

The Hamlyn Symposium on Medical Robotics

2022



Proceedings

26 - 29th June 2022

Daniel Elson, Stamatia Giannarou, George Mylonas, Ferdinando Rodriguez y Baena, Riccardo Secoli, Alexander Thompson (Editors)

Proceedings of the 14th

Hamlyn Symposium on Medical Robotics 2022

Imperial College London and the Royal Geographic Society,
London London, United Kingdom
26th - 29th June, 2022

Published by:

The Hamlyn Centre Imperial College London
E- Print, London, United Kingdom — June 2022

<https://www.imperial.ac.uk/hamlyn-centre/>

ISSN 2755-0036

Preface

This year we celebrate the 14th anniversary of the [Hamlyn Symposium on Medical Robotics](#). Hosted by Professor The Lord Ara Darzi, Professor Ferdinando Rodriguez y Baena, and the team of the Hamlyn Centre at Imperial College, the symposium attracts an international audience with clinical, scientific, and engineering expertise, and this year proved to be our most vibrant yet.

After a cancelled meeting in 2020, a “virtual symposium year” in 2021 and everything that happened in between, we were excited to be able to host this symposium as an in-person event, which was held at the Royal Geographical Society on the 26th to 29th June 2022. The theme of the meeting was "*MedTech Reimagined*", with a fantastic line-up of scientists, engineers and clinicians in medical robotics and allied technologies.

The topics covered this year included:

- Smart Devices
- Soft and Continuum Robotics
- Magnetic Technology
- Surgical Guidance
- Neurosurgery
- Clinical Insights

We were delighted to have distinguished keynote speakers from the UK and USA. [Professor Jaydev Desai](#), Director of the Georgia Center for Medical Robotics and Associate Director of the Institute for Robotics and Intelligent Machines, gave a talk on Monday morning on "*Robotic Transcatheter and Endovascular Interventions*", followed by [Professor Laura Marcu](#) from the University of California at Davis, who closed the day with her lecture on "*FLIM-guided robotic surgery*". [Professor John Skinner](#), the current President of the British Orthopaedic Association, opened the second day with his keynote lecture on "*The Adoption of Robotic Technology for Orthopaedic Surgery in Healthcare Systems*", while this year's Storz-Hopkins lecture was delivered by [Professor Alex Golby](#), a distinguished Professor of Neurosurgery and Professor of Radiology at Harvard Medical School. Her talk was on "*Optimizing surgery for patients with brain tumors: The right information at the right time in the right place*".

We were also excited to announce our customary *Industry Forum*, where leading industry representatives engaged in a moderated panel discussion around key topics affecting healthcare and technological developments in this space.

This year, the Forum focused on industrial orthopaedic robotics, a growing field that is slowly becoming more mainstream, thanks to recent technological developments, strategic mergers and acquisitions, and growing acceptance within the patient and clinical community.

The discussion revolved around the following key questions:

- What does the future of this technology hold?
- What is the commercial strategy behind the major players offering robotic systems today?
- What outstanding barriers remain, which prevent widespread adoption of CAOS technology?
- How can clinicians, scientists and industry work together to break some of these barriers?

The industry panel featured [Mr Ori Hadomi](#), Vice President of Strategic Initiatives and Partnerships, Medtronic Inc; [Mr Branko Jaramaz](#), Senior Director, Research and Development, Smith and Nephew; [Mr Thomas Küenzi](#), Senior Director Velys R&D, DePuy Synthes; [Mr Jim Nevelos](#), Vice President of Advanced Technology and Research (Joint Replacement), Stryker Corp; [Mr Brian Uthgenannt](#), Global Marketing Manager, Corin Group; and [Mr Felix Wandel](#), Vice President of Robotics and Technology (EMEA), Zimmer Biomet.

In addition, we held a *Funders' Forum* session centred around international funding opportunities to engage with clinicians, technologists, Small and Medium-size Enterprises and healthcare providers in the UK and abroad. Funding representatives were invited to join the session, with a view to share upcoming opportunities to fund research in healthcare technologies with our audience, and avenues to pursue international partnerships and collaborations.

The goal of the event was to follow up on "**Recommendation H: SUPPORT**" in the UK-RAS-sponsored [White Paper on Surgical Robotics](#). This recommendation encourages funding agencies to explore joint funding schemes to facilitate further international collaborations in surgical robotics. The panel included: [Dr. Françoise J. Siepel](#), Operational Coordinator, Digital Innovation Hubs in Healthcare Robotics (DIH HERO, H2020); [Ms Philippa Hemmings](#), Head of Healthcare Technologies, EPSRC, UK; and [Mr Michael Wolfson](#), Program Director, Division of Discovery Science & Technology (Bioengineering), NIH, USA.

We were also delighted to see that the Symposium workshops have continued to grow and flourish, many of these organised by early career researchers. A total of 12 workshops were delivered, covering areas ranging from clinical applications of robotic navigation to low-cost medical robotics, human augmentation; challenges in deploying robotic applications, micro/nano robotics; sensing and biophotonics; and recent advances in surgical autonomy. We have received accreditation for these workshops from the Royal College of Surgeons and were proud to deliver a programme that enables the Continued Professional Development (CPD) of clinicians and engineers in these fields. A detailed programme for each of our workshops is listed on our symposium [website](#). We believe these have played a crucial role in providing a platform for the formulation of new ideas and future collaborations.

One of our longstanding Symposium highlights was the [Surgical Robot Challenge](#). This year we received 14 entries, from teams in Italy, Pakistan, Hong Kong, China, Switzerland, UK, USA and Israel. To increase accessibility to the challenge, we opted for an online delivery medium this year and each team was asked to submit their video entries and presentations in digital form. The challenge was sponsored by Intuitive Surgical, Cambridge Consultants and the Wellcome Trust. Applications were not restricted to a particular focus area, but needed to demonstrate innovation, application and design in how robots can improve procedures leading to quicker recovery, smaller scars, less blood loss, less pain, earlier return to work and less stay in hospital.

Prizes were awarded in the following categories:

- Best Application
- Best Innovation
- Best Design

We showcased the entries at the Hamlyn Symposium via a highlights video and announced the winners at the award ceremony. All entries can be viewed on our [YouTube](#) channel.

Organising an international meeting of this scale involves a huge amount of effort and a dedicated team. We would like to thank our extraordinary Programme Committee and workshop organisers for dedicating their valuable time to ensure timely review of the submitted papers and delivering an excellent symposium programme. We are grateful to all of our sponsors, particularly the Wellcome Trust through its Institutional Translational Partnership Award (iTPA), for supporting the Symposium and affiliated workshops. Special thanks go to the Royal College of Surgeons of England for arranging CPD accreditation of the Symposium workshops.

Importantly, we would like to take this opportunity to express our gratitude to the team who have worked tirelessly behind the scenes to make the 2023 symposium a success and for their efforts in managing all aspects of the Symposium organisation, from programme preparation and publicity to registration and logistics. In particular, we would like to thank Marianne Knight, the Hamlyn Centre's Director of Operations, and her operational team: Karina Aashamar, Alia Talaat Ahmed, Salzitsa Anastasova-Ivanova, Robert Merrifield. And a big Thank You to our Hamlyn Centre members, who have helped to make the Symposium a memorable experience for all. Lastly, special thanks go to Lady Hamlyn. None of this would be possible

Hamlyn Symposium on Medical Robotics 2022

without the generous philanthropic support from both the Helen Hamlyn Trust and Lady Hamlyn herself. It has been a great honour and privilege to have had the opportunity to establish, develop and lead the Hamlyn Centre to its current internationally leading status, supported by so many talented researchers.

Professor The Lord Ara Darzi and Professor Ferdinando Rodriguez y Baena
Hamlyn Symposium on Medical Robotics 2022

Organisation

Co-Chairs

Professor The Lord Darzi of Denham
Professor Ferdinando Rodriguez y Baena

Programme Committee

Ferdinando Rodriguez y Baena (Chair)	Imperial College London, UK
Kaspar Althoefer	Queen Mary University of London, UK
William Anderson	John Hopkins Medicine, USA
Christos Bergeles	King's College London, UK
Darwin Caldwell	Instituto Italiano di Tecnologia, Italy
Philip Chiu	The Chinese University of Hong Kong, China
Howie Choset	Carnegie Mellon University, USA
Kevin Cleary	Children's National Hospital, USA
Peter Culmer	University of Leeds, UK
Dana Damian	The University of Sheffield, UK
Brian Davies	Imperial College London, UK
Elena De Momi	Politecnico di Milano, Italy
Simon DiMaio	Intuitive Surgical Inc, USA
Sanja Dogramadzi	University of Sheffield, UK
Pierre DuPont	Harvard University, USA
Daniel Elson	Imperial College London, UK
Leonard Fass	Imperial College London, UK
Gabor Fichting	Queen's University, Canada
Fanny Ficuciello	University of Naples Federico II, Italy
Paolo Fiorini	University of Verona, Italy
Stamatia Giannarou	Imperial College London, UK
Kanako Harada	University of Tokyo, Japan
S. Duke Herrell	Vanderbilt University, USA
Jaesung Hong	DGIST, South Korea
Pierre Jannin	INSERM, France
Branko Jaramaz	Smith and Nephew, USA
Leo Joskowicz	Hebrew University of Jerusalem, Israel
Peter Kazanzides	Johns Hopkins University, USA
Gernot Kronreif	ACMIT, Austria
Daniel Leff	Imperial College London, UK
Benny Lo	Imperial College London, UK
Thomas Looi	Sick Kids Toronto, Canada
Jacques Marescaux	IRCAD, France
Leonardo Mattos	Istituto Italiano di Tecnologia, Italy
Arianna Menciassi	Scuola Superiore Sant'Anna, Italy
Yoav Mintz	Hadassah Medical Center, Israel
George Mylonas	Imperial College London, UK
Marcia O' Malley	Rice University, USA
Sebastien Ourselin	King's College London, UK

Rajni Patel	Western University, Canada
Kawal Rhode	King's College London, UK
Cameron Riviere	Carnegie Mellon University, USA
Nicolas Rojas	Imperial College London, UK
Ichiro Sakuma	University of Tokyo, Japan
Riccardo Secoli	Imperial College London, UK
Pallav Shah	Imperial College London, UK
Bruno Siciliano	University of Naples Federico II, Italy
Stefanie Speidel	National Center for Tumor Diseases, Germany
Danail Stoyanov	University College London, UK
Lee Swanstrom	University of Strasbourg, France
Amir Szold	Assia Medical Group, Israel
Russell Taylor	Johns Hopkins University, USA
Alex Thompson	Imperial College London, UK
Pietro Valdastri	University of Leeds, UK
Bob Webster	Vanderbilt University, USA
Helge Wurdemann	University College London, UK
Sheng Xie	University of Leeds, UK

Additional Reviewers

Sara Abad, Mohammed Al-Nuaimi, John Bason Mitchell, Sebastian Bodenstedt, Joseph Bolarinwa, Timothy Brumfiel, Guido Caccianiga, Marco Caianiello, Lin Cao, Digby Chappell, Wei Chen, Angus Clark, Francesco Cursi, Joseph Davids, Hadi El Daou, Joshua Fleck, Enrico Franco, George Freeman, Wenlong Gaozhang, Arincheyan Gerald, Reza Haghighi Osgouei, Mohammad Hossein Hamedani, Mohammad Holdar, Xue Hu, Cristina Iacono, Alexander C. Jenke, Dominic Jones, Joanna Jones, Alexandros Kogkas, Ka-Wai Kwok, Dongmyoung Lee, Maria Leiloglou, Kelin Li, Zheng Li, Zhenhong Li, Alix Macklin, Erin Mahan, Nils Marahrens, Andrea Mariani, Murilo Marques Marinho, Majed Melibary, Shuhei Miyashita, Rocco Moccia, Laura Morchi, Konstantinos Mountris, Sina Najjari, Anh Nguyen, Andrew Orekhov, Linda Patern, Micha Pfeiffer, Kun Qian, Duncan Raitt, Dominik Rivoir, Mark Runciman, Seyed Mohammad Hadi Sadati, Mohamed Sallam, Bruno Scaglioni, Alice Segato, Fan Shao, Neel Shihora, Avinash Kumar Singh, Edoardo Sinibaldi, Canberk Sozer, William Spittal, John Swensen, Izadyar Tamadon, Fabio Tatti, Selene Tognarelli, Samyakh Tukra.


Local Organising Team

Marianne Knight (Operational Lead)
Karina Aashamar
Salzitsa Anastaova-Ivanova
Daniel Elson
Stamatia Giannarou
Robert Merrifield
George Mylonas
Riccardo Secoli
Alia Talaat
Alex Thompson

TABLE OF CONTENTS






Monday, June 27th

Session 1: Smart Devices









- 1 Robotic System with Intuitive Control for Endoscopic Bone Cyst Surgery** 
Subin Lee (DGIST, South Korea)
Seunguk Kim (DGIST, South Korea)
Rene Marcel Solzbacher (DGIST, Germany)
Hyunwook Kim (DGIST, South Korea)
Sanghyun Joung (AIRS Inc., South Korea)
Jaesung Hong (DGIST, South Korea)
- 3 Design and Experimental Evaluation of the SOFTScreen Capsule System in a Colon Phantom** 
Vanni Consumi (University College London, UK)
Lukas Lindenroth (UCL University College London, UK)
Danail Stoyanov (UCL University College London, UK)
Agostino Stilli (UCL University College London, UK)
- 5 Answering the FDA'S Call to Action: Using Steerable Sheaths and Mirrors to Prevent ERCP Infections** 
Joshua Gafford (EndoTheia, Inc., United States)
Scott Webster (EndoTheia, Inc., United States)
Patrick Anderson (EndoTheia, Inc., United States)
Stanley Herrell (Vanderbilt University Medical Center, United States)
Keith Obstein (Vanderbilt University Medical Center, United States)
Daniel Rucker (University of Tennessee - Knoxville, United States)
Robert Webster III (Vanderbilt University, United States)
- 7 Validation of a Proof-of-Concept System for Personalised Computer-Assisted Treatment of Knee Osteochondral Lesions** 
Fabio Tatti (Imperial College London, UK)
Branislav Jaramaz (Smith & Nephew Inc., United States)
Ferdinando Rodriguez Y Baena (Imperial College London, UK)
- 9 Design and Characterization of Robotically-Guided Ultrasonic Bone Cutting for Laminectomies and Facetectomies**
Luke MacLean (Johns Hopkins University, United States)
Nicholas Theodore (Johns Hopkins University, United States)


Session 2: Soft and Continuum Robotics

- 11 Pop-up Soft Robot for Minimally Invasive Surgery** 
Mark Runciman (Hamlyn Centre, Imperial College London, London, UK)
James Avery (Hamlyn Centre, Imperial College London, London, UK)
George Mylonas (Hamlyn Centre, Imperial College London, London, UK)
- 13 A Simple and Powerful Instrument for Robotic Flexible Endoscopy** 
Giuliano A. Giacoppo (Institute of Medical Device Technology, University of Stuttgart, Germany)
Ada L. Bachmann (Institute of Medical Device Technology, University of Stuttgart, Germany)
Peter P. Pott (Institute of Medical Device Technology, University of Stuttgart, Germany)

- 15** **Shape Sensing for a Soft Continuum Manipulator Using Electrical Impedance Tomography (EIT)** 
Amirhosein Alian (Imperial College London, UK)
Emilia Zari (Imperial College London, UK)
James Avery (Imperial College London, UK)
Enrico Franco (Imperial College London, UK)
Mark Runciman (Imperial College London, UK)
Ferdinando Rodriguez Y Baena (Imperial College London, UK)
George Mylonas (Imperial College London, UK)
- 17** **A Haptic Feedback Glove for Minimally Invasive Surgery** 
Arincheyan Gerald (Boston University, United States)
Rukaiya Batliwala (Boston University, United States)
Jonathan Ye (Boston University, United States)
Patra Hsu (Boston University, United States)
Hiroyuki Aihara (Harvard University, United States)
Sheila Russo (Boston University, United States)
- 19** **Design and Validation of Zero-Slack Separable Manipulator for Intracardiac Echocardiography**
Christian Debuys (Texas A&M University, United States)
Florin Ghesu (Siemens Healthineers, United States)
Reza Langari (Texas A&M University, United States)
Young-Ho Kim (Siemens Healthineers, United States)
- 21** **Multifunctional Hybrid Module for Manipulators** 
Canberk Sozer (The University of Sheffield, UK)
Sujit Kumar Sahu (Scuola Superiore Sant'Anna Pisa, Italy)
Linda Paterno (Scuola Superiore Sant'Anna Pisa, Italy)
Arianna Menciassi (Scuola Superiore Sant'Anna Pisa, Italy)
- 23** **Finite Element Dynamics of a Concentric Tube Robot Motion and Interaction with Environment Using SOFA-Framework** 
Katie Zuo (King's College London, UK)
Benjamin Jackson (King's College London, UK)
Ross Henry (King's College London, UK)
Christos Bergeles (King's College London, UK)
S.M.Hadi Sadati (King's College London, UK)
- 25** **A Sensorized Needle-Insertion Device for Characterizing Percutaneous Thoracic Tool- Tissue Interactions** 
Rachael L'Orsa (University of Calgary, Canada)
Kourosh Zareinia (Ryerson University, Canada)
David Westwick (University of Calgary, Canada)
Garnette Sutherland (University of Calgary, Canada)
Katherine Kuchenbecker (Max Planck Institute for Intelligent Systems, Germany)
- 27** **Toward Bipolar Electrosurgery with Concentric Tube Robots** 
Jesse d'Almeida (Vanderbilt University, United States)
Margaret Rox (Vanderbilt University, United States)
Robert Webster (Vanderbilt University, United States)
- 29** **Design of a Robotic Traction Device for Endoscopic Submucosal Dissection** 
Flora Fung Leung (The Chinese University of Hong Kong, Hong Kong)
Chun Ping Lam (The Chinese University of Hong Kong, Hong Kong)
Lap Wing Cheung (The Chinese University of Hong Kong, Hong Kong)
Donald Ngo Fung Ip (The Chinese University of Hong Kong, Hong Kong)
Yeung Yam (The Chinese University of Hong Kong, Hong Kong)
Philip Wai Yan Chiu (The Chinese University of Hong Kong, Hong Kong)
Ka Chun Lau (The Chinese University of Hong Kong, Hong Kong)

Poster Teasers 1

- 31 Understanding Different Inflated Balloon Catheter Behaviours via Computational Modelling** 
- Junke Yao* (University College London, UK)
Giorgia Bosi (University College London, UK)
Gaetano Burriesci (University College London, UK)
Helge Wurdemann (University College London, UK)
- 33 Robotic Surgery – Implications for Informed Consent** 
- Jessica Henley* (Memorial University of Newfoundland, Canada)
Joannie Neveu (Memorial University of Newfoundland, Canada)
Doug Angel (Memorial University of Newfoundland, Canada)
Simon Kirby (Memorial University of Newfoundland, Canada)
- 37 Generalization for Deep Reinforcement Learning for Inverse Kinematics of Concentric Tube Robots** 
- Keshav Iyengar* (UCL, UK)
Sarah Spurgeon (University College London, UK)
Danail Stoyanov (University College London, UK)
- 39 Towards Autonomous Robotic Ultrasound Scanning Using Pneumatically Attachable Flexible Rails** 
- Aoife McDonald-Bowyer* (University College London, UK)
Solene Dietsch (University College London, UK)
Emmanouil Dimitrakakis (University College London, UK)
Joanna Coote (University College London, UK)
Lukas Lindenroth (University College London, UK)
Danail Stoyanov (University College London, UK)
Agostino Stilli (University College London, UK)
- 41 Automatic Vessel Recognition and Segmentation: a Novel Deep Learning Architecture with Transfer Learning Approach** 
- Giovanni Faoro* (Scuola Superiore Sant'Anna, Italy)
Stefano Pane (Scuola Superiore Sant'Anna, Italy)
Veronica Iacovacci (Scuola Superiore Sant'Anna, Italy)
Sara Moccia (Scuola Superiore Sant'Anna, Italy)
Arianna Menciacchi (Scuola Superiore Sant'Anna, Italy)
- 43 A Novel, Research-Orientated Organ Perfusion Platform** 
- Morenike Magbagbeola* (University College London, UK)
Katie Doyle (University College London, UK)
Zainab Rai (University College London, UK)
Lukas Lindenroth (University College London, UK)
George Dwyer (University College London, UK)
Agostino Stilli (University College London, UK)
Brian Davidson (University College London, UK)
Danail Stoyanov (University College London, UK)
- 45 A Temporal Learning Approach to inpainting Endoscopic Specularities and Its Effect on Image Correspondence** 
- Rema Daher* (University College London, UK)
Francisco Vasconcelos (University College London, UK)
Danail Stoyanov (University College London, UK)
- 47 Detector-Free Dense Feature Matching for Fetoscopic Mosaicking** 
- Sophia Bano* (University College London, UK) *Francisco Vasconcelos* (University College London, UK) *Anna David* (University College London Hospital, UK)
Jan Deprest (University Hospital Leuven, Belgium)
Danail Stoyanov (University College London, UK)

- 49 Deep Learning-Based Plane Pose Regression Towards Training in Freehand Obstetric Ultrasound** 
Chiara Di Vece (University College London, UK)
Brian Dromey (University College London, UK)
Francisco Vasconcelos (University College London, UK)
Anna L David (Institute for Women's Health, University College London, UK)
Donald M Peebles (Institute for Women's Health, University College London, UK)
Danail Stoyanov (University College London, UK)
- 51 Deep Reinforcement Learning Based Semi-Autonomous Control for Robotic Surgery** 
Ruiqi Zhu (Imperial College London, UK)
Dandan Zhang (Imperial College London, UK)
Benny Lo (Imperial College London, UK)
- 53 Human Machine Interfaces for Robot-Assisted Colonoscopy: a Clinical Survey** 
Martina Finocchiaro (Universitat Politècnica de Catalunya, Spain)
Alberto Arezzo (University of Torino, Italy)
Arianna Menciassi (Sant'Anna, Italy)
Alicia Casals (Universitat Politècnica de Catalunya, Spain)
Albert Hernansanz (UPC (Universitat Politècnica de Catalunya), Spain)
Gastone Ciuti (The Biorobotics Institute, Italy)
- 55 A Soft Palpation Sensor for Early Detection of Biological Tissue Abnormalities Based on Electrical Impedance Tomography** 
Saina Akhond (Imperial College London, UK)
James Avery (Imperial College London, UK)
George Mylonas (Imperial College London, UK)
- 57 Proof-of-Concept Investigation of an Instrument-Mounted Markerless Tracking System for Robot-Assisted Orthopaedic Surgery** 
Fabio Tatti (Imperial College London, UK)
Xue Hu (Imperial College London, UK)
Ferdinando Rodriguez Y Baena (Imperial College London, UK)
- 59 A Physical Simulator Integrated with Soft Sensing for Mastering the Manipulation of Vascular Structures in Robotic Surgery** 
Andrea Mariani (The BioRobotics Institute, Scuola Superiore Sant'Anna, Italy)
Dario Galeazzi (The BioRobotics Institute, Scuola Superiore Sant'Anna, Italy)
Selene Tognarelli (The BioRobotics Institute, Scuola Superiore Sant'Anna, Italy)
Arianna Menciassi (The BioRobotics Institute, Scuola Superiore Sant'Anna, Italy)
- 61 Robotic Telemanipulation System for Minimally Invasive Surgery Using a Passive Universal Joint and Inertial Sensors** 
Max B. Schäfer (University of Stuttgart, Institute of Medical Device Technology, Germany)
Moritz Hemmer (University of Stuttgart, Institute of Medical Device Technology, Germany)
Anja M. Glöckner (University of Stuttgart, Institute of Medical Device Technology, Germany)
Peter P. Pott (University of Stuttgart, Institute of Medical Device Technology, Germany)
- 63 Dense 3D Reconstruction Through Lidar: a New Perspective on Computer-Integrated Surgery** 
Guido Caccianiga (Haptic Intelligence Department, Max Planck Institute for Intelligent Systems, Germany)
Katherine J. Kuchenbecker (Haptic Intelligence Department, Max Planck Institute for Intelligent Systems, Germany)
- 65 Development of a Wearable Fluorescence Sensor for Non-Invasive Monitoring of Gut Permeability** 
Elena Monfort-Sanchez (Imperial College London, UK)
Dr James Avery (Imperial College London, UK)
Dr Alex J. Thompson (Imperial College London, UK)
Prof Ara Darzi (Imperial College London, UK)






- 67 Nonlinear Trajectory Following Control for a Bio-Inspired Steerable Needle** 
Zejian Cui (Imperial College London, UK)
Abdulhamit Donder (Imperial College London, UK)
Ferdinando Rodriguez Y Baena (Imperial College London, UK)
- 69 Multi Jet Fusion of Nylon-12: a Viable Method to 3D-Print Concentric Tube Robots?** 
Kalani Picho (Worcester Polytechnic Institute, United States)
Brandon Persons (Worcester Polytechnic Institute, United States)
Jesse d'Almeida (Vanderbilt University, United States)
Nicholas Pacheco (Worcester Polytechnic Institute, United States)
Colin Reynolds (Worcester Polytechnic Institute, United States)
Loris Fichera (Worcester Polytechnic Institute, United States)
- 71 Design, Realization and Preliminary Validation of an Active Physical Simulator for the Study of Pelvic Floor Damages During Childbirth** 
Giulia Modarelli (University of Pisa, Italy)
Sabina Maglio (Scuola Superiore Sant'Anna - The Biorobotic Institute, Italy)
Selene Tognarelli (The BioRobotics Institute - Scuola Superiore Sant'anna, Italy)
Arianna Menciassi (Sant'Anna, Italy)

Session 3: Magnetic Technology


- 73 Mechanical Reinforcement Towards Fully Soft Magnetic Endoscopic Endonasal Surgical Manipulators** 
Zaneta Koszowska (University of Leeds, UK)
Giovanni Pittiglio (University of Leeds, UK)
James Chandler (University of Leeds, UK)
Michael Brockdorff (University of Leeds, UK)
Pietro Valdastri (University of Leeds, UK)
- 75 Magnetic Endoluminal Devices Can Assist in Their Own Insertion** 
Nicholas Posselli (University of Utah, United States)
Emma Pinegar (University of Utah, United States)
Jake Abbott (University of Utah, United States)
- 77 Dual-Arm Platform for Control of Magnetically Actuated Soft Robots** 
Michael Brockdorff (University of Leeds, UK)
Giovanni Pittiglio (University of Leeds, UK)
Tomas da Veiga (University of Leeds, UK)
James Chandler (University of Leeds, UK)
Pietro Valdastri (University of Leeds, UK)
- 79 A Navigation Console to Steer Magnetic Instruments Under Radiological Guidance for Neuro-Vascular Interventions** 
Roland Dreyfus (Multi-Scale Robotics Lab, ETH Zurich, Switzerland)
Quentin Boehler (Multi-Scale Robotics Lab, ETH Zurich, Switzerland)
Christophe Chautems (Multi-Scale Robotics Lab, ETH Zurich, Switzerland)
Bradley Nelson (Multi-Scale Robotics Lab, ETH Zurich, Switzerland)
- 81 Toward Targeted Therapy in the Brain by Leveraging Screw-Tip Soft Magnetically Steerable Needles** 
Trevor J Schwehr (Johns Hopkins University, United States)
Adam J Sperry (University of Utah, United States)
John D Rolston (University of Utah, United States)
Matthew D Alexander (University of Utah, United States)
Jake J Abbott (University of Utah, United States)
Alan Kuntz (University of Utah, United States)

Tuesday, June 28th

Session 4: Surgical Guidance


- 83 Studying the Usability of Forbidden Region Virtual Fixtures for Safer Robotic Assisted Minimally Invasive Surgery** 
Martina Favaretto (Politecnico di Milano, Italy)
Aldo Marzullo (University of Calabria, Italy)
Elena De Momi (Politecnico di Milano, Italy)
- 85 ISurgeon: Augmented Reality Telestration for Improved Surgical Training** 
Thomas Fuchs (Department of General, Visceral and Transplantation Surgery, Heidelberg University Hospital, Germany)
Eleni Felinska (Department of General, Visceral and Transplantation Surgery, Heidelberg University Hospital, Germany)
Alexandros Kogkas (Department of Surgery and Cancer, Faculty of Medicine, Imperial College London, UK)
George Mylonas (Department of Surgery and Cancer, Faculty of Medicine, Imperial College London, UK)
Beat Müller-Stich (Department of General, Visceral and Transplantation Surgery, Heidelberg University Hospital, Germany)
Felix Nickel (Department of General, Visceral and Transplantation Surgery, Heidelberg University Hospital, Germany)
- 87 The Design of a Biomimetic Whisker-Based System for Clinical Gastrointestinal Diseases Screening** 
Zeyu Wang (The Hamlyn Centre/ Dept of Surgery and Cancer, Imperial College London, UK)
Junhong Chen (The Hamlyn Centre/ Dept of Surgery and Cancer, Imperial College London, UK)
Ruiyang Zhang (The Hamlyn Centre/ Dept of Surgery and Cancer, Imperial College London, UK)
Benny Lo (The Hamlyn Centre/ Dept of Surgery and Cancer, Imperial College London, UK)
- 89 Vision-Based Robot Localisation for Ductoscopic Navigation** 
Rema Daher (Imperial College London, UK)
Connah Kendrick (Manchester Metropolitan University, UK)
Moi Hoon Yap (Manchester Metropolitan University, UK)
Daniel Leff (Imperial College London, UK)
Stamatia Giannarou (Imperial College London, UK)
- 91 A Mixed Reality System for Human Teleoperation in Tele-Ultrasound** 
David Black (University of British Columbia, Canada)
Septimiu Salcudean (University of British Columbia, Canada)

Session 5: Neurosurgery






- 93 Collaborative Robotic Ultrasound Tissue Scanning for Surgical Resection Guidance in Neurosurgery** 
Alistair Weld (Imperial College London, UK)
Michael Dyck (Technical University of Munich, Germany)
Julian Klodmann (Technical University of Munich, Germany)
Giulio Anichini (Imperial College London, UK)
Luke Dixon (Imperial College London, UK)
Sophie Camp (Imperial College London, UK)
Alin Albu-Schäffer (Technical University of Munich, Germany)
Stamatia Giannarou (Imperial College London, UK)
- 95 Head-Mounting Surgical Robots for Passive Motion Compensation** 
Nicholas Posselli (University of Utah, United States)
Paul Bernstein (Moran Eye Center, University of Utah, United States)
Jake Abbott (University of Utah, United States)

- 97 Towards an MRI-Conditional Robot for Intracerebral Hemorrhage Evacuation** 
Anthony Gunderman (Georgia Institute of Technology, United States)
Saikat Sengupta (Vanderbilt University Medical Center, United States)
Dimitri Sigounas (George Washington University, United States)
Kevin Cleary (Children's National Hospital, United States)
Yue Chen (Georgia Institute of Technology, United States)
- 99 Bimanual Endoscopic Robot for Neurosurgery** 
Pierre Dupont (Boston Children's Hospital / Harvard Medical School, United States)
Karl Price (Boston Children's Hospital / Harvard Medical School, United States)
Joseph Peine (Boston Children's Hospital / Harvard Medical School, United States)
Margherita Mencattelli (Boston Children's Hospital / Harvard Medical School, United States)
Ashkan Pourkand (Boston Children's Hospital / Harvard Medical School, United States)
Thomas Looi (Sick Kids Hospital, Canada)
James Drake (Sick Kids Hospital, Canada)
Yash Chitalia (Boston Children's Hospital / Harvard Medical School, United States)
- 101 Towards a Procedure Optimised Steerable Microcatheter for Neurosurgical Laser Ablation**
Ayhan Aktas (Imperial College London, UK)
Ali Anil Demircali (Imperial College London, UK)
Riccardo Secoli (Imperial College London, UK)
Burak Temelkuran (Imperial College London, UK)
Ferdinando M Rodriguez Y Baena (Imperial College London, UK)
- 103 Design of a Meso-Scale Grasper for Robotic Pediatric Neuroendoscope Tool**
Timothy A. Brumfiel (Medical Robotics and Automation (RoboMed) Laboratory, United States)
Kent K. Yamamoto (Medical Robotics and Automation (RoboMed) Laboratory, United States)
Asif Rashid (George W. Woodruff School of Mechanical Engineering, Georgia Institute of Technology, United States)
Akiyuki Shigematsu (Medical Robotics and Automation (RoboMed) Laboratory, Japan)
Coley Chapman (George W. Woodruff School of Mechanical Engineering, Georgia Institute of Technology, United States)
Shreyes N. Melkote (George W. Woodruff School of Mechanical Engineering, Georgia Institute of Technology, United States)
Joshua J. Chern (Children's Healthcare of Atlanta, United States)
Jaydev P. Desai (Medical Robotics and Automation (RoboMed) Laboratory, United States)
- 105 Robotic Curvilinear Laser Thermal Therapy Probe for Transforaminal Hippocampotomy** 
Daniel Esser (Vanderbilt University, United States)
John Peters (Vanderbilt University, United States)
Abby Grillo (Vanderbilt University, United States)
Sarah Garrow (Vanderbilt University, United States)
Tyler Ball (Vanderbilt University Medical Center, United States)
Robert Naftel (Vanderbilt University Medical Center, United States)
Dario Englot (Vanderbilt University Medical Center, United States)
Joseph Neimat (University of Louisville, United States)
Will Grissom (Vanderbilt University, United States)
Eric Barth (Vanderbilt University, United States)
Robert Webster III (Vanderbilt University, United States)
- 107 A Steerable Guide for MRI-Guided Laser Interstitial Thermal Therapy**
Jin Seob Kim (Johns Hopkins University, United States)
Ryan Fischer (University of Miami, United States)
Iahn Cajigas (University of Miami, United States)
Michael Ivan (University of Miami, United States)
Doyoung Chang (University of Miami, United States)
- 109 In Vitro Navigation of a Magnetic Sphere Using a Model Predictive Controller for Neurovascular Targeted Drug Delivery Applications** 
Derick Sivakumaran (Magnebotix AG, Switzerland)
Fabian Christopher Landers (ETH Zürich, Switzerland)
Quentin Boehler (ETH Zurich, Switzerland)





Christophe Chautems (ETH Zurich, Switzerland)
Salvador Pané (ETH Zurich, Switzerland)
Bradley J. Nelson (ETH Zurich, Switzerland)

- 111 An MRI Compatible MR-Guided High-Intensity Focused Ultrasound Neonatal Neurosurgery Platform for Intraventricular Hemorrhage** 
- Hrishikesh Raghuram* (University of Toronto, Canada)
Benjamin Keunen (The Hospital for Sick Children, Canada)
Nathan Soucier (University of Toronto, Canada)
Thomas Looi (The Hospital for Sick Children, Canada)
Samuel Pichardo (University of Calgary, Canada)
Adam Waspe (The Hospital for Sick Children, Canada)
James Drake (The Hospital for Sick Children, Canada)

Poster Teasers 2

- 113 The Fulcrum Effect in the Control of Electromechanical Articulated Laparoscopic Instruments**
- Amir Szold* (Assia Medical Group, Israel)
- 115 Inexact Multi-Task Learning for Fetal Anastomoses Detection** 
- Alessandro Casella* (Politecnico di Milano, Istituto Italiano di Tecnologia, Italy)
Gaia Romana De Paolis (Politecnico di Milano, Italy)
Elena De Momi (Politecnico di Milano, Italy)
Dario Paladini (Istituto Giannina Gaslini, Italy)
Sara Moccia (The Biorobotic Institute, Sant'Anna, Italy)
Leonardo Mattos (Istituto Italiano di Tecnologia, Italy)
- 117 EndoVine: Soft Robotic Endoscope for Colonoscopy** 
- Ameya Pore* (University of Verona, Italy)
Nicola Piccinelli (University of Verona, Italy)
Giacomo De Rossi (University of Verona, Italy)
Matteo Piano (University of Verona, Italy)
Daniele Meli (University of Verona, Italy)
Diego Dall'Alba (University of Verona, Italy)
Riccardo Muradore (University of Verona, Italy)
Paolo Fiorini (University of Verona, Italy)
- 119 Development and Control of a Robotic Simulator for Peristaltic Motion** 
- Jarrett Ten* (University of Sheffield, UK)
Quentin Lahondes (University of Sheffield, UK)
Shuhei Miyashita (University of Sheffield, UK)
Dana Damian (University of Sheffield, UK)
- 121 Envisioning Robotic Exoscope: Concept and Preliminary Results** 
- Alice Valeria Iordache* (Politecnico di Milano, Italy)
Alessandro Casella (Politecnico di Milano, Istituto Italiano di Tecnologia, Italy)
Elisa Iovene (Politecnico di Milano, Italy)
Junling Fu (Politecnico di Milano, Italy)
Federico Pessina (Humanitas Research Hospital, Italy)
Marco Riva (Humanitas Research Hospital, Italy)
Giancarlo Ferrigno (Politecnico di Milano, Italy)
Leonardo Mattos (Istituto Italiano di Tecnologia, Italy)
Elena De Momi (Politecnico di Milano, Italy)
- 123 Minimum-Parameter Adaptive Propulsion Matrix of Screw-Type Magnetic Capsule Endoscopes** 
- Adam J Sperry* (University of Utah, United States)
Jake J Abbott (University of Utah, United States)

- 125 Cable-Driven Linear Haptic Display for Medical Interventions** 
Max B. Schäfer (University of Stuttgart, Institute of Medical Device Technology, Germany)
Julia Nawratil (University of Stuttgart, Institute of Medical Device Technology, Germany)
Moritz Hemmer (University of Stuttgart, Institute of Medical Device Technology, Germany)
Sophie Weiland (University of Stuttgart, Institute of Medical Device Technology, Germany)
Peter P. Pott (Institut für Medizingerätetechnik, Universität Stuttgart, Germany)
- 127 Comparison of Performance Metrics for Real-Time Haptic Feedback in Surgical Skill Training** 
Lianne R. Johnson (Rice University, United States)
Michael D. Byrne (Rice University, United States)
Marcia K. O'Malley (Rice University, United States)
- 129 Predictable Therapeutic Microswarm Dispersion for Targeted Drug Delivery Application** 
Kiana Abolfathi (School of Computer Science and Electronic Engineering, University of Essex, UK)
Mohammad Reza Hairi Yazdi (School of Mechanical Engineering, University of Tehran, Iran)
Ali Kafash Hoshidar (School of Computer Science and Electronic Engineering, University of Essex, UK)
- 131 Modeling Telescoping Tendon-Actuated Continuum Robots** 
Yash Chitalia (Boston Children's Hospital and Harvard University, United States)
Abdulhamit Donder (Boston Children's Hospital & Harvard Medical School, United States)
Pierre Dupont (Boston Children's Hospital and Harvard University, United States)
- 133 Preliminary Findings of a Multimodal Sensor System for Measuring Surgeon Cognitive Workload** 
Ravi Naik (Imperial College London, UK)
Kaizhe Jin (Imperial College London, UK)
Alexandros Kogkas (Imperial College London, UK)
Hutan Ashrafian (Imperial College London, UK)
Ara Darzi (Imperial College London, UK)
George Mylonas (Imperial College London, UK)
- 135 Reinforcement Learning for Path Generation for Surgical Robot Maneuver** 
Junhong Chen (Imperial College London, UK)
Zeyu Wang (Imperial College London, UK)
Ruiqi Zhu (King's College London, UK)
Ruiyang Zhang (Imperial College London, UK)
Weibang Bai (Imperial College London, UK)
Benny Lo (Imperial College London, UK)
- 137 Augmented Reality for Seamless Human Robot Interaction in Surgery** 
Hisham Iqbal (Imperial College London, UK)
Ferdinando Rodriguez Y Baena (Imperial College, UK)
- 139 A Modular ROS-Based dVRK Teleoperation Controller Architecture** 
Radian Gondokaryono (University of Toronto; PCIGITI Sickkids Hospital, Canada)
Mustafa Haiderbhai (University of Toronto; PCIGITI Sickkids Hospital, Canada)
Adnan Munawar (John Hopkins University, United States)
Thomas Looi (PCIGITI Sickkids Hospital, Canada)
James Drake (PCIGITI Sickkids Hospital, Canada)
Lueder Kahrs (University of Toronto; PCIGITI Sickkids Hospital, Canada)
- 141 FMRI and MEG Compatible Hand Motion Sensor** 
Lingyu Lyu (Imperial College London, UK)
Elena Monfort-Sanchez (Imperial College London, UK)
Mark Runciman (Imperial College London, UK)
George Mylonas (Hamlyn Centre for Robotic Surgery, UK)
James Avery (Imperial College London, UK)

- 143 Signature Robot: a Miniature Robot for Orthopaedic Surgery** 
Spyridon Souipas (Imperial College London, UK)
Stephen Laws (Imperial College London, UK)
Ferdinando Rodriguez Y Baena (Imperial College, UK)
Brian Davies (Imperial College London, UK)
- 145 Optimizing Continuum Robot Tendon Routing for Minimally Invasive Brain Surgery** 
Margaret Rox (Vanderbilt University, United States)
Aidan Copinga (University of Utah, United States)
Robert Naftel (Vanderbilt University Medical Center, United States)
Robert Webster (Vanderbilt University, United States)
Alan Kuntz (University of Utah, United States)
- 147 Design, Fabrication, and Evaluation of a Biomimetic Soft Peristaltic Pump for Biomedical Applications** 
Sina Najjari (University of Leeds, UK)
Peter Culmer (University of Leeds, UK)
Ali Alazmani (University of Leeds, UK)
- 149 Distal Joint Rotation Mechanism for Endoscopic Robot Manipulation** 
Lap Wing Cheung (Chinese University of Hong Kong, Hong Kong)
Ka Chun Lau (Chinese University of Hong Kong, Hong Kong)
Flora Leung (The Chinese University of Hong Kong, Hong Kong)
Donald Ngo Fung Ip (The Chinese University of Hong Kong, Hong Kong)
Henry Chow (The Chinese University of Hong Kong, Hong Kong)
Philip Wai Yan Chiu (The Chinese University of Hong Kong, Hong Kong)
Yeung Yam (The Chinese University of Hong Kong, Hong Kong)

Session 6: Clinical Insights

- 151 3D Printed Cups for Acetabular Reconstruction: a 3D-CT Implant Study**
Anna Di Laura (Royal National Orthopaedic Hospital & UCL, UK)
Johann Henckel (Royal National Orthopaedic Hospital, UK)
Martin Belzunce (Royal National Orthopaedic Hospital, UK)
Harry Hothi (Royal National Orthopaedic Hospital & UCL, UK)
Alister Hart (Royal National Orthopaedic Hospital & UCL, UK)
- 153 Results of in Vivo Cardiac Arrhythmia Ablations with an Electro-Magnetic Navigation System** 
Christophe Chautems (ETH Zurich, Switzerland)
Nikola Cesarovic (ETH Zurich, Switzerland)
Peter Bode (University of Zurich, Switzerland)
Bradley Nelson (ETH Zurich, Switzerland)
Firat Duru (University Heart Center Zurich, Switzerland)
- 155 A Drop-in Robotic Gamma Probe for Minimally Invasive Radioguided Surgery**
Tom Pampiglione (University College London Hospital, UK)
Lluís Fumado (Hospital Del Mar, Spain)
Maarten Ruben Grootendorst (Lightpoint Medical Ltd., Netherlands)
Kunal Vyas (Lightpoint Medical Ltd., UK)
Manish Chand (University College London Hospital, UK)
- 157 The Virtuoso Surgical System: First Live Animal Experience**
Richard Hendrick (Virtuoso Surgical, Inc., United States)
Neal Dillon (Virtuoso Surgical, Inc., United States)
Lauren Branscombe (Virtuoso Surgical, Inc., United States)
Trevor Bruns (Virtuoso Surgical, Inc., United States)
Evan Blum (Virtuoso Surgical, Inc., United States)
Moffat Oresi (Virtuoso Surgical, Inc., United States)
Stephanie Amack (Virtuoso Surgical, Inc., United States)
S. Duke Herrell III (Vanderbilt University Medical Center, United States)
Robert Webster III (Vanderbilt University, United States)

159 Neurosurgical Robotics: Pushing the Boundaries with a Single Platform for the Sacrum to the Cranium 

Brendan F. Judy (Johns Hopkins Hospital, Baltimore, Maryland, USA, United States)
A. Daniel Davidar (Johns Hopkins Hospital, Baltimore, Maryland, USA, United States)
Andrew Hersh (Johns Hopkins Hospital, Baltimore, Maryland, USA, United States)
Carly Weber-Levine (Johns Hopkins Hospital, Baltimore, Maryland, USA, United States)
Amanda N. Sacino (Johns Hopkins Hospital, Baltimore, Maryland, USA, United States)
Brian Y. Hwang (Johns Hopkins Hospital, Baltimore, Maryland, USA, United States)
Tej D. Azad (Johns Hopkins Hospital, Baltimore, Maryland, USA, United States)
Ann Liu (Johns Hopkins Hospital, Baltimore, Maryland, USA, United States)
Joshua Materi (Johns Hopkins Hospital, Baltimore, Maryland, USA, United States)
Tara Dedrickson (Johns Hopkins Hospital, Baltimore, Maryland, USA, United States)
William S. Anderson (Johns Hopkins Hospital, Baltimore, Maryland, USA, United States)
Nicholas Theodore (Johns Hopkins Hospital, Baltimore, Maryland, USA, United States)

161 Index of Authors

Robotic System with Intuitive Control for Endoscopic Bone Cyst Surgery

S. Lee¹, S. Kim¹, R.M. Solzbacher¹, H. Kim¹, S. Joung², J. Hong¹

¹Department of Robotics Engineering, DGIST

²AIRS Inc.

jhong@dgist.ac.kr

INTRODUCTION

With a rise in total joint replacement and bone tumor surgeries, complications such as osteolysis increasingly occur. Osteolysis can promote bone cysts to form, which reduces bone density and can delay the recovery process by causing fractures [1]. To prevent these fractures, bone cysts are often surgically removed.

Conventional bone cyst surgery requires a large incision to gain access to the entire lesion. Through this access window, the cyst is removed using a curet. The inside of the bone is cleaned by following suction and irrigation before it is injected with a drug to promote bone regeneration [2]. The large access window for reaching the lesion may weaken the bone and can be the cause of additional fractures, further delaying the patient's recovery. Preventative measures such as internal plate fixation also require additional scans and expose the patient to more radiation.

The da Vinci Surgical System (da VinciTM Surgical System, Intuitive Surgical Inc, Sunnyvale, CA, USA) is used for minimally invasive surgery on soft tissue. Due to the limited bending and drilling functions, the robot is not applicable to the lesion inside bone. Various continuum robots [3][4] have been developed to overcome this limitation. However, the developed robots have difficulty removing hard, fibrous membrane inside the lesion because of their insufficient rigidity.

In this study, we propose a robotic compliant joint based endoscopic surgery system for minimally invasive bone cyst surgery. The proposed system includes a flexible bone drilling instrument with high rigidity which removes the bone cyst, and a roboticized commercial flexible endoscope to provide visual feedback as well as suction and irrigation to clean the lesion. An intuitive control device with auto-rotation display is integrated. Several experiments in which simulated lesions have been removed from cow femurs have been performed to evaluate the system.

MATERIALS AND METHODS

The proposed system consists of three parts as shown in Fig 1. The drilling robot for removing the bone cyst, the endoscopic robot to provide visual feedback as well as suction and irrigation, and the control device to manipulate the drilling and endoscopic robot.

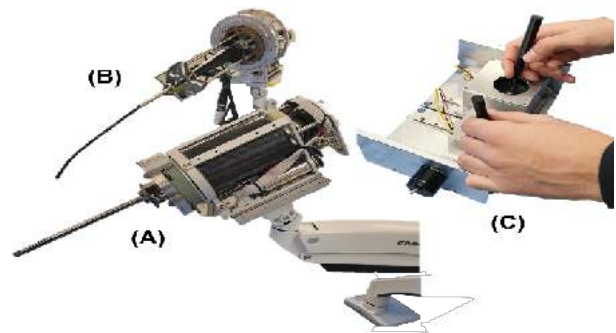


Fig. 1 (A) Drilling robot, (B) endoscopic robot, (C) leader devices

A. Drilling robot

The curved drilling instrument is actuated by the drilling robot giving it 3 degrees of freedom (DOF) (bend, rotate, translate). The notched compliant joint of the drilling instrument enables the drill to bend inside of the lesion after being inserted into the port. An additional DOF is used to rotate the drill bit, located at the distal end of the instrument. Bending of drilling instrument is enabled by the deformation of the notches from wire tension. Compared to other continuum robots, our robot can hold high wire tension because due to high intrinsic rigidity from the shape of the notches. For additional rigidity, two separate motors are used for each of the two bending wires. This enables counter-tensioning between the two wires. The high bending rigidity enables the drill to be precisely positioned during drilling despite repulsive forces being generated during the cyst removal.

B. Endoscopic Robot

The endoscopic robot provides visual feedback through 3 degrees of freedom (bend, rotate, translate) by using a motorized commercial endoscope (Olympus CYF-VHA). Cleaning inside the bone is performed through suction and irrigation added to the robot.

C. Control Device

Two control devices are used to manipulate the drilling and endoscopic robots respectively. It consists of a joystick and a linear guide with an encoder. The joystick controls the bending and rotation motion with each axis representing one motion, while the linear guide with the encoder controls translation separately. A joystick without spring-return is used for strict alignment with the drilling robot. The position of the joystick represents the position of the bend and rotation

axes of the robot. Safe and intuitive control is possible because the surgeon can deduce the current robot position from the position of the joystick.

In addition, as the surgeon rotates the endoscope, the frame of reference rotates, making it more difficult to remain oriented and moving the drill in the correct direction. To overcome this issue, the endoscope video feed is counter-rotated against the endoscope rotation, enabling the view to remain unrotated regarding the determined view axis (Fig 2). As such, the endoscope can be manipulated freely without confusing surgeon's sense of direction.

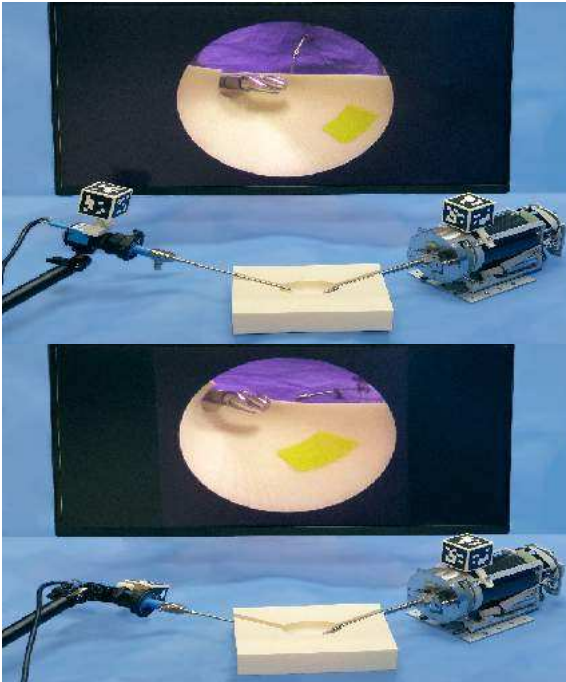


Fig. 2 (Top) 0° Endoscope with endoscopic view. (bottom) 90° Endoscope with adjusted endoscopic view (auto-rotation)

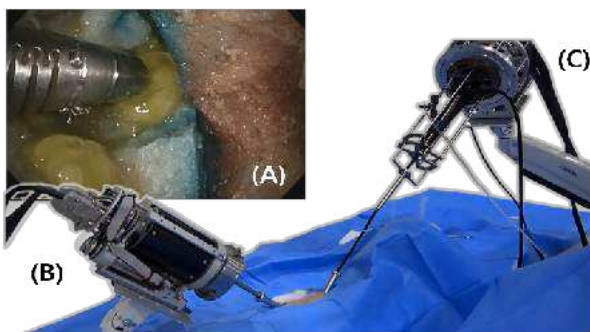


Fig. 3 (A) Experimental setup with endoscopic view, (B) drilling robot, (C) endoscopic robot

D. Experiment

To evaluate the feasibility of the proposed system animal experiments were conducted on cow femurs. Prior to the experiment, lesions were simulated by drilling out part of the femurs and filling it with agarose which has similar characteristics with a bone cyst. During the experiment, ports were drilled based on MRI

scans of the femur. The drilling and endoscopic robots were inserted through the ports and removed the simulated bone cyst (Fig 3). To clean up the removed lesion, suction and irrigation of the endoscopic robot was used.

RESULTS

The experiments were conducted by three orthopedic surgeons. Without previous experience using the proposed robotic system, they were able to control the robot with little practice before the experiments. It was possible to approach to the entire lesion using the bendable drill. Because the drill has high rigidity and enough speed to drill the lesion, it was easy to remove the lesion from the bone. In consequence, the experiments verified the feasibility of the proposed system in terms of ability to remove bone cysts.

DISCUSSION

The proposed system is expected to reduce recovery time and decrease the risk of additional fracture due to the minimally invasive approach. The system's capability of removing bone cysts has been verified through a series of phantom and animal experiments. It is possible to apply the robot to various other orthopedic surgeries with requirements for high flexibility and high rigidity. The system will be further developed regarding user feedback, including both visual and force feedback. In addition, control interface modifications based on the kinematics will be developed for intuitive control by combining rotation and bending motions of the robot.

ACKNOWLEDGMENT

This work was supported by the Ministry of Trade, Industry & Energy (MOTIE, Korea), Ministry of Science & ICT (MSIT, Korea), and Ministry of Health & Welfare (MOHW, Korea) under the Technology Development Program for AIBio-Robot-Medicine Convergence (20001688).

REFERENCES

- [1] J. Pretell-Mazzini, R. Murphy, I. Kushare and J. Dormans, "Unicameral Bone Cysts", *Journal of the American Academy of Orthopaedic Surgeons*, vol. 22, no. 5, pp. 295-303, 2014. Available: 10.5435/jaaos-22-05-295.
- [2] H. Hou, K. Wu, C. Wang, S. Chang, W. Lin and R. Yang, "Treatment of Unicameral Bone Cyst", *Journal of Bone and Joint Surgery*, vol. 93, no. 1, pp. 92-99, 2011. Available: 10.2106/jbjs.j.01123
- [3] F. Alambeigi et al., "A Curved-Drilling Approach in Core Decompression of the Femoral Head Osteonecrosis Using a Continuum Manipulator", *IEEE Robotics and Automation Letters*, vol. 2, no. 3, pp. 1480-1487, 2017. Available: 10.1109/lra.2017.2668469.
- [4] H. Watanabe, K. Kanou, Y. Kobayashi and M. Fujie, "Development of a "steerable drill" for acl reconstruction to create the arbitrary trajectory of a bone tunnel", 2011 IEEE/RSJ International Conference on Intelligent Robots and Systems, 2011. Available: 10.1109/iros.2011.6094654.

Design and experimental evaluation of the SOFTScreen Capsule System in a Colon Phantom

Vanni Consumi¹, Lukas Lindenroth¹, Danail Stoyanov¹, Agostino Stilli¹

¹Wellcome/EPSCRC Centre for Interventional and Surgical Sciences, University College London, UK

vanni.consumi.20@ucl.ac.uk

INTRODUCTION

Colorectal cancer (CRC) is nowadays one of the deadliest cancer but the high surviving rate is achievable if the disease is diagnosed and treated at the early stage. However, the standard procedure represents a discomfortable treatment for many patients at the point that many are discouraged in undergoing routine screening program. In fact, the clinician has to insert and guide by hand a semi-flexible tubular colonoscope and might apply significant forces and torques on the colon walls, with the complications of creating loops in the intestine, tissue damage or even perforation. For this reason, research in capsule robotic colonoscopy is in high demand [1]; the main objective of robotics in this field is to design a system capable of navigating inside the large intestine in order to provide visual inspection of the lumen, possibly, carrying surgical tools required in the colonoscopy procedure, i.e. polypectomy, without the creation of large pushing forces and loops.

Human colon is about 130 cm long and composed by 4 consecutive tracts, joint at different angles, named sigmoid, descending, transverse and ascending colon. The diameter the tubular organ can changes from 25 mm to 70 mm, reaching up to 80 mm if insufflated with CO₂ gas, often adopted in colonoscopy. Nonetheless, colon wall is a multilayers membrane that consists of four main layers (mucosa, submucosa, muscularis externa and serosa) which makes the membrane very compliant to large deformation and very slippery, being the internal wall of the colon characterized by continuous secretion of mucus. Due to both the morphology and the frictional behaviour of the colon, the design of robots that are able to crawl the intestine and perform the screening of the organ is a challenge. Various locomotion strategies for micro robotic devices have been explored, such active capsules inspired by bio-mimetic locomotion strategies, such insect or caterpillar, or by use of locomoting members to self-propel once inside the colon such wheels or tracks [2]. Nonetheless, current robotic solutions are still far away to replace the standard colonoscopy due to the challenges in integrating reliable locomotion strategy in small size robots able to face the complex environment represented by the colon.

In this work, we discuss the design and the features of the SOFTScreen system [3], discussing the testing of its locomotion capability inside a silicone phantom resembling the colon surface.

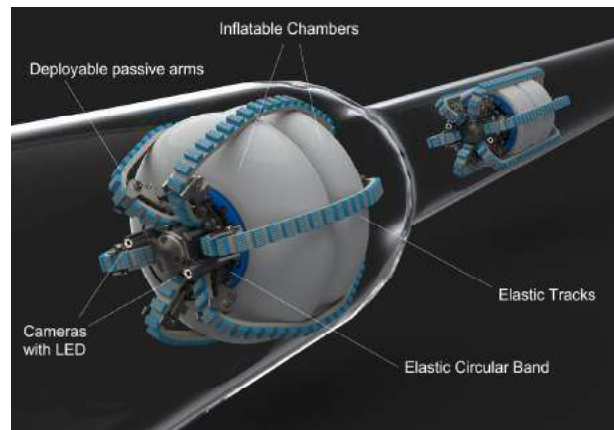


Fig. 1 Render of the SOFTScreen System navigating inside a transparent pipe, before and after a variation in diameter of the canal. The robot embeds six elastic tracks, two inflatable toroidal chambers to adapt to changing in diameter, two front cameras for inspection, and two elastic bands to recall the two sets of six radially deployable arms that passively bend during the inflation (tethers not shown in the figure).

MATERIALS AND METHODS

The SOFTScreen system represented in Fig. 1 is a cylindrical capsule designed to make use of soft materials, such silicone, to achieve traction and adaptability inside the human large intestine. The propulsion of the proposed robot is based on the motion of 6 elastic silicone tracks, all engaging a single worm-gear which is powered by on-board electric brushless motor (Model 315170, Maxon Motor™, Sashseln, Switzerland). The capability to adapt to the changing diameter of the colon is achieved by the inflation of two inflatable, silicone, toroidal chambers through two external pressure regulators (VPPX, FESTO™, Esslingen am Neckar, Germany) connected to the robot via soft tethers. When the internal motor drives the worm gear, the tracks create a continuous loop, and the toothed part of the tracks that is in contact with the wall of the colon will produce traction force by friction: the capsule will propel itself forward and backward inside the lumen according to the direction of the motor. The tracks are spaced symmetrically along the cylindrical shape of the robot to produce uniform contact along the perimeter while the inflation of the chambers aims at enlarging the diameter of the robot to control the

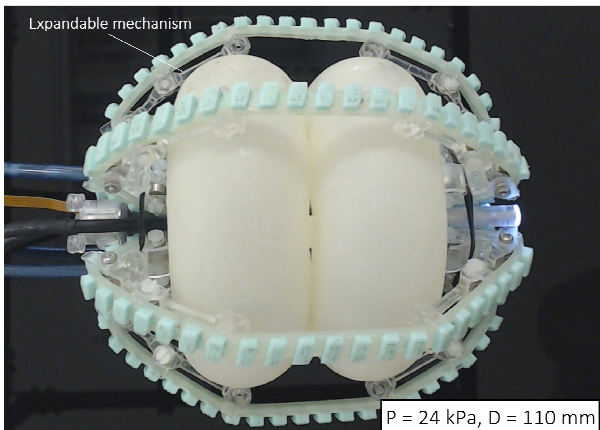


Fig. 2 Inflated configuration of the large-scale prototype reaching almost double of its initial diameter. The two chambers are inflated through external pressure regulators connected to the robot. Upon inflation, the expandable arms of the robot open in accordance to the deformation.

number of tracks in contact (by lifting the tracks up to the colon wall), the frictional force responsible for the motion, as well as it contributes to self-centre the axis of the front camera to the axis of the lumen investigated (Fig. 2). The chambers, one at front and one at the back of the robot, are inflated independently and, like the tracks, are made of Smooth-On™ silicones, all but the side of the teeth responsible of the traction treated with additive SLIDE™ STD (Smooth-On Inc., Easton, PA, US), to ensure safety and compliance to colon tissue. The rigid chassis is 3D printed and it serves to house the motor and to secure the inflatable chambers. Additionally, the chassis mounts twelve deployable arms, two for each track, that can open passively in accordance with the deformation of the chambers to prevent the creation of high contact forces between inflated chambers and surrounding tracks (Fig.2). When no pressure is delivered to the chambers, the arms are recalled by the mean of two elastic bands, one front and one back.

The large scale prototype of the system (2.5:1 scale) has been designed taking into account the future miniaturization of all the parts and its locomotion was tested inside a silicone colon phantom (circa 500 mm long), composed of two straight segments and a 90° elbow, with uneven internal surface and internal diameter of circa 85 mm. The current prototype mounts two 4.5 mm diameter off-the-shelf endoscopes but they haven't been included for this navigation experiments to reduce the drag force of the cables.

Speed of the prototype was measured in two configurations: in Case 1 no inflation is applied to the chambers, in Case 2 both chambers are inflated at 16 kPa and the external diameter results circa 85 mm (Fig. 3). These two cases were experimented inside the phantom both supported with circular rigid and inside the phantom fully collapsed (Fig. 3).

RESULTS

The SOFTScreen capsule navigated successfully multiple times inside the phantom in each of the

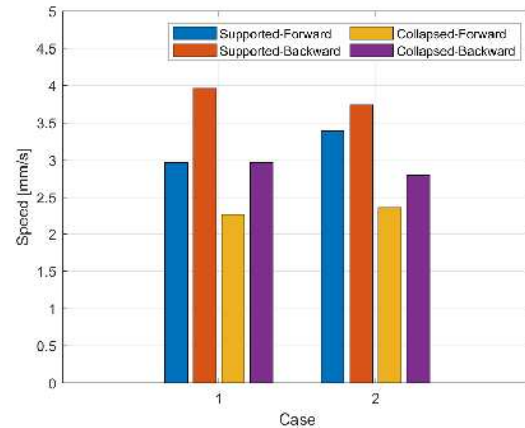


Fig. 3 Speed of the robot both not inflated (case 1) and inflated (case 2) inside Supported and Collapsed phantom.

conditions considered, both forward and backward (Fig. 3). During tests, motor's speed was kept at around 6000 RPM and robot resulted generally faster inside the Supported case and in backward direction.

DISCUSSION

The SOFTScreen capsule is a track-based robotic system which aims at integrating a robust locomotion along with the use of two chambers to adapt to the varying diameter of the colon and to self-centre its cameras for an efficient visual field inside the large intestine. Preliminary navigation testing was carried out inside a soft phantom with promising outcome: in particular, although the system doesn't have a steering mechanism, the loop motion of the tracks was observed to be useful for the capsule to approach and move forward in proximity of the curvature considered in this experiment. Moreover, the pressure differential between the two toroidal chambers can be used to control the tilt angle of the cameras with respect to the axis of the lumen so that it's possible to point the camera to specific target (such polyps).

Future work will further investigate the locomotion capabilities of the current prototype inside a more complex and curved scenario resembling the colon, as well as the construction of the real scale prototype will be carried out.

REFERENCES

- [1] I. Kassim, L. Phee, W. S. Ng, F. Gong, P. Dario, and C. A. Mosse, "Locomotion techniques for robotic colonoscopy," *IEEE Eng. Med. Biol. Mag.*, vol. 25, no. 3, pp. 49–56, 2006, doi: 10.1109/MEMB.2006.1636351.
- [2] D. Lee, S. Joe, J. Choi, B. I. Lee, and B. Kim, "An elastic caterpillar-based self-propelled robotic colonoscope with high safety and mobility," *Mechatronics*, vol. 39, pp. 54–62, 2016, doi: 10.1016/j.mechatronics.2016.08.002.
- [3] V. Consumi, L. Lindenroth, D. Stoyanov, and A. Stilli, "SoftSCREEN-Soft Shape-shifting Capsule Robot for Endoscopy based on Eversion Navigation," doi: 10.12809/hkmj154685.

Answering the FDA’s Call To Action: Using Steerable Sheaths and Mirrors to Prevent ERCP Infections

J. B. Gafford¹, S. J. Webster¹, P. A. Anderson¹, S. D. Herrell^{1,2,4}, K. L. Obstein^{2,4},
D. C. Rucker^{1,3}, and R. J. Webster III^{1,2,4}

¹*EndoTheia, Inc.*

²*Vanderbilt University Medical Center*

³*The University of Tennessee, Knoxville, Mechanical Engineering*

⁴*Vanderbilt University, Mechanical Engineering; Institute for Surgery and Engineering (VISE)*
{joshua.gafford, robert.webster}@endotheia.com

INTRODUCTION

Endoscopic Retrograde Cholangiopancreatography (ERCP) is the gold standard treatment for a variety of disorders of the pancreaticobiliary system. In ERCP, the biliary tract is accessed from the duodenum using a specialized endoscope called a duodenoscope. It enters the body transorally, navigates through the stomach, past the pylorus, and into the duodenum. Then, various flexible tools are passed through the duodenoscope and aimed sideways at its tip, under side-view camera visualization. An elevator mechanism integrated into the duodenoscope tip is used to control tools to cannulate the major duodenal papilla to access the bile duct.

An FDA review in 2019 found that many post-ERCP deaths and infections over the past few years have been due to multi-drug-resistant bacteria transferred between patients undergoing ERCP. The root cause was determined to be the duodenoscopes themselves, which were transmitting harmful bacteria (including *Escherichia coli*, *Staphylococcus*, and carbapenem-resistant *Enterobacteriaceae*) between patients in 5.4% of all cases [1], [2]. Furthermore, the FDA linked the high infection rates directly to the elevator mechanism, which contains moving parts with small gaps that harbor bacteria and are difficult to clean and sterilize between cases [2]. These realizations led to the August 2019 call-to-action by the FDA [3], which recognized that a paradigm shift in duodenoscope technology was needed. The FDA call-to-action emphasizes the urgent need to develop “innovative device designs, such as those with disposable components” [3], and urges hospitals to rapidly adopt these technologies, once available.

To answer this call to action, we are developing a fully disposable ERCP system (Figs. 1 and 2) that enables

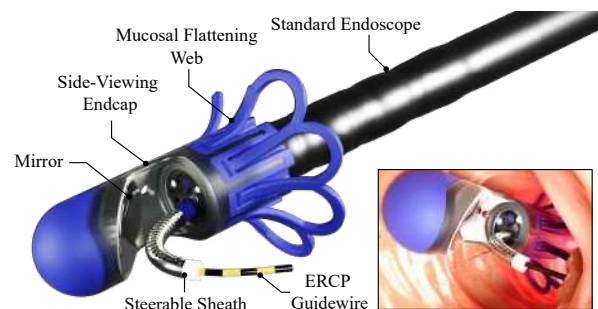


Fig. 1: ERCP System consisting of a disposable steerable sheath and side-viewing endcap (inset shows a clinical rendering of the system being used to cannulate the major duodenal papilla).

physicians to perform ERCP using standard, forward-viewing upper-GI endoscopes, which are inherently much easier to clean due to their simpler construction, and are far less likely to transmit infections to patients [4] ($\ll 0.0001\%$ infection rate [5]), compared to duodenoscopes with their complicated reprocessing protocols and fundamentally difficult-to-clean design. Such a device could potentially curb infection rates in ERCP, sparing many patients from unnecessary sickness or death due to contaminated duodenoscopes.

MATERIALS AND METHODS

Our system combines two fully disposable components: a flexible physician-controlled steerable sheath, and a distally-mounted side-viewing endcap, as shown in Fig. 2 (a). The steerable sheath passes through standard endoscope ports, and carries within itself the standard guidewires, cannulas, sphincterotomes, and baskets that are used in ERCP interventions. The sheath is coupled to a

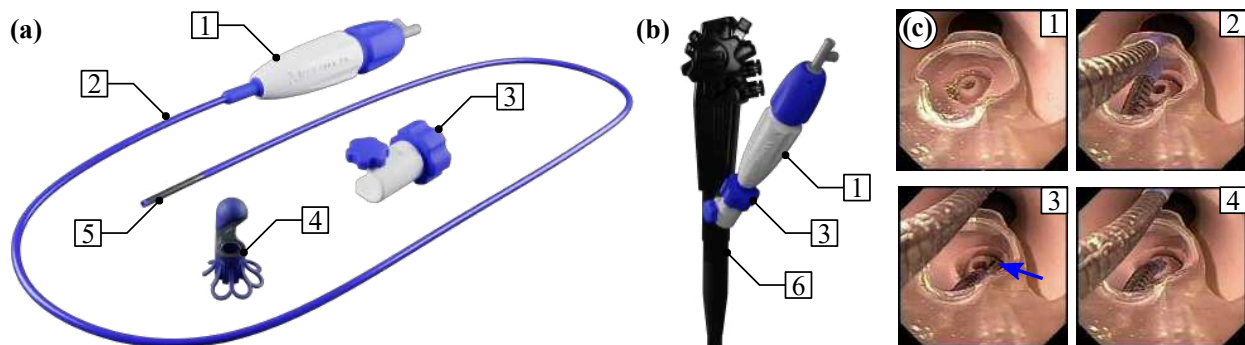


Fig. 2: (a) ERCP System: (1) user interface, (2) flexible braid-reinforced transmission, (3) endoscope locking mechanism, (4) disposable endcap, (5) steerable sheath, (b) system mounting scheme to a standard endoscope handle (6), (c) endoscope view during an in vitro feasibility study: (1) papilla is initially visualized in the side-viewing mirror, (2) the steerable sheath is brought into the endoscope field-of-view, (3) the guidewire is advanced out of the tip of the steerable sheath (blue arrow), (4) the sheath is deflected further to cannulate the papilla.

user interface that is rigidly mounted to the working port of the endoscope channel, and enables the physician to control the insertion, retraction, rotation, and deflection of the steerable sheath (and, accordingly, tools passed through the sheath) to facilitate papilla cannulation. The sheath utilizes a tendon-less actuation methodology, enabled by two micromachined Nitinol tubes nested inside one-another, implementing the concentric agonist-antagonist actuation scheme that enables distal steerability through the transmission of a differential force applied axially along the length of the tubes [6].

The disposable endcap press-fits onto the distal tip of the endoscope, and contains within itself an angulated mirror surface that re-directs a portion of the endoscope’s native field-of-view to the side to facilitate visualization of the papilla. The endcap features an atraumatic tip to facilitate device insertion, as well as a matrix of flexible interconnected protruding ‘arms’ that evert when the endoscope is withdrawn, thereby flattening mucosal folds to enhance visualization.

To enable cannulation of even the most extreme papilla orientations, the sheath was designed to deflect up to 135 degrees using analytical methods presented in [6]. While the sheath tip (which implements the concentric push-pull paradigm) is comprised of Nitinol, a long flexible transmission constructed of braid-reinforced Nylon tubing couples the Nitinol sheath to the user interface to facilitate the transfer of axial forces and torques to the sheath. The UI mounts rigidly onto the endoscope’s working channel via a scope locking mechanism, as shown in Fig. 2 (b).

RESULTS

We investigated the feasibility of our disposable ERCP system at both visualizing and cannulating the major duodenal papilla. Experiments were performed in a high-fidelity synthetic ERCP trainer (the Chamberlain Group, LLC, Great Barrington, MA, USA). The endcap was affixed to a standard Olympus GIF-1T140 gastroscope,

and navigated to the site of the papilla. The sheath was passed through the gastroscope, and the proximal user interface was locked onto the endoscope handle via the scope lock. The endcap and steerable sheath were used in tandem to cannulate the papilla with a standard ERCP guidewire (Boston Scientific Jagwire, 3.9F). The cannulation sequence is shown in Fig. 2 (c). The total cannulation time was 36 seconds.

DISCUSSION

The feasibility study presented in this paper represents a pivotal first-step towards safer, duodenoscope-less ERCP. Responding directly to the FDA’s call-to-action for safer, disposable tools for ERCP, we have developed a platform enabling ERCP to be performed using much easier-to-sterilize forward-viewing endoscopes. Preliminary results in a clinical training phantom demonstrate the promise of such an approach, and current efforts are focused on commercialization and regulatory approval.

Conflict of Interest Disclosure: The authors have research-related financial interests in EndoTheia, Inc.

REFERENCES

- [1] FDA, “The FDA Continues to Remind Facilities of the Importance of Following Duodenoscope Reprocessing Instructions: FDA Safety Communication,” 2019.
- [2] R. M. Humphries and G. McDonnell, “Superbugs on duodenoscopes: The challenge of cleaning and disinfection of reusable devices,” *Journal of Clinical Microbiology*, vol. 53, no. 10, pp. 3118–3125, 2015.
- [3] FDA, “FDA recommends health care facilities and manufacturers begin transitioning to duodenoscopes with disposable components to reduce risk of patient infection,” 2019.
- [4] P. Wang, T. Xu, S. Ngamruengphong, M. A. Makary, A. Kalloo, and S. Hutfless, “Rates of infection after colonoscopy and esophagogastroduodenoscopy in ambulatory surgery centres in the USA,” *Gut*, vol. 67, pp. 1626–1636, 2018.
- [5] J. Kovaleva, F. T. M. Peters, H. C. V. D. Mei, and J. E. Degener, “Transmission of Infection by Flexible Gastrointestinal Endoscopy and Bronchoscopy,” *Clinical Microbiology Reviews*, vol. 26, no. 2, pp. 231–254, 2013.
- [6] K. Oliver-Butler, J. A. Childs, A. Daniel, and D. C. Rucker, “Concentric push-pull robots: Planar modeling and design,” *IEEE Transactions on Robotics*, pp. 1–15, 2021.

Validation of a Proof-of-Concept System for Personalised Computer-Assisted Treatment of Knee Osteochondral Lesions

F. Tatti¹, B. Jaramaz², and F. Rodriguez y Baena¹

¹*Mechatronics in Medicine Laboratory, Imperial College London, UK*

²*Smith & Nephew Inc., USA*

{f.tatti,f.rodriguez}@imperial.ac.uk; branko.jaramaz@smith-nephew.com

INTRODUCTION

The number of total and partial knee arthroplasties performed annually in the United Kingdom increased steadily between 2003-2019. Over the past two years, the COVID-19 pandemic has created a backlog of delayed arthroplasties that will require several years to clear [1]. Early intervention through targeted treatment of focal cartilage lesions could alleviate some of the burden by avoiding or postponing the need for more complex and invasive procedures, but such interventions are still uncommon [2]. Among the key challenges of these procedures is the difficulty of ensuring correct positioning and a good congruence between the implant and patient anatomy, which are critical for success [3].

In this regard, Computer-Assisted Orthopaedic Surgery (CAOS) could be of assistance, as it provides valuable metrics to inform the selection and placement of an implant, and minimise the error between planning and execution. CAOS systems promise to bring more quantitative data and objective metrics into the operating theatre, informing the surgeons' decisions, thus allowing them to tailor each intervention to the patient's needs [4]. This work presents the validation of a novel computer-assisted surgical workflow for the treatment of osteochondral lesions. The software uses intraoperative information on the patient's anatomy and lesion to help clinicians optimise the selection of an implant and its pose. The software was combined with the existing capabilities of the NAVIO™ surgical system (Smith & Nephew inc.) [5], creating a complete workflow that incorporates both surgical planning and assisted bone preparation.

MATERIALS AND METHODS

In the context of a government funded industry-academia partnership with a large orthopaedics robot manufacturer (Smith & Nephew, inc), we created a software module that generates a parametric description of the shape and size of an osteochondral defect (OCD), and uses it to optimise the selection of an implant and its pose. The software module requires two inputs: a 3D model of the patient's femur and a vector of points representative of the defect's contour. The size and elongation of the defect are captured by fitting a 2D ellipse to its contour,

while the anatomical shape is described by fitting an elliptic or hyperbolic paraboloid to the external surface. The 3D model of the femur is assumed to be constructed by means of a statistical shape model, therefore ignoring the presence of a defect and reconstructing the missing cartilage surface, as if the defect were not present. The shape of the available implants is described using the same mathematical model employed for the defect geometry.

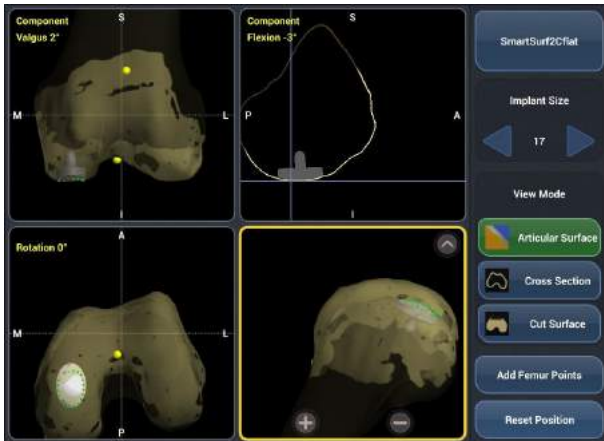
The software automatically rates the similarity between the shape of each implant and the femur surface, by comparing the defect's parametric description with that of the implants. A list of options is then presented to the surgeon, in which the implants are ordered from the best to worst match. When an implant is selected from the list, the software co-registers the implant's and femur's outer surfaces using the Iterative Closest Point (ICP) algorithm [6], providing a suggested pose. The surgeon is free to make adjustments to this initial pose, using the NAVIO's interactive planning user interface (see Figure 1a).

We validated our work by creating a total of 6 artificial lesions on the medial and lateral condyle of 3 different plastic bones, and using the described system to select an appropriate implant and optimise its pose. The phantom bones were then cut using the NAVIO system and a 3D-printed mock of the selected implant was inserted. The accuracy of the implant's position was assessed by using a tracked probe to collect the position of four divots on the surface of the 3D printed implant. Figure 1b shows the successful planning and placement of an implant prototype, and the frame of reference used to compute the implantation error.

RESULTS

The software selected an appropriate implant in all of the test cases, and the automatically generated pose required only minor adjustments. The overall procedure including patient registration, planning and bone preparation required less than 30 minutes per case.

The average \pm sd root mean squared (RMS) distance between the surface of the bone model and the outer surface of the implant at its planned position was 0.64



(a) Screenshot of the planning user interface.



(b) Implant pose accuracy verification.

Fig. 1: Osteochondral defect repair setup.

± 0.06 mm across all tested lesions, indicating a good congruence between the implant and bone anatomy. The translational and rotational errors between planned and achieved implant position are shown in Figure 2. The RMS error across all lesions was 0.49 mm, 0.65 mm, and 0.26 mm in the medio-lateral, anterior-posterior, and superior-inferior direction respectively. The RMS rotational error was 1.05°, 1.50°, and 1.89° in flexion-extension, varus-valgus, and implant rotation.

DISCUSSION

The available biomechanical evidence indicates that a proud implant has a significant negative effect on peak contact pressure [3]. The presented system addresses this issue by maximising the shape similarity between implant and bone anatomy, with positive results.

The translational implantation error was comparable to that obtained with the same surgical system for total knee replacement, while the rotational error was slightly larger [7]. This could be attributed to the use of small implants with a single fixation post. Nevertheless, the accuracy of implant placement compares favourably to previous studies on osteochondral graft transplantation of the knee, both with freehand and navigated technique [8].

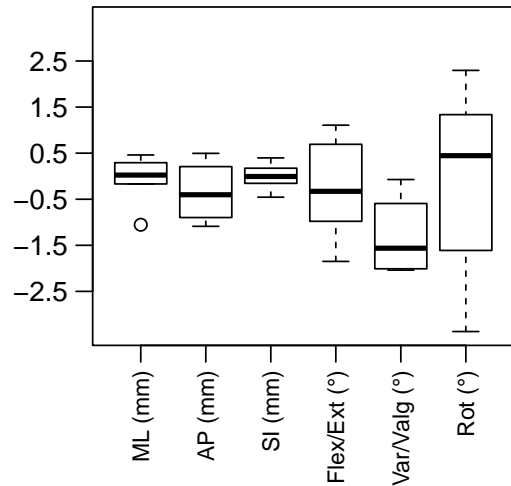


Fig. 2: Implant pose error. Medio-lateral, anterior-posterior, and superior-inferior translational error. Rotational error in flexion-extension, varus-valgus, and implant rotation.

Overall, this work represents a successful in-vitro validation of a prototype system for computer-assisted osteochondral defect repair. While further testing is required to fully demonstrate clinical viability, this initial result is promising and demonstrates that the proposed system could help clinicians accurately plan and execute OCD repair procedures.

ACKNOWLEDGEMENTS

The authors thank Hisham Iqbal, Dylan Hower, Patricia Murtha, Darren Wilson, Daniel Farley, and Graham Bennet for their support. The study received funding from INNOVATE UK under project number 103950.

REFERENCES

- [1] National Joint Registry, *18th Annual report*, 2021.
- [2] A. Fuchs, H. Eberbach, K. Izadpanah *et al.*, "Focal metallic inlay resurfacing prosthesis for the treatment of localized cartilage defects of the femoral condyles: a systematic review of clinical studies," *Knee Surg Sports Traumatol Arthrosc*, vol. 26, pp. 2722–2732, 2018.
- [3] C. Becher, R. Huber, H. Thermann, H. Paessler, and G. Skrbensky, "Effects of a contoured articular prosthetic device on tibiofemoral peak contact pressure: a biomechanical study," *Knee Surgery, Sports Traumatology, Arthroscopy*, vol. 16, pp. 56–63, 2008.
- [4] F. Picard, A. Deakin, P. Riches *et al.*, "Computer assisted orthopaedic surgery: Past, present and future," *Med Engineering and Physics*, vol. 72, pp. 55–65, 2019.
- [5] R. Mitra and B. Jaramaz, "Navio surgical system — handheld robotics," in *Handbook of Robotic and Image-Guided Surgery*. Elsevier, 2020, pp. 443–457.
- [6] P. Besl and N. McKay, "A method for registration of 3-d shapes," *IEEE Trans. Pattern Analysis and Machine Intelligence*, vol. 14, pp. 239–256, 1992.
- [7] S. Han, D. Rodriguez-Quintana, A. Freedhand, K. Mathis, A. Boiwka, and P. Noble, "Contemporary robotic systems in total knee arthroplasty: A review of accuracy and outcomes," *Orthopedic Clinics*, vol. 52, pp. 83–92, 2021.
- [8] D. Koulalis, P. Di Benedetto, M. Citak, P. O'Loughlin, A. Pearle, and D. Kendoff, "Comparative study of navigated versus freehand osteochondral graft transplantation of the knee," *The American journal of sports medicine*, vol. 37, pp. 803–807, 2009.

Design and Characterization of Robotically-Guided Ultrasonic Bone Cutting for Laminectomies and Facetectomies

L.J. MacLean^{1,2}, N Theodore²

¹Whiting School of Engineering, Johns Hopkins University, USA

²Department of Neurosurgery, Johns Hopkins University School of Medicine, USA
lmaclea2@jh.edu

INTRODUCTION

Computer-navigated and robotic guidance systems facilitate accurately placing pedicle screws in the spine. [1] The clinical success of robotics has generated interest in extending these methods to other spinal procedures. [1] Bone cutting is particularly interesting but traditional osteotomies are challenging to robotically guide. [1-2] Fortunately, the development of ultrasonic bone cutting has led to more precise osteotomies that may be better suited for robotics. [3] These bone scalpels oscillate based on a piezoelectric crystal and can be optically tracked. [3]

We propose that robotically guiding an ultrasonic bone scalpel will allow for precisely navigated osteotomies. This system offers several clinical benefits including reduced accidental damage (e.g. nerve roots), minimally invasive surgery (MIS), and reduced blood loss. [1-3] Accurately knowing the cut positions could also help alignment corrections. [4] Here, we evaluate the accuracy of a basic design configuration with a cervical spine phantom undergoing laminectomies and facetectomies. We hypothesize that robotically guided ultrasonic bone cutting will improve the spatial precision and facilitate MIS. This work aims to demonstrate the initial proof-of-concept for robotically guided ultrasonic bone cutting.

MATERIALS AND METHODS

We used a UR5 robot (Teradyne inc) which is a six-jointed unit that allows for accurate positioning of the guide. The Nexus® harmonic bone scalpel (Misonix inc) was chosen with a 20mm end-blade operating at 22.5kHz. A solution of 0.9% saline was run through the cannulated lumen of the blade to prevent burning of the phantom material during cutting. Two different custom end-effectors were 3D printed for the robot in PLA using the Ultimaker S3 printer. The first end effector rigidly attached the scalpel to the robot so that all degrees of freedom are robotically controlled and such that force measurements of the bone-blade interaction can be measured. The second is a cannulated guide which allowed for the surgeon to control axial translation and is more comparable to pedicle screw guides. A key fit between a scalpel attachment and the guide cannula prevents roll rotation about the lengthwise axis of the tool. The experimental setup is shown in figure 1.

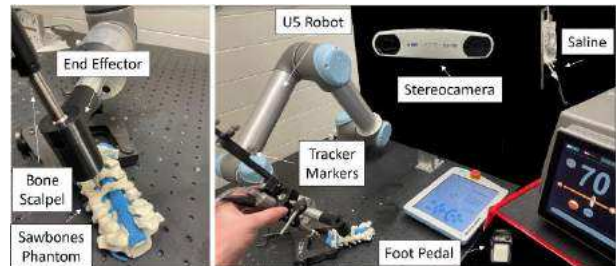


Fig. 1 Experimental setup (A) Close view of cutting guide and phantom, and (B) Large view of support technologies

The surgical phantom was a CI-CVII Sawbones™ spine model. A rubber spinal cord with nerve roots was included to assess potential damage. An O-arm (Medtronic plc) took a Cone-Beam CT (CBCT) of the model prior to cutting. This scan was loaded into 3D Slicer™ for planning the cutting trajectories. Orthogonal views were used to manually mark the laminectomies and facetectomies (Fig. 2). Each facetectomy involved cutting the superior and inferior articular processes.

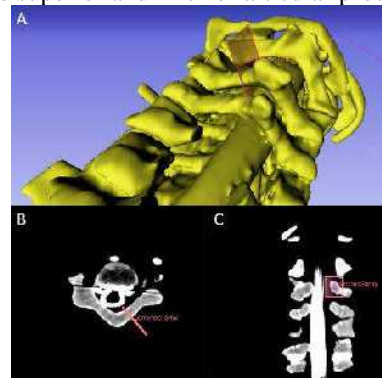


Fig. 2 Cut plane planning (A) 3D Rendering for Visualization, (B) Axial view with slice, and (C) Coronal view with slice

The phantom was rigidly clamped to the workbench and registered to a Polaris Vicra® tracking system (NDI inc) with a pointwise registration by digitizing the lateral and spinous processes. Four tracking markers were attached to the bone scalpel via a 3D-printed attachment, and a spin calibration determined the tooltip position. Finally, the tracked tool was attached to the robot to compute a transform between the robot and the phantom. The virtual cut planes are then mapped to the robot coordinate frame. The joint angles and kinematics for the robot are set using a custom Python terminal. Three cuts, and consequently three positions were required for most trials. For the rigidly attached tool, the forces were recorded throughout the cutting process.

A total of 32 cuts for accuracy trialing were performed. Laminectomies were performed with guidance for CII to CIII, with rigid attachment from CIV to CV and then freehand from CVI to CVII. Facetectomies were performed via guidance for root-levels C3 to C4, via fixed robotics for C5 and freehand for C6 to C7. Another CBCT is then taken of the cut phantom. Actual cut planes were compared against the planned cuts by calculating the Root-Mean Squared (RMS) positional error between the planes. We also measured the force-velocity relationship based on a separate set of 30 axial cuts.

RESULTS

All three techniques being (1) robotic guidance (with the cannula end-effector), (2) rigid attachment and (3) freehand were accurate for the laminectomies and facetectomies. The pooled RMS errors indicate the robotic approaches slightly outperformed the freehand technique, but these methods sometimes made incomplete cuts. Guidance had an RMS error of 1.57 ± 0.65 mm with 100% percent completion of the laminectomy cuts but only 62.5% of the facetectomy cuts. The rigid attachment had an RMS error of 1.43 ± 0.49 mm but only completely made 50% of both the laminectomy and facetectomy cuts. The freehand cuts had an RMS error of 2.94 ± 0.81 mm but completed 100% of both the laminectomies and facetectomies. (Fig. 3)

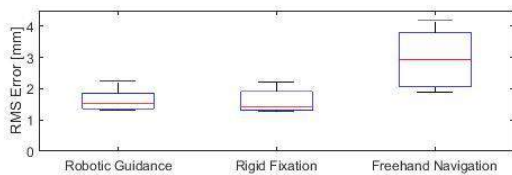


Fig. 3 Pooled accuracy results based on the RMS Error of the difference between the planned and actual osteotomy planes

The data was also subdivided between the level, side and superior/inferior (for the facetectomy), but none had a significant impact on the accuracy. All three techniques had similar accuracy between the laminectomies and the facetectomies. The force-velocity curve suggests that the cutting force initially increases with velocity, then plateaus before then beginning to increase again.

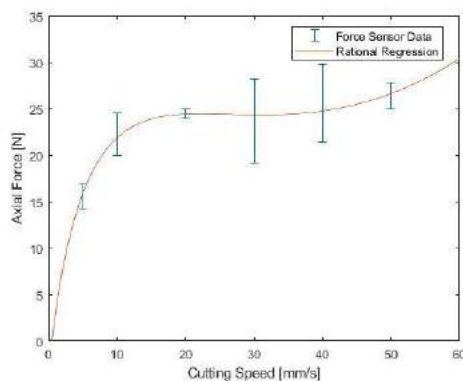


Fig. 4 The cutting force measured from the UR5 force logger as a function of the cutting speed of the ultrasonic bone scalpel

DISCUSSION

The results demonstrate that robotically assisted ultrasonic bone cutting is feasible and may have the potential to address limitations of traditional methods. [3] The accuracy results suggest that even a simple proof-of-concept robot may improve accuracy. Incomplete cutting of the bone segment occurred when the cutting paths were insufficiently deep or when guide positioning prevented sufficient lateral cutting. Both problems can be addressed by improving upon the current path planning. The force measurements are in contrast to traditional methods where faster cuts lead to greater force [5] This is likely caused by the unique cutting action of the piezoelectric unit. [3] The motor is able to compensate for increased cutting speed up to a point (creating the plateau region), before reaching maximum power when the force begins to increase again. [3] These findings may inform a force-based control strategy.

Accuracy improvements with other surgical tools generally lead to improved clinical outcomes. This bone-cutting system may also be generalizable to other instruments such as curettes or ultrasonic milling for discectomies. This proof-of-concept trialing suggests the possibility of a broader range of robotically-guided tools. Key limitations include the use of sawbones instead of cadaveric bone, only examining the cervical spine, and testing performed by a single user. Future work will address more general and more realistic contexts. Further, this work only considered laminectomies and facetectomies but wedge osteotomies for alignment correction will be considered in the future. Next steps include improving the path planning and automation.

This work demonstrates the feasibility of robotically guided ultrasonic bone cutting for spinal surgery. The reported accuracy is encouraging, and weaknesses, such as the path planning sensitivity, can likely be overcome. The unique force-velocity curve may allow for force control in the future. These results justify the continued development of robotic bone cutting.

REFERENCES

- [1] Staub BN, Sadrameli SS. The use of robotics in minimally invasive spine surgery. *J Spine Surg.* 2019 Jun; 5(Suppl1): S31-S40.
- [2] Hartl R, Lam KS, Wang J, Korge A, Kandziora F, Audigé L. Worldwide Survey on the Use of Navigation in Spinal Surgery. *World Neurosurg.* 2013 Jan; 79(1):162-72.
- [3] Hu Z, Ohnmeiss DD, Lieberman IH. Use of an ultrasonic osteotome device in spine surgery: experience from the first 128 patients. *Eur Spine J.* 2013 Dec; 22(12): 2845-9.
- [4] Galbusera F, Bassani T, La Barbera L, Ottardi C, Schlanger B, Brayda-Bruno M, Villa T, Wilke HJ. Planning the Surgical Correction of Spinal Deformities: Toward the Identification of the Biomechanical Principles by Means of Numerical Simulation. *Front Bioeng Biotechnol.* 2015; 3: 178.
- [5] James TP, Pearlman JJ, Saigal A. Predictive force model for haptic feedback in bone sawing. *Med Eng Phys.* 2013 Nov; 35(11): 1638-44.

Pop-Up Soft Robot for Minimally Invasive Surgery

Mark Runciman, James Avery, George Mylonas

Hamlyn Centre, Imperial College London, London, UK

m.runciman@imperial.ac.uk

INTRODUCTION

Colorectal cancer was estimated to have caused the second highest number of cancer-related deaths globally in 2020, and the third highest number of incidences [1]. As a result, there is an intense research focus on developing improved screening and treatment options. Among recently developed surgical techniques for early colorectal cancers is Endoscopic Submucosal Dissection (ESD), which offers patient benefits such as reduced recurrence rate, the possibility of removing large early cancers *en bloc*, and increased resection rate [2], in comparison to the more common procedure Endoscopic Mucosal Resection (EMR). However, procedure times and perforation rates are higher for ESD as a result of the high technical difficulty [3].

Robotic devices may simplify difficult ESD procedures, lessening the learning curve and/or reducing the staff required; however, there is no standard flexible robotic endoscope in spite of recent advances. Challenges facing designers of robotic devices include reducing patient discomfort and achieving cecal intubation rates comparable to standard endoscopy [4]. Cecal intubation is achieved when the endoscopist successfully reaches the cecum with the endoscope, and bulky robotic mechanisms can make navigation and insertion harder and cause increased patient discomfort, resulting in the need for sedation or longer procedure times.

Here we present an inflatable robot capable of volume, size, and stiffness changes as an answer to the need for surgical robots that can achieve access to the proximal colon. To the authors' knowledge it is the first robot for minimally invasive surgery whose structure and actuators were made using laser welding manufacture, and the design is low-profile and low-cost as a result. This work builds on the inflatable Cyclops robot [5] but replaces the long force transmission cables with soft hydraulic actuators as described in [6]. As such, both the robot's structure and actuators are made from flexible plastic film. One of the main benefits of this construction is that the robot can easily be collapsed to a small size by folding and/or rolling, then deployed by pressurising the structure. The robot therefore has two states: an inactive, deflated, flexible state, and an active, pressurised, rigid state. The folded state can be approximated by a cuboid of 25 x 7.5 x 100 mm and the deployed state by a cylinder of approximately 44 mm in diameter and 100 mm in length. The tip position of a single 3 mm diameter flexible instrument can be controlled by the robot while in its active state. The ranges of motion in the local

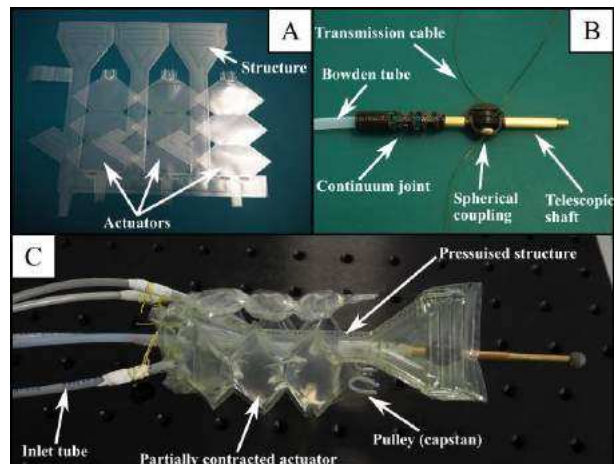


Fig. 1 Inflatable robotic device A) Laser-welded actuators affixed to laser-welded structure during construction. B) Shaft assembly with PTFE Bowden tube, 3D printed continuum joint, telescopic shaft, and spherical coupling connecting the transmission cables to the shaft. C) Complete robot with pneumatically pressurised structure and hydraulic actuators.

coordinates of the robot are approximately 47.0 mm, 92.5 mm, and 89.0 mm in the X, Y, and Z directions, respectively. The X axis is positive along the shaft, the Y axis horizontal and the Z axis vertical.

MATERIALS AND METHODS

A hybrid parallel mechanism was chosen as a trade-off between the number of actuators and the degrees of freedom, resulting in a polar robot whose tip can be positioned with 3 degrees of freedom. The robot is composed of a shaft assembly, inflatable structure, and soft actuators. The structure and actuators, shown in Figure 1A, were manufactured using laser welding of thin plastic films, described in [5], to create sealed chambers. The structure and actuators were welded separately, the excess material removed from each, then the actuators manually welded to the structure at specific anchor points. The shaft assembly, Figure 1B, consists of a 3D printed passive continuum joint, a telescopic brass shaft, and a 3D printed spherical coupling to attach the three transmission cables to the shaft. Except for the shaft assembly, all parts of the robot are capable of reversible changes in volume, shape, and rigidity. The proximal end of the continuum joint couples to the inflatable structure to provide a lever point. The parallel mechanism controls the point through which the shaft intersects the plane made by the locations where the cables enter the inflatable structure. In this way the pitch and yaw of the shaft are determined. The length of the telescopic shaft is changed by actuating a flexible tube through a Bowden tube connected at the base of the continuum joint.

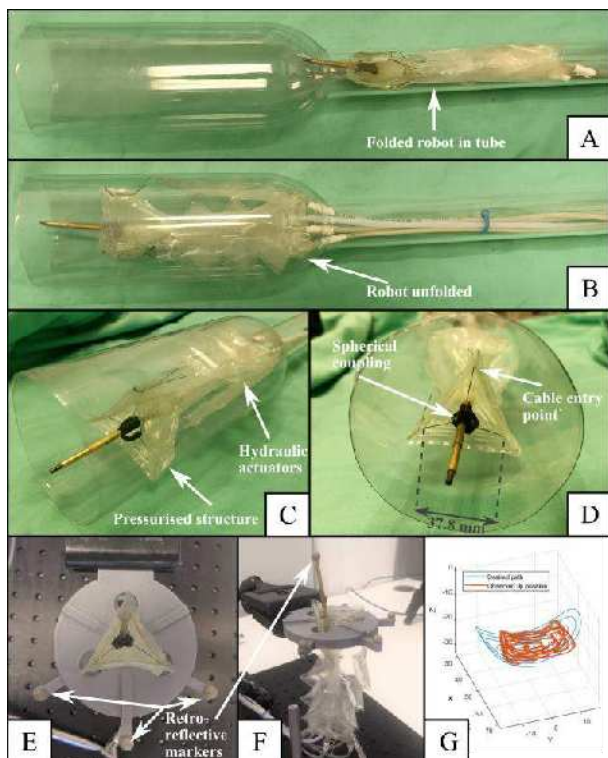


Fig. 2 Deployment and use of deformable robot. A) Passing through insertion tube B) Unfolding at target C) Pressurised robot ready to use D) Close-up showing cable entry points, spherical coupling, and telescopic shaft E&F) Path scanning experiment setup G) Result of path scanning experiment – ten repetitions of spiral path projected on cylinder.

The contraction of the soft hydraulic actuators is determined by controlling their volume, as discussed in [6], which was achieved in this work using individual syringe pumps. A block and tackle pulley arrangement was used between the structure and each actuator to double the stroke, thereby reducing the required actuator length by a factor of two.

An optical tracking system (Optitrack, NaturalPoint Inc.) was used to observe the position of the tip during a path scanning task. A retroreflective marker was placed on the tip of the robot, with others in a reference pattern defining the cable entry plane and the centre of the planar parallel mechanism. The setup is shown in Figures 2 E and F.

RESULTS

Figure 2A-D shows the robot was able to deform before its deployment and subsequent use. In Figure 2A the deflated robot was folded and rolled around the shaft assembly, then passed through an insertion tube to a larger void, Figure 2B. For deployment, Figure 2C, the inflatable structure was pressurised to 2 bar absolute using a pneumatic regulator (PRE1-U08, AirCom, Germany). Pressurising the structure caused it to unfold, increase its size and rigidity, and correctly position the cable entry points of the integrated parallel mechanism relative to each other. As such, the robot was able to scan complex paths. Figure 2G shows the result of scanning a spiral pattern projected onto a cylinder aligned with the robot's central axis.

DISCUSSION

The robot was made from low-cost materials using rapid manufacturing techniques, creating the possibility for single-use and even patient-specific robotic devices for minimally invasive surgery. Additional automated manufacturing steps such as laser cutting could further reduce assembly times and increase scalability. Benefits of this approach in a fully developed system could include infection control and reduction in operational costs that could make robotic surgery more accessible. The ongoing aim of this project is to create pop-up soft robotic devices capable of accurate and precise path scanning for diagnostic and therapeutic uses.

The inflatable robot was able to pass through an insertion tube, pop up by inflating its support structure, and scan a complex path. The path scanning was more inaccurate than anticipated due to bending of the structure, however, in another tracing task, a human user manually compensated for the robot's motion in real time to successfully trace a circle. Therefore, the authors expect that inaccuracies may be compensated for in future versions of the device with a stiffer structure and by using visual servoing, for example. Other innovations for future versions could involve replacement of the brass shafts with plastic shafts to make the device MRI compatible. The length of the robot could be greatly reduced, for example, by changing the design of the pulley mechanism.

REFERENCES

- [1] J. Ferlay *et al.*, “Cancer incidence and mortality worldwide: Sources, methods and major patterns in GLOBOCAN 2012,” *International Journal of Cancer*, vol. 136, no. 5, pp. E359–E386, 2015, doi: 10.1002/ijc.29210.
- [2] P. Russo, S. Barbeiro, H. Awadie, D. Libânio, M. Dinis-Ribeiro, and M. Bourke, “Management of colorectal laterally spreading tumors: a systematic review and meta-analysis,” *Endoscopy International Open*, vol. 07, no. 02, pp. E239–E259, 2019, doi: 10.1055/a-0732-487.
- [3] J. H. Kim *et al.*, “Risk factors associated with difficult gastric endoscopic submucosal dissection: predicting difficult ESD,” *Surgical Endoscopy*, vol. 31, no. 4, pp. 1617–1626, 2017, doi: 10.1007/s00464-016-5149-6.
- [4] Z. Li and P. W. Y. Chiu, “Will the robot take over endoscopy?,” *Endoscopy*, vol. 47, no. 09, pp. 773–774, 2015.
- [5] M. Runciman, J. Avery, M. Zhao, A. Darzi, and G. P. Mylonas, “Deployable, Variable Stiffness, Cable Driven Robot for Minimally Invasive Surgery,” *Frontiers in Robotics and AI*, vol. 6, 2020, doi: 10.3389/frobt.2019.00141.
- [6] M. Runciman, J. Avery, A. Darzi, and G. Mylonas, “Open Loop Position Control of Soft Hydraulic Actuators for Minimally Invasive Surgery,” *Applied Sciences*, vol. 11, no. 16, 2021, doi: 10.3390/app11167391.

A simple and powerful instrument for robotic flexible endoscopy

Giuliano A. Giacoppo, Ada L. Bachmann, Peter P. Pott

Institute of Medical Device Technology, University of Stuttgart
giuliano.giacoppo@imt.uni-stuttgart.de

INTRODUCTION

To enable more complex operations in single-port surgery, endoluminal surgery, and natural orifice surgery, endoscopic robots are equipped with multiple instrument channels [1, 2]. Such surgery often requires retracting tissue to create sufficient work space for the actual operation. E.g. during a cholecystectomy, the liver must be lifted with an instrument, which requires a payload force of up to 3 N [3].

A cable-driven instrument was developed, which can be used through a working channel of a robotic flexible endoscope. This paper describes the required tensile force to handle a payload force of 3 N deriving specifications for an actuation unit. Therefore, the way the force ratio behaves when the entire length of the instrument's active section of 75 mm is used, and how the force ratio behaves when a length of 50 mm is used, were investigated. It is intended to provide a simple and powerful instrument to enable more complex surgery with robotic flexible endoscopes.

MATERIALS AND METHODS

The instrument is divided into a passive and an active part that can be classified as a pseudocontinuum discrete joint robot [4]. This active part consists of 12 segmented joints in x-direction and 12 segmented joints in y-direction with

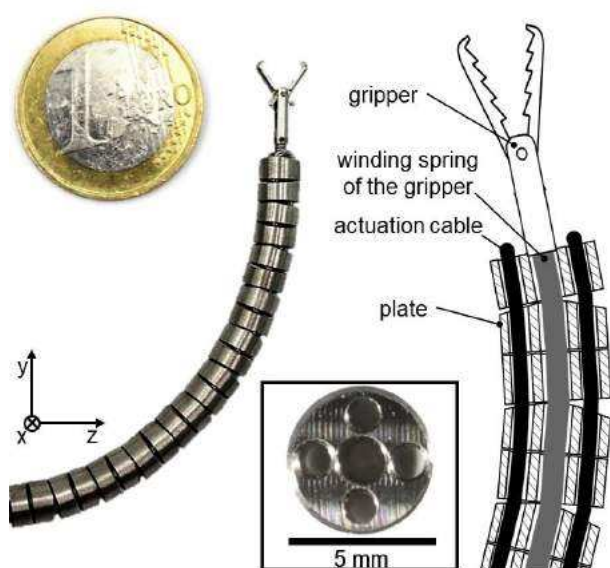


Fig. 1 Active section of the instrument with 12 segmented joints in x-direction and 12 segmented joints in y-direction resulting in 25 plates with 5 holes and the gripper at the tip.

a gripper at the tip (see Fig. 1). The gripper with an outer diameter of 1.8 mm, and its winding spring (\varnothing 1.6 mm), serves as a backbone for the 25 plates (Ti6Al4V Grade 5). These circular plates are angled 8.5° on one side, 2.5 mm high, and have an outer diameter of 5 mm, with five drill holes to guide the cable pulleys. The central hole (\varnothing 1.6 mm) of the plates houses the winding spring of the gripper. The four outer holes (\varnothing 1.2 mm) guide the cables (\varnothing 0.8 mm, 7 x 7, 1.4401 – AISI 316 located on a 1.6 mm circle) for actuation. With these plates, the active part (75 mm length) can be angled in two perpendicular planes up to 102° . The passive part (1750 mm length) with cable guides is used to overcome the distance in the working channel. To achieve this, the passive part consists of four wrap springs ($\varnothing_{\text{Out}} = 1.50$ mm; $\varnothing_{\text{Spring}} = 0.20$ mm) as an extension of the Bowden cable cores. The entire bundle is covered with silicone and has an outer diameter of 5.5 mm.

The actuation of the robotic instrument is achieved via lightweight and cost-effective twisted-string actuators [1]. To be able to design the system, the required tensile force has to be known. According to the theoretical consideration, the required tensile force

$$F_T = \frac{l}{x} \cdot F_P \quad (1)$$

results from the quotient of the length l of the active part and the distance x of the central axis to the cable are multiplied by the payload F_P (see Fig. 2). However, the friction is not taken into account. The actual required tensile force is to be determined by measurements in a test rig similar in design to LAU [5].

To determine the necessary cable force to achieve a payload of 3 N at the tip of the gripper, the active section in a measurement setup is in the extended state as shown in Fig. 2. This involves an isometric force measurement with a load cell (KD40s, ME-Meßsysteme, Henningsdorf, DE) on the Bowden cable and the gripper. Two

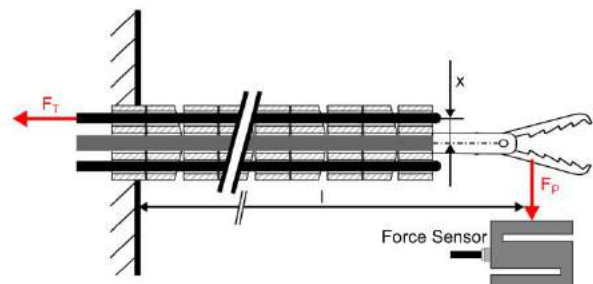


Fig. 2 Schematic representation of the measurement setup. The tensile force F_T is applied and the resulting payload F_P is measured.

different lengths of the active part are examined. The full 75 mm length of the active part with 12 joints and a shortened version with 7 joints (50 mm) are used.

RESULTS

For both lengths 75 mm (12 joints) and 50 mm (7 joints), Fig. 3 shows the required tensile force in the Bowden cable and theoretical tensile force over the payload. A larger gradient of the required tensile force compared to the theoretical relationship can be seen for both lengths. The instrument with 7 joints and an active length of 50 mm requires a tensile force of 254 N to achieve a maximum payload of 4.8 N.

A maximum payload of 2.7 N is achieved with the instrument of 12 joints and an active length of 75 mm, for which a tensile force of 160 N is required.

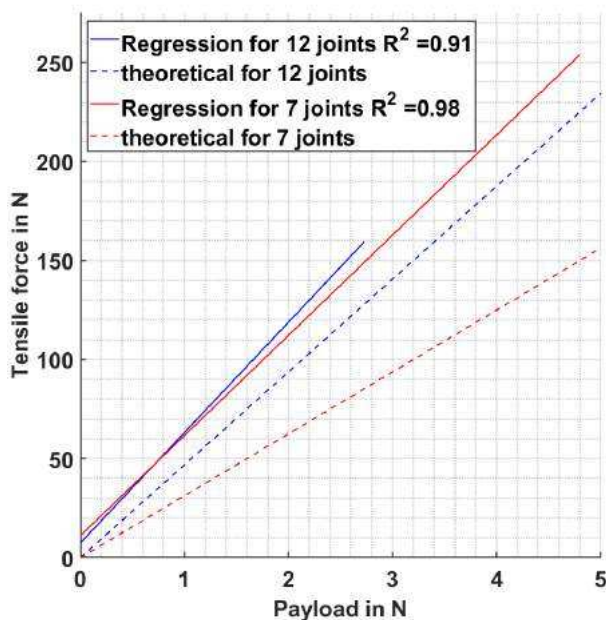


Fig. 3 Required tensile force to lift a payload for 12 joints with a total length of 75 mm and for 7 joints with a total length of 50 mm.

DISCUSSION

With the presented instrument, it is possible to handle a payload force of up to 4.8 N. It can be used for robotic flexible endoscopy to create additional work space, such as lifting the liver during a cholecystectomy.

Using 12 joints, only a maximum payload of 2.7 N can be applied. If the tensile force is increased to achieve a higher payload, the instrument breaks out to the side.

Since the frictional force acts in the direction of motion the core in the Bowden cable should in theory align axially without a contact surface. Thus, no friction should occur for the straight instrument (Fig. 2). Nevertheless, the measurements show that this ideal condition could not be achieved in the straight state and that high frictional forces have to be overcome already in this case.

In the application, however, it can be assumed that the passive part will adopt an unknown curvature to reach the target location of the operation. This would lead to increased friction, which has to be compensated with a higher tensile force.

Furthermore, it can be observed that the gradient of the regression line is higher than the theoretical line. This indicates that for a given payload, a higher tensile force must be applied since the friction force must also be compensated.

Therefore, the friction effect cannot be neglected. One approach to reduce the friction effect is to superimpose a longitudinal vibration (dithering) on the actuation cable [6].

The required tensile force results from the instrument's geometry. Since the passive part also has a considerable length, friction arises over the entire device.

These design limitations derive from the fact that the instrument is guided through a working channel. Therefore, a small outer diameter is necessary to ensure insertion and removal.

With these measurements, the tensile force of 254 N is needed in practice to achieve a 4.8 N payload. This is sufficient to achieve the requirements of a payload for a cholecystectomy. With this knowledge, a sufficient motorized actuation unit can be designed to integrate this into a flexible robotic instrument.

In the future, more sophisticated tests should be performed under experimental conditions. A tissue phantom should be used to investigate the behavior of the instrument under realistic conditions.

REFERENCES

- [1] Schlesiger D, Giacoppo GA, Schäfer MB, Pott PP. Twisted string actuation with position feedback for robotic endoscopy. *Current Directions in Biomedical Engineering*. 2021;7(2):343-346.
- [2] Visconti TA, Otoch JP, Artifon EL. Robotic endoscopy. A review of the literature. *Acta Cirúrgica Brasileira*. 2020; 35.
- [3] Hwang M, Kwon D. K-FLEX: A flexible robotic platform for scar-free endoscopic surgery. *The International Journal of Medical Robotics and Computer Assisted Surgery*. 2020;16(2):e2078
- [4] Burgner-Kahrs J, Rucker DC, Choset H. Continuum Robots for Medical Applications: A Survey. *IEEE Transactions on Robotics*. 2015;31(6):1261-80.
- [5] Lau KC, Leung YY, Chiu PWY, Yam Y, Lau JYW, Poon CCYP. A Flexible Surgical Robotic System for Removal of Early-Stage Gastrointestinal Cancers by Endoscopic Submucosal Dissection. *IEEE Transactions on Industrial Information*. 2016;12(6):2365-74.
- [6] Matich S, Neupert C, Kirschniak A, Schlaak HF, Pott PP. 3-D force measurement using single axis force sensors in a new single port parallel kinematics surgical manipulator. *IEEE/RSJ International Conference on Intelligent Robots and Systems (IROS)*. 2016

Shape Sensing for a Soft Continuum Manipulator using Electrical Impedance Tomography (EIT)

A. Alian, E. Zari, J. Avery, E. Franco, M. Runciman, F. Rodriguez y Baena, and G. P. Mylonas

The Hamlyn Centre for Robotic Surgery, Imperial College London
a.alian21@imperial.ac.uk

INTRODUCTION

Soft robots offer numerous advantages for use in medical applications due to their flexibility, maneuverability and inherent softness, which increase safety in surgical procedures by reducing trauma and recovery time for patients. In recent years, soft continuum manipulators able to navigate unconstrained areas opened new opportunities in minimally invasive surgery (MIS) and endoscopic applications. A compelling requirement yet to be fulfilled is the integration of a robust proprioceptive sensing system in the manipulator. The solutions that have been explored in the literature include optical fibers and electromagnetic (EM) sensors. However, both methods have disadvantages: aside from their high cost, optical fibers have bulky hardware that is difficult to integrate in a soft continuum robot and can affect its bending, while EM trackers are sensitive to metallic tools or other EM devices [1].

Here, we investigate a sensing approach based on electrical impedance tomography (EIT) for a 1 DOF inextensible manipulator that employs hydraulic actuation. Our system consists of a Flexible Printed Circuit (FPC) with 13 electrodes embedded in the soft continuum robot. Saline is used as a conductive actuation fluid and the voltage differences detected by the electrodes are used to measure the deformations of the manipulator upon pressurization. Having low profile and biocompatible components, and leaving adequate space for additional instruments are the main advantages of EIT in medical applications. This method shows promising results and we believe that it can inspire a new generation of autonomous soft continuum robots.

MATERIALS AND METHODS

In order to evaluate the performance of the proposed sensing scheme, a number of experiments have been conducted on a continuum manipulator prototype, consisting of an hydraulically-driven soft actuator and an FPC for sensing. The soft manipulator has been fabricated following the process outlined in [2] using Ecoflex 00-50 silicone rubber, and it has a semi-circle cross-section with an outer diameter of 12 mm, a total active length of 90 mm and 4 mm wall thickness.

The FPC consists of 13 evenly spaced electrodes on a polyamide flex film which is inserted in the inner chamber of the actuator (see Figure 1.a). The EIT technique [3] has been used to detect deformations of the manipulator induced by both internal pressure and external forces. To record the changes of the impedance, electrical current is injected through a pair of electrodes and the resultant voltages are measured simultaneously from the remaining pairs. To estimate the shape deformations, EIT provides two alternatives, one of which is using the measured voltages directly and assigning them to particular deformations. Another alternative is using the voltages to numerically compute a series of partial differential equations based on the finite element method through the inverse problem in EIT [4]. The output of this numerical approach are EIT reconstruction images that visualize the conductivity changes due to the shape deformations.

Two experiments have been carried out to evaluate the accuracy and sensitivity of EIT in this application. The experimental setup incorporates the continuum manipulator equipped with 13-electrode FPC, a syringe pump, and a data acquisition interface for EIT measurements. 0.9% saline solution has been used as the actuation fluid of the robot, and a protocol with 84 channels has been adopted for EIT measurements. The specified protocol assigns 12 injection pairs as 1-2, 1-3, 1-4 and so forth, and allocates electrodes 1-7, 2-8, 3-9 and so forth to measurement pairs. These 84 channels are recorded in 0.4 second time steps by the EIT system (Eliko Quadra). During the first experiment which is conducted to assess the sensitivity of EIT, the manipulator is actuated through a syringe pump while the voltages are recorded. To ensure the stability of the output voltage, the supply pressure is maintained constant in six intervals and the shape deformations of the manipulator are captured by camera. In the second experiment, instead of being pressurized, the continuum manipulator is manually pinched with different intensity at two locations along its length. The aim of this experiment is to validate the capability of EIT to localize external forces and potential obstacles.

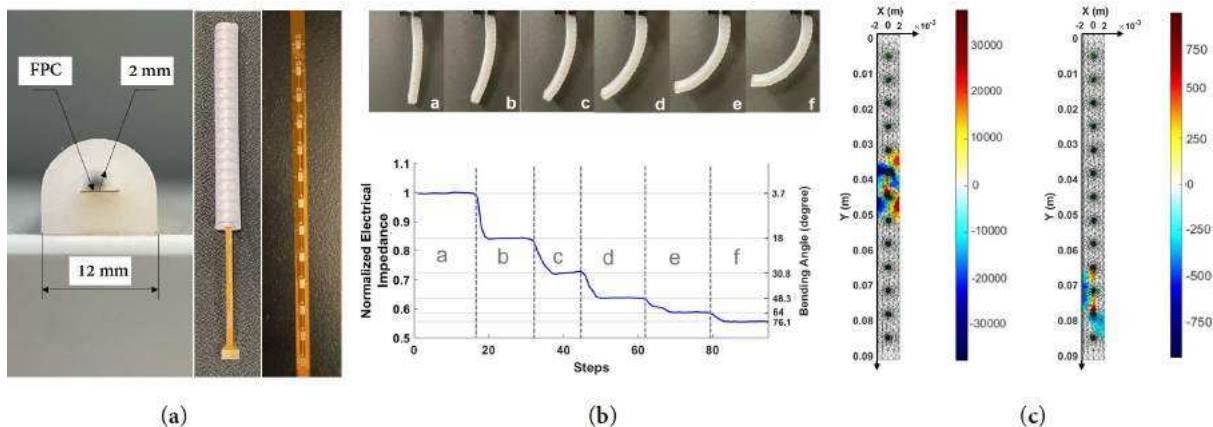


Fig. 1 Soft continuum manipulator and results of EIT experiments. a) Cross sectional area of the bending actuator with the integrated FPC. b) Top: six configurations at which the pressure remained constant with their corresponding bending angles in degree. Bottom: plot of the normalized resultant impedance changes in one EIT channel. c) Localizing the external force at the middle and lower section of the manipulator from changes in conductivity. The numbers on the colorbars are in S/m.

RESULTS

The impedance changes measured with EIT to detect the deformations caused by the hydraulic pressure for the first experiment are normalized and depicted in Figure 1.b. It can be observed that the EIT system is sensitive to deformations and can identify shape changes. Figure 1.b shows that the impedance changes from the initial bending angle of 3° to the angle of 76° ranges up to 45% of the maximum value of the impedance. The highest drop in the impedance occurs between the transition from configuration *a* to *b* by 16%, while the lowest occurs by 3% between *e* and *f*. This degree of sensitivity can be leveraged to provide precise feedback signals for closed-loop control systems. It can be seen in the figure that the impedance declines as the soft actuator bends. This decrease can be attributed to the fact that pressurizing the actuator inflates the inner chamber and increases its cross sectional area (CSA). Since the distance between the electrodes on the FPC is fixed, this increase in the CSA results in a lower impedance. The reconstructed EIT images localizing the deformations induced by an external load during the second experiment are shown in Figure 1.c. These images signify the changes in the conductivity of each element in the meshed model of the actuator used for the inverse problem of EIT. These results support the idea that EIT can be utilized for localizing external forces as the relevant conductivity changes correspond to the spots at which the pinching occurred. In particular, the conductivity decreases at the pinching site as this has reduced the CSA and increases either side as CSA increases.

DISCUSSION

A soft continuum manipulator with an integrated EIT sensing scheme has been presented and produced using an easy and repeatable manufacturing procedure. The

results of the experiments indicate that the EIT system is able to detect the deformations of the manipulator and to localize external forces. Although the fabricated prototype has only 1 DOF, we believe that this sensing approach could be extended to n DOF systems. A limitation of this method is the inextensible characteristic of the FPC, which could be overcome by using a stretchable substrate instead of the polyamide film. In addition, further experiments will be conducted to optimize the measurement protocol. Future work aims at creating a numerical model able to relate the conductivity changes detected by the electrodes to the deformations of the manipulator.

ACKNOWLEDGMENTS

This work is partially supported by a research collaboration with the Multi-Scale Medical Robotics Centre, The Chinese University of Hong Kong.

REFERENCES

- [1] S. K. Sahu, C. Sozer, B. Rosa, I. Tamadon, P. Renaud, and A. Menciassi, "Shape Reconstruction Processes for Interventional Application Devices: State of the Art, Progress, and Future Directions," *Frontiers in Robotics and AI*, vol. 8, no. November, pp. 1–26, 2021.
- [2] P. Polygerinos, Z. Wang, J. T. Overvelde, K. C. Galloway, R. J. Wood, K. Bertoldi, and C. J. Walsh, "Modeling of Soft Fiber-Reinforced Bending Actuators," *IEEE Transactions on Robotics*, vol. 31, no. 3, pp. 778–789, 2015.
- [3] J. Avery, M. Runciman, A. Darzi, and G. P. Mylonas, "Shape sensing of variable stiffness soft robots using electrical impedance tomography," *Proceedings - IEEE International Conference on Robotics and Automation*, vol. 2019-May, pp. 9066–9072, 2019.
- [4] K. Y. Aristovich, G. S. D. Santos, B. C. Packham, and D. S. Holder, "A method for reconstructing tomographic images of evoked neural activity with electrical impedance tomography using intracranial planar arrays," *Physiological Measurement*, vol. 35, no. 6, pp. 1095–1109, 2014.

A Haptic Feedback Glove for Minimally Invasive Surgery

Arincheyan Gerald¹, Rukaiya Batliwala¹, Jonathan Ye¹, Patra Hsu²,
Hiroyuki Aihara³, and Sheila Russo^{1,4}

¹*Department of Mechanical Engineering, Boston University,*

²*Department of Biomedical Engineering, Boston University,*

³*Brigham and Women's Hospital, Harvard Medical School*

⁴*Materials Science & Engineering Division, Boston University,*
russos@bu.edu

INTRODUCTION

Robot-assisted minimally invasive surgery (MIS) has countless benefits over open surgery, from shorter recovery times and lower risk procedures for the patient to higher accuracy and broader capabilities for the surgeon [1]. However, a significant detriment to these procedures is that current systems lack haptic feedback. The lack of haptic feedback in MIS forces the surgeon to depend merely on visual cues, such as the deformation of tissue under load, to estimate the forces [1]. The likely outcome of misreading these cues is torn tissue, patient discomfort or broken sutures [2]. Moreover, haptic feedback is specifically vital for robot-assisted endoscopy procedures. A recent study evaluating an Endoscopic Operation Robot (EOR) concluded that haptic feedback is beneficial in remote manipulation of flexible endoscopes. When haptic feedback was absent there were more incidences of overstretching of sigmoid colon in a colonoscopy training model [3]. This work presents a soft robotic glove that provides haptic feedback for endoscopic procedures (Fig. 1, A). In our previous work, we introduced a soft robotic sleeve [4] that can detect forces between a colonoscope and colon walls during navigation. The glove receives force input from the soft robotic sleeve wrapped around the colonoscope (Fig. 1, B). Any incident force on the sleeve, during endoscopic navigation, is relayed to the surgeon as haptic feedback through proportional inflation of the glove's pneumatic actuators.

MATERIALS AND METHODS

The glove design consists of three finger actuators. The actuators are attached to the main glove piece in a modular fashion using adjustable straps. The finger actuators are designed to be wrapped around the proximal phalanges on the dorsal side of the hand. This allows the surgeon to operate the endoscope without the actuators hindering their finger dexterity. Loss of finger dexterity could hamper handling and manipulation of the endoscope during the surgery. Current commercial haptic feedback gloves use vibrotactile or linear resonant

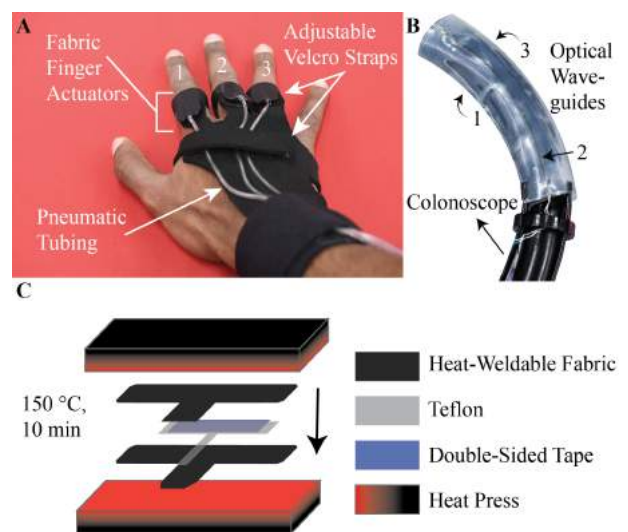


Fig. 1 A) Haptic feedback glove showing soft actuators (numbered) and tubing. B) Soft robotic sleeve showing three optical waveguides [4]. C) Fabrication diagram of finger actuators.

actuators (LRAs) mounted onto the palm and fingertips [5]. This can affect palm and fingertip dexterity, rendering such gloves unsuitable for haptic feedback in endoscopies. The number of finger actuators in the proposed glove can be varied depending on the number of sensors attached to the endoscope. The finger actuators are made from a combination of materials. First, heat weldable fabric (Seattle Fabrics, Inc.) and Teflon (McMaster-Carr Supply Company) are laser-cut into a T shaped pattern. Then, the Teflon is sandwiched between two pieces of the heat weldable fabric (Fig. 1, C) and sealed together using a heat press at 150° C for 10 min. This forms a completed actuator with the Teflon creating space for an air pocket. Tubing and Velcro® straps are then attached to the actuator. The main glove serves as a connection between the finger actuators and the wrist, providing a secure fit. It is made from Neoprene and has Velcro® straps to adjust to the user's hand size. The soft robotic sleeve used in this study has three

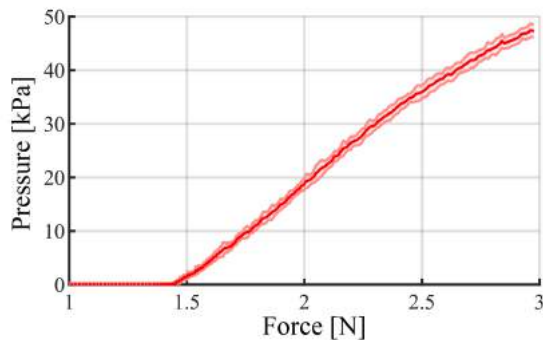


Fig. 2 Test results displaying actuator inflation pressure in response to incident force on soft robotic sleeve.

optical waveguides [4] to serve as force sensors, and each of them is connected to a finger actuator. The actuators are arranged on the glove to match the spatial orientation of waveguides of the sleeve, i.e., the actuator on the index finger maps force input from the leftmost waveguide. (Fig. 1, A-B). The glove is connected to a fluidic control board, with solenoid valves (GVP-321C-24D, Nitra[®] Pneumatics) and an Arduino[®] Mega 2560 micro-controller. The control algorithm uses pulse width modulation (PWM) to vary the duty cycle controlling the solenoid valve, based on the input from the soft robotic sleeve. Thus, the magnitude of incident force on the soft sensors determines the value of the duty cycle, triggering a proportional inflation of the actuators.

RESULTS

A. Force Calibration

The soft robotic sleeve was subject to a force compression calibration test using an indenter fixed to an Instron testing machine. As the indenter presses down on the optical waveguide sensors, light transmission decreases and this causes a change in signal voltage. The control algorithm then triggers inflation of the actuators in the glove. The test was performed over a range of 0-3 N. The PWM duty cycle is adjusted so that forces greater than 1.5 N trigger actuator inflation [4]. This is to ensure that the surgeon is notified of potentially dangerous forces to the colon wall while ignoring smaller, inconsequential forces. This threshold can be changed as necessary. As seen in Fig. 2, as the force increases beyond 1.5 N, the actuators inflate and the internal pressure rises linearly to about 50 kPa. This demonstrates the ability of the actuators to apply haptic feedback in a manner proportional to the incident force on the sensor. The actuators inflate to max pressure in 103 ms.

B. In-Vitro Validation

An *in-vitro* test was performed by imitating a colonoscopy procedure. The soft robotic sleeve was wrapped around a colonoscope model. An artificial colon model was created from thermoplastic elastomer (TPE) (Stretchlon[®] 200, FibreGlast, USA) and the colonoscope was inserted into it (Fig. 3, A). During navigation, when the colonoscope pushes on the colon wall, the light transmission in the optical waveguides decreases and the voltage values drop. This increases the value of the duty cycle and triggers the inflation of the

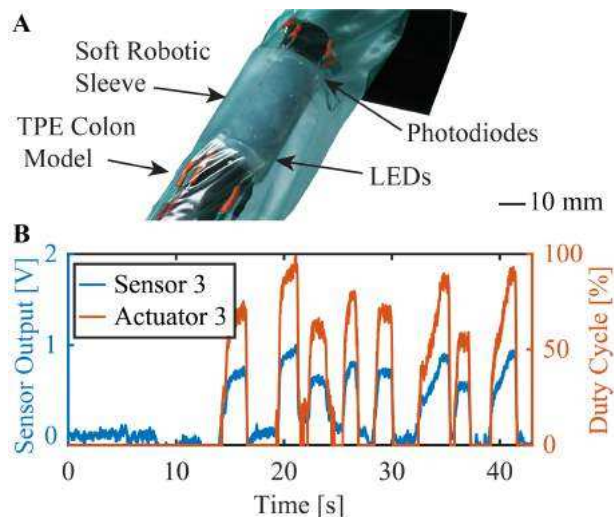


Fig. 3 *In-vitro* validation test. A) Setup. B) Results.

actuators on the haptic glove. As seen in Fig. 3, B, when a sensor (i.e., optical waveguide) on the colonoscope pushes against the colon wall, the voltage difference and duty cycle increase and results in inflation of the glove's actuator. This demonstrates the preliminary viability of the haptic glove in endoscopic procedures.

DISCUSSION

The goal of this study was to evaluate the feasibility of a soft glove to provide haptic feedback to a surgeon during an endoscopic procedure. We concluded that the glove successfully pressurizes the fingers of the wearer proportional to the force exerted on a colon wall during a colonoscopy procedure, and thus provides continuous haptic feedback. The next steps for this study would be to determine the adaptability of the haptic glove to various users (i.e., expert and novice endoscopists) and validate its usability in a clinical colonoscopy setting. Future work will also incorporate a gyroscopic sensor to ensure that the actuators spatially map force even when the colonoscope is rotated.

ACKNOWLEDGMENTS

This work was supported by the National Institute of Biomedical Imaging and Bioengineering of the National Institutes of Health under award number R21EB029154 and by the the National Center for Advancing Translational Sciences, National Institutes of Health, through BU-CTSI Grant Number 1UL1TR001430. Its contents are solely the responsibility of the authors and do not necessarily represent the official views of the NIH.

REFERENCES

- [1] N. Enayati, E. D. Momi, and G. Ferrigno, "Haptics in robot-assisted surgery: Challenges and benefits," *IEEE Reviews in Biomedical Engineering*, vol. 9, pp. 49–65, 2016.
- [2] A. Okamura, "Methods for haptic feedback in teleoperated robot-assisted surgery," *Industrial Robot: An International Journal*, vol. 31, pp. 499–508, 12 2004.
- [3] K. Kume, N. Sakai, and T. Goto, "Haptic feedback is useful in remote manipulation of flexible endoscopes," *Endoscopy International Open*, vol. 06, pp. E1134–E1139, 9 2018.
- [4] M. McCandless, A. Gerald, A. Carroll, H. Aihara, and S. Russo, "A soft robotic sleeve for safer colonoscopy procedures," *IEEE Robotics and Automation Letters*, vol. 6, pp. 5292–5299, 7 2021.
- [5] M. Caeiro-Rodríguez, I. Otero-González, F. A. Mikic-Fonte, and M. Llamas-Nistal, "A systematic review of commercial smart gloves: Current status and applications," *Sensors*, vol. 21, 4 2021.

Design and validation of zero-slack separable manipulator for Intracardiac Echocardiography

Christian DeBuys^{1,2}, Florin Ghesu¹, Reza Langari², and Young-Ho Kim¹

¹Siemens Healthineers, Digital Technology & Innovation, Princeton, NJ, USA

²Texas A&M University, College Station, TX, USA

¹{christian.debuys, florin.ghesu, young-ho.kim}@siemens-healthineers.com, ²{cldebuys, rlangari}@tamu.edu

INTRODUCTION

Intracardiac echocardiography (ICE) catheter, known to have a strong ability to visualize cardiac structures and blood flow from within the heart, is now being favorably used in cardiac catheterization and electrophysiology as an advanced imaging approach. However, clinicians require substantial training and experience to become comfortable with steering the catheter to localize and measure the area of treatment to watch for complications while device catheters are deployed in another access. Thus, it is reasonable that a robotic-assist system to hold and actively manipulate the ICE catheter could ease the workload of the physician.

There exist commercially-available robotic systems [1] and research prototypes [2, 3] for ICE catheter manipulation. They all use existing commercially available ICE catheters (e.g. ACUSON AcuNav ICE catheter family, Siemens Healthineers) based on multiple tendon-sheath mechanism (TSM). To motorize the existing TSM-based ICE catheter, the actuators interface with the outer handle knobs to manipulate four internal tendons. However, in practice, the actuators are located at a sterile, safe place far away from the ICE handle [3]. Thus, to interface with knobs, there exist multiple coupled gear structures between two, leading to a highly nonlinear behavior (e.g. various slack, elasticity) alongside hysteresis phenomena in TSM [2].

Since ICE catheters are designed for single use, the expensive actuators need to be located in a safe place so as to be reusable. Moreover, these actuators should interface as directly as possible with the tendons for accurate tip controls. In this paper, we introduce a separable ICE catheter robot with four tendon actuation: one part reusable and another disposable. Moreover, we propose a practical model and calibration method for our proposed mechanism so that four tendons are actuated simultaneously allowing for precise tip control and mitigating issues with conventional devices such as dead-zone and hysteresis with simple linear compensation. We consider an open-loop controller since many available ICE catheters are used without position-tracking sensors at the tip due to costs and single use.

MATERIALS AND METHODS

Figure 1 explains an overview of the new concept design of ICE catheter robot. The proposed robotic system consists of two parts: “The back portion” contains four Faulhaber linear motors (LM 1483-080-11-C) with motor drivers mounted to a plastic core. The plastic core contains a channel along its central axis for the ultrasound (US) cable and its connector, which are shown in blue in Fig. 1(a). The inter-

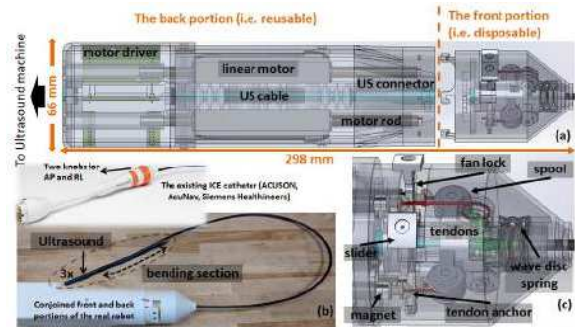


Fig. 1: An overview of the catheter robot.

face from one catheter tendon in “the front portion” shown in Fig. 1(c) to its respective linear motor is as follows: 1) the tendon (green) from the catheter is bent 90 degrees around a low-friction roller and is wrapped around and fastened to the small radius of the spool, 2) a separate tendon (red) is wrapped around and fastened to the large radius of the spool and then attached to the tendon anchor, and 3) the tendon anchor is held in place by the fan lock until the catheter is clipped together and the motor rod has connected to the tendon anchor via magnetic force. The different radii of the spools serve to increase the pulling force of the motors with a 3:1 ratio.

The clipping system functions like closing a child-proof medicine bottle. The clinician pushes the disposable part into the catheter body until it makes contact, pushes slightly farther and twists, then releases to lock the mechanism. Inside the device, the motors move their rods until their magnets make contact with the magnets on the tendon anchors. Finally, the clinician pushes the sliders apart to manually open the fan-lock, and the motors are free to pull on the tendons.

The robot has two degrees of freedom, anterior/posterior (AP) curvature κ_x and right/left (RL) curvature κ_y , and four linear actuators, making this a redundant system with four inputs and two outputs. Whole body translation/rotation are not handled in this paper. A redundant control scheme is used with a constant curvature assumption to resolve and take advantage of this redundancy, in which the energy of the control input is minimized while respecting feasibility constraints (such as requiring a minimum tension for all tendons) as in [4]. We define the robot’s configuration $q = [\kappa_x, \kappa_y]^T$, where curvature is chosen rather than bending angle to obtain linear kinematic and static equations as in [5], and axial compression is considered negligible. We assume quasi-static motion of the catheter governed by the following moment balance equation:

$$\begin{bmatrix} K_b & 0 \\ 0 & K_b \end{bmatrix} \begin{bmatrix} \kappa_x \\ \kappa_y \end{bmatrix} = \begin{bmatrix} -d_{y1} & -d_{y2} & \cdots & -d_{yn} \\ d_{x1} & d_{x2} & \cdots & d_{xn} \end{bmatrix} \begin{bmatrix} T_1 \\ T_2 \\ \vdots \\ T_n \end{bmatrix} \quad (1)$$

where K_b is bending stiffness of the bending section, d_{xi} and d_{yi} are the i^{th} tendon's x and y coordinates relative to the central axis, T_i is the tension in the i^{th} tendon, and $n = 4$ for our device. We can write Eq.(1) in matrix form as $\mathbf{K}\mathbf{q} = \mathbf{D}\boldsymbol{\tau}$. To convert our control input from actuator forces $\boldsymbol{\tau}$ to actuator displacements \mathbf{y} , we consider the conservation of strain equation in [5].

$$\mathbf{y} = (\mathbf{D}^T \mathbf{L}_0 \mathbf{K}^{-1} \mathbf{D} + \mathbf{L}_t \mathbf{K}_t^{-1}) \boldsymbol{\tau} = \mathbf{G}\boldsymbol{\tau} \quad (2)$$

\mathbf{L}_0 , \mathbf{L}_t , and \mathbf{K}_t are diagonal matrices containing the undeformed bending section length l_0 , the unstretched tendon lengths $l_{t,i}$, and the length-normalized tendon stiffnesses $k_{t,i}$, respectively. \mathbf{G} is the compliance matrix. Combining Eq. (1) and (2) we obtain the forward kinematics.

$$\mathbf{q} = \mathbf{K}^{-1} \mathbf{D} \mathbf{G}^{-1} \mathbf{y} \quad (3)$$

\mathbf{K} is diagonal and thus invertible, and \mathbf{G} is invertible for any configuration of non-slack tendons. All parameters in the equations must be determined empirically. \mathbf{L}_0 , \mathbf{L}_t , and \mathbf{K}_t can be measured directly; \mathbf{K} and \mathbf{D} can be approximated by the following parameter identification procedure:

1. Make initial guess for parameters (K,D).
2. Input motor position trajectories which should achieve desired bending angle as calculated from inverse kinematics and redundant control input.
3. Update parameter guesses based on difference between desired and measured bending angle.
4. Repeat steps 2 and 3 until parameter values converge.

The desired bending angle was changed to desired curvature and then converted to the desired motor position inputs using the parameter estimates and by inverting Eq. (3). The inverse kinematics were solved with an energy minimizing redundant control input which included minimum tension constraints to prevent slack [4].

The proposed methods were validated with three trials on a test bed by following a desired sinusoidal output for bending angle in the AP/LR direction. For each trial, the robot followed two cycles of the sinusoid, and the ground truth output angle was measured with an EM sensor, which was only used to evaluate performance. Tip position and bending angle errors were described as mean absolute error (MAE) and standard deviation (StD). Performance was evaluated without and with simple hysteresis compensation. The simple hysteresis compensation involved adjusting the input angle by a constant ± 10 degrees depending on the direction of motion. The backlash width (about 20°) was obtained based on the unique physical properties of the catheter [2].

RESULTS

Figure 2 shows one example of bending angle for without and with our simple hysteresis compensation. The control of all tendons simultaneously allowed the removal of tendon slack and thereby deadzone present in conventional catheters. The overall performance evaluation is described in Table 1. The tip pose errors (MAE) are reported as 4.8 mm and 6.1° . With hysteresis compensation, the position and orientation errors are improved 31% and 47%, respectively.

Table 1: Mean Absolute Error (MAE) and Standard Deviation (StD) for Tip Position and Bending Angle

	Position [mm]	StD	Angle [deg]	StD
no comp.	4.80	1.97	6.11	4.03
comp.	3.31	2.02	3.26	2.90
% reduction	31.0		46.6	

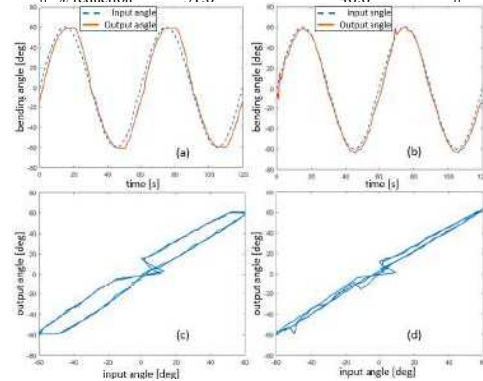


Fig. 2: One result for AP bending: (a) Time versus output angle without compensation (b) Time versus output angle with hysteresis compensation (c)(d) The input angle versus the output angle without/with hysteresis compensation

DISCUSSION

Our proposed design and models are validated in a simple scenario. We plan to investigate more sophisticated controls (e.g., a predictive or learning-based) for complicated scenarios with a systematic evaluation. In the future, we will mount the device to a manipulator which adds whole-body translation and rotation to evaluate control in the full workspace.

DISCLAIMER

The concepts and information presented in this paper are based on research results that are not commercially available.

ACKNOWLEDGEMENT

Research reported in this publication was supported in part by the National Institute of Biomedical Imaging and Bioengineering of the National Institutes of Health under award number R01EB028278. The content is solely the responsibility of the authors and does not necessarily represent the official views of the National Institutes of Health.

REFERENCES

- [1] Stereotaxis, "Stereotaxis v-drive robotic navigation system," 2020, <http://www.stereotaxis.com/products/!vdrive>.
- [2] D.-H. Lee, Y.-H. Kim, J. Collins, A. Kapoor, D.-S. Kwon, and T. Mansi, "Non-linear hysteresis compensation of a tendon-sheath-driven robotic manipulator using motor current," *IEEE Robotics and Automation Letters*, vol. 6, no. 2, 2021.
- [3] Y.-H. Kim, J. Collins, Z. Li, P. Chinnadurai, A. Kapoor, C. H. Lin, and T. Mansi, "Automated catheter tip repositioning for intra-cardiac echocardiography," 2022.
- [4] S. Fang, D. Franitza, M. Torlo, F. Bekes, and M. Hiller, "Motion control of a tendon-based parallel manipulator using optimal tension distribution," *IEEE/ASME Transactions on Mechatronics*, vol. 9, no. 3, pp. 561–568, 2004.
- [5] D. B. Camarillo, C. R. Carlson, and J. K. Salisbury, "Configuration tracking for continuum manipulators with coupled tendon drive," *IEEE Transactions on Robotics*, vol. 25, no. 4, pp. 798–808, 2009.

Multifunctional hybrid module for manipulators

Canberk Sozer¹, Sujit Kumar Sahu^{2,3,4}, Linda Paterno^{2,3}, Arianna Menciassi^{2,3}

¹Department of Automatic Control and Systems Engineering, The University of Sheffield, UK

²The BioRobotics Institute, Scuola Superiore Sant'Anna Pisa, Italy

³Department of Excellence in Robotics & AI, Scuola Superiore Sant'Anna Pisa, Italy

⁴ICube, CNRS, University of Strasbourg, INSA Strasbourg, Strasbourg, France

c.sozer@sheffield.ac.uk

INTRODUCTION

The modularity concept in manipulators relies on connecting multiple elementary structures to achieve more complex and functional systems [1]. It has promising advantages, such as affordability and higher robustness [2], and allows for better adaptability to changing needs, e.g. enlarging the system workspace. Thus, modularity is highly desired in soft robotics applications, from minimally invasive surgery [3] to deep-sea exploration [4].

In this context, the hybrid soft-rigid approach is an effective method that combines different materials to allow for the main benefits of soft (i.e., compliance and a high degree of freedom) and rigid (i.e., force generation and precision) structures [5].

This study proposes a novel hybrid soft-rigid module that combines actuation in 3D space, proprioceptive sensing, and controllable variable stiffness. The general-purpose module has major advantages, such as compactness, lightweight, low-cost, and easy fabrication using a conventional 3D printer. The design and experimental characterization are here reported. The serial integration of three modules is finally shown.

MATERIALS AND METHODS

The overview of the module is given in Fig. 1a. The module is a compact and low-cost solution that combines actuation in 3D space, variable stiffness - both controlled by air pressure -, and proprioceptive sensing. The module is 17 mm in outer diameter with a 3 mm working channel at the centre and 35 mm in length. The weight of the module is 7 g, and the material cost is less than €3 per module.

The module consists of rigid parts (VisiJet M3 Crystal, 3D Systems, USA), rigid yet compliant springs (751-663, RS PRO, UK), soft chambers (Ecoflex 00-50, Smooth-On, USA), and soft stiffness pads (Dragon Skin 10 Medium, Smooth-On, USA) (Fig. 1b).

For actuation, three spring-reinforced soft actuators are equally placed around the module with a 120° distribution, providing the motion ability in 3D space. Each actuator consists of a soft cylindrical pressure chamber and a spring. Upon pressurization of an actuator, the spring limits the radial expansion of the soft chamber but allows for elongation. Thanks to the

rigid ball joint as a rotation centre, the elongation of the actuators allows for omnidirectional bending of the module up to 30° (Fig. 1c). The total bending angle can be increased by integrating multiple modules serially.

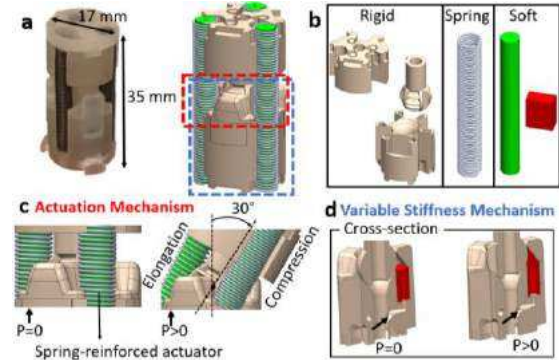


Fig. 1 (a) Overview of the module; (b) module components; (c) actuation and (d) variable stiffness mechanisms.

The spring as a reinforcement element did not only limit the radial expansion of the pressurized soft actuator but also behaved like an inductive sensor for proprioceptive sensing at the same time. The change in the length due to elongation and compression changes the inductance of the spring. The relationship between induced voltage, current, and the geometrical properties of the sensor can be written as follows:

$$V_L = \frac{\mu n^2 A}{l} \frac{dI_L}{dt} \quad (1)$$

where V_L is the induced voltage, μ , n , A , l are core permeability, number of turns, cross-sectional area, and length of the spring, respectively, and $\frac{dI_L}{dt}$ is the rate of current change through the sensor. Eq. (1) shows that the induced voltage is inversely correlated with the length of the sensor. Therefore, it is expected that while the induced voltage of the sensor of the pressurized actuator decreases due to the elongation, the induced voltage of the other two sensors increases due to the compression. Thus, by measuring the voltage of three sensors simultaneously, the bending angle and direction of the module can be estimated.

For variable stiffness, three stiffness pads were placed into the dedicated slots in the bottom rigid part. Upon

pressurization (Fig. 1d), the top membrane of the stiffness pads expands toward the ball joint, and the increased friction between the membrane and joint surface reduces the motion ability of the joint, thus resulting in stiffness enhancement of the module. This approach allowed for tuning the stiffness of the module without position dependency. The bottom rigid part has been designed to pressurize three pads simultaneously to increase the uniformity of the applied force to the ball joint at the centre. The pressure is distributed to the three pads through a structural airway within the rigid structure. Therefore, one inflation tube is enough to control the stiffness of the entire module.

RESULTS

Fig. 2a shows the relationship between applied pressure and bending angle of the module when one actuator is pressurized up to 200 kPa. The module reaches 30° at 120 kPa pressure. Although the pressure continues to increase up to 200 kPa, the bending angles remain the same due to the rigid structure design. The maximum standard deviations for 5 trials were calculated as $\pm 4.4^\circ$ at around 10°, where the friction between rigid parts is maximum. Indeed, the actuators were installed to the rigid structure with pre-elongation. Although this enabled to keep the rigid parts together, increased the friction in between.

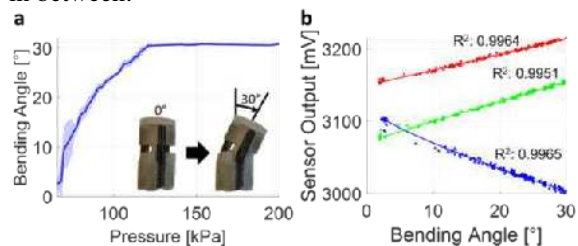


Fig. 2 Relationship between (a) the applied pressure - bending angle and (b) the bending angle - induced voltage at the three sensors (given with R^2 errors to the fitted power curve). Blue colour represents the pressurized actuator. Red and green colours indicate passively compressed actuators. Fig. 2b demonstrates the induced voltage change at the three springs while one actuator is pressurized to bend the module up to 30°. Manual fabrication of the actuators and their instalment inaccuracies to the rigid structure caused variations (i.e., 3153, 3104, and 3076 mV) when they are in the same length at 0° straight position. According to the power curve fitting to 5 trials, the induced voltage at the elongated actuator decreases (100 mV) while the induced voltage at the passively compressed other two actuators increases (80 and 61 mV), thus providing sufficient change to be correlated with the bending angle and bending direction of the module.

Fig. 3 presents the controllable variable stiffness capability of the module. For this experiment, stiffness pads were pressurized up to 500 kPa with 100 kPa intervals when the module was fixed at 0°. Then, a force sensor was pushed toward the module for 3 mm and the force was recorded. Finally, the recorded last force value was divided by the displacement (i.e., 3 mm). According to the average

of 5 trials, upon pressurization, the stiffness of the module can be increased by up to 95% (from 0.12 to 0.23 N/mm) in a controllable way.

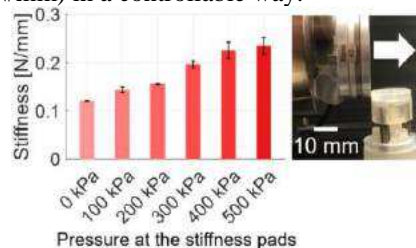


Fig. 3 Experimental result of the relationship between pressure at the stiffness pads and the stiffness of the module.

DISCUSSION

The study reports the design and experimental characterization of a module that is compact, low-cost, lightweight, and easy to fabricate using a conventional 3D printer.

The module that combines actuation in 3D space, proprioceptive sensing, and controllable variable stiffness is proposed as a general-purpose technology. Therefore, it can be adapted to use in a wide range of applications. For example, a multifunctional endoscope can be built by integrating multiple modules for steering a biopsy forceps in the tortuous shape of the colon. As shown in Fig. 4a, both single and double curvature can be achieved by tuning the actuation and variable stiffness structure, properly. Alternatively, an ultrasound tool can be attached to the tip of the endoscope (Fig 4b) to deliver non-invasive ultrasound therapy.

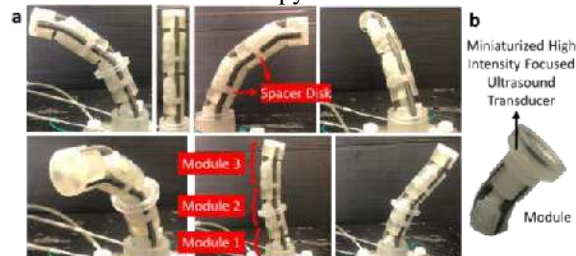


Fig. 4 Modular manipulator by integrating three modules in various configurations.

REFERENCES

- [1] S. S. R. Chennareddy, A. Agrawal, and A. Karupiah, 'Modular Self-Reconfigurable Robotic Systems: A Survey on Hardware Architectures', *J. Robot.*, vol. 2017, pp. 1–19, 2017.
- [2] C. Zhang, P. Zhu, Y. Lin, Z. Jiao, and J. Zou, 'Modular Soft Robotics: Modular Units, Connection Mechanisms, and Applications', *Adv. Intell. Syst.*, vol. 2, no. 6, p. 1900166, Jun. 2020.
- [3] A. Arezzo *et al.*, 'Total mesorectal excision using a soft and flexible robotic arm: a feasibility study in cadaver models', *Surg. Endosc.*, vol. 31, no. 1, pp. 264–273, Jan. 2017.
- [4] B. T. Phillips *et al.*, 'A Dexterous, Glove-Based Teleoperable Low-Power Soft Robotic Arm for Delicate Deep-Sea Biological Exploration', *Sci. Rep.*, vol. 8, no. 1, p. 14779, Dec. 2018.
- [5] C. Sozer, L. Paternò, G. Tortora, and A. Menciassi, 'A Novel Pressure-Controlled Revolute Joint with Variable Stiffness', *Soft Robot.*, p. soro.2020.0196, Jul. 2021.

Finite Element Dynamics of a Concentric Tube Robot Motion and Interaction with Environment Using SOFA-framework

Katie Zuo, Benjamin Jackson, Ross Henry,
Christos Bergeles, S.M.Hadi Sadati*

School of Biomedical Engineering & Imaging Sciences, King's College London, UK.

**smh_sadati@kcl.ac.uk*

INTRODUCTION

The concept of continuum and soft robotics has opened new abilities that were previously unachievable by rigid robotics alone, such as squeezing, growing, and morphing to their environments. As an example, Concentric Tube Robots (CTR) are continuum robots made of a series of pre-curved, elastic tubes where each tube can individually be rotated, as well as extended and recalled; interactions between each tube allows for turns and twists, giving control over the length and configuration of the robot. CTRs can assist in minimally invasive surgery (MIS) to access difficult to reach areas, due to the intricate human anatomy, with advantages including single-site entry and their malleable nature [1]. However, utilizing CTRs, and continuum robots in general, are not without their own challenges. Due to the complex nature of a continuum structure, fast and accurate simulations are still in development and require specific skills to operate. These simulations are not usually accurate due to the complex behaviours of the materials used and their deformable nature.

SOFA (Simulation Open Framework Architecture) was introduced as an open-source platform to address some of the challenges with real-time physics-based simulation of interaction with deformable tissue in medical applications and later for modelling soft robots. More specifically, a BeamAdapter plugin² was developed based on interpolation of a continuous geometry over multiple consecutive Timoshenko beam segments to address the simulation challenges of neurovascular interventions using interleaved catheters and guidewires [2]. The BeamAdapter plugin has been also utilized for interactive planning of coil embolization in brain aneurysms [3] and interactive training system for interventional electrophysiology procedures [4].

We have recently developed a Reduced-Order dynamic model for CTRs based on the shape interpolation of the robot backbone and showcased its real-time performance, correct estimation of the path-dependent motions and snapping instances, accurate simulations of stable and post-snapping motions in an experimental comparative study [5]. In this paper, we outline the process and the code on how a CTR model can be implemented into an example scene provided as a part of the SOFA-framework 'BeamAdapter' plugin [2]. The

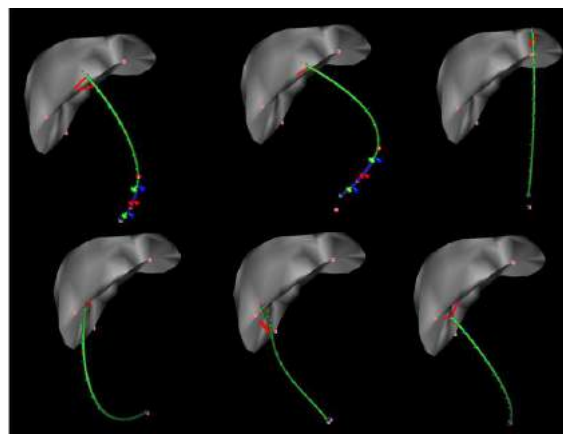


Fig. 1. FEM simulation of a CTR interaction with a liver.

simulation results are evaluated experimentally. We showcased a more complex simulation scenarios with the robot interactions with a deformable model of a liver (see Fig. 1), and a brief discussion on how the results from this study can guide the further development of the plugin.

MATERIALS AND METHODS

SOFA Framework: 'BeamAdapter' plugin: Real-time Finite Element Model (FEM) for dynamic simulations of a CTR and its interactions with a realistic and deformable organ anatomy have yet to be developed. The example scene that is provided with the plugin contains three precurved tubes (a catheter, a guide sheath, and a coil), a keyboard control interface for linear and rotational actuation of the tubes, and collision models for their interaction with a FEM of a sample vascular system. The plugin supports 2D (circular) or 3D (spiral) initial shape for the tubes, with options to alter parameters such as the tube inner and outer diameters, material density, Young's modulus, and Poisson's ratio to aid in its realistic interactions between different materials. The simulation accuracy and numerical performance can be adjusted to achieve the desired system behaviour or real-time performance.

CTR Model implementation & Experimental Verification: The example scene from the BeamAdapter plugin repository was adapted to model a 3-tube CTR (see Fig. 2). The parameters of a 2-tube CTR setup, as in [5] (see Fig. 3), was used to experimentally validate the presented model. The model parameters used are summarized in Table I.

An experimental scenario consisting of independent 550 deg clockwise and counter clockwise rotation (u_ϕ) of

This work was supported in part by ERC Starting under Grant 714562, by core funding from the Wellcome/EPSCRC Centre for Medical Engineering, Wellcome Trust [WT203148/Z/16/Z], and an NIHR Cardiovascular MIC Grant.

²<https://github.com/sofa-framework/BeamAdapter>

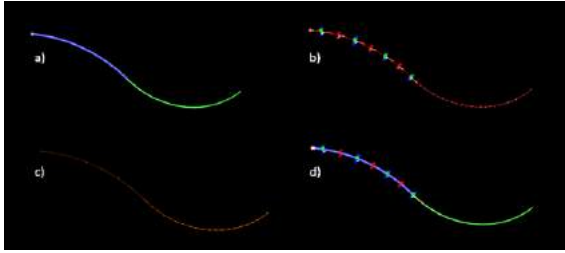


Fig. 2. Representations of different mappings used to model a 3-tube CTR using SOFA: (a) visual model, (b) behaviour model, (c) collision model, (d) visual and behaviour model.

each tube (see Fig. 4) was replicated through the plugin keyboard control interface ‘InterventionalRadiologyController’. The resulting return-motion-cycle for each tube consisted of two snapping instances to highlight the model capability in capturing system unstable configurations and the resulting rapid motion. The CTR tip position, which is associated with the last defined state in the scene, was recorded using the ‘WriteState’ module and plotted in Matlab for comparison with the experimental data and a dynamic modeling framework recently presented in [5].

RESULTS

The developed model could effectively interact with the deformable model of a liver while preserving the simulation real-time performance and numerical stability (see Fig. 1).

The FEM simulation results in comparison with the experimental data (exp) and a recently introduced Reduced-Order Model (ROM) for a CTR dynamics, based on shape interpolation, are presented in Fig. 4. The SOFA-based FEM simulations neither could predict the snapping instances nor simulate the resulted rapid motion. Even though the utilized theory by the BeamAdapter plugin accounts for the damping and torsional stresses, there is no specific parameter to change a tube shear modulus or material damping values in the scene. In our simulation based on ROM techniques, we found it crucial to be able to fine-tune the values for the material damping, shear, and Young’s moduli independently to be able to capture the snapping behavior and hysteresis effects in the motion of a real CTR (see Fig. 4). Our results highlighted the potential and roadmap to improve the BeamAdapter plugin for FEM of a CTR dynamics.

DISCUSSION

In this paper, we utilized the SOFA-framework BeamAdapter plugin to present the first Finite Element model for the dynamics of a CTR dynamics and its interaction with a deformable environment, in this case a liver. Such a simulation framework has substantial application in modeling, control, automation, and user training for medical CTRs. Our experimental study highlighted the need for improving the plugin by providing access to the tubes’ material shear modulus and damping, the possibility to pre-program and record the

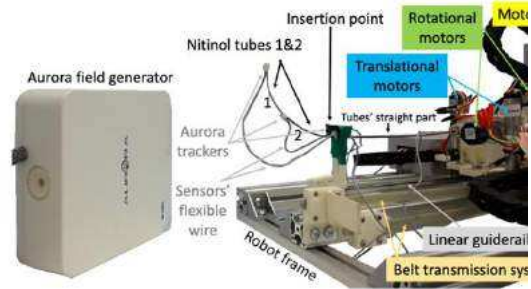
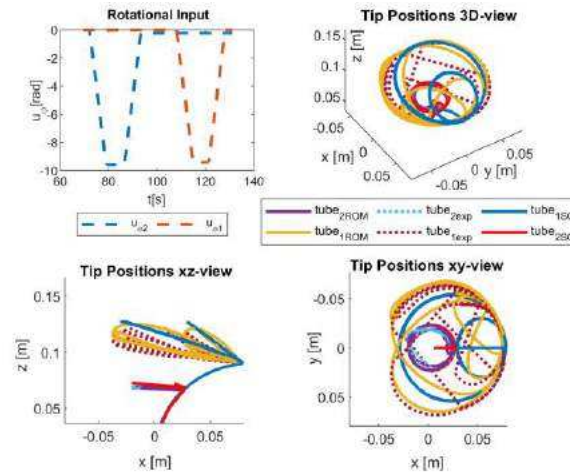


Fig. 3. CTR experimental setup as in [5].

Table 1. CTR setup parameters to use with wireRestShape module from BeamAdapter plugin.

Tube #	1 (inner)	2 (outer)
Inner Radius [mm]	0.35	0.7
Outer Radius [mm]	0.55	0.9
Overall Length [mm]	309	275
Straight Length [mm]	164	161
Curve Mean Diameter [mm]	136	157.5
Curvature Correction Factor	1.214	1.174
Initial Inserted Length [mm]	134	77
Young’s Modulus* [GPa]	77	74.4
Material - Density [Kg/m ³]	Niti - 6450	Niti - 6450



system input values, and easier means to record the configuration of the individual tubes’ tip.

REFERENCES

- [1] Z. Mitros et al. ‘From Theoretical Work to Clinical Translation: Progress in Concentric Tube Robots’, Annual Rev Control, 2021.
- [2] Y. Wei et al. ‘A (near) real-time simulation method of aneurysm coil embolization’, Aneurysm, InTech, 2012.
- [3] J. Dequidt et al. ‘Towards interactive planning of coil embolization in brain aneurysms,’ MICCAI, 2009.
- [4] H. Talbot et al. ‘Interactive training system for interventional electrophysiology procedures,’ Med Image Anal, Elsevier, 2017.
- [5] S. Sadati et al. ‘Real-Time Dynamics of Concentric Tube Robots with Reduced-Order Kinematics Based on Shape Interpolation,’ IEEE RA-L, 2022.

A Sensorized Needle-Insertion Device for Characterizing Percutaneous Thoracic Tool-Tissue Interactions

Rachael L'Orsa^{1,2,3}, Kouros Zareinia⁴, David Westwick¹,
Garnette Sutherland², and Katherine J. Kuchenbecker³

¹Department of Electrical and Software Engineering, University of Calgary,

²Surgical Performance Laboratory, Project neuroArm, University of Calgary,

³Haptic Intelligence Department, Max Planck Institute for Intelligent Systems,

⁴Department of Mechanical and Industrial Engineering, Ryerson University
ralorsa@ucalgary.ca

INTRODUCTION

Tube thoracostomy (TT), where a tube is placed between the lungs and the chest wall to drain air and/or fluids introduced by injury or disease, is a crucial procedure with both routine and emergent applications. It has high complication rates (up to 37.9%) [1], particularly for residents [2] and emergency physicians [3]. Inadvertent tissue punctures during insertion can cause severe complications, including rare immediate fatality [4]. We propose semi-automating TT tool insertion, as merging the accurate haptic sensing capabilities of a medical robot with the dexterity and perspicacity of a physician could help protect against non-target tissue puncture. To avoid insertional complications, operators must a) position and b) orient tools correctly, and must c) halt insertion immediately upon breaching the parietal pleural membrane. We focus here on preliminaries required for c) and leave a) and b) to future work. We report a prototype sensorized needle-insertion device named NIDO that records manual tool-tissue interactions with *ex vivo* porcine ribs, a realistic tissue phantom for TT [5], from contact to puncture of the parietal pleura. The acquired dataset showcases tissue characteristics and informs future puncture detection algorithms.

MATERIALS AND METHODS

NIDO combines a linear stage (DDS300-E/M with BBD201 controller from Thorlabs, USA) with a six-axis force/torque sensor (Mini40 with amplifier from ATI, USA), a three-axis accelerometer (EVAL-ADXL354BZ from Analog Devices, USA), two cameras (C922s from Logitech, Switzerland), and a custom tissue mount. Data are collected via a multifunction I/O device (USB-6215 from National Instruments, USA) communicating with QUARC real-time control software (Quanser, Canada) in Simulink 9.1 (Mathworks, USA) on a desktop PC (Zoostorm with i5-6400 processor). The two audio/video streams are recorded simultaneously at 60 frames per second via OBS Studio (H. Bailey and OBS Project

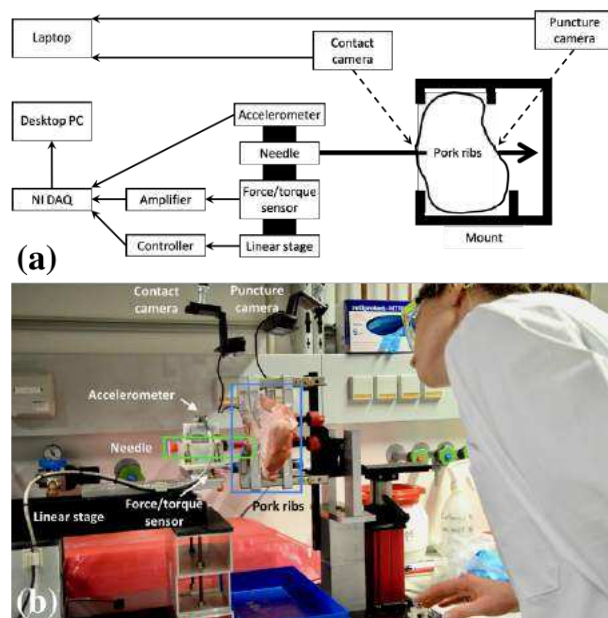


Fig. 1 (a) Block diagram of the system. (b) NIDO being used to collect *ex vivo* insertion data.

contributors) on a laptop (Dell Latitude with i7-6600U processor). Both computers use Windows 10. Figure 1 (a) depicts NIDO's system-level design, while Fig. 1 (b) shows the physical apparatus in use.

Operators manually advance the stage carriage such that a bevel-tip 9 cm, 18G needle (Cook Medical, USA) contacts and punctures intercostal spaces within fresh, room-temperature, commercially available pork ribs. Rib sections are secured at four corners in the custom mount, which positions the ribs perpendicularly to the needle-insertion axis and allows for natural intercostal tissue displacement in response to needle forces. Manual taps on the NIDO frame synchronize the audio/video streams with their data counterparts during each trial. An author manually labels contact and puncture events in trial videos, and post-processing scripts in Matlab r2020a (Mathworks, USA) map event labels to data streams.

TABLE I Mean and standard deviation of insertion force, velocity, penetration depth, and duration for all trials.

Collection	n	Mean Force [N]	Maximum Force [N]	Mean Velocity [mm/s]	Maximum Velocity [mm/s]	Penetration Depth [mm]	Duration [s]
Session 1	28	1.8 ± 0.5	3.3 ± 1.3	18.9 ± 6.0	81.1 ± 23.8	33.7 ± 10.2	2.3 ± 0.7
Session 2	17	2.0 ± 0.8	4.1 ± 1.7	29.3 ± 9.1	92.0 ± 39.3	38.5 ± 3.2	1.8 ± 0.5
Session 3	18	0.5 ± 0.1	1.0 ± 0.2	22.5 ± 6.4	54.6 ± 13.3	19.0 ± 2.3	1.5 ± 0.5
All sessions	63	1.5 ± 0.8	2.9 ± 1.7	22.7 ± 8.2	76.5 ± 30.1	30.8 ± 10.5	1.9 ± 0.7

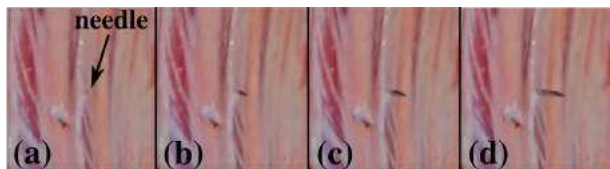


Fig. 2 The needle ruptures the pleural membrane in stages: (a) membrane displacement, (b) tip perforation, (c) bevel emanation, and (d) full needle penetration.

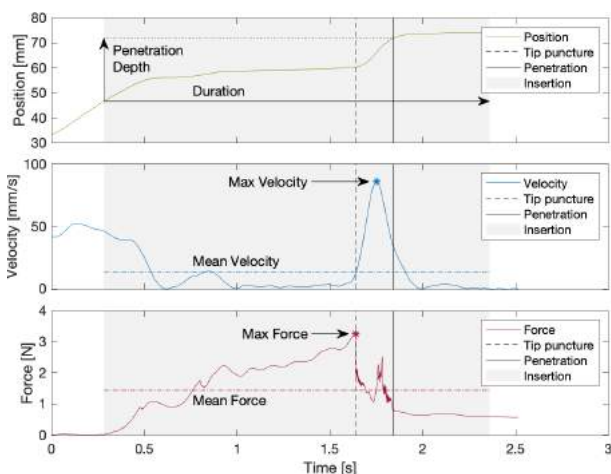


Fig. 3 Position, velocity, and force during a typical Session 1 trial, with forward (gray) needle motion and metrics labeled.

Basic statistical measures are extracted and analyzed in Minitab 21 (Minitab Inc., USA).

RESULTS

Non-medical operators performed 63 manual insertions across three sessions, where each session had its own tissue sample. Visible membrane rupture occurs in stages (Fig. 2); we define puncture as needle tip perforation because it provides the most reliable force signature. Generally it presents as the first rapid decrease in force (dashed line in Fig. 3) and can accompany both increasing and decreasing needle velocity due to the manual nature of insertions. Tissue inhomogeneity can yield a region characterized by one or more rapid force decreases between tip puncture and full needle penetration, i.e., between dashed and solid vertical lines. Table I lists mean and max force, mean and max velocity, penetration depth, and duration within sessions and overall. Table II contains the results of a three-way analysis of variance, which identifies sessions as a statistically significant factor affecting maximum insertion force.

TABLE II Analysis of variance (ANOVA) for maximum insertion force, $\alpha = 0.05$.

Source	DF	Adj SS	Adj MS	F-Value	P-Value
Session	2	20.8	10.4	7.47	0.001
Mean Velocity	1	0.1	0.1	0.05	0.820
Max Velocity	1	2.9	2.9	2.06	0.157

DISCUSSION

We present a sensorized data-collection device and apply it to a critical step in tube thoracostomy using an *ex vivo* model. We report the haptic response of the parietal pleura, which is poorly documented in the literature. Metrics varied significantly across sessions due to the different tissue samples employed, matching anecdotal physician reports of high inter-patient variability. The identified force maximums will inform future tissue phantom and robot designs, and patterns visible in the data will be used to develop real-time methods for pleural membrane puncture identification. Tissue variation due to the time interval between harvesting and experimentation is a limitation of this work. Furthermore, it is important to consider live pleura with respiratory rhythm and pulsatile blood flow, versus an *ex vivo* model such as this. Next steps include automating needle insertion to enable consistent tissue characterization and analyzing how a wider range of factors affect puncture force.

ACKNOWLEDGMENTS

The authors thank M. Wieland and P. Kress for their assistance. We acknowledge funding from the Vanier Canada Graduate Scholarship, the Alberta Innovates Technology Futures Graduate Student Scholarship, and the German Academic Exchange Service (DAAD).

REFERENCES

- [1] C. Platnick, C. E. Witt, F. M. Pieracci, C. K. Robinson, R. Lawless, C. C. Burlew, E. E. Moore, M. Cohen, and K. B. Platnick, "Beyond the tube: Can we reduce chest tube complications in trauma patients?" *Am J Surg*, vol. 222, no. 5, pp. 1023–1028, 2021.
- [2] V. Kong, G. Oosthuizen, B. Sartorius, C. Keene, and D. Clarke, "An audit of the complications of intercostal chest drain insertion in a high volume trauma service in South Africa," *Ann R Coll Surg Engl*, vol. 96, no. 8, pp. 609–613, 2014.
- [3] M. Careau, C. Malo, V. Boucher, and M. Émond, "P110: Chest tube thoracostomy in the ED: predictors of complications," *CJEM*, vol. 22, no. S1, pp. S104–S105, 2020.
- [4] S. Metsel, Z. Ram, I. Priel, D. Nass, and P. Lieberman, "Another complication of thoracostomy—perforation of the right atrium," *Chest*, vol. 98, no. 3, pp. 772–773, 1990.
- [5] C. Van Doormaal, D. Howes, C. Salazar, and C. Parker, "An innovative and inexpensive pork ribs model for teaching tube thoracostomy," *Ann Emerg Med*, vol. 58, no. 4, p. S215, 2011.

Toward Bipolar Electrosurgery with Concentric Tube Robots

Jesse F. d’Almeida¹, Margaret Rox¹, and Robert J. Webster III¹

¹*Department of Mechanical Engineering, Vanderbilt University, Nashville, TN, 37212*
jesse.f.dalmeida@vanderbilt.edu

INTRODUCTION

Some of the earliest clinical motivations for concentric tube robots (CTRs) involved procedures which are often accomplished via electrosurgery [1], [2]. However, the development of electrosurgery in physical prototypes was initially left to future work, as early research focused on mechanics-based models and model-based control methods [3], [4]. In recent years, monopolar electrosurgery has been delivered through CTRs in physical prototypes [5], [6]. Since the ground is attached elsewhere on the patient’s body, monopolar tools typically simply require an exposed metal tip to cut.

Bipolar tools, in contrast, carry two electrodes, are traditionally made in the shape of a forceps with each jaw containing one of the electrodes. Bipolar electrosurgery has several general advantages over monopolar, in applications where it can be used, including more localized heating and lower voltages, which lead to a lower risk of injury to the patient [7]. Motivated by these advantages, a bipolar electrosurgery forceps has been designed for delivery through for CTRs [8].

In this paper we propose an alternate approach in which the CTR itself acts as one of the active electrodes, with the other delivered through the CTR’s central lumen. We demonstrate teleoperated tissue cutting using a concentric tube robot equipped with this approach to electrosurgery.

MATERIALS AND METHODS

While typical bipolar electrosurgery tools include two electrodes, incorporating two of these down the central lumen of a CTR with appropriate insulation either limits the diameters of the electrodes, or requires relatively larger-diameter concentric tube robots than may otherwise be desirable. Fortunately though, the CTR itself is made of conductive metal (a nickel-titanium alloy called Nitinol) and can function as one of the electrodes. This leaves the entire internal lumen for the other electrode. The following describes our preliminary tests in developing this prototype bipolar tool.

A. Design of the Electrosurgery Tool

We chose 30 AWG wire to function as our active electrode, as it is rated for a high level of current while being small enough (1.2 mm diameter with insulation) to fit within the inner tube of the existing tube set on the

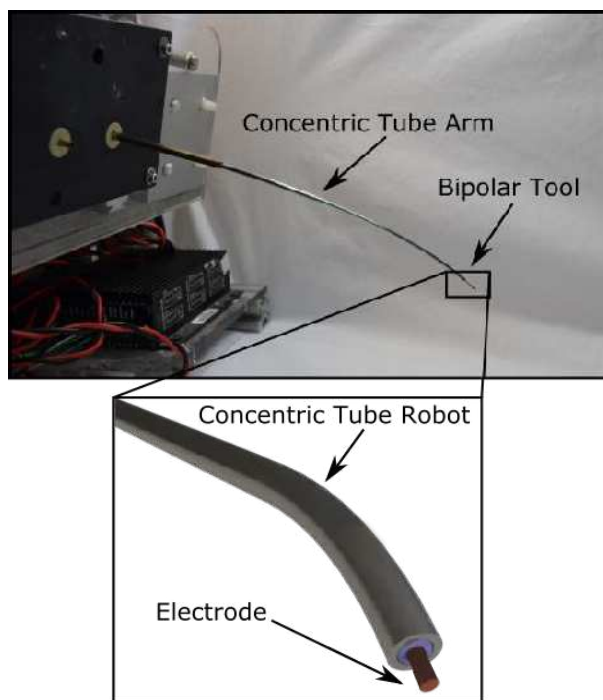


Fig. 1 (Top) Image of the electrosurgery tool mounted to the bimanual robot (Bottom) Close up model of the electrosurgery tool in which a wire passing through the concentric tubes acts as the active electrode to bring power to the tip of the tool and the nitinol tube itself functions as the return path for the current.

robot. We further selected wire with a silicone insulation that was capable of withstanding temperatures of 200°C, so that the wire would not melt during use. The wire was passed through the central lumen of our CTR prototype, and a cable was soldered to the inner tube to attach to an electrosurgical unit (ESU). For our ESU we used an RF Cautery generator (Basco India, Chennai, India). A small section of exposed wire protruded from the tip of the tube, enabling current to flow between this active section and CTR itself when in contact with tissue or in a saline solution. A model of the system is shown in Figure 1. Our ESU is capable of producing 100 W on a 100 ohm load for bipolar cutting, at frequencies of 2MHz. We selected the ESU intensity setting of 1.5 for cutting tissue. We also used a thermal imaging camera to estimate the heat produced by the tool while operational.

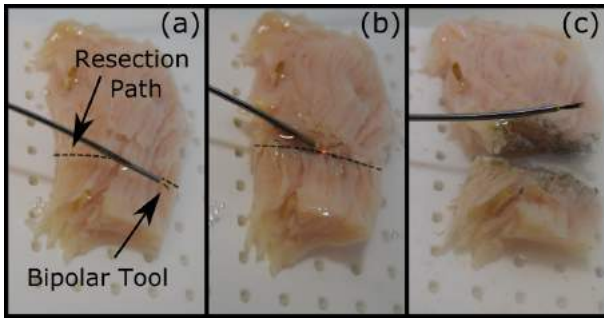


Fig. 2 The experimental results of resection with the robotically operated electro-surgery tool in which chicken breast was cut along the dotted line; shown before (left), during (middle) and after (right) the experiment.

TABLE I Tube Parameters used in CTR

Tube	OD (mm)	ID (mm)	Curvature (m^{-1})
Inner	1.68	1.34	4.5
Middle	2.32	1.87	2.1
Outer	3.80	2.75	0

B. Teleoperated Electrosurgical Tissue Cutting

The robot we used for testing was previously developed in [9], which uses a three tube manipulator and can be teleoperated via a Phantom Omni haptic device (3D Systems, Rock Hill, South Carolina, USA). The tube set, with parameters shown in Table I, consisted of a straight outer tube and curved middle and inner tubes.

To validate the performance of the electro-surgery tool, we sought to emulate the resection of a tumorous portion of tissue by using the bipolar tool to cut apart a portion of chicken breast tissue. A piece of tissue was secured to a 3D printed platform and submerged in a bowl of saline solution. We then teleoperated the robot with our bipolar tool attached to manually resect the desired portion of tissue.

RESULTS

We were successfully able to teleoperate the robot with the electro-surgery tool to resect a portion of chicken breast tissue. The results of this experimental resection are shown in Figure 2. A thermal image of the tool in operation is shown in Figure 3.

DISCUSSION

This paper describes our initial work toward integrating bipolar electro-surgery into a concentric tube robot. With minimal cost and effort, we were able to successfully create a concentric tube robot capable of cutting chicken breast. Much future work remains to be done to optimize electro-surgical cutting, including in-depth evaluation of all materials choices, tool tip geometry as it relates to not only cutting but also coagulation, and electrical voltages and power levels used. Ideally bipolar electro-surgery involves the generation of local plasma at the cutting tip, which requires an ESU capable of sophisticated closed-loop control of the cutting process based on electrical feedback. The

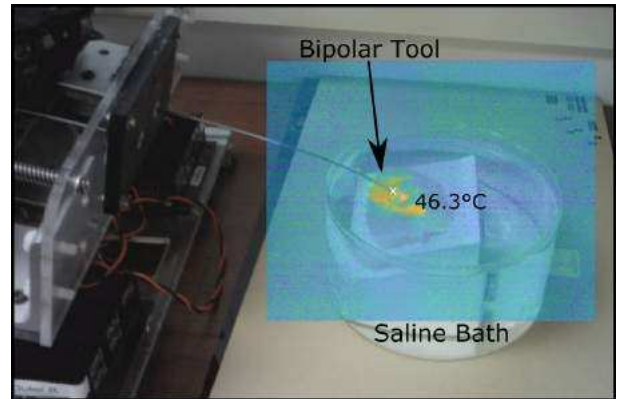


Fig. 3 Thermal image of bipolar tool cutting chicken breast along a path overlaid on the optical image. The maximum temperature in this instance was measured to be 43.6° .

ESU we used in this paper, while inexpensive, is not designed to facilitate plasma-based cutting. Furthermore, integration of our electro-surgery concept into a complete system suitable for deployment in a practical operating room will also be needed before these results can be clinically deployed.

REFERENCES

- [1] R. J. Hendrick, C. R. Mitchell, S. D. Herrell, and R. J. Webster, "Hand-held transendoscopic robotic manipulators: A transurethral laser prostate surgery case study," *Int J Rob Res*, vol. 34, no. 13, pp. 1559–1572, Nov 2015.
- [2] C. Bergeles, A. H. Gosline, N. V. Vasilyev, P. J. Codd, P. J. del Nido, and P. E. Dupont, "Concentric tube robot design and optimization based on task and anatomical constraints," *IEEE Transactions on Robotics*, vol. 31, no. 1, pp. 67–84, 2015.
- [3] D. C. Rucker, B. A. Jones, and R. J. Webster III, "A geometrically exact model for externally loaded concentric-tube continuum robots," *IEEE Transactions on Robotics*, vol. 26, no. 5, pp. 769–780, 2010.
- [4] P. E. Dupont, J. Lock, B. Itkowitz, and E. Butler, "Design and control of concentric-tube robots," *IEEE Transactions on Robotics*, vol. 26, no. 2, pp. 209–225, 2010.
- [5] E. J. Butler, R. Hammond-Oakley, S. Chawarski, A. H. Gosline, P. Codd, T. Anor, J. R. Madsen, P. E. Dupont, and J. Lock, "Robotic neuro-endoscope with concentric tube augmentation," in *2012 IEEE/RSJ International Conference on Intelligent Robots and Systems*, 2012, pp. 2941–2946.
- [6] L. Harvey, R. Hendrick, N. Dillon, E. Blum, L. Branscombe, S. Webster, R. J. Webster III, and T. Anderson, "A Novel Robotic Endoscopic Device Used for Operative Hysteroscopy," *Journal of Minimally Invasive Gynecology*, vol. 26, no. 7, pp. S8–S9, 11/2019 2019. [Online]. Available: <https://doi.org/10.1016/j.jmig.2019.09.03>
- [7] G. A. Vilos and C. Rajakumar, "Electrosurgical Generators and Monopolar and Bipolar Electro-surgery," *Journal of Minimally Invasive Gynecology*, vol. 20, no. 3, pp. 279–287, may 2013.
- [8] C. Lutfallah, T. Looi, and J. Drake, "A novel bipolar cautery tool for minimally-invasive neuroendoscopic procedures," in *2020 42nd Annual International Conference of the IEEE Engineering in Medicine Biology Society (EMBC)*, 2020, pp. 6062–6065.
- [9] J. Burgner, P. J. Swaney, D. C. Rucker, H. B. Gilbert, S. T. Nill, P. T. Russell III, K. D. Weaver, and R. J. Webster III, "A Bimanual Teleoperated System for Endonasal Skull Base Surgery," in *IEEE/RSJ International Conference on Intelligent Robots and Systems*, 2011, pp. 2517–2523.

Design of a Robotic Traction Device for Endoscopic Submucosal Dissection

Flora Fung LEUNG¹, Chun Ping LAM¹, Lap Wing CHEUNG¹, Donald Ngo Fung IP¹, Yeung YAM^{1,3,4}, Philip Wai Yan CHIU^{2,3,4}, *Ka Chun LAU^{1,4}

¹Department of Mechanical and Automation Engineering; ²Department of Surgery; ³Chow Yuk Ho Technology Centre for Innovative Medicine; ⁴Multi-scale Medical Robotics Center, The Chinese University of Hong Kong
fleung@link.cuhk.edu.hk, *Corresponding author: kclau@mrc-cuhk.com

INTRODUCTION

Endoscopic Submucosal Dissection (ESD) for the removal of large lesions en-bloc is an emerging endoscopic technique [1]. However, the often blocked surgical view by dissected mucosa prolongs the time for operation, steepens the learning curve, and increases the risk of complications. Traction assisting methods are used widely to increase exposure to the submucosal surgical field. Cost-effective methods such as magnetic anchor and clip-and-string offer effective independent retraction but limiting to uni-direction. Secondary hand methods, including the use of external forceps, double-balloon, and robotic-assisted systems [2], are more dexterous in tissue manipulation but suffer from coupling lifter and dissector motion. Recent bimanual endoscopic robots prompt to provide an optimal solution but the long development time and large investment involved hinder the ready applicability of these complex systems. In this work, we aim to explore a portable robotic platform that provides dexterous tissue manipulation to comprehend the dynamics in ESD, as an alternate and reference to the more advanced robotic platform.

MATERIALS AND METHODS

The robotic traction device (RTD) we proposed consists of a passive bending section, a flexible robotic lifter, an actuation unit, and a single-hand controller as figure 1 shows. The passive bending overtube is customizable for most commercial endoscopes. It provides an over-the-scope accessory channel for the robotic lifter. A flexible 4-Degree-of-Freedom (DoF) robotic lifter is developed for three-dimensional tissue manipulation. The articulated continuum structure allows bending in pitch-yaw directions and translation in the proximal-distal direction. An open-close single-DoF gripper is equipped at the tip to provide grasping motion. Such arrangement forms a cylindrical workspace with two proximally convex dome-shaped bases. The isolated translation allows intuitive adjustment for the optimal traction strength without relocation of the grasper.

The robotic lifter has a diameter of 3.8 mm, a 9.9 mm commercial gastroscope is used and the overtube diameter is 19 mm. A 4.2 mm working channel made of ePTFE is used. The passive bending overtube is produced by FDM process (PLA) and the robotic lifter is produced by CNC machining (PEEK and SUS316). Most actuators of the robotic lifter are placed proximally utilizing the

tendon-sheath mechanisms (TSM), one actuation unit consisting of a DC motor and a rack-and-pinion mechanism is developed for the translation of the robotic lifter and is attached to the endoscope's controller.

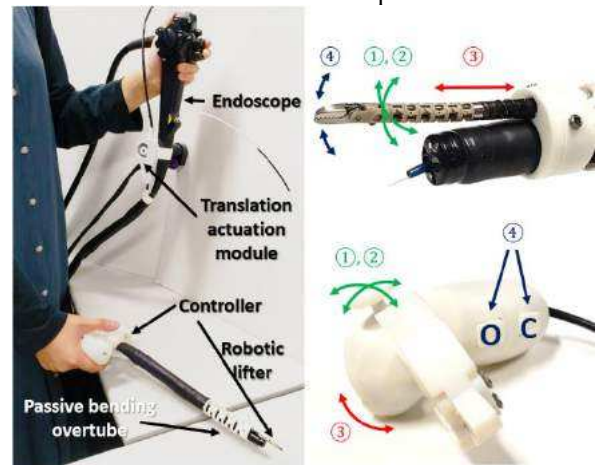


Fig. 1 Left: the overview and the components of the robotic traction device (RTD); right: the motion mapping between the robotic traction device and the hand-held controller.

Decoupling between the robotic lifter and the endoscope is achieved by the distally mounted overtube. As the robotic lifter engages, it “stiffens” the overtube and partially constrained the bending section of the endoscope. As a result, the unconstrained part of the endoscope moves pseudo-independently from the robotic lifter, as demonstrated in figure 2. During RTD-assisted ESD, a well-exposed view of the submucosal surgical site can be obtained and maintained stably throughout the dissection thanks to this unique decoupling feature.



Fig. 2 A silicon rubber mimicked mucosa tissue is used to demonstrate an RTD-assisted endoscopic resection, both the lifter and the dissector can be controlled independently, and their motions are decoupled.

Besides, some critical design criteria are addressed to ensure the usability of the platform, in particular: 1) To prevent degradation of overall flexibility, hinge joints are used for the passive bending overtube to minimize the stiffness added to the endoscope. 2) The hand-held

controller is developed for the sole operation of both the endoscope and the dexterous robotic instrument.

The continuum section of the robotic lifter has a maximum bending angle of 120 degrees and is modeled with the piecewise constant curvature assumption. A feedforward controller runs at 50 Hz to compensate for the friction loss. The lifting force of the robotic lifter is measured to be $\sim 1\text{N}$. In an experiment, a weight of 100g was fixed at the tip of the robot arm and lifted repeatedly for 10 times from the neutral position. No twisting and significant buckling of the manipulator was observed.

RESULTS

RTD-assisted ESD was performed on an explanted pig stomach to verify the feasibility of the system. On a pre-marked, injected, and initially incised target area, ESD was performed with RTD installed on a commercial endoscope and a needle knife through its working channel. The operator has no experience in controlling an endoscope. Figure 3 shows the experimental setup. A specimen of 35 mm size was dissected in 30 minutes. Although the dissection time is shorter than the average ESD operation time for specimens of similar size, the results cannot be compared directly due to the ease of conditions with the explanted model used. The experiment aims to perform a preliminary test on the platform built, whereas the effectiveness of the system should be studied with more subjects in a more controlled and realistic environment. The experiment result confirmed the effectiveness and potential of the proposed system in providing multidirectional and independent tissue traction motion in conventional ESD. Figure 4 shows a typical lifting, pulling, advancing, and cutting motion during the ESD. The future clinical study will focus on animal tests to further evaluate the performance of RTD.

DISCUSSION

Among the conventional traction methods developed by the industry and the more advanced bimanual robotic platforms [3], the proposed traction device provides a practical solution that can be seamlessly adapted into current procedures. Although not being the first to propose similar ideas, the significance of this work is the decoupled motion between the lifter and dissector which is not achieved by others. The two-step stiffness feature of the endoscope through changing the insertion stage of the flexible robotic lifter makes the surgeons capable of 1) performing usual endoscopy when the lifter is retracted and, 2) conducting ESD procedures when the lifter is inserted for traction and the workspace of the endoscope is partially constrained to the distal section.

The main limitation of the proposed system is the size of the overtube and the inevitable loss of flexibility at the lifter engaged stage. The optimal overtube sizes for the upper and lower GI tract are less than 14 mm and 18 mm respectively. The diameter of the overtube can be reduced with a finer manufacturing method and stronger materials. Additional features such as a tapered tip can be added to ensure smooth insertion. The loss of flexibility causes the proposed platform insufficient to cover

operations in some special cases such as retroflexion. Other approaches such as a more dexterous or variable stiffness overtube might be explored in the future to improve this aspect.



Fig. 3 Ex-vivo test setup: a commercial endoscope system, and the diathermy machine; the passive bending overtube and the translation actuation module were installed on the endoscope to channel the robotic lifter; a cart for actuation motors is located beside the operator who held the controllers of the endoscope and the robotic lifter in separate hands.

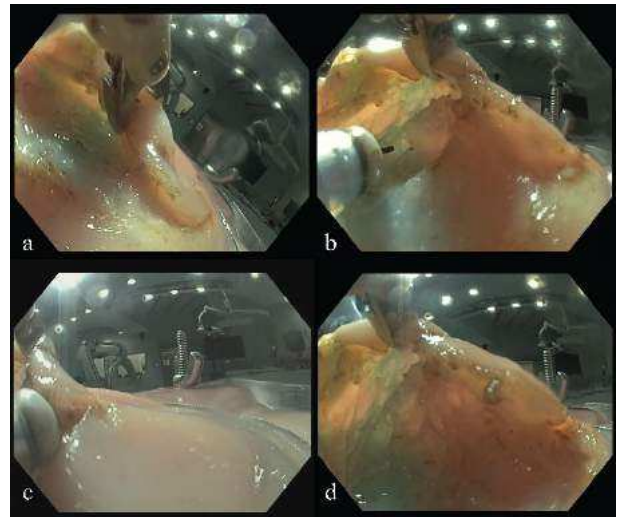


Fig. 4 Typical dissection with RTD-assisted ESD: (a) positioning and grasping the edge of the dissected mucosa; (b) retracting the tissue towards the upper-left direction, advancing the endoscope closer to the dissection site where the robotic lifter holds and pulls the tissue towards proximal direction; (c) holding the position of the lifter during dissection and (d) resultant dissection plane remains horizontal to the gastric wall.

This work is supported by InnoHK funding.

REFERENCES

- [1] S. Oka *et al.*, "Advantage of endoscopic submucosal dissection compared with EMR for early gastric cancer," *Gastrointest. Endosc.*, vol. 64, no. 6, pp. 877–883, 2006, doi: 10.1016/j.gie.2006.03.932.
- [2] D. H. Lee, M. Hwang, and D. S. Kwon, "Robotic endoscopy system (easyEndo) with a robotic arm mountable on a conventional endoscope," *Proc. - IEEE Int. Conf. Robot. Autom.*, vol. 2019-May, pp. 367–372, 2019, doi: 10.1109/ICRA.2019.8793626.
- [3] K. C. Lau, E. Y. Y. Leung, P. W. Y. Chiu, Y. Yam, J. Y. W. Lau, and C. C. Y. Poon, "A Flexible Surgical Robotic System for Removal of Early-Stage Gastrointestinal Cancers by Endoscopic Submucosal Dissection," *IEEE Trans. Ind. Informatics*, vol. 12, no. 6, pp. 2365–2374, 2016, doi: 10.1109/TII.2016.2576960.

Understanding Different Inflated Balloon Catheter Behaviours via Computational Modelling

J. Yao¹, G.M. Bosi¹, G. Burriesci^{1,2}, and H. Wurdemann¹

¹*Mechanical Engineering, University College London, UK*

²*Bioengineering at Ri.MED Foundation, Palermo, Italy*

junke.yao.19@ucl.ac.uk

INTRODUCTION

Balloon aortic valvuloplasty (BAV), a minimally invasive intervention, uses a balloon catheter to dilate the narrowed aortic valve as pre-dilatation or post-dilatation during the treatments of aortic stenosis. However, the instability of the inflated balloon by blocking the pulsating blood flow and the cardiac contraction causes the risk of tissue damage. Although a technique named rapid ventricle pacing (RVP) has been introduced to reduce the cardiac output for balloon stabilisation during its inflation, RVP is still associated with several complications. Several studies have introduced new balloon designs with considering non-occlusive configuration to improve the stability of the balloon catheter [1], [2], but sufficient data and understanding of their clinical outcome is still required. Therefore, using a commercially available valvuloplasty balloon catheter to achieve stability and avoid the use of RVP is worth to be investigated. In this study, to study the level of balloon inflation that allows for its stabilization during heart systole, a Finite Element (FE) model of the balloon catheter is created to simulate inflation and deflation procedures. Then, a Fluid-Structure Interaction (FSI) model is used to simulate how the displacement of the balloon along the aortic root varied by the different internal volumes under the blood flow.

MATERIALS AND METHODS

A. Simulation Models

The numerical model was created based on an Edwards 9350BC23 balloon catheter (Edwards Lifesciences, Irvine, USA), which is a standard shape balloon catheter. The inflated unstretched balloon diameter was 20.75 mm with a total length of 79.6 mm, whose tapered ends were attached to the catheter shaft. The 2.8 mm catheter was curved to the upper wall of the aortic arch (Fig. 1). The materials of the balloon and the catheter were modelled as isotropic, linear elastic with Young's modulus of 600 MPa and 1 GPa, Poisson ratio of 0.45 and 0.4 and density of 1256 kg/m³ and 1100 kg/m³, respectively[3]. The idealised aortic arch was designed with a diameter of 25 mm and a thickness of 1.5 mm, where a 100 mm straight section was regarded as ascending aorta ending

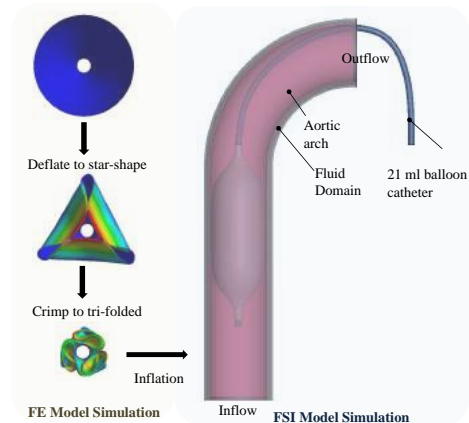


Fig. 1 Simulations of FE model and FSI model

with an arch of 50 mm radius, assumed as a rigid body. The blood flow was assigned as a Newtonian incompressible fluid having a density of 1060 kg/m³ and a dynamic viscosity of 4.0×10^{-3} Pa · s.

B. Simulations of Balloon FE Model

To describe the deflation and inflation procedures, the balloon was crimped to a tri-folded configuration and then inflated to its nominal internal volume (21 ml). Suction pressure (1 atm) was applied on the surface of the balloon to form a star-shaped configuration and then an iris mechanism was used to crimp the balloon into a tri-folded state as shown in Fig. 1. Subsequently, the unloaded deflated balloon model was imported to investigate the inflation process by applying pressure until reaching its nominal volume. During the whole procedure, the ends of the balloon were constrained in three directions.

C. Fluid-Structure Interaction Simulation

The unloaded balloon models with different internal volumes were imported into an FSI model, where the inlet boundary as a parabolic velocity profile with 1.3 m/s maximum value at the systole peak and zero pressure outlet boundary are used for the fluid domain. The simulation time was set to 0.2 seconds, which was close to the time of systole.

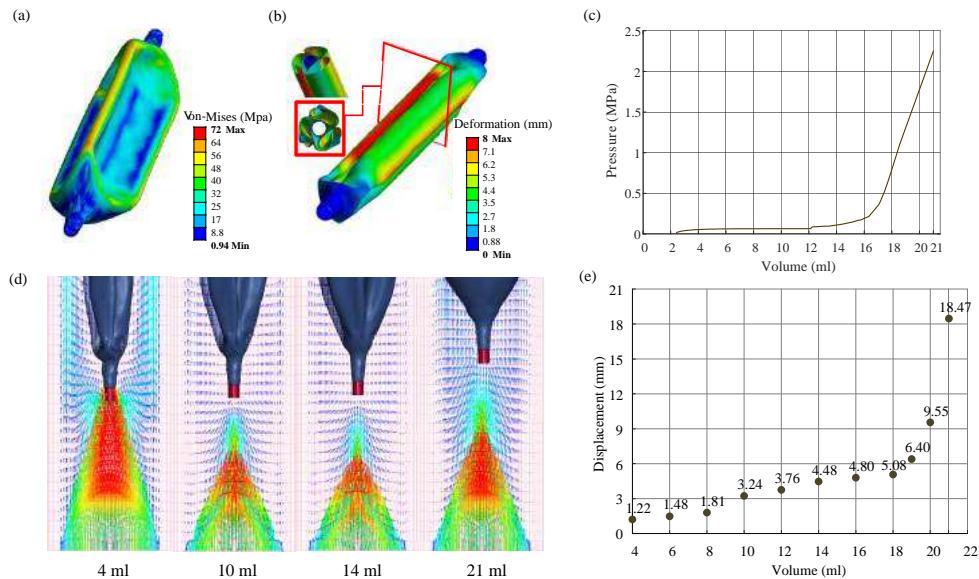


Fig. 2 Simulation results. (a)The von Mises stress distribution of deflation via pressurization; (b)The deformation of the tri-folded configuration; (c)The pressure-volume curve of the inflation simulation; (d)The velocity distribution with different internal volume; (e)The change of the maximum displacement by the increase of the internal volume.

RESULTS

During the deflation simulation, the ratio of kinetic energy to the total internal energy remained lower than 5%, which ensured that the internal forces were negligible and no unrealistic dynamic effect occurred. The balloon model was firstly deflated to a star shape with maximum von Mises stress 72 MPa at the end of the simulation (Fig. 2(a)). Then the balloon was crimped as tri-folded with 9 mm diameter in Fig. 2(b), which had an internal volume of 2.16 ml as the potential residual fluid. For the inflation procedure, the internal volume balloon reached 21 ml at the end with a diameter of 23.3 mm. The internal volume varied with the applied pressure is shown in Fig. 2(c), where the volume increased during a low value of the pressure until it reached 12 ml and it required higher applying pressure to have the same increment of the volume after 16 ml. FSI simulation has ten inflation levels simulated: 4 to 20 ml with 2 ml increment, and 21 ml. In Fig. 2(d), it shows the velocity distribution from the inlet section to the middle of the aortic straight part at 0.9 s, where the flow velocity reaches the highest value of 1.225 m/s and the displacement of 21 ml balloon is obviously larger than others. The maximum displacement verse volume is plotted in Fig. 2(e), where the displacements are 1.22, 1.48 and 1.81 mm for 4 to 8 ml and shows a jump from 8 to 10 ml (3.24 mm). For the 20 ml balloon, the maximum value jumps to 9.55 mm and increases to 18.47 mm for the 21 ml balloon.

DISCUSSION

A successful process for the FE model of balloon catheter deflation and inflation operations, as well as FSI simulations for the interaction between a balloon catheter and blood flow, were described in the current study. The pressure-volume curve of the numerical

balloon model inflation shows a similar trend with experimental data in a previous study [4]. For the FSI model, the maximum displacement has two jumps when increasing the inflation level from 8 to 10 ml and 18 to 20 ml. These sudden increases in balloon displacement show that there is a volume threshold permitting the balloon to cause considerable displacement and another amount that forces the balloon's displacement to expand abruptly in Fig. 2(e). The small value (<1.5 mm) of the displacement can be inferred that the balloon in this situation is relatively stable. Therefore, by regularly deflating the balloon to a 'safe volume' (i.e. <10 ml) during systole and inflating it to the nominal volume to induce valve expansion during diastole several times until successful dilatation, it is possible to achieve stabilisation while avoiding the complications associated with RVP. To the authors' knowledge, this model is the first attempt to use FSI modelling with two-way strong coupling to simulate a balloon catheter and aorta under realistic loading conditions. In the future, incorporating the aortic sinus and leaflets to give the different blood pressure on the balloon will allow the simulation to be more accurately represented.

REFERENCES

- [1] H. S. Weich *et al.*, "Balloon Aortic Valvuloplasty Using a Non-Occlusive Balloon Catheter: First Animal Experience," *Cardiovascular Engineering and Technology*, vol. 11, pp. 59–66, 2020.
- [2] S. Toggweiler *et al.*, "Simplifying transfemoral accurate neo implantation using the trueflow nonocclusive balloon catheter," *Catheterization and Cardiovascular Interventions*, vol. 96, no. 6, pp. 640–645, 2020.
- [3] B. Benedetta *et al.*, "Numerical model of a valvuloplasty balloon: in vitro validation in a rapid-prototyped phantom," *BioMed Eng OnLine*, vol. 15, no. 37, pp. 1–6, 2016.
- [4] A. Palombi *et al.*, "Sizing the aortic annulus with a robotised, commercially available soft balloon catheter: In vitro study on idealised phantoms," *IEEE ICRA*, 2019.

Robotic Surgery – Implications for Informed Consent

Jessica Henley, M.Eng,

Simon Kirby, MD

Memorial University of Newfoundland –
Faculty of Medicine

INTRODUCTION

Informed consent can be a complicated medico-legal process to ensure that a patient understands the risks involved with medical treatment or procedure. Surgeons in particular continue to face legal liability on the claim that informed consent was not properly achieved before surgery, which is likely to be further complicated by evolving technological advances in medicine [1],[2]. Robotic surgery introduces ambiguity for physicians to achieve informed consent. In addition to explaining the procedure according to the plan, the physician must describe the risk inherent to the technology that could create risk during the procedure. In the relatively new and ever-progressing world of surgical robotics, the surgeon may not have a complete understanding of what can go wrong based on their knowledge of the technology. This ambiguity leaves room for legal vulnerability for both the physician and the patient in achieving informed consent, as well as ambiguity in who can be held responsible.

With the development and implementation of surgical robotics, no standardized protocol or training has been developed for how to approach informed consent discussions with patients. This poster considers the implications of surgical robotics on informed consent.

METHODS

A scoping review using the PRISMA-ScR methodology was conducted to identify published issues and contributing factors that influence the ability of physicians to achieve informed consent when advising patients on surgical robotic procedures. The review was conducted using PubMed, Scopus, Embase and Engineering Village. A search string consisting of a combination and synonyms of the terms "robotic", "surgery" and "informed consent" in the title and abstract of papers published before 2021 was used to find eligible publications. Initial results returned 159 papers. Titles and abstracts were hand-searched for relevance to the research question, eliminating 122 papers, with 37 remaining. With duplicates removed, 30 papers were included for full review. Thematic analysis was performed on 30 papers to identify the main factors that influence the acquisition of informed consent. The findings were grouped in an Ishikawa diagram to demonstrate the root cause and effect.

RESULTS

An Ishikawa root cause analysis diagram (Figure 1) was developed to demonstrate the various factors found to contribute to the complexity of gaining informed consent

for procedures using a robotics approach. Categories of causes that may be considered include (i) patient factors such as expectations, beliefs, attitudes, comorbidities, etc.; (ii) physician factors, including judgment, knowledge, and experience; (iii) organizational characteristics, including education, policy, leadership, and staffing; and (iv) technical/equipment factors including haptic feedback, the possibility for malfunction, etc. Results are summarized in Table 1 with the frequency of themes discussed within the literature

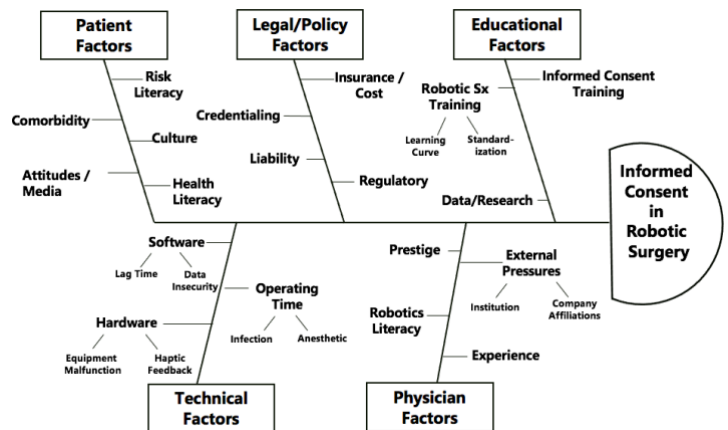


Figure 1 – Ishikawa Root Cause Analysis

PHYSICIAN FACTORS

Inadequate physician understanding of tech (12)
Prestige/reputation (9)
Lack of independent outcomes reporting (7)
Inexperience (6)

LEGAL/POLICY

Cost/Insurance (15)
Legal factors (liability, litigation) (14)
Ununiform credentialing (10)
Regulatory inadequacies (6)

PATIENT FACTORS

Patient factors (10) – comorbidities
Patient understanding of risk (9) – culture, education
Media /Beliefs (6)

TECHNOLOGICAL

Technological factors (18)
Software (12) – lag-time, algorithm, personal data
Hardware (9) - haptic feedback, arm malfunction

EDUCATIONAL

Inadequate training (21)
Steep learning curve (14)
Inadequate research to prove patient benefit (11)

ORGANIZATIONAL

Industry conflict of interest (11)
Institutional factors (6)

Table 1 – Themes in Literature

Other significant findings included suggestions for what details need to be explicitly included in the informed consent discussion.

DISCUSSION

The acquisition of truly informed consent requires patient and physician understanding of the risks and benefits of the procedure, as well as the consequences of choosing an alternate intervention. With the breadth of things that could go wrong during any procedure, either with the surgeon, the anesthetic, or the patient, it is nearly impossible for a physician to know, let alone describe, all the possible scenarios that could occur. The use of robotic and advanced technology certainly adds to this.

An overarching theme within the literature cites inadequate training in robotic surgery and a lack of

standardized credentialing. 21 papers discuss that training has historically been poor and called for improvements in training and a standardized curriculum. Since the publication of many of the reviewed papers, a standardized curriculum was validated in 2015[3]. However, more recent papers (n=11) still discuss the insufficient training, suggesting improvements must continue to ensure surgeons are adequately trained. In addition, 10 papers cite the need for uniform credentialing to ensure that surgeons have comparable experience and education to be considered fully trained to practice robotic surgery.

The literature agrees that surgeons are often unaware of the breadth of errors that could occur in robotic surgery. Authors (n=14) suggest that surgeons' understanding of robotic complications is lacking. Several authors (n=9) discussed the lack of reporting outcomes and complications in robotic procedures, which could certainly prevent the dissemination of common errors for other surgeons to learn from. The conclusions of 7 papers suggested that robotic surgery training needs to formally include error recognition and contingency planning within its curriculum and that the ICD should explicitly include potential errors and a conversion-to-conventional discussion. However, authors (n=3) also suggest that patient understanding of technical procedures is more difficult to achieve in robotic surgery, due to the complexity of explaining possible errors and patient factors like culture and education [4,5,6].

Discussion of alternative approaches is mandatory within the definition of informed consent. 13 papers discuss the lack of published research and data to confirm the benefit of robotics, and there is no consensus for any procedure that robotic surgery is the standard of care. Some authors (n=8) suggested that this lack of proven benefit over the conventional approach must be disclosed to patients in the ICD. Two authors additionally suggested that the surgeon should disclose their motivation for using robotics, whether it be from preference, ergonomic benefit, or increased training, since proven superiority is not implied [4,5].

The literature suggests that physicians should discuss certain details explicitly when obtaining informed consent. Char et. al [7] suggested that patients consider the physician's volume of procedures essential to making an informed decision, with 7 authors in agreement. Several authors (n=6) suggested that the innovative nature of the procedure or technology must be discussed explicitly with the patients. Regulatory bodies, such as the FDA, have also released statements encouraging surgeons to have a more open dialogue about the risk and benefits of robotic-assisted surgery with particular emphasis on surgeon experience [8].

This research attempts to expose some of the areas which may dispose the patient to unintended consequences of

robotic surgery that are not overtly discussed by physicians when obtaining informed consent.

CONCLUSIONS AND RELEVANCE

Validated curriculums have been developed for robotic surgery training but focus on technical skills and not on patient rights and safety. We recommend incorporating specific training for informed consent discussion within robotic surgery training. We suggest training include the risks and failures possible with robotic technology, as well as contingency plans on how to abort the robotic approach and convert to conventional alternatives. In addition, formalized training should be implemented at the medical school/residency education level regarding general informed consent including altering informed consent discussions when using innovative technology like robotic surgery.

Clinical simulation should be considered an appropriate tool for teaching these skills with standardized patients. This could be added to the residency curriculum, to ensure residents are entrustable in informed consent skills before commencing independent practice. Other suggestions from the literature proposed the creation of a Frequently Asked Questions database and hotline for patient questions [9], and the production of general patient guidelines for robotic surgery by international surgical societies [6].

These recommendations will help protect patients from harm and surgeons from liability in the informed consent discussion.

REFERENCES

- [1] C. M. P. Association, "Risk Fact Sheet," 2016.
- [2] M. Hanson and D. Pitt, "Informed consent for surgery: risk discussion and documentation.," *Can. J. Surg.*, vol. 60, no. 1, pp. 69–70, Feb. 2017
- [3] Reitman, AM.; Moreno, JD. Ethics guidelines for innovative surgery: Recommendations for national policy. *Ethical guidelines for innovative surgery*. 2006.
- [4] Nestor, M.W., Wilson, R.L., "An anticipatory ethical analysis of robotic assisted surgery". 2019. *Business and Professional Ethics Journal*.
- [5] Wightman, S.C., David, E.A., Atay, S.M., Kim, A.W., Angelos, P., "The ethics of robotic surgical systems is a conversation of informed consent". *Video-Assisted Thoracic Surgery*. 2020.
- [6] Ferrarese, A. et al., "Informed consent in robotic surgery: Quality of information and patient perception". 2016.
- [7] Char, S.J.L., Hills, N.K., Lo, B., Kirkwood, K.S., "Informed consent for innovative surgery: A survey of patients and surgeons". 2013. *Surgery (United States)*.
- [8] US Food and Drug Administration. Caution when using robotically-assisted surgical devices in women's health including mastectomy and other cancer-related surgeries: FDA safety communication. 2019
- [9] Graur, F., et. al., "Ethics in robotic surgery and telemedicine". 2010. *Mechanisms and Machine Science*

APPENDIX A – Literature Reviewed

- [1] Di Paolo M., "Bioethical approach to robot-assisted surgery". 2019. *British Journal of Surgery* (2019) 106:10 (1271-1272). Date of Publication: 1 Sep 2019. DOI 10.1002/bjs.11288
- [2] Angelos P., "The ethics of introducing new surgical technology into clinical practice the importance of the patient-surgeon relationship". 2016. *JAMA Surgery* (2016) 151:5 (405-406). Date of Publication: 1 May 2016. DOI 10.1001/jamasurg.2016.0011
- [3] Bareeq RA, Jayaraman S, Kiaii B, Schlachta C, Denstedt JD, Pautler SE., "The role of surgical simulation and the learning curve in robot-assisted surgery". 2008. *J Robot Surg*. DOI 10.1007/s11701-008-0074-x
- [4] Char, S.J.L., Hills, N.K., Lo, B., Kirkwood, K.S., "Informed consent for innovative surgery: A survey of patients and surgeons". 2013. *Surgery (United States)*. DOI 10.1016/j.surg.2012.08.068
- [5] Collins JW, Wisz P., "Training in robotic surgery, replicating the airline industry. How far have we come?". 2020. *World J Urol*. DOI 10.1007/s00345-019-02976-4
- [6] Dickens, B.M., Cook, R.J., "Legal and ethical issues in telemedicine and robotics". 2006. *International Journal of Gynecology and Obstetrics*. DOI 10.1016/j.ijgo.2006.04.023
- [7] Ferrarese, A., Pozzi, G., Borghi, F., Pellegrino, L., Di Lorenzo, P., Amato, B., Santangelo, M., Niola, M., Martino, V., Capasso, E., "Informed consent in robotic surgery: Quality of information and patient perception". 2016. *Open Medicine (Poland)*. DOI 10.1515/med-2016-0054
- [8] Geiger, J.D., Hirschl, R.B., "Innovation in surgical technology and techniques: Challenges and ethical issues". 2015. *Seminars in Pediatric Surgery*. DOI 10.1053/j.sempedsurg.2015.02.008
- [9] Lam, K., Purkayastha, S., Kinross, J.M., "The ethical digital surgeon". 2021. *Journal of Medical Internet Research*. DOI 10.2196/25849
- [10] Larson, J.A., Johnson, M.H., Bhayani, S.B., "Application of surgical safety standards to robotic surgery: Five principles of ethics for nonmaleficence". 2014. *Journal of the American College of Surgeons*. DOI 10.1016/j.jamcollsurg.2013.11.006
- [11] Lendvay TS, Hannaford B, Satava RM., "Future of robotic surgery". 2013. *Cancer J*. DOI 10.1097/PPO.0b013e31828bf822
- [12] Lim PC, Kang E., "How to prepare the patient for robotic surgery: before and during the operation". 2017. *Best Pract Res Clin Obstet Gynaecol*. DOI 10.1016/j.bpobgyn.2017.04.008
- [13] Mavroforou, A., Michalodimitrakis, E., Hatzitheofilou, C., Giannoukas, A.D., "Legal and ethical issues in robotic surgery". 2010. *International Angiology*. DOI
- [14] Mohan A, Wara UU, Arshad Shaikh MT, Rahman RM, Zaidi ZA., "Telesurgery and Robotics: An Improved and Efficient Era". 2021. *Cureus*. DOI 10.7759/cureus.14124
- [15] Mueller, P.S., Hook, C.C., "Technological and treatment imperatives, life-sustaining technologies, and associated ethical and social challenges". *Mayo Clinic Proceedings*. 2013. DOI: 10.1016/j.mayocp.2013.05.005
- [16] Nestor, M.W., Wilson, R.L., "An anticipatory ethical analysis of robotic assisted surgery". 2019. *Business and Professional Ethics Journal*. DOI 10.5840/bpej201812675
- [17] O'Sullivan, S., Nevejans, N., Allen, C., Blyth, A., Leonard, S., Pagallo, U., Holzinger, K., Holzinger, A., Sajid, M.I., Ashrafian, H., "Legal, regulatory, and ethical frameworks for development of standards in artificial intelligence (AI) and autonomous robotic surgery". 2019. *International Journal of Medical Robotics and Computer Assisted Surgery*. DOI 10.1002/rcs.1968
- [18] Sauerland S, Brockhaus AC, Fujita-Rohwerder N, Saad S., "Approaches to assessing the benefits and harms of medical devices for application in surgery". 2014. *Langenbecks Arch Surg*. DOI 10.1007/s00423-014-1173-y
- [19] Sharkey, N., Sharkey, A., "Robotic surgery: On the cutting edge of ethics". 2013. *Computer*. DOI 10.1109/MC.2012.424
- [20] Strong, V.E., Forde, K.A., MacFadyen, B.V., Mellinger, J.D., Crookes, P.F., Sillin, L.F., Shadduck, P.P., "Ethical considerations regarding the implementation of new technologies and techniques in surgery". 2014. *Surgical Endoscopy*. DOI 10.1007/s00464-014-3644-1
- [21] Vvedenskaya, E., "Bioethical aspects of robotics in surgery". 2021. *Jahr*. DOI 10.21860/J.12.1.7
- [22] Wightman, S.C., David, E.A., Atay, S.M., Kim, A.W., Angelos, P., "The ethics of robotic surgical systems is a conversation of informed consent". 2020. *Video-Assisted Thoracic Surgery*. DOI 10.21037/vats.2020.02.02
- [23] Zorn KC, Gautam G, Shalhav AL, Clayman RV, Ahlering TE, Albala DM, Lee DI, Sundaram CP, Matin SF, Castle EP, Winfield HN, Gettman MT, Lee BR, Thomas R, Patel VR, Leveillee RJ, Wong C, Badlani GH, Rha KH, Eggener SE, Wiklund P, Mottrie A, Atug F, Kural AR, Joseph JV; Members of the Society of Urologic Robotic Surgeons., "Training, credentialing, proctoring and medicolegal risks of robotic urological surgery: recommendations of the society of urologic robotic surgeons". 2009. *J Urol*. DOI 10.1016/j.juro.2009.05.042
- [24] Schiff D, Borenstein J. "How Should Clinicians Communicate With Patients About the Roles of Artificially Intelligent Team Members?" *AMA J Ethics*. 2019. doi: 10.1001/amajethics.2019.138.
- [25] Woo YJ, Handy JR Jr, Sade RM. "First in line for robotic surgery: Would you want to know? J

- Thorac Cardiovasc Surg. 2019. DOI
10.1016/j.jtcvs.2018.11.025.
- [26] Sheetz KH, Dimick JB. "Is It Time for Safeguards in the Adoption of Robotic Surgery?" JAMA. 2019 May 28;321(20):1971-1972. doi: 10.1001/jama.2019.3736.
- [27] Graur, F., Frunza, M., Elisei, R., Furcea, L., Scurtu, L., Radu, C., Szilaghy, A., Neagos, H., Muresan, A., Vlad, L., "Ethics in robotic surgery and telemedicine". 2010. Mechanisms and Machine Science. DOI 10.1007/978-90-481-9689-0_53
- [28] Conti, Adelaide(1); Azzalini, Elena(2); Amici, Cinzia(3); Cappellini, Valter(3); Faglia, Rodolfo(3); Delbon, Paola(4), "An ethical reflection on the application of cyber technologies in the field of healthcare". 2018. Advances in Service and Industrial Robotics - Proceedings of the 26th International Conference on Robotics in Alpe-Adria-Danube Region, RAAD 2017. DOI
- [29] McLean TR., "The legal and economic forces that will shape the international market for cybersurgery". 2006. Int J Med Robot. DOI 10.1002/rcs.109
- [30] Satava, R.M., "Laparoscopic Surgery, Robots, and Surgical Simulation: Moral and Ethical Issues". 2002. Surgical Innovation. DOI 10.1177/155335060200900408

Generalization for Deep Reinforcement Learning for Inverse Kinematics of Concentric Tube Robots

K. Iyengar¹, S. Spurgeon², and D. Stoyanov¹

¹*Department of Computer Science, University College London*

²*Department of Electronic and Electrical Engineering, University College London*
keshav.iyengar@ucl.ac.uk

INTRODUCTION

Concentric tube robots (CTRs) are a class of continuum robot that depend on the interactions between neighbouring, concentrically aligned tubes to produce the curvilinear shapes of the robot backbone [1]. The main application of these unique robots is that of minimally invasive surgery (MIS), where most of the developments for CTRs have been focused. Due to the confined workspaces and resulting extended learning times for surgeons in MIS, dexterous, compliant continuum robots such as CTRs have been under development in preference to the mechanically rigid and limited degrees-of-freedom (DOF) robots used in interventional medicine today. The precurved tubes in CTRs, sometimes referred to as active cannulas or catheters, are manufactured from super-elastic materials like Nickel-Titanium alloys with each tube nested concentrically. From the base, the individual tubes can be actuated through extension and rotation, which results in the bending and twisting of the backbone as well as access to the surgical site through the channel and robot tip. Clinically, CTRs are motivated for use in brain, cardiac, gastric surgery as well other procedures [2].

Due to tube interactions, modelling and control is non-trivial. Position control for CTRs has relied on model development, and although a balance between computation and accuracy has been reached in the literature [1], there remain issues such as performance in the presence of tube parameter discrepancies and the impact of unmodelled physical phenomena such as friction and permanent plastic deformation. This motivates the development of an end-to-end model-free control framework for CTRs. We extend our previous model-free deep reinforcement learning (deepRL) method [3] with an initial proof of concept for generalization. The task we give the agent then is to control the end-effector Cartesian robot tip position by means of actions that represent changes in joint values to reach a desired position in the robot workspace whilst considering a specific CTR system.

A hurdle with using deep learning approaches for control of CTRs is the limitation of CTR system generalization. Deep learning methods rely on the data given and cannot

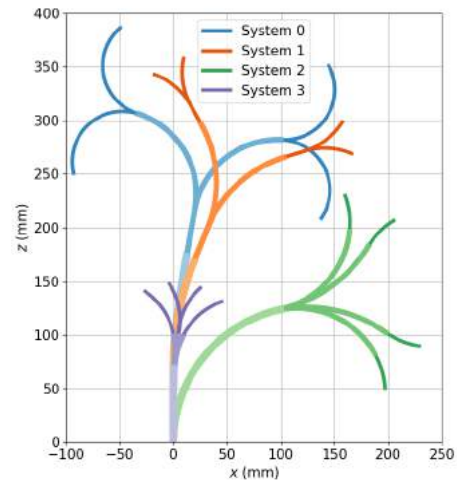


Fig. 1 CTR systems generalized over ordered from longest to shortest.

inherently differentiate between CTR systems. Thus, deep learning methods have been investigated for single CTR systems only. For deep learning methods to be viable, they must be able to generalize over multiple CTR systems.

MATERIALS AND METHODS

The CTR system generic deepRL method described below will seek to generalize over four CTR systems which each have different tube parameters as shown in Fig. 1. These parameters include, stiffness, inner and outer diameters, curved and straight lengths etc. The objective is to obtain good performance across CTR systems with a single control policy. For generalization, a system specifier, $\psi = \{0, 1, 2, 3\}$, was appended to the state, s_t , for the agent to differentiate the CTR systems. During training, a discrete uniform distribution is sampled to determine the system parameters to be used in the simulation for that episode. The simulation, using the exact kinematics from Rucker et al. [4], generates desired goals, G_d , within the workspace of the selected CTR system during the start of an episode and determines the current robot tip position or achieved goal, G_a . During the episode, the agent tries to reach

TABLE I

System	Errors (mm) ± std	Errors (% length) ± std	Success rate
1	0.77 ± 0.65	0.16 ± 0.065	94.0%
2	0.75 ± 0.48	0.17 ± 0.18	94.1%
3	0.63 ± 0.26	0.20 ± 0.08	99.3%
4	0.64 ± 0.22	0.3 ± 0.13	99.3%

this desired goal. Both these goals are included in the state which is defined as

$$s_t = \{\gamma_1, \gamma_2, \gamma_3, G_a - G_d, \delta(t), \psi\} \quad (1)$$

where γ_i is the cylindrical representation [5] for tube i . Tubes are ordered innermost to outermost. The cylindrical representation is defined as:

$$\gamma_i = \{\gamma_{1,i}, \gamma_{2,i}, \gamma_{3,i}\} = \{\cos(\alpha_i), \sin(\alpha_i), \beta_i\} \quad (2)$$

with rotation and extension of tube i represented as α_i and β_i respectively. The agent can take an action a or a change in joint position at each timestep t such that

$$a_t = \{\Delta\beta_1, \Delta\beta_2, \Delta\beta_3, \Delta\alpha_1, \Delta\alpha_2, \Delta\alpha_3\}. \quad (3)$$

The agent receives a reward r_t if the current achieved tip position G_a is within a goal tolerance $\delta(t)$ to the desired tip position G_d . The reward, r_t is defined as:

$$r_t = \begin{cases} 0 & \text{if } e_t \leq \delta(t) \\ -1 & \text{otherwise} \end{cases}. \quad (4)$$

where e_t is the Euclidean distance or l_2 norm $\|G_a - G_d\|_2$ between the achieved and desired goal.

Using deep deterministic policy gradient (DDPG) [6] with hindsight experience replay (HER) [7], the training parameters are as follows. The number of training timesteps was 3 million, buffer size was 500,000 with the policy network having 3 hidden networks with 256 units per layer, the initial goal tolerance and final goal tolerance were 20 mm and 1 mm applied over 1.5 million steps using a decay function [3]. Zero-mean Gaussian noise of 1.8 mm was applied to $\Delta\beta_i$ and 0.025 radians to $\Delta\alpha_i$.

RESULTS

A generic policy for all four systems was trained then using the trained policy, 1000 evaluation episodes were performed for each CTR system, resulting in 4000 evaluation episodes in total. For training results, a success rate of 100% was achieved with a mean error of 0.7 mm in the final 100 episodes. For each respective system, the mean and standard deviation errors were 0.77 mm and 0.65 mm, 0.75 mm and 0.48 mm, 0.63 mm and 0.26 mm and 0.64 mm and 0.22 mm. The success rate for each system was 94.0%, 94.1% 99.3% and 99.3%. These results are summarized in Table I. As longer CTR systems will have larger errors, usually error metrics are represented as a percentage of robot length. Even still, we find larger errors found in robot systems with larger workspaces.

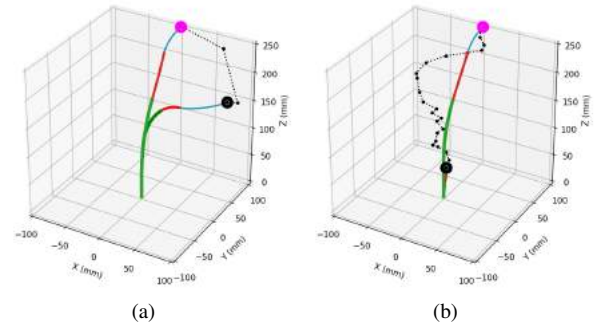


Fig. 2 System 0 (a) and system 1 (b) inverse kinematic solutions for the same desired goal.

Visualized in Fig. 2 is an example of the same desired end-effector position with two different initial joint configurations, resulting in two different final inverse kinematics solutions for system 0 Fig. 2a and system 1 Fig. 2b using the same policy. The desired goal position was (0, 100, 250) mm. The final joint configuration in Figure 2a was $\beta = [-7.63, -4.78, 0.0]$ mm, $\alpha = [65.83, 200.19, 120.77]^\circ$ with a tip error of 0.58 mm and for Fig. 2b $\beta = [-4.72, -3.54, -0.09]$ mm and $\alpha = [62.61, 193.39, 172.42]^\circ$ with a tip error of 0.65 mm.

DISCUSSION

The method is able to generalize over four distinct CTR systems however evaluation metrics across systems differ as seen in Table I. In other words, error metrics is biased to smaller robot workspaces even when represented as a percentage of robot length. System 0, the system with the longest overall length performs worst in evaluation whereas system 3 performs best. In the future, we plan on including CTR system parameters to fully generalize.

REFERENCES

- [1] H. B. Gilbert, D. C. Rucker, and R. J. Webster III, "Concentric tube robots: The state of the art and future directions," *Robotics Research*, pp. 253–269, 2016.
- [2] H. Alfalahi, F. Renda, and C. Stefanini, "Concentric tube robots for minimally invasive surgery: Current applications and future opportunities," *IEEE Transactions on Medical Robotics and Bionics*, vol. 2, no. 3, pp. 410–424, 2020.
- [3] K. Iyengar and D. Stoyanov, "Deep reinforcement learning for concentric tube robot control with a goal-based curriculum," in *2021 IEEE International Conference on Robotics and Automation (ICRA)*, 2021, pp. 1459–1465.
- [4] D. C. Rucker, B. A. Jones, and R. J. Webster III, "A geometrically exact model for externally loaded concentric-tube continuum robots," *IEEE transactions on robotics*, vol. 26, no. 5, pp. 769–780, 2010.
- [5] R. Grassmann, V. Modes, and J. Burgner-Kahrs, "Learning the forward and inverse kinematics of a 6-dof concentric tube continuum robot in se(3)," in *2018 IEEE/RSJ International Conference on Intelligent Robots and Systems (IROS)*, 2018, pp. 5125–5132.
- [6] T. P. Lillicrap, J. J. Hunt, A. Pritzel, N. Heess, T. Erez, Y. Tassa, D. Silver, and D. Wierstra, "Continuous control with deep reinforcement learning," *arXiv preprint arXiv:1509.02971*, 2015.
- [7] M. Andrychowicz, F. Wolski, A. Ray, J. Schneider, R. Fong, P. Welinder, B. McGrew, J. Tobin, P. Abbeel, and W. Zaremba, "Hindsight experience replay," *arXiv preprint arXiv:1707.01495*, 2017.

Towards Autonomous Robotic Ultrasound Scanning using Pneumatically Attachable Flexible Rails

A. McDonald-Bowyer¹, S. Dietsch¹, E. Dimitrakakis¹, J. Coote¹, L. Lindenroth¹, D. Stoyanov¹, and A. Stilli¹

¹Wellcome/EPSRC Centre for Interventional and Surgical Sciences (WEISS)
a.mcdonald-bowyer.19@ucl.ac.uk

INTRODUCTION

Robotic-assisted partial nephrectomy (RAPN) is a surgical procedure that employs robotics to remove a portion of diseased kidney. During the procedure, a drop-in Ultrasound (US) probe is used to identify the resection margins. Although the robot facilitates the task, the scanning of the kidney proves challenging due to slippage and requires a highly skilled surgeon [1]. In previous work [2], we presented a Pneumatically Attachable Flexible (PAF) rail to enable stable, track-guided US scanning of the kidney during RAPN. In [3] and [4], we have investigated the autonomous deployment of the PAF rail on the surface of the organ and their use in intraoperative organ manipulation. In [5], Wang et al. studied the 3-D reconstruction of a mass embedded in a kidney phantom when the PAF rail guides the US probe. In this work, we investigate autonomous control during the US scanning using the PAF rails, specifically using fibre-optic shape-sensing data as the input for path-planning. First, we present the design and fabrication of the sensorized PAF rail; then we assess the performance of real-time curvature sensing with the sensorized PAF rail system on rigid and soft phantoms; finally, we demonstrate how the PAF rail local shape data can be used to plan a trajectory and autonomously guide an intraoperative US probe.

MATERIALS AND METHODS

Design and Fabrication of Sensorized PAF Rail - We updated the design of the PAF rail based on the optimisation design study firstly presented in [2] and later in [5]. We incorporated a 1 mm channel along its internal perimeter to embed fine bore low-density polyethylene (LDPE) tubing (0.86 mm ID, 1.52 mm OD), which houses a multi-core shape sensing fibre (FBGS International, Jena, Germany). Each core contains 25 FBGs spaced at 10 mm intervals. The PAF rail was manufactured using injection moulding of DragonSkin™30 silicone (Smooth-On, Macungie, PA, US).

Design and Fabrication of Phantoms - We laser cut seven concentric ($R = 30, 50, 70, 90, 110$ mm) grooves (see Fig. 1a) into a sheet of acrylic plastic to evaluate the curvature sensing performance of the bare fibre. Phantoms of the same curvature range were fabricated in

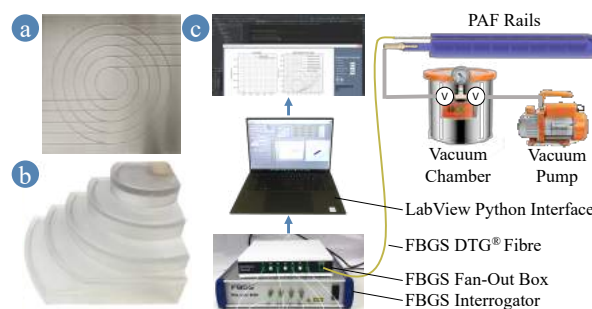


Fig. 1 a) Acrylic laser-cut plate. b) Rigid curvature block. c) Hardware schematic: The shape-sensing fibre is threaded through the fine-bore tubing and fixed at the distal end with Sil-Poxy Silicone adhesive. The rail is then attached to a 12-litre vacuum chamber via a barb connector and tubing, which is vacuumized by a 3 CFM single-stage vacuum pump. The fibre is connected to an optical interrogator via a multi-core fibre fan-out.

rigid plastic (see Fig. 1b), hard silicone rubber (Smooth-On, DragonSkin™30) and soft silicone rubber (Smooth-On, EcoFlex™00-20). These materials were chosen to reflect the large range of mechanical properties of kidney tissue reported in the literature [6] [7]. Finally, we created a negative mould from segmented CT images to fabricate a geometrically realistic kidney phantom. We cast tissue-mimicking material (polyvinyl alcohol - PVA) following the procedure in [8] and included a spherical structure of stiffer PVA to replicate a mass.

Curvature Sensing - First, we examined the curvature sensing performance of the bare shape-sensing fibre to set the ground truth comparison. We recorded and averaged the curvature over 30 iterations after threading the fibre along each groove of the acrylic plate. Then, we embedded the fiber in the PAF rails. A pneumatic circuit was set up as shown in Fig. 1c. The PAF rail was suctioned to each surface of the rigid curvature block and soft curvature phantoms while we recorded the sensed curvature for 5 seconds. *Autonomous Ultrasound Scanning* - As a proof-of-concept, we automated the track-guided US scan using the first generation da Vinci surgical robot [9] and the sensorized PAF rails. We equipped the first da Vinci Patient Side Manipulator (PSM1) with the EndoWrist® Prograsp™ Forceps paired with the drop-in US probe BK X12C4 (BK-Medical Holding Inc., Peabody, Massachusetts), as shown in Fig. 2. The PAF rail is suctioned to the kidney

TABLE I DS30 Sensed Curvature Errors

R (mm)	Max ϵ ($\times 10^{-2} mm^{-1}$)	(%)	Mean ϵ ($\times 10^{-2} mm^{-1}$)	(%)
30	2.64 ± 0.91	8.80	5.68 ± 0.25	18.9
50	1.6 ± 0.89	3.20	3.51 ± 0.25	7.02
70	0.57 ± 1.15	0.81	2.38 ± 0.33	3.40
90	0.39 ± 1.11	0.43	1.82 ± 0.34	2.02
110	0.11 ± 0.95	0.10	1.49 ± 0.28	1.35

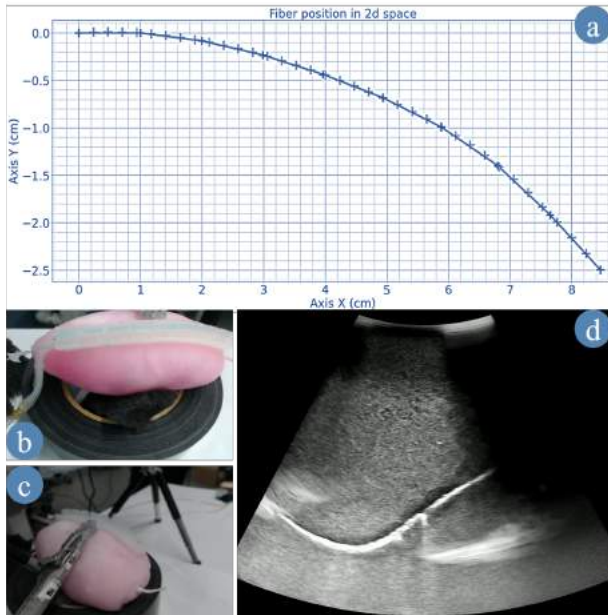


Fig. 2 Feasibility study snapshot. a) Computed drop-in US trajectory. b) Camera top view. c) Camera lateral view. d) Stream snapshot recorded with the drop-in US probe.

phantom while the PSM1/US probe pair is manually positioned perpendicular to the first fibre grating. A snapshot of the sensed fibre shape is taken, converted to a trajectory and relayed to the dVRK to control the PSM1 using the Robot Operating System (ROS). It executes a scan of the phantom, delivering a real-time US stream.

RESULTS

The average sensing error of the bare FBGS fibre is 1.02 ± 0.03 (2.9%) (Fig. 3). When embedded in the rail and tested on the rigid phantoms, the average sensing error increases to 6.5%. Sensing accuracy deteriorates with smaller radius of curvature, from 1.25% at $R = 110$ mm to 18.9% at $R = 30$ mm (see Table I). The trajectory

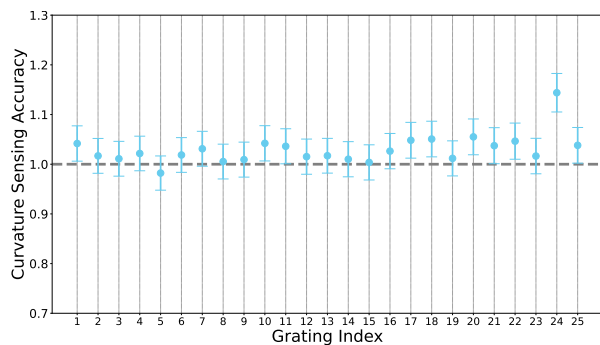


Fig. 3 Curvature sensing accuracy at each grating position along the fibre. Accuracy is defined as the ratio of sensed curvature to geometric curvature. For perfect sensing, we would expect a value of 1 for each grating.

for PSM1 was successfully obtained from the sensorized rail (Fig. 2d) and the trajectory was executed by PSM1. The probe maintained contact with the rail for 20 mm and an US stream was obtained (Fig. 2a).

DISCUSSION

We autonomously guided an ultrasound probe during the scan of a kidney phantom from the sensed curvature of the PAF rails. Here, we present promising results but, further study is needed to improve the US trajectory accuracy as we made several assumptions. Namely, curvature uniformity along the width of the rail, we manually positioned the probe perpendicular to the rail to reduce the problem from 3-D to 2-D planning, and we did not account for the offset between the US probe and the PSM1 tip.

As expected, we experienced larger curvature sensing errors of the sensorized PAF rails at tighter radii ($R = 30$ mm). However, in this context, the PAF rails are oriented along the long axis of the kidney. In this region, R ranges between 70 and 110 mm which corresponds to a sensing accuracy range of 1.35% - 3.4%. Or to a maximum position error of 0.024 mm and 1.16 mm for the full length of the rails. These results are satisfactory for path planning.

Overall, we demonstrate the applicability of shape sensing in soft robotics to automate an intraoperative robotic US scan. In a further study, we aim to perform multiple US swipe sequences to enhance the US scan quality and compare the robot performance against clinical standards. Another improvement would be to develop a calibration process to remove systematic errors when the rail is under suction.

REFERENCES

- [1] C. G. Rogers *et al.*, "Robotic Partial Nephrectomy for Complex Renal Tumors: Surgical Technique," *European Urology*, vol. 53, no. 3, pp. 514–523, 3 2008.
- [2] A. Stilli *et al.*, "Pneumatically Attachable Flexible Rails for Track-Guided Ultrasound Scanning in Robotic-Assisted Partial Nephrectomy: A Preliminary Design Study," *IEEE ROBOTICS AND AUTOMATION LETTERS*, vol. 4, no. 2, 2019.
- [3] C. D'Etorre *et al.*, "Semi-Autonomous Interventional Manipulation using Pneumatically Attachable Flexible Rails," *IEEE International Conference on Intelligent Robots and Systems*, pp. 1347–1354, 11 2019.
- [4] C. D'Etorre *et al.*, "Autonomous pick-and-place using the dVRK," *International Journal of Computer Assisted Radiology and Surgery*, vol. 16, no. 7, p. 1141, 7 2021.
- [5] C. Wang *et al.*, "Ultrasound 3D reconstruction of malignant masses in robotic-assisted partial nephrectomy using the PAF rail system: a comparison study," *International Journal of Computer Assisted Radiology and Surgery (2020)*, vol. 15, no. 7, pp. 1147–1155, 5 2020.
- [6] F. Adams *et al.*, "Soft 3D-Printed Phantom of the Human Kidney with Collecting System," *Annals of Biomedical Engineering*, vol. 45, no. 4, pp. 963–972, 4 2017.
- [7] C. L. Cheung *et al.*, "Use of 3-dimensional printing technology and silicone modeling in surgical simulation: development and face validation in pediatric laparoscopic pyeloplasty," *Journal of surgical education*, vol. 71, no. 5, pp. 762–767, 2014.
- [8] E. C. Mackle *et al.*, "Wall-less vascular poly(vinyl) alcohol gel ultrasound imaging phantoms using 3D printed vessels," <https://doi.org/10.1117/12.2510033>, vol. 10870, pp. 66–72, 2 2019.
- [9] "The da Vinci Research Kit (dVRK) – Intuitive Foundation." [Online]. Available: <https://www.intuitive-foundation.org/dvrk/>

Automatic Vessel Recognition and Segmentation: a novel Deep Learning Architecture with Transfer Learning Approach

Giovanni Faoro, Stefano Pane, Veronica Iacovacci, Sara Moccia, Arianna Menciacchi

The BioRobotics Institute, Scuola Superiore Sant'Anna, Pisa, Italy

Department of Excellence in Robotics and AI, Scuola Superiore Sant'Anna, Pisa, Italy
giovanni.faoro@santannapisa.it

INTRODUCTION

Ultrasound (US) imaging stands as a valid alternative to X-rays based methodologies for navigation and intraoperative tracking of vascular probes, thanks to its non-ionizing nature. However, US images quality is highly operator dependent, being subject to probe's orientation and contact force. In recent years, researchers have worked to develop Robotic US Systems (RUSS), granting the acquisition of good quality real-time US images, without the need of an expert operator [1]. Besides, to facilitate US images analysis, deep learning strategies have been developed. Applications in the field include the automatic segmentation of vessels, which is fundamental during endovascular procedures.

Intraoperatively, an automatic method to classify images based on the presence of vessels and selectively segment only vascular images would be valuable. For example, during hand-held probe procedures it would increase the quality of information feedback. In RUSS, it would enable automatic adjustment of probe positioning serving as alternative to manual positioning by highly trained sonographers. Additionally, a method for precisely discriminating the presence of vessels in the image plane could increase safety in visual-servoing platforms, by preventing possible control instabilities generated by imaging artifacts. However, segmentation architectures typically assume that the processed image contains vessels to be segmented [2], but this is not granted in real intraoperative settings especially at the beginning of the procedure when the imaging probe is not yet optimally positioned.

To address these unmet needs, in this paper we propose a multi-task convolutional neural network (CNN) architecture able to distinguish between vessel and no vessel images, in addition to segmenting them. The goal of such architecture is to enable robust and automatic US images analysis in real intraoperative settings.

MATERIALS AND METHODS

One of the most common deep learning architectures for medical image segmentation is U-Net, which is characterized by a contracting (encoder) and an expansion (decoder) path [3]. To accomplish our goal, we built a multi-task architecture, as a modified version of U-Net (Fig. 1), by adding a classification branch after

the contracting path that is able to detect the presence of vessels in the image. The classification branch is made of flatten layer, dense layer (activated with the rectified linear unit), dropout (with 0.5 probability), dense layer (activated with the hyperbolic tangent function), dropout (with 0.5 probability) and dense layer (activated with the softmax function). In our multi-task architecture, the contracting path is shared among classifier final layers and segmentation decoder, minimizing the computational cost.

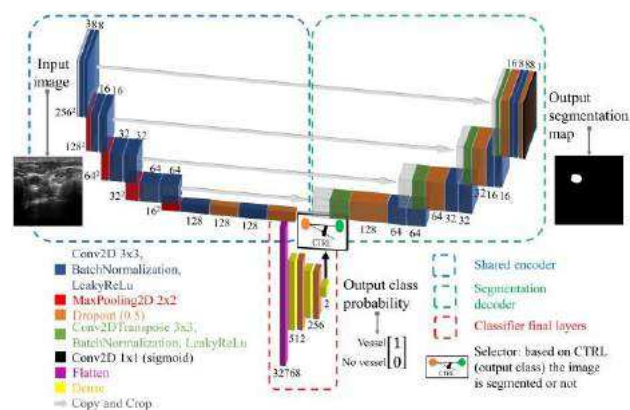


Fig.1 Our multi-task CNN architecture for vessel detection and segmentation from US images. The encoder path is shared to minimize computation; based on the output class probability the input image is further processed for vessel segmentation or not.

Our multi-task CNN is fed with images with size 256x256 pixels and provides as output a 2x1 probability vector, representing the class probability (vessel or no vessel image), and a 256x256 probability map, representing the segmentation output. Classification and segmentation branches were trained separately, considering categorical cross-entropy (for the classification task) and Dice loss (for the segmentation task). The Dice loss is defined as 1- Dice Similarity Coefficient (DSC), which is computed as two times the cardinality of output and ground truth intersection over the sum of cardinalities. To tackle overfitting issues relevant to the relatively small size of our dataset, we decided to exploit transfer learning [4].

We collected two small datasets of common carotid artery (CCA) US images available online¹: 240 B-mode

¹ <https://splab.cz/en/research/zpracovani-medicinskychsignalu/database/artery>, 17/01/2022, 16:50
https://www.researchgate.net/publication/261703132_100-IMT-Images_of_the_CCA, 17/01/2022, 16:50

images (120 with no vessel, 60 with vessels in long axis, 60 with vessels in short axis) were used to train the classifier, 240 B-mode images (120 with vessels in long axis, 120 with vessels in short axis) to train the segmentation network. Gold-standard (GS) annotation was obtained semi-automatically by using GIMP environment (GNU Image Manipulation Program 2.10.28). The images from the datasets had different size and were resized to 256x256 pixels.

Initial CNN weights were retrieved from a state-of-the-art U-Net architecture trained on US images [5], since transfer learning is expected to achieve better performances when original and target tasks are similar [4]. The encoder layers were frozen and the two datasets were used to fine-tune the classification branch and the U-Net decoder path.

The multi-task CNN was implemented with TensorFlow and Keras libraries and ran on NVIDIA Tesla K80 GPU provided by Google Collaboratory. The classifier was trained with SGD optimizer (learning rate: 0.001, momentum: 0.8). The segmentation branch was trained with Adam optimizer with a learning rate of 0.03, adapted during learning with an InverseTimeDecay routine. Batch size was set to 20 and the maximum number of epochs to 100, but early stopping with a patience of 10 was used to avoid overfitting. 6-fold cross-validation was used for robust testing. For each fold, training images were doubled in number by applying horizontal flip. Training images were further split, after shuffle, into training set (80%) and validation set (20%). Supplementary data augmentation techniques, as random rotation, zoom and shift, were applied online during training.

Architecture performances were evaluated defining True Positive (TP), True Negative (TN), False Negative (FN) and False Positive (FP) outputs in accord to the GS annotation. These were used for the computation of standard metrics as: accuracy (defined as $TP+TN$ over the sum of all) and F1 score (defined as $2TP$ over $2TP+FP+FN$) for the classification task; DSC for the segmentation task.

RESULTS

The average accuracy and F1 score for the classification task were 93.54% and 92.06%, respectively, with an average computation time on Google Colab of 5.01 ± 0.61 ms per image (Fig. 2a). The average DSC for the segmentation task was higher than 90%, i.e., 92.22%, with an average computation time of 8.95 ± 1.04 ms per image, enabling real-time applications (Fig. 2b).

DISCUSSION

Deep learning architectures able to perform vessel detection and segmentation together, as the one proposed here, would be valuable in real life dynamic environments, both in hand-held and robot-held probe procedures. By exploiting transfer learning, we were able to achieve promising segmentation performances (DSC equal to 92.22%) with a relatively small dataset

(i.e., 240 images), compared to a previous work that shows CCA segmentation training a U-Net with over 2000 images [2]. Additionally, the proposed architecture allowed real-time deployment.

These preliminary results indicate that such multi-task CNN could be efficiently integrated in a robotic platform, potentially enabling robust visual-servoing procedures for, e.g., catheter navigation or aortic screening. Additionally, applications can be enlarged to different districts by further fine-tuning the network.

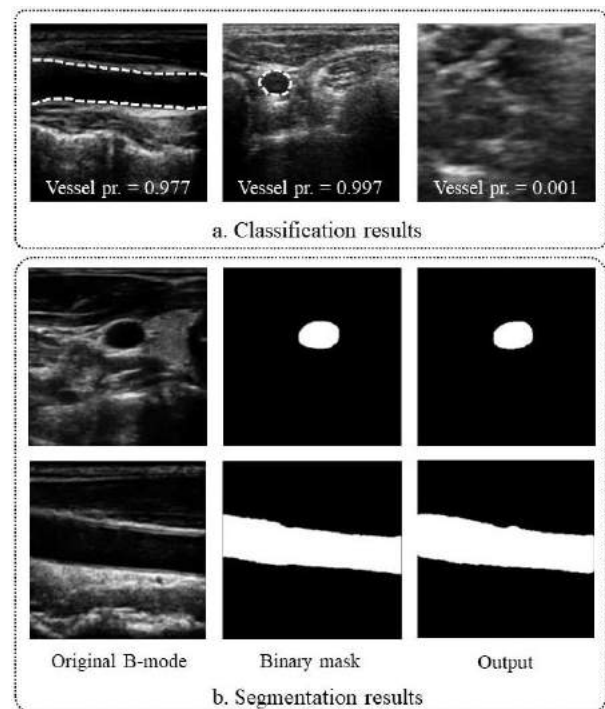


Fig. 2 Results in classification and segmentation tasks. a. Different B-mode images with the output vessel probability. From left to right, a TP long axis view, TP short axis view and a TN background images are shown. b. Segmentation results on a vessel short axis (first row) and long axis (second row) view.

REFERENCES

- [1] Z. Jiang, Z. Li, M. Grimm, M. Zhou, M. Esposito, W. Wein, W. Stechele, T. Wendler and N. Navab, Autonomous Robotic Screening of Tubular Structures based only on Real-Time Ultrasound Imaging Feedback, *IEEE Transactions on Industrial Electronics*, 2021
- [2] M. Xie, Y. Li, Y. Xue, L. Huntress, W. Beckerman, S. Rahimi, J. Ady, U. Roshan, Vessel lumen segmentation in carotid artery ultrasounds with the U-Net convolutional neural network, *IEEE International Conference on Bioinformatics and Biomedicine*, 2020
- [3] N. Siddique, S. Paheding, C. P. Elkin, and V. Devabhaktuni, U-Net and its variants for medical image segmentation: A review of theory and applications, *IEEE Access*, vol. 9, pp. 82031-82057, 2021
- [4] M. H. Hesamian, W. Jia, X. He, P. Kennedy, Deep Learning Techniques for Medical Image Segmentation: Achievements and Challenges, *J Digit Imaging*, 32:582-596, 2019
- [5] Guo Y, Duan X, Wang C, Guo H, Segmentation and recognition of breast ultrasound images based on an expanded U-Net, *PLoS ONE* 16(6): e0253202, 2021

A Novel, Research-Orientated Organ Perfusion Platform

M. Magbagbeola¹, K. Doyle¹, Z.L. Rai^{1,2,3}, L. Lindenroth¹, G. Dwyer¹,

A. Stilli¹, B.R. Davidson^{1,2,3}, D. Stoyanov¹

¹Wellcome/EPSRC Centre for Interventional and Surgical Sciences (WEISS), University College London,

²Centre for Surgical Innovation, Organ Repair and Transplantation (CSIORT), University College London

³Royal Free Hospital NHS Trust, London

Abstract— This paper presents a low-cost, versatile, organ perfusion machine designed for use in research. The modular and adaptable nature of the system allows for additional sensing equipment to be added or adapted for specific use. A feedback controller was implemented and tested on a porcine liver to maintain input pressure of the perfusate into the hepatic artery (HA). The results confirmed the effectiveness of the controller for maintaining input through the HA in a timely manner.

I. INTRODUCTION

Perfusion machines have the potential of extending the period during which an organ remains viable ex vivo from hours to days [1-4]. The ability to preserve organs in controlled physiological conditions can provide answers to basic scientific questions in a variety of research avenues. Additionally, a perfused whole organ can be used in the context of surgical training, making this platform a versatile option for the academic community. Perfusion machines such as the OrganOx Metra (OrganOx Metra, OrganOx, Oxford, United Kingdom) have recently been used successfully in clinical settings [4, 5]. However, due to the high cost of the commercial perfusion platforms, and the lack of open access software, these machines have been inaccessible to the wider research community. The academic community may therefore benefit from a similar form of perfusion machine designed specifically for use in a research setting. A novel perfusion system has been developed to evaluate organs in a manner that allows real-time monitoring and process control of physiological parameters such as flow rate, pressure, oxygenation, and pH. These parameters are in-built in the system and can be adjusted as required. By utilising cleanable, reusable components, this system provides an affordable alternative to commercially available, clinical perfusion machines, with a total parts cost of approximately £11,000. This paper presents preliminary findings on the system performance when applied to the perfusion of a porcine liver.

II. MATERIALS AND METHODS

A porcine liver obtained from an abattoir, was selected for preliminary testing of the proposed machine. The organ was suspended via a perforated plastic film over the organ chamber and any runoff perfusate from the liver was collected and returned to the 4 L reservoir. Additionally, the output flow

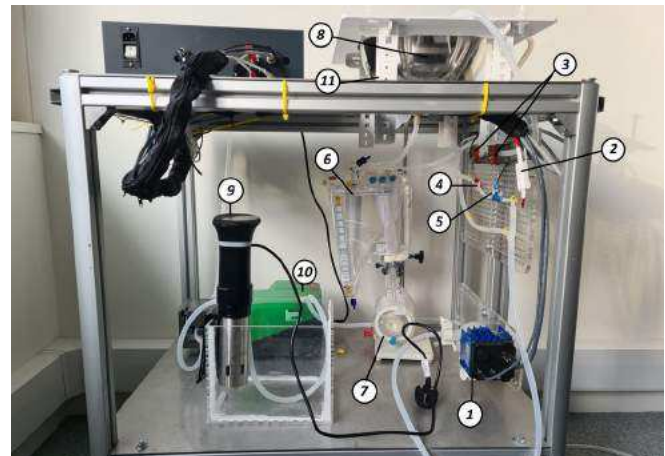


Figure 1: An overview of a research-oriented perfusion system. (1) centrifugal pump, (2) pressure sensor, (3) flow sensors, (4) temperature sensor, (5) oxygen sensor, (6) reservoir, (7) oxygenator, (8) organ chamber, (9) heat exchanger, (10) peristaltic pump, (11) load cells.

of perfusate from the liver was returned to the reservoir where it was filtered. Four load cells were placed directly beneath the four supports of the organ chamber in a square arrangement to evaluate the weight distribution of the liver throughout the perfusion. A single centrifugal pump (PuraLev 1200 MU, Levitronix GmbH, 8005 Zurich, Switzerland) circulated the perfusate throughout the system flow circuit while pressure (Single Use Pressure Sensors, PendoTECH, Princeton NJ 08540, USA) and flow (SONOFLOW co.55/100, SONOTEC, 06112 Halle, Germany) sensors monitored the input and the output pressure and flow rates of the perfusate. A single oxygen (EOM-(t)-FOM, PreSens Precision Sensing GmbH, 93053 Regensburg, Germany), and temperature (Pt100, PreSens Precision Sensing GmbH, 93053 Regensburg, Germany) sensor was used to monitor the perfusate travelling into the input of the organ. The perfusate was warmed, using a heat exchanger, to a temperature of 29°C while the oxygenator re-oxygenated the heated blood from the reservoir before pumping it back through the system. Fig.1 gives an overview of the system. A single-board computer (Raspberry Pi 4, Raspberry Pi Foundation, Cambridge CB2 1NF, UK) controlled all peripherals, and were communicated with using a combination of MODBUS (pumps, flow and pressure sensors), RS-232 (oxygen sensor), and RS-485 (pH

sensors) communication protocols. An analog-to-digital converter (Waveshare 32-bit AD/DA board, Waveshare Electronics, Shenzhen, China) is used to interface between the Raspberry Pi and the pressure sensors. The software architecture is implemented using ROS2, an open-source software framework for robotic applications, to ensure modularity of system components. All sensor data are displayed in real time via a laptop interface and the output recorded for further analysis.

The system is designed to enable fine control of all peripherals but was primarily used in this study to control and maintain pressure through either of the two input vessels, the portal vein (PV) and hepatic artery (HA). Pressure can be controlled via the centrifugal pump or by using a closed-loop proportional-integral-derivative (PID) controller. PID is a commonly used feedback controller designed to regulate process variables such as pressure or flowrate. A desired HA input pressure can be established and maintained by adjusting an actuator that minimises the difference between the desired value and the current state. The gain parameters of the PID controller were tuned using the Ziegler-Nichols tuning method and chosen based on achieving the shortest settling time while minimising potential overshoots. The following parameters were obtained: $K_p = 5$, $K_i = 2$, and $K_d = -0.5$.

III. RESULTS

In the preliminary test conducted, the system was set to perfuse the porcine liver for approximately 20 minutes. Throughout the experiment, step signals of 15 mmHg – 30 mmHg were used to test the system's adaptability and response. Pressure readings for blood flow into the liver via the HA are shown in Fig.2 and indicate that the controller achieved a settling time of approximately 20 s and a small overshoot (less than 2 mmHg). Steady state appears to be achieved within 6 s – 10 s and remains stable over time. A larger overshoot of approximately 3 mmHg occurs with sudden large decreases in pressure. A RPM limit placed on the centrifugal pump limited the maximum attainable pressure reading to 28 mmHg – 30 mmHg.

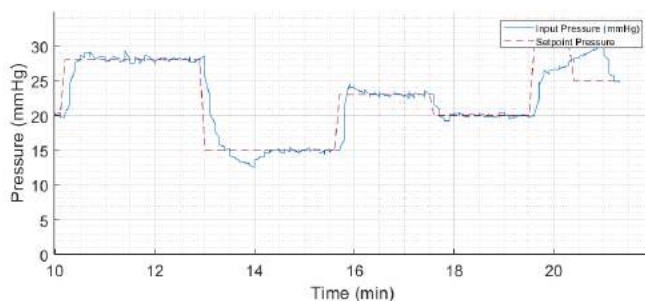


Figure 2: Snapshot of pressure sensor output while under the pressure controller. Red line indicates the desired input pressure while the blue indicates the input pressure reading.

IV. DISCUSSION AND CONCLUSION

In this study, we presented a novel computer assisted perfusion machine that has the versatility to benefit the wider



Figure 3: Figure shows a fully perfused liver. Stable pressure and flow are maintained into and out of the major blood vessels.

research community. The proposed system has the capability of fine-tuned control of pressure and flow as well as real-time monitoring of multiple parameters. Further sensors can be easily integrated, and the machine can be customised to meet the needs of the user thanks to the underlying software architecture. The efficacy of the system was tested in this study by assessing its ability to maintain a stable input pressure through the HA of a porcine liver.

While machine perfusion has been shown to be invaluable in clinical practice, it has been too costly for continuous use in research. For example, the Organ Ox Metra costs approximately £30,000 per device per year on lease and uses single-use consumables, adding to the overall cost (approx. £6,000 per use). The perfusion machine, being reusable, adaptable, and customisable, can assist researchers in monitoring and controlling several key parameters relevant to their respective discipline or area of interest at a lower cost (approx. £11,000) than commercially available alternatives. Our results demonstrate that whole ex-vivo organ perfusion with this system is feasible and a promising alternative to current commercial perfusion devices. Fig. 3 shows an image of the porcine liver following perfusion.

Work is currently underway to test this system on the porcine pancreas and, in the future, on human organs. This is in part to investigate a new loco-regional ablation treatment on ex-vivo perfused human organ.

REFERENCES

- [1] Leemkuil M, Lier G, Engelse MA, Ploeg RJ, de Koning EJP, t Hart NA, et al. Hypothermic Oxygenated Machine Perfusion of the Human Donor Pancreas. *Transplant Direct*. 2018;4(10):e388.
- [2] Branchereau J, Renaudin K, Kervella D, Bernadet S, Karam G, Blanco G, et al. Hypothermic pulsatile perfusion of human pancreas: Preliminary technical feasibility study based on histology. *Cryobiology*. 2018;85:56-62.
- [3] Hamaoui K, Papalois V. Machine Perfusion and the Pancreas: Will It Increase the Donor Pool? *Curr Diab Rep*. 2019;19(8):56.
- [4] Javanbakht M, Mashayekhi A, Trevor M, Branagan-Harris M, Atkinson J. Cost-utility analysis of normothermic liver perfusion with the OrganOx metra compared to static cold storage in the United Kingdom. *Journal of medical economics*. 2020;23(11).
- [5] Nasralla D, Coussios CC, Mergental H, Akhtar MZ, Butler AJ, Ceresa CDL, et al. A randomized trial of normothermic preservation in liver transplantation. *Nature*. 2018;557(7703).

A Temporal Learning Approach to Inpainting Endoscopic Specularities and Its effect on Image Correspondence

Rema Daher¹, Francisco Vasconcelos¹, and Danail Stoyanov¹

¹Computer Science Department, Surgical Robot Vision Group, University College London
rema.daher.20@ucl.ac.uk, f.vasconcelos@ucl.ac.uk, danail.stoyanov@ucl.ac.uk

This work was supported by WEISS at UCL(203145Z/16/Z) and H2020 FET(GA863146)

INTRODUCTION

Computer vision has been utilized to analyze minimally invasive surgery videos and aid with polyp detection, tool localization, and organ 3D modelling tasks. However, irregular light patterns such as saturation, specular highlights, or extreme contrasts occlude texture and hinder these tasks. In this work, specular highlights were removed and the occluded data was reconstructed. To do that, an unsupervised temporal generative adversarial network (GAN) was used to inpaint specular highlights spatially and temporally. Due to the absence of a dataset with ground truth occluded textures, the network was trained on the in-vivo gastric endoscopy dataset (Hyper-Kvasir [1]) with specular highlight masks that were automatically created and processed to act as pseudo ground truths. Ablation studies and direct comparison with other methods were used to show the improved results of our system. In addition, the results on various datasets show the generalizability of our network on different environments and procedures as shown in Fig. 1. Finally, experiments also show the positive effect of inpainting on other computer vision tasks under the umbrella of 3D reconstruction and localization in endoscopy including feature matching as well as optical flow and disparity estimation.

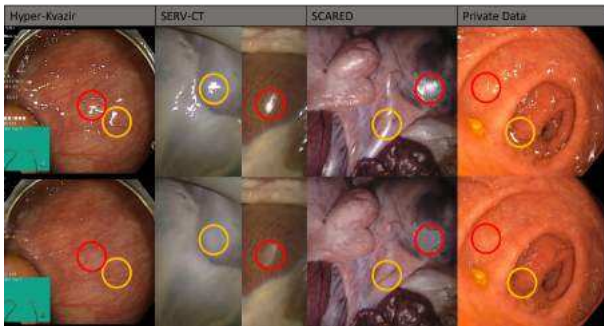


Fig. 1 Some motivational results of the specular highlight inpainting system on various datasets.

MATERIALS AND METHODS

The network architecture for inpainting is based on the Spatio-Temporal Transformer Network (STTN) proposed by [2]. STTN is a GAN mainly made up of spatial-temporal transformers that take as input feature vectors

generated using a 2D convolutional encoder. The vector outputs from the transformers are fed into a decoder to generate the inpainted images.

Some modification were performed to transform STTN from the task of object removal in diverse scenes to specularity removal in endoscopic videos.

First, their model is trained on inpainting diverse videos using random masks with frame ensured continuity. For the case at hand, a pseudo ground truth was created for training. To create this pseudo ground truth, specularities were first segmented from Hyper-Kvasir dataset using the chromatic characteristics of specular highlights [3]. After segmentation, the outputted masks are processed to cover specularity-free regions by using position translation and overlap clipping. Now that these masks cover up visible or unoccluded texture, this texture acts as pseudo ground truth to the inpainting output of these translated masks.

The pseudo ground truth was used for training the model; however, this model was first initialized by another model trained on temporally continuous random masks with endoscopic videos. The model was pretrained because having randomly located masks with various sizes can help the model learn missing textures of various regions of the gastrointestinal tract, whereas specularity masks can be limited to small sizes with certain textures for example. With these modifications, the proposed system becomes as is depicted in Fig. 2.

RESULTS AND DISCUSSION

Several experiments were performed to assess our system's inpainting ability. First, two models were analyzed, $Model_{S,C}$, which was trained from scratch using pseudo ground truth and $Model_{T,C}$, which was also trained on the pseudo ground truth, but it was initialized with another model trained on spatially consistent random shaped masks. Quantitative and qualitative analysis showed that $Model_{T,C}$ outperformed $Model_{S,C}$ in inpainting. Visually, with transfer learning, more details are captured as opposed to training from scratch. This was also evaluated quantitatively using Peak Signal to Noise Ratio (PSNR) and Mean Square Error (MSE) metrics ($Model_{S,C}$: PSNR=28.896, MSE=120.613. $Model_{T,C}$: PSNR=29.542, MSE=104.719)

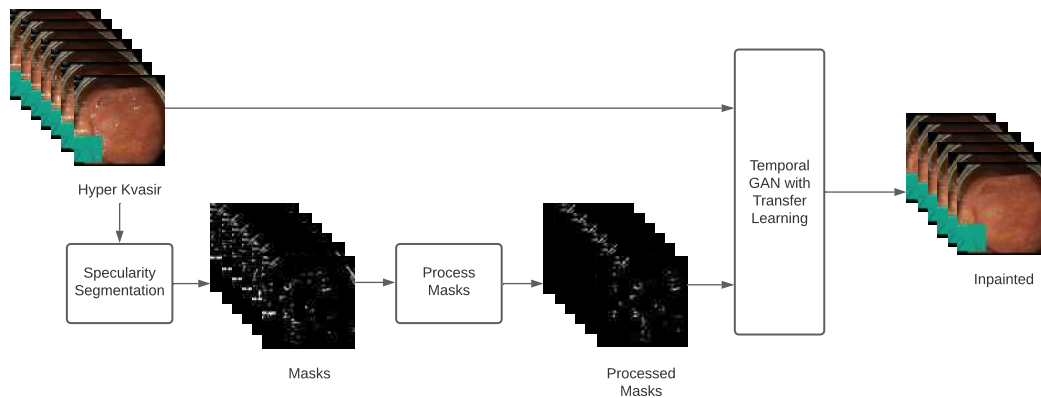


Fig. 2 The flowchart of the proposed system.

Other learning approaches that solve this problem do not have a temporal component [4], [5] and since they are not open source, an ablation study is used. To do that, the model was tested on one frame at a time, which made it act as a model with no temporal component, $Model_{T,C,NT}$. The model was also compared to a non-learning-based method represented as $Model_{Trad}$ and to the STTN model $Model_{STTN}$. Visually, the proposed $Model_{T,C}$ showed the most detailed inpainting, also shown through quantitative analysis in Table I.

Models	$\blacktriangle PSNR_{mean}$	$\blacktriangledown MSE_{mean}$
$Model_{T,C}$	29.542	104.719
$Model_{STTN}$	28.683	119.541
$Model_{Trad}$	19.909	895.222
$Model_{T,C,NT}$	29.284	112.717

TABLE I $PSNR_{mean}$ and MSE_{mean} values

$Model_{T,C}$ was tested on private data from a different hospital and on in-vivo data (SERV-CT [6], SCARED [7]). This showed the model’s generalizability (Fig. 1).

The effect of inpainting specular highlights in endoscopy on disparity, feature matching, and optical flow was analysed. The results showed improvement in disparity with inpainting through visual and quantitative analysis on the basis of bad3% error, root mean square error (RMS), and the endpoint error (EPE) metrics.

As for feature matching, visually, the original frame pair matches count is higher than those generated from the inpainted frame pair. Thus, without inpainting specular highlights, lower quality feature matches are generated. Visual analysis on optical flow estimation showed that results were significantly better with inpainting giving smoother and more homogeneous optical flows.

For the quantitative analysis of both feature matching and optical flow, no direct ground truth was present. That is why, camera pose estimation was performed using matches that were generated from feature matching and optical flow separately with the results shown in Table II. For feature matching, quantitative results were improved, whereas, the optical flow results did not show any significant change; in fact, the results were even

degraded slightly with inpainting.

Statistics	Feature Matching	Optical Flow
RTE	% 11.72	% 1.73
RRE	% 30.12	-% 1.59
Inliers	% 25.17	-% 4.82

TABLE II Mean of the difference between the feature-/optical-flow-based pose estimation results of original versus inpainted sequences in terms of Relative Translation and Rotation Errors and RANSAC Inliers.

CONCLUSION

In this work, an unsupervised inpainting system was proposed to remove specular highlights from endoscopic videos using pseudo ground truth and transfer learning. Experiments showed improvement on previous methods, generalizability on different datasets, and a positive effect on other computer vision tasks.

REFERENCES

- [1] H. Borgli, V. Thambawita, P. H. Smedsrud, S. Hicks, D. Jha, S. L. Eskeland, K. R. Randel, K. Pogorelov, M. Lux, D. T. D. Nguyen *et al.*, “Hyperkvasir, a comprehensive multi-class image and video dataset for gastrointestinal endoscopy,” *Scientific Data*, vol. 7, no. 1, pp. 1–14, 2020.
- [2] Y. Zeng, J. Fu, and H. Chao, “Learning joint spatial-temporal transformations for video inpainting,” in *European Conference on Computer Vision*. Springer, 2020, pp. 528–543.
- [3] O. El Meslouhi, M. Kardouchi, H. Allali, T. Gadi, and Y. A. Benkaddour, “Automatic detection and inpainting of specular reflections for colposcopic images,” *Central European Journal of Computer Science*, vol. 1, no. 3, pp. 341–354, 2011.
- [4] S. Ali, F. Zhou, A. Bailey, B. Braden, J. E. East, X. Lu, and J. Rittscher, “A deep learning framework for quality assessment and restoration in video endoscopy,” *Medical Image Analysis*, vol. 68, p. 101900, 2021.
- [5] P.-R. Siavelis, N. Lamprinou, and E. Z. Psarakis, “An improved gan semantic image inpainting,” in *International Conference on Advanced Concepts for Intelligent Vision Systems*. Springer, 2020, pp. 443–454.
- [6] P. Edwards, D. Psychogyios, S. Speidel, L. Maier-Hein, and D. Stoyanov, “Serv-ct: A disparity dataset from ct for validation of endoscopic 3d reconstruction,” *arXiv preprint arXiv:2012.11779*, 2020.
- [7] M. Allan, J. Mcleod, C. Wang, J. C. Rosenthal, Z. Hu, N. Gard, P. Eisert, K. X. Fu, T. Zeffiro, W. Xia *et al.*, “Stereo correspondence and reconstruction of endoscopic data challenge,” *arXiv preprint arXiv:2101.01133*, 2021.

Transformer-based Feature Matching for Fetoscopic Mosaicking

Sophia Bano¹, Francisco Vasconcelos¹, Anna L. David², Jan Deprest³, and Danail Stoyanov¹

¹Wellcome/EPSCRC Centre for Interventional and Surgical Sciences & Department of Computer Science, University College London, UK

²Fetal Medicine Unit, University College London Hospital, UK

³Department of Development and Regeneration, University Hospital Leuven, Belgium
sophia.bano@ucl.ac.uk

INTRODUCTION

Twin-to-twin transfusion syndrome (TTTS) is a rare fetal anomaly that affects the twins sharing a monochronic placenta. It is caused by abnormal placental vascular anastomoses on the placenta, leading to uneven flow of blood between the two fetuses [1]. Fetoscopic Laser Photocoagulation (FLP) is used to treat TTTS, however, this procedure is hindered because of difficulty in visualizing the surgical environment due to limited surgical field-of-view, unusual placenta position, limited manoeuvrability of the fetoscope and poor visibility due to fluid turbidity and occlusions (Fig. 1). This adds to the surgeon's cognitive load and may result in increased procedural time and missed treatment, leading to persistent TTTS. Fetoscopic video mosaicking can create a virtual expanded field-of-view (FOV) image of the fetoscopic environment, which may support the surgeons in localizing the vascular anastomoses during the FLP procedure.

Classical video mosaicking techniques perform handcrafted feature detection, description (i.e. SIFT, SURF, ORB, etc) and feature matching in consecutive frames and homography estimation for image stitching. However, these methods perform poorly on the in vivo fetoscopic videos due to low resolution, poor visibility, floating particles and texture paucity or repetitive texture. Deep learning-based sequential mosaicking [2] method overcomes the limitation of feature-based mosaicking methods, but results in drifting error when stitching non-planar views. A recent intensity-based image registration [3] method relies on placental vessel segmentation maps for registration. This facilitated in overcoming some visibility challenges, however, this method fails when the predicted segmentation map is inaccurate or inconsistent across frames or in views with thin or no vessels. In the paper, we propose the use of transformer-based detector-free local feature matching (LoFTR) method [4] as a dense feature matching technique for creating reliable mosaics with minimal drifting error. Using the publicly available dataset [3], we experimentally show the robustness of the proposed method over the state-of-the-art vessel-based method.

*This work was supported by the Wellcome/EPSCRC Centre for Interventional & Surgical Sciences (203145Z/16/Z), EPSCRC (EP/P027938/1, EP/R004080/1, NS/A000027/1, EP/P012841/1); and the Royal Academy of Engineering Chair in Emerging Technologies Scheme.

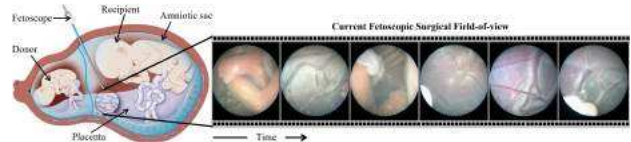


Fig. 1 During FLP, a fetoscope, having limited field-of-view, is inserted into the amniotic cavity and is used to localize and ablate the vascular anastomoses sites.

MATERIALS AND METHODS

A. Detector-Free Feature Representation

The recently proposed LoFTR [4] method first establish pixel-wise dense matches at a coarse level and later refine the good matches at a fine level. Given two consecutive frames F^t and F^{t+1} , a standard convolutional neural network architecture is used to extract dense features at coarse, $\tilde{F}^t, \tilde{F}^{t+1}$ (at $1/8^{th}$ of input resolution), and fine, \hat{F}^t, \hat{F}^{t+1} (at $1/2^{th}$ of input resolution), levels from both frames. The coarse local features, $\tilde{F}^t, \tilde{F}^{t+1}$, becomes the input to the LoFTR module. LoFTR uses transformer with positional encoding, and self and cross-attention layers to transform \tilde{F}_1, \tilde{F}_2 into position and context dependent local features, denoted as $\tilde{F}_{tr}^t, \tilde{F}_{tr}^{t+1}$, that can be matched easily.

B. Feature Matching

The coarse level matches \mathcal{M}_c between $\tilde{F}_{tr}^t, \tilde{F}_{tr}^{t+1}$ are established by using a differential matching layer, which gives a confidence matrix \mathcal{P}_J . The matches in \mathcal{P}_J with confidence higher than a predefined threshold and that also satisfies the mutual nearest neighbour criteria are selected as \mathcal{M}_c . Finally, coarse (\mathcal{M}_c) to fine (\mathcal{M}_f) matches are obtained by taking local window size from fine-level features, \hat{F}^t, \hat{F}^{t+1} , at each coarse match positions, applying a LoFTR module to obtained the fine transformed representation and correlating them. For more detail, please refer to [4], in which it is shown that LoFTR produces high-quality matches even in regions having low-textures and are affected by motion blur or repetitive patterns; making it an ideal matching module for fetoscopic mosaicking.

C. Registration and Mosaicking

A circular mask covering only the fetoscopic FOV is used to remove matches from the unwanted blank re-

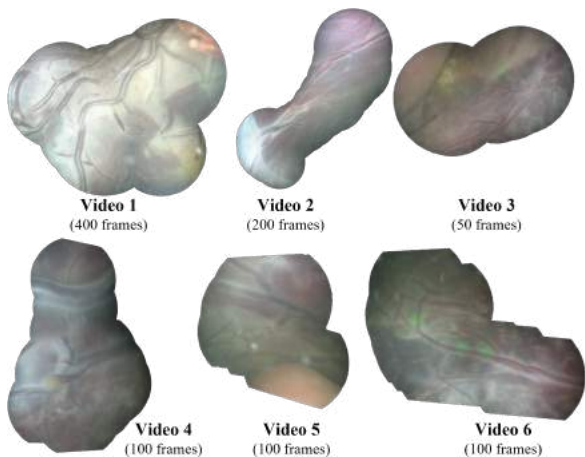


Fig. 2 Visualization of the generated mosaic using the proposed LoFTR-based method for the 6 in vivo clips.

gions. The registration between two consecutive frames, F^t and F^{t+1} , is approximated as an affine transformation [3] using RANdom SAMple Consensus (RANSAC) method. The obtained transformation is refined by using only the inliers with the Levenberg-Marquardt method that further reduces the reprojection error. Left-hand matrix multiplication is applied to the pairwise transformations to obtain the relative transformations of all frames in a video with respect to the first frame [2], following by image blending to generate an expanded FOV image.

RESULTS AND DISCUSSION

For the experimental analysis, we used the publicly available fetoscopy placenta dataset [3] that contains 6 in vivo fetoscopy video clips from 6 different TTTS procedures. The LoFTR matching model, pretrained on the ScanNet dataset [4], is used for obtaining the fine-level matches between two consecutive frames. Since groundtruth transformations are not available, we use the 5-frame structural similarity index measure (SSIM) presented in [3] for the quantitative evaluation of mosaics. The proposed LoFTR-based method is also compared with the state-of-the-art vessel-based [3] method (Fig. 3). The qualitative analysis on all 6 video clips is also performed (Fig. 2).

From Fig. 3, we can observe that the proposed LoFTR-based method performed significantly better on all video clips (except video 1) resulting in significantly low interquartile range and high median 5-frame SSIM when compared to the vessel-based [3] method. Video 1 contains heavy amniotic fluid particles dynamically floating in the in vivo environment, which affects the performs of the LoFTR resulting in inaccurate transformation estimation. In a vessel-based method, such particles are already filtered during vessel segmentation. Video 2-6 have dynamically changing non-planar views with some videos having low illumination and some frames having either no or very thin vessels. This negatively influences the vessel-based method, resulting in increase drifting error. LoFTR-based method, on the other hand, showed

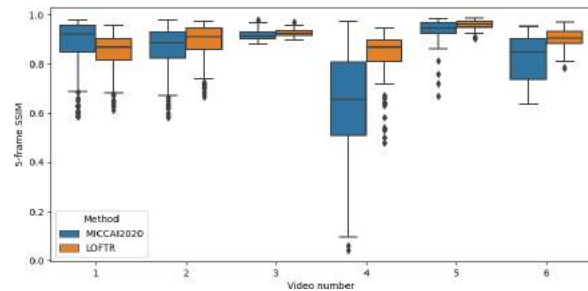


Fig. 3 Quantitative comparison of the proposed LoFTR-based method with the vessel-based (MICCAI2020) method [3] using the 5-frame SSIM metric.

robustness even in regions having low-textures (very thin or no vessels) and low illumination. This is also evident from the qualitative results (Fig. 2 which can be compared with the qualitative results presented in [3]. In the case of Video 1, discontinuities are visible in the generated mosaic. In the case of Video 2-6, the generated mosaics are reliable and accurate without any visible discontinuities, which is also inline with the observations drawn from the quantitative results.

CONCLUSIONS

We propose a fetoscopic video mosaicking method that benefited from the detector-free feature matching with transformers (LoFTR) [4] method, resulting in generating reliable virtual expanded field-of-view image of the intraoperative fetoscopic environment. Using the publicly available fetoscopy placenta dataset [3], we experimentally showed that the proposed LoFTR-based method outperformed the state-of-the-art vessel-based [3] fetoscopic mosaicking method. The proposed method is robust even in low-textured and low illumination non-planar views, which shows the potential of facilitating the surgeons during the TTTS procedure. Future work involves validating the proposed method on the larger FetReg [5] dataset.

REFERENCES

- [1] A. Baschat, R. H. Chmait, J. Deprest, E. Gratacós, K. Hecher, E. Kontopoulos, R. Quintero, D. W. Skupski, D. V. Valsky, Y. Ville *et al.*, “Twin-to-twin transfusion syndrome (TTTS),” *Journal of Perinatal Medicine*, vol. 39, no. 2, pp. 107–112, 2011.
- [2] S. Bano, F. Vasconcelos, M. Tella-Amo, G. Dwyer, C. Gruijthuisen, E. Vander Poorten, T. Vercauteren, S. Ourselin, J. Deprest, and D. Stoyanov, “Deep learning-based fetoscopic mosaicking for field-of-view expansion,” *International journal of computer assisted radiology and surgery*, vol. 15, pp. 1807–1816, 2020.
- [3] S. Bano, F. Vasconcelos, L. M. Shepherd, E. Vander Poorten, T. Vercauteren, S. Ourselin, A. L. David, J. Deprest, and D. Stoyanov, “Deep placental vessel segmentation for fetoscopic mosaicking,” in *Medical Image Computing and Computer-Assisted Intervention*. Springer, 2020, pp. 763–773.
- [4] J. Sun, Z. Shen, Y. Wang, H. Bao, and X. Zhou, “LoFTR: Detector-free local feature matching with transformers,” in *Conference on Computer Vision and Pattern Recognition*, 2021, pp. 8922–8931.
- [5] S. Bano, A. Casella, F. Vasconcelos, S. Moccia, G. Attalakos, R. Wimalasundera, A. L. David, D. Paladini, J. Deprest, E. De Momi, L. S. Mattos, and D. Stoyanov, “Fetreg: Placental vessel segmentation and registration in fetoscopy challenge dataset,” *arXiv preprint arXiv:2106.05923*, 2021.

Deep Learning-based Plane Pose Regression towards Training in Freehand Obstetric Ultrasound

Chiara Di Vece¹, Brian Dromey^{1,2}, Francisco Vasconcelos¹,
Anna L. David^{2,3}, Donald Peebles^{2,3}, and Danail Stoyanov¹

¹Wellcome/EPSRC Centre for International and Surgical Sciences, University College London

²Elizabeth Garrett Anderson Institute for Women’s Health, University College London

³NIHR UCL Hospitals Biomedical Research Centre, University College London

chiara.divece.20@ucl.ac.uk

INTRODUCTION

In obstetrics ultrasound (US) training, the learner’s ability to mentally build a three-dimensional (3D) map of the fetus from a two-dimensional (2D) US image represents a major challenge. Pre-defined anatomical planes, known as standard planes (SPs), retain a significant clinical relevance. Their correct acquisition requires extensive experience due to the complexity of SP definition, their high intra- and low inter-class variation. Previous work proposed automating the extraction of SPs from data acquired with a simplified protocol rather than assisting operators in acquiring typical freehand 2D SPs. These methods, based on traditional machine learning (ML) approaches [1] or convolutional neural network (CNN) [2], are mostly confined to selection or classification of SPs. Automatic approaches for the localisation of planes in 3D volumes are based either on supervised learning (SL) [3] or reinforcement learning (RL) [4]. The first ones, even though effective, can mainly localize one single plane at a time or are tailored to just one organ. Also, they attempt to learn a mapping from high-dimensional volumetric data to low-dimensional abstract features directly, making the training difficult. In the second case, most of the available solutions employing deep reinforcement learning (DRL) are based on robotic navigation and are used at the point of care. To the best of our knowledge, there are no available training systems to guide the sonographers in freehand obstetric US. Currently, training in obstetric US is focused on SPs recognition. The autonomous probe navigation towards SPs remains a highly challenging task due to the need to interpret variable and complex images and their spatial relationship. Our work aims to develop a real-time training platform to guide inexperienced sonographers in acquiring proper obstetric US images that could be potentially deployed for existing US machines.

MATERIALS AND METHODS

The development of our training system has been divided into five main blocks (Figure 1).

1. Unity simulator for volume reconstruction and synthetic images acquisition: The fetal volume can be

sliced with arbitrarily oriented planes. The user can visualize them and annotate the standard ones. Besides, the environment can be used for the automated generation of supervised data using pre-acquired 3D US volumes.

2. Plane pose regression system: We use a regression CNN to estimate the 6D pose of arbitrarily oriented US planes using a continuous rotation representation [5]. Our method is purely image-based and, therefore, does not require tracking sensors. Besides, it differs from traditional slice-to-volume registration methods since it does not require a previously acquired volume of the same subject being scanned. Instead, we predict poses relative to a generalized brain center, where training and test data belong to different subjects. The network was trained on synthetic images acquired from phantom US volumes and fine-tuned on real scans. Training data was generated by slicing US volumes in Unity at random coordinates and more densely around the manually annotated transventricular (TV) SP.

Network architecture. We used ResNet-18 as a backbone for feature extraction. We modified the network by re-initialising the fully connected layer and adding a regression head to directly output the rotation and translation representations. The input is the US image I (128×128) obtained by slicing the volume. The CNN predicts the 6D pose $\theta_{Pred} = (t'_x, t'_y, t'_z, \alpha'_x, \alpha'_y, \alpha'_z)$. Specifically, the network outputs a vector of nine parameters $\theta_{Out} = (t_1, t_2, t_3, r_1, \dots, r_6)$; the first three are used for the translation and the last six for the rotation, then used internally by our CNN to reconstruct the rotation matrix \mathbf{R}' in the forward pass.

Loss function. We used the mean squared error (MSE) between predicted $(\mathbf{t}', \mathbf{R}')$ and ground truth (\mathbf{t}, \mathbf{R}) values: $\mathcal{L}_{Tot} = \frac{1}{N} \sum_{t=1}^N \|\mathbf{R}' - \mathbf{R}\|_2 + \lambda \frac{1}{N} \sum_{t=1}^N \|\mathbf{t}' - \mathbf{t}\|_2$, where N denotes the total number of images I within one training epoch, and λ the hyperparameter balancing between the rotation and translation losses.

Experiments. Our framework is implemented in *PyTorch* and trained using a Tesla® V100-DGXS-32GB GPU of an NVIDIA DGX station for 50 epochs with batch size of $K = 100$, Adam optimiser and weighting factor $\lambda = 0.01$. We performed two experiments.

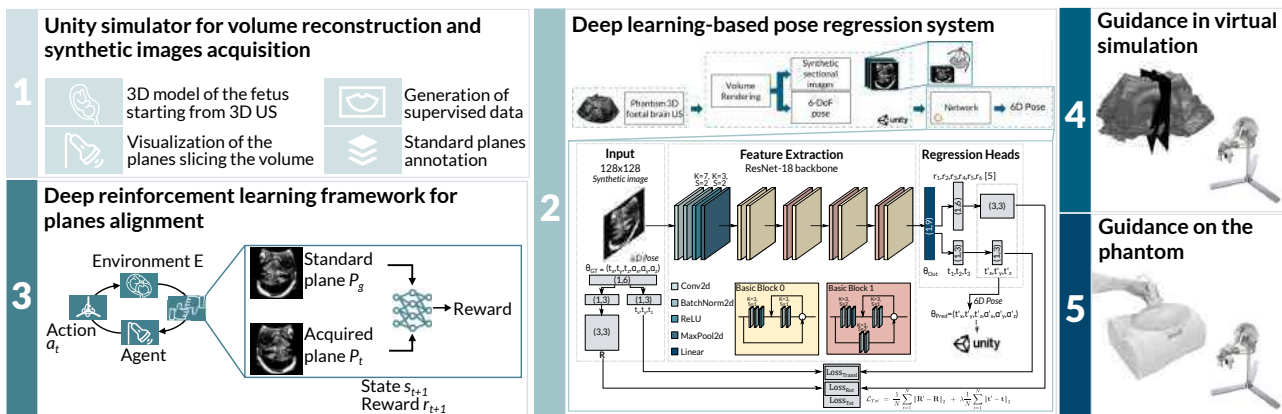


Fig. 1 Overall structure of the training system for obstetric US acquisitions using vision-based DRL

- *Experiment 1: (1.1)* Training (4 scans, 75088 images) and testing (2 scans, 37544 images) on phantom data (same phantom, 23 weeks) with weights from ImageNet; *(1.2)* Training (2 scans of one fetus of 23 weeks, 38754 images) and testing (2 scans of another fetus of 24 weeks, 38754 images) on real data with weights from the case 1.1. The test sets are divided into random planes (*Test RP*) and planes around the TV SP (*Test SP*). For translation, we employed the Euclidean distance between the two planes (*mm*). For rotation, we display errors as the geodesic distance to ground truth ($^{\circ}$) defined as $Error_{Rot} = \arccos((\mathbf{R}^{-1}_{00} + \mathbf{R}^{-1}_{11} + \mathbf{R}^{-1}_{22} - 1)/2)$.
- *Experiment 2:* We fed sectional images of the TV SPs into the network to estimate their pose as a sanity test. We plotted back the two planes within the volume into Unity to visually evaluate the distance between the annotated TV SPs and the predicted ones (2.1, 2.2).

3. DRL framework for planes alignment: The process reminds of the sonographers’ behaviour as they continuously manipulate (*action*) the US probe (*agent*) to scan the maternal abdomen (*environment*) while visualising the intermediate planes P_t on the screen (*state*) until the SP P_g is acquired (*reward* and *terminal state*).

4. Guidance in simulation: Once the direction to align the plane P_t to the standard one P_g is found, the users could be guided through a haptic device by making them *feel* a force pointing towards the correct direction.

5. Guidance on the phantom/patient: The system could be developed as an interface and tested in a clinical setting, with validation studies with novice operators.

RESULTS

Considering the pose regression experiments, for phantom data, the median errors are 0.90 mm/1.17 $^{\circ}$ and 0.44 mm/1.21 $^{\circ}$ for random planes and planes close to TV one, respectively. For real data, testing on a fetus of 24 weeks, these errors are 1.89 mm/2.75 $^{\circ}$ and 1.03 mm/0.86 $^{\circ}$. The average inference time is 2.97 ms per plane. Figures 2 reports the translation and rotation error distributions and the sanity test results for phantom and real data.

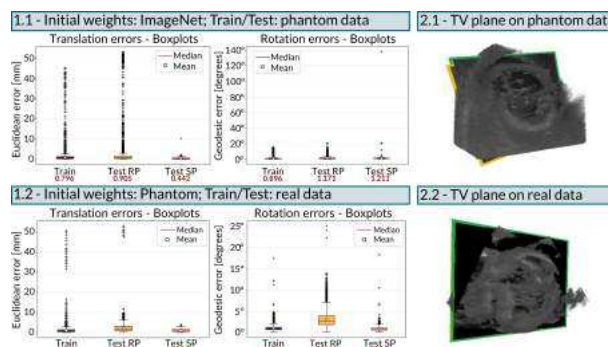


Fig. 2 Left: Translation and rotation error distributions in phantom (1.1) and real (1.2) US data for planes at random coordinates (Test RP) and around the annotated TV SP (Test SP). Right: Visual evaluation of TV SP prediction on phantom (2.1) and real (2.2) US data

DISCUSSION

Our regression CNN can reliably localize US planes within the fetal brain in the phantom, regularly used for clinical training and evaluation of skills; it successfully generalizes pose regression to an unseen fetal brain without the need for real ground truth data in real-time or 3D volume scans of the patient beforehand. Future development will expand the prediction to volumes of the whole fetus and assess its potential for vision-based, freehand US assisted navigation for acquiring SPs.

REFERENCES

- [1] D. Ni *et al.*, “Standard Plane Localization in US by Radial Component Model and Selective Search,” *US in Medicine and Biology*, vol. 40, no. 11, pp. 2728–2742, 2014.
- [2] C. Baumgartner *et al.*, “SonoNet: Real-Time Detection and Localisation of Fetal Standard Scan Planes in Freehand US,” *IEEE Transactions on Medical Imaging*, vol. 36, no. 11, 2017.
- [3] A. Schmidt-Richberg *et al.*, “Offset regression networks for view plane estimation in 3D fetal US,” in *Medical Imaging*, 2019.
- [4] K. Li *et al.*, “Autonomous navigation of an us probe towards standard scan planes with deep reinforcement learning,” *IEEE International Conference on Robotics and Automation*, pp. 8302–8308, 2021.
- [5] Y. Zhou *et al.*, “On the continuity of rotation representations in neural networks,” in *Proceedings of the IEEE Computer Society Conference on Computer Vision and Pattern Recognition*, 2019, pp. 5738–5746.

Deep Reinforcement Learning Based Semi-Autonomous Control for Robotic Surgery

Ruiqi Zhu¹, Dandan Zhang^{1,2}, and Benny Lo¹

¹*The Hamlyn Centre, Imperial College London*

²*Department of Engineering Mathematics, University of Bristol*

INTRODUCTION

In recent year, autonomy has been widely introduced into surgical robotic systems to assist surgeons to carry out complex tasks reducing the workload during surgical operation [1]. Most of the existing methods normally rely on learning from demonstration [2], which requires a collection of Minimally Invasive Surgery (MIS) manoeuvres from expert surgeons. However, collecting such a dataset to regress a template trajectory can be tedious and may induce significant burdens to the expert surgeons.

In this paper, we propose a semi-autonomous control framework for robotic surgery and evaluate this framework in a simulated environment. We applied deep reinforcement learning methods to train an agent for autonomous control, which includes simple but repetitive manoeuvres. Compared to learning from demonstration, deep reinforcement learning can learn a new policy by altering the goal via modifying the reward function instead of collecting new dataset for a new goal. In addition to the autonomous control, we also created a handheld controller for manual precision control. The user can seamlessly switch to manual control at any time by moving the handheld controller. Finally, our method was evaluated in a customized simulated environment to demonstrate its efficiency compared to full manual control.

MATERIALS AND METHODS

The customized simulator is developed based on Asynchronous Multi-Body Framework (AMBF) [3] as shown in Fig.1 (a). The aim is to implement semi-autonomous control for the peg transfer task. The task is segmented into two parts, automatic coarse control and manual override precision control. The coarse control includes controlling the gripper to approach the peg and modify its orientation to an appropriate pose for a grasp. The precision control includes fine-tuning the gripper's orientation, grasping and transferring the peg. The control flow chart is shown in Fig.1 (b). For training an agent to operate in the simulator with deep reinforcement learning methods, we built an environment via Robot Operating System (ROS). With the interface, the environment can feedback reward, image frame and information telling whether the termination state is reached.

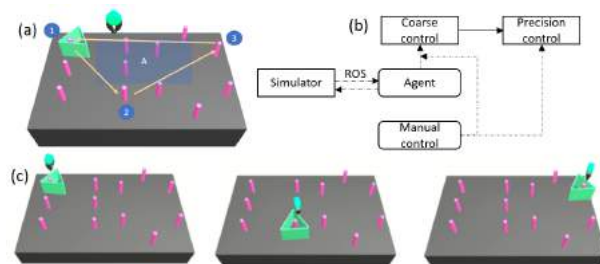


Fig. 1 The illustration of the evaluation task(a), the control flow chart(b), the final frame of episodes with different initialization (c).

Double Deep Q Network (DDQN) [4] was used to optimize the agent for automating the coarse control. In addition, a handheld controller was developed for the user to override the system and carry out precision control.

Coarse Control. For the coarse control, we considered it as a Markov Decision Process defined by a tuple $\{S, A, T, R, \gamma\}$ which represents state space, action space, transition probability, reward function and discount factor. In this experiment, as it was visual-based, the agent only received an image frame after taking a step without knowing the actual state information. visual perception offers the agent the potential of inferring the varying target state. In this experiment, we clipped the frame to the region of interest to reduce the computation load and then stacked four consecutive frames as the input to the deep neural network, so that it can infer the actual state. We would like to hold the end-effector at a consistent height since we want to avoid the danger of the end-effector colliding with other objects. The action space was $\{dx, dy, d\phi\}$, the position movement along x and y axis in Cartesian space and the roll angle of the end-effector in Euler space. The action space was discretized with a precision of $6mm, 8mm, 10rads$ respectively with ranges $[-6mm, 6mm], [-8mm, 8mm], [-10rads, 10rads]$. Narrowing the action space by discretization can bring faster convergence and save training time and computation. To encourage the agent to approach the target, and modify its orientation when the distance d is less than the threshold $d_{threshold}$ of $10mm$, the reward function was defined as shown in Equation 1,

TABLE I Evaluation Results

	Manual	Semi-autonomous
M	329mm	136mm
T	94s	76s

where d_t , $\Delta\theta_t$ refer to the distance to the target and the deviation to the desired orientation angle which is perpendicular to the closest side of the target at time step t respectively. The discount factor γ was set as 0.95.

$$r_{t+1} = \begin{cases} (d_t - d_{t+1})|d_t - d_{t+1}|, & \text{if } d_{t+1} > d_{t\text{threshold}} \\ (\Delta\theta_t - \Delta\theta_{t+1})|\Delta\theta_t - \Delta\theta_{t+1}|, & \text{otherwise} \end{cases} \quad (1)$$

DDQN was used to optimize the objective $J_\theta = \sum_{t=0}^{T-1} \gamma^t r_{t+1}$. The action value update equation is shown as following, where $a_{t+1}^* = \arg \max_{a_{t+1}} Q(s_{t+1}, a_{t+1} | \theta)$.

$$Q(s_t, a_t | \theta) = r(s_t, a_t, s_{t+1}) + \gamma Q(s_{t+1}, a_{t+1}^* | \theta') \quad (2)$$

The decoupling of the selection of the best action and the action value estimation of next state can reduce over-estimation and therefore stabilize the training process. In addition, the use of target network θ' can further stabilize the training [5].

Precise Control. For the manual override precision control, we designed and developed a handheld controller as shown in Fig.2 (a). A depth camera was used to track the 3-D position of the tooltip of the 3-D printed handheld controller using library *OpenCv*, and an IMU sensor was attached at the end of the controller to track its 3-D orientation. Then, the pose was mapped onto the gripper in the simulator for the manual override control. In addition, a footpedal was used to control the clutch of the gripper.

RESULTS

The training of the agent took around 150 episodes to reach the convergence, as shown in Fig.2 (c). In addition, after the convergence, the steps required to complete an episode also converged indicating that it has learned a stable and efficient policy as shown in Fig.2 (d). The final frames of episodes with different initialized target positions are shown as Fig.1 (c). For all three different target positions, the agent can successfully control the gripper to approach the target and modify its orientation to an appropriate position for a grasp.

As for the manual override control, we evaluated the correspondence between the mapped gripper trajectory and the controller trajectory qualitatively as shown in Fig.2 (b). It indicates that the gripper trajectory can correspond to the controller trajectory.

We have conducted a user study to validate the proposed framework. The evaluation task is illustrated in Fig.1 (a). First, the gripper needs to grasp the target at position 1 and transfer the target to position 2. After that, the gripper is reset to a position within region A. The process is repeated to transfer the target from position

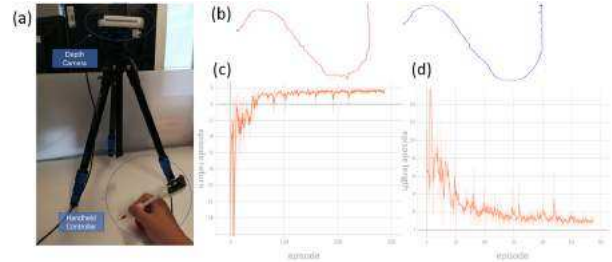


Fig. 2 The setup for manual override control (a), the qualitative results (b): gripper trajectory (red), controller trajectory (blue), episode vs. episode return (c), episode vs. episode length (d).

2 to position 3 and from position 3 to position 1. Participants were asked to carry out this procedure for 9 times. The average controller travel length M and task completion time T were recorded for evaluation. The evaluation results are shown on Table I. It indicated that with the proposed framework, the travel length was reduced by around 58.7% and the completion time was reduced by around 19.1%.

DISCUSSION

In this paper, we proposed a deep reinforcement learning based semi-autonomous control framework. It uses the DDQN to implement the automatic coarse control while the user only need to focus on fine control and make the decision at critical points. The user study showed that the method can reduce the controller travel length by a great margin and the completion time as well. This demonstrates the potential of the proposed method in automating repetitive tasks and reducing the cognitive loads on the surgeons in MIS operations. However, the reduction margin of the completion time was not as high as expected and this was because when starting the fine control after the coarse control phase, the user usually needed to identify the relative pose of the end-effector to the target by moving the controller slightly. Thus, future work includes enabling seamless collaborative control by offering visual or force feedback. In addition, further work will be carried out on transferring the learned policy to the da Vinci surgical Robotic platform.

REFERENCES

- [1] M. Yip and N. Das, "Robot autonomy for surgery," in *The Encyclopedia of MEDICAL ROBOTICS: Volume 1 Minimally Invasive Surgical Robotics*. World Scientific, 2019, pp. 281–313.
- [2] J. Chen, D. Zhang, A. Munawar, R. Zhu, B. Lo, G. S. Fischer, and G.-Z. Yang, "Supervised semi-autonomous control for surgical robot based on bayesian optimization," in *2020 IEEE/RSJ International Conference on Intelligent Robots and Systems (IROS)*. IEEE, 2020, pp. 2943–2949.
- [3] A. Munawar, Y. Wang, R. Gondokaryono, and G. S. Fischer, "A real-time dynamic simulator and an associated front-end representation format for simulating complex robots and environments," in *2019 IEEE/RSJ International Conference on Intelligent Robots and Systems (IROS)*. IEEE, 2019, pp. 1875–1882.
- [4] H. Van Hasselt, A. Guez, and D. Silver, "Deep reinforcement learning with double q-learning," in *Proceedings of the AAAI conference on artificial intelligence*, vol. 30, no. 1, 2016.
- [5] V. Mnih, K. Kavukcuoglu, D. Silver, A. A. Rusu, J. Veness, M. G. Bellemare, A. Graves, M. Riedmiller, A. K. Fidjeland, G. Ostrovski *et al.*, "Human-level control through deep reinforcement learning," *nature*, vol. 518, no. 7540, pp. 529–533, 2015.

Human Machine Interfaces for robot-assisted colonoscopy: a clinical survey

M. Finocchiaro^{1,2,3}, A. Arezzo⁴, A. Menciasci^{2,3}, A. Casals¹, A. Hernansanz^{1*}, G. Ciuti^{2,3*}

¹ Center of Research in Biomedical Engineering, Universitat Politècnica de Catalunya,

²The BioRobotics Institute and ³Department of Excellence in Robotics & AI, Scuola Superiore Sant'Anna,

⁴Department of Surgical Sciences, University of Torino

* These senior authors equally contributed to this work.

martina.finocchiaro@upc.edu

INTRODUCTION

Over the years, the continuous development of intraluminal procedures resulted in strong benefits for the patients, *i.e.*, reduced blood loss, lower risks of infections, diminished scaring impact and quicker recovery time [1]. However, these improvements imposed high mental and physical stress to the clinicians [2], [3]. In this context, the introduction of robotic technologies has resulted in notable improvements in terms of endoscopes flexibility and control stability, by designing multi-steerable snake-like robots and endoscopic capsules. Nevertheless, it also introduces additional degrees of freedom (DOF) to control and sensing information to process, posing the basis for a new framework of human-robot interaction and high-level telemanipulation control [4]. Besides the mechanical design of the surgical device, the Human Machine Interface (HMI, *i.e.*, the interface used to maneuver the endoscope, together with the adopted control strategy and the quality of the feedback received during the interventions) has an important impact over the outcomes of the procedure. Accordingly, all these factors can vary the difficulty of the tasks and are strictly connected to the users' physical and mental stress, influencing their final performances [5]. Focusing on one intraluminal intervention, *i.e.*, robot-assisted colonoscopy, a variety of HMI have been designed in the last decades, including different input devices, assistive tools and feedback [6]. However, few studies aiming at assessing the best features of the HMI have been performed so far [7]–[9], leading to a lack of knowledge about the optimal HMI able to minimize the cognitive and physical load of the operators and maximize their performance. Herein, we present the results of a survey administered to more than 70 endoscopists across different European countries, to get insights about the clinicians' desires on the next generation HMI for robot assisted colonoscopy.

MATERIALS AND METHODS

A group of 71 endoscopists, both gastroenterologist (80%) and colorectal surgeons (20%), with different

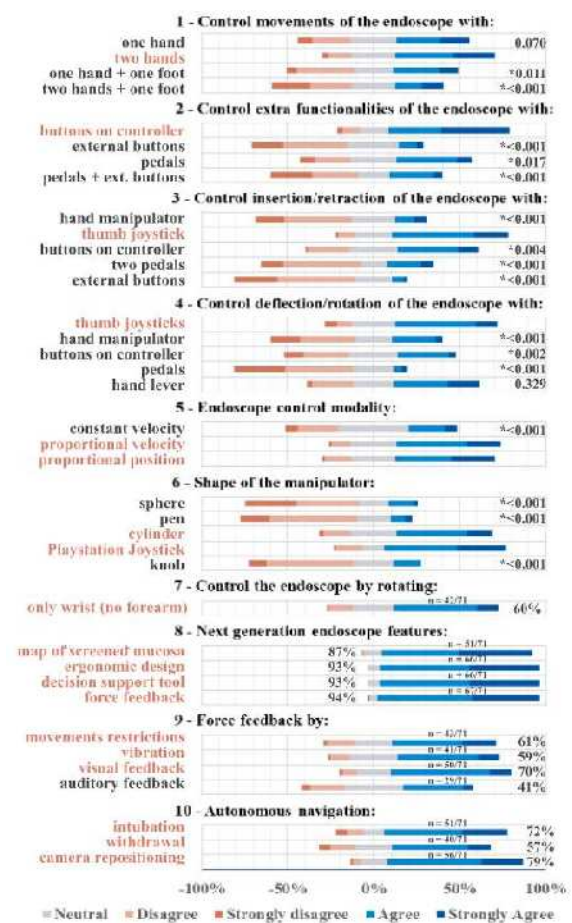


Fig. 1 Summary of the questions and answers provided by 71 endoscopists using a 5-point Likert scale. From questions 1-6, the clinicians' preferred option is highlighted in pink, and the respective *p-values* (preferred option vs other option) of the Wilcoxon signed rank test are reported. For questions 7-10 the answers collecting a percentage of agreement (*agree + strongly agree*) > 50% are highlighted in pink. The number of subjects agreeing (*n*) and their percentage with respect to the total number of subjects interviewed is reported.

levels of experience (15% with less than 2 years, 58% with more than 10 years, and 27% in the middle), filled an anonymous online survey (available at [10])

comprising 38 questions. The questionnaire (Fig. 1) asked to rate with a Likert scale (1 to 5) the level of agreement regarding the inclusion of several features on the next generation HMI for robot-assisted colonoscopy. Explanatory graphics were provided to help understanding the questions, which were conceived jointly by both clinicians and engineers. Consensus measure [11] was used to assess the dispersion of the clinicians' answers, whereas subjects' preferences were estimated comparing the distributions of the medians through the Wilcoxon signed rank test. The percentage of subjects agreeing with each statement was computed by summing all the *agree* and *strongly agree* answers.

RESULTS

The average consensus computed was 0.78 ± 0.04 , indicating a high degree of agreement among the clinicians for each question. Accordingly, the subjects expressed their preference in controlling the endoscope with two hands without using pedals and activating the extra functionalities with buttons integrated in the controller (Fig. 1). The clinicians prefer to control the insertion and retraction of the endoscope by moving a joystick placed on top of the controller with a thumb (up/down), instead of pushing/pulling a manipulator towards the monitor, pressing pedals, or using buttons. Same preferences were expressed for controlling the deflection and rotation of the endoscope (*i.e.*, moving thumbs joystick up-down/right-left). Regarding the control strategy, similarly high rates were given to the proportional velocity control (*i.e.*, the velocity of the tip is proportional to the joystick displacement from its rest-position) and the proportional position control (*i.e.*, the whole deflection of the tip is proportionally mapped on the joystick range of motion), both *p value* <0.001. The manipulator shape is preferred to be cylindrical or Playstation® joystick style, and allowing manipulation by moving only the wrist, without involving the forearm. Force feedback (*e.g.*, to assist the navigation, provide contact forces, attract the camera towards important spots *etc.*) is highly requested (94%) either with haptic constrains (movement restriction and vibration) or with visual information. In addition, all the clinicians highly recommend the insertion of (1) optional autonomous navigation for intubation, withdrawal and tip repositioning, (2) an intelligent tool for decision support during the examination and diagnosis, and (3) a virtual map showing the parts of the mucosa not visualized during the screening. Finally, up to 93% of the clinicians interviewed agree on the need of a more ergonomic design with respect to the conventional colonoscope to reduce the physical load.

DISCUSSION

Results show clear preferences of the clinicians for most of the questions, pointing the high consensus and the outcome of the statistical tests. Considering the inquiries related to the physical aspects of the HMI, the platform commercially available best fitting all the clinicians' desires are the Playstation® style joystick and the 6-

DOF Haptic device (Touch Haptic device, 3D System), which might increase the easiness of use of the controls and reduce the physical load. However, the information collected could drive the design of new custom interfaces, best fitting all the requests. On the software side, clear interest has been shown in the adoption of intelligent tools assisting both navigation and decision-making.

ACKNOWLEDGMENTS

This work was supported by the ATLAS project, which has received funding from the European Union's Horizon 2020 research and innovation program under the Marie Skłodowska-Curie grant agreement No 813782.

REFERENCES

- [1] V. Vitiello, S. L. Lee, T. P. Cundy, and G. Z. Yang, "Emerging robotic platforms for minimally invasive surgery," *IEEE Rev. Biomed. Eng.*, vol. 6, pp. 111–126, 2013, doi: 10.1109/RBME.2012.2236311.
- [2] D. E. Yung, T. Banfi, G. Ciuti, A. Arezzo, P. Dario, and A. Koulaouzidis, "Musculoskeletal injuries in gastrointestinal endoscopists: A systematic review," *Expert Review of Gastroenterology and Hepatology*, vol. 11, no. 10. Taylor and Francis Ltd, pp. 939–947, 2017, doi: 10.1080/17474124.2017.1356225.
- [3] F. O. Marcondes, R. A. Gourevitch, R. E. Schoen, S. D. Crockett, M. Morris, and A. Mehrotra, "Adenoma Detection Rate Falls at the End of the Day in a Large Multi-site Sample," *Dig. Dis. Sci.*, vol. 63, no. 4, 2018, doi: 10.1007/s10620-018-4947-1.
- [4] J. P. Desai, R. V. Patel, A. Ferreira, and S. Agrawal, *The Encyclopedia of Medical Robotics*, vol. 1. WORLD SCIENTIFIC, 2018.
- [5] O. F. Ahmad *et al.*, "Artificial intelligence and computer-aided diagnosis in colonoscopy: current evidence and future directions," *Lancet Gastroenterol. Hepatol.*, vol. 4, no. 1, pp. 71–80, 2019, doi: 10.1016/S2468-1253(18)30282-6.
- [6] G. Ciuti *et al.*, "Frontiers of Robotic Colonoscopy: A Comprehensive Review of Robotic Colonoscopes and Technologies," *J. Clin. Med.*, vol. 9, no. 6, p. 1648, May 2020, doi: 10.3390/jcm9061648.
- [7] G. Ciuti *et al.*, "A comparative evaluation of control interfaces for a robotic-aided endoscopic capsule platform," *IEEE Trans. Robot.*, vol. 28, no. 2, pp. 534–538, 2012, doi: 10.1109/TRO.2011.2177173.
- [8] E. Rozeboom, J. Ruiter, M. Franken, and I. Broeders, "Intuitive user interfaces increase efficiency in endoscope tip control," *Surg. Endosc.*, vol. 28, no. 9, pp. 2600–2605, 2014, doi: 10.1007/s00464-014-3510-1.
- [9] C. Fan, H. Clogenson, P. Breedveld, J. J. van den Dobbelen, and J. Dankelman, "Comparison of two control methods for minimally invasive surgical instruments," *J. Med. Devices, Trans. ASME*, vol. 6, no. 2, pp. 3–8, 2012, doi: 10.1115/1.4006544.
- [10] <https://forms.office.com/r/rE945RK1Y4>
- [11] W. J. Tastle and M. J. Wierman, "An information theoretic measure for the evaluation of ordinal scale data," *Behav. Res. Methods*, vol. 38, no. 3, pp. 487–494, 2006, doi: 10.3758/BF03192803.

A Soft Palpation Sensor for Early Detection of Biological Tissue Abnormalities based on Electrical Impedance Tomography

S. Akhond, J. Avery, and G. Mylonas

The Hamlyn Centre, Imperial College London, London, UK
s.akhond17@imperial.ac.uk

INTRODUCTION

We propose a soft inflatable sensor to detect tissue anomalies for internal examination of organs, especially in cases which are difficult to visualise, and where external palpation by physicians is not possible or informative. Rectal cancer is one of the most common cancers in the world, with over one third of cases diagnosed at a late stage. Assessment of elastic properties of colorectal tissue has been shown to offer potential improvements to tumour diagnostic accuracy, and early detection of precancerous tumours that are not visible through endoscopic imaging [1]. The proposed sensor provides a novel approach for sensing small lesions that are not easily detected by the current visualisation methodologies. The sensor includes an inflatable unit which is used to distend the tissue analogous to a palpation task. Any variation in tissue stiffness will cause a change in the shape of the soft inflatable unit, which is detected using the principles of Electrical Impedance Tomography [2]. A prototype has been designed and tested against a silicone phantom simulating a tissue with abnormalities.

MATERIALS AND METHODS

Fig. 1(a) proposes a soft inflatable cylindrical sensor, with a diameter of 15 mm and height of 9 mm, whose shape changes when it is pressed against tissues of different stiffness. The idea of Electrical Impedance Tomography (EIT) [2], [3] is to apply currents to different electrodes and measure the voltages across them to infer any non-uniform conductivity inside the body [4]. The sensor's design and working principle are inspired by EIT. In abstract, the shape changes are inferred via changes in the voltages across electrodes. Regions with higher stiffness values cause greater deformation in the shape of the sensor and hence, higher change in voltage signals are expected. The sensor is comprised of a thin membrane (1 mm) which is supported by a thicker silicone layer (Ecoflex 00-30) referred to as rigid base in Fig. 1(a). The membrane was inflated using 0.5% saline solution via an inlet tube of 5 mm outer diameter. Two electrodes (copper wires of 0.4 mm diameter) were integrated within the saline chamber. One electrode is fixed in the centre point of the rigid base. The second electrode is embedded within the soft membrane allowing it to move closer or further away from the

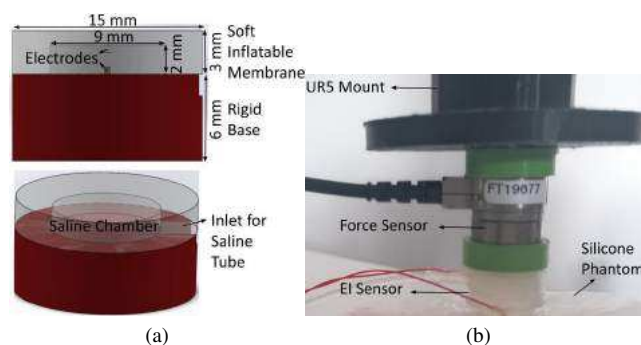


Fig. 1 (a) Sensor Design and (b) attachment to UR5 arm for palpation task.

first electrode as it is pressed against tissues of different stiffness values. As such, any change observed in the voltage values corresponds to the change in distance between the two electrodes. 0.5 ml of 0.9% saline solution is injected causing the membrane to inflate to a dome shape. A current of 2 mA at a frequency of 5 kHz is applied using a Howland current source. The voltage across the electrodes is measured using a National Instruments Corp USB-6363 DAQ at a rate of 50 kHz.

The sensor was tested against a 110x70x25 mm tissue simulating phantom of Ecoflex 00-20. Seven spherical nodules (hard beads), with diameters $d = [4, 6, 8, 10, 12, 14, 16]$ mm, were integrated at a depth of 3 mm during the silicone curing process to simulate tissue abnormalities. The chosen nodule sizes and depth were representative of cancerous tumours in colon tissue [1]. A Universal Robot UR5 arm is used to perform the palpation task. The sensor was mounted on UR5 arm as shown in Fig. 1(b). In addition, a force-torque sensor Nano 17 (ATI Industrial Automation) was placed between the UR5 mounting plate and the proposed soft sensor to measure applied forces. Initially, the sensor is placed just in contact with the silicone phantom - the initial contact point is determined by the force sensor readings. The sensor then indents the tissue vertically with a frequency of 1 Hz. The experiment is repeated with an indentation depth of 3 mm and 5 mm. The palpation task is performed at the location of each hard nodule and on the soft silicone in the neighbourhood of each nodule. The average demodulated amplitude of 10 voltage sine waves was measured.

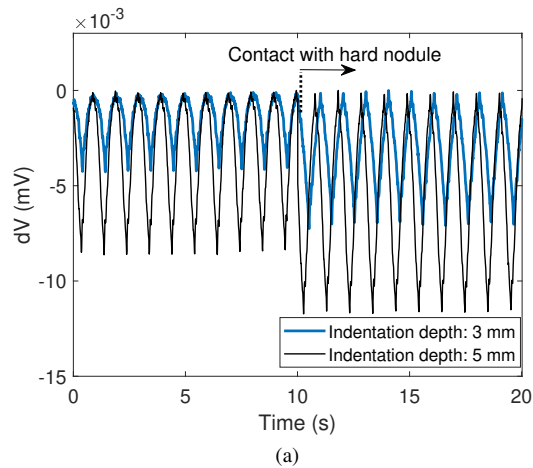


Fig. 2 Change in voltage during palpation upon contact with soft region of silicone phantom and 4 mm hard nodule. Experiment was repeated for indentation depths of 3 mm (blue line) and 5 mm (black line).

RESULTS

Fig. 2 shows the changes in voltage values dV as the sensor is in contact with the soft tissue and the 4 mm hard nodule. The hard nodule is detected for an indentation depth of 3 mm (equal to the nodule depth) and also in the case of deeper indentation (5 mm).

Fig. 3 compares the performance of the sensor to that of the commercially available ATI Nano 17 force torque sensor. The sensor is able to identify nodules both smaller and larger than the sensing area of 9 mm. A heatmap of the change in voltage values in Fig. 4, demonstrates that the sensor can successfully detect the presence of hard nodules in all seven locations. The locations are identified as a change in amplitude of voltages detected between palpating a nodule and a neighbouring soft section on the phantom. As such, the heatmap does not represent the size of nodules detected. Comparison of nodule size and more accurate localization is the subject of a future study.

DISCUSSIONS

This work proposed a new palpation sensor design, inspired by ideas in EIT. The sensor successfully detects small (4 mm) nodules in the model silicone phantom, which would not be visible during existing imaging techniques such as endoscopy. In addition, the sensor has a soft structure as opposed to the commercially available Nano 17 sensor and has a considerably lower cost. The soft nature of the sensor, along with its material choice (silicone, low currents, and non-ferromagnetic) make it safe for use in internal examination and minimally invasive surgery, and MR compatible. Moreover, the small size (15 mm in diameter) and soft structure of the sensor allows it to be attached to a conventional endoscope in the future and navigated inside the colon during endoscopy. However, a soft actuation platform is needed for implementation of the sensor to palpate movable soft tissue (e.g. the colon) and is the subject of further studies.

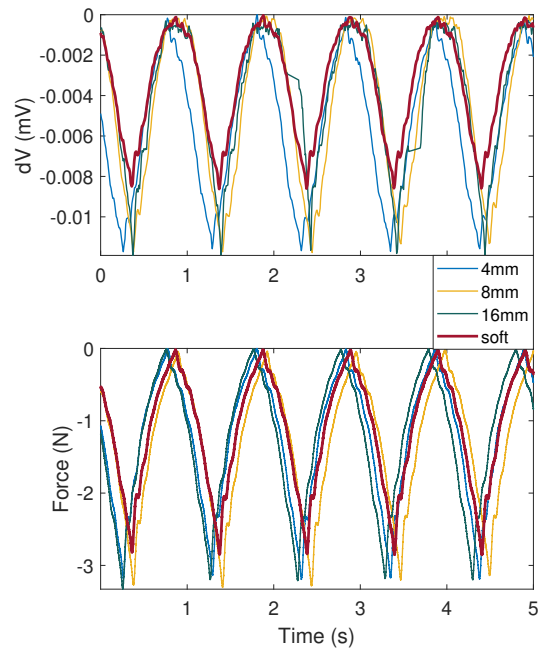


Fig. 3 Comparison of the proposed palpation sensor's performance (top) against an ATI Nano 17 Force sensor (bottom). The red signal corresponds to the sensor's output upon contacting the soft tissue. The experiment was repeated for 3 nodule sizes of $d = \{4, 8, 16\}$ mm.

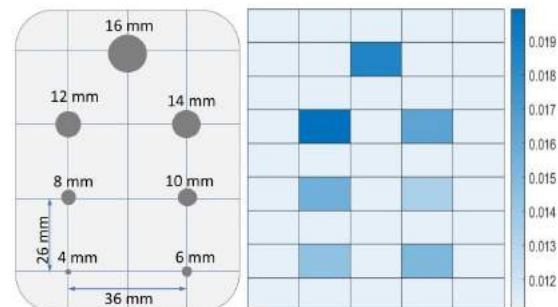


Fig. 4 Sketch of silicone phantom model and hard nodule placements (left) and a heatmap of phantom obtained by the palpation sensor (right).

ACKNOWLEDGEMENTS

The work was supported by CRUK award C57560/A30036.

REFERENCES

- [1] S. Kawano, M. Kojima, Y. Higuchi, M. Sugimoto, K. Ikeda, N. Sakuyama, S. Takahashi, R. Hayashi, A. Ochiai, and N. Saito, "Assessment of elasticity of colorectal cancer tissue, clinical utility, pathological and phenotypical relevance," *Cancer science*, vol. 106, no. 9, pp. 1232–1239, 2015.
- [2] D. Haemmerich, D. J. Schutt, A. S. Wright, J. G. Webster, and D. M. Mahvi, "Electrical conductivity measurement of excised human metastatic liver tumours before and after thermal ablation," *Physiological measurement*, vol. 30, no. 5, p. 459, 2009.
- [3] J. Avery, M. Runciman, A. Darzi, and G. P. Mylonas, "Shape sensing of variable stiffness soft robots using electrical impedance tomography," in *2019 International Conference on Robotics and Automation (ICRA)*. IEEE, 2019, pp. 9066–9072.
- [4] D. Holder, "Part 1 of electrical impedance tomography: Methods, history and applications," *Bristol: Institute of Phys. Publ*, pp. 54–64, 2004.

Proof-of-concept investigation of an instrument-mounted markerless tracking system for robot-assisted orthopaedic surgery

F Tatti, X Hu, and F Rodriguez y Baena

Mechatronics in Medicine Laboratory, Imperial College London, U.K.

{f.tatti, xue.hu17, f.rodriguez}@imperial.ac.uk

INTRODUCTION

Intraoperative patient registration and tracking are key enabling components of Computer-Assisted Orthopaedic Surgery (CAOS). Optical tracking systems that detect rigidly-attached reference frames with reflective markers are the standard in current CAOS systems, due to their large field of view and high accuracy [1], [2].

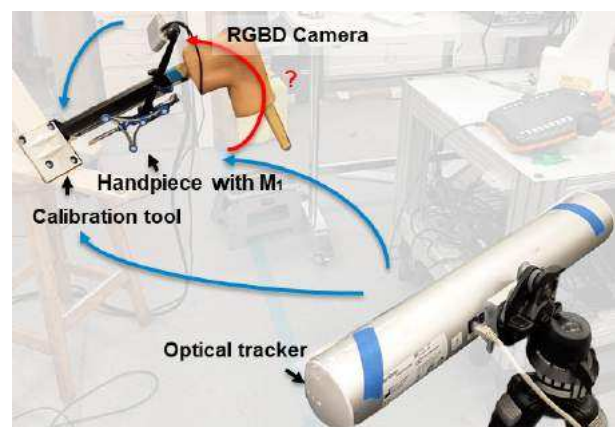
Recent improvements in depth sensing technology have led to the widespread availability of RGBD stereo-cameras. Their adoption in CAOS is appealing, as it would allow to reconstruct a patient's anatomy with a simple 'snapshot' of the scene [3], [4]. However, integrating such cameras into a CAOS system would not be straightforward, as would require changes to the layout traditionally used in current systems. Indeed, while the camera is normally positioned laterally to the patient, a markerless system would need to look directly into the surgical incision, at a much closer distance so as to maximise the density of points in the Region-of-Interest (RoI). While these constraints present some challenges, the light weight and small form factor of many state-of-the-art RGBD cameras allow to envision solutions that would not be possible with bulkier systems.

In this abstract we present a preliminary study for an integrated solution composed of a lightweight RGBD camera connected to the robot-assisted burring tool of a commercial CAOS system. We present preliminary results on the tracking accuracy of the system, and discuss the advantages and disadvantages of such a solution.

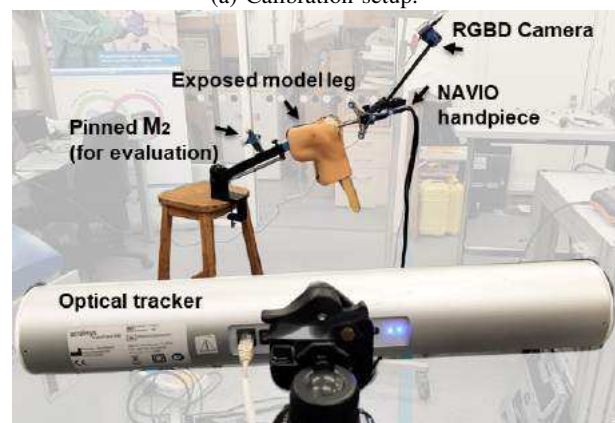
MATERIALS AND METHODS

The Acusense camera (Revopoint 3D Technologies Inc, Shenzhen, China) was selected for this study. It is a highly-compact RGBD camera, with an approximate weight of 100 g and sub-millimetre 3D reconstruction accuracy.

The camera was rigidly attached to the robotic handpiece of the NAVIO™ surgical system (Smith & Nephew inc.), using a custom-made 3D-printed adapter, as seen in Figure 1a. The handpiece itself has a rigidly-attached reference frame with optical markers M_1 for reliable tool tracking. The custom adapter placed the camera at 36 cm from the tip of the handpiece.



(a) Calibration setup.



(b) Registration accuracy testing setup.

Fig. 1 An overview of the system setup.

The system was tested by moving the tip of the handpiece across the surface of a plastic knee anatomical model. The output of the RGBD camera was processed in real time with a deep-learning based algorithm that segments the target femur points from the depth captures and registers them to a pre-scanned reference model. This process is described in detail in [4]. The markerless tracking and registration yield the pose of the tracked femur in the RGBD camera space (*i.e.*, $F^{(D)}(t)$).

In order to assess the accuracy of the registration between the segmented femur and the reference model, a fusionTrack500 optical tracker (Atracsys LLC, Switzer-

land) was used to obtain gold standard reference measurements, by tracking two reference frames rigidly attached to the handpiece (M_1) and femur model (M_2) respectively. The optical tracker was considered as the world frame W . The ground truth femur pose was thus expressed as:

$$F_{gt}^{(D)}(t) = {}^D T_{M_1} \times {}^{M_1} T_W(t) \times {}^W T_{M_2}(t) \times F_{gt}^{(M_2)} \quad (1)$$

where ${}^W T_{M_1}(t)$ and ${}^W T_{M_2}(t)$ are the optically-tracked poses of the reference frames. $F_{gt}^{(M_2)}$ is the initial femur pose registered in the marker frame, and ${}^D T_{M_1}$ is the relative static pose between the reference frame of the RGBD camera and the rigid marker M_1 . These two matrices are unaffected by the movement of the handpiece and thus only need to be calibrated once.

The calibration of ${}^D T_{M_1}$ was computed by using a custom 3D-printed tool S with a known feature-rich 3D surface and reflective markers embedded at known locations. The calibration setup is shown in Figure 1a. The surface of the calibration tool was acquired with the RGBD camera and registered to the CAD model using the Iterative Closest Point (ICP) algorithm for ${}^S T$. The poses of the reflective markers on the handpiece and calibration tool were both acquired using the optical tracker, allowing for the desired calibration to be computed.

A gold-standard reference for the anatomy of the model leg was obtained by digitising the surface of the plastic femur with a tracked probe and recording the position of the probe's tip relative to the optical reference frame attached to the leg. The points were subsequently co-registered with a previously obtained high-resolution scan of the plastic femur, to obtain $F_{gt}^{(M_2)}$.

The accuracy of the markerless registration was assessed by placing the tip of the handpiece in contact with the plastic bone and comparing the pose of the femur estimated from the RGBD data with the reference pose obtained from the optical tracker. To avoid interference between the two cameras, the handpiece was rigidly fixated to a holder and the RGBD and gold standard measurements were obtained sequentially. The setup is shown in Figure 1b.

RESULTS

The detection of the target anatomy was stable and continuous when moving the tool across the bone surface. The overall error was found to be $6.16 \pm 2.68^\circ$ in rotation and $6.03 \pm 2.26\text{mm}$ in translation, in line with previous literature. Figure 2 shows the distribution of quantified errors in 3D. The lowest rotational error shows in the transverse plane, which was expected as this is the rotation best constrained by the morphology of the point cloud.

DISCUSSION

This study provides some initial insights into the feasibility of an instrument-mounted markerless tracking system for robot-assisted orthopaedic surgery. From a technical point of view, such a system would have the advantage of enabling robot assisted cut without

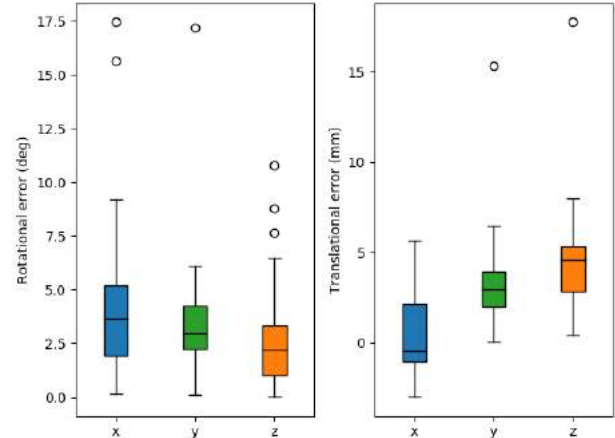


Fig. 2 Markerless registration accuracy results.

tracking any additional instrumentation. Furthermore, this configuration would also minimise line-of-sight concerns and place the camera at an optimal distance from the target anatomy, optimising both the quality of 3D reconstruction and the density of points in the RoI. Some limitations and drawbacks should however be considered: firstly, while the results obtained are in line with the state of the art (see [4], [5]), a higher bone registration accuracy would be required for an effective use of the markerless tracking in the control of the assisted cut, in order to ensure accurate placement of the implant. Secondly, while close proximity of the camera to the surgical site ensures optimal visibility and 3D reconstruction in a controlled lab environment, in a real surgery it would pose sterility challenges, and expose the camera to the risk of occlusion from blood splatter or debris during bone machining.

Altogether, markerless registration and tracking hold great promise for the next generation of CAOS systems. The fast pace at which this technology is evolving justifies optimism, and further research into this space will help the CAOS community gain a better understanding of the best use of these systems.

ACKNOWLEDGEMENTS

This study was partially funded by INNOVATE UK under project number 51235.

REFERENCES

- [1] F. Picard, A. Deakin, P. Riches, K. Deep, and J. Baines, "Computer assisted orthopaedic surgery: Past, present and future," *Medical Engineering and Physics*, vol. 72, pp. 55–65, 2019.
- [2] G. Figueras-Benítez, L. Urbano, A. Acero, M. Huerta, and M. Castro, "Surgical navigation systems: A technological overview," in *Proc. VII Int. Conf. on Elec. Eng. Surg. navigation systems*, 2014.
- [3] J. Ogor, G. Dardenne, S. Sta, J. Bert, H. Letissier, E. Stindel, and C. Hamitouche, "Towards markerless 3d pose estimation for computer assisted orthopaedic surgery: a comparison study of depth cameras," in *CAOS 2020*, 2020.
- [4] X. Hu, H. Liu, and F. Rodriguez y Baena, "Markerless navigation system for orthopaedic knee surgery: A proof of concept study," *IEEE Access*, vol. 9, 2021.
- [5] X. Hu, A. Nguyen, and F. Rodriguez y Baena, "Occlusion-robust visual markerless bone tracking for computer-assisted orthopaedic surgery," *IEEE Trans. Instrumentation and Measurement*, in press.

A Physical Simulator Integrated with Soft Sensing for Mastering the Manipulation of Vascular Structures in Robotic Surgery

A. Mariani, D. Galeazzi, S. Tognarelli, A. Menciacchi

The BioRobotics Institute, Scuola Superiore Sant'Anna, Pisa, Italy

an.mariani@santannapisa.it

INTRODUCTION

Robot-assisted minimally invasive surgery requires the surgeon to learn the new control dynamics of the surgical instruments and, usually, how to deal with the loss of haptic feedback. Indeed, excessive forces applied to delicate tissues – as blood vessels – may cause dramatic intraoperative events, such as major bleeding [1]. Training plays a paramount role to prevent the onset of such adverse events. Nowadays, simulation has come to the forefront to acquire technical skills since it excludes patients from the learning stage. The ideal simulator for surgical training should be able to reproduce the target anatomy with high-fidelity [2]. This is even more fundamental if its aim is teaching tissue manipulation. In this context, tool-tissue interaction and consequent tissue deformation need to be fully realistic [3]. Secondly, the ideal simulator should provide objective assessment of the skill that the simulator is meant to teach [4].

In this work, we introduce a sensorized physical simulator that could be helpful in teaching novices how to reduce tension on vascular structures. On the one hand, physical simulators can reproduce tissue interaction with higher realism than virtual or computer-based simulators. On the other hand, sensorization can guarantee quantitative metrics to assess the surgeon's practical skills and possibly to provide trainees with concurrent (i.e., real-time) feedback to optimize learning.

MATERIALS AND METHODS

Design and fabrication – We focused on robot-assisted thoracoscopic surgery (RATS) to define the target anatomy to simulate. This choice was motivated both by the criticality of tissue manipulation in this kind of procedures and by the expertise of our clinical partner (i.e., Prof. Franca Melfi and her robotic surgery team at the University of Pisa). Indeed, they often require the application of a mechanical stapler on major blood vessels to isolate the lobe to operate. During this task, the most common error for novice surgeons is the exertion of excessive tension on blood vessels [5]. This can lead to the rupture of blood vessels and thus to severe bleeding. In robot-assisted lung lobectomy, vascular injuries are reported in 2.4% of total cases and 87% of such intraoperative events lead to a conversion to open thoracotomy [6]. Specifically, we selected the left inferior pulmonary vein (LIPV) as the vascular structure to simulate. Fig. 1A visually summarizes the fabrication and sensorization of the LIPV simulator.

In details, to create an anatomically accurate model, computed tomography images of an adult human thorax

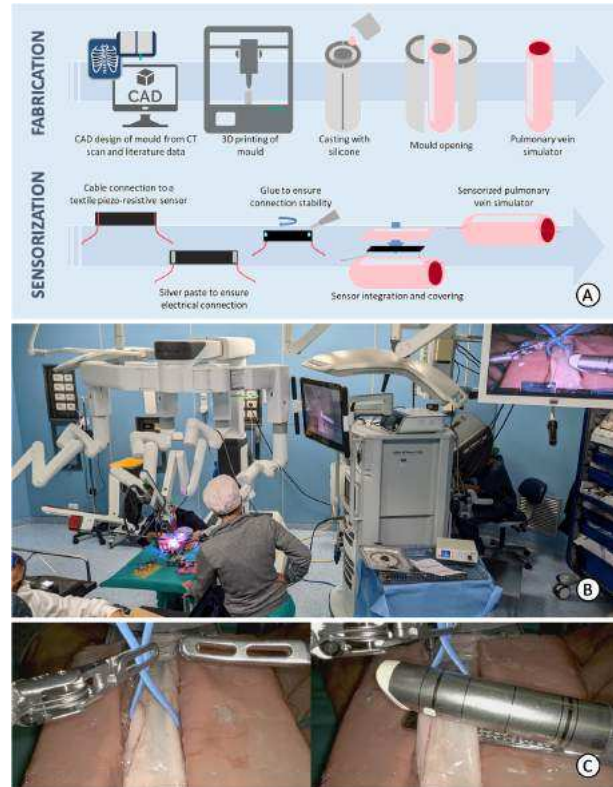


Figure 1. A) Fabrication and sensorization processes. B) A da Vinci Xi Surgical System was used for the preliminary validation of the simulator. C) Two snapshots from the task execution: the surgeon initially passes a blue vessel loop under the vein simulator (left), and later inserts the robotic stapler while raising the vein by taking advantage of the loop (right).

from 3D Slicer library were analyzed. The LIPV simulator was fabricated using the cast molding technique. The mold was designed using SolidWorks software moving from the 3D Slicer segmentation of the LIPV as a reference. Literature data regarding LIPV dimensions were considered to refine the model [7]. The mold was then printed in resin with a ProJet MJP 3600 max machine (by 3D Systems, Rock Hill, SC). Silicone Ecoflex-30 (by Smooth-On, Macungie, PA) was used for the simulator casting. This material was chosen as its elastic modulus is close to the one of pulmonary veins [8].

Severe bleeding of blood vessels is associated to excessive strain [1]. Thus, our sensorization was meant to sense the longitudinal strain ϵ applied to the vein simulator. We aimed at performing such a sensorization without compromising the realism of the simulator. For this reason, we resorted to soft sensors. Specifically, highly stretchable textile sensors were considered since they can be easily integrated into elastic structures and

they also provide a cheap solution. In particular, the conductive polymer LG-SLPA (by Eeonyx Corporation, Pinole, CA) was chosen. The textile was integrated to the simulator by using silicone glue. The conductive polymer LG-SLPA behaves like a variable resistor. It was integrated in a simple voltage divider configuration and an Arduino Mega 2560 was used to power the circuit and to read data. To characterize the sensor, a VT-80 Linear Stage (by Physik Instrumente, Karlsruhe, Germany) was used to impose a linear longitudinal strain to the LIPV simulator. To compute the characterization curve of the sensor, linear interpolation was later applied.

Preliminary validation – We focused on the *construct validity* of the simulator (i.e., its capability to distinguish between users with heterogeneous levels of expertise). The experiments were performed using a da Vinci Xi Surgical System (by Intuitive Surgical Inc., Sunnyvale, CA) (Fig. 1B). The surgical instrument mounted on the left patient-side manipulator was a prograsp forceps. On the right manipulator, there was a tip-up fenestrated grasper, later substituted with a stapler 30 at the end of the task. The LIPV simulator was integrated with a clamping system to pre-tension the vein as in physiological conditions ($\epsilon=0.13$) and a silicon-based support board. This study involved a task resembling the LIPV isolation and stapling. A video showing a repetition of the tasks is available at <https://bit.ly/3Lc3ona>. This task required to: a) pass a vessel loop under the LIPV to later raise the LIPV (Fig. 1C, left), and b) insert the robotic stapler under the LIPV (Fig. 1C, right). Four users with medical background and different levels of RATS expertise joined this study. This group included: a surgeon and proctor (MAS) with more than 20 years of experience in RATS, an expert surgeon (EXP) with 5 years of experience in RATS, a surgeon (SUR) with a single year of experience in RATS, a surgical resident (RES) with no specific experience in RATS, yet surgical education. Each user performed the task 3 times. Strain values were recorded along each task repetition and the maximum strain applied to the vessel during the task was computed and averaged across the 3 repetitions (ϵ_{\max}).

RESULTS

Sensor characterization – The characterization test of the sensorized simulator showed a linear behavior of the resistance variation with respect to the longitudinal strain, with the presence of a small hysteresis (Fig. 2A). The root mean squared error (linear interpolation) was 0.03, corresponding to 4% of the full-scale output. It was considered sufficiently small for the application.

Construct validity – Fig. 2B shows ϵ_{\max} as a function of the user's expertise. It is possible to notice a distinct trend: the higher the experience, the lower the maximum strain applied to the vascular structure.

DISCUSSION

This work introduces an anatomy-based simulator of pulmonary vein integrated with soft textile sensing. Sensor data can be processed to extract a simple metric related to the vessel strain and this information was

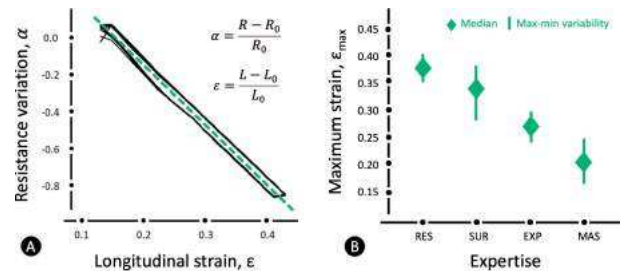


Figure 2. A) Data from uniaxial tensile test (black) and calibration curve (green). B) Proof of the *construct validity* of the simulator (expertise levels defined in the *Methods* section).

proven to objectively discriminate medical users with heterogeneous levels of expertise. This feature (*construct validity*) plays a relevant role in training and education, as it can be used to assess when the trainee has learnt how to master a certain skill. The possibility to assess skills by using a sensor makes the evaluation totally objective, as well as independent from the presence of a proctor. In addition to skill assessment, sensor data can be used to provide a warning feedback to the trainee (e.g., using a buzzer). A strain-based feedback could optimize learning the robot-assisted manipulation of vascular structures (where haptic feedback is usually missing) by teaching the maximum strain that can be applied.

Extensive validation (on a wider population) is required to assess the real usefulness of this platform in training curricula and in different surgical specialties that involve the manipulation of vascular structures. A study on the simulator's mechanical properties is needed to properly assess its high-fidelity. Also, testing the reproducibility of the developed simulator is necessary.

REFERENCES

- [1] M. F. Berry, "Pulmonary Artery Bleeding During Video-Assisted Thoracoscopic Surgery: Intraoperative Bleeding and Control," *Thorac. Surg. Clin.*, vol. 25, no. 3, 2015.
- [2] C. S. Abdelshehid et al., "High-fidelity simulation-based team training in urology: Evaluation of technical and nontechnical skills of urology residents during laparoscopic partial nephrectomy," *J. Surg. Educ.*, vol. 70, no. 5, 2013.
- [3] C. L. Cheung, et al., "Use of 3-dimensional printing technology and silicone modeling in surgical simulation: Development and face validation in pediatric laparoscopic pyeloplasty," *J. Surg. Educ.*, vol. 71, no. 5, 2014.
- [4] S. S. Vedula, et al., "Objective Assessment of Surgical Technical Skill and Competency in the Operating Room," *Annu Rev Biomed Eng.*, vol. 19, 2018.
- [5] S. L. Meyerson et al., "Needs assessment for an errors-based curriculum on thoracoscopic lobectomy," *Ann. Thorac. Surg.*, vol. 94, no. 2, 2012.
- [6] R. J. Cerfolio, et al., "Incidence, Results, and Our Current Intraoperative Technique to Control Major Vascular Injuries During Minimally Invasive Robotic Thoracic Surgery," *Ann. Thorac. Surg.*, vol. 102, no. 2, 2016.
- [7] K. Iso et al., "Wall thickness of the pulmonary vein-left atrial junction rather than electrical information as the major determinant of dormant conduction after contact force-guided pulmonary vein isolation," *J. Interv. Card. Electrophysiol.*, vol. 46, no. 3, 2016.
- [8] J. Banks, et al., "The physical properties of human pulmonary arteries and veins," *Clin. Sci. Mol. Med.*, vol. 55, no. 5, 1978.

Robotic Telemanipulation System for Minimally Invasive Surgery using a Passive Universal Joint and Inertial Sensors

Max B. Schäfer, Moritz Hemmer, Anja M. Glöckner, Peter P. Pott

*Institute of Medical Device Technology, University of Stuttgart, Germany
max.schaefer@imt.uni-stuttgart.de*

INTRODUCTION

Robot-assisted surgery (RAS), such as minimally invasive surgery (MIS), performed by means of master-slave telemanipulation systems, has the potential to improve both the surgical outcome in certain procedures and ergonomic aspects for the surgeon [1, 2]. Regarding the widespread use and the levels of complexity and resource consumption, there is a considerable gap between sophisticated RAS systems and conventional minimally invasive procedures. Designing a simplified RAS system for versatile applications could ease this gap, thus it leads to a more widespread use.

During surgical procedures, space around the situs is limited, which is further aggravated by bulky RAS systems. Even the setup of multiple manipulator arms is challenging due to additional space-consuming equipment. The design of the manipulator's kinematics has a strong influence on this issue. By using a stiff connection between the instrument and the manipulator's tool center point (TCP) and a zero-force constraint in the invariant trocar point, in RAS systems it is commonly tried to avoid lateral forces onto the abdominal wall, referring to less trauma for the patient [3]. However, it remains unclear if there is a quantifiable advantage of this feature compared to conventional laparoscopy where those lateral forces are commonly accepted. Further, this approach leads to a relatively large range of motion of the manipulator's TCP. Using a passive universal joint between the manipulator's TCP and the surgical instrument and accepting the occurrence of lateral forces, might lead to a more compact manipulator design [cf. 4]. Aiming for widespread usage, further simplifications are required. Using standard and off-the-shelf components, such as conventional surgical tools, will potentially increase the applicability to different surgical procedures and will ease the integration into existing infrastructure. Our work aims on the investigation of various aspects regarding the simplification of RAS systems. Thus, there is a need for a reconfigurable and easy to adapt master-slave telemanipulation setup. In this paper, the kinematic approach and the setup of the components are described.

MATERIALS AND METHODS

A seven degree of freedom (DOF) articulated robotic arm (Panda, Franka Emika GmbH, Germany) is used as the manipulator of the telemanipulation setup. Due to its kinematic redundancy, any TCP pose can be achieved with arbitrary joint configurations, which has advantages regarding the collaboration with staff around the situs.

Conventional laparoscopic instruments by Karl Storz (KARL STORZ SE & Co. KG, Germany) can be mounted to the manipulator via a mechanical interface. The mechanical interface is attached to the manipulator's TCP by a passive universal joint and contains an inertial measurement unit (IMU) GY-521 with an MPU-6050 chip (InvenSense Inc., CA, USA) for the orientation determination. Additionally, a HEX 21 6-axis force and torque sensor (Wittenstein SE, Germany) is integrated into the mechanical interface, enabling the measurement of interaction forces at the instrument's tip.

As a first input device, a Falcon (formerly Novint Technologies Inc., New Mexico, USA) is used. It allows to command translational movements in 3 DOF and to provide feedback forces. The components of the telemanipulation setup are depicted in Fig. 1.

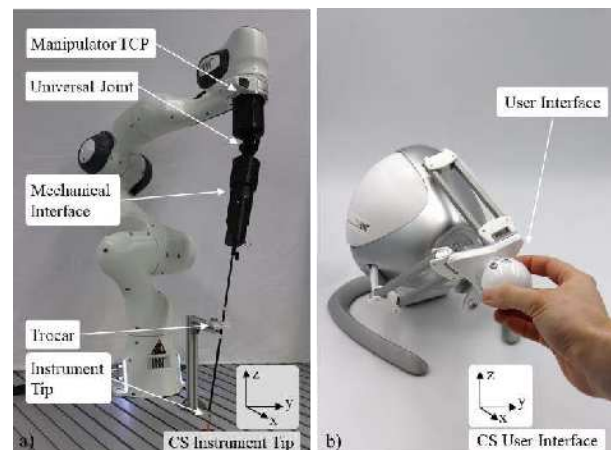


Fig. 1 Manipulator with mechanical interface and instrument (a), and Novint Falcon input device (b).

The movements of the user interface of the input device are mapped to the tip of the instrument with an adjustable ratio of motion scaling. Due to the passive universal joint and the varying penetration depth of the instrument in the trocar point, the IMU is required to obtain the orientation of the instrument's longitudinal axis. With the position of the manipulator's TCP, the orientation of the mechanical interface, and the known length of the surgical instrument, the position of the instrument's tip is determined.

The overall communication follows a master-slave architecture. The master consists of the input device while the slave consists of the manipulator, IMU, and the force-/torque sensor. Both subsystems are connected to a workstation. The input device is connected via USB and controlled in a 1 kHz control loop via a C++ application. The manipulator is connected to the workstation by

TCP/IP and communicates via the provided SIMULINK (The MathWorks Inc., MA, USA) library. Force-/torque sensor and IMU are read out via a Raspberry Pi 4 Model B (Raspberry Pi Foundation, Cambridge, UK) using the MATLAB (The MathWorks Inc.) Support Package for Raspberry Pi Hardware. Interprocess communication on the workstation is achieved via a shared memory concept.

To achieve a soft behavior of the manipulator and of the instrument's tip, and the ability to exert and compensate for interaction forces, force control is required. The force control is implemented as a task space impedance controller at the manipulator TCP, neglecting trocar friction and trocar point and instrument deformation. Stiffness matrix K_m and damping matrix D_m are based on a harmonic oscillator with damping ratio of 1 (critically damped) and mass of 1 kg (approximate endeffector mass), resulting in the following equation:

$$D_m = 2\sqrt{K_m} \quad (1)$$

To determine a suitable translational stiffness, measurements were performed evaluating onset latency, settling time, steady state error, and overshoot. Therefore, a step function with an amplitude of 10 mm was commanded to the manipulator, resembling a sudden input movement from a user. The desired stiffness was increased in steps of $100 \text{ N}\cdot\text{m}^{-1}$ from $1000 \text{ N}\cdot\text{m}^{-1}$ to $2000 \text{ N}\cdot\text{m}^{-1}$. For every stiffness, 10 measurements were carried out.

Furthermore, the overall system latency was evaluated using a high-speed camera (MiniVis EoSens, High Speed Vision GmbH, Ettlingen, Germany) with a frame rate of 1000 fps and a spatial resolution of 560×148 pixels. An overall number of 10 measurements were performed.

RESULTS

Preliminary tests confirm the proposed kinematic setup and show robust operation. In the case of a 1:1 ratio of motion scaling, the required range of motion of the manipulator's TCP is only dependent of the penetration depth and the resulting leverage ratio. Thus, the required range of motion is relatively compact. The chosen control strategy in the task space allows to collaboratively interact with the manipulator at any of its limbs. This enables staff to manually change joint configurations without influencing the position of its TCP.

Fig. 2 shows the mean values and standard deviations for onset latency, settling time, steady state error, and overshoot. As expected, the onset latency drops with higher stiffness. The settling time decreases up to a stiffness of $1500 \text{ N}\cdot\text{m}^{-1}$, afterwards a strong increase can be seen, which is caused by a positive overshoot. With a stiffness of $1600 \text{ N}\cdot\text{m}^{-1}$, the remaining offset is at its minimum, and the strong increase for higher stiffnesses can be explained by slight oscillations of the system for higher stiffnesses. A stiffness of $1500 \text{ N}\cdot\text{m}^{-1}$ was finally chosen to ensure a short onset latency while still showing a stable behavior. This results in translational damping of $77.5 \text{ N}\cdot\text{s}\cdot\text{m}^{-1}$. Using these stiffness and damping values, mean overall system latency is 61.5 ms (SD = 7.8 ms).

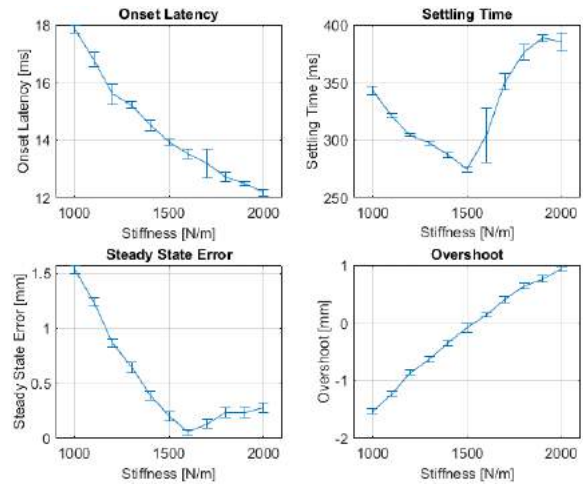


Fig. 2 Mean values and standard deviations for onset latency, settling time, steady state error, and overshoot.

DISCUSSION

The suggested kinematic approach using a passive universal joint allows for a reduced range of motion of the manipulator's TCP. However, the magnitude of the forces on the abdominal wall needs to be investigated. In this work, a 7 DOF robot was used, however, a manipulator with less DOF, such as a 4 DOF SCARA kinematic, would be sufficient, due to the universal joint, and would allow compact manipulator designs.

Using an IMU for obtaining the instrument's orientation, brings up the issue of sensor drift over time. Since the user is a part of the feedback loop, it might be negligible, however, the sensor drift must be further quantified.

In this work, a fixed trocar point is used. Disturbances, such as slight movements of the patient and the soft behavior of the abdominal wall might lead to a changing position of the trocar point. This can be handled by permanently recalculating the intersection point of two consecutively measured orientations of the instrument.

The latency of the system is sufficiently small [5]. However, the biggest influence was observed to be the communication between workstation and manipulator which will also be addressed in the future.

REFERENCES

- [1] Kwak JM, Kim SH. Robotic Surgery for Rectal Cancer: An Update in 2015. *Cancer Res Treat.* 2016; 48(2):427-435.
- [2] Wee IJY, Kuo L-J, Ngu JC-Y. A systematic review of the true benefit of robotic surgery: Ergonomics. *Int J Med Robotics Comput Assist Surg.* 2020; 16:e2113.
- [3] Kuo CH, Dai JS, Dasgupta P. Kinematic design considerations for minimally invasive surgical robots: an overview. *Int J Med Robotics Comput Assist Surg.* 2012; 8: 127-145.
- [4] Ghodoussi M, Butner SE, Wang Y. Robotic surgery - the transatlantic case. *Proceedings 2002 IEEE Int Conf on Robotics and Automation*, 2002, pp. 1882-1888 vol.2.
- [5] Anvari M, Broderick T, Stein H, Chapman R, Ghodoussi M, Birch DW, Mckinley C, Trudeau P, Dutta S, Goldsmith CH. The impact of latency on surgical precision and task completion during robotic-assisted remote telepresence surgery. *Comput Aided Surgery.* 2005; 10:2, 93-99.

Dense 3D Reconstruction Through Lidar: A New Perspective on Computer-Integrated Surgery

Guido Caccianiga and Katherine J. Kuchenbecker

Haptic Intelligence Department, Max Planck Institute for Intelligent Systems
{caccianiga, kjk}@is.mpg.de

INTRODUCTION

Technical innovations in sensing and computation are quickly advancing the field of computer-integrated surgery. From one side, spectral imaging and biophotonics are strongly contributing to intraoperative diagnostics and decision making. Simultaneously, learning-based algorithms are reshaping the concept of assistance and prediction in surgery. In this fast-evolving panorama, we strongly believe there is still a need for *robust geometric reconstruction of the surgical field* whether the goal is traditional surgical assistance or partial or full autonomy.

3D reconstruction in surgery has been investigated almost only in the space of mono and stereoscopic visual imaging because surgeons always view the procedure through a clinical endoscope. Compared to using traditional computer vision, deep learning has made significant progress in creating high-quality 3D reconstructions and dense maps from such data streams, especially for monocular simultaneous localization and mapping (SLAM) [1]. The main limitations are linked to reliability, generalization, and computational cost.

Meanwhile, *lidar* (light detection and ranging) has greatly expanded in use, especially in SLAM for robotics, terrestrial vehicles, and drones. Lidar sensors explicitly measure the depth field rather than inferring it from camera images. The technology is evolving quickly thanks to the upsurge of mixed and augmented reality in consumer mobile devices [2]: high-resolution, short-range, miniaturized lidar sensors are expected soon.

In parallel to these developments, the concept of multiple-viewpoint surgical imaging was proposed in the early 2010's in the context of magnetic actuation and micro-invasive surgery [3]. In routine clinical practice, however, the use of multiple trans-abdominal cannulae still limits the kinematics of the camera and instruments to have a fixed pivot point at the body wall. For this reason, here we propose an approach in which *each surgical cannula can potentially hold a miniature lidar*. We envision that exploring this powerful sensing technology and enabling multi-viewpoint imaging without disrupting the current surgical workflow will yield far more accurate and complete 3D reconstructions of the surgical field, which opens new opportunities for the future of computer-integrated surgery.

MATERIALS AND METHODS

We chose a simulated surgical scene composed of custom silicone organs arranged to reproduce a human

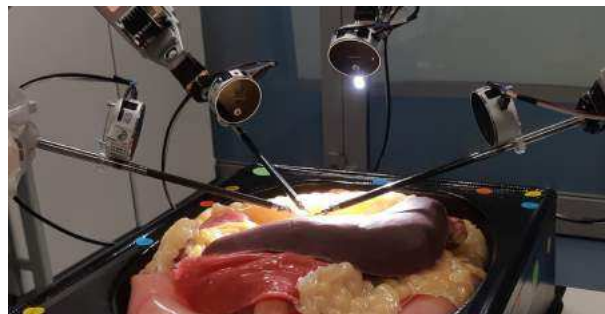


Fig. 1 Our experimental setup featuring a da Vinci Si, four puck-shaped Intel L515 high-resolution lidar cameras attached to the cannulae, and custom organs [4] located within an EASIE-R whole-abdomen surgical simulator.

abdomen [4] (Fig. 1). A ground-truth (GT) measurement of this scene was meticulously acquired using an Artec Eva HD (0.1 mm accuracy) 3D scanner (Fig. 3d). An Intel L515 high-resolution (1024×768, 30 fps) lidar camera was then attached to each of the four cannulae of an Intuitive Surgical da Vinci Si (Fig. 1). We programmed the L515s' lasers and infrared receivers to produce point clouds at close range (≥ 5 cm); they interface with our Ubuntu 20.04 workstation through the RealSense SDK and ROS wrappers. A Raspberry Pi 4B externally triggers the four lidars to sequentially capture their point clouds. We record the stereo images of the da Vinci endoscope (1920×1080, 30 fps) using a DeckLink Duo 2 with custom ROS drivers [5]. We performed 3D reconstruction from the endoscope images using the pre-trained HSM network because it performed best on the SERV-CT surgical dataset [6].

All five resulting point clouds (endoscope and four lidars) were imported into Artec Studio 16 and independently registered to the GT surface via a robust proprietary alignment procedure based on geometry features. Then the registered point clouds were exported to CloudCompare for computational evaluation. For each cloud, we first calculated a scalar field (*point-to-GT*) representing the signed distance of each recorded point to the GT surface (Fig. 2a-f); non-zero values show sensing errors. We then evaluated how well each sensor covers the surgical scene by sampling the entire GT surface (constant density of one point per mm^2) and calculating a second set of scalar fields (*GT-to-point*) for the signed distance from each GT vertex to the closest point in a surface created from the selected point cloud (Fig. 2g-l); unseen GT points have high distance.

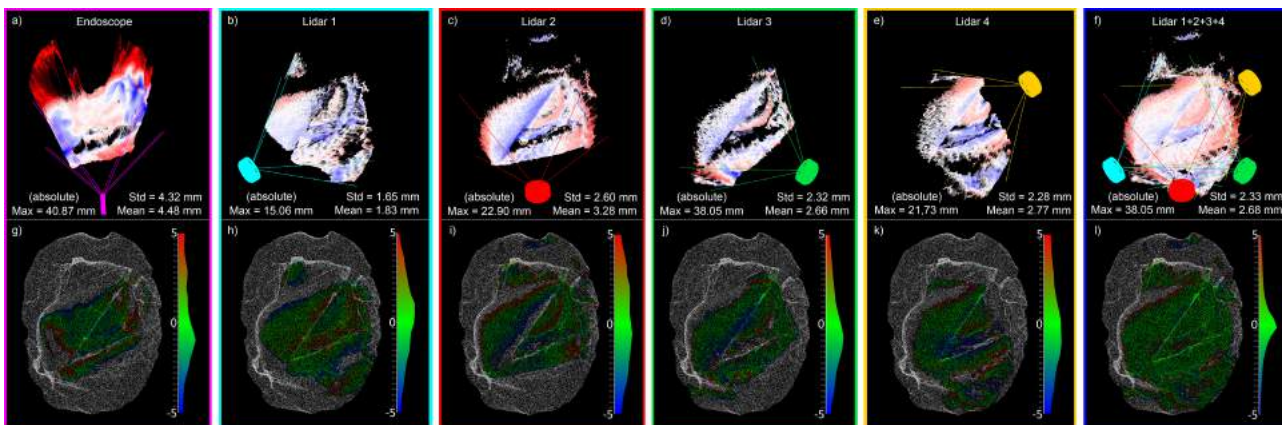


Fig. 2 The point clouds (a–f) from each sensor color-mapped with the *point-to-GT* scalar fields (red: positive error, blue: negative). Statistics are calculated from the absolute scalar values. For each point cloud (a–f), the respective *GT-to-point* scalar field distribution is shown (g–l) in the ± 5 mm range. Green areas highlight the portion of the ground truth surface that is reconstructed accurately.

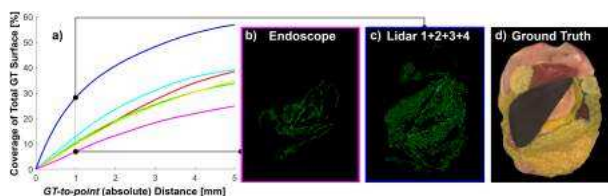


Fig. 3 a) Percentage of total ground truth surface covered by each sensor for an increasing *GT-to-point* error range. b, c) areas covered by the endoscope (magenta) and the four lidars combined (blue) for the ± 1 mm error range. d) Ground truth.

RESULTS

The *point-to-GT* scalar fields depicted in Fig. 2(a–e) show the overall accuracy of each camera with respect to the GT. Maximum, mean, and standard deviation of the distances for each point cloud are reported. Figure 2(f) shows the result of overlapping the four lidar point clouds to characterize the total potential coverage of a multi-viewpoint approach. To better address scene coverage while also considering point-placement accuracy, the *GT-to-point* scalar fields are plotted in the ± 5 mm range and shown in Fig. 2(g–l) with their error distributions.

Figure 3 shows the percentage of the total surface of the GT seen by each sensor for an allowed error range between 0 mm and ± 5 mm. Each lidar accurately sees about 50% more of the GT surface than the endoscope. The inset images show, in comparison, the coverage of the endoscope and the four combined lidars at a conservative error tolerance of ± 1 mm. For each GT vertex covered by multiple lidars, we chose the point with minimum error to provide an upper bound on performance that could be expected from this method.

DISCUSSION

We proposed a novel approach to dense 3D reconstruction using lidars attached to the surgical cannulae. Direct comparison between lidar from different viewpoints and a state-of-the-art 3D reconstruction method on stereoendoscope images showed that lidar-generated point clouds achieve better accuracy and scene coverage. Furthermore, lidars have the advantage of directly

producing measured point clouds, removing the computational effort and delay of estimating depth from the pixel disparity. This experiment especially hints at the potential of lidar imaging when deployed in a multiple-viewpoint approach.

Aligning point clouds to the GT a posteriori allowed quantitative analysis, but continuous cloud-to-cloud alignment should be implemented for real-world usage. Another limitation for clinical testing and translation of the proposed setup is the physical size of the lidars we used (36 mm \times 30 mm minimum chip size). We envision new surgical procedures where multiple miniaturized sensors could be directly embedded in cannulae, as [7] did with cameras, or, if untethered, grasped and assembled on instruments or magnetically controlled from the outside. Such technologies will enable novel computer-integrated systems that could help surgeons during the critical steps of complex procedures by providing omnidirectional visualization, AR pre-operative overlays, safety enhancement, and real-time pseudo-haptic cues.

REFERENCES

- [1] D. Recasens, J. Lamarca, J. M. Fácil, J. M. M. Montiel, and J. Civera, “Endo-depth-and-motion: Reconstruction and tracking in endoscopic videos using depth networks and photometric constraints,” *IEEE RA-L*, vol. 6, no. 4, pp. 7225–7232, 2021.
- [2] M. Vogt, A. Rips, and C. Emmelmann, “Comparison of iPad Pro’s LiDAR and TrueDepth capabilities with an industrial 3D scanning solution,” *Technologies*, vol. 9, 2021.
- [3] Y.-H. Su, K. Huang, and B. Hannaford, “Multicamera 3D viewpoint adjustment for robotic surgery via deep reinforcement learning,” *JMRR*, vol. 06, p. 2140003, 3 2021.
- [4] E. D. Gomez, “The role of haptic tool vibrations in skill acquisition and assessment in minimally invasive robotic surgery,” Master’s thesis, University of Pennsylvania, 2013.
- [5] M.-P. Forte, R. Gourishetti, B. Javot, T. Engler, E. T. Gomez, and K. J. Kuchenbecker, “Design of interactive AR functions for robotic surgery and evaluation in dry-lab lymphadenectomy,” *IJMRAS*, pp. 1–21, Nov. 2021.
- [6] P. J. E. Edwards, D. Psychogyios, S. Speidel, L. Maier-Hein, and D. Stoyanov, “SERV-CT: A disparity dataset from cone-beam cone-beam CT for validation of endoscopic 3D reconstruction,” *Medical Image Analysis*, p. 102302, 2021.
- [7] A. Afifi, C. Takada, Y. Yoshimura, and T. Nakaguchi, “Real-time expanded field-of-view for minimally invasive surgery using multi-camera visual simultaneous localization and mapping,” *Sensors*, vol. 21, pp. 1–20, 3 2021.

Development of a wearable fluorescence sensor for non-invasive monitoring of gut permeability

Elena Monfort Sánchez, James Avery, Ara Darzi, Alex J. Thompson

*Hamlyn Centre, Imperial College London, London, UK,
e.monfort-sanchez19@imperial.ac.uk*

INTRODUCTION

Inflammatory bowel disease, coeliac disease, and malnutrition have all been linked to changes in intestinal function, particularly gut permeability [1]. Endoscopic biopsies and histopathology, together with chemical tests such as Lactulose:Mannitol assays, are the techniques currently used to assess permeability in the clinic. However, those methods are either invasive, unable to offer comprehensive diagnoses, or challenging to perform in infants [2]. Further, the mechanisms and interactions behind the gut's function in the aforementioned (and additional) disorders are currently not well understood. As a result, novel diagnostic technologies that provide non-invasive and accurate measurements of intestinal permeability (and other aspects of gut function) could have major therapeutic implications [3].

Recent studies in both humans and animals have shown the potential of transcutaneous fluorescence spectroscopy to provide information relevant to gastrointestinal (GI) function – including gut permeability – in a non-invasive manner (e.g. [4-7]). This method entails oral administration of a fluorescent contrast agent combined with the use of a wearable probe to non-invasively measure the permeation of the contrast agent from the gut into the blood stream, thereby facilitating measurements of gut leakiness/permeability and other clinically relevant GI functions [4-7]. However, the devices that have been used for this purpose are laser-based, large and expensive, which make them unsuitable for large scale clinical deployment [4-7].

To address the above limitations, here we report preliminary results from a compact fluorescence spectroscopy sensor for transcutaneous monitoring of gut function. The primary functionality of the device is to detect fluorescence signals at the skin as an orally ingested contrast agent (fluorescein) permeates through the gut barrier into the blood stream. For the developed sensor, the optical system, electronic design, and optical and temperature safety assessments are reported below, along with preliminary results demonstrating the potential for clinical use.

METHODS

Optical system. The overall concept of the compact fluorescence spectroscopy sensor is represented in Figure 1A. Excitation light is provided by a light emitting diode (LED), which is separated from the detection

components (Photodiodes, PDs) to minimise the effect of light leaking directly from the LED to the PDs. Optical fibres (200 μm diameter) transport light from the LED to the tissue and back to the PDs, with custom 3D printed mounts used to ensure secure placement at the fingertip. All electronic and optical components are encapsulated inside two 12x9.4x3.4 cm metallic boxes (LED and PDs separated).

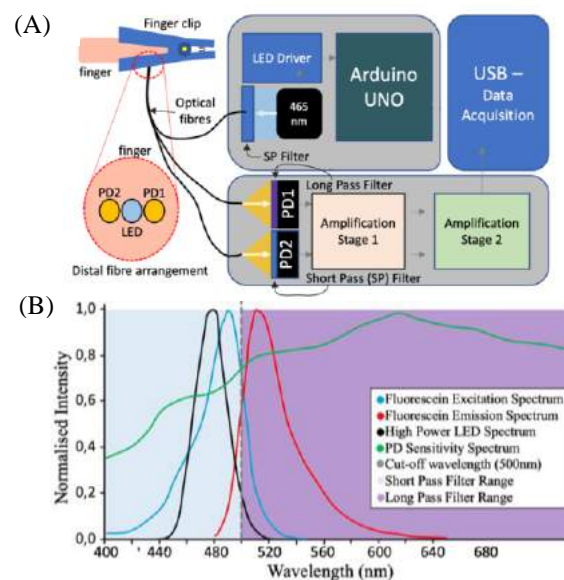


Figure 1. (A) Diagram of the developed fluorescence sensor. 250 μm spacing between Optical fibres at the finger clip; (B) Spectra of the optical components used in the compact fluorescence sensor. Spectral data was obtained from the datasheets of each component.

The sensor aims to detect the fluorescence emission from fluorescein (a clinically approved fluorescent contrast agent) in the blood stream. To achieve this, the sensor employs one high power LED (465 nm peak intensity) for excitation and two Silicone PIN PDs for detection (one for detection of the fluorescence signal; one for detection of the backscattered LED signal, which is used for normalisation). Because the PDs have broad sensitivity spectra, with 70% relative sensitivity at 500 nm, we incorporated three flexible reflective optical filters (cut-off wavelength at 500 nm; two short pass, one long pass filter) into the system to remove the wavelengths that will negatively affect the collected data. Figure 1B shows the spectral characteristics of each optical component in the system.

Electronic design. Since the fluorescein dose is dispersed throughout the vascular system, the expected

fluorescence intensity at the sensor is small. For that reason, the electronic circuitry is designed to amplify the signal as much as possible while also minimising the noise. This is achieved by a two-staged amplification cascade. The first stage uses a very-low input bias transimpedance amplifier (TIA; ADA4530) to convert the input PD current into amplified voltage. The second stage employs standard non-inverting amplification to further amplify and filter the signal.

RESULTS

Optical power/temperature safety assessment. As shown in Figure 1A, the output from the 465 nm high power LED is directed onto the human finger (through use of an optical fibre). Because the measurements are collected on the fingertip, the LED power, at both the tip of the optical fibre and surface of the LED, need to be controlled using both software and hardware such that the emission from the LED is always skin-safe. The maximum allowable power (MAP) when in contact with the skin was calculated as $63 \mu\text{W}$ [8]. An LED driver was used to control the input current and restrict the LED power. To achieve the MAP the LED current was limited to 80mA. To confirm the optical safety of the sensor, we measured the LED emission power for 3h (Figure 2 (left axis)). The average optical power of the LED at the tip of the fibre was $57.36 \mu\text{W}$ (with optical filters) and $92.3 \mu\text{W}$ (without filters).

Although the LED is not in contact with the skin, its temperature also needed to be controlled so that it did not affect the circuitry or the performance of the LED itself (105°C maximum operating temperature). The LED temperature was analysed for approx. 3 hours, with a current limit of 80mA. MAX31855 Thermocouple was used. Figure 2 (right axis) shows the temperature of the LED as a function of time with an On/Off period of 3s. After 3h, the temperature does not reach values above 35°C (not affecting the circuitry and skin-safe with temperature $< 45^\circ\text{C}$ at all times).

Proof-of-concept results. The performance of this prototype sensor was tested on different concentrations of fluorescein diluted in water (concentration range: 0– $1.7 \mu\text{g}$ fluorescein per ml water; chosen to approximate the expected signal levels at the fingertip following ingestion of fluorescein). At the same time, an Ocean Insight spectrometer (FLAME-S-VIS-NIR-ES) was used to collect spectra for each concentration, with illumination provided by a 488 nm laser source (Figure 3). The collected data demonstrated the potential of the prototype sensor to detect fluorescein at signal levels expected *in vivo*.

DISCUSSION

We have reported the progress in development of a compact fluorescence spectroscopy sensor to non-invasively study human gut permeability. The optical and electronic design mimics the performance of the laser-based, trolley-mounted system presented in [6]. In addition, power and temperature assessments have been carried out to confirm the safety of the sensor. Safety and

stability were achieved with an 80 mA LED drive current and 50% duty cycle (with 3 s On/Off switching). Importantly, a 3 s switching time will be sufficient for clinical monitoring of gut permeability, as changes in fluorescence intensity are expected over timescales of minutes-hours rather than seconds (e.g. measurements were made at 1 min intervals in [5,7]). Finally, preliminary results demonstrated the capability of the sensor to detect fluorescein fluorescence in simple phantoms at concentrations close to those expected *in vivo* following oral ingestion of the contrast agent. Overall, the results presented in this paper indicate the potential of the compact fluorescence sensor for safe and effective clinical monitoring of gut permeability in the future. The presented sensor is also significantly cheaper ($\sim\text{£}2.5\text{k}$, with potential for further cost reductions) than the existing technology ($\sim\text{£}10\text{k}$, [5,7]). Ongoing work is now focussed on deploying the sensor in a clinical trial.

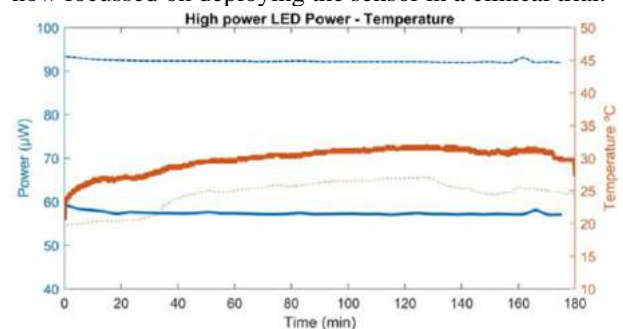


Figure 2. Optical power and temperature safety results. (left axis, blue) LED Power at the tip of the optical fibre with (bold) and without (dotted) the optical filters. (right axis, orange) LED temperature (bold) and internal temperature (dotted).

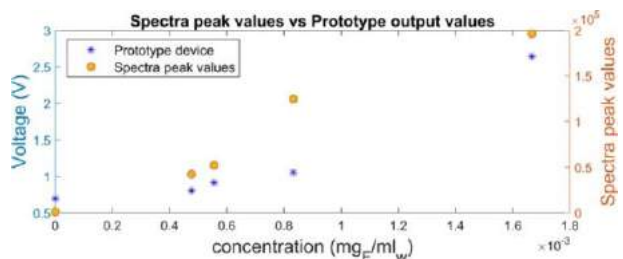


Figure 3. Sensor output voltages (blue) and spectral peak intensities (orange) as functions of fluorescein concentration.

REFERENCES

- [1]. Graziani *et al*, *European review for medical and pharmacological sciences*, 23(2), 795-810 (2019). https://doi.org/10.26355/eurev.201901_16894
- [2]. Salles Teixeira *et al*, *Nutricion hospitalaria*, 29(2), 269–281 (2014). <https://doi.org/10.3305/nh.2014.29.2.7076>
- [3]. Thompson *et al*, *Gut*, 70, 1580-1594 (2021). <https://doi.org/10.1136/gutjnl-2020-323609>
- [4]. Dorshow *et al* *Scientific Reports*, 7, 10888 (2017). <https://doi.org/10.1038/s41598-017-09971-y>
- [5]. Maurice *et al*, *Scientific Reports*, 10, 16169 (2020). <https://doi.org/10.1038/s41598-020-73149-2>
- [6]. Mbuki *et al*, *Transactions of The Royal Society of Tropical Medicine and Hygiene*, trab083 (2021), <https://doi.org/10.1093/trstmh/trab083>
- [7]. Lett *et al*, *Biomedical Optics Express*, 12, 4249-4264 (2021). <https://doi.org/10.1364/BOE.424252>
- [8]. International Commission on Non-Ionizing Radiation Protection (ICNIRP), "ICNIRP guidelines on limits of exposure to laser radiation of wavelengths between 180 nm and 1,000 microns," *Health Phys.* 105(3), 271–295 (2013)

Nonlinear Trajectory Following Control for a Bio-Inspired Steerable Needle

Zejian Cui¹, Abdulhamit Donder¹, and Ferdinando Rodriguez Y Baena¹

¹*Department of Mechanical Engineering, Imperial College London,
zejian.cui19@imperial.ac.uk; a.donder18@imperial.ac.uk; f.rodriquez@imperial.ac.uk*

INTRODUCTION

Research in minimally invasive surgery has placed great focus on percutaneous intervention, leading to a booming research interest in steerable needles [1]. Such systems, compared with rigid needles, enjoy the advantage of following a curvilinear trajectory towards a target that lies under anatomical tissue surrounded by vessels while avoiding obstacles along the path. Amongst these, a bio-inspired programmable bevel-tip steerable needle (PBN) has been developed, which can steer in any direction in three-dimensional space without causing tissue damage due to torsion; its steering behaviour has been described by a mechanics-based model[2]. To further investigate needle tracking performance under the newly-developed needle model, this paper presents a tailored closed-loop controller which characterizes needle movement by applying an underactuated Autonomous Underwater Vehicle (AUV) model.

MATERIALS AND METHODS

A. Mechanics-based 3D PBN model

An interlocked four-segment steerable needle prototype that can steer in any direction in the 3D space within a predefined workspace has been developed and is currently undergoing preclinical trials on the ovine model. In [2], a mechanics-based Euler-Bernoulli beam model has been developed which establishes needle tip curvatures κ_P as a function of needle absolute offsets at the proximal end O and a vector of needle parameters μ . We define a nonlinear function f to calculate needle tip curvature κ_P as

$$\kappa_P = f(O, \mu) \quad (1)$$

It is also required that a permissibility condition must be satisfied so that the needle can move as a single body during insertion. Details are illustrated in [2], and here we summarize it as a function of needle absolute offsets as below

$$PM(O) = 1 \quad (2)$$

B. Trajectory following controller design

Based upon the aforementioned needle model, we have developed an overall trajectory following control strategy, which consists of a High-level controller (HLC) and

a Low-level controller (LLC). The HLC takes inspiration from the AUV model, with the current and target needle poses as inputs and the linear moving velocity and rotational speeds around body frame axes as outputs. These HLC outputs are subsequently sent to the LLC, which interprets them into optimized needle inputs, with individual motion commands for each segment. The HLC considers the needle tip as an underactuated AUV following a reference trajectory and corrects the needle navigation path when it strays from the reference one. We assume there exists linear and rotational control inputs for the PBN except for the rotational speed around the needle axis, which is considered null. Built upon modified AUV kinematics and error dynamics as described in [3], the HLC control law is derived as follows. Denoting the needle tip is moving forward at the speed of v and steering around its body frame axes y_b and z_b at rates of ω_y and ω_z respectively, we have

$$\begin{cases} v = v_d + v_d(\cos \psi_e \cos \theta_e - 1) + \gamma^2 x_e \\ \vec{\omega} = \vec{\omega}_d + \mathbf{b}_1^{-1}(\vec{\theta})(\vec{\mathbf{q}} + (\mathbf{B}_1(\vec{\theta}_d) - \mathbf{B}_1(\vec{\theta}))\vec{\omega}_d + \vec{\mathbf{p}}) \end{cases} \quad (3)$$

where $\gamma > 0$ is a non-negative HLC parameter, and $\vec{\mathbf{q}}$ and $\vec{\mathbf{p}}$ are as expressed as

$$\vec{\mathbf{q}} = \left[0, -\frac{z_e v_d}{k_2}, \frac{y_e v_d \cos \theta_e}{k_3} \right]^T$$

$$\vec{\mathbf{p}} = [k_1 \sin \phi_e, k_2 \sin \theta_e, k_3 \sin \psi_e]^T$$

where k_1, k_2, k_3 are three other non-negative HLC parameters, definitions of other parameters can be directed to [3].

After the HLC generates outputs as v, ω_y and ω_z , v , the needle insertion speed, can be directly controlled via the needle actuation box as in [2], while ω_y and ω_z need to be further converted into executable needle inputs by the LLC. From curvature and rotation speed relationships, we first convert ω_y and ω_z desired needle tip curvatures $\kappa_d = [\kappa_{1d}; \kappa_{2d}]$, and based on (1) we let the LLC conduct an inverse mapping to generate needle offset movements commands. An open-source software tool CasADi, for numerical optimization and optimal control [4], is adopted. The process of finding needle

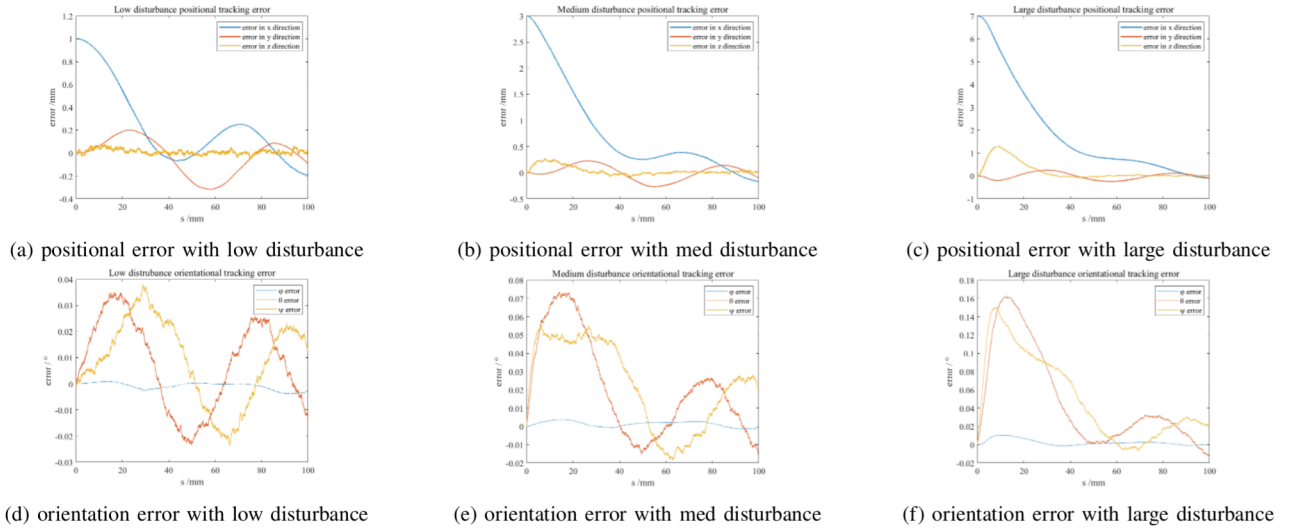


Fig. 1 Euclidean errors during PBN navigation under different initial disturbances

offsets O corresponding to a reference tip curvature κ_d can be summarized into an optimization problem as

$$\text{minimize } J = \frac{1}{2} O^T Q O \quad (4)$$

$$\text{subject to } f(O, \mu) = \kappa_d \quad (5)$$

$$PM(O) = 1$$

where $O \in \mathbb{R}^{4 \times 1}$ is a column vector storing absolute offsets and $Q \in \mathbb{R}^{4 \times 4}$ is a weight matrix storing relative contributions of needle segments towards the overall control efforts.

C. Simulation

To analyze the performance of the combined control strategy, we present a trajectory tracking simulation conducted in Matlab 2020a (Mathworks inc.). Tracking performance is evaluated based on average positional errors between target and actual needle tip points along the course. A reference trajectory of insertion length $s = 100$ mm, whose curvatures along the path follow the following relationships, is selected.

$$\kappa_{ref}(s) = \begin{bmatrix} \kappa_{1ref} \\ \kappa_{2ref} \end{bmatrix} = 0.007 \begin{bmatrix} \cos\left(\frac{4\pi s}{100}\right) \\ \sin\left(\frac{4\pi s}{100}\right) \end{bmatrix} mm^{-1} \quad (6)$$

For the HLC, controller parameters are tuned experimentally and in this case we choose $k_1 = 5$, $k_2 = 3.5$, $k_3 = 5$, $\gamma = 1$. For the LLC, we consider driving each segment requires equal amount of effort and thus $\mathbf{Q} = \mathbf{I}^{4 \times 4}$. Needle parameters selected remain the same as in [2]. To simulate initial disturbances, three cases with disturbances on position and orientation being $\pm [1\text{mm}, 0^\circ]$, $\pm [3\text{mm}, 1^\circ]$ and $\pm [7\text{mm}, 3^\circ]$, are exerted respectively. To simulate noises in needle position gathered by hypothetical position sensors, random noises with magnitude of 1mm and 5° are added.

RESULTS

The average Euclidean position error during trajectory tracking under low, medium and large disturbances were found to be 0.3480 mm, 0.8256 mm

and 1.9043 mm respectively; the average Euclidean orientation errors in angle ϕ , θ and ψ were $[-0.0009^\circ, 0.0077^\circ, 0.0092^\circ]$, $[0.0013^\circ, 0.0215^\circ, 0.0233^\circ]$ and $[0.0025^\circ, 0.0489^\circ, 0.0513^\circ]$ respectively. The percentage of curvature references provided by the HLC to the LLC the value of which was found to exceed the maximum needle steering angle took up 99.84 %, 99.82 % and 99.87 % of all control steps under these three cases, respectively (shown in Figure 1).

DISCUSSION

The simulation results demonstrate that the combined controller is able to guide the PBN towards the reference trajectory under different initial perturbations and environmental disturbances, leading to a reduction in both position and orientation errors. However, we also notice that there always remains a certain amount of Euclidean error oscillating towards the end, which might be attributed to needle steerability limitations. This limitation implies that at each control step, the needle may fail to arrive at the desired state defined by the HLC and hence Euclidean errors persist and accumulate as the needle navigates. Experimental validation will follow in future work.

REFERENCES

- [1] N. J. van de Berg, D. J. van Gerwen, J. Dankelman, and J. J. van den Dobbelsteen, "Design choices in needle steering—a review," *IEEE/ASME Transactions on Mechatronics*, vol. 20, no. 5, pp. 2172–2183, 2015.
- [2] T. Watts, R. Secoli, and F. R. Y. Baena, "A Mechanics-Based Model for 3-D Steering of Programmable Bevel-Tip Needles," *IEEE Transactions on Robotics*, vol. 35, no. 2, pp. 371–386, 2019.
- [3] Y. Nakamura and S. Savant, "Nonlinear tracking control of autonomous underwater vehicles," in *Proceedings 1992 IEEE International Conference on Robotics and Automation*, 1992, pp. A4–A9 vol.3.
- [4] J. A. E. Andersson, J. Gillis, G. Horn, J. B. Rawlings, and M. Diehl, "CasADi – A software framework for nonlinear optimization and optimal control," *Mathematical Programming Computation*, In Press, 2018.

Multi Jet Fusion of Nylon-12: A Viable Method to 3D-print Concentric Tube Robots?

K. Picho, B. Persons, J.F. d’Almeida, N.E. Pacheco, C. Reynolds, L. Fichera

Department of Robotics Engineering, Worcester Polytechnic Institute, USA
kmpicho@wpi.edu

INTRODUCTION

Concentric Tube Robots (CTRs) are needle-sized flexible manipulators well suited for minimally invasive surgery. The body of a CTR consists of a set of pre-curved tubes nested telescopically within each other, as shown in Fig. 1. Each tube can be translated and rotated independently. During actuation, the tubes interact elastically with each other, creating tentacle-like bending motions. CTRs are usually made of superelastic Nickel-Titanium (Nitinol), a metal alloy capable of withstanding large amounts of strain (typically up to 6-8%) without undergoing plastic deformation. Strain recovery is key for the operation of a CTR, as it enables the body of the robot to undergo substantial yet reversible bending.

In recent years, different groups have investigated the viability of 3D-printing CTRs using materials other than Nitinol [1-2]. This research is motivated by the fact that Nitinol can be a challenging material to work with: to build CTRs, Nitinol tubing must first be formed into a prescribed curved shape through an annealing treatment, which, as previous work has shown, can be complex, time-consuming, and error-prone [3]. Correct execution of this process requires specialized expertise as well as equipment that may not be readily available in a robotics laboratory. 3D-printing promises to overcome these challenges by providing a way to rapidly prototype CTRs. This would not only benefit CTR research, but it would also enable new appealing capabilities, such as the ability to create patient- or procedure-specific robots.

In this paper, we present a study on the viability of fabricating CTRs using Multi Jet Fusion (MJF) of Nylon-12, a type of elastic polymer commonly used in additive manufacturing [4]. We note that Nylon-12 was already evaluated for the purpose of building CTRs in [2], but fabrication was performed with Selective Laser Sintering (SLS), which produced unsatisfactory results. Our study is the first study to evaluate the suitability of MJF to 3D-print CTRs.

MATERIALS AND METHODS

MJF is a novel additive manufacturing technology developed by Hewlett-Packard (Palo Alto, CA, USA) [4]. Parts are built by depositing successive layers of material powder, which are then heated and fused. This process is similar to SLS, but powder heating uses infrared light (as opposed to a laser in SLS), in combination with chemical agents that facilitate heat absorption. MJF can create parts with mechanical properties and finish similar to those printed with SLS [4]. Unlike SLS, however, the



Fig. 1: 3D-printed Concentric Tube Robot.

unique treating agents that MJF uses help to create tiny features. Thus, MJF is capable of higher dimensional accuracy, finer resolution, and smaller wall thicknesses, which all significantly aid in the printing of CTRs. For this study, MJF fabrication of the tubes was outsourced to Protolabs (Maple Plain, MN, USA).

Stress-Strain Characterization: As a first step in our study, we performed a tensile test to experimentally characterize the stress-strain curve of Nylon-12 parts created with MJF. This test was carried out according to the ASTM D638 protocol, using specially designed “dog-bone” shaped parts and an Instron 5500R Universal Testing Machine (Instron, Norwood, MA, USA). This test enabled us to estimate the linear elastic range of the material and the Young’s Modulus, which are necessary to model the mechanics of CTRs [5].

Fatigue Testing: Prior work found Nylon-12 tubes printed via SLS to be brittle and prone to breaking [2]. To verify if Nylon-12 tubes created with MJF can withstand multiple bending cycles, we performed a fatigue test. This test used a tube with an outer diameter of 3.2 mm, a wall thickness of 0.6 mm, and a 28.26 mm radius of curvature. The tube was straightened by pulling it inside a straight hollow shaft and then pushed back out. This process was automated by attaching the proximal end of the tube to a motorized stage and repeated for 200 cycles. Photographs were taken every 10 cycles to document the conditions of the tube.

In-Plane Bending Verification: We performed an experiment to verify if the in-plane bending model for concentric tubes proposed by Webster *et al.* in [5] can be used with the tubes considered in this study. Briefly, the model in [5] assumes that concentric tubes apply moments to one another by virtue of their different pre-curvatures and bending stiffnesses. If two concentric tubes are aligned so that they bend in the same plane, their equilibrium curvature is simply described by $\kappa = \frac{E_1 I_1 k_1 + E_2 I_2 k_2}{E_1 I_1 + E_2 I_2}$, where the subscripts indicate the tube number, E is the Young’s Modulus, k is the pre-curvature, and I is the second moment of area.

The experiment is illustrated in Fig. 2: two tubes are nested inside each other so that their curved sections overlap completely, and the equilibrium curvature is then estimated from images. The experiment used the

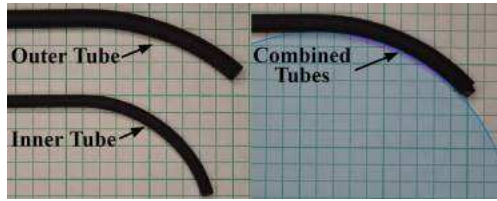


Fig. 2: In-plane bending test. Photographs of the tubes are taken before and after insertion with a Nikon D5100 DSLR camera. The equilibrium curvature is measured by manually digitizing three points along the curve, and then using a circle fit in MATLAB to estimate the corresponding radius.

combinations of inner/outer tubes listed in Table 1. All the tubes used in these trials have a wall thickness of 0.6 mm and a distal curved section of 50 mm. Each trial was repeated 11 times.

RESULTS

Stress-Strain Characterization: Fig. 3 shows the stress-strain curve estimated in the tensile test. The curve increases linearly until approximately 2% strain before entering the region of plastic deformation. Breakage of the dog bone part occurred at 17.7% strain. The Young's Modulus was estimated to be 1.51 GPa. These results are consistent with those reported in other studies [4].

Fatigue Testing: The tube was able to withstand all 200 bending cycles without any macroscopic or otherwise apparent sign of breakage. We did observe a progressive loss of pre-curvature of the tube, as documented in Fig. 4. We attribute the loss of curvature to plastic deformation: as can be verified using Eq. (1) in [5], the strain experienced by the material in the tube during straightening reached nearly 6%.

In-Plane Bending Experiment: Results are reported in Table 1. The in-plane bending model from [5] was able to predict the radius of curvature of the combined tubes, with RMSEs ranging between 0.3 and 1.9 mm.

DISCUSSION

Results suggest that MJF of Nylon-12 may be a viable process to build CTRs. Tubes can be printed in small diameters (the smallest tube in this paper has outer diameter equal to 2.2 mm) and can withstand hundreds of bending cycles without breaking. Although the maximum recoverable strain was not determined, it would be reasonable to assume a value between 2-3% based on the stress-strain curve in Fig. 3. This value is **Table 1:** Experimental conditions and results for the in-plane bending experiments. OD: Outer Diameter. R: Radius of Curvature. R*: Equilibrium Radius of Curvature predicted by the model in [5]. RMSE: Root-Mean-Square Error. All units are in millimeters.

Trial	Outer Tube		Inner Tube		Combined Tubes	
	OD	R	OD	R	R*	RMSE
1	3.8	69.0	2.2	21.9	54.7	1.7
2	3.8	39.9	2.2	22.1	36.4	0.8
3	5.4	68.6	3.8	43.2	64.0	1.9
4	5.4	34.5	3.8	70.9	36.8	0.3

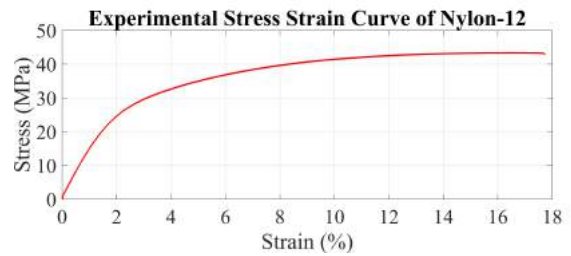


Fig. 3: Stress strain curve for MJF-printed Nylon-12.

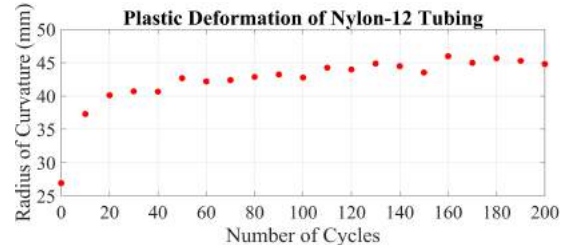


Fig. 4: Progressive loss of pre-curvature observed during fatigue testing.

lower than what is achievable with Nitinol (6-8%), implying that CTRs made of Nylon-12 will not be able to achieve the same range of bending motions as those made of Nitinol. This was expected, as superelastic Nitinol is and remains the most suitable material for CTRs. MJF of Nylon-12 offers the convenience to rapidly prototype CTRs at the expense of limiting the robot's reachable workspace. One important limitation of this study is that it did not investigate the mechanics of concentric Nylon-12 tubes subject to rotation. We plan to conduct a complete verification of the CTR kinematics model in [5] in future work.

The dimensions and pre-curvatures of the component tubes in a CTR are critical design parameters, as they determine the robot's reachable workspace. Several groups have recently explored algorithms that produce optimal designs for a given application. Until now, however, these algorithms have been of limited application due to the difficulty of sourcing Nitinol tubing with specific prescribed dimensions and pre-curvatures. By enabling the creation of tubes in virtually any arbitrary dimensions and curvatures, MJF promises to overcome these challenges and open up the way to the creation of procedure- and patient-specific robots.

REFERENCES

- [1] Amanov E, Nguyen TD, Burgner-Kahrs J. Additive manufacturing of patient-specific tubular continuum manipulators. SPIE Medical Imaging 2015.
- [2] Morimoto TK, Okamura AM. Design of 3-D printed concentric tube robots. IEEE Transactions on Robotics. 2016 Sep 23;32(6):1419-30.
- [3] Gilbert HB, Webster RJ. Rapid, reliable shape setting of superelastic nitinol for prototyping robots. IEEE robotics and automation letters. 2015 Dec 11;1(1):98-105.
- [4] Cai C, et al. Comparative study on 3D printing of polyamide 12 by selective laser sintering and multi jet fusion. Journal of Materials Processing Technology. 2021 Feb 1;288:116882.
- [5] Webster RJ, Romano JM, Cowan NJ. Mechanics of precurved-tube continuum robots. IEEE Transactions on Robotics. 2008 Nov 11;25(1):67-78.

Design, realization and preliminary validation of an active physical simulator for the study of pelvic floor damages during childbirth

G. Modarelli¹, S. Maglio², S. Tognarelli², A. Menciassi²

¹University of Pisa, Pisa, Italy

²The BioRobotics Institute, Scuola Superiore Sant'Anna, Pisa, Italy
sabina.maglio@santannapisa.it

INTRODUCTION

Pelvic floor (PF) is a muscle-fascial system that inferiorly closes the pelvis. It is really important in woman's life because it guarantees the correct positioning of the pelvic organs, the urines and feces continence and evacuation, and it allows sexual activity and childbirth [1]. Dysfunctions of PF involve important physical and psychological consequences in the daily life of a woman and significant expenses for their treatment. Vaginal delivery represents one of the main risk factor for the onset of PF disorders.

Pelvic muscles in pregnant women show very different elastic characteristics if compared with non-pregnant women's muscles. Moreover, they undergo considerable stretching during the passage of the foetus, that often results in a medium and/or long-term tissues injury. Thus, dedicated studies could both pave the way to a better comprehension of this phenomena, and improve the use of prevention clinical techniques, i.e., c-section. High-fidelity and active physical simulators deepen the study of the factors characterizing a clinical event and allow the doctor to have a physical support and real time feedback, which are essential for technique refinement and knowledge transfer in the clinical practice. Currently, there are only birth simulators available on the market, in which the PF is merely an additional element recreated at a low-fidelity level in terms of anatomical and physiological features. In addition, commercial simulators equipped with PF are limited in number and entirely passive, hence they don't provide any feedback to the clinician.

In this framework, the aim of this paper is to realize a sensorized physical simulator of maternal PF that can be used both as a teaching and/or a training system for gynaecologists and obstetrics. The innovative features of the proposed simulator are the following: i) high-fidelity reconstruction of the maternal PF anatomy; ii) use of soft materials able to replicate the biomechanical properties of human tissues; iii) active evaluation of the muscle deformation induced by the foetal head (FH) passage through the PF structure.

MATERIALS AND METHODS

By combining anatomical data with literature information, a 3D model of the maternal PF was reconstructed and utilized for muscle fabrication through molding technique (Figure 2). Ecoflex 0030 silicone (Smooth-On, PA, USA) was used for

reproducing the biomechanical behavior of the PF muscles. Its elastic modulus of $E=0.068$ MPa is close to the pregnant woman muscles modulus, i.e., $E=0.06$ MPa [2]. The tendons structures of the PF are then replicated for guaranteeing the right positioning of the muscle component (Figure 2 for details). Finally, a female pelvis model with standard dimensions was found for bones replication [3].

In order to record the muscle deformation during the delivery simulation, elastic sensors capable to follow the elongation of the PF are required. Commercial sensors were discarded because commonly they are rigid and thus they do not meet the silicone elasticity and integration requirements. As an alternative, a specific elastic conductive fabric (Med-tex P130, Shieldex, Germany) was investigated for fabricating a custom home-made resistive sensor. Conductive fabric has been already demonstrated as a valid solution for soft applications [4], allowing to evaluate the elongation by changing its resistance. Finally, signal acquisition is ensured by firm electrical connections made of conductive wires properly hand-stitched on the fabric mesh. Electronic components for signal conditioning and acquisition are required.

To evaluate the sensors resistance-elongation relation, several tensile tests were performed by using the Instron 5965 machine (Instron, USA). Rectangular shaped textile samples were stretched from 0% to 100% - in order to cover the entire human tissue stretch range - for 5 cycles at 400 mm/min speed. Test was repeated 3 times. The components were integrated and the final device was validated both on the bench and with clinicians. In order to calibrate the simulator and to collect data that can be used for comparing the obtained system with literature, a descent of the FH through the PF was simulated by using the Instron machine. A vertical descent of 100 mm at 150 mm/min speed was repeated 3 times; applied forces and sensor elongation were acquired from the Instron and simulator electronics, respectively. As in the literature, it was used a rigid FH approximating a 10 cm sphere made of PETG realized by means of the FDM technique.

Ultimately, to complete the preliminary system validation phase, a pre-clinical testing protocol was realized by involving expert gynecologists at Azienda Ospedaliero Universitaria Pisana. The tests were performed by combining our simulator with a commonly used FH simulator. The descent of the FH through the PF was reproduced. Five different positions

that the FH might assume during the delivery were simulated by the clinicians. Tests were repeated 3 times.

RESULTS

Three different sensors were made in order to cover the muscular areas mostly stressed during childbirth: 2 rectangles of 51mmx6.5mm in size were positioned between the pubic symphysis and the perineal body; 1 smaller rectangle of 44mmx6.5mm was integrated near the perineal body. Sensors signal was acquired using a Wheatstone bridge. The electronic circuit was powered and managed through the Arduino Mega 2560 board (Arduino, Italy). By combining the elongation applied by the Instron machine on the sensors samples with their resistance values, the sensor calibration curve was obtained (Figure 1). As shown in the figure, the resistance increases linearly up to 60% of the elongation and decreases linearly from 60% to 100%. An equal and opposite behaviour was observed during the shortening phase of the sensor. The acquired signal proved to be accurate, showing an identical behaviour over time and during multiples tests.

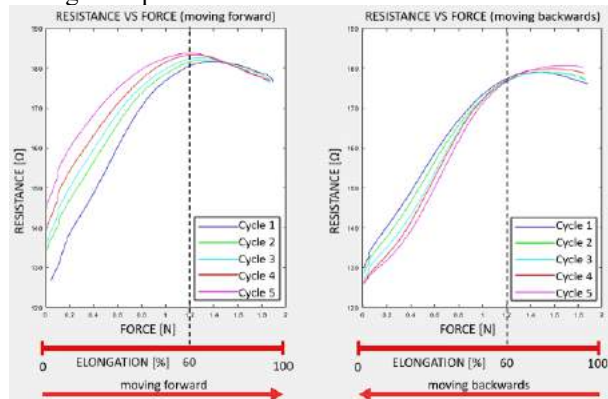


Fig. 1 Resistance VS Force calibration curves of a single sensor: moving forward (left) and moving backward (right).

The integrated system is reported in figure 2. Pelvis bones were made of PETG through a FDM printer (i3 MK3S+, Prusa Research, Czech Republic). The resistive sensors, made with Med-tex P130 fabric, were integrated on the PF structure using Ecoflex 0010 silicone. Muscles and bones were glued together through a thin inextensible fabric replicating PF tendons in the corresponding anatomical position.

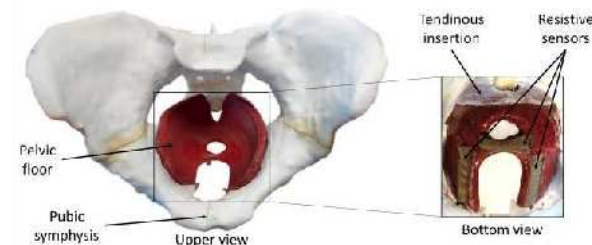


Fig. 2 Complete simulator. On the left upper view and on the right bottom view.

The forces acquired during the test simulating FH descent with the Instron machine (i.e., 45N as peak force) are similar to those found in literature (i.e., 30 N

as peak force) [5]. Moreover, the sensor resistance-elongation curve acquired with the final system, show the same behaviour obtained for the single sensor, demonstrating the system robustness and the analysis repeatability.

From the tests with three expert gynaecologists (Figure 3), it was possible to replicate the literature findings in terms of which one of the reproduced foetal positions (e.g., occiput anterior (OA) position - baby facing towards mamma's spine) causes greater muscle distension, resulting in an increased possibility of PF injury and/or the onset of PF dysfunction in the postpartum period. The obtained results (Figure 3A) confirmed that all the integrated sensors worked correctly during the tests. In addition, sensors provided different output signals, showing different peak values (point of instantaneous main contact between FH and PF) at different descent instants.

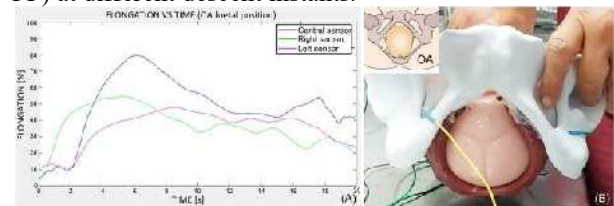


Fig. 3 Test conducted with expert gynaecologist. A) Elongation VS Time curves extracted from the integrated sensors; (B) Testing set-up.

DISCUSSION

The described active high-fidelity simulator showed good potentialities and it could be considered a valid system for PF damages evaluation. Clinicians confirmed the simulator is anatomically and physiologically faithful to human anatomy. Resistive textile sensors allowed to monitor the elongation of the PF tissues during the FH descent. The device, therefore, represents a promising tool that can be included both in training courses for experienced and non-experienced clinicians, and in gynecological education lessons.

Future efforts will be dedicated to a structured test protocol with at least 40 trainees (expert and residents). Additionally, a simple solution for fixing the system to the gynecological table during the test protocol will be identified for avoiding to affect the experimental data with drawbacks due to a not-stable manual held.

REFERENCES

- [1] G. Bolis. Manuale di Ginecologia e Ostetricia. II. EdiSeS.
- [2] S. Badir et al. A novel procedure for the mechanical characterization of the uterine cervix during pregnancy. *J. Mech. Behav. Biomed. Mater.* 2013; 27:143–153.
- [3] “Sketchfab.” <https://sketchfab.com/3d-models/female-human-pelvis-9c4180fe752e4340a2ea90d5a8ad2bf3>.
- [4] A. Atalay et al. Batch Fabrication of Customizable Silicone-Textile Composite Capacitive Strain Sensors for Human Motion Tracking. *Adv. Mater. Technol.* 2017; 2(9): 1–8.
- [5] M. E. T. Silva et al. Study on the influence of the fetus head molding on the biomechanical behavior of the pelvic floor muscles, during vaginal delivery. *J. Biomech.* 2015; 48(9): 1600–1605.

Mechanical Reinforcement towards Fully Soft Magnetic Endoscopic Endonasal Surgical Manipulators

Z Koszowska¹, G Pittiglio¹, J H Chandler¹, M Brockdorff¹, and P Valdastrì¹

¹*School of Electronic and Electrical Engineering
STORM lab, University of Leeds
elzmk@leeds.ac.uk*

INTRODUCTION

Endoscopic Endonasal Surgery (EES) targets the sinuses or base of the skull for treatment of lesions, tumors or polyps. The endonasal approach for these procedures is much safer than a craniotomy approach, involving removing part of the skull to access the operating site. Even though current EES is highly beneficial, technological limitations are still present [1]. EES is performed by inserting a rigid endoscope and accompanying tools through the nostrils. The coupled constraints of narrow, curved anatomy with straight and rigid tools present a significant challenge in EES, limiting visibility and maneuverability within the workspace. Enhancing the flexibility and controllable Degrees of Freedom (DoF) of the tools could make procedures safer and easier to perform. Most of the proposed robotic solutions for EES are mechanically driven with sizes close to standard and do not address the issue of miniaturisation or delicate tissue interaction [2], [3]. The field of soft robotics may offer solutions to the issues faced in EES, allowing small compliant manipulators with increased DoF for superior maneuverability and safer tissue interactions. Of these robotic designs, the relatively new field of Soft Magnetic Manipulators (SMMs) presents some notable advantages when designing for small scales. SMMs can be entirely soft and can be magnetically pre-programmed to produce desired deformations under exposure to specific and controlled external magnetic fields [4]. External, remote actuation of this type thus enables extreme miniaturization without loss of controllable DoFs, which is often impossible to achieve with other approaches due to the accommodation of onboard actuation. Due to these advantages magnetically actuated devices can be very beneficial in medical environment – specifically for improving navigation through tortuous anatomical pathways and difficult to access surgical sites, such as in EESs. In this paper we investigate the application of soft continuum magnetic manipulators to EES procedures. In combination, the presented approach aims to enable delicate interaction with tissue, and higher maneuverability with respect to current EES tools; overcoming issues associated with torsion.

MATERIALS AND METHODS



Fig. 1 Experimental set up: a manipulator with optical markers, robotic arms with External Permanent Magnets (EPMs) and frame with optical markers.

A magnetic agent with a magnetic moment m is subject to magnetic force (F) and torque (τ), under an applied field B , respectively as

$$\vec{F} = (\vec{m} \cdot \nabla) \vec{B} \quad (1)$$

$$\vec{\tau} = \vec{m} \times \vec{B}. \quad (2)$$

The magnetisation direction of a controlled body is a crucial element when it comes to magnetic actuation of soft structures. According to (2), when the magnetisation direction of the magnetic body aligns with the applied external magnetic field direction, it is subject to no resultant torque. If not aligned, magnetic torque will tend to rotate the body; it can be expressed as the cross product of magnetisation direction and applied external magnetic field (2). Using this phenomenon, the magnetic manipulator can be pre-programmed in a manner to achieve desired deflection, when exposed to specific external magnetic fields.

In cases where the angle between the magnetisation vector and applied magnetic field is higher than 90° , SMMs will commonly twist around the z axis of the manipulator, rather than producing expected deflection. The concept of constraining torsion in magnetic soft robots was explored by [4], through the addition of helical fibres; succeeding with twist reduction of 67 %. To address the issue of twisting, we consider a manipulator design with a monolithic elastic double helix reinforcement structure. Pursuing a geometrical solution to the torsional effect maintains the benefits of fully soft

TYPE	OD (mm)	ID (mm)	R	h (mm)	w (mm)
CYL	3.5	N/A	N/A	N/A	N/A
SMM 1	3.5	1	30	0.5	1.25
SMM 2	3.5	1	12.5	1.5	1.25

TABLE I Design parameters of SMMs including geometrical variation of helical reinforcement (Fig.1).

structure without a need for inclusion of hard structures such as springs or fibres. Figure (2) shows the design parameters in Y-Z and X-Z planes, related to the double helix SMM design. This results in relatively low stiffness along X and high stiffness along Y directions. Such stiffness variability allows for minimal bending in the Y direction and torsion around Z direction, while keeping high deflection in the X direction.

A cylinder and two designs of mechanical reinforcement with varied geometrical parameters were considered as defined in Table I.

Basing on clinical needs for miniaturisation, the outer diameter of the manipulators is set to 3.5 mm. The core cylinder diameter and width of the helices was held constant across designs (Table I). All samples were fabricated by casting, with 3D printed moulds (Grey V4 resin, Form III, Formlabs, USA). Equal parts of Dragon Skin™ 30 (Smooth-On, Inc., U.S.A.) A and B were mixed with 100 wt% of hard magnetic micro-particles (Nd-FeB with an average 5 μm diameter and intrinsic coercivity of $H_{ci} = 9.65$ kOe, MQFP-B+, Magnequench GmnH, Germany). The magnetic slurry was then treated in a high vacuum-mixer (ARV- 310, THINKYMIXER, Japan) for 90 seconds at a speed of 1400 rpm and pressure of 20.0 kPa. The degassed slurry was injected in to the closed molds and cured at 45° for 30 minutes. To track samples during characterization with the dual arm system, a frame with optical markers was attached to the tip (Fig.1). Each design was fabricated twice to be magnetised in along their X and Y axes to allow comparison of stiffness variability between the axes. (Fig. 2).

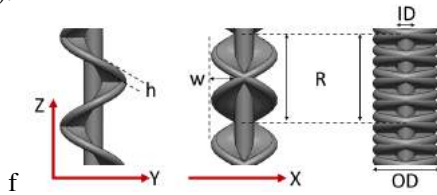


Fig. 2 Examples of monolithic reinforcement design, where h is the helix thickness; w is helix width; ID is the core diameter; R is number of revolutions per unit length and OD is an overall diameter.

Three candidate designs (Table I) magnetised in X and Y directions were evaluated by recording data on manipulator deformation under varied conditions of external magnetic fields applied by dual arm robotic system with permanent magnets (Fig.1). The tip poses of manipulators are recorded via an Optitrack system with optical markers attached to the manipulator during testing. The bending information around X, Y and Z was obtained from rotation of the rigid body.

RESULTS

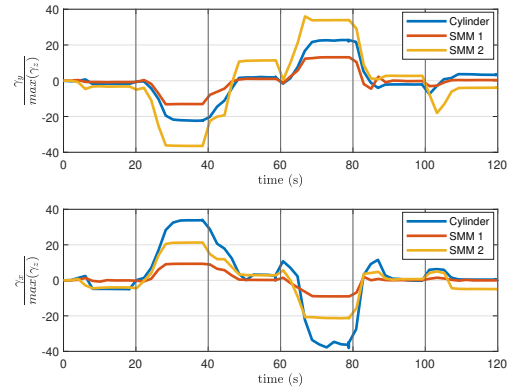


Fig. 3 Results of testing 3 candidate designs under different magnetic field conditions as a ratio of deflection to torsion. Top: Samples magnetized in X direction; Bottom: Samples magnetized in Y direction.

An optimal geometry for this type of manipulator should show minimal twisting behaviour and maximum deflection in the easy axis, therefore we consider a ratio of bending in the magnetized direction to the maximum recorded torsion for all six samples. In the case of magnetization along X, the optimal design is expected to have the highest ratio and the lowest in case of magnetization along Y. In the Fig. 3(top), SMM2 shows a greater ratio than a cylinder of the same diameter. In addition, the ratio value for SMM1 is lower than the value for both, cylinder and SMM2. In the Fig. 3(bottom), SMM1 shows the lowest ratio of all three samples. However, analysing both plots, it can be seen that only the design SMM2 shows desired behaviour in both magnetization cases.

DISCUSSION

Results collected for three candidate designs showed that the SMM2 design reduces torsion while keeping high deflection in X direction and relatively low deflection in Y direction. Therefore from samples tested in this paper, SMM2 is an optimal design to be used as a soft magnetic manipulator for EES. Future work will include investigation on a greater range of designs, varying more parameters of reinforcing geometry.

REFERENCES

- [1] S. Chalongsongse, S. Chumnanvej, and J. Suthakorn, "Analysis of Endonasal Endoscopic Transsphenoidal (EET) surgery pathway and workspace for path guiding robot design," *Asian Journal of Surgery*, vol. 42, no. 8, pp. 814–822, 2019. [Online]. Available: <https://doi.org/10.1016/j.asjsur.2018.12.016>
- [2] H. S. Yoon, J. H. Jeong, and B. J. Yi, "Image-Guided Dual Master-Slave Robotic System for Maxillary Sinus Surgery," *IEEE Transactions on Robotics*, vol. 34, no. 4, pp. 1098–1111, 2018.
- [3] S. Coemert, R. Roth, G. Strauss, P. M. Schmitz, and T. C. Lueth, "A handheld flexible manipulator system for frontal sinus surgery," *International Journal of Computer Assisted Radiology and Surgery*, vol. 15, no. 9, pp. 1549–1559, 2020. [Online]. Available: <https://doi.org/10.1007/s11548-020-02220-0>
- [4] P. Lloyd, Z. Koszowska, M. D. Lecce, O. Onaizah, J. H. Chandler, P. Valdastrì, L. Wang, P. Lloyd, O. Onaizah, and C. Jh, "Feasibility of Fiber Reinforcement Within Magnetically Actuated Soft Continuum Robots," vol. 8, no. July, pp. 1–10, 2021.

Magnetic Endoluminal Devices Can Assist In Their Own Insertion

Nicholas R. Posselli, Emma K. Pinegar, and Jake J. Abbott

Department of Mechanical Engineering and Robotics Center, University of Utah
{nicholas.posselli, emma.pinegar, jake.abbott}@utah.edu

INTRODUCTION

In the design of long, flexible medical devices that are inserted into a lumen by pushing them from their proximal end (e.g., catheters, scopes, cochlear-implant electrode arrays), there is a fundamental trade-off between making the device flexible/soft to safely conform to the environment, and making the device stiff to enable the device to be inserted without buckling [1]. A number of continuum medical devices have incorporated magnetic actuation [2]–[5], typically at the distal end to magnetically steer the device in a desired direction. This type of magnetic actuation can reduce insertion forces and/or delay buckling by reducing the total friction between the continuum device and the environment. However, because the magnetic actuation is limited to the distal end, its effectiveness is reduced with increased insertion depth. Our group recently proposed a magnetic-actuation concept for soft endoluminal robots in which the soft robot has two or more axially magnetized permanent magnets distributed along its length, with the magnetization direction alternating between neighboring magnets, and a rotating external magnet is used to induce a traveling wave in the soft device, causing it to crawl in a deterministic and reversible direction [6]. In this paper, we extend the concept in [6] to soft continuum devices that are inserted by pushing them from their proximal end (Fig. 1). Our basic hypothesis is that if the magnetic-actuation concept is sufficient to cause crawling in untethered devices, it will also reduce the insertion forces required to insert continuum devices. We will show that this is, in fact, the case. We will also show that, in limiting cases, it is even possible to reduce the insertion forces to zero such that the continuum device inserts itself without any proximal-end push.

MATERIALS AND METHODS

We fabricated a simple continuum device comprising ring magnets with 1 mm inner diameter (dia.), 2 mm outer dia., and 1 mm thickness attached every 26 mm along the length of a Tygon tube with 0.75 mm outer dia. and 0.254 mm inner dia., using cyanoacrylate, such that the magnetization directions alternate between neighboring magnets (Fig. 2(b)).

This work was supported by the National Science Foundation under Grant 1830958. N. R. Posselli and E. K. Pinegar contributed equally.

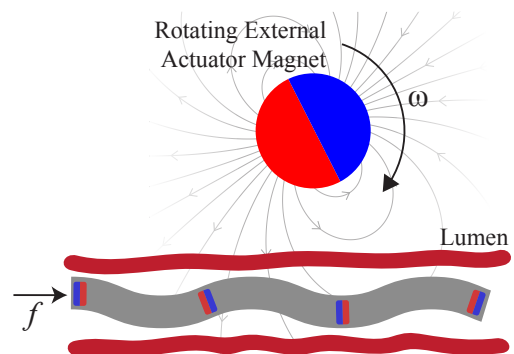


Fig. 1 Schematic of a flexible/soft continuum device, which has permanent magnets with alternating axial magnetization embedded along its length, being inserted into a lumen by applying an insertion force f at its proximal end while an external magnetic-field source, rotating with angular velocity ω , generates a nonuniform rotating field that induces a traveling wave to assist in the insertion of the device. The embedded magnets in closest proximity to the external magnet are the most greatly affected. The embedded magnets can be rings, to maintain a working channel in the continuum device.

We created an artificial lumen environment comprising a Tygon 3603 tube with 4 mm inner dia. wrapped into a planar spiral. We placed a 51 mm cubic NdFeB permanent magnet above the spiral such that its axis of rotation is approximately collinear with the spiral's axis, and its magnetization direction is orthogonal to this axis (Fig. 2(a)). This setup approximates magnetic actuation of a cochlear-implant electrode array [2], but it also lets us explore the physics of this magnetic-actuation concept in a truly open-loop fashion in which the behavior of the external magnet is invariant to the state of the continuum device. We conducted an experiment in which we placed the external magnet at five heights above the planar spiral between 70 mm and 190 mm, as well as with the external magnet completely removed, while rotating the external magnet at a somewhat-arbitrary angular velocity of 7.2 rad/s while manually inserting the continuum device as deep as possible until buckling prevented further insertion (ten trials in each configuration).

We conducted a second experiment in which we stretched the artificial lumen out in a straight horizontal line (Fig. 2(e)), and oriented the external magnet to match the configuration shown in Fig. 1, with its axis of rotation orthogonal to the lumen's axis. The

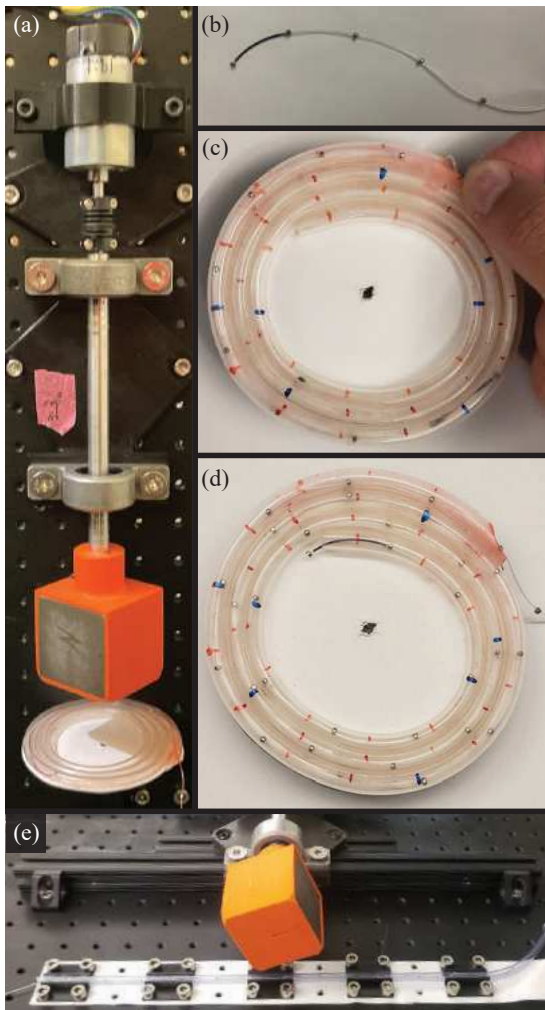


Fig. 2 (a) Experimental setup comprising a cubic permanent magnet rotated by a motor, at a reconfigurable height above an artificial lumen wrapped into a planar spiral. (b) Magnetic continuum device, with distal segment painted for visualization. (c) Example of buckling preventing deeper insertion at less than one complete turn of the spiral. (d) Example with continuum device having reached the final depth of the lumen at more than three full turns of the spiral. (e) Experimental setup comprising a cubic permanent magnet rotated by a motor, with manual horizontal translation at a fixed height, above an artificial lumen in a straight line.

experimenter moved the rotating external magnet to keep it approximately 60 mm behind the distal tip of the continuum device at a fixed height of 72 mm, again with an angular velocity of 7.2 rad/s, while manually inserting the continuum device as deep as possible (ten trials). We also performed ten insertion trials with the external magnet completely removed.

RESULTS

The results of the first experiment are shown in Fig. 3: the magnetic actuation resulted in much deeper insertion (up to the full 770 mm) than we could obtain without any magnetic actuation (up to 265 mm). Analysis of variance

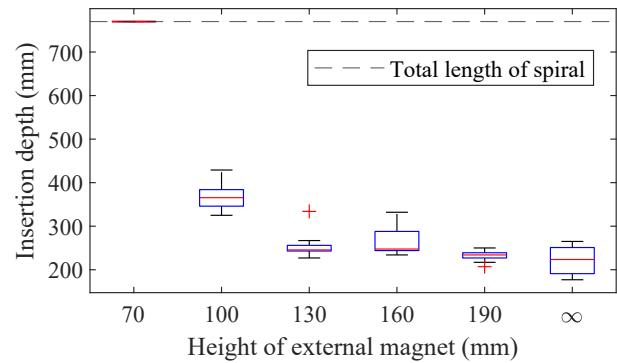


Fig. 3 Box-whisker plots showing results of ten insertion trials in planar-spiral at six magnet configurations.

indicates that external magnet height has a statistically significant effect ($p < 0.001$).

In the second experiment, the insertion depth was 337 mm (the full length of the straight artificial lumen) in all ten trials with magnetic assistance, and fell within the range 69–143 mm without magnetic assistance. During both experiments, we observed that for external magnet heights 72 mm and below, once the continuum device was inserted to some specific critical depth into the artificial lumen, it began to insert itself without any manual insertion force applied at the proximal end.

DISCUSSION

We have demonstrated a simple magnetic design and open-loop-actuation concept that both creates a pulling effect and inhibits the friction build-up that would eventually lead to buckling, which enables deeper insertion of a device than could be achieved otherwise. Further, given ideal conditions, it enables a continuum endoluminal device to insert itself into a lumen. Of course, our *in vitro* experiments are still fairly different from biological lumens, but the physical principles are likely to translate. We have not yet attempted to optimize the separation distance between the continuum device's magnets or the rotation frequency of the applied field. It is our conjecture that the actuation principles demonstrated here for spiral and straight paths could be applied to insertions along more general paths. However, there are still many unanswered questions about how that should best be done.

REFERENCES

- [1] A. Loeve *et al.*, "Scopes too flexible...and too stiff," *IEEE Pulse*, vol. 1, no. 3, pp. 26–41, 2010.
- [2] L. Leon *et al.*, "An in-vitro insertion-force study of magnetically guided lateral-wall cochlear-implant electrode arrays," *Otol. Neurotol.*, vol. 39, no. 2, pp. e63–e73, 2018.
- [3] J. J. Abbott *et al.*, "Magnetic methods in robotics," *Annu. Rev. Control Robot. Auton. Syst.*, vol. 3, pp. 57–90, 2020.
- [4] Z. Yang and L. Zhang, "Magnetic actuation systems for miniature robots: A review," *Adv. Intell. Syst.*, vol. 2, p. 2000082, 2020.
- [5] L. Pancaldi *et al.*, "Locomotion of sensor-integrated soft robotic devices inside sub-millimeter arteries with impaired flow conditions," *Adv. Intell. Syst.*, p. 2100247, 2022.
- [6] L. N. Pham *et al.*, "Soft endoluminal robots propelled by rotating magnetic dipole fields," *IEEE Trans. Med. Robot.*, vol. 2, no. 4, pp. 598–607, 2020.

Dual-Arm Platform for Control of Magnetically Actuated Soft Robots

M. Brockdorff¹, G. Pittiglio¹, T. da Veiga¹, J. H. Chandler¹, and P. Valdastri¹

¹*STORM Lab UK, University of Leeds,
elmbr@leeds.ac.uk*

INTRODUCTION

The present work discusses a novel approach for remote magnetic actuation. In the following, we present a full characterization of the dual External Permanent Magnet (dEPM) actuation system. Herein, we discuss how this system can be applied to fully control the magnetic field in a predefined workspace. We discuss how it can generate a *homogeneous magnetic field*, in every direction and control every *independent* gradient in the same workspace. We prove how up to 8 Degrees of Freedom (DOF), 3 independent field components and 5 gradients directions, can be controlled fully independently.

The rise in popularity of magnetic actuation comes from the fact that it allows for the control of wireless magnetic micro-robots and magnetic Soft Continuum Robots (SCRs), which bring about a reduction in size when compared to their non-magnetic counterparts. SCRs have a theoretical infinite number of DOFs and thus, can adapt to various nonlinear environments, minimising contact and pressure on surrounding tissue. While successful multi-DOFs magnetic actuation has been demonstrated at small scale [1], by using systems of *coils*, large-scale manipulation is yet to be fully proven. In fact, it might require several independently-controlled coils [2] to be effective along any possible direction of motion. Despite their ability to generate both homogeneous fields [3] and gradients [2], systems of coils are less scalable, compared to permanent magnet-based magnetic field control systems [3]. In fact, due to lower field density, energy-consumption and need for high-performance cooling systems, they are generally characterized by limited workspace [4].

By further developing the idea of remotely actuating 1 Internal Permanent Magnet (IPM) (internal since, generally, inside the human body) with 1 External Permanent Magnet (EPM) [5], we discuss how 2 robotically actuated EPMs are able to magnetically manipulate 2 IPMs, independently. This is achieved by independently controlling the torque (magnetic field) and the force (field gradients) applied to each IPM.

MATERIALS AND METHODS

Magnetic manipulability is the measure of the number of magnetic DOFs that can be magnetically manipulated by a magnetic actuation system. This means that, given a set of inputs, we aim to measure the number of variables

that can be independently actuated. In the following, we prove that with 2 EPMs ($M = 2$) we can control 8 DOFs of 2 orthogonal IPMs ($N = 2$) in the same point of the workspace. Assuming that 2 IPMs are in the same point within the workspace, they will experience the same magnetic field (B) and magnetic field jacobian ($dB = \frac{\partial B}{\partial p}$). This will induce a magnetic wrench on the IPMs consequent to its magnetization m_i and location p_i as shown in (1).

$$w_i = \begin{pmatrix} 0_{3,3} & m_{i*} \\ m_{i*} & 0_{3,3} \end{pmatrix} \begin{pmatrix} B(p) \\ dB(p) \end{pmatrix}. \quad (1)$$

$$w_i = S_i U$$

Where $w_i = \begin{pmatrix} \tau_i \\ f_i \end{pmatrix}$ and τ_i and f_i refer to the respective torque and force on the agent i . Here we introduce the operator $\cdot_+ : \mathbb{R}^3 \rightarrow \mathbb{R}^{3 \times 5}$ which rearranges any vector $v \in \mathbb{R}^3$, as well as the operator $\cdot_\times : \mathbb{R}^3 \rightarrow \mathbb{R}^{3 \times 3}$ as $v_\times = (v \times e_1 \mid v \times e_2 \mid v \times e_3)$. Where e represents the canonical basis of \mathbb{R}^3 .

Finding the rank of S allows us to determine the number of controllable DOFs. It is known that for any agent i , $rank(S_i) = 5$ [6]. Moreover, one can notice that maximum manipulability can be obtained when the 2 agents are orthogonal. This comes from the fact that with this configuration $S = (S_1^T S_2^T)^T$ and $m_1 \times m_2 \neq 0$. Resulting in $rank(S) = 8$, thus proving that with $M =$

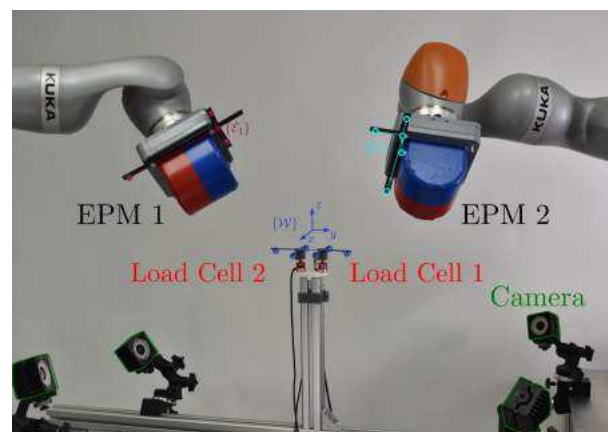


Fig. 1 Setup for magneto-mechanical actuation experiments using the dEPM setup

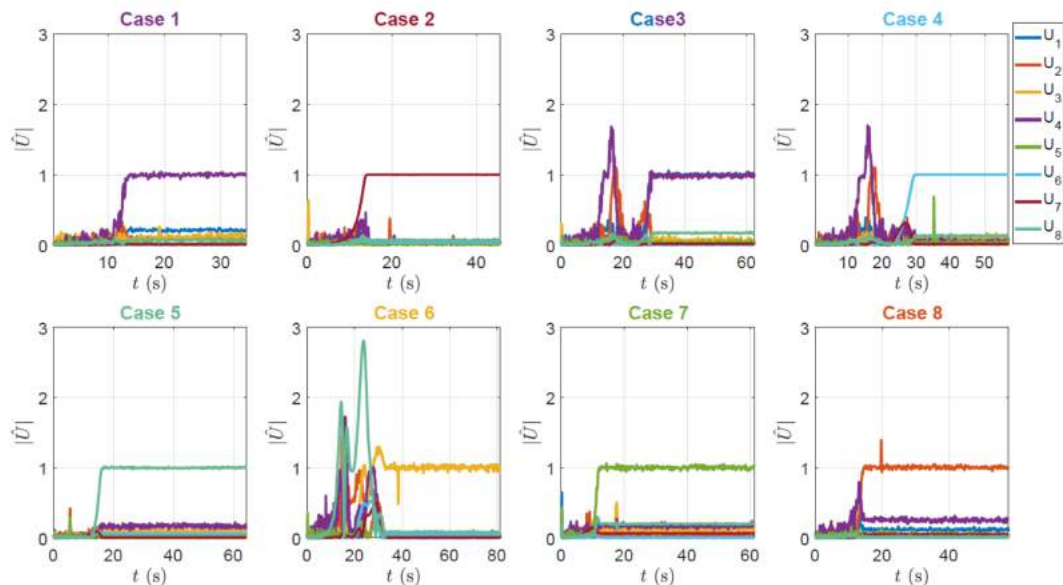


Fig. 2 Normalized response for magnetic field and differentials. Title colors are referred to the component activated for each case.

$N = 2$ we can control 8 independent magnetic DOFs. Since 2 EPMS are used, we refer to this actuating system as the dEPM system.

Finding 8 independent DOFs is equivalent to finding 8 poses of the EPMS that lead to 8 orthogonal directions of the wrench onto the IPMs. Thus, obtaining 8 independent $U(T)$, where $T = 1, 2, \dots, 8$. Due to the nonlinearities associated with solving (1), we opted for a direct analysis of primitive poses which show independent activation of field and differential component. To achieve *independent field control* we look for configurations where the magnets are aligned. In contrast, to obtain independent components of U related to the *differentials* of the field, we consider solutions with no field components. This is achieved by positioning the EPMS in opposite directions.

RESULTS

Validation of the proposed inferences were performed through a series of experiments, aimed at proving the 8 DOFs manipulation capabilities. This was done by using 8 configurations of the EPMS for which we can control, independently, the 8 components of the field U . Each experiment was performed by placing 2 IPM coupled 6-axis load cells ($12.7 \times 12.7 \times 12.7 \text{ mm}^3$ Nano17 Titanium, ATI, USA) between 2 robotic arms (LBR iiwa 14, KUKA, Germany); each manipulating one of the actuating EPMS (Cylindrical permanent magnet with a diameter and length of 101.6 mm and an axial magnetization of 970.1 Am^2 (N52)), as shown in Fig. 1. Two load cells were used, each with a IPM attached to it, with IPMs orthogonal to each other. By measuring the wrench induced by each unique pose of the EPMS and inverting (1) by use of the Moore-Penrose pseudoinverse, U for each pose was measured. The

normalized results for each case (independent actuation of each component of U) can be seen in Fig. 2.

DISCUSSION

The present work discussed the manipulation capabilities of robotically manipulated magnetic sources. In particular, we showed that 2 actuated EPMS are able to independently manipulate 8 DOFs. Both theoretical dissertation and experiments prove that the proposed approach can achieve the same capabilities as coil based actuation [6]. The findings can be used to potentially improve a vast range of diagnostic and interventional medical procedures through the employment of smaller and softer instruments. For example, applying the dEPM system to actuate multi-DOFs magnetic SCRs.

REFERENCES

- [1] S. Salmanipour, O. Youssefi, and E. D. Diller, "Design of Multi-Degrees-of-Freedom Microrobots Driven by Homogeneous Quasi-Static Magnetic Fields," *IEEE Transactions on Robotics*, vol. 37, no. 1, pp. 246–256, 2021.
- [2] M. Richter, V. K. Venkiteswaran, and S. Misra, "Multi-Point Orientation Control of Discretely-Magnetized Continuum Manipulators," *IEEE Robotics and Automation Letters*, vol. 6, no. 2, pp. 3607–3614, 2021.
- [3] J. J. Abbott, E. Diller, and A. J. Petruska, "Magnetic Methods in Robotics," *Annual Review of Control, Robotics, and Autonomous Systems*, vol. 3, no. 1, pp. 57–90, may 2020. [Online]. Available: <https://doi.org/10.1146/annurev-control-081219-082713>
- [4] M. Yousefi and H. Nejat Pishkenari, "Independent position control of two identical magnetic microrobots in a plane using rotating permanent magnets," *Journal of Micro-Bio Robotics*, vol. 17, no. 1, pp. 59–67, jun 2021. [Online]. Available: <https://doi.org/10.1007/s12213-021-00143-w> <https://link.springer.com/10.1007/s12213-021-00143-w>
- [5] G. Pittiglio, J. H. Chandler, M. Richter, V. K. Venkiteswaran, S. Misra, and P. Valdastrì, "Dual-Arm Control for Enhanced Magnetic Manipulation," in *2020 IEEE/RSJ International Conference on Intelligent Robots and Systems (IROS)*, 2020, pp. 7211–7218.
- [6] S. Salmanipour and E. Diller, "Eight-Degrees-of-Freedom Remote Actuation of Small Magnetic Mechanisms," in *2018 IEEE International Conference on Robotics and Automation (ICRA)*, 2018, pp. 3608–3613.

A navigation console to steer magnetic instruments under radiological guidance for neuro-vascular interventions

R. Dreyfus¹, Q. Boehler¹, C. Chautems¹, B.J. Nelson¹

¹Multi-Scale Robotics Lab, ETH Zurich

dreyfusr@ethz.ch

INTRODUCTION

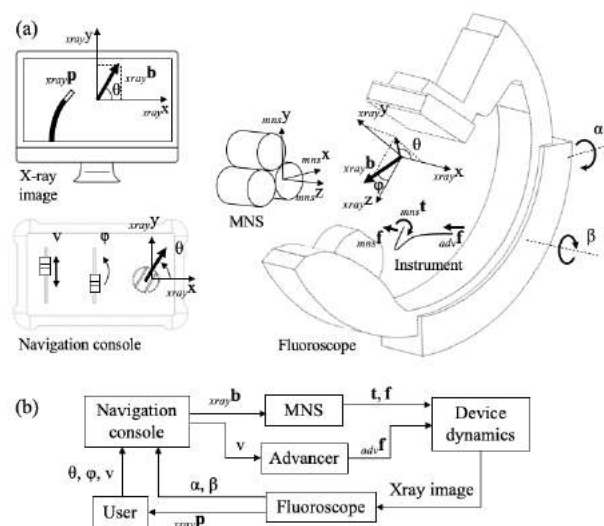
The gold-standard for treating some neurovascular diseases such as ischemic stroke is an effective and minimal invasive endovascular technique. The primary instruments used are catheters and guidewires that are inserted into the vasculature through a small incision at the groin [1]. Some instruments have a curved tip allowing for easier access of different vessels as they bifurcate and are navigated by pushing, pulling, and rotating. In cerebrovascular interventions, interventional neuroradiologists are often faced with tortuous and complex anatomies that can be challenging to navigate and require a high level of skill and expertise [2].

An alternative to manual catheter and guidewires is a robotic approach using robotic magnetic navigation (RMN). In RMN, magnetic instruments composed of a flexible magnetic tip are redirected by the external magnetic field generated by a magnetic navigation system (MNS) [3]. In neurovascular radiology, where the instruments are navigated under radiological guidance, x-ray images of the patient anatomy and the instruments are displayed on a monitor. Under these circumstances, the steering of magnetic catheters and guidewires can be challenging, because they are 3D objects moving in a 3D environment, whereas the operator is provided a 2D image on a 2D display. Companies such as Stereotaxis make use of graphical representations of the magnetic field, the magnetic instrument, and the patient anatomy to help the operator in making the mental transformations [3]. Adding visual cues such as graphical overlays or a separate monitor have the potential to divert the doctor's gaze away from the x-ray image. This can lead to loss of focus and potentially increase risk. In this work, we propose a new interface that allows the steering of magnetic instruments without the need of additional visual feedback other than the already available 2D fluoroscope image.

MATERIALS AND METHODS

In radiological interventions, the emitter and collector of the x-ray fluoroscope are often rotated around the patient to obtain more favourable views (α and β in dFig 1(a)). Hence, the coordinate frame centered on the x-ray image is generally not aligned with the coordinate frame of the MNS (subscripted as mns and $xray$ in dFig 1(a)). For intuitive handling, it is crucial to define the field inputs in the fluoroscope's frame of reference.

This allows the user to steer the magnetic instrument in the image without having to maintain a mental model of all the necessary geometric transformations. As a consequence, the orientation of the imaging device must be constantly updated. This can be achieved by adjusting the fluoroscope orientation manually or by accessing the angles α , β directly from the imaging device or from sensors attached to it.



dFig 1 (a) The magnetic instrument is steered with the magnetic field ${}_{xray}\mathbf{b}$ generated by the MNS and inserted by the advancer at speed v . The field induces torques and forces ${}_{mns}\mathbf{t}$ and ${}_{mns}\mathbf{f}$ acting on the magnetic tip of the instrument and the advancer applies a pushing force on the proximal side ${}_{adv}\mathbf{f}$. The magnetic instrument is imaged with an x-ray fluoroscope that provides visual feedback. The user steers the instruments with the navigation console by changing the magnetic field ${}_{xray}\mathbf{b}(\theta, \varphi)$ in the fluoroscope's frame of reference. (b) Block diagram of the control scheme. Inputs to the navigation console from the user are θ , φ and v .

As a second measure to make steering more intuitive, we introduce the concept of absolute field control. By absolute field control, we rotate the magnetic field in absolute coordinates rather than changing the direction in relative steps. To this end, we developed a navigation console that maps the orientation of the user inputs one-to-one to the orientation of the magnetic field.

The new interface was tested in the setup seen in Fig 2(a). The MNS used is a three-coil electro-magnetic navigation system (eMNS) capable of generating magnetic fields at a magnitude of 25 mT, 20 cm away from the coils' surface. The magnetic field induces torques on the magnets embedded in the instruments,

causing their tip to align in the direction of the applied field. A magnetic catheter and a magnetic guidewire are navigated inside a silicone phantom model (Trandomed 3D Inc.) in the aortic arch and the M1 coronary arteries. The model is filled with a water-soap solution and navigation is performed under no-flow condition. The magnetic instruments are inserted and retracted by a remote-controlled robotic advancer unit and imaged by a C-arm fluoroscope (Ziehm Imaging Inc.). During instrument navigation, the operator is not provided with any visual feedback of the current magnetic field direction.

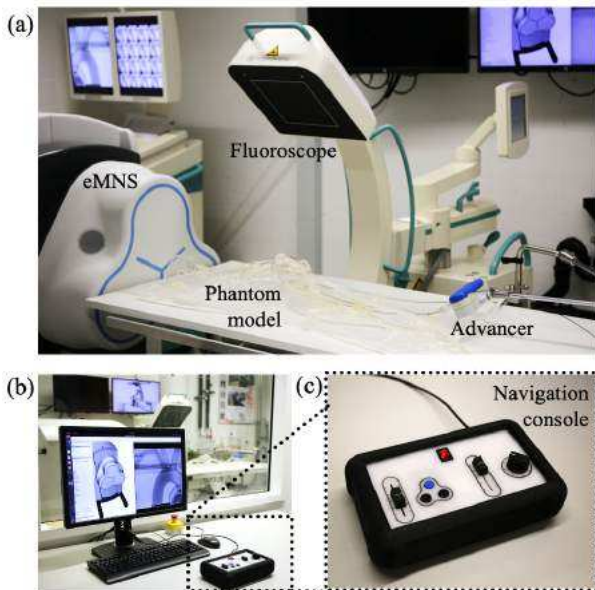


Fig 2 (a) Overview of the test setup, (b) user interface with monitor and x-ray image, (c) navigation console.

RESULTS

The realisation of the navigation console can be seen in Fig 2(c). We chose to map the in-plane azimuth angle of the magnetic field θ to a rotary knob and the off-plane inclination angle φ to a linear joystick. The dials on the navigation console are directional and reflect the current direction of the magnetic field at all times, as illustrated in Fig 3. To know the current state of the magnetic field, the operator can simply touch the dials on the console or look at them. In addition to the magnetic field inputs, the device has programmable buttons and a linear joystick to control the catheter insertion speed. The interface was tested on a setup replicating the arrangement found in a clinical setting Fig 2(a). A 4 Fr magnetic catheter and 2 Fr guidewire were successfully navigated in the aortic arch Fig 3(a) and M1 cerebral arteries Fig 3(b) of the phantom model. The interface and control strategy were demonstrated to be effective in steering the magnetic instrument without the need of additional visual cues other than the already available x-ray image.

DISCUSSION

We introduced a new human machine interface that allows for magnetic catheter and guidewire steering. The

interface does not depend on additional visual feedback other than what is already available in a standard operating room. The interface is intuitive and promises a shallow learning curve for new adopters, good catheter and guidewire control, improving patient safety, and simple integration in the operating room infrastructure.

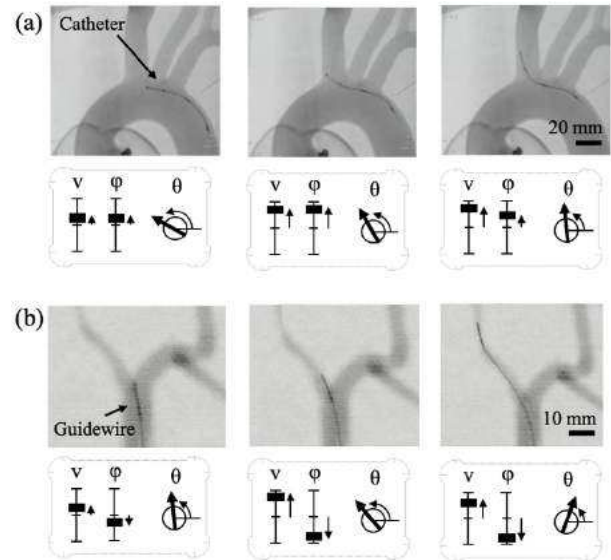


Fig 3 Navigating a 4 Fr catheter cross the aortic arch (a) and a 2 Fr guidewire in the M1 coronary arteries (b) in a silicone phantom model under no-flow conditions. In-plane steering is done with the θ -dial, off-plane adjustments with the φ -joystick, and insertion-retraction with the v -joystick.

ACKNOWLEDGEMENT

This work was supported by the Swiss National Science Foundation through grant number 200020B_185039, by the ITC-InnoHK funding, and by the ERC Advanced Grant 743217 Soft Micro Robotics (SOMBOT).

REFERENCES

- [1] G. Britz, "An overview of neurovascular disease management," *Methodist DeBakey cardiovascular journal*, vol. 10, no. 4. Methodist DeBakey Heart & Vascular Center, pp. 212–213, Oct. 01, 2014. doi: 10.14797/mdcj-10-4-212.
- [2] F. J. A. Mont'Alverne *et al.*, "Unfavorable vascular anatomy during endovascular treatment of stroke: Challenges and bailout strategies," *Journal of Stroke*, vol. 22, no. 2. Korean Stroke Society, pp. 185–202, 2020. doi: 10.5853/jos.2020.00227.
- [3] T. Krings *et al.*, "Magnetic versus manual guidewire manipulation in neuroradiology: In vitro results," *Neuroradiology*, vol. 48, no. 6, pp. 394–401, Jun. 2006, doi: 10.1007/s00234-006-0082-3.

Toward Targeted Therapy in the Brain by Leveraging Screw-Tip Soft Magnetically Steerable Needles

Trevor J. Schwehr¹, Adam J. Sperry¹, John D. Rolston²,
Matthew D. Alexander^{2,3}, Jake J. Abbott¹, and Alan Kuntz⁴

¹Department of Mechanical Engineering, ²Department of Neurosurgery, ³Department of Radiology and Imaging Sciences, and ⁴School of Computing, University of Utah
alan.kuntz@utah.edu

INTRODUCTION

Steerable needles capable of taking curvilinear trajectories through tissue enable the ability to avoid anatomical obstacles and home in on targets [1]. Steerable needle designs that are pushed into tissue from their base struggle to take tight curvatures without damaging tissue due to the needle cutting laterally through tissue [2]–[4]. We propose a new type of steerable needle that can take much tighter curvatures safely. This needle pulls itself through tissue via a screw tip, with rotation ω imparted at its base (Fig. 1(a)), either by hand or with a robotic insertion system. The needle is steered by applying a magnetic field \mathbf{b} (units T), and thus a magnetic steering torque $\boldsymbol{\tau} = \mathbf{m} \times \mathbf{b}$ (units N·m), to a magnetic dipole \mathbf{m} (units A·m²) at the needle's tip via, e.g., an external permanent magnet. As the needle's body only needs to transmit rotation to its tip and not an axial insertion force, our design leverages extremely soft tubing for its shaft, which enables the shaft to have low bending stiffness and impart low forces on surrounding tissues. We note that magnetic torque scales with distance as $\|\boldsymbol{\tau}\| \propto d^{-3}$, which is more favorable at clinical scale than force $\|\mathbf{f}\| \propto d^{-4}$ [5], which has been proposed as a way to pull soft steerable needles in tissue [6].

Our design enables paths with high curvature, unlocking clinical applications such as targeted therapy in brain tissue. Consider the case of stereotactic ablation in which the hippocampus and the amygdala are ablated via energy application (e.g., laser or radiofrequency) in order to treat epilepsy [7] (Fig. 1(b)). To minimize damage to healthy brain tissue, this procedure is currently performed by inserting a straight instrument into the structures and ablating in a series of cylindrical shapes. Unfortunately, due to the straight nature of the tool, the desire to not ablate brain tissue outside of these structures, and the inability to safely create multiple passes at these brain structures, this results in only partially ablating the intended structures [8].

This work was supported in part by the National Science Foundation under Grant 1830958. T. J. Schwehr and A. J. Sperry contributed equally. T. J. Schwehr is now with the Department of Mechanical Engineering, Johns Hopkins University.

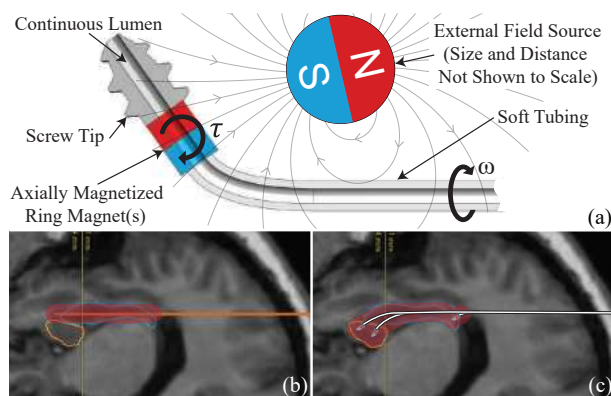


Fig. 1 (a) Cross-section schematic of the needle concept and depiction of the field of an external permanent magnet being used to steer the needle. Our two control variables are ω and τ . (b) Straight needle insertion and region of ablation with sub-optimal coverage of the hippocampus (blue) and amygdala (orange). (c) Steerable needle insertion and possible region of ablation with three branching paths that more closely follow the shape of the hippocampus and amygdala.

In this work, we demonstrate the ability to leverage our highly curved needle to more closely conform to these brain structures' complex geometries, conceptually opening the door to better ablation patterns (where the ablation probe could be delivered through, or embedded in, the lumen of the steerable needle). To do so, our needle takes a complex path that incorporates multiple branching points wherein our needle is partially retracted and then steered forward along new paths (Fig. 1(c)). We demonstrate such a complex, multi-branch path in brain simulating gelatin, covering a planar representation of the relevant brain structures segmented from the real patient scan of Fig. 1, at correct anatomical scale.

MATERIALS AND METHODS

Our prototype needle (Fig. 2(a)) is constructed from the tip of a No. 2 brass screw (major dia. 2.2 mm, minor dia. 1.4 mm) with a machined lumen of 0.5 mm dia. The screw tip is affixed to four axially magnetized Grade-N50 NdFeB ring magnets—each with 0.5 mm inner dia. (ID), 1 mm outer dia. (OD), 0.5 mm height—acting as one large magnet. They are affixed using cyanoacrylate

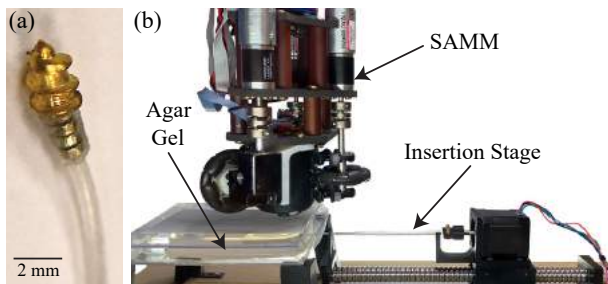


Fig. 2 (a) Image of the tip of the needle prototype. (b) Experimental setup with the SAMM positioned above the tip of the needle in the agar gel. The needle is inserted via a robotic insertion stage.

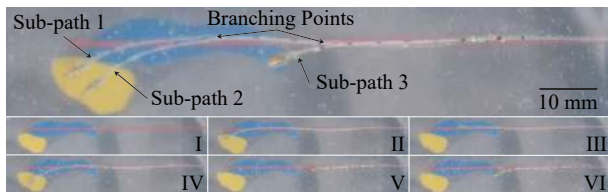


Fig. 3 (Top) Composite image of the branching paths achieved with our needle, with at-scale image of brain structures. (Bottom) Chronological image sequence.

to a Tygon tube with 0.25 mm ID and 0.76 mm OD. We inserted our needle into a custom 25 mm thick 0.5 wt% agar gel phantom (Fig. 2(b)) that has been previously established to have similar mechanical properties to human brain [9]. A robotic stage inserts the needle by rotating the needle at its base and simultaneously moving forward in a coordinated fashion. We generate the torque at the needle tip to achieve steering by actively actuating the spherical-actuator-magnet manipulator (SAMM) to change the applied magnetic field using its 50.8 mm diameter spherical permanent magnet [10]. In our experiments we repositioned the SAMM periodically during insertion to be directly above the needle tip with steering torque in the desired direction of curvature.

A correctly scaled image of the brain, with the hippocampus and the amygdala regions highlighted, was placed above the agar gel such that it could be seen through the agar by a camera below. Closing the loop visually, a human operator then attempted to steer a three-branched, curved trajectory that ensured that the aggregate path covered the geometry of both brain structures assuming cylindrical ablation around the needle tip trajectory (see Fig. 1(c) for the desired trajectory).

RESULTS

Figure 3 shows a three-stage branching path achieved by our needle. Sub-path 1 is the first insertion of the needle. Sub-paths 2 and 3 were achieved by partially retracting the needle to the respective branching point then reinserting while steering in the new direction of each sub-path. We achieved a 26 mm minimum radius of curvature using an applied field strength of 73 mT. We performed additional experiments to verify the ability to: steer in 3D, by steering out of the horizontal plane (Fig. 4(a)); and advance through, and steer in, *ex vivo* ovine brain tissue (Fig. 4(b)).

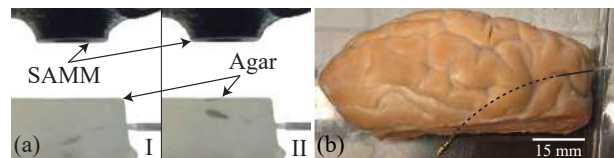


Fig. 4 (a) Demonstration of out-of-plane steering (side view). We steered down (I), partially retracted, then steered up (II). (b) Example of steering through ovine brain (top-down view). We steered the needle open-loop by estimating the needle tip's pose based on expected curvature and translation. In this case, the needle was rotated at its base by hand rather than with the robotic insertion stage. Due to the open-loop nature of this experiment, this curvature should not be assumed maximal.

DISCUSSION

These results demonstrate the potential of this needle design to precisely navigate with high curvature to a particular region of interest in the brain for targeted therapies such as energy-based ablation. They further demonstrate the potential to take branching paths when necessary, potentially enabling complete coverage of a region while minimizing travel through healthy tissue. We note that, given that the OD of the commercial ring magnets we employ in this work is smaller than the minor diameter of the screw tip in our prototype, we could increase the steering torque by 117% via custom magnets, or we could decrease the size of our screw tip by 27% via a custom screw (potentially with a different material and/or thread height as well).

Magnetic steering requires knowledge of the five-degree-of-freedom pose of the needle's tip. In our closed-loop experiments this was possible due to the transparency of the phantom, but limited our experiments to be in a plane. To further evaluate the performance of this needle in opaque tissues (such as the brain) with 3D regions of interest, closed-loop control and localization without line-of-sight is required. Such localization can be achieved through medical-imaging (e.g., CT, fluoroscopy) or potentially through magnetic localization.

REFERENCES

- [1] R. J. Webster III *et al.*, "Nonholonomic modeling of needle steering," *Int. J. Robot. Res.*, vol. 25, no. 5-6, pp. 509–525, 2006.
- [2] K. B. Reed *et al.*, "Robot-assisted needle steering," *IEEE Robot. Autom. Mag.*, vol. 18, no. 4, pp. 35–46, 2011.
- [3] M. Rox *et al.*, "Decoupling steerability from diameter: Helical dovetail laser patterning for steerable needles," *IEEE Access*, vol. 8, pp. 181 411–181 419, 2020.
- [4] A. Hong *et al.*, "Magnetic control of a flexible needle in neurosurgery," *IEEE Trans. Biomed. Eng.*, vol. 68, no. 2, pp. 616–627, Feb. 2021.
- [5] J. J. Abbott *et al.*, "Magnetic methods in robotics," *Annu. Rev. Control Robot. Auton. Syst.*, vol. 3, pp. 57–90, 2020.
- [6] M. Ilami *et al.*, "Magnetic needle steering in soft phantom tissue," *Sci. Rep.*, vol. 10, p. 2500, 2020.
- [7] M. Cossu *et al.*, "RF-ablation in periventricular heterotopia-related epilepsy," *Epilepsy Res.*, vol. 142, pp. 121–125, 2018.
- [8] S. S. Grewal *et al.*, "Laser ablation for mesial temporal epilepsy: a multi-site, single institutional series," *J. Neurosurg.*, vol. 130, pp. 2055–2062, 2018.
- [9] D. C. Stewart *et al.*, "Mechanical characterization of human brain tumors from patients and comparison to potential surgical phantoms," *PLOS ONE*, vol. 12, no. 6, p. e0177561, Jun. 2017.
- [10] S. E. Wright *et al.*, "The spherical-actuator-magnet manipulator: a permanent-magnet robotic end-effector," *IEEE Trans. Robot.*, vol. 33, no. 5, pp. 1013–1024, 2017.

Studying the Usability of Forbidden Region Virtual Fixtures for Safer Robotic Assisted Minimally Invasive Surgery

Martina Favaretto¹, Aldo Marzullo², and Elena De Momi¹

¹*Department of Electronics, Information and Bioengineering, Politecnico di Milano,*

²*Department of Mathematics and Computer Science, University of Calabria*

INTRODUCTION

Forbidden Region Virtual Fixture (FRVF) have been researched in recent years to improve the safety of RAMIS. In fact, most of the commercially available RAMIS systems, such as the da Vinci Surgical System, are currently lacking haptic interfaces, limiting the perception of the surgeon of the patient's anatomy and overburdening the visual channel [1]. The absence of haptic feedback can compromise the procedure's safety as the surgeon is unaware of the force applied with the instrument on sensitive anatomical structures. Moreover, especially for novice surgeons who are not proficient in the control of the surgical robot, the unnoticed collision of the surgical tools with the patient's anatomy is an additional risk factor. FRVF can prevent the surgical instruments from getting excessively close to sensitive anatomical structure by returning a feedback force to the surgeon, who is notified of the proximity and can move the instrument in a safer position.

Although FRVF is a promising technique, there are conflicting opinions among surgeons on their real usability, as the force might disturb the execution of the procedure. In this letter, we present a user study on a simplified FRVF scenario, with the aim of evaluating the system's effectiveness and usability.

MATERIALS AND METHODS

A. The FRVF system

The designed FRVF system is based on the knowledge of the real-time relative position in the surgical scene of the anatomical structure to be protected and of the surgical instruments. In absence of exteroceptive sensors, this requires building a computational representation of the interaction. The forbidden region is defined starting from the 3D mesh of the anatomical structure to be protected, which can be obtained from pre-operative images. For simplicity, the structure is assumed to be rigid. The mesh is registered intraoperatively using a set of points of the real anatomical structures obtained using the robot's arm as a localizer. A safety region of width r is identified around the anatomy, as shown in Figure 1.

The position and orientation of the surgical instruments are identified using the robotic arm's kinematic

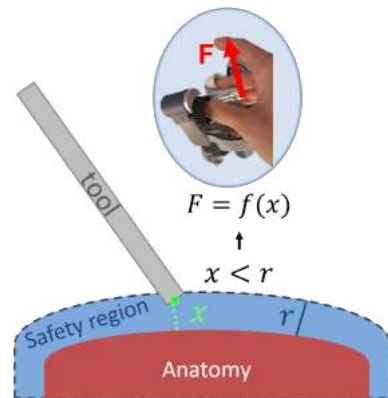


Fig. 1 FRVF system's scheme: when the instrument is inside the safety region, a feedback force is returned to the master manipulator. x is the tool's distance from the anatomy, r is the width of the safety region.

to recover the position of the tool's tip and of the remote center of motion (rcm). The entire body of the instrument is represented as a cylinder with radius equal the radius of the instrument and oriented as the segment connecting the tip and the rcm . In particular, the shortest Euclidean distance x between the cylinder and the 3D mesh is used.

Whenever the surgical instruments are inside the safety region, a force is computed according to the visco-elastic model in Eq. 1 and returned to the master manipulator.

$$\vec{F} = \begin{cases} k(r-x) \cdot \vec{n} + b(0-\dot{x}) \cdot \vec{n} & \text{if } x \leq r \\ 0 & \text{if } x > r \end{cases} \quad (1)$$

In Eq. 1, k and b are respectively the elastic and the dumping constants, while \vec{n} is the outward normal to the anatomy's surface at its closest point to the instrument. The force is therefore directed to push the tool out of the safety region. A threshold force was set at 5N to prevent damaging to the manipulators' actuators. Notably, no torque is applied to the manipulator, as no desired orientation is imposed.

B. Evaluation of the FRVF system

The evaluation of the system was carried out on a complete da Vinci Research Kit with the contribution

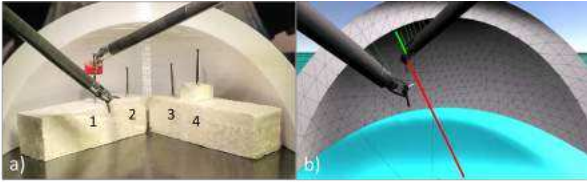


Fig. 2 a) experimental setup. b) computational representation of the interaction. The green line represent the minimum distance of cylinder from the mesh, while the red line indicates the direction of the force feedback to the master manipulator.

of ten un-experienced users. Each user was asked to perform the task in Figure 2: first the red ring is picked up with the right tool, then it is inserted in the first two nails with an up-bottom motion, passed on to the left tool to repeat the movement on the last two nails and finally placed back at the center of the board. The task is inspired by robotic prostatectomy procedures, where the surgeon is forced to work in proximity to the pubic bone structure [2], often colliding with the instrument on it and creating small damages. The goal of the task is to verify whether the presence of the FRVF can reduce the chances of collision of the instruments with the white structure, here representing the pubic bone, without hindering the execution of the task. The experiment was repeated by each user under three different conditions:

- **Control:** execution without force feedback;
- **$r = 2$ cm:** force feedback with safety distance of 2 cm;
- **$r = 2.5$ cm:** force feedback with safety distance of 2.5 cm;

A wider safety region is expected to guarantee a safer execution, but might complicate the execution of the task, as the force feedback starts to act farther away from the pubic bone, where the rings are located.

The order of execution of the tasks was picked randomly for each user to rule out a possible bias in the results. Practice time was given at the beginning of the experiment to reduce the impact of the learning effect.

The utilized values of k and b were respectively 250 N/m and 8 N·s/m. The average and minimum distance from the structure were recorded during the execution of the task as well as the number of collision events. To evaluate the potential hindering of the execution instead, the execution time was used as performance metric.

RESULTS

The distance data are shown in Figure 3. Statistical relevance was established with a Wilcoxon test (significance level 0.05). Both the average and the minimum distance from the anatomy resulted significantly higher when the force feedback was active with respect to the control condition (for $r = 2$ cm p-values are 0.0257 and 0.0257 respectively, for $r = 2.5$ cm they are 0.0028 and 0.0312). However, no significant difference is found between the $r = 2$ cm and $r = 2.5$ cm conditions.

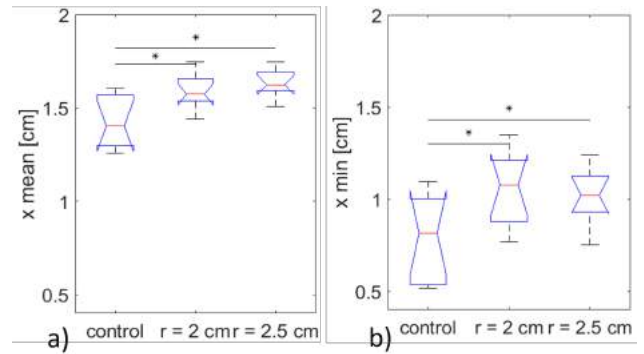


Fig. 3 Average (a) and minimum (b) distance of the surgical instruments from the bone structures.

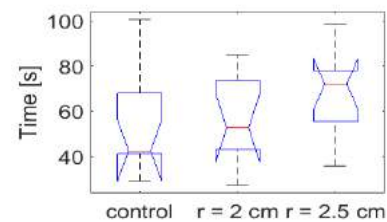


Fig. 4 Execution times.

Additionally, no collision events were recorded while 8 collisions occurred without force feedback. Regarding the execution time, shown in Figure 4, no significant differences were found among the three experimental conditions, even though a trend of increasing times is visible.

DISCUSSION

Results show that the tested FRVF system is effective in preventing collisions and allows to perform the tested task within a safer distance from the simulated pubic structure. Moreover, the force feedback generated for the two tested values of the safety radius r did not significantly hinder the execution of the task, which was carried out with execution times comparable to the control. These results suggest that, when the force parameters are properly tuned for a specific application, the FRVF can bring a significant advantage to the user. The next step will be to extend the user study to a pool of surgeons to have a more robust evaluation of the system's usability. Additionally, we plan to include an AR interface in the system to get a comparison of the usefulness of different types of augmentation for collision avoidance.

REFERENCES

- [1] A. N. Healey, "Speculation on the Neuropsychology of Teleoperation: Implications for Presence Research and Minimally Invasive Surgery," *Presence: Teleoperators and Virtual Environments*, vol. 17, no. 2, pp. 199–211, 2008.
- [2] "Periurethral suspension stitch during robot-assisted laparoscopic radical prostatectomy: Description of the technique and continence outcomes," *European Urology*, vol. 56, no. 3, pp. 472–478, 2009.
- [3] S. A. Bowyer, B. L. Davies, and F. Rodriguez y Baena, "Active constraints/virtual fixtures: A survey," *IEEE Transactions on Robotics*, vol. 30, no. 1, pp. 138–157, 2014.

iSurgeon: Augmented reality telestration for improved surgical trainingT.E. Fuchs ¹, E.A. Felinska ¹, A. Kogkas ^{2,3}, G.P. Mylonas ^{2,3}, B.P. Müller-Stich ¹, F. Nickel ¹¹Department of General, Visceral and Transplantation Surgery, Heidelberg University Hospital, 69120 Heidelberg, Germany.²Hamlyn Centre for Robotic Surgery, Imperial College London, London, SW7 2AZ, UK.³Department of Surgery and Cancer, Faculty of Medicine, Imperial College London, London, SW7 2AZ, UK.

felix.nickel@med.uni-heidelberg.de

INTRODUCTION

Minimally invasive surgery (MIS) has become the gold standard in many surgical procedures [1]. Although it provides a better outcome for patients it has a slower learning curve [2, 3]. In laparoscopic surgery trainees need to learn how to interpret the operative field displayed on the laparoscopic screen. Experts currently guide trainees only verbally during laparoscopic surgical procedures. We developed the iSurgeon which allows the instructor to make hand gestures that are detected by an RGB-D camera (colour resolution: 1920x1080 pixels, 30 fps, depth resolution: 512x424 pixels, 30 fps) and displayed on the laparoscopic screen in augmented reality (AR) to provide visual expert guidance (telestration) [4]. Thus, the expert can provide clearer instructions by using gestures in addition to verbal instructions. This study analysed the effect of iSurgeon guided instructions on the gaze behaviour of instructor and trainee during laparoscopic surgery. We also aimed to find out if the iSurgeon affects the performance and the cognitive workload of the trainees.

MATERIALS AND METHODS

In a randomized-controlled cross-over trial, 40 laparoscopically naive medical students performed 7 basic laparoscopic tasks. One porcine laparoscopic cholecys-

tectomy (task 8) was performed with iSurgeon or with verbal instructions only. Task 8 was divided into 3 steps: A: preparation of cystic artery and duct; B: clipping and cutting of the cystic artery and duct; C: preparation of the gallbladder from the liver bed. We used Pupil Core eye-tracking glasses (Pupil labs GmbH, Berlin, Germany) to capture the instructor's and the students' gazes. Gaze behaviour was evaluated for tasks 1-7 by measuring the gaze latency, gaze convergence and collaborative gaze convergence. The gaze latency was considered as the time from instruction until the first fixation of the trainee's gaze on a target area [5]. The gaze convergence was the absement, namely the integral of the gaze displacement, between the instruction and the first fixation of the trainee on the target area [6]. The collaborative gaze convergence was the absement of the instructor's and trainee's gaze over the time needed to merge over a target area [5]. The performance was measured by the number of errors in tasks 1-7 and with the global and specific Objective Structured Assessments of Technical Skills (OSATS) checklists in task 8 [7, 8]. Furthermore, the total time needed to complete the tasks was measured. Subjective workload of the participant was measured by a questionnaire consisting of 6 questions which were answered on visual analogue scales. Each scale delivered a score between 0 (low workload) and 100 (high workload). As another cognitive workload measure, we analysed the blink rate in all



Fig. 1 Left: Instructor (1) and trainee (2) wear Pupil Core eye-tracking glasses connected to separate laptops (3). When using the iSurgeon the instructor (1) works with hand gestures detected by a sensor (4) to instruct the participant (2). The gestures are projected on a screen (5) connected to a laparoscopic tower (6). Tasks are performed in a box trainer (7). Right: The expert's hand is displayed on the laparoscopic screen while he instructs the trainee to perform a porcine laparoscopic cholecystectomy (task 8).

task	Gaze Latency (sec)			Gaze Convergence (pixels*sec)			Collaborative Gaze Convergence (pixels*sec)		
	iSurgeon	Verbal	p-val.	iSurgeon	Verbal	p-val.	iSurgeon	Verbal	p-val.
1	0.14 ± 0.07	0.42 ± 0.13	< 0.01	0.01 ± 0.01	0.08 ± 0.03	< 0.01	0.03 ± 0.03	0.10 ± 0.04	< 0.01
2	0.15 ± 0.08	4.26 ± 1.73	< 0.01	0.01 ± 0.02	1.10 ± 0.55	< 0.01	0.02 ± 0.03	1.03 ± 0.41	< 0.01
3	0.28 ± 0.24	1.86 ± 0.91	< 0.01	0.03 ± 0.04	0.50 ± 0.28	< 0.01	0.04 ± 0.07	0.62 ± 0.23	< 0.01
4	0.14 ± 0.09	1.46 ± 0.60	< 0.01	0.01 ± 0.01	0.33 ± 0.22	< 0.01	0.02 ± 0.02	0.34 ± 0.25	< 0.01
5	0.14 ± 0.11	2.18 ± 1.63	< 0.01	0.01 ± 0.01	0.62 ± 0.59	< 0.01	0.04 ± 0.04	0.67 ± 0.45	< 0.01
6	0.16 ± 0.15	2.11 ± 1.12	< 0.01	0.01 ± 0.04	0.53 ± 0.42	< 0.01	0.04 ± 0.06	0.49 ± 0.38	< 0.01
7	0.13 ± 0.11	0.76 ± 0.65	< 0.01	0.00 ± 0.02	0.19 ± 0.18	< 0.01	0.03 ± 0.04	0.26 ± 0.21	< 0.01

Fig. 2 Results of gaze latency, gaze convergence and collaborative gaze convergence presented in medians ± interquartile ratios.

tasks [9]. Within-group comparison was done with the Wilcoxon rank-sum test (tasks 1-7) and between-group comparison with the Mann-Whitney U test (task 8). The effects of modality and task type to each metric were assessed with two-way repeated measures ANOVA.

RESULTS

There was a significant main effect of instruction modality (iSurgeon, Verbal) in tasks 1-7 on gaze latency ($F(1,39)=762.5$, $p<0.01$, $\eta_p^2=0.95$), gaze convergence ($F(1,39)=482.8$, $p<0.01$, $\eta_p^2=0.93$) and collaborative gaze convergence ($F(1,39)=408.4$, $p<0.01$, $\eta_p^2=0.91$) Fig. 2). The number of errors was significantly lower in tasks 1-7 while using iSurgeon (0.18 ± 0.56 vs. 1.94 ± 1.80 , $F(1,39)=433.5$, $p<0.01$, $\eta_p^2=0.92$) and the score ratings for task 8 were significantly higher with iSurgeon (global OSATS: 29 ± 2.5 vs. 25 ± 5.5 , $p<0.01$; task specific OSATS: 60 ± 3 vs. 50 ± 6 , $p<0.01$). While instructed with iSurgeon, participants completed some tasks significantly faster (tasks 2-6, $p<0.01$). No significant difference in task duration was shown for tasks 1, 7 and 8. The workload questionnaire for tasks 1-7 resulted in significantly less workload with iSurgeon ($p<0.01$), whereas it was not significantly lower in task 8 ($p=0.12$). The blink rate was significantly lower in tasks 3-7 ($p<0.01$).

DISCUSSION

AR based telestration with the iSurgeon successfully improved laparoscopic surgical performance. Trainee's gaze behaviour was improved by reducing the time from instruction to fixation on targets and leading to a higher convergence of the instructor's and the trainee's gazes during the task [6]. Also, the convergence of trainee's gaze and target areas increased with the iSurgeon. This suggests that AR based telestration works by means of guiding the trainees' gazes.

The performance in terms of errors and achieved points in the scores was improved by the iSurgeon. However, the time needed to complete the task was reduced only in some tasks. Possible reasons for that are the composition of the tasks. Task 1 and 7 might have been easier to perform in general or the verbal instructions were clearer in these tasks. This would also explain why the iSurgeon did not have a huge effect on the task duration. Further, the complexity of cholecystectomy might have

been too high for laparoscopically naïve students resulting, regardless of the instruction modality, in no difference in task duration. The cognitive workload measured by the questionnaire was lower in most of the tasks with the iSurgeon suggesting that participants felt more comfortable while being instructed with iSurgeon. Though, the blink rate as another possible indicator for cognitive workload was not significantly different in three of the eight tasks. A possible explanation for that might be that task 8 was too complex for the participants. That might have caused the cognitive workload to be not alleviated significantly in comparison to the already high workload caused by the complex task itself. Further studies are needed to exactly analyse the effect of the iSurgeon on surgeons with different experience levels.

REFERENCES

- [1] Buia, A., F. Stockhausen, and E. Hanisch, *Laparoscopic surgery: A qualified systematic review*. World J Methodol, 2015. 5(4): p. 238-54.
- [2] Caroff, D.A., et al., *Association of Open Approach vs Laparoscopic Approach With Risk of Surgical Site Infection After Colon Surgery*. JAMA Netw Open, 2019. 2(10): p. e1913570.
- [3] Harrysson, I.J., et al., *Systematic review of learning curves for minimally invasive abdominal surgery: a review of the methodology of data collection, depiction of outcomes, and statistical analysis*. Ann Surg, 2014. 260(1): p. 37-45.
- [4] Nickel, F., A. Cizmic, and M. Chand, *Telestration and Augmented Reality in Minimally Invasive Surgery: An Invaluable Tool in the Age of COVID-19 for Remote Proctoring and Telementoring*. JAMA Surg, 2021.
- [5] Kwok, K.W., et al., *Collaborative gaze channelling for improved cooperation during robotic assisted surgery*. Ann Biomed Eng, 2012. 40(10): p. 2156-67.
- [6] Chetwood, A.S., et al., *Collaborative eye tracking: a potential training tool in laparoscopic surgery*. Surg Endosc, 2012. 26(7): p. 2003-9.
- [7] Martin, J.A., et al., *Objective structured assessment of technical skill (OSATS) for surgical residents*. Br J Surg, 1997. 84(2): p. 273-8.
- [8] Nickel, F., et al., *Direct Observation versus Endoscopic Video Recording-Based Rating with the Objective Structured Assessment of Technical Skills for Training of Laparoscopic Cholecystectomy*. Eur Surg Res, 2016. 57(1-2): p. 1-9.
- [9] Richstone, L., et al., *Eye metrics as an objective assessment of surgical skill*. Ann Surg, 2010. 252(1): p. 177-82.

The Design of a Biomimetic Whisker-based System for Clinical Gastrointestinal Diseases Screening

Zeyu Wang, Junhong Chen, Ruiyang Zhang, and Benny Lo

The Hamlyn Centre/ Dept of Surgery and Cancer, Imperial College London
zeyu.wang20@imperial.ac.uk

INTRODUCTION

The prevalence of gastrointestinal diseases, manifesting as many broad and confusing symptoms such as malabsorption, malnutrition, and even neurologic dysfunction[1], has become a socio-economic burden for present-day society. Extensive clinical studies illustrate that early screening for gastrointestinal diseases is of vital importance for reducing mortality and improving life expectancy.

The conventional screening method is endoscopy, featured by high sensitivity in diagnoses of mucosal diseases[2]. Its minimally invasive nature makes it extensively carried out in hospitals. However, the highly confined and challenging working conditions including darkness, glare, reflection, bleeding caused by biopsy, blur, and defocus can all prevent optical sensors from working optimally, even lead to missing diagnosis[3]. Meanwhile, the diagnosis bias induced by endoscopist differences has a significant effect [4]. In addition, the tactile sensory modality is desired in surgical practice, which is the foundation of efficient force feedback in minimally invasive surgery.

Inspired by the sensory mechanism of rat whisker, which shows great potential in texture discrimination and distance estimation tasks[5], in this paper, a biomimetic artificial whisker system is proposed for clinical gastrointestinal disease screening. Unlike optical sensing methods, this tactile sensing is a strong complement to the conventional vision-based methods, especially in situations where optical devices cannot work well, a totally lightless environment for instance. Utilizing the analog front end (AFE) technology, the system inherent noise is minimized, which suppresses detection error in experiments. An end-to-end deep learning algorithm is proposed to provide diagnostic outcomes assisting clinical decisions and avoiding subjective bias. A medical phantom-based pilot study was conducted to demonstrate the detection accuracy of the proposed with three common tissue structures, which are normal tissue, ulcerative colitis, and ulcerative cancer. The results have shown the proposed can reach 100% in distinguishing the different types of tissues, and demonstrated the potential of this novel system for advancing endoscopy.

MATERIALS AND METHODS

In this section, the system framework design, modeling analysis, and detailed implementation are present.

A. System framework design

Fig.1 illustrates the framework of the proposed method. During the screening procedure, the proposed whisker-based system enters the intestinal tract or gastric environment, characterized by surface pathological changes caused by specific diseases. Along the trajectory of clinical inspection, the different response signals, which reflect the specific pathological information, will be generated from the proposed system. Combined with deep learning-based algorithms, a whisker-based system has great potential in providing a close-loop screening capability of the perception, analysis, and even diagnosis without human intervention.

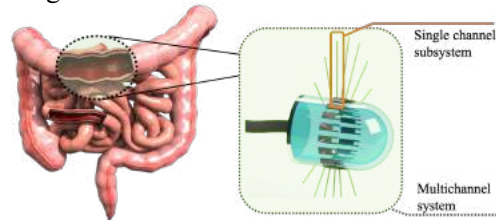


Fig. 1 Conceptual design of the proposed system.

B. Modelling analysis for parameter optimization

Different transduction solutions and movement patterns will contribute to diverse system performance. By modeling analysis, design parameters can be optimized.

As shown in Fig. 2, the artificial whisker can be modeled as a cantilever beam with a free end, which satisfies the Bernoulli-Euler equation according to the mechanics of materials theory[6]. The E and I are Young's modulus of elasticity of the beam material, and the cross-sectional area momentum of inertia, respectively.

Although the analytic solution is difficult to get for this dynamic model, in this paper, a deep learning algorithm was utilized to parameterize this relationship to achieve data interpretation for better diagnosis. Meanwhile, noise control is crucial for detection accuracy.

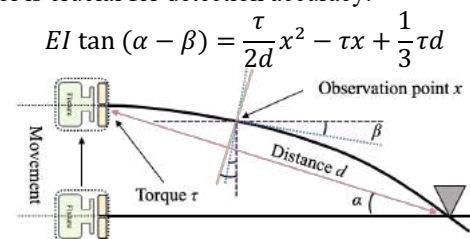


Fig. 2 The cantilever beam like model of the whisker-based system.

C. System implementation

Firstly, a whisker-based sensor is designed for tactile information acquisition. Generally, this kind of sensor

consists of a whisker shaft and a transducer that simulates real skin follicles. Here, a PVDF film is used as a transducer utilizing piezoelectric properties. Its large dynamic range, high electromechanical conversion sensitivity, and stable chemical properties make it an ideal candidate for implantable medicine and in-vivo monitoring. However, the generated signal of the PVDF film is ultra-weak charge variation with an ultra-high output impedance. Hence, a pre-processing circuit, a charge amplifier, is proposed for impedance matching.

Subsequently, the ultra-weak analog voltage signal generated from the proposed sensor is captured and analyzed in the cascade subsystem. As shown in Fig. 3, a signal conditioning circuit is proposed for achieving those purposes. The analog signal is fed into an anti-aliasing circuit for filtering. Afterward, the output signal is routed into an analog-front-end system to complete multi-stage programable amplification, high-precision analog-to-digital conversion, and low-pass filtering processes. In this way, the original deformation signal is converted into a digitalized signal, which is the basis of the high-level interpretation and disease screening. To keep signal accuracy and a wide frequency response range, the gain is adjusted to a moderate value to suppress the noise level. A 24-bits high-precision ADC is integrated to compensate for the limitation of the insufficient gain. The serial peripheral interface (SPI) protocol is utilized for timing control, data/instruction interaction between the microprocessor unit (MCU) and the AFE system.

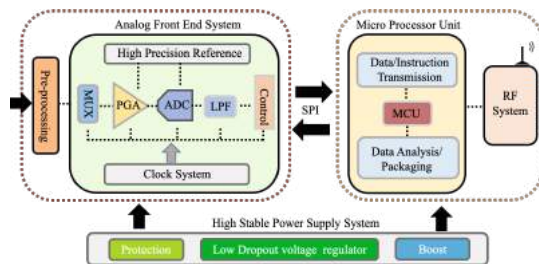


Fig. 3 The structure of the signal conditioning circuit.

RESULTS

To assess the clinical application potentials, a pilot study, abnormal tissue screening, is conducted after exploring the electrical characteristic of the proposed system.

A phantom is used for the abnormal tissue screening task. Three classes were defined, which are normal, cancer, and ulcerative colitis. Although the model is different from a real intestinal track, the different diseases have their own unique common topologies and surface textural changes. Hence, by constructing a large dataset, a fast screen procedure could be achieved theoretically. A deep neural network consisting of 4 layers of 1-dimensional Convolutional Neural Network (CNN), and 1 layer of Long-Short Term Memory (LSTM) structure, is deployed for the classification task. For each class, there are 120 samples, and train data is set as 80 samples, and test data is set to 40 samples.

After iterative training, the test accuracy can reach 100%, showing the great potential of the proposed system as a novel sensing modality for improving clinical disease

screening. In the future, a large-scale database can be built through extensive clinical or preclinical trials, so as to train and deploy artificial intelligence algorithms with enhanced disease detection ability, higher accuracy, and improved robustness, namely, self-learning capability.

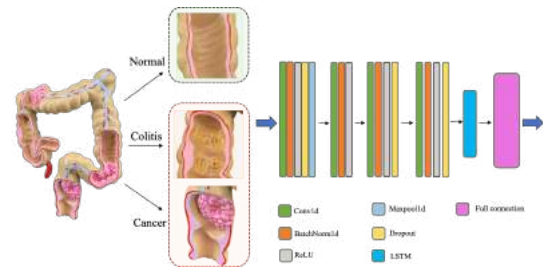


Fig. 4 Experimental setup and structure of the end-to-end algorithm.

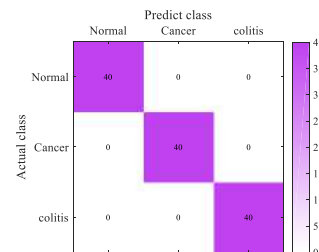


Fig. 5 The confusion matrix of the pilot study.

DISCUSSION

In this paper, a biomimetic whisker-based system with artificial intelligence-enabled self-learning capability is proposed for clinical gastrointestinal diseases screening. In the future, the property of the whisker shaft, and motion speed will be further explored to optimize system performance. Meanwhile, a large-scale database will be built through extensive clinical and preclinical experiments to enhance the robustness of the system.

ACKNOLEGMENT

This work is supported by the Multiscale Medical Robotic Centre, InnoHK, funded by the HK Innovation and Technology Commission.

REFERENCES

- [1] H. L. Hofer and J. A. Bell, "Chapter 3 - Gastrointestinal Diseases," in *Ferrets, Rabbits, and Rodents (Second Edition)*, K. E. Quesenberry and J. W. Carpenter, Eds. Saint Louis: W.B. Saunders, 2004, pp. 25–40.
- [2] G. Berci and K. A. Forde, "History of endoscopy," *Surg Endosc*, vol. 14, no. 1, pp. 5–15, Jan. 2000.
- [3] S. B. Ahn, and C. S. Eun, et.al "The Miss Rate for Colorectal Adenoma Determined by Quality-Adjusted, Back-to-Back Colonoscopies," *Gut Liver*, vol. 6, no. 1, pp. 64–70, Jan. 2012.
- [4] T. de Lange, S. Larsen, and L. Aabakken, "Inter-observer agreement in the assessment of endoscopic findings in ulcerative colitis," *BMC Gastroenterol*, vol. 4, p. 9, May 2004.
- [5] J. H. Solomon and M. J. Hartmann, "Robotic whiskers used to sense features," *Nature*, vol. 443, no. 7111, Art. no. 7111, Oct. 2006.
- [6] L.-W. Cai, *Fundamentals of Mechanical Vibrations*. John Wiley & Sons, 2016.

Vision-based Robot Localisation for Ductoscopic Navigation

Rema Daher¹, Connah Kendrick², Moi Hoon Yap²,
Daniel Leff¹, and Stamatia Giannarou¹

¹*Department of Surgery and Cancer, Imperial College London*

²*Department of Computing and Mathematics, Manchester Metropolitan University
stamatia.giannarou,d.leff@imperial.ac.uk*

INTRODUCTION

Earlier detection of small invasive and non-invasive cancers such as ductal carcinoma in-situ could be achieved through systematic interrogation of the mammary duct network. Conventional ductoscopy has failed to penetrate practice because current platforms are unwieldy, inflexible, and cannot safely, swiftly and smoothly navigate down the complex tree-like structure of mammary ducts. Moreover, poor quality views with white light endoscopic visualisation within 1mm ducts hinders cancer exclusion, hence the reported low specificity [1]. Recently, the "MAMMOBOT" has been developed, which is a flexible steerable endoscopic robotic system that can safely navigate mammary ducts [2].

Ductoscopic navigation through mammary duct trees can be challenging due to the small field-of-view (FOV), coupled with the paucity of salient duct luminal features. Furthermore, tissue deformation and the complexity of the ductal tree anatomy make navigation disorientating, even for experienced operators. Intraoperative localisation and guidance are therefore essential for thoroughly examining ductal trees, targeting and retargeting pathological sites and deploying sensing probes in-vivo while keeping optimal tissue contact.

Navigation systems based on electromagnetic (EM) tracking and image registration have been extensively investigated to assist camera localisation during endoscopic examinations. EM-based systems require additional equipment in the clinical setup and are sensitive to sensor calibration, field distortion and tissue deformation [3]. Image registration systems localise the camera by maximising the similarity between the endoscopic image and a virtual camera view created using a patient specific computer tomography (CT) model [4], [5]. Thus far, the endoscopic navigation methods have focused on bronchoscopic examinations.

This paper presents a vision-based navigation framework for robot localisation during ductoscopic examinations. A 3D model of the mammary duct tree was created by a CT scan of a custom-made phantom. Camera localisation is achieved by matching ductoscopic views with virtual views from the CT model.

MATERIALS AND METHODS

A. Mammary duct tree model

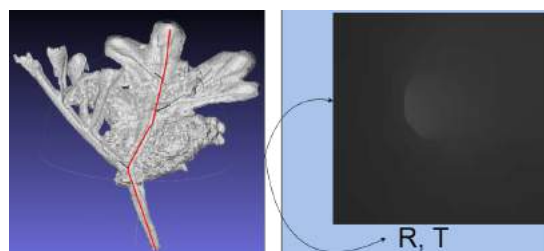


Fig. 1 Visualisation of virtual camera inside a CT model.

A bespoke breast phantom with realistic ductal pathways was created. For this purpose, the 3D model of the internal structures of a female adult's breast was used and a life-size branch of the ductal tree was 3D printed to be used for reference. The ductal tree branch of our phantom was then created by sculpting a magnified version of the 3D printed branch. The sculpted branch was used as a mould to create the ductal branch of 2–3 mm diameter, with shore 2A platinum silicone.

The CT images of the phantom were used by the MiTiSegmenter program [6] that reconstructs 3D structures from CT image with high accuracy. From this a virtual camera fly through of ductal structures was performed, using Unity. The camera's FOV was set to 60 degrees with a minimum and maximum clipping distance of 0.1 and infinity, respectively. Due to working in a virtual environment and unity limitations with working with such small details, we scale the 3D model to generate a smooth flight path. During the fly through, we used shader enabled z-pass to acquire depth images of the ductal structure. Each depth frame stores the camera's location and rotation as shown in Fig. 1.

B. Vision-based camera localisation

To assist robot navigation during endoscopic examinations of the mammary duct tree, the camera is localised by matching ductoscopic images with virtual camera views generated from the 3D model described above. Since camera localisation methods based on depth information has proven to be more robust to illumination variations when compared to methods relying on intensity or gradient information, in our work, depth maps

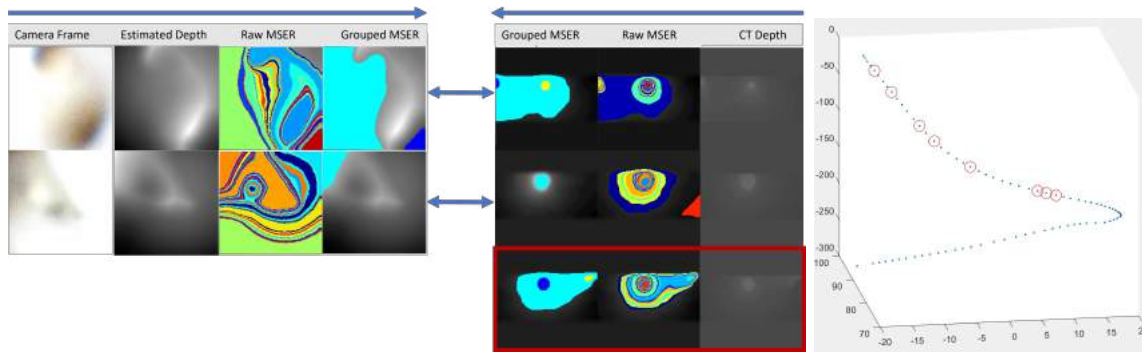


Fig. 2 (Left) Bifurcation localization correspondence results. (Right) Localization path output.

are generated and used to extract geometric features that represent the structure of the mammary duct tree.

Depth is estimated from the ductoscopic images using the Shape from Shading method in [7] for depth recovery of endoscopic data. Then, geometric features are extracted from the depth maps of the ductoscopic data and the depth maps generated from the 3D model using the Maximally Stable Extremal Region Detector (MSER). More specifically, bifurcations are detected and their number, shape, size and spatial association are used to represent parts of the ductal tree [4].

The camera state is defined by the distance of the camera location from the entry point along the path, the rotation with respect to the initial orientation of the virtual camera along the path, and the pathway branch where the camera is located. Camera localisation is achieved by estimating the state of the virtual camera which gives the view with the highest similarity to the ductoscopic video frame. Particle swarm optimisation is applied to minimise the matching cost for continuous tracking.

RESULTS

To enable navigation inside the narrow mammary ducts, in our work the Optivu Micro Modular Flexible Forward View fiberscope (Optimax Ltd) of 0.5mm diameter was used to capture ductoscopic data of our breast phantom.

A path through the phantom was selected as shown in Fig. 1 in red. In Fig. 2 (left), two ductoscopic video frames with bifurcations are shown together with their estimated depth maps and extracted geometric features. As it can be observed, the first bifurcation was successfully identified and corresponded to the correct virtual view from the 3D model, shown on the first row of the CT data. For the second bifurcation, the correspondence was one frame apart, meaning that virtual CT frame n was chosen instead of $n - 1$, which is shown in the red box in Fig. 2. This is mainly due to the region filtering which over-suppressed the extracted regions due to the low quality of the ductoscopic data. In Fig. 2 (right), the virtual camera path is shown in blue and the estimated camera poses using our localization method are shown as red circles along the path.

A limitation of our work was the Rigidity of the fiberscope, making manual movement of the phantom

necessary for the camera to see the bifurcations, which corrupted the EM data. Thus, the virtual camera path instead of the EM data was shown in red in Fig. 2 (right).

These results show that the proposed method can successfully localise the camera inside our breast phantom despite the low quality of the captured ductoscopic data and the presence of significant specular highlights.

DISCUSSION

In this paper, we have presented a robot localisation framework to assist ductoscopic navigation through the mammary duct tree. Our framework has been validated on phantom data and the results verify its good performance in the mammary duct tree under challenging conditions such as, low video data quality and specular highlights. The end goal is to incorporate the proposed navigation approach into MAMMOBOT, an integrated platform for a millimetre-scale growing robot with navigation and tissue characterisation capabilities.

ACKNOWLEDGEMENT

This work is supported by the Cancer Research UK Early Detection Committee - Innovation Award (C52190/A30051).

REFERENCES

- [1] L. Waaijer, J. Simons, I. Borel Rinkes, P. Van Diest, H. Verkooijen, and A. Witkamp, "Systematic review and meta-analysis of the diagnostic accuracy of ductoscopy in patients with pathological nipple discharge," *Journal of British Surgery*, vol. 103, no. 6, pp. 632–643, 2016.
- [2] P. Berthet-Rayne, S. H. Sadati, G. Petrou, N. Patel, S. Giannarou, D. R. Leff, and C. Bergeles, "Mammobot: A miniature steerable soft growing robot for early breast cancer detection," *IEEE Robotics and Automation Letters*, vol. 6, no. 3, pp. 5056–5063, 2021.
- [3] X. Luo, K. Mori, and T. M. Peters, "Advanced endoscopic navigation: surgical big data, methodology, and applications," *Annual review of biomedical engineering*, vol. 20, pp. 221–251, 2018.
- [4] M. Shen, S. Giannarou, P. L. Shah, and G.-Z. Yang, "Branch: Bifurcation recognition for airway navigation based on structural characteristics," in *International Conference on Medical Image Computing and Computer-Assisted Intervention*. Springer, 2017, pp. 182–189.
- [5] M. Shen, Y. Gu, N. Liu, and G.-Z. Yang, "Context-aware depth and pose estimation for bronchoscopic navigation," *IEEE Robotics and Automation Letters*, vol. 4, no. 2, pp. 732–739, 2019.
- [6] "https://github.com/connahkendrickmmu/mitisegmenter."
- [7] M. Visentini-Scarzanella, D. Stoyanov, and G.-Z. Yang, "Metric depth recovery from monocular images using shape-from-shading and specularities," in *2012 19th IEEE International Conference on Image Processing*, 2012, pp. 25–28.

A Mixed Reality System for Human Teleoperation in Tele-Ultrasound

D. G. Black¹ and S. E. Salcudean¹

¹*Robotics and Control Lab, University of British Columbia
dgblack@ece.ubc.ca*

INTRODUCTION

Many applications including telemedicine, manufacturing, and maintenance profit from remote guidance. Existing approaches to tele-ultrasound (US) include robotic teleoperation as well as multimedia applications that combine verbal and graphical guidance. Robotic US systems can provide high precision, low latency, and haptic feedback [1][2][3]. One system has demonstrated clinical utility in trials [4], and much recent work has focused on autonomous robotic US [5]. However, the issues of safe human-robot interaction and guaranteed robust autonomy remain difficult, especially from a regulatory perspective. Further limitations include restricted workspaces, time consuming set-up, large physical size that prevents use in ambulances, and cost, especially compared to inexpensive US systems.

Conversely, systems sold by Clarius Mobile Health Corp. and Butterfly Network use a wireless US probe with images and video conferencing available via a cloud interface on a mobile phone application. Though inexpensive and flexible, the desired probe pose and force are given verbally or with some overlays of arrows or pointers on the US image, which is very inefficient, leading to high latency and low precision.

We present a novel concept of “Human Teleoperation” through mixed reality which bridges the gap between these two methods. In this control framework, the human follower is controlled as a flexible, cognitive robot such that both the input and the actuation are carried out by people, but with near robot-like latency and precision. This allows teleguidance that is more precise, intuitive, and low latency than verbal guidance, yet more flexible, inexpensive, and accessible than robotic teleoperation. This short paper summarizes the concepts and introduces a new design of the communication system to use a secure, high-speed, network-agnostic WebRTC interface. More details and results can be found in [6].

MATERIALS AND METHODS

The tele-US system consists of the follower side and the expert side, which communicate wirelessly over the Internet. The follower wears a mixed reality (MR) headset (HoloLens 2 in our implementation) which projects a virtual US transducer into the follower’s scene. The expert controls the virtual probe using a haptic controller (Phantom Desktop, 3D Systems, Inc.) to input the desired pose and force. The follower tracks the



Fig. 1 The teleoperation concept. Frames 1-3: follower matches the virtual probe precisely, starting in a random pose. Frame 4: the expert moves the virtual probe, and the real one quickly tracks the motion.

virtual probe with his/her real probe, as seen in Fig. 1. Thus the expert, in real time, receives the US images, a video stream of the patient with the virtual and real probes in position (called an MR capture), and is in verbal communication with the follower. Additionally, the follower can send a spatial mesh of the patient, generated by the HoloLens 2, to the expert. The mesh is rendered haptically as a virtual fixture for the Phantom Desktop, giving the expert the sensation that they are physically interacting with the tissue. This spatial mapping also provides the expert-to-follower coordinate transform. The system is shown in Fig. 2.

The effectiveness of the approach was demonstrated first using a WebSocket server and Robot Operating System (ROS) on a local wireless network (WLAN). Refer to [6] for details. We measured the data latencies, the actual end-to-end teleoperation latency, and the positional precision. Additionally, two procedures were carried out on two patients each to compare Human Teleoperation to verbal guidance and to direct US by the expert. These procedures involved quantitative endpoints so the numerical measurements (inferior vena cava diameter and kidney length) could be compared between methods. However, the US images, video feed, and spatial meshes require a large bandwidth while haptic feedback and MR teleoperation necessitate very low latencies for stable and transparent teleoperation. A Web Real Time Communication (RTC)-based system is more suitable to meet these requirements and support tele-US at large distances. This framework provides a direct peer-to-

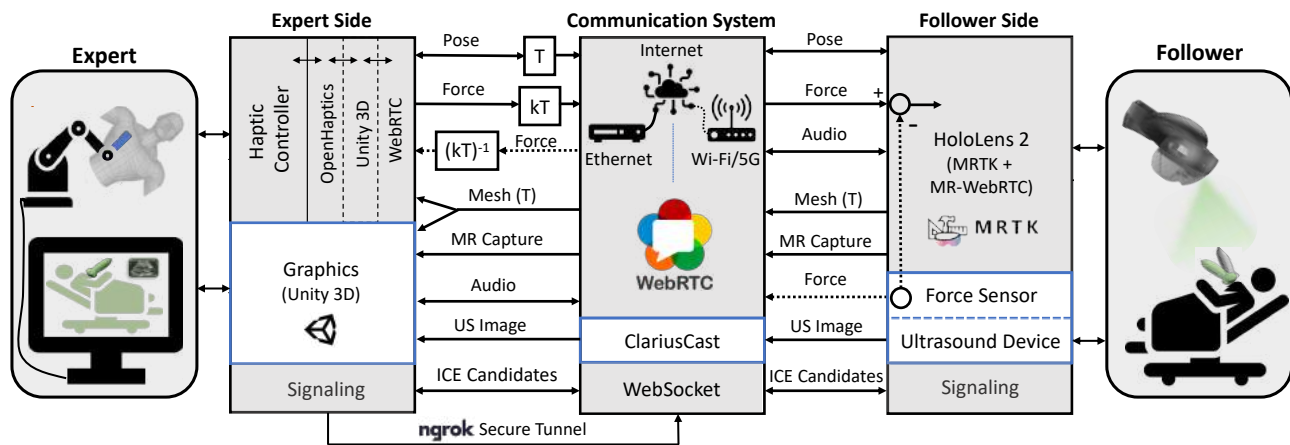


Fig. 2 System Architecture. k is a scaling factor for the force while T is the transform from expert to follower coordinates, obtained from the mesh. The force feedback (dotted lines) has not yet been implemented.

peer connection over UDP between the expert and follower, thus removing server-related delays. Any dropped packets are quickly replaced with new information, and local consistency checks are in place, so the higher speeds of UDP are preferable to the reliability of TCP. An implementation of this system is in place, and in collaboration with Rogers Communications, a Canadian telecommunications company, the communication is set up to run over the 5G radio access network (RAN). The 5G network holds promise for achieving the required bandwidth and latency, and this will be tested using the sub-6GHz and mm-wave bands. Latency results from initial tests with WebRTC are presented for comparison to the WebSocket-based communication.

RESULTS

Our latency tests on the WebSocket implementation showed on average 11.4 ms delay for pose and force transmission. In contrast, the preliminary WebRTC implementation has delays of only 5.4 ms on average for the same local network and it can run over the Internet. In addition, the latency of the MR capture over WebRTC is 160ms whereas with Windows Device Portal it was found to be ≥ 4 seconds, and with ROS it was infeasibly slow. The mean end-to-end teleoperation latency was measured through two trials to be 270 ms, with mean error in pose tracking of 7 mm and 6° .

While no patient tests have yet been carried out with the WebRTC implementation, our WebSocket results show average time taken to complete the procedures to be 65 seconds for direct US, 214 seconds for verbal guidance, and 73 seconds for Human Teleoperation. The average measurement error compared to direct US was 6 mm for verbal guidance and 3 mm for Human Teleoperation.

DISCUSSION

The teleoperation latency is greater than that of any of the data channels individually because it is limited by the response time of the human follower. However, the latency of 270 ms is permissible even for haptic feedback without greatly degrading the user experience.

Additionally, the new WebRTC implementation is shown to be much faster and more appropriate for teleultrasound at large distances. The effectiveness of the concept is shown most clearly in the patient tests, where it greatly outperformed verbal teleguidance in efficiency and precision. These tests were preliminary and had a small sample size, but nonetheless revealed a clear difference between methods. No quantitative comparison to robotic teleoperation has yet been made, but the benefits of this system compared to robotics lie in cost, ease of deployment, acceptance in communities, and flexibility.

Ongoing and future work includes utilizing 5G to perform remote tests, exploring how to improve the human-computer interaction, and investigating reinforcement learning for autonomous US guidance. We also plan on integrating force sensing on an US probe to allow the study of stable and transparent force reflection in bilateral teleoperation under time delays imposed by the human response time.

REFERENCES

- [1] S. E. Salcudean, G. Bell, S. Bachmann, W.-H. Zhu, P. Abolmaesumi, and P. D. Lawrence, "Robot-assisted diagnostic ultrasound—design and feasibility experiments," in *International Conference on Medical Image Computing and Computer-Assisted Intervention*. Springer, 1999, pp. 1062–1071.
- [2] M. Akbari, J. Carriere, T. Meyer, R. Sloboda, S. Husain, N. Usmani, and M. Tavakoli, "Robotic ultrasound scanning with real-time image-based force adjustment: Quick response for enabling physical distancing during the covid-19 pandemic," *Frontiers in Robotics and AI*, vol. 8, 2021.
- [3] C. Delgorgue, F. Courrèges, L. A. Bassit, C. Novales, C. Rosenberger, N. Smith-Guerin, C. Brù, R. Gilbert, M. Vannoni, G. Poisson *et al.*, "A tele-operated mobile ultrasound scanner using a light-weight robot," *IEEE transactions on information technology in biomedicine*, vol. 9, no. 1, pp. 50–58, 2005.
- [4] P. Vieyres, G. Poisson, and *et al.*, "A tele-operated robotic system for mobile tele-echography: The otelo project," in *M-health*. Springer, 2006, pp. 461–473.
- [5] S. Wang, J. Housden, Y. Noh, D. Singh, and A. Singh, "Robotic-assisted ultrasound for fetal imaging: Evolution from single-arm to dual-arm system," in *Annual Conference Towards Autonomous Robotic Systems*, vol. 11650, July 2019, pp. 27–38.
- [6] D. Black, Y. O. Yazdi, A. H. H. Hosseinabadi, and S. Salcudean, "Human teleoperation - a haptically enabled mixed reality system for teleultrasound," *TechRxiv*, /08/19 2021.

Collaborative Robotic Ultrasound Tissue Scanning for Surgical Resection Guidance in Neurosurgery

Alistair Weld*¹, Michael Dyck*^{2,3}, Julian Klodmann², Giulio Anichini⁴, Luke Dixon⁴, Sophie Camp⁴, Alin Albu-Schäffer^{2,3}, and Stamatia Giannarou¹

¹ *Hamlyn Centre for Robotic Surgery, Imperial College London,*

² *Institute of Robotics and Mechatronics, German Aerospace Center,*

³ *Department of Informatics, Technical University of Munich,*

⁴ *Department of Neurosurgery, Charing Cross Hospital, Imperial College London, UK*
a.weld20@imperial.ac.uk, michael.dyck@dlr.de

INTRODUCTION

The main goal of surgical oncology is to achieve complete resection of cancerous tissue with minimal iatrogenic injury to the adjacent healthy structures. Brain tumour surgery is particularly demanding due to the eloquence of the tissue involved. There is evidence that increasing the extent of tumour resection substantially improves overall and progression-free survival. Realtime intraoperative tools which inform of residual disease are invaluable. Intraoperative Ultrasound (iUS) has been established as an efficient tool for tissue characterisation during brain tumour resection in neurosurgery [1].

The integration of iUS into the operating theatre is characterised by significant challenges related to the interpretation and quality of the US data. The capturing of high-quality US images requires substantial experience and visuo-tactile skills during manual operation. Recently, robotically-controlled US scanning systems have been proposed (see e.g. [2]) but the scanning of brain tissue poses major challenges to robotic systems because of the safety-critical nature of the procedure, the very low and precise contact forces required, the narrow access space and the large variety of tissue properties (hard skull, soft brain structure).

The aim of this paper is to introduce a robotic platform for autonomous iUS tissue scanning to optimise intraoperative diagnosis and improve surgical resection during robot-assisted operations. To guide anatomy specific robotic scanning and generate a representation of the robot task space, fast and accurate techniques for the recovery of 3D morphological structures of the surgical cavity are developed. The prototypic DLR MIRO surgi-

cal robotic arm [3] is used to control the applied force and the in-plane motion of the US transducer. A key application of the proposed platform is the scanning of brain tissue to guide tumour resection.

MATERIALS AND METHODS

Intraoperative Surgical Navigation. The 3D reconstruction of surgical scenes is uniquely challenging due to textureless surfaces, occlusions, specular highlights and tissue deformation. To deal with these challenges, we develop a novel deep learning approach that utilises stereo vision for geometric focused depth estimation. Our method advances conventional 3D reconstruction approaches which are based on the direct regression of depth information, by developing a neural network which learns to replicate the behaviour of a structured light projector. Geometric awareness is enforced through the learning of the reflection of light off surfaces.

A Unet architecture has been designed to take a stereo image as input and to predict how the projected structured light should appear on the surfaces on the left and right images, separately. Specifically, we are predicting binary code structured light, which consists of vertical bars of white and black colour. To predict these binary patterns, we purpose our neural network to be a Sigmoid binary classifier. So the neural network should be predicting whether or not a pixel should have a value of 1 or 0, where white corresponds to the value 1 and black to the 0. These predicted binary codes can then be processed into disparity or depth maps, using 2D cross correlation over the epipolar lines of the stereo images.

Collaborative Robotic Tissue Scanning. To fulfil the safety critical requirements of robotic iUS scanning and to cope with the low stiffness of brain tissue we develop an impedance controller using task-specific coordinates defined with respect to the surface of the anatomy of interest. The recovered 3D morphological structure is utilised to represent the anatomical surface

*These authors contributed equally to the work. This project was supported by UK Research and Innovation (UKRI) Centre for Doctoral Training in AI for Healthcare (EP/S023283/1), the Royal Society (URF\R\2 01014), the NIHR Imperial Biomedical Research Centre and the International Graduate School of Science and Engineering (IGSSE); TUM Graduate School

as a triangular mesh. We define the task coordinates as the orientation of the US probe axis to coincide with the surface normal and its distance d to the surface. Controlling this distance allows us to realise different scenarios of probe-tissue interaction, such as contact avoidance with a safety margin for re-scanning and updating the 3D structure of the tissue surface, contact establishment, or interaction with a desired contact force. We obtain a planar representation of the anatomical surface, described by 2D (u, v) -coordinates. Scanning trajectories along the surface can be planned in 2D and automatically executed. The (u, v) -coordinates with zero impedance allows the clinician to move along the surface, while the controller is taking care of probe orientation and contact forces.

Controlling the robot at different distances to the tissue implicitly creates a foliation of the Cartesian space, parallel surfaces, obtained by shifting the original tissue surface along its normal direction. We define the planar (u, v) -coordinates in a novel way that allows for consistent impedance control along and in-between all leaves of the foliation. This novel concept allows to control and continuously adapt desired interaction forces between US probe and tissue, capable of safe US scanning on tissues as soft as the human brain. Due to the use of the unified impedance control framework in [4], passivity and stability are guaranteed.

RESULTS

Due to the lack of publicly available datasets containing binary code structured light patterns, our proposed model has been trained and tested on simulated data of real objects, created with VisionBlender [5]. Results so far have shown successful depth estimation, without requiring training on depth ground truth. The validation mean absolute error was 1.4 pixels , where the mean ground truth disparity of the objects is 16.1 pixels . Early comparison to direct depth regressing networks, has indicated to an improved robustness to pixel perturbation (brightness and contrast) by up to 50% , using our technique. Our model will be further validated on a dataset which we are currently developing with images of ex vivo and medical phantoms as shown in Fig. 1. Fig. 2 shows the performance of the developed impedance controller in a realistic simulation, tracking a trajectory along a discretised surface patch ($d = 0$, establish contact), a positive leaf ($d > 0$, avoid contact) and negative leaf ($d < 0$, apply a particular force), with the corresponding control errors (e_u , e_v , e_d). We demonstrate consistency of the planar (u, v) -coordinates and accurate tracking behaviour along all leaves, with a root mean squared error (RMSE) in the controlled distance of $RMSE_d = 0.369 \text{ mm}$. The higher errors in u most likely arise from dynamic coupling and lack of feedforward control terms in the presented experiment.

DISCUSSION

In this paper, we have presented a robotic platform for iUS tissue scanning which will optimise diagno-

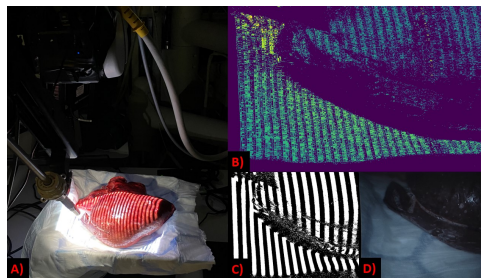


Fig. 1 A) camera, projector setup with sheep's kidney B) generated depth map C) binarised structured light pattern D) laproscopy image.

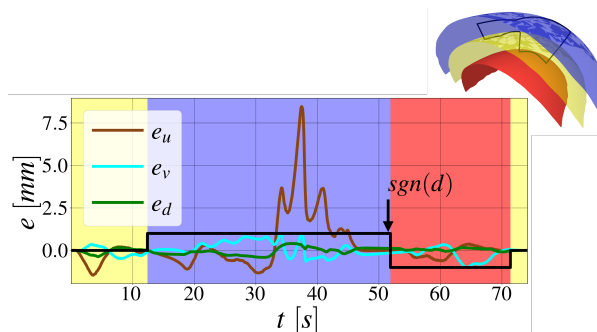


Fig. 2 Error e in (u, v) -coordinates, distance d for trajectory (upper right) along tissue surface (yellow, $d_{des} = 0 \text{ mm}$), positive leaf (blue, $d_{des} = 50 \text{ mm}$) and negative leaf (red, $d_{des} = -50 \text{ mm}$). The black graph depicts the signum function of the desired distance d , where $sgn(d) = \pm 1$ corresponds to $d_{des} = \pm 50 \text{ mm}$, respectively.

sis with the aim of improving both the efficacy and safety of tumour resection. The development of the above technologies will have a significant impact on the surgeon's sensing, completeness and safety during tumour resection and ultimately on the management of the patient. Our future work will focus on further improving the control, as well as validating the proposed visual servoing setup on ex vivo and medical phantoms.

REFERENCES

- [1] R. Sastry et al., "Applications of ultrasound in the resection of brain tumors," *Journal of Neuroimaging*, vol. 27, no. 1, 2016.
- [2] F. von Haxthausen, S. Böttger, D. Wulff, J. Hagenah, V. García-Vázquez, and S. Ipsen, "Medical robotics for ultrasound imaging: current systems and future trends," *Current Robotics Reports*, vol. 2, no. 1, pp. 55–71, 2021.
- [3] U. Seibold, B. Kübler, T. Bahls, R. Haslinger, and F. Steidle, "The dlr mirosurge surgical robotic demonstrator," ser. The Encyclopedia of Medical Robotics, J. P. Desai and R. V. Patel, Eds. WORLD SCIENTIFIC, October 2018, vol. 1, pp. 111–142. [Online]. Available: <https://elib.dlr.de/131078/>
- [4] A. Albu-Schäffer, C. Ott, and G. Hirzinger, "A unified passivity-based control framework for position, torque and impedance control of flexible joint robots," *The international journal of robotics research*, vol. 26, no. 1, pp. 23–39, 2007.
- [5] J. Cartucho, S. Tukra, Y. Li, D. S. Elson, and S. Giannarou, "Visionblender: a tool to efficiently generate computer vision datasets for robotic surgery," *Computer Methods in Biomechanics and Biomedical Engineering: Imaging & Visualization*, vol. 9, pp. 331 – 338, 2021.

Head-mounting Surgical Robots for Passive Motion Compensation

Nicholas R. Posselli¹, Paul S. Bernstein², and Jake J. Abbott¹

¹*Dept. of Mechanical Engineering and Robotics Center, University of Utah*

²*Dept. of Ophthalmology and Visual Sciences, Moran Eye Center, University of Utah*
nicholas.posselli@utah.edu, paul.bernstein@hsc.utah.edu, jake.abbott@utah.edu

INTRODUCTION

Many up-and-coming therapeutic protocols in ophthalmology are technically difficult, near/beyond the limits of human ability, and are being attempted by only a few surgeons. For example, subretinal injection of stem cells or gene therapies requires placement of a fine cannula in the subretinal space, holding that position steady for ~90 s to inject a bleb of fluid. Surgeon hand tremor places a limit on achievable precision. A wide variety of robot-assisted surgical systems have been proposed to improve the precision of eye surgery [1]. However, there has not been much consideration of patient head motion, which is common among patients undergoing eye surgery under monitored anesthesia, a.k.a. conscious sedation, which makes a patient calm and somewhat sleepy during a surgery, but the patient may still be awake. Head motion in this state is due to breathing, talking, snoring, and other (in)voluntary motions of the patient. Of the 16% of patients who snore under monitored anesthesia, half have sudden head movement during surgery [2]. Movement must be compensated by the surgeon, to the best of their ability, to avoid complications. Benchtop experiments with artificial or enucleated (i.e., *ex vivo*) eyes, which are typical in the development of robotic systems, do not capture the effect of patient motion. Limited *in vivo* studies in humans have placed the patient under general anesthesia [3], [4], which is not typical of eye surgery and results in reduced patient movement (the patient is still breathing, of course). Any clinical robotic system must deal with patient motion. Active compensation (i.e., closed-loop control) can involve sensing the force between the surgical instrument and the eye, or using visual-servoing techniques, or some combination of both [1].

Two groups (including ours) have developed compact telerobotic systems motivated by the prospect of mounting the robot directly to the patient's head to passively compensate for patient motion [5], [6]. However, to date, neither has actually mounted their robot on a living human, let alone quantify the benefits of head mounting. Mounting a robot to a patient's head is not

Research reported in this publication was supported by the National Eye Institute of the National Institutes of Health under Award Number R21EY027528. The content is solely the responsibility of the authors and does not necessarily represent the official views of the National Institutes of Health.



Fig. 1 Radiotherapy immobilization system modified to enable surgical robots to be quick-connected magnetically through a standard surgical draping (not shown). System shown fitted with one robot and counterweights for balance. (Inset) In this study, tracking markers placed on the robot and goggles are used to quantify the displacement of the robot relative to the goggles (i.e., the eye) due to breathing/snoring motion of the wearer.

a trivial task. The only way to rigidly mount a robot to a patient's head would be to drill into the skull, which is very invasive compared to current eye surgery. With alternative methods, the soft tissue surrounding the skull makes a truly rigid connection essentially impossible. In [5], the authors proposed a mechanism that would allow their manipulator to be pressed against the patient's face to form a semi-rigid connection. In a more recent work, they proposed a mechanism that would semi-rigidly fix the patient's head with respect to the surgical bed, using granular jamming, and then the robot would be mounted on that head-fixation system [7]. An alternate strategy is to mount directly to the patient's eye, but thus far this has been limited to one-degree-of-freedom robots [8]. In this paper, we introduce a noninvasive head-mounting concept, based on a modified radiotherapy immobilization system, which enables one or more robots to be mounted semi-rigidly to a patient's head (Fig. 1), and we perform an experiment that highlights the potential benefits of this form of head mounting.

MATERIALS AND METHODS

We modified a CIVCO Solstat Immobilization System with a U-shaped 8-mm-thick aluminum mounting plate to enable one or more surgical robots to be mounted with high stiffness at the connection (Fig. 1). We modified the



Fig. 2 Control conditions: (C1) Head resting on pillow; (C2) Strap holding head tightly on pillow.

Solstat's quick-release clips, which attach the custom-fit thermoplastic face mask, to accommodate the additional thickness of the plate. The Solstat's masks are already compatible with the standard surgical draping. On/off magnets in the aluminum plate enable the robot(s) to be attached after the draping is applied. We removed the Solstat's component used to rigidly attach it to a table (during radiotherapy), enabling it to fit on a Stryker stretcher pillow. The weight of the robot(s) is carried by the Solstat, not felt by the wearer. Since we only used one robot (which is a modification of [6]), counterweights were used to eliminate an applied moment.

We performed an experiment to quantify eye movement relative to a static world frame (i.e., the Leica ophthalmic microscope) in three conditions—the head resting on the pillow (C1), the head strapped down to the pillow (C2), and wearing our head-mounting device on the pillow (C3)—and in the final condition, to quantify the movement of the head-mounted robot relative to the eye (C4). C1 and C2 (Fig. 2) represent cases where a surgical robot would be mounted to the bed or bedside table. The position of the eye was tracked using a Sony PMW-10MD camera recording video through the lens of the microscope, using a colored marker attached to swim goggles that are effectively rigidly connected to the skull due to their tight fit in the eye sockets (Fig. 1); the robot was similarly tracked in C4. For each condition, video was recorded for 11 inhale-exhale cycles (i.e., trials), each starting fully exhaled, for gentle (but not shallow) breathing and for deep snoring-like rapid inhalations. The wearer kept his body otherwise still and relaxed. The markers were localized in the images during post-processing. Scale bars of known length on the markers were used to determine the conversion from pixels to millimeters, with the assumption that the markers primarily moved in a horizontal plane. The 2D vector displacement relative to the initial condition was recorded, and converted to a scalar magnitude.

RESULTS

Figure 3 shows peak movement of the goggles relative to the world frame (and thus the eye relative to a hypothetical bed/table mounted robot) was as high as 2.2 mm for gentle breathing and 5.2 mm during snoring-like movements with the control conditions; the head strap was ineffective at mitigating these relatively small motions. The largest movement of our head-mounted

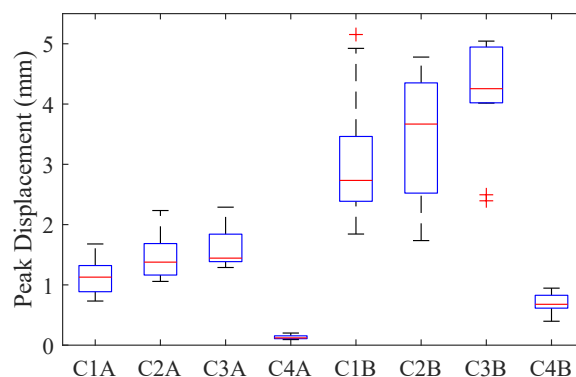


Fig. 3 Box-whisker plots ($N = 11$) of peak displacement of goggles with head resting on pillow (C1), head strapped to pillow (C2), and when using the head-mounting system (C3), as well as the head-mounted robot relative to the goggles (C4), for gentle breathing (A) and deep snoring-like rapid inhalation (B).

robot relative to the goggles (and thus to the eye) was 0.2 mm for gentle breathing and 0.9 mm for snoring-like movements. Analysis of variance, using a Bonferroni correction, indicates that these differences are significant ($p < 0.001$) for both types of movement. Our head-mounting device itself did not reduce patient motion.

DISCUSSION

These results highlight the potential for head-mounting teleoperated surgical robots to provide substantial passive motion compensation for improved precision and patient safety. In our experiments, no instruments were inserted in the eye, which would further stabilize the eye and reduce relative motion. Also, we rested the head-mounting device on the pillow, which may not be optimal. Finally, passive compensation should be viewed as complementary to active compensation.

REFERENCES

- [1] E. Vander Poorten *et al.*, "Robotic retinal surgery," in *Handbook of Robotic and Image-Guided Surgery*, M. H. Abedin-Nasab, Ed. Elsevier, 2019, ch. 36, pp. 627–672.
- [2] C. A. McCannel *et al.*, "Snoring is associated with unexpected patient head movement during monitored anesthesia care vitreoretinal surgery," *Retina*, vol. 32, no. 7, pp. 1324–1327, 2012.
- [3] T. L. Edwards *et al.*, "First-in-human study of the safety and viability of intraocular robotic surgery," *Nat. Biomed. Eng.*, vol. 2, p. 649–656, 2018.
- [4] A. Gijbels *et al.*, "In-human robot-assisted retinal vein cannulation, a world first," *Ann. Biomed. Eng.*, vol. 46, p. 1676–1685, 2018.
- [5] M. A. Nasser *et al.*, "The introduction of a new robot for assistance in ophthalmic surgery," in *Proc. Int. Conf. IEEE Eng. Med. Biol. Soc.*, 2013, pp. 5682–5685.
- [6] M. Nambi *et al.*, "A compact telemanipulated retinal-surgery system that uses commercially available instruments with a quick-change adapter," *J. Med. Robot. Res.*, vol. 1, no. 2, p. 1630001, 2016.
- [7] M. A. Nasser *et al.*, "A targeted drug delivery platform for assisting retinal surgeons for treating age-related macular degeneration (AMD)," in *Proc. Int. Conf. IEEE Eng. Med. Biol. Soc.*, 2017, pp. 4333–4338.
- [8] S. Guo *et al.*, "Demonstration of optical coherence tomography guided big bubble technique for deep anterior lamellar keratoplasty (DALK)," *Sensors*, vol. 20, no. 2, p. 428, 2020.

Towards an MRI-Conditional Robot for Intracerebral Hemorrhage Evacuation

A.L. Gunderman¹, S. Sengupta², D. Sigounas³, K. Cleary⁴, Y. Chen¹

¹Department of Biomedical Engineering, Georgia Institute of Technology/Emory University,

²Institute of Imaging Science, Vanderbilt University Medical Center

³George Washington University

⁴Children's National Hospital
agunderman3@gatech.edu

INTRODUCTION

Stroke is the second leading cause of death worldwide, causing over six million deaths in 2019 [1]. Intracerebral hemorrhage (ICH), a subcategory of hemorrhagic strokes, accounts for 20% of total stroke deaths, with a one year mortality rate as high as 65% [2]. Forty percent of these deaths occur within two days of symptom onset [2], suggesting a benefit to early hemorrhage evacuation following clinical decompensation [3]. Despite the need for urgency, “watchful waiting” or conservative management has been a common treatment modality due to the potential cortical disruption and brain shift associated with large craniotomies [3]. However, in recent years, minimally invasive surgery has proven to be a safer alternative to larger, open craniotomies for hemorrhagic clot evacuation [3] and is an increasingly accepted method of treatment for patients with a deep-seated hematoma 30-50 mL in volume [4]. Unfortunately, minimally invasive methods are complicated by lack of adequate visualization, which is necessary to account for brain shift and deformation during the evacuation procedure.

In recent studies, there has been a push for coupling minimally invasive robotic interventions with different intraprocedural visualization techniques. Using the concentric tube robot (CTR), several groups have used interventional CT [5], endoscopic cameras [6], and interventional MRI [7] to guide minimally invasive neurosurgical procedures. However, each imaging modality comes with corresponding pitfalls. CT applies ionizing radiation to the patient, requiring a cost-benefit balance between dynamic visualization and ionizing radiation exposure. Endoscopic cameras possess a limited field-of-view, preventing full dynamic brain visualization. MRI, though it provides superior imaging quality without a detrimental impact on the patient, is restricted by the inability to use ferromagnetic materials, i.e., magnets, steel, iron, etc., and the reduction in image quality by non-ferromagnetic metals, such as nitinol.

In this paper, we build upon our work in [7], aiming to ameliorate the reduction of imaging quality associated with the use of metallic materials by developing a plastic MRI-compatible robotic system for MRI-guided ICH removal. This paper presents the first use of off-the-shelf plastic tubes for CTR, and characterizes the robot's accuracy, MRI-compatibility, and evacuation feasibility for ICH evacuation in phantom trials.

MATERIALS AND METHODS

Our robotic system is a frameless stereotactic CTR that consists of three modular components (Fig. 1): (1) a three degree of freedom concentric tube module (CTM), (2) a universal pneumatic transmission module (PTM), and (3) a custom designed stereotactic frame (SF). The three degree of freedom CTM utilizes a one degree of freedom outer tube stage (translation) and a two degree of freedom inner tube stage (translation and rotation). The CTM is made entirely of plastic (nylon concentric tubes, nylon lead screws, IGUS bearings, and polylactic acid chassis) and carbon fiber (linear guide rails), eliminating MR-imaging distortion. The CTM marries to the PTM through a series of plastic dowel pins, snap-fit latches, and splined transmission shafts. The PTM consists of three pneumatic bi-directional radial inflow turbines, which were modified from our prior work [8] to be reduced in size and parametrically modifiable. These motors are driven by 10-meter pneumatic lines routed through the MRI waveguide, decoupling the ferromagnetic interaction between the compressor and air distribution (valves and electronics) and the MRI. The motors are controlled using an adaptive control algorithm implemented through MATLAB and a DMC-4163 Galil motion controller.

In our envisioned clinical workflow, the SF would be mounted to the skull such that the desired vector between the hematoma and burr hole location is aligned with the robot's insertion vector. The clinician would then drill the burr hole and the patient would be placed in the MRI. After the patient is placed in the MRI bore, the robot would be mounted to the SF from the superior end of the MRI bore and registered to the MRI's coordinate system using rigid body registration with respect to the SF's fiducials. The MRI's workstation would then be used to provide dynamic information

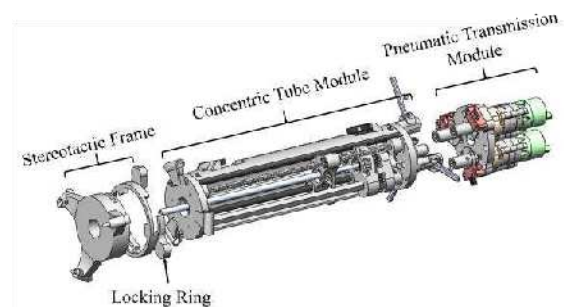


Fig. 1 MRI-compatible ICH concentric tube robot deconstructed into its three separate modules.

about the clot, informing the clinician how to position the robot for optimal clot evacuation.

The robot's tip accuracy and MRI compatibility were validated in 70 cm wide bore, Philips 3 Tesla Ingenia Elition MRI System. Fig. 2A shows the general experimental setup. During the experiment, the phantom is placed in front of the robot with a pair of single loop imaging coils on either side of it. The robot was first localized using MR visible fiducials placed on the SF using scout imaging. Following localization, ten target locations were selected at different depths in a Knox gelatin phantom (Kraft Foods Global, Inc., USA) around the rotational axis of the inner tube (OD/ID: 6/4 mm, curvature 0.05 mm^{-1}) in the MR coordinate system. Inverse kinematics were used to determine the joint space parameters needed to reach the target and the robot was moved to that position. The accuracy was then quantified as the difference between the desired location and the robot's final location.

RESULTS

The robot was able to maintain a tip accuracy of $3.40 \pm 0.48 \text{ mm}$. Fig. 2B shows an example image of the MRI image with the robot at its resulting position calculated by the inverse kinematics (red dot) next to its desired target position (green star).

MRI compatibility was determined by comparing a control image of a bottle phantom without the robot in the MRI bore to an image of the bottle phantom with the robot operating in the MRI bore (Fig. 3). No obvious image artifact, contrast or SNR changes were observed.

DISCUSSION

This paper presented a preliminary study of the first ever MR-compatible plastic tube CTR. The targeting

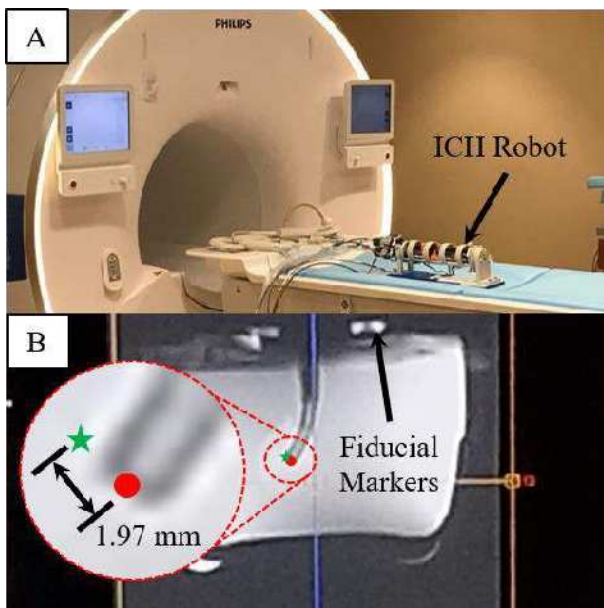


Fig. 2 (A) The robot can be seen placed on the MRI bed prior to accuracy characterization. (B) An example MRI image of the ICH robot inside the phantom with a targeting accuracy of 1.97 mm. The resulting position (red dot) can be seen next to the desired position (green star).

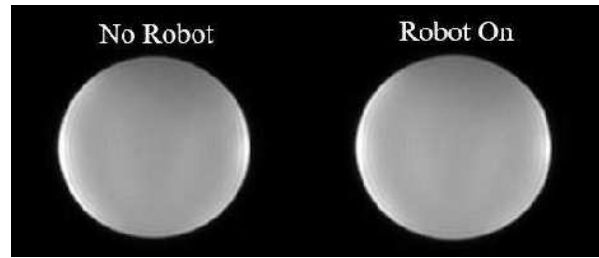


Fig. 3 (A) The resulting images of the phantom bottle imaged by the MRI with (left) no robot in the bore and (right) the robot operating in the bore. No appreciable difference in SNR was observed.

tests validated the accuracy of the robot's inverse kinematics with the primary cause of error to be robot registration. The robot was operable within the MRI without impacting image quality. Additionally, the large inner diameter of the inner tube was able to efficiently evacuate a 15 mL clot volume of water at a vacuum pressure of 20 mmHg in under 2 seconds guided by continuous image guidance, clearly indicating the feasibility of this robot for evacuation.

REFERENCES

- [1] Xiong, Ruochu, Fangye Li, and Xiaolei Chen. "Robot-assisted neurosurgery versus conventional treatment for intracerebral hemorrhage: A systematic review and meta-analysis." *Journal of Clinical Neuroscience* (2020).
- [2] Hannah, Theodore C., Rebecca Kellner, and Christopher P. Kellner. "Minimally Invasive Intracerebral Hemorrhage Evacuation Techniques: A Review." *Diagnostics* 11, no. 3 (2021): 576.
- [3] Zhou, Xinyu, Jianjun Chen, Qi Li, Gaoping Ren, Guoen Yao, Ming Liu, Qiang Dong et al. "Minimally invasive surgery for spontaneous supratentorial intracerebral hemorrhage: a meta-analysis of randomized controlled trials." *Stroke* 43, no. 11 (2012): 2923-2930.
- [4] Wang, Weijun, Ningquan Zhou, and Chao Wang. "Minimally invasive surgery for patients with hypertensive intracerebral hemorrhage with large hematoma volume: a retrospective study." *World neurosurgery* 105 (2017): 348-358.
- [5] I. S. Godage, A. A. Ramirez, R. Wirz, K. D. Weaver, J. Burgner-Kahrs and R. J. Webster, "Robotic intracerebral hemorrhage evacuation: An in-scanner approach with concentric tube robots," 2015 IEEE/RSJ International Conference on Intelligent Robots and Systems (IROS), 2015, pp. 1447-1452, doi: 10.1109/IROS.2015.7353558.
- [6] Bruns, Trevor L., Andria A. Ramirez, Maxwell A. Emerson, Ray A. Lathrop, Arthur W. Mahoney, Hunter B. Gilbert, Cindy L. Liu et al. "A modular, multi-arm concentric tube robot system with application to transnasal surgery for orbital tumors." *The International Journal of Robotics Research* 40, no. 2-3 (2021): 521-533.
- [7] Chen, Yue, Isuru S. Godage, Saikat Sengupta, Cindy Lin Liu, Kyle D. Weaver, and Eric J. Barth. "MR-conditional steerable needle robot for intracerebral hemorrhage removal." *International journal of computer assisted radiology and surgery* 14, no. 1 (2019): 105-115.
- [8] Chen, Yue, Isuru S. Godage, Zion Tsz Ho Tse, Robert J. Webster, and Eric J. Barth. "Characterization and control of a pneumatic motor for MR-conditional robotic applications." *IEEE/ASME Transactions on Mechatronics* 22, no. 6 (2017): 2780-2789.

Bimanual Endoscopic Robot for Neurosurgery

Karl Price¹, Joseph Peine¹, Yash Chitalia¹, Margherita Mencattelli¹, Ashkan Pourkand¹, Thomas Looi², James Drake², Pierre E. Dupont¹

¹Cardiac Surgery, Boston Children's Hospital, Harvard Medical School, Boston, MA USA

²Neurosurgery Department, Sick Kids Hospital, Toronto, Canada

INTRODUCTION

In recent decades, improvements in neurosurgical care have been driven by technological advances such as frameless stereotaxy and endoscopy. Endoscopy enables navigation through the clear fluid-filled ventricular system of the brain instead of through healthy brain tissue enabling minimally invasive treatment of tumors, cysts, hydrocephalus and epileptogenic lesions [1]. Twenty percent of brain tumors lie either adjacent to, or inside, the ventricles, and endoscopy has had a major impact in their treatment leading to reductions in morbidity and procedure time [2].

Despite this progress, significant difficulties remain. A major challenge is that most endoscopes force clinicians to perform one-handed surgery even though many neurosurgical tasks require two hands. For example, one hand can retract healthy tissue while the second removes a lesion.

A second challenge is that existing tools are mounted on straight rigid shafts. This forces the surgeon to pivot the endoscope about the burr hole in the skull to move the tool inside the brain. This pivoting motion can damage healthy brain tissue adjacent to the surgical corridor and so limit the size of tumors that can be safely accessed endoscopically.

An ideal system for overcoming these limitations would enable the endoscope orientation to remain relatively fixed during a procedure and allow the surgeon to manipulate multiple dexterous tools within a workspace volume located at the endoscope's tip. The contribution of this paper is to present a robotic two-armed endoscope (Fig. 1) that overcomes these challenges along with preliminary validation results for a bimanual task.

Notable prior results on the design of multi-armed robotic neuroendoscopes include [3-5]. The present work differs from those results in that both the arms and the tools (e.g., forceps, scissors, bipolar cautery, suction) are designed as small, easily-sterilizable and replaceable modules that can be individually swapped during a procedure. This enables intraoperatively exchange of either a tool or a robotic arm without the risk involved in removing and reinserting the endoscope in the brain.

ROBOT DESIGN

The robot design is scalable. Current prototype dimensions are shown in Fig. 2. When fully extended, the 2.8mm diameter arms are 35mm long and trace out circles which are also 35mm in diameter. The arms are delivered with a center-to-center spacing of 8mm through

a 10×12mm trocar with an integrated camera and LED illumination. By rotating and translating the trocar about its axis, the overlapping workspaces of the two arms can access a cylindrical workspace shown in red with a diameter of 43mm.



Fig. 1. Bimanual neuroendoscopy robot.

Each arm is constructed from a balanced pair of precurved superelastic tubes such that relative rotation of the tubes causes their curvature to vary between straight and maximally curved [6]. Combined with extension and retraction, each arm possesses three degrees of freedom. Tip-deployed tools, such as the scissors and forceps of Fig. 1, can also roll about the axis of the arm. Arm and tool motion are controlled using haptic interfaces.

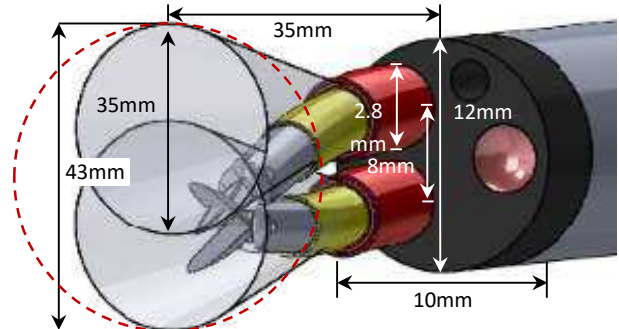


Fig. 2. Dimensions of robot arms, workspace and trocar. Note that arm lengths and workspaces are not to scale. Gray circles show workspaces of individual arms. Red dashed circle shows workspace accessible by rotating the trocar about its axis.

The entire robot is depicted in Fig. 3a with the arm and tool modules shown in Figs. 3b and 3c, respectively. These modules are inserted through the trocar module and clamp to mating drive system components as shown in Fig. 3a. To reduce the complexity and size of the arm and tool modules while making them more easily sterilizable, all the motors for driving the arms and tools

are incorporated in the drive system instead of the modules themselves. A sterile drape (not shown) can be used to separate the drive system (all motors and electronics) from the sterile arm, tool and trocar modules.

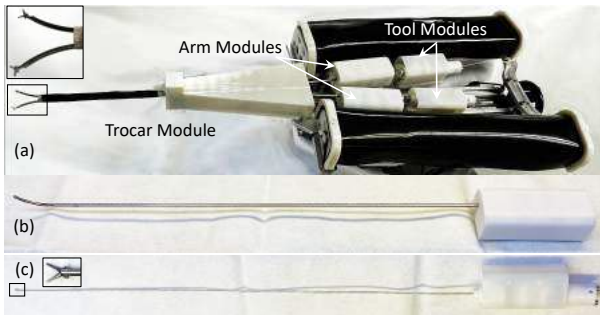


Fig. 3. Modular endoscopic robot. (a) Robotic system with inset showing arms and tools. (b) Removable arm module. (c) Removable tool module.

EXPERIMENTAL EVALUATION

An underwater hidden peg transfer task was used to compare the robotic system with a standard endoscope and a single straight tool. The pegs are hidden behind an opaque elastic membrane (shown semi-transparent in Fig. 4a) with a 6mm diameter circular hole. The task is to move the rings between the corresponding top / bottom pegs while minimizing motion of the endoscope – which would create pressure against the surrounding brain tissue during actual surgery. The goal of this task is to explore motions associated with debulking a tumor that is large relative to the diameter of the endoscope trocar.

The challenge of the task is that the elastic membrane, which represents the tumor-encasing membrane, blocks the view of the rings and pegs. In the manual version, the endoscope trocar must be inserted through the hole in the membrane and trocar pivoting about a point located 9.5cm above the membrane (simulated burr hole in skull) is needed to move the rings between initial and destination pegs. This is challenging because the endoscope tends to slip out of the membrane hole as it moves (tops of pegs are 1cm below membrane).

In the robotic version of this task, the trocar can remain stationary while one arm is used to push back the membrane and the second arm grasps and moves the peg. This is shown in Fig. 4b where the right arm has stretched the hole in the membrane up and to the right revealing a peg and ring which can now be grasped by the left arm.

Metrics for comparing robot and manual performance were task time, ring drops and trocar pivoting. For fairness of comparison, a manual endoscope was fabricated using the same camera as the robot. The manual forceps were also identical to those used on the robot. Manual trocar pivoting was measured using an electromagnetic tracking system.

For these initial tests, a single operator performed training trials with both systems until they felt comfortable. Ten trials were then performed with each system. Table 1 lists the results of the experiments. Use of the robot reduced task time by 37% and decreased ring drops by 86%. Furthermore, the robot trocar remained

stationary for the entire task while the manual trocar had to pivot about the simulated burr hole by 13deg in both coordinate directions of the peg plane. While not measured by the metrics, the operator indicated a higher stress level using the manual endoscope.

DISCUSSION

This abstract introduces a bimanual endoscopic robot design enabling intraoperative swapping of tools and arms. Initial evaluation on a task modeling tumor debulking demonstrates how the use of two steerable arms can improve task performance. These results suggest that a modular robot system enabling bimanual neuroendoscopy holds the potential to markedly expand the number of intracranial procedures amenable to a minimally invasive approach.

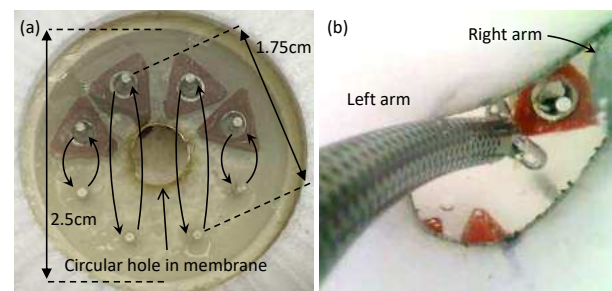


Fig. 4. Hidden peg transfer task. (a) Opaque membrane shown semi-transparent for visualization. (b) Robot endoscope view. Right arm pulls back membrane while left arm reaches for ring.

Table 1. Hidden Peg Transfer Task Metrics (10 trials)

Metric	Manual System	Robotic System
Total task time (min:sec)	2:18±0:45	1:27±0:16
Ring drops	2.1±1.9	0.3±0.5
Trocar pivoting with respect to x and y axes of peg plane (deg)	±6.5	0

REFERENCES

- [1] Cinalli G, Cappabianca P, de Falco R, Spennato P, Cianciulli E, Cavallo LM, Esposito F, Ruggiero C, Maggi G, de Divitiis E. Current state and future development of intracranial neuroendoscopic surgery. *Expert Rev Med Devices*. 2005 May;2(3):351-73.
- [2] Badie B, Brooks N, Souweidane MM. Endoscopic and minimally invasive microsurgical approaches for treating brain tumor patients. *Journal of neuro-oncology*. 2005 69(1-3):209-219.
- [3] Nishizawa, K, Fujie, MG, Hongo K, Dohi T, Iseki, H. Development of surgical manipulator system "HUMAN" for clinical neurosurgery. *Japan Medical Association Journal*, 2006 49(11-12), 335-344.
- [4] Azimian H, Looi T, Drake J. A Dual-Arm Robotic Neuroendoscope: Early Results. *Proc Hamlyn Symposium on Medical Robotics 2016*:34-35.
- [5] Rox MF, Ropella DS, Hendrick RJ, et al. Mechatronic Design of a Two-Arm Concentric Tube Robot System for Rigid Neuroendoscopy. *IEEE ASME Trans Mechatron*. 2020;25(3):1432-1443.
- [6] Dupont PE, Lock J, Itkowitz B, Butler, E. Design and Control of Concentric Tube Robots. *IEEE Transactions on Robotics* 2010; 26(2):209-225.

Towards a Procedure Optimised Steerable Microcatheter for Neurosurgical Laser Ablation

A. Aktas¹, A. A. Demircali², R. Secoli³, B. Temelkuran², F. Rodriguez y Baena¹

¹*The Mechatronics in Medicine Lab, Imperial College London*

²*Department of Metabolism, Digestion and Reproduction, Imperial College London*

³*The Hamlyn Centre for Robotic Surgery, Imperial College London*

[a.aktas20, f.rodriguez}@imperial.ac.uk

INTRODUCTION

Minimally invasive surgery (MIS) has seen significant growth over the last two decades due to its great benefits to surgical outcomes. In MIS neurosurgical procedures such as biopsy, ablation, and fluid delivery/extractions, it is common practice to use straight catheters. The success of these procedures derives from the precision and accuracy of reaching the surgical target without damaging healthy structures, which is not often possible due to limitations of the tool design. To overcome these, researchers continue to work on improving procedural delivery via robotic steerable needles with multiple design choices [1]. Within this area of research, the first robotic ecosystem, code-name EDEN2020 (Enhanced Delivery Ecosystem for Neurosurgery in 2020), was developed to provide a clinical tool to assess the potential of Convection Enhanced Delivery (CED) of chemotherapeutics along preferential pathways that align to anisotropic brain structures [2]. This task is possible only with a flexible delivery system.



Fig. 1 EDEN2020 robotic system

The EDEN2020 robotic ecosystem shown in Fig. 1, employs a Programmable Bevel-tip Needle (PBN) with a multi-lumen design to embed sensing and drug delivery conduits for CED. Watts et al. [3] presented the first clinically viable PBN prototype with a 2.5 mm outer diameter (Fig. 2a), which was manufactured

using extrusion of a medical-grade polymer. Although a diameter of 2.5 mm is clinically applicable, a further size reduction would be necessary for the application of diagnostic and therapeutic procedures involving deep-seated tissue structures, such as in Thermal Interstitial Laser Therapy (LiTT) [4]. Standard extrusion methods have limited capacity for complex geometry such as the PBN; therefore, we explored a different method to reduce the overall size of MIS tools.

This paper presents a new manufacturing method for PBNs that employs thermal drawing technology [5], which was previously applied to the manufacture of complex and irregular shapes at the micro-nano scale, with less material and lower cost. Our efforts to date have resulted in a 1.3 mm outer diameter PBN, demonstrating a 50% reduction in size but with equivalent performance to our most successful prototypes to date.

MATERIALS AND METHODS

A preform to fiber thermal drawing process is a fabrication method to produce longitudinally uniform fibers by heating the preform to its viscous liquefaction point and rolling it into meters to kilometers-long fibre while preserving cross-sectional structure [6]. Thermal drawing has been employed in several application areas in the literature, including optical communication, microfluidics, electronics, and textiles [7]. After the Additive Manufacturing methods were introduced, producing more complex and arbitrary structures with specific materials became possible. Hence, the 3D-printing thermal drawing method was chosen to produce each PBN segment. The 3D printed preform design was completed using standard Computer-Aided Design (CAD) software (SolidWorks, Dassault Systemes, France). During prototype (preform) development, several design approaches were considered and optimised attractively to reach the targeted segment dimensions and sliding performance of the interlocking mechanism by considering the effect of thermal expansion. A commercially available Ultimaker 3 Extended printer was used with PC material (Ultimaker PC Transparent, 2.85 mm filament, Netherlands) with 0.4AA print core (non-abrasive plastics) and layer thicknesses of 0.1 mm. Compared to the default speed

of 250 mm/s, the print core travel speed was adjusted to 40 mm/s to create smoother surfaces. For transparent PC printing, the following temperatures were taken into account: nozzle temperature $T_n = 270\text{ }^\circ\text{C}$ and bed temperature $T_b = 107\text{ }^\circ\text{C}$. The dimensions of the 3D printed preform were 40 mm in diameter and 100 mm in length. The central lumen of the preform was 8.6 mm in diameter, and the targeted draw ratio was 40 to reach 0.21 mm central lumen. Calculation of fibre to be drawn can be done by assuming that the amount of preform fed in a radiative 3-zone furnace and drawn fibre are equal (feed-through speed $v_f = 2.5\text{ m/min}$ and drawing speed $v_d = 1.4\text{ m/min}$). Thus, square of draw ratio \times preform length can yield for the fibre to be drawn ($40^2 \times 0.1 = 160\text{ m}$ fibre). The feed-through speed was also increased and optimised to avoid the 3D printed preform shrinking during the draw due to voids in its layers. The temperature of the 3-zone furnace used for thermally drawing the fiber was as follows: top zone: $140\text{ }^\circ\text{C}$, middle zone: $200\text{ }^\circ\text{C}$, and bottom zone: $85\text{ }^\circ\text{C}$. The thermal drawing process produced a long PBN shaped fiber segment with a radius of 0.65 mm, and afterward, the long fiber segment was trimmed to the desired length (200 mm). A complete needle assembly was created by assembling four individual shorn segments and assembly performed by hand. To compare the performance of PBN shaped fibres, the flexural stiffness and tensile stress of individual segments are tested. Additionally, the interlocking mechanism's breakout force between two assembled segments is measured.

RESULTS

The cross-section comparison between the previous segment and thermally drawn (TD) PBN segment is given in Fig. 2b. The results show that we achieved a diameter almost half the size of the current state of the art. Although there are inaccuracies in the interlocking mechanism (Fig. 2b), these do not affect the sliding behaviour or breakout strength between the segments, hence demonstrating the viability of thermal drawing as an alternative to extrusion.

TABLE I Mechanical features

	Mean Flexural Stiffness (N/mm)	Mean Tensile Stress (MPa)	Mean Interlocking Breakout Force (N)
2.5mm Extruded	0.023	13.10	5.47
2.5mm TD	0.38	53.66	18.52
1.3mm TD	0.031	51.45	10.94

The mean flexural stiffness, tensile stress, and interlocking mechanism breakout force values of the thermally drawn and extruded samples are given in Table 1. In order to have a better curvature performance, segment rigidity plays a critical role during the insertion of the segments. The thermal drawing method has higher stiffness compared to the extruded method for the same segment sizes. As a result of the increased stiffness, the catheter curvature performance is reduced, while

the interlocking strength is improved. With the 1.3 mm segment prototype, the effect on steering performance is mitigated (30% worse), while interlock strength is improved (50% better). Qualitatively, the thermally drawn segments work more efficiently, moving with respect to one another without separating and more fluidly than with the extruded 2.5 mm prototype. Comparing the thermal drawing method with extrusion, the former does not need additional post-production processing (e.g., nano-coating to improve the sliding behavior), representing a marked advantage.

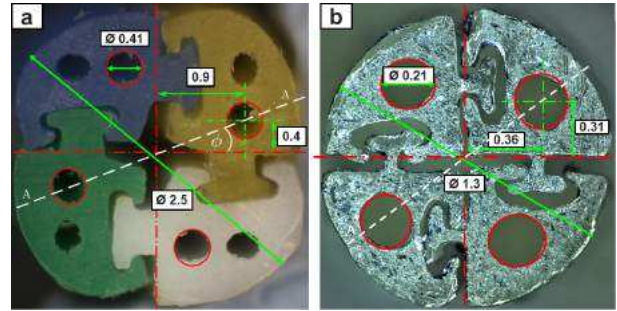


Fig. 2 a) Extruded PBN, b) Thermally Drawn PBN

DISCUSSION AND CONCLUSION

The manufacture of the PBN catheter with a 50% reduction in size to the state of the art opens door to its application to a wider range of diagnostic and therapeutic interventions. However, though our thermal drawing method is advantageous, it results in a stiffer structure compared to previous systems due to the choice of a harder material. A thorough examination of the effect of this change on the curvature performance of the needle will be part of future work. In addition, the use of different materials and molding methods will be investigated, alongside the integration of this newly developed catheter within EDEN2020's ecosystem for precision neurosurgery, paving the way for the eventual application of our needle steering technology to LiTT.

REFERENCES

- [1] N. J. van de Berg, D. J. van Gerwen, J. Dankelman, and J. J. van den Dobbelsteen, "Design choices in needle steering: a review," *IEEE/ASME Transactions on Mechatronics*, vol. 20, no. 5, pp. 2172–2183, Oct 2015.
- [2] A. Jamal, A. Bernardini, and D. Dini, "Microscale characterisation of the time-dependent mechanical behaviour of brain white matter," *Journal of the Mechanical Behavior of Biomedical Materials*, vol. 125, p. 104917, 2022.
- [3] T. Watts, R. Secoli, and F. Rodriguez y Baena, "A mechanics-based model for 3-d steering of programmable bevel-tip needles," *IEEE Transactions on Robotics*, vol. 35, no. 2, pp. 371–386, 2018.
- [4] M. Pinzi, B. Hwang, V. N. Vakharia, J. S. Duncan, F. Rodriguez y Baena, and W. S. Anderson, "Computer assisted planning for curved laser interstitial thermal therapy," *IEEE Transactions on Biomedical Engineering*, 2021.
- [5] R. Chen, A. Canales, and P. Anikeeva, "Neural recording and modulation technologies," *Nature Reviews Materials*, vol. 2, no. 2, pp. 1–16, 2017.
- [6] L. van der Elst, C. F. de Lima, M. G. Kurtoglu, V. N. Koraganji, M. Zheng, and A. Gumennik, "3d printing in fiber-device technology," *Advanced Fiber Materials*, pp. 1–17, 2021.
- [7] W. Yan, A. Page, T. Nguyen-Dang, Y. Qu, F. Sordo, L. Wei, and F. Sorin, "Advanced multimaterial electronic and optoelectronic fibers and textiles," *Advanced materials*, vol. 31, no. 1, p. 1802348, 2019.

Design of a Meso-Scale Grasper for Robotic Pediatric Neuroendoscope Tool

T.A. Brumfiel¹, K.K. Yamamoto¹, A. Rashid², A. Shigematsu¹, C. Chapman²
S.N. Melkote², J.J. Chern³, J.P. Desai¹

¹The Medical Robotics and Automation Lab, Georgia Institute of Technology

²George W. Woodruff School of Mechanical Engineering, Georgia Institute of Technology

³Children's Healthcare of Atlanta

tbrumfiel3@gatech.edu

INTRODUCTION

Endoscopic third ventriculostomy (ETV) is a procedure to relieve intracranial pressure by creating a hole at the bottom of the third ventricle, allowing cerebrospinal fluid (CSF) to drain [1]. Many neurosurgical procedures, such as ETV, make use of surgical graspers to collect biopsy samples [2]. Grasping forces exerted by neurosurgical tools on brain tissue have been indicated to range from 0 – 0.3 N for 70% of neurosurgical procedures [3]. Perforating the bottom of the third ventricle in ETV has even been measured to require less than 0.01 N [4].

This paper focuses on the design and evaluation of a meso-scale surgical grasper to be integrated within our previously developed neurosurgical continuum robot [5]. Fig.1(a) shows the schematic of the proposed integration of the grasper with the continuum robot. The grasper developed was machined using a multi-axis CNC mill (CNC Mini-Mill/GX, Minitech Machinery Corp., GA, United States) and a femtosecond laser (WS-Flex Ultra-Short Pulse Laser Workstation, Optec, Frameries, Belgium) and was actuated with a single cable to allow for compatibility with most flexible surgical robots. With the use of micro-machining processes and a tendon-actuated mechanism, the meso-scale, steerable neurosurgical grasper had a 1.93 mm OD, appropriate for high-precision neurosurgical procedures and to be introduced through the working channel of commercially available endoscopic tools.

MATERIALS AND METHODS

The proposed grasper design differentiated from recently developed surgical graspers by size, which remained in the 3-4 mm OD range [6], [7]. The grasper consisted of a scissor linkage system with a compression spring encapsulating the input linkage as shown in Fig.1(a)(inset). This allowed for the grasper to be actuated exclusively by the tension of a nitinol (NiTi) tendon, making it compatible for tendon-driven endoscopic tools as compared to commercially available rigid graspers and forceps. Each grasper (Fig.1(b-1)) was machined from 1.5 mm thick 316L stainless steel sheets using a 5-axis CNC micro-mill. The steel sheets were fixed to a Delrin block using high strength adhesives and machined using micro end mills with diameters of 0.3-1.0 mm at spindle speeds

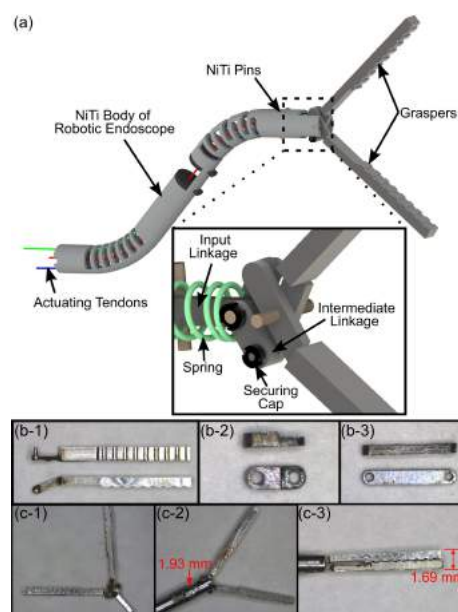


Fig. 1 The (a) proposed robotic endoscope and grasper design with (inset) details of the grasper linkage system shown. Images of the (b-1) machined graspers, (b-2) intermediate links, and (b-3) input linkage. The images of (c-1) the assembled linkage system, (c-2) the linkage system inside of its 1.93 mm tube sheath, and (c-3) the closed grasper.

ranging from 10k-55k rpm. Each grasper component was then finalized on a femtosecond laser where its final features were refined.

The graspers contained a 0.4 mm extrusion in which intermediate linkages (Fig. 1(b-2)) were placed over and secured using a stainless steel cap, each machined using a femtosecond laser. The intermediate linkages had a length, width, and thickness of 1.6 mm, 0.6 mm, and 0.4 mm, respectively, and contained a step on the side that interfaced with the input linkage (Fig. 1(b-3)) to ensure all faces mated properly. The intermediate linkages were then constrained to one end of the input linkage using NiTi tubes (OD 0.3 mm) with NiTi caps to hold the assembly together. The input link, machined from 0.4 mm stainless steel on the femtosecond laser, had a length and width of 3 mm and 0.6 mm, respectively. Holes were machined on each side to allow for assembly with the intermediate linkages and for securing a tendon for actuation.

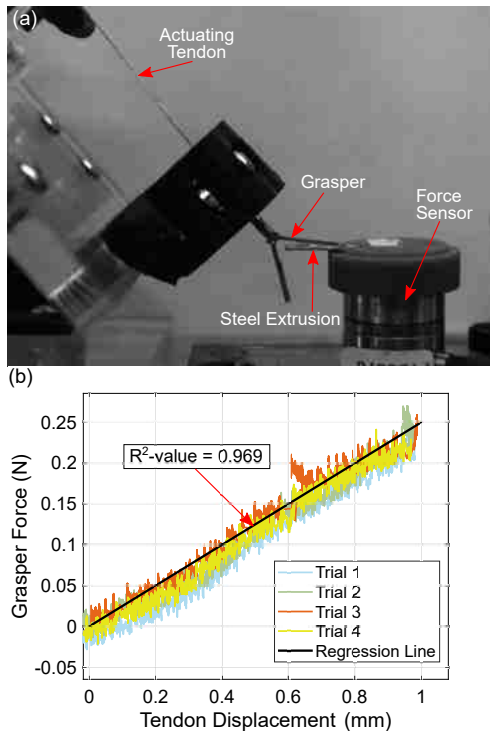


Fig. 2 (a) Image of the grasper force evaluation setup and (b) the results of grasping forces as a function of the tendon displacement.

Assembly of the graspers consisted of sliding each linkage on its respective shaft and securing it laterally through the use of the machined securing caps. The caps were attached with stainless steel and NiTi flux to keep respective metal components secured. The assembled linkage system, shown in Fig. 1(c-1), was then placed into a 1.93 mm OD NiTi tube. NiTi tubes of 0.3 mm OD were placed inside the said tube, acting as a wall for the spring to compress against. The input linkage and tendon were routed through the spring and pins. The compression spring provided a force for opening the graspers when the tendon was released from tension. The final grasper assembly is shown in Fig. 1(c-2) and Fig. 1(c-3) in its open and closed configurations respectively, where the closed configuration is measured to have an OD of 1.69 mm.

To evaluate the grasping force capabilities, one interior face of the graspers was placed against a steel beam extruding outward from a 6-axis force sensor (ATI Industrial Automation, NC, USA). The force acting downward throughout actuation was taken to be the applied grasping force. The input link was linearly translated using a Kevlar tendon secured to a lead-screw assembly actuated by a brushed DC motor (Maxon Precision Motors, MA, United States). The experimental assembly, shown in Fig. 2(a), was observed using a CMOS camera (Zelux™ 1.6 MP, Thorlabs Inc., NJ, United States) throughout each experimental trial.

RESULTS

The motor was commanded to move the initially slacked tendon from 0–1 mm at a rate of 0.016 mm/s followed by a 30 second rest period. The recorded grasping forces

for four trials of motion are shown in Fig. 2(b) where the applied force is shown to be linear with respect to tendon stroke with an R^2 -value of 0.969. The average maximum force was recorded to be 0.246 N, which falls in the range of forces required for a large number of neurosurgical interventions [3].

While conducting tests, the grasper was observed to lack the ability to fully return to its open configuration with the aid of the compression spring. This is hypothesized to be due to friction and interstitial spacing introduced by assembly errors. Reducing friction, improving securing methods, and refining the assembly procedure are ongoing work.

DISCUSSION

The development of a meso-scale grasper for use in a neurosurgical robotic endoscope tool was presented in this work. This significantly smaller grasper used actuation strategies compatible with those of current tendon-driven continuum surgical tools and can provide forces in the range of existing clinical graspers. Future works will focus on the improvement of the mechanical design, integration into existing steerable robotic endoscopic tools, and incorporation of grasper force estimation through tendon force feedback and shape sensing.

ACKNOWLEDGEMENT

Research reported in this publication was supported in part by the Eunice Kennedy Shriver National Institute Of Child Health and Human Development of the National Institutes of Health under Award Number R21HD101321. The content is solely the responsibility of the authors and does not necessarily represent the official views of the National Institutes of Health.

REFERENCES

- [1] A. V. Kulkarni, J. M. Drake, C. L. Mallucci, S. Sgouros, J. Roth, and S. Constantini, "Endoscopic third ventriculostomy in the treatment of childhood hydrocephalus," *The Journal of Pediatrics*, vol. 155, no. 2, pp. 254–259.e1, 2009.
- [2] A. I. Ahmed, M. J. Zaben, N. V. Mathad, and O. C. Sparrow, "Endoscopic biopsy and third ventriculostomy for the management of pineal region tumors," *World Neurosurgery*, vol. 83, no. 4, pp. 543–547, 2015.
- [3] L. S. Gan, K. Zareinia, S. Lama, Y. Maddahi, F. W. Yang, and G. R. Sutherland, "Quantification of forces during a neurosurgical procedure: A pilot study," *World Neurosurgery*, vol. 84, no. 2, pp. 537–548, 2015.
- [4] H. J. Marcus, K. Zareinia, L. S. Gan, F. W. Yang, S. Lama, G.-Z. Yang, and G. R. Sutherland, "Forces exerted during microneurosurgery: a cadaver study," *The International Journal of Medical Robotics and Computer Assisted Surgery*, vol. 10, no. 2, pp. 251–256, 2014.
- [5] Y. Chitalia, S. Jeong, K. K. Yamamoto, J. J. Chern, and J. P. Desai, "Modeling and control of a 2-dof meso-scale continuum robotic tool for pediatric neurosurgery," *IEEE Transactions on Robotics*, vol. 37, no. 2, pp. 520–531, 2021.
- [6] Y. Fujisawa, K. Kiguchi, K. Harada, M. Mitsuishi, M. Hashizume, and J. Arata, "Compact 4dof robotic forceps with 3.5 mm in diameter for neurosurgery based on a synthetic elastic structure," in *2017 International Symposium on Micro-NanoMechatronics and Human Science (MHS)*, 2017, pp. 1–3.
- [7] W. Lai, L. Cao, Z. Xu, P. T. Phan, P. Shum, and S. J. Phee, "Distal end force sensing with optical fiber bragg gratings for tendon-sheath mechanisms in flexible endoscopic robots," in *2018 IEEE International Conference on Robotics and Automation (ICRA)*, 2018, pp. 5349–5255.

Robotic Curvilinear Laser Thermal Therapy Probe for Transforaminal Hippocampotomy

Daniel S. Esser¹, John E. Peters¹, Abby M. Grillo¹, Sarah J. Garrow², Tyler Ball³, Robert Naftel³, Dario J. Englot³, Joseph Neimat⁴, William A. Grissom², Eric J. Barth¹, and Robert J. Webster III¹

¹*Department of Mechanical Engineering, Vanderbilt University,*

²*Department of Biomedical Engineering, Vanderbilt University*

³*Department of Neurological Surgery, Vanderbilt University Medical Center*

⁴*Department of Neurological Surgery, University of Louisville*

Robert.Webster@Vanderbilt.edu

INTRODUCTION

Epilepsy affects an estimated one out of 150 people, with 30% of patients unresponsive to existing drug-based therapies for seizure management. Hippocampal resection can be a curative procedure for drug-resistant temporal lobe epilepsy [1], however, current rates of surgical resection are limited by perceived and real risks of undergoing neurosurgery [2].

Laser Interstitial Thermal Therapy (LITT) is a less invasive alternative to surgical resection, which heats brain tissue causing thermal necrosis [3]. Existing commercial LITT tools (Medtronic, Monteris) are straight probes which are inserted through the skull. Reaching deep brain targets such as the hippocampus requires traversing significant amounts of potentially eloquent brain tissue [3]. Deploying LITT using curved needles to avoid critical neural structures has been proposed and explored in simulation and computational design [4], [5], but has yet to be demonstrated experimentally. The purpose of this paper is to describe the first experimental prototype of a needle that can deliver LITT along a curved trajectory.

MATERIALS AND METHODS

Our novel approach to LITT delivery to the hippocampus through the foramen ovale is shown in Fig. 1a. A helical needle with a curvature of $\kappa = 47.141/m$ and a torsion of $\tau = 80.95rad/m$ was fabricated by shapsetting a .045" OD / .039" ID nitinol tube. Design parameters for the helical needle were determined using a path planning optimization technique described in [5]. The highest curvature patient-specific needle from that study is used here, since it represents the greatest potential for optical bend losses. A 200 μm , bend insensitive multimode fiber (Newport MKS: F-MBB) was integrated into the helical needle to form the curvilinear laser delivery probe, which was powered by a 15W, 980nm clinical laser (BW Tek: BWF5-980-15).

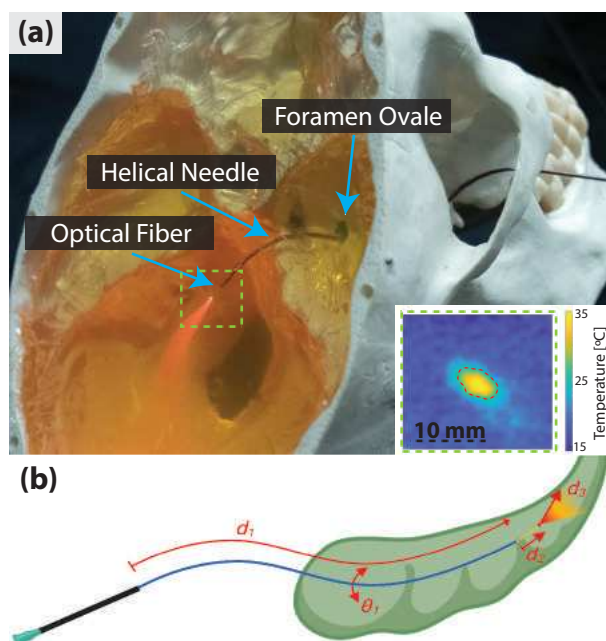


Fig. 1 (a) Helical needle delivered through the foramen ovale in a skull model filled with gelatin; red laser indicating fiber output. Inset: Thermal image of gelatin phantom after irradiation. (b) LITT delivery system degrees of freedom.

The probe was delivered using a pneumatically driven MR-compatible robot, described in [6] using a follow-the-leader approach. Our robot degrees of freedom are shown in Fig. 1b; d_1 and θ_1 are the translational and rotational pneumatically driven degrees of freedom of the helical needle, d_2 is the translation of the optical fiber out of the helical needle, and d_3 is the laser intensity, which affects the size of the treatment zone. The insertion DOFs (d_1, d_2) have a maximum travel of 120mm, while the laser can be controlled to create an ablation volume (d_3) of up to 15 mm in diameter. The pneumatic robot and laser were controlled using Simulink.

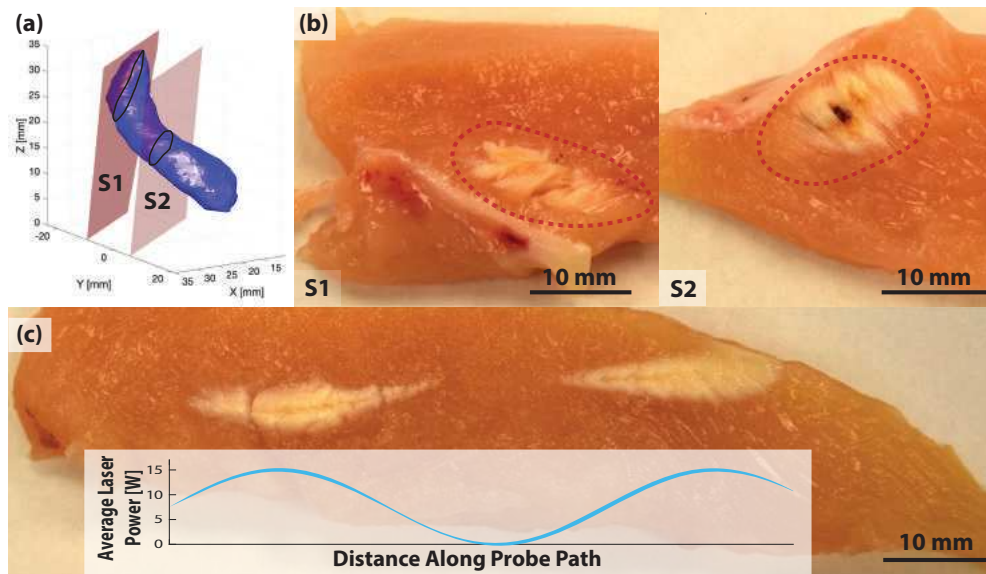


Fig. 2 (a) Segmentation of a human hippocampus from [5]. (b) Histology following ablation in chicken breast along a curvilinear trajectory matching the shape of the human hippocampus in a. (c) Modulating laser power with fixed translational speed to create a varying lesion diameter. (d) Helical path following demonstration.

RESULTS

The curvilinear laser ablation probe was first tested in a skull model filled with gelatin to demonstrate the ability of the helically curved needle to navigate through the facial-skeletal structures (Fig. 1a). A transverse view of the thermal treatment zone after irradiation with 3W for 30s was imaged using an IR-camera in the gelatin phantom. The dashed red line indicates a temperature rise of $> 10^{\circ}\text{C}$ above ambient temperature, which is an approximate threshold for thermal necrosis. The lesion size can be adjusted by varying the laser power or translation rate along the ablation path.

Subsequently, the curvilinear ablation probe was validated in *ex-vivo* chicken breast. The segmented MRI scan of a human hippocampus used to optimize the needle shape and trajectory is shown in Fig. 2a. The laser ablation probe was deployed 59 mm into *ex-vivo* chicken breast, and ablation was performed by robotically retracting the probe at a constant speed with incident power of 2.75 W for a duration of 11.5 min. Histological cross sections after the curvilinear ablation are shown in Fig. 2b, corresponding to approximate slices in the planned ablation volume in Fig. 2a. In Fig. 2c, we demonstrate the ability of the robotic system to create lesions with varying diameters; while the probe is translated through the tissue at a rate of 6 mm/s, the laser power is modulated sinusoidally over time. The ability for the needle tip to follow a helical path was confirmed using a magnetic tracker (Northern Digital) in Fig. 2d.

DISCUSSION

The integration of a curvilinear robotic delivery system with a laser therapy tool enables more precise thermal treatment zones due to the ability to control both path rates and laser power simultaneously to selectively ablate various lesion shapes and sizes, while navigating around anatomical constraints. We have demon-

strated that with open-loop control of our robotic system, it is possible to ablate a volume of tissue that matches a pre-operative segmented MR scan of a hippocampus. To reduce the chance of tissue charring effects, we plan to integrate fluid or CO_2 cooling in future versions of the probe, and monitor tip temperature. We also plan to create an optical/thermal model to relate probe speed and laser power to the volume of necrotic tissue. Subsequently, the curvilinear LITT system will be integrated with real-time MRI thermometry for closed-loop control. This prototype combining curved needles and laser thermal therapy is a promising first step towards robotic LITT delivery for enhanced and targeting of deep brain structures using a minimally-invasive approach.

REFERENCES

- [1] H. Choi, R. L. Sell, L. Lenert, P. Muennig, R. R. Goodman, F. G. Gilliam, and J. B. Wong, "Epilepsy surgery for pharmacoresistant temporal lobe epilepsy: A decision analysis," *JAMA - Journal of the American Medical Association*, vol. 300, no. 21, 2008.
- [2] S. G. Uijl, F. S. Leijten, K. G. Moons, E. P. Veltman, C. H. Ferrier, C. A. van Donselaar, M. Aramideh, C. J. Vecht, L. Wagner, E. Strijks, G. Hageman, R. S. Holscher, and D. Oenema, "Epilepsy surgery can help many more adult patients with intractable seizures," *Epilepsy Research*, vol. 101, no. 3, 2012.
- [3] J. T. Willie, N. G. Laxpati, D. L. Drane, A. Gowda, C. Appin, C. Hao, D. J. Brat, S. L. Helmers, A. Saindane, S. G. Nour, and R. E. Gross, "Real-time magnetic resonance-guided stereotactic laser amygdalohippocampotomy for mesial temporal lobe epilepsy," *Neurosurgery*, vol. 74, no. 6, 2014.
- [4] M. Pinzi, V. N. Vakharia, B. Y. Hwang, W. S. Anderson, J. S. Duncan, and F. R. Y. Baena, "Computer Assisted Planning for Curved Laser Interstitial Thermal Therapy," *IEEE Transactions on Biomedical Engineering*, vol. 68, no. 10, 2021.
- [5] D. B. Comber, E. B. Pitt, H. B. Gilbert, M. W. Powelson, E. Matijevich, J. S. Neimat, R. J. Webster, and E. J. Barth, "Optimization of curvilinear needle trajectories for transforaminal hippocampotomy," *Operative Neurosurgery*, vol. 13, no. 1, 2017.
- [6] D. B. Comber, J. E. Slightam, V. R. Gervasi, J. S. Neimat, and E. J. Barth, "Design, Additive Manufacture, and Control of a Pneumatic MR-Compatible Needle Driver," *IEEE Transactions on Robotics*, vol. 32, no. 1, 2016.

This work was funded by NIH R01 NS120518.

A Steerable Guide for MRI-guided Laser Interstitial Thermal Therapy

J.S. Kim¹, R. Fischer², I. Cajigas³, M. Ivan³, D. Chang²

¹Department of Mechanical Engineering, Johns Hopkins University,

²Department of Interventional Radiology, University of Miami,

³Department of Neurological Surgery, University of Miami,

doyoungchang@gmail.com

INTRODUCTION

Laser interstitial thermal therapy (LITT) is capable of generating precise ablative lesions under real-time magnetic resonance imaging (MRI) thermometry for the treatment of epilepsy and brain tumors[1]. The Visualase Thermal Therapy System (Medtronic, Inc) is a minimally-invasive LITT platform that delivers laser light through a fiber optic cable ensheathed in a cooling catheter. Currently, the 3-mm diffusing tip may create ablation lesions of a 1cm sphere along a linear trajectory, requiring multiple probe placements to treat lesions shaped irregularly or surrounded by critical structures.

In this paper, we present the development of a steerable guide for the Visualase system that enables deployment of the laser fiber along a controlled curved trajectory with micro-adjustability to further enhance its dexterity and treat lesions up to 5cm in diameter. Catheter insertion experiments were performed in tissue-mimicking gelatin phantoms to investigate the safety of the steerable guide system and verify the accuracy of the mathematical trajectory prediction model.

MATERIALS AND METHODS

The steerable guide system consists of three major components: (a) Steerable stylet, (b) Visualase catheter guide and (c) Rigid cannula. It has three degrees of freedom, which are the rotation and curvature amount of the stylet and the insertion depth of the straight and curved sections, respectively.

For placement, first, the rigid cannula is placed to insert the catheter along a straight path up to the point where the desired curved trajectories should start. The steerable stylet that allows a curved deployment is placed within the catheter. This stylet is used to deploy the catheter beyond the cannula along a specified radial direction (θ) and curvature trajectory (ϕ) as illustrated in Fig 1. The curvature is achieved using a tendon-driven mechanism, where a tendon runs along the length of a cannula that has a notch on one side towards its distal end to allow it to flex once tension is applied. A knob at the stylet base is used to control the tension amount, which in turn determines the curvature of the catheter when exiting the rigid cannula. Once the tension amount is pre-determined, the stylet acts as a pre-curved needle allowing the catheter to be deployed along a curved path without damaging the surrounding healthy tissue. The

whole catheter assembly can be rotated about the cannula axis using a control knob to control the direction of the curved trajectory about its axis.

For LITT, the rigid cannula may be placed using CT or MRI stereotactic navigation. Then, the curved catheter may be deployed with real-time MRI guidance to enable tracking and micro-adjustments. For MRI compatibility, all parts were 3D printed with the Form 2 (Formlabs, USA). Nitinol tubes and wire were used for the stylet and rigid needle guide. Once positioned, the stylet is retracted, and the optical fiber can be placed within the catheter for ablation. Subsequent curved paths may be repeatedly achieved through the single insertion point.

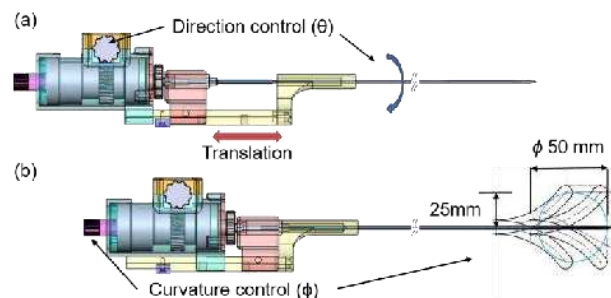


Fig. 1 Steerable guide system for Visualase LITT in (a) retracted and (b) extended positions

However, the achievable curvature is limited to a certain amount using this method alone as the rigid cannula suppresses the needle from being curved when tension is pre-applied. This causes the friction between the catheter and rigid cannula to increase, making it difficult to push out. Moreover, the bond between the stylet and tendon may break as the pre-applied tension increases. One way to achieve high curvature would be to gradually increase the tension amount simultaneously while pushing the curved catheter out of the rigid cannula. However, the trajectory would be inconsistent and there is risk of tissue damage in case of a sudden change of tension amount, causing a sweeping motion.

A passive tension control mechanism has been developed to overcome this limitation, where a 3D printed elastic spring is placed between the tendon and translational screw that controls the tension. When the applied tension is higher than a predefined level, the spring is compressed which effectively acts as a stress relieving mechanism as in Fig 2(a). This decreases the tension load and prevents the stylet from being damaged. When the catheter is

pushed out of the rigid cannula, the spring is restored as in Fig 2 (b), increasing the tension and curving the stylet. The mechanism works in the reverse order of the insertion in case of the retraction of the catheter.

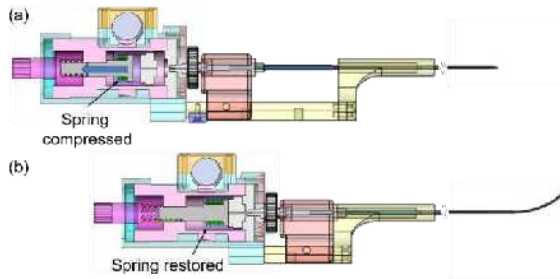


Fig. 2 3D printed spring being (a) compressed while stylet is retracted and (b) restored during catheter deployment along curved trajectory

RESULTS

Experiments were performed by inserting the stylet into a tissue-mimicking gelatin phantom along various predefined curvature trajectories. The phantom was fabricated using Knox gelatin (Kraft Foods Global Inc., USA), which has been previously reported to have similar insertion force profile to that of brain tissue [2]. A grid paper was placed under the phantom so that an image of the trajectory could be recorded and analyzed. For each different trajectory trial, the rigid cannula was first inserted. Then, a preset tension amount was applied to the stylet and the catheter was inserted without any further adjustments. A new gelatin phantom block was used for each trial. The curvature controlling knob value was tested from 0° to 240° with an increment of 10° . A maximum tip displacement of 25mm was achieved, which translates to a workspace of 5cm in diameter.

A mathematical model of the needle trajectory has been developed to predict the needle tip position (x_{tip}) and catheter curvature trajectory for a given tension control knob value. We model the catheter-needle system as an inextensible rod and apply the general rod theory combined with the Lie group theory, which has successfully been used in modelling flexible needle steering [3]. The general governing equations for the inextensible rod are written as

$$\frac{d}{ds} B\omega(s) + \omega \times (B\omega) + e_3 \times f = -m_{ext} \quad (1)$$

$$\frac{df}{ds} + \omega \times f = -f_{ext} \quad (2)$$

where B denotes the stiffness matrix, f_{ext} and m_{ext} respectively denote the external moment and force per unit length applied along the needle, and $f(s)$ denotes the internal force distribution along the rod. The internal moment to the curvature is computed as

$$m(s) = B\omega(s) \quad (3)$$

where $\omega(s)$ denotes the angular deformation of the rod. Using the Lie-group-theory, this can be expressed as [3]

$$\omega = [\omega_1, \omega_2, \omega_3]^T = (R^T(s) \frac{dR(s)}{ds})^V \quad (4)$$

The position of the point along the rod is then computed by considering the inextensibility condition as

$$r(s) = \int_0^s R(\sigma) e_3 d\sigma \quad (5)$$

where $R(s)$ is determined by solving (4). Using this model and the boundary conditions of the steerable guide, we use numerical optimization techniques to calculate the predicted needle trajectory and tip displacement. The average and standard deviation of tip position error (between predicted and actual needle tip position) in gelatin was 0.70 mm and 0.43 mm respectively.

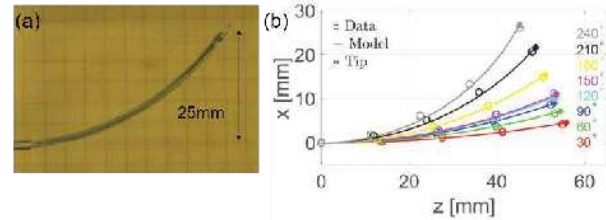


Fig. 3 (a) Example image of curved trajectory with tip displacement of 25mm and (b) plot of predicted curvature model and experimental data comparison

DISCUSSION

In this paper, we have presented a novel steerable guide for the Visualase MRI-guided LITT system. The system was able to successfully deploy the catheter along a curved trajectory without causing tissue damage and was able to achieve variable curvatures. A mathematical model was developed to predict the trajectory and tip position of the catheter and its accuracy was validated.

The proposed system provides several benefits: 1) Increased ablation volume of up to 5cm in diameter from a single insertion point. 2) Access to tumors that are currently unreachable lesions due to surrounding critical structures. 3) Quick touch-up without increasing the risk of complications in case of incomplete ablation. 4) Micro adjustments to the probe trajectory in case of deviations from the planned trajectory caused by needle deflection or tissue deformation. As such, the proposed device would greatly minimize the invasiveness, operation time, cost and ultimately the efficacy of LITT.

ACKNOWLEDGEMENT

The authors greatly thank Medtronic for supporting this research project through ERP ID# ERP-2019-11909.

REFERENCES

- [1] C. Banerjee, B. Snelling, M. H. Berger, A. Shah, M. E. Ivan, and R. J. Komotar, "The role of magnetic resonance-guided laser ablation in neurooncology," *Br J Neurosurg*, vol. 29, pp. 192-6, Apr 2015.
- [2] D. S. Minhas, J. A. Engh, M. M. Fenske, and C. N. Riviere, "Modeling of needle steering via duty-cycled spinning," *Annu Int Conf IEEE Eng Med Biol Soc*, vol. 2007, pp. 2756-9, 2007.
- [3] J. S. Kim, J. Guo, M. Chatrasingh, S. Kim, and I. Iordachita, "Shape determination during needle insertion With curvature measurements," in *2017 IEEE/RSJ International Conference on Intelligent Robots and Systems (IROS)*, 2017, pp. 201-208.

In Vitro Navigation of a Magnetic Sphere using a Model Predictive Controller for Neurovascular Targeted Drug Delivery Applications

D. Sivakumaran^{1,2}, F. C. Landers², Q. Boehler², C. Chautems²,
S. Pané², and B. J. Nelson²

¹MagnebotiX AG, Zurich Switzerland,

²Multi-Scale Robotics Lab, ETH Zurich
derick.sivakumaran@magnebotix.com

INTRODUCTION

The conventional systemic administration of drugs has been utilized in medicine for centuries. However, systemic drug administration limits the kind of drugs and the minimally required doses for treatment inside the human body. Furthermore, directly delivering pharmaceuticals to the location inside the body where they are needed would increase their efficacy while limiting side effects and opening new possibilities in drug development [1]. In the following, this direct transport will be referred to as Targeted Drug Delivery (TDD).

Navigation inside the human body is challenging, and several factors, such as biocompatibility, controllability, and scalability, need to be considered. Magnetic navigation is a promising technique for enabling TDD inside the human body for several reasons [2]:

- The magnetic fields and gradients in the range required for magnetic navigation are considered biocompatible.
- Magnetic fields and gradients are highly controllable.
- Magnetic fields and gradients offer good scaling properties and are thus applicable for small-scaled objects fitting into the human vasculature.

Some research attention has been directed towards in-silico simulations of the forces and flows inside the vasculature [3]. However, due to non-linear forces inside blood vessels, pulsatile flows, and the elastic nature of the human vasculature, an experimental platform is required to verify and improve navigation strategies.

In this work, we focused on magnetic navigation inside a two-dimensional (2D) model of the main vasculature of the human brain (namely the circle of Willis), see Figure 1. We manipulated a small-scaled untethered magnetic sphere inside an electromagnetic navigation system (eMNS), consisting of eight electromagnets to show remote magnetic navigation. Control of untethered devices inside a blood vessel is a challenging task for many reasons, including non-linear flows, friction forces, and the presence of a non-Newtonian fluid, i.e., blood. Using a model predictive controller (MPC), we were

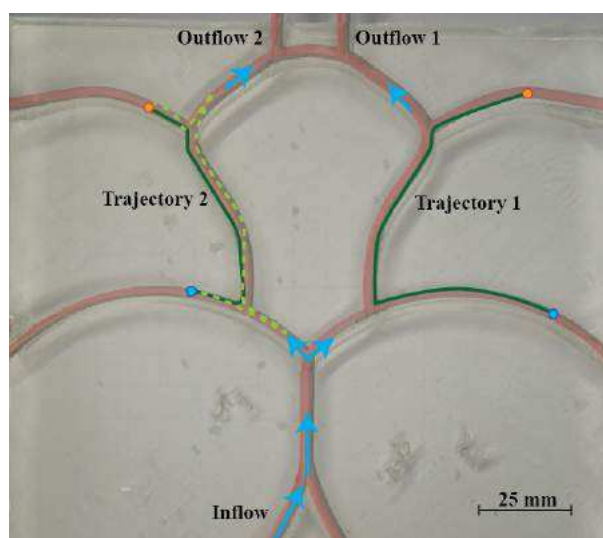


Fig. 1 The camera image from the vessel-like in vitro model with an overlay of the CAD. The blue circles represent the starting point and the orange ones the target points for the two trajectories. The solid green lines represent the optimal path. The dashed green line is an example path followed by the magnetic sphere during an experiment for the second trajectory. The direction of the flow is indicated by the light blue arrows.

able to show in-flow navigation and a high degree of controllability in reaching the target bifurcation.

MATERIALS AND METHODS

To find the optimal control inputs an MPC was developed that loads the geometric model, gets the actual position of the magnetic sphere from a camera, takes into account the forces of the eMNS and gravity and calculates the trajectory for a certain time horizon for different magnetic fields [4]. The MPC applies the field in a direction for which the estimated position at the end of the time horizon is the closest to the desired target position (see Fig. 2). The MPC can be manually tuned by setting the length of the time horizon, the magnitude of the magnetic field and gradient, and the number of directions in which to simulate a magnetic gradient.

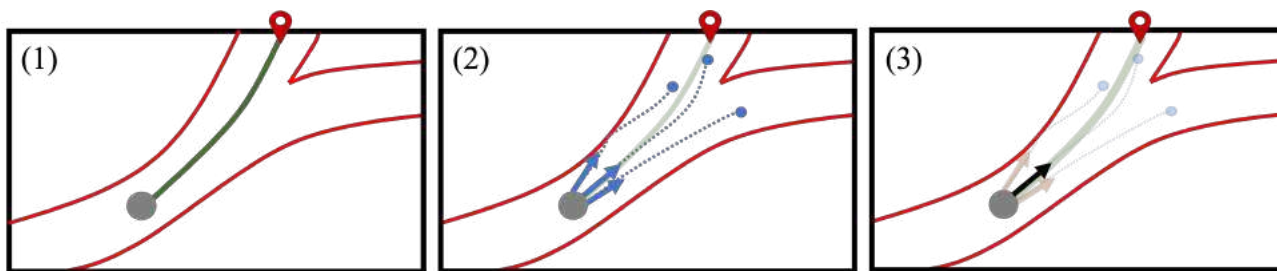


Fig. 2 The functioning of the MPC: (1) Find optimal path to target. (2) Simulate trajectory for different directions of gradients. (3) Chose gradient direction for which the simulated end position has the smallest distance to the target.

In Figure 1 the vessel-like in vitro model is depicted. It is a 20 cm × 20 cm 2D silicone model that captures the main vessels of the circle of Willis and has similar dimensions. It was fabricated by 3D-printing the geometry with polyvinyl alcohol (PVA) and placing it inside a container and pouring a silicon mix into the container. After curing the 3D print could be dissolved with water, leaving a vessel structure with a diameter of 4 mm as previously designed in the silicon block. For the experiments a spherical Neodymium magnet with diameter of 1.5 mm and a remanence magnetization of 1.17 T was used. The magnetic sphere was tracked on the camera image using a background subtraction algorithm from the open source computer vision library [5].

RESULTS

The model shown in Figure 1 has eight openings. For the following experiments six of them were sealed and the other two were chosen to be the inflow and outflow point respectively. Water flow was created using a peristaltic pump with a constant flow rate of 0.13 m/s. The MPC was evaluated by measuring the success rate of navigating the magnetic sphere from a position along the streamline to a branch that was not in the main direction of the flow.

In Figure 1 the point of inflow and outflow for the two trajectories are labeled as well as the initial starting points and targets. The experiment for both trajectories were repeated five times. In each iteration the MPC could successfully navigate the magnetic sphere to the desired targets. Seven out of ten times it did so with less than four control inputs (i.e., number of times the magnetic gradient was changed, see Table I). Except for two iterations the navigation took less than 40 seconds. In 80% of the time the magnetic sphere had to be controlled against the flow for a short distance (see Fig. 1). However, switching start and target position and using the MPC for the reverse navigation was unsuccessful.

TABLE I Mean and standard deviation of the number of control inputs and the navigation time

	Control inputs		Time [s]	
	mean (std)	mean (std)	mean (std)	mean (std)
Trajectory 1	3.2 (1.6)	42.4 (27.8)		
Trajectory 2	3.6 (0.9)	24.7 (6.0)		

DISCUSSION

In this work the performance of an MPC, which took into account the force of an eMNS and gravity to model the trajectory of an untethered magnetic sphere, was tested in a 2D vasculature in vitro model. It was able to navigate to the intended branch of a bifurcation, despite the flow of water dragging it away to the other branch.

The described experiment gave valuable insight into the dynamics of a small object in a confined space and actuated with an eMNS. For example, the duration of the navigation task suggest that for faster flow the MPC needs to increase the rate at which new control inputs are given to the eMNS. When expanding to a 3D model the MPC can be adapted quickly. However, in that case the tracking becomes more challenging. It has to be evaluated if navigation is still possible when using pulsatile flow with higher flow rate, i.e., similar to the fluiddynamic conditions inside the blood vessel.

In the future, we plan to increase the complexity of the vasculature model further, enable feedback control with angiography data and further improve our control algorithm to enable TDD via magnetic navigation in a clinical setting.

ACKNOWLEDGEMENT

The authors would like to thank Vitaly Pustovalov for his help in conducting the experiments. This project has received funding from the European Union's Horizon 2020 Proactive Open program under grant agreement No 952152.

REFERENCES

- [1] Z. Zhao, A. Ukidve, J. Kim, and S. Mitragotri, "Targeting strategies for tissue-specific drug delivery," *Cell*, vol. 181, pp. 151–167, 4 2020. [Online]. Available: <https://pubmed.ncbi.nlm.nih.gov/32243788/>
- [2] J. J. Abbott, E. Diller, and A. J. Petruska, "Magnetic methods in robotics," *Robotics, and Autonomous Systems Annu. Rev. Control Robot. Auton. Syst.* 2020, vol. 13, pp. 57–90, 2020. [Online]. Available: <https://doi.org/10.1146/annurev-control-081219->
- [3] T. D. Do, Y. Noh, M. O. Kim, and J. Yoon, "In silico magnetic nanocontainers navigation in blood vessels: A feedback control approach," *Journal of Nanoscience and Nanotechnology*, vol. 16, pp. 6368–6373, 6 2016.
- [4] L. Arcese, M. Fruchard, and A. Ferreira, "Endovascular magnetically guided robots: Navigation modeling and optimization," *IEEE Transactions on Biomedical Engineering*, vol. 59, pp. 977–987, 4 2012.
- [5] G. Bradski, "The OpenCV Library," *Dr. Dobb's Journal of Software Tools*, 2000.

An MRI Compatible MR-Guided High-Intensity Focused Ultrasound Neonatal Neurosurgery Platform for Intraventricular Hemorrhage

H. Raghuram^{1, 2}, B. Keunen², N. Soucier^{1, 2}, T. Looi^{1, 2}, S. Pichardo³
A.C. Waspe^{1, 2}, J.M. Drake^{1, 2}

¹The Hospital for Sick Children, Canada

²University of Toronto, Canada

³University of Calgary, Canada

rishi.raghuram@mail.utoronto.ca

INTRODUCTION

Intraventricular Hemorrhage (IVH) is a serious neurovascular complication in neonates that can lead to blood clots forming in the ventricular system [1]. Magnetic resonance-guided high-intensity focused ultrasound (MRgHIFU) has been investigated as a non-invasive treatment for clot lysis [2][3]. However, current MRgHIFU systems are not suitable for treating IVH in neonates.

We have developed an MRgHIFU platform optimized for the neonatal brain, which facilitates ergonomic patient positioning and directs treatment through their anterior fontanelle. This platform is based on an MRI-compatible robot designed by our group [4]. This paper describes the optimization of the MRgHIFU platform and its initial validation for treating IVH.

MATERIALS AND METHODS

Treatment is delivered using a 256-element phased-array concave HIFU transducer sourced from a Sonalleve V1 table (Profound Medical, Toronto, CA). The MRgHIFU platform has five degrees of freedom to move the transducer (Fig.1). The platform's electronics and control system are interfaced with a Sonalleve V1 matching circuit, controller board and generator cabinet. Treatment is guided using an Achieva 3.0T TX MRI (Philips Healthcare, Best, NL). We developed an open-source software to interface with the MRI, move the platform, and control HIFU treatment [5].

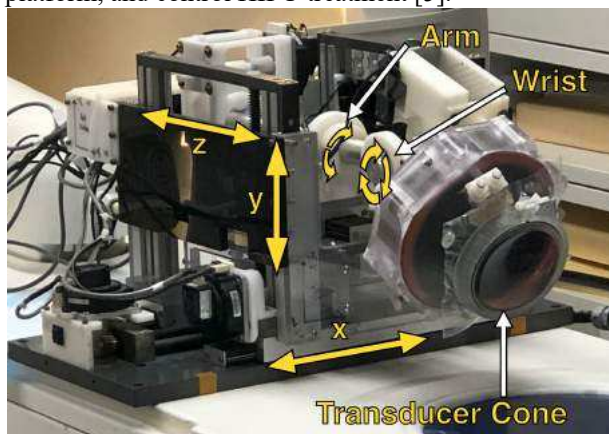


Fig.1: The MRgHIFU platform's five degrees of freedom and coordinate convention.

To optimize the platform to treat IVH, the HIFU transducer was encased in a 3D printed reservoir (transducer cone), which was filled with degassed deionized water. This maintained acoustic coupling during treatment and made it possible to position the transducer above a neonatal patient's head inside an MR-compatible incubator.

Integrating the transducer cone affected the platform's targeting, which required updating and optimizing the MR-compatible robot's hardware and electronics. Some major changes included redesigning the worm drive assemblies, changing the location of limit switches, and redefining the maximum operating range within the MR-bore. Additionally, vitamin E fiducial markers were embedded into the transducer cone's exterior and used to co-register the robot and MR coordinate spaces (Fig.2A). This also allowed overlaying the HIFU focal point and beam path onto MR scans during treatment (Fig.2B).

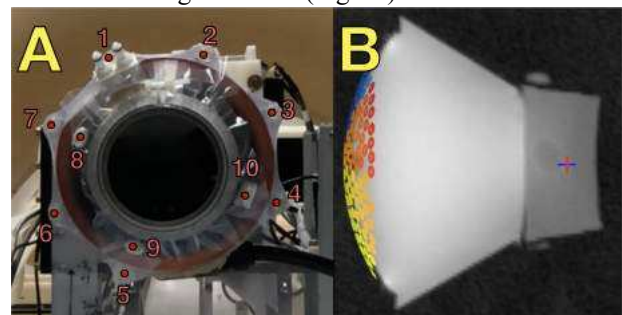


Fig.2: (A) Ten vitamin E fiducial markers (red dots) are embedded onto the transducer cone's exterior. (B) HIFU transducer (coloured circles) and focal point (crosshair) overlaid onto a pre-treatment MRI scan of a phantom.

We first optimized the MRgHIFU platform's targeting ability through simulated brain matter. Subsequently, we validated the platform's ability to lyse blood clots embedded into a brain-mimicking phantom.

Brain-mimicking phantoms were developed to test the platform in a controlled setting. These phantoms emulated the acoustic properties of brain matter, allowed localization of HIFU lesions (both visually and in MR scans), and had interior cavities to imitate the cerebral ventricles.

The platform's targeting accuracy was quantified according to performance criteria outlined in ISO Standard 9283:1998 [6]. HIFU treatment was

delivered to specific coordinates in the phantom and the geometric distance between the intended and actual target locations was measured using T2-weighted MRI scans. An ablation procedure (100W for 30s) was used to create a thermal lesion in the phantom and demarcate the HIFU focal point's location.

The clot lysis efficacy was validated by clotting whole porcine blood inside cavities cast within the phantoms according to an *in vivo* IVH piglet model developed by our group [3]. A boiling histotripsy procedure (500W, 10ms pulse duration, 1.0% duty cycle, and 40s duration) was used to induce acoustic cavitation at the HIFU focal point and cause lysis. After treatment, the remaining solid blood clot mass was used to quantify clot lysis efficacy and the phantom's cavities were inspected for any collateral damage.

RESULTS

The platform could successfully manipulate the transducer cone inside the MR bore and maintain coupling with the phantoms in all the experiments. HIFU treatment was successful and monitored using our open-source software. A total of 127 points were included in the targeting assessment and the platform demonstrated an accuracy of 0.6mm and a precision of 1.2mm (Fig.3). A total of 9 phantoms were included for the quantification of clot lysis efficacy. The platform lysed an average of $97.0\% \pm 2.57\%$ of the initial clot mass. The progression of clot lysis was monitored by T2-weighted MR scans (Fig.4). No apparent collateral damage was observed after treatment.

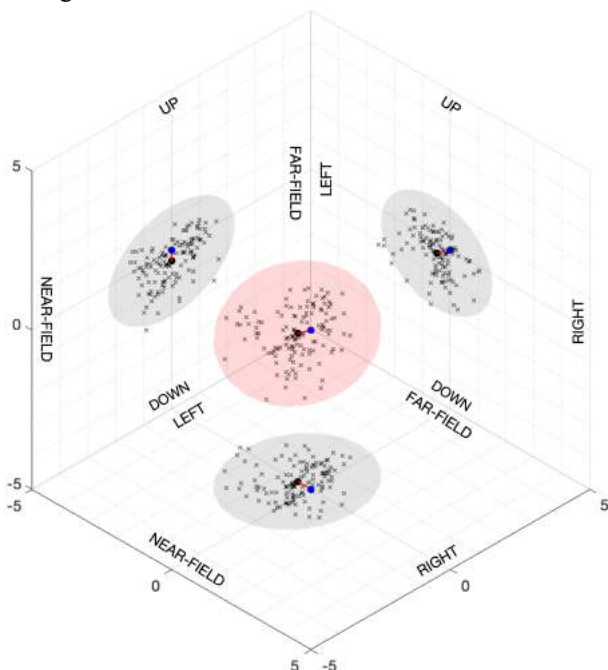


Fig.3: Targeting assessment data plotted on a 3D scatter plot. The targeting accuracy is represented as the distance between the intended (blue circle) and actual (black circle) target locations. The targeting precision is represented by the elliptical 99.7% confidence interval (red ellipsoid).

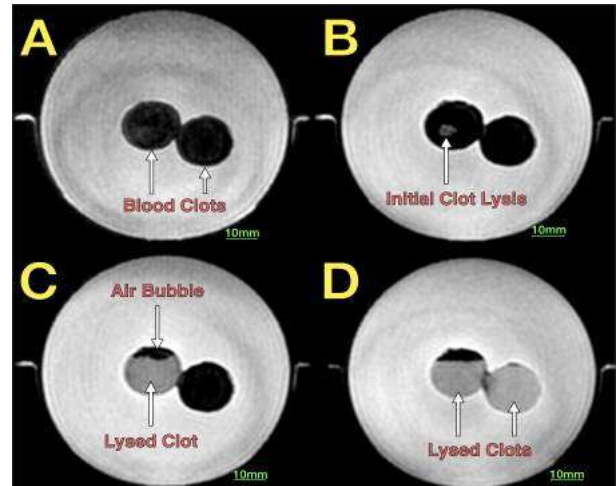


Fig.4: The progression of clot lysis in T2-weighted MR Scans. The phantom and embedded clot can be seen (A) before treatment, (B) after a single sonication point, (C) after half of the clot was treated, and (D) after both halves were treated.

DISCUSSION

The results demonstrate the MRgHIFU platform's high targeting ability and validated its clot lysis efficacy when targeting through simulated brain matter. The developments made after the integration of the transducer cone rectified the targeting ability. Moreover, the platform's accuracy and precision suggest its suitability for the small ventricles in a neonatal brain. Additionally, the platform's ability to lyse a substantial amount of clot mass can provide a greater degree of freedom to optimize treatment for specific patient cases.

These results serve as a successful initial verification of our MRgHIFU platform's potential as a non-invasive treatment of the blood clots in the ventricles of neonates suffering from IVH. Future work will focus on assessing the platform's efficacy at lysing blood clots in an *in vivo* survival study.

REFERENCES

- [1] J. J. Volpe, *Neurology of the Newborn*, 6th ed. Elsevier Inc., 2017.
- [2] A. Burgess *et al.*, "High-intensity focused ultrasound (HIFU) for dissolution of clots in a rabbit model of embolic stroke," *PLoS One*, vol. 7, no. 8, pp. 1–7, 2012, doi: 10.1371/journal.pone.0042311.
- [3] T. Looi *et al.*, "An MR-based quantitative intraventricular hemorrhage porcine model for MR-guided focused ultrasound thrombolysis," *Child's Nerv. Syst.*, vol. 34, no. 9, pp. 1643–1650, 2018, doi: 10.1007/s00381-018-3816-8.
- [4] K. D. Price *et al.*, "Design and validation of an MR-conditional robot for transcranial focused ultrasound surgery in infants," *Med. Phys.*, vol. 43, no. 9, pp. 4983–4995, 2016, doi: 10.1118/1.4955174.
- [5] S. Pichardo *et al.*, "Proteus: A software platform for multisite development of MRI-guided focused ultrasound applications," 2019.
- [6] International Organization for Standardization, "ISO 9283:1998 Manipulating industrial robots - Performance criteria and related test methods," vol. 1988. 1988.

The fulcrum effect in the control of electromechanical articulated laparoscopic instruments

Amir Szold^{1,2}

¹Medical Director, Assia Medical Group, Tel Aviv, Israel,

²CMO, Human Xtensions LTD, Kfar Neter, Israel

INTRODUCTION

TM

The HandXTM (Fig. 1A)[1] is an electromechanical, handheld, laparoscopic device which operates a fully articulating set of 5mm instruments; e.g., needle-holder, grasper, and mono-polar hook. Laparoscopic minimally invasive surgery, presents control difficulties to the surgeon due the "fulcrum effect" [2], [3]. In laparoscopic surgery, elongated surgical instruments are inserted through trocars (ports) in the abdomen of the patient. This creates a fulcrum effect while operating these instruments, where, for example, left and up maneuvers by the surgeon's hand are translated into right and down movements of the instrument's end-effector.

The HandXTM's sphere-like control interface (CI) allows the surgeon to manipulate the articulated instruments' end-effector 90° in all directions. The HandXTM brings the dexterity and ease of robotic surgery into the palm of the surgeon, whilst maintaining a small footprint in the operating room, unlike other commercially available surgical robotics platforms. Moreover, in times of an increasing awareness for healthcare system costs, it offers the possibility to improve surgeon's dexterity, precision and ergonomics in a more cost-effective manner than other platforms.

The HandXTM, being a digital electromechanical device, allows rapid performance improvements to be made by simply applying software updates. The control design implemented in the device (Robo-style, Fig. 1B) maps the surgeon's motions directly to the instrument end-effector; i.e., if the surgeon is pointing the CI to the right the end-effector articulates right), and the same for the vertical motion (up-up, and down-down). However, the position of the end-effector in 3D Cartesian space is inverse, due to the fulcrum effect

- as discussed above. Crothers et al. [2] have shown that surgeons can overcome this fulcrum effect and can manipulate laparoscopic tools in a smooth and efficient fashion.

As discussed, applying improvements to the HandXTM control design is simple, hence, as a part of an ongoing research and development process, we implemented an inverse, fulcrum-like, control design to the CI (Lapro-style, Fig. 1B); i.e., if the surgeon is pointing the CI to the right, the end-effector articulates left and the same for the vertical motion (up-down, down-up).

Here we describe our findings in a comparative research, testing performance and adaption, between the

different control designs of the HandXTM's CI.

MATERIALS AND METHODS

A. Participants

A total of 17 participants were included in this study. Participants were divided into four user groups, based on their background and experience with the HandX device: (1) HX naïve group (N=6), which had no significant previous experience with the device; (2) HX intermediate group (N=4), which had some previous experience with the device; (3) HX skilled group (N=3), which had a significant experience with the device, and also included one surgeon; and (4) surgeon group (N=4), which had no previous experience with the device, but had an experience performing laparoscopic procedures.

B. Apparatus

Prior to the experiment, participants were given a general overview of the experimental protocol and were asked to perform a tip-positioning skill tasks on surgical training setup (Fig. 2A) using the HandXTM in both CI control methods.

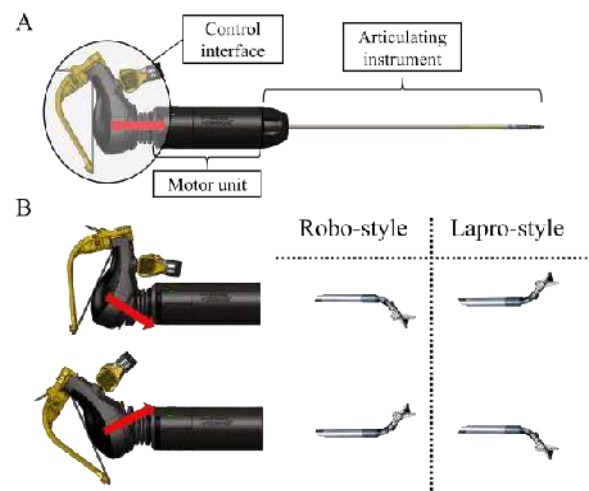


Fig. 1 The HandXTM device. (A) The device; (B) the difference in the end-effector's articulation between the Robo-style control and the Lapro-style control. The red arrow signifies the pointing direction of the control interface, held by the surgeon.

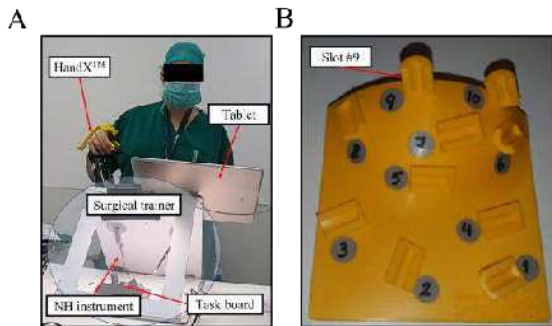


Fig. 2 The experiment setup. (A) The surgeon holding the HandX™ device, in front of the surgical trainer; (B) the tip positioning skill task.

The tip-positioning skill task (Fig. 1B) is consisted of 10-numbered slots, where each slot is situated at a different orientation on the task board. This task simulates the maneuverability and dexterity needed in a surgical scenario, and which the HandX™ provides to the user. The goal in this task is to position the end-effector of the instrument (HX needle holder (NH)) in

each of the slots, going from 1 to 10 as fast as possible. Upon completion, task completion time is measured, and a performance metric (slot rate [1/minute]) is calculated.

Performing the task, participants were situated in front of a surgical trainer, as in Fig. 2A, and held the HandX™ device in their right hand. The NH instrument,

connected to the device was inserted into the task board workspace through a port in the surgical trainer. Participants viewed the task board via a tablet, situated above a dedicated port in the surgical trainer allowing the entire workspace to be observed.

C. Protocol

Participants completed the experiment protocol which included:

- 1) **Tutorial of device usage.** Participants were asked to read the device's instruction prior to performing the experiment, and were given a device usage tutorial.
- 2) **Tip positioning skills task.** Participants performed the skill task with the HandX™ in each control configuration, in succession.
- 3) **Semi-structured post-interviews.** Participants were given a questionnaire to fill out about their experience with each control configuration.

D. Data Measures and Analysis

Performance data (slot rate metric) and subjective feedback (questionnaire) were collected. A paired t-test was conducted for each group (separately) to determine the effect of the control configuration.

RESULTS

Table I summarizes the performance metric for the tip positioning task, averaged for each group, and sub-groups. In both the naive and surgeon groups, the step

rate was significantly higher in the inverted control (Lapro-style) than in the direct control (Robo-style) - $t=5.202$ ($p<0.001$) for the HX naive group, and $t=8.49$ ($p<0.001$) for the surgeon group. These results suggest that for non-skilled users the Lapro-style control may be more natural. For the intermediate group inverted control step rate was also higher but not significantly. Lastly, for the HX skilled group the Lapro-style control step rate was significantly lower ($t=-3.859$, and $p<0.01$) which may suggest that the skilled participants' previous experience had impaired their ability to use the device using the Lapro-style.

The filled out questionnaire and the verbal comments, made by the participants revealed that the reactions to the Lapro-style, as well as the experience with it, were very positive towards that control style, and most participants (excluding the HX expert group) had favored it over the Robo-style control.

TABLE I Statistical analysis of the step rate. Bold cells are statistically significant ($p<0.05$)

Group	Robo-style	Lapro-style	Difference	Significance
HX naïve	1.7 ±	9.52 ±	7.82 ±	$t=5.202$,
HX intermediate	1.70 7.52 ±4.10	1.23 10.04 ±4.61	0.65 2.52 ±2.47	$p<0.001$ $t=1.368$, $p=0.78$
HX skilled	17.5 ±3.77	9.29 ±4.32	-8.21 ±7.44	$t=-3.859$, $p<0.01$
Surgeons	3.95 ±2.08	19.58 ±5.26	15.63 ±3.88	$t=8.49$, $p<0.001$

DISCUSSION

The HandX™ is a digital electromechanical device which allows rapid testing of features that can increase performance to be made by simply applying software changes. Here we implemented a control design change in the form of the Lapro-style. This modification significantly improved intuitiveness in naive HandX™ users, both surgeons and non-surgeons. These suggest that operating an articulating instrument in a fulcrum-effected environment, e.g., laparoscopic surgery, may require the control interface to be consistent with the fulcrum effect as well. This is an example of how the HandX digital platform can empower the minimal invasive surgical landscape by allowing rapid improvements with personalized digital platforms that combine the power of robotics with the ease and affordability of hand-held solutions.

REFERENCES

- [1] "Human xtensions website." [Online]. Available: <https://www.human-x.com>
- [2] I. R. Crothers, A. G. Gallagher, N. McClure, D. T. D. James, and J. McGuigan, "Experienced laparoscopic surgeons are automated to the "fulcrum effect": An ergonomic demonstration," *Endoscopy*, vol. 31, no. 05, pp. 365–369, 1999, 365.
- [3] C. Gruijthuisen, L. Dong, G. Morel, and E. V. Poorten, "Leveraging the fulcrum point in robotic minimally invasive surgery," *IEEE Robotics and Automation Letters*, vol. 3, no. 3, pp. 2071–2078, 2018.

Inexact Multi-Task Learning for Fetal Anastomoses Detection

Alessandro Casella^{1,2}, Gaia Romana De Paolis², Elena De Momi², Dario Paladini³, Sara Moccia⁴, and Leonardo S. Mattos¹

¹*Department of Advanced Robotics, Istituto Italiano di Tecnologia, Genoa, Italy*

²*Department of Electronics, Information and Bioengineering, Politecnico di Milano, Milan, Italy*

³*Department of Fetal and Perinatal Medicine, Istituto “Giannina Gaslini”, Genoa, Italy*

⁴*The BioRobotics Institute and Department of Excellence in Robotics & AI, Scuola Superiore Sant’Anna, Pisa, Italy*

INTRODUCTION

Twin-to-Twin Transfusion Syndrome (TTTS) is a rare pathology that may affect monochorionic twin pregnancies. TTTS depends on the unbalanced blood transfer from one twin (the donor) to the other (the recipient) through abnormal placental vascular anastomoses. Currently, the treatment for TTTS consists of the photo-ablation of abnormal anastomoses in fetoscopic laser surgery [1]. Residual anastomoses still represent a major complication [2] and their identification is not a trivial task. Visual challenges such as small field of view, amniotic fluid turbidity, low-resolution imaging, and unfavourable views are due to the position of the insertion site for the tools. To support surgeons, researchers are working on vessel and placenta segmentation [3], [4]. Recently, [5] presented the first multi-centre large-scale dataset to improve the current state-of-the-art in segmentation and registration in fetoscopy. However, to date, there is no work in the literature on anastomosis detection. There is also no available datasets for this task.

This work aims to develop a deep-learning-based framework for anastomosis detection in intra-operative fetoscopic videos from inexact labels. Considering the challenges of labelling anastomoses, we propose a weakly-supervised strategy by training a multi-task convolutional neural network (CNN) for (i) segmenting vessels in the fetoscopy frame and (ii) classifying frames as containing anastomoses or not. Relying on class activation mapping (CAM), anastomosis detection is then accomplished.

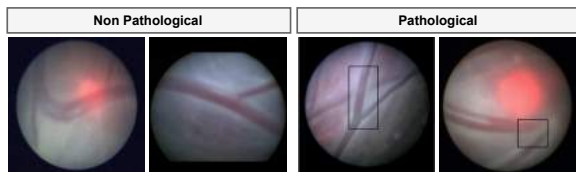


Fig. 1: A sample of the anastomoses dataset. Black bounding boxes highlight the pathological anastomosis.

MATERIALS AND METHODS

In this work, we want to exploit the representation learning capability of CNNs for inexact supervised anastomoses detection. CNNs can extract meaningful features from data, and CAM can be used for investigating the

CNN visual encoding process and localising anastomoses. As shown in Fig. 2, the proposed framework is composed by a backbone and three branches. The backbone comprises (i) a dense-feature encoder and (ii) a Feature Pyramid Network (FPN) decoder. The decoder is connected to a Y-shape head consisting of two branches, for vessel segmentation and frame classification. The localisation branch extracts activation maps from the last three segmentation blocks of the encoder to perform anastomoses detection with CAM.

The encoder is based on the DenseNet121 architecture. Dense connectivity in DenseNet is implemented to improve gradients’ flow among layers, avoiding the problem of gradient vanishing in deeper layers and improve network training efficiency. The decoder is designed as FPN to leverage feature hierarchy and semantics learning at different scales. All the feature maps from each pyramid level in the FPN are processed by a segmentation block to produce rough segmentation maps, one at each pyramid scale. The segmentation block contains a 3×3 convolution followed by *Group Normalisation* and *ReLU* activation. The partial segmentation maps are summed up and processed by the Y-shape head. The segmentation branch in the Y-shape head consists of 1×1 convolution for channel reduction, bilinear upsampling to recover the original size, and sigmoid activation. The classification branch is made of a Global Average Pooling (GAP) layer followed by three fully connected layers. We add one dropout layer to each of the first two layers to regularise the training process [6]. In the localisation branch, we compute the weighted sum of all Gradient-weighted Class Activation Map (Grad-CAM) for the segmentation blocks in the decoder, which represents the feature map response at each scale. The overall activation map is then rescaled using MinMax scaling, and a threshold is applied to extract regions of interest that may contain anastomoses. We experimentally found that 0.75 is a reasonable threshold value.

A. Experimental protocol

To develop and test our framework, we built a dataset by merging a publicly available dataset¹ presented in [4] that we extended with additional data collected at

¹<https://www.ucl.ac.uk/interventional-surgical-sciences/fetoscopy-placenta-data>

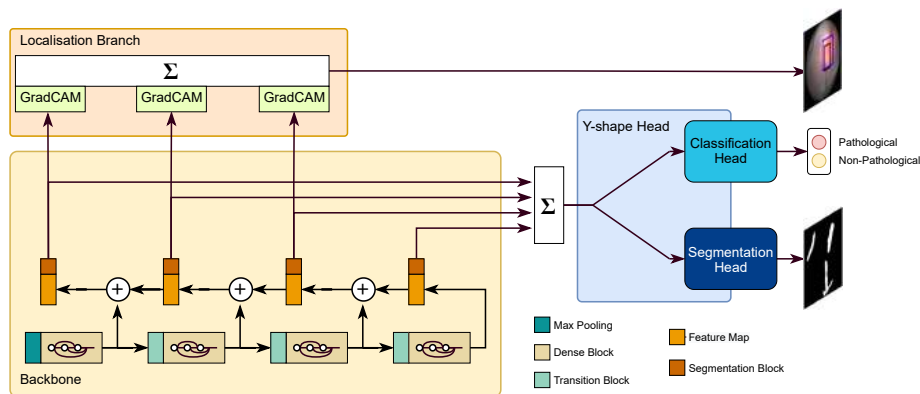


Fig. 2: Overview of the proposed WAYNet framework.

TABLE I: Results of the ablation studies for the backbone network. In the baseline the Segmentation Head is missing.

		Classification			Segmentation	Detection
		Acc	Rec	Prec	IoU	IoU
Baseline	ResNet50	0.6200	0.0570	0.7500	-	0.0424
	ResNet50	0.6827	0.5377	0.6064	0.5770	0.0062
Fine-Tuning	Dense	0.7380	0.5849	0.6966	0.5426	0.0217
	ResNet50	0.9889	0.9811	0.9905	0.5976	0.0570
Multi-Task	Proposed	0.9668	0.9906	0.9292	0.5314	0.2206

Istituto Giannina Gaslini, Italy for a total of 18 TTTS procedures. We manually extracted 1476 frames and asked an expert clinician to annotate vessels and the presence of pathological anastomoses in each frame. The 27.6% of frames includes pathological anastomosis. A sample of our dataset is shown in Fig. 1. For testing the detection performance, we further annotated 83 frames from 3 additional patients with bounding boxes. The overall framework was trained end-to-end using a combination ($L_{Overall}$) of two loss functions. $L_{Overall}$ is defined as: $L_{Overall} = L_S + L_C$, where L_S is the binary cross entropy used for the segmentation task and L_C is the weighted cross entropy used for the classification task. We used a weighted cross entropy to account for class imbalance.

We evaluated the performance of the proposed framework in terms of accuracy (Acc), recall (Rec), and precision ($Prec$) for the classification task. As for the segmentation and detection task, intersection over union (IoU) was utilized. A Wilcoxon test assessed the statistical significance of the results.

In the ablation study, we investigated several configurations and training strategies for our framework. The **Baseline** consists of a classification network based on ResNet50. In **fine-tuning** configurations (ResNet50 and Dense-FPN), we trained the backbone on vessel segmentation and then on the classification task, while in **Multi-Task** tests (ResNet50 and Proposed), we trained the backbone on both tasks end-to-end.

RESULTS

As shown in Table I, the proposed framework achieved good performance in classification ($Acc = 0.9668$, $Rec = 0.9906$, $Prec = 0.9292$) and segmentation ($IoU = 0.5314$). For anastomoses detection we achieved an $IoU = 0.2206$. Our framework performed comparably with the other

tested approaches for the classification and segmentation task, while it showed by far the best performance for the anastomosis detection task.

CONCLUSIONS AND DISCUSSION

This paper presented a first step towards the automatic localisation of anastomoses in TTTS surgical videos. Our framework showed promising results and outperformed tested approaches for weakly-supervised anastomoses detection from inexact labels. The vessel segmentation and anastomoses classification performance of our framework is reliable, with few misclassifications. Sometimes pathological and non-pathological anastomoses may look very similar, affecting classification performance, especially with such small datasets. Contrastive learning approaches might tackle this challenge. However, the high imbalance between classes could be an issue for those techniques. Collecting more data and data stratification are reasonable improvements to our experimental protocol. Despite achieving promising results, there is still work to do to tackle the complexity of the task.

REFERENCES

- [1] Roberts et al. Interventions for the treatment of twin-twin transfusion syndrome. *Cochrane Database of Systematic Reviews*, 2014(1), 2014.
- [2] Lopriore, et al. Residual Anastomoses After Fetoscopic Laser Surgery in Twin-to-Twin Transfusion Syndrome: Frequency, Associated Risks and Outcome. *Placenta*, 28(2-3):204–208, 2 2007.
- [3] Casella, et al. A shape-constraint adversarial framework with instance-normalized spatio-temporal features for inter-fetal membrane segmentation. *Medical Image Analysis*, 70:102008, 2021.
- [4] Bano, et al. Deep placental vessel segmentation for fetoscopic mosaicking. In *International Conference on Medical Image Computing and Computer-Assisted Intervention*, pages 763–773. Springer, 2020.
- [5] Bano et al. FetReg: Placental Vessel Segmentation and Registration in Fetoscopy Challenge Dataset. *ArXiv*, 2021.
- [6] Lee, et al. Robust tumor localization with pyramid grad-cam. *ArXiv*, abs/1805.11393, 2018.

EndoVine: Soft Robotic Endoscope for Colonoscopy

Ameya Pore*, Nicola Piccinelli*, Giacomo De Rossi*, Matteo Piano,
Daniele Meli*, Diego Dall’Alba*, Riccardo Muradore*, and Paolo Fiorini*

*University of Verona, Italy
[name].[surname]@univr.it

INTRODUCTION

Colonoscopy is the gold standard examination procedure for screening colorectal cancer (CRC), providing the ability to inspect the lower digestive tract [1]. Standard colonoscopy is carried out with a minimally invasive approach based on a flexible endoscope controlled by the steering knobs. However, for routine screening, the intrusive nature of the intervention, the rigidity of the device and the lack of intuitiveness in steering can make the experience highly unpleasant to the recipient [2]. Patient discomfort and pain are due to tissue stretching and friction as the endoscope is pushed through the colon [1]. Furthermore, the use of rigid instruments introduces risks such as tissue perforation and anaesthesia-related adverse events [2]. Overcoming the design limitations of the flexible endoscope by using soft material can reduce both tissue stretching and friction, making it more tolerable for the patient.

Soft everting robots that show growth from the tip have demonstrated successful application in navigating highly constrained environment without damaging it. Tip-extending soft robots, called vine robots, take flexible film as body material and air pressure as input power to propel forward [3]. Natural orifice intraluminal procedures that operate through constrained bodily lumens such as colon, oesophagus, and trachea, represent suitable scenarios for vine robots. Recent work has investigated soft pressure-driven colonoscope via inflation of tip balloons [4], which may cause harmful local tissue stretching. Another work by Dehghani et al. developed a pneumatically driven colonoscopy robot [5]; however, their prototype does not allow retraction of the tip and does not provide room for instruments. Retraction of vine robots is believed to be a challenging problem due to the buckling of the robots [3].

Therefore, in this abstract, we present an Endoscopic Vine robot (EndoVine) designed for colonoscopy with a novel retraction mechanism. EndoVine comprises a double inverted soft inflatable sleeve that propels the tip using internal pneumatic propulsion. It will be equipped with an internal flexible channel for the camera, light source and working instruments to enable bowel inspection. The soft robotic body has been designed to be disposable, reducing the risk of infection transmission, which is a concern with traditional flexible endoscope

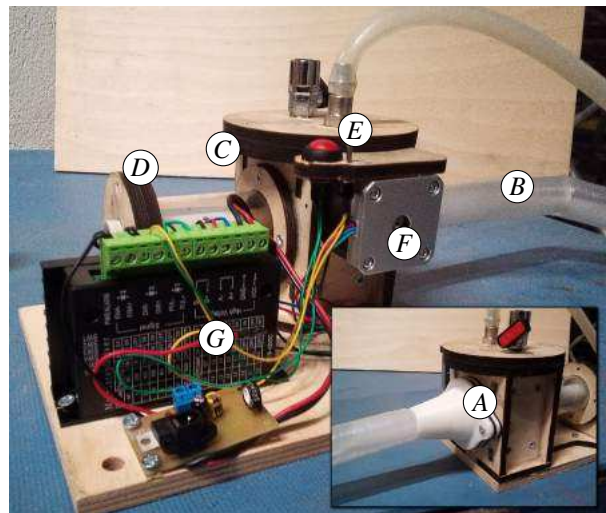


Fig. 1 The prototype of the EndoVine robot used in the experiments. (a) the anatomical interface, (b) the robot sleeve, (c) the airtight chamber, (d) the opening for the instrument insertion, (e) the air pressure connector, (f, g) the motor and its controller.

[5]. In the following sections, we present the design of EndoVine and demonstrate its feasibility in navigating and retracting the colonic tract in a controlled manner. For the experiments, a simplified colon model was created referring to the CT colonography dataset [6] considering the opinion of the domain expert to conform with the shape and size of the average human colon. The colon model was 3D printed with a rigid polymer.

MATERIALS AND METHODS

EndoVine improves the technology of vine robots [3] making it suitable for colonoscopy with the adoption of a sleeved pressure chamber (Fig. 1). This approach allows for a free instrument channel in the centre of the robot through which the protruding tip carries a soft, bendable tube. The concept is based on the robotic growth inside the cavity to protect the surrounding sensitive tissue when instruments are inserted. By the properties of vine robots, the expansion occurs only at the tooltip, thus leaving the material in contact with the tissue static, reducing the overall friction.

The robot consists of a main pressurised airtight chamber, with the entry for the instrument channel on its



Fig. 2 The experimental setup. The EndoVine travels through the rectum (A) into the sigmoid curve (B). It adapts its shape to overcome the curve to reach the splenic flexure (C).

posterior side. There is an anatomical interface on the anterior side of the chamber from where the robot's sleeve grows. The airtight chamber has an electric stepper motor used to control the tip's eversion speed and provide the retraction of the robot's body. During retraction, the pressure is decreased while the stepper motor wraps the sleeve along a rigid tube at the posterior of the airtight chamber. The electric motor, using a set of rollers internal to the airtight chamber, wraps and unwraps the sleeves along the tube while the instrument channel goes through the back port. This is possible because the pressure of the sleeve keeps the internal instrument channel rigidly coupled to it.

The instrument channel for this preliminary setup is a silicon tube with 10 mm diameter. The soft sleeve is made with natural rubber latex and polymers, complying with ASTM F1671 clinical specifications. It has a diameter of 38 mm when inflated to be compatible with the anatomical dimension of the human colon.

RESULTS

The experiments show a preliminary evaluation of the navigation capabilities of our prototype using the colon model in Fig. 2. The air pressure to inflate the soft sleeve is tuned up to 0.15 bar maximum to reduce the risk of rupture and high forces on the surrounding anatomy. The entire length of the sleeve has been lubricated with Vaseline to reduce friction. The robot, as shown in Fig. 2, can traverse through the sigmoid curve and approach the splenic flexure, which are considered challenging bending curves [5]. To visualise the robot moving through the phantom, please refer to the supplementary video ¹, where a rollout of the experiment is shown. The tip stops at approximately 60% of the colon length due to the current maximum length (46 cm) of the sleeve and the internal channel. The total navigation time is ~ 90 s comparable with that of standard endoscopists. Although representative of the general conformation and size of a real adult colon, the rigid colon model used to test the platform does not allow any flexing to accommodate the protruding robot tip.

DISCUSSION

The soft robot endoscope solution for colonoscopy could positively impact in the early detection of CRC by reduc-

ing patient discomfort and enhancing social acceptance. The sleeved pressure chamber solution proposed in this abstract introduces an inner flexible channel, which will pave the way towards safe, non-traumatic, intra-operative flexible instruments insertion. The current prototype requires further design and development: in particular, buckling shall be avoided during retraction. This can be done improving the wrapping mechanism in the posterior of the airtight chamber. Active steering mechanism at the tip of the robot will also be implemented to ensure successful navigation across challenging bends of the colonic tract, avoiding undesired pushing and friction on anatomical walls. Moreover, a more accurate selection of sleeve and inner chamber material will be required for the feasibility of a clinical application. We will finally perform more advanced testing of our prototype on more realistic deformable anatomical manikins with a longer sleeve and wider inner channel to improve navigation at most challenging colon bending and minimise the overall intrusiveness of the device.

ACKNOWLEDGEMENTS

This work was supported by the ATLAS project. The ATLAS project has received funding from the European Union's Horizon 2020 research and innovation programme under the Marie Skłodowska Curie grant agreement No 813782.

REFERENCES

- [1] G. Ciuti *et al.*, "Frontiers of robotic colonoscopy: a comprehensive review of robotic colonoscopes and technologies," *Journal of Clinical Medicine*, vol. 9, no. 6, p. 1648, 2020.
- [2] H.-E. Huang *et al.*, "Autonomous navigation of a magnetic colonoscope using force sensing and a heuristic search algorithm," *Scientific reports*, vol. 11, no. 1, pp. 1–15, 2021.
- [3] L. H. Blumenschein *et al.*, "Design, modeling, control, and application of everting vine robots," *Frontiers in Robotics and AI*, vol. 7, 2020.
- [4] L. Manfredi *et al.*, "A soft pneumatic inchworm double balloon (spid) for colonoscopy," *Scientific Reports*, vol. 9, 2019.
- [5] H. Dehghani *et al.*, "Design and preliminary evaluation of a self-steering, pneumatically driven colonoscopy robot," *Journal of medical engineering & technology*, vol. 41, no. 3, pp. 223–236, 2017.
- [6] K. Clark, B. Vendt, K. Smith, J. Freymann, J. Kirby, P. Koppel, S. Moore, S. Phillips, D. Maffitt, M. Pringle *et al.*, "The cancer imaging archive (tcia): maintaining and operating a public information repository," *Journal of digital imaging*, vol. 26, no. 6, pp. 1045–1057, 2013.

¹Supplementary Video: <https://youtu.be/ahpHrZtOfmU>

Development and Control of a Robotic Simulator for Peristaltic Motion

Jarrett Ten¹, Quentin Lahondes¹, Shuhei Miyashita¹⁻², Dana Damian^{1,2}

*Automatic Control and Systems Engineering Department, University of Sheffield,
Portobello Ln, Sheffield S1 3JD, UK,*

²*Insigneo Institute for in silico Medicine, University of Sheffield, UK
jarrettten@gmail.com, d.damian@sheffield.ac.uk*

INTRODUCTION

Up to 33.5% of patients suffering from gastrointestinal (GI) malignancies endure at least one non-lethal operative complication [1]. This signals a need for a change to traditional invasive surgical methods. In this regard, in vivo medical robots (IMR) are seeing fast-paced progress providing efficient therapies and reducing patient trauma. IMRs aim to travel throughout the body via peristalsis through the gastrointestinal tract (GIT), conducting diagnostics and microsurgeries from within. Peristalsis can be defined as the repeated waves of circular contractions and relaxations of the gut wall forcing contents (bolus) along the GIT. Many of these technologies feature novel designs, smart materials and complex control to match the dynamic conditions of the treated disease [2]. Examples include the capsule endoscopic robot capable of providing visual diagnostics of the GIT [3], deployable patch and plug aimed at removing and patching stomach ulcers [4], and robotic implants for tissue regeneration [5]. At the same time, it is critical to also develop testing platforms which can exhibit realistic biological conditions to extensively optimise and validate these novel technologies towards their progression to the clinic.

Numerous gastrointestinal simulators (GIS) have been developed to evaluate IMRs and have shown to reduce cost and length of testings, and improve the ethicality of the medical industry by limiting the number of animal trials conducted. However, currently developed GIS such as the Human Gastric Simulator [6] and the Mechanical Gastric Simulator [7] are focused on replicating chemical digestion, but gave limited attention on realistic mechanical digestion, utilising gravity as an aid to the mechanical digestion process. This then limited the accuracy of the simulated motion, restraining the ability to understand the influence of the GIT on the movements of IMRs and to critically evaluate their performances. In addition, few studies quantify in vivo peristaltic motion consisting of periodic contractions and dilations of the GIT which further complicates the evaluation of developed GIS and its ability to critically assess IMRs. This paper introduces a novel simulator that replicates the peristaltic motion of the GIT to enhance the optimisation and testing of IMRs.

MATERIALS AND METHODS

Model: A simple peristaltic wave can be described as a sinus function of an (x) coordinate and time (t) as seen

in equation (1). Where r is the radius of the GI tubular organ at time t , r_0 is the initial radius of the GI tubular organ, a is the amplitude of the wave, X is the wavelength and v is the wave speed [8].

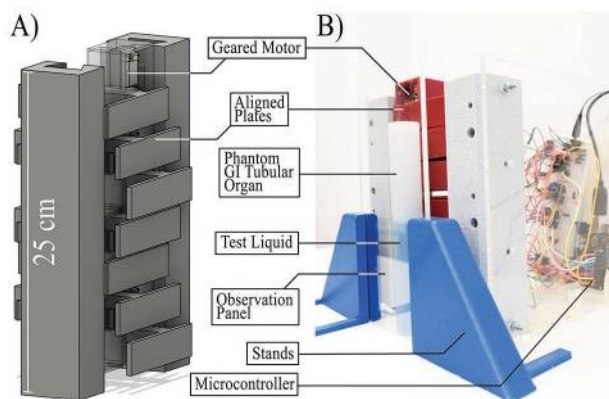


Fig. 1. A) Computer aided design of the simulator (25x4x5 cm) showing peristaltic motion B) Experimental setup of the simulator (in red) with the phantom organ filled with test liquid, placed inbetween the simulator and the observation panel.

$$r(x, t) = r_0 + a \sin\left[\frac{2\pi}{\lambda}(x - vt)\right] \quad (1)$$

Simulator: To reproduce the in vivo behaviour of peristaltic motion, the simulator possesses an array of seven aligned plates successively compressing and relaxing the phantom organ (Figure 1A). The aligned plates are controlled independently and individually by a single microcontroller equipped with four motor drivers and a DC motor for each plate. To obtain sufficient actuation force, the motors were equipped with gear boxes of ratio 298:1 and are connected to a rack and pinion system to achieve the displacement needed to simulate peristaltic motion. To replicate the mechanical properties of the GIT, a GI phantom tubular organ was fabricated using Ecoflex-0050; a silicone rubber known for its mechanical similarities with GIT tissues [9].

Experimental Setup: The simulator was placed vertically with the phantom organ in between the plates and an observation panel made out of acrylic (Figure 1B). The phantom organ was then filled with dyed water. The simulator aims to provide a one-dimensional wave of contractions, which deforms the phantom organ and displaces the bolus along the wave.

Experimental Procedure: a , X and v of equation (1) were varied via the microcontroller in an open-loop control system and the resultant motion of the displaced water level was recorded and imported into Tracker

(<https://physlets.org/tracker/>). For each of the variables, three trials were performed.

Characterisation of Peristaltic Motion: To allow a comparison between the simulated motion with in vivo peristaltic motion, the vertical displacement of the test sample was evaluated against tracking data of a patient swallowing water [10]. The parameters were model-matched by selecting the best a , X and v to match with the patient-specific waveform resulting in a model for peristaltic motion as shown in equation (2).

$$r(x, t) = r_0 + 0.02\sin\left[-\frac{2\pi}{16}\left(\frac{x}{16} - 0.061t\right)\right] \quad (2)$$

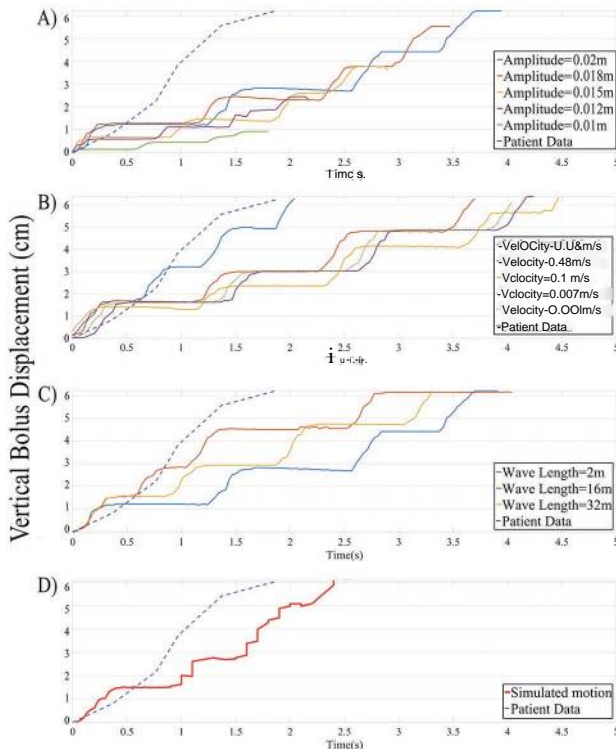


Fig. 2. Raw vertical bolus displacement plotted against time with the end point defined and overlaid with patient data with varying A) amplitude B) wave velocity C) wave length. D) vertical bolus displacement of a test sample in a model-matched simulator overlaid with patient data.

Accuracy of the Simulated Peristaltic Motion: The matched model highlighted in equation (2) was implemented into the simulator to further evaluate its ability to accurately mimic peristaltic motion.

RESULTS

Variations of a , X and v are shown in Figure 2A, 2B and 2C. The obtained results have been plotted against patient-specific data and can be seen in Figure 2D. With Figure 2D it can be seen that the obtained waveform more closely resembles that of the patient specific data, hence having a shorter waveform when compared to Figures 2A, 2B and 2C. It is also noted from 0-0.5 seconds the accuracy optimised settings allowed the simulator to effectively mimic the motion of peristalsis to transport a bolus upwards within the phantom organ. However, from 0.5 seconds onwards, the simulator's performance

deviated from patient data due to the lack of force exerted by a single compression plane and the inability to evenly contract around the phantom organ.

DISCUSSION

This study presents the development of a mechanical peristaltic motion simulator for the simulation and evaluation of IMRs as it travels throughout the GIT. In combination with a developed phantom organ, the developed simulator is able to replicate peristaltic waves with variable amplitudes, wavelengths and velocities to allow benchtop studies of the GI physiology and pathologies. The performance of the simulator was evaluated through calculating the mean relative error between in vivo data and the obtained experimental results, and it indicated a similarity of 79.9% was achieved. However, the accuracy of the simulator was limited by the width of the aligned plates which restricts the simulator to a resolution of 15.1 mm. In addition, the current simulator is restricted to uni-axial contractions and will be addressed in future work. We envisage the use of this simulator to better evaluate future IMRs, to reduce the number of animal trials conducted and develop safer, more ethical medical robots and devices.

REFERENCES

- [1] Rady MY., Ryan T., Starr NJ., Perioperative Determinants of Morbidity and Mortality in Elderly Patients Undergoing Cardiac Surgery, *Critical Care Medicine*, Volume 26, Issue 2, Page 225-245, 1998.
- [2] Guang-Zhong Yang, Steve H. Collins, Paolo Dario, Peer Fischer, Ken Goldberg, Cecilia Laschi, Marcia K. McNutt, Five years of Science Robotics, *Science Robotics*, 6, 61, (2021).
- [3] Kim, L., S. C. Tang, and S. -S. Yoo., Prototype Modular Capsule Robots for Capsule Endoscopies, 13th International Conference on Control, Automation and Systems (ICCAS), IEEE, 2013.
- [4] D'Argente D.P., Perry A., Iwata S., Iwasaki Y., Will H., Fabozzo I., Iwase A., Damian, D., Rus D., Miyashita, S., Programmable Medicine: Autonomous, Ingestible, Deployable Patch and Plug for Stomach Ulcer Therapy, *IEEE International Conference on Robotics and Automation (ICRA)*, Page 1511 - 1518, 2018.
- [5] Mohamed Atwya, Can Kavak, Elodie Alisse, YanQiang Liu, Dana D. Damian, Flexible and Expandable Robot for Tissue Therapies - Modeling and Design, *IEEE Transactions on Biomedical Engineering*, 68,2, (568-578), (2021).
- [6] Kong F., Singh R.P., A Human Gastric Simulator (HGS) to Study Food Digestion in Human Stomach, *Journal of Food Science*, Volume 75, 2010.
- [7] Barrows L., Retamal C., Torres H., Zuniga R.N, Troncoso E., Development of an in vitro mechanical gastric system (MGS) with realistic peristalsis to assess lipid digestibility, *Food Research International*, Volume 90, Page 216-225, 2016
- [8] Ono M., Kata S., A Study of an Earthworm Type Inspection Robot Movable in Long Pipes, *International Journal of Advanced Robotic Systems*, Volume 7, issue 1, 2010.
- [9] Leonardo M., Gioia L., Tommaso M., Leonardo R., Arianna M., Comparative Analysis of Occlusion Methods for Artificial Sphincters, *Artificial Organs*, Issue 44, Page 995-1005, 2020.
- [10] Shaughnessy EE., Towbin A., Prosser J., Neonate with Choking, *JAMA Pediatr*, Volume 169, Issue 3, Page 281-282, 2015.

Envisioning Robotic Exoscope: Concept and Preliminary Results

Alice Valeria Iordache^{1,*}, Alessandro Casella^{1,2,*}, Elisa Iovene¹, Junling Fu¹, Federico Pessina³, Marco Riva³, Giancarlo Ferrigno¹, Leonardo S. Mattos², and Elena De Momi¹

¹Department of Electronics, Information and Bioengineering, Politecnico di Milano, Milan, Italy

²Department of Advanced Robotics, Istituto Italiano di Tecnologia, Genoa, Italy

³Humanitas Research Hospital, Milan, Italy

*These authors contributed equally.

INTRODUCTION

The introduction of a surgical microscope in neurosurgery increased the spectrum and safety of interventions. The surgeon operates with both hands on the patient while also controlling the visualization system to provide the proper view. Despite the benefits of the microscope, low ergonomics may lead to long-term effects on the musculoskeletal system. The bulky binocular system may limit the setup's flexibility, hindering robotics integration into the operating theatre.

Recently, the introduction of the exoscopes overcame those limitations by enabling a flexible and ergonomic working environment, combined with improved image quality. The exoscope is fixed on the surgical field through pneumatic arm holders that the surgeon can move manually or through foot control. Although providing the surgeon with enhanced vision, the complexity of its use has emerged as a limiting factor [1]. The continuous switching from operation theatre and visualization system reduces the smoothness of the surgical procedure, and the steep learning curve of the foot pedal [2] leads to switching to the conventional microscope in most cases. Visual servoing

techniques [3] have been primarily studied in the context of camera automation in minimally invasive laparoscopy [4]. Its potential has become even more significant in the context of neurosurgery, as the only solution for tracking instruments is to employ vision sensors. However, visual servoing techniques for exoscope automation are currently limited due to open challenges in neurosurgical practices. This work proposes a framework for an autonomous vision-guided camera holder that tracks and follows a selected surgical instrument based on a visual servoing technique. We envision this solution to automate the exoscope in neurosurgery, providing intuitive control of the system and reducing surgeon workload and operating time.

MATERIALS AND METHODS

A. Visual Servoing Framework

In this study, a markerless position-based visual servoing framework was implemented as illustrated in Fig. 1. A 7 DOF serial manipulator (KUKA LwR 4+) was used with a stereo camera mounted in an eye-in-hand configuration to simulate the exoscope system. An object-detection

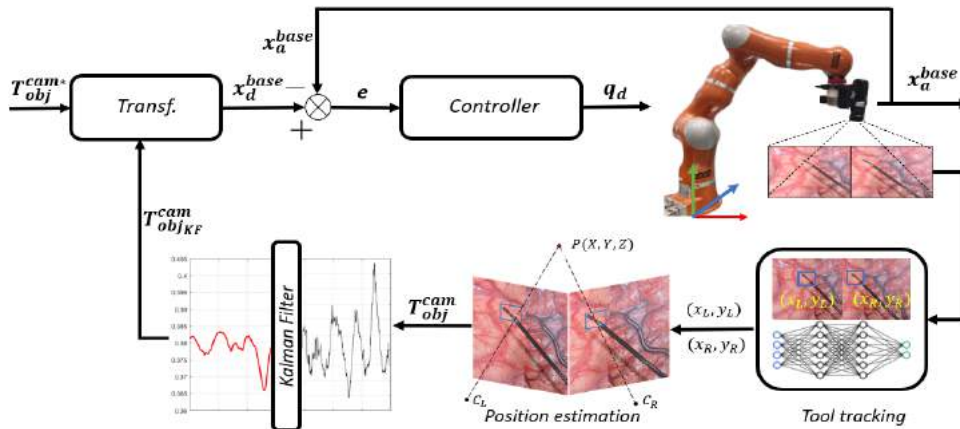


Fig. 1 System's overview: tool coordinates (x_R, y_R) and (x_L, y_L) are identified in the image space. The position $P(X, Y, Z)$ in the 3D space is estimated and filtered by the Kalman Filter T_{objKF}^{cam} . This, together with the desired position T_{obj}^{cam*} , are transformed and used to compute the desired position of the camera x_d^{base} . The desired and actual position of the camera, x_a^{base} , are used to calculate the error signal e . The controller computes the required joint positions q_d that compensate for the error.

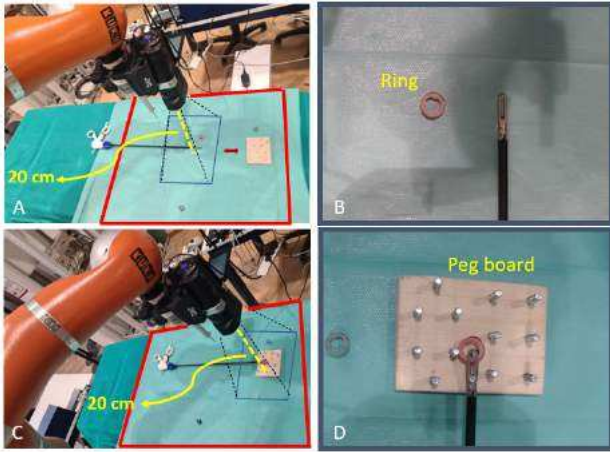


Fig. 2 Design of the task, only one ring is seen by the camera, camera need to be moved to reach the pegboard.

neural network *Yolov3*[5] was trained to identify the tip of a surgical instrument from the images acquired by the 3D camera. The training dataset was composed of 5000 images, 1800 were extracted from the *EndoVis 2017 challenge dataset* [6] while the remaining were recorded and manually annotated.

The position reconstruction was computed by triangulation using DLT, while the Kalman filter was applied, considering a three-dimensional constant velocity model of the instrument's motion. The desired position of the instrument with respect to the camera T_{obj}^{cam} was defined in such a way that the instrument is kept at the center of the image. Only motions along the *XY*-plane have been implemented since, in neurosurgery, movement along the depth is only required for focus adjustments. Finally, a position controller was employed to compensate for the error between the desired and actual position of the camera.

B. Experimental protocol

In order to test the usability of the system, a user study was carried out on ten non-medical subjects. The designed task was a pick-and-place in which users were asked to use a surgical instrument to pick up, one at a time, four randomly distributed rings in a defined workspace and place them on a target pegboard, as shown in Fig. 2. The distance in the *Z* direction between the camera and the task space was 0.2m and was kept fixed to provide a reduced Field of View (FoV) and force the user to move the camera to complete the task. Users were asked to perform the task exclusively by observing the scene on an external monitor where the camera FoV was displayed. The task was executed in two different modalities:

- 1) *Autonomous Camera Control (ACC)*: the user was able to activate and deactivate the autonomous motion of the camera by pressing a foot pedal.
- 2) *Joystick Control (JC)*: the user was able to move the camera using a foot-controlled joystick each time a different view of the scene was needed.

Three repetitions were performed for both modalities.

RESULTS AND DISCUSSION

The systems' functionality was evaluated in terms of tool's position density inside the image plane and execution time. Fig. 3 shows that in *ACC*, the density is higher at the center of the image than in *JC*. This proves that the *ACC* is more effective at keeping the instrument in the center of the image, providing a better view of the scene, which is crucial for optimal task performance. As for the execution

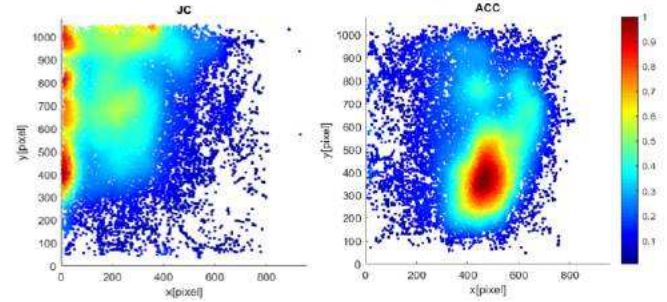


Fig. 3 Normalized instrument's tip density inside the image plane for the *JC* and *ACC* modalities

time, *ACC* showed better results, as illustrated in Table I. The mean and standard deviation of the execution time for the three repetitions are reported.

TABLE I Mean execution time, *std* and p-value for the three repetitions of the *JC* and *ACC* modalities.

Repetition	1		2		3	
	<i>JC</i>	<i>ACC</i>	<i>JC</i>	<i>ACC</i>	<i>JC</i>	<i>ACC</i>
Exec. time[s]	112 ±11.8	82.6 ±24.6	105.3 ±14.4	80.2 ±26.2	104.9 ±18.1	73.1 ±18.5
p-value	**		**		**	

This demonstrates that *ACC* reduces completion time by allowing the user to focus only on the main task and consequently perform better. Statistical analysis was conducted for all repetitions using the Wilcoxon signed-rank test with a 5% level of significance.

CONCLUSIONS AND DISCUSSION

Preliminary results have shown that the proposed marker-less visual servoing system has significant advantages over the currently used system. However, translating this system into operating room requires further improvements. Future studies will focus on the improvement of the tracking and control module.

REFERENCES

- [1] Mamelak, et al. A high-definition exoscope system for neurosurgery and other microsurgical disciplines: Preliminary report. *Surgical Innovation*, 15(1):38–46, 2008. PMID: 18388000.
- [2] Maurer, et al. Evaluation of a novel three-dimensional robotic digital microscope (aeos) in neurosurgery. *Cancers*, 13(17), 2021.
- [3] Chaumette and Hutchinson. Visual servo control. i. basic approaches. *Robotics Automation Magazine, IEEE*, 13:82 – 90, 01 2007.
- [4] Gruijthuijsen, et al. Robotic endoscope control via autonomous instrument tracking, 2021.
- [5] Redmon and Farhadi. *Yolov3: An incremental improvement*. 04 2018.
- [6] Allan, et al. 2017 robotic instrument segmentation challenge, 2019.

Minimum-parameter Adaptive Propulsion Matrix of Screw-type Magnetic Capsule Endoscopes

Adam J. Sperry and Jake J. Abbott

Department of Mechanical Engineering and Robotics Center, University of Utah
adam.sperry@utah.edu, jake.abbott@utah.edu

INTRODUCTION

Capsule endoscopes are employed for non-invasive video-based inspection of the intestines. Active control of such capsules continues to be an active area of research [1]. The most popular and seemingly most viable method to actively traverse the length of the small intestine involves equipping the capsule with an internal permanent magnet and an external screw-like thread (which would be coated in something like ice for swallowing) and rotating the capsule with an externally applied magnetic field such that rotation is converted to translation via the screw threads [2]–[7]. Empirical models of this method of locomotion have been proposed [3], [5], as have analytical models [2], [4], [7]. The model commonly used to describe the locomotion of screw-type capsules in a lumen (see, e.g., [4], [7]) is

$$\begin{bmatrix} v \\ \omega \end{bmatrix} = \begin{bmatrix} \alpha & \beta \\ \beta & \gamma \end{bmatrix} \begin{bmatrix} f \\ \tau \end{bmatrix} = P^{-1} \begin{bmatrix} f \\ \tau \end{bmatrix} \quad (1)$$

where f (units N) and τ (units N·m) are the non-lumen force and torque applied to the capsule along the lumen (e.g., due to magnetism and gravity), v (units m·s⁻¹) and ω (units rad·s⁻¹) are the resulting linear and angular velocity of the capsule through the lumen (see Fig. 1), and α , β , and γ (with consistent units) are the parameters that make up the inverse of the symmetric propulsion matrix P [8]; it can be shown that both P and P^{-1} must be positive-definite. Advanced control systems can make use of the model of (1) for optimal propulsion and localization (e.g., as an *a priori* process model in a Kalman filter [7]). However, the locomotion properties of these screw-type capsules change substantially as a function of the properties of their lumen environment (e.g., lubrication, lumen diameter). We have come to realize that adaptive controllers capable of updating the propulsion matrix to better reflect the capsule's current environment can lead to better controllers, but adaptive controllers come with their own challenges related to stability and convergence.

The model of (1) has the same structure used for flagella-like magnetic microswimmers [8]. Fluid viscosity appears linearly in each of the propulsion-matrix parameters such that it can be factored out, leaving purely geometry-dependent terms [8]. As such, the propulsion matrix describing a given microswimmer has only a

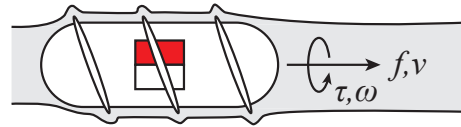


Fig. 1 An applied force f and torque τ on a screw-type capsule results in a linear velocity v and angular velocity ω . All four vectors are assumed to be aligned with the lumen.

single parameter that can vary as a function of the fluid environment, since the geometry-dependent terms are constant. Given the other similarities between the models used for magnetic microswimmers and screw-type capsules, in this paper we experimentally investigate if the propulsion matrix (and its inverse) of a screw-type capsule can be expressed as the product of a constant positive-definite symmetric matrix and a single scalar parameter that varies as a function of the environment.

MATERIALS AND METHODS

Experiments were conducted to determine the propulsion matrix for a screw-type capsule (mass 10.1 g, length 42.0 mm, diameter 13.5 mm without thread, 1 mm thread height, 13.5 mm thread pitch, rigidly embedded 4.76 mm cubic NdFeB Grade-52 permanent magnet with 0.126 A·m² dipole magnitude and Allegro A1392 Hall-effect sensors) in a lubricated rigid tube (inner diameter 19.1 mm). Three commercial water-based lubricants of different viscosities were used to simulate variations in the environment that may be encountered in the intestines: a liquid (Equate™ Personal Lubricant Liquid), a thin jelly (Equate™ Personal Lubricant Jelly), and a thick jelly (Kroger® Lubricating Jelly). The experiments consisted of two parts (Fig. 2). To estimate α and β , we applied constant force (via gravity) and no torque to the capsule by dropping the capsule through the tube at a 31° incline. The resulting average linear and angular velocity were measured via video recording at 60 FPS. To measure angular velocity, the capsule was marked with lines indicating fixed angular increments. Both average velocities were computed as the total distance traveled divided by the total time. 10 trials were conducted for each lubricant and an average was taken over these trials, and the measured velocity-force correspondences were used to estimate α and β . To

estimate γ , we used tri-axial Helmholtz coils (described in [9]) to apply a rotating uniform magnetic field to the capsule with constant angular velocity 0.4 Hz and constant field strength (5 mT) sufficient to maintain the capsule in synchronous rotation. Under these conditions, a constant torque and no force is applied to the capsule and torque measurements can be used with the observed angular velocity to estimate γ . Alternatively, we use a relationship that does not require torque measurements (which is valid only under zero-force conditions)

$$\gamma = \beta \frac{\omega}{v} \quad (2)$$

to compute γ from an observation of both the linear and angular velocity of the capsule. Using this relationship, it is possible to determine P^{-1} even for capsules that do not have embedded magnetic sensors. 10 trials were conducted for each lubricant and average velocities were taken over these trials. As the capsule advanced through the tube, the tube was moved in the opposite direction to keep the capsule in the central workspace of the Helmholtz coils.

RESULTS

The estimated inverse propulsion matrices for the environments simulated by each of the three qualitatively distinct lubricants are given below.

$$\begin{aligned} P_{\text{liquid}}^{-1} &= \begin{bmatrix} 11.9 & 231 \\ 231 & 197927 \end{bmatrix} \\ &= 197927 \begin{bmatrix} 6.0 \times 10^{-5} & 0.0012 \\ 0.0012 & 1 \end{bmatrix} \end{aligned} \quad (3)$$

$$\begin{aligned} P_{\text{thin jelly}}^{-1} &= \begin{bmatrix} 8.82 & 153 \\ 153 & 109114 \end{bmatrix} \\ &= 109114 \begin{bmatrix} 8.1 \times 10^{-5} & 0.0014 \\ 0.0014 & 1 \end{bmatrix} \end{aligned} \quad (4)$$

$$\begin{aligned} P_{\text{thick jelly}}^{-1} &= \begin{bmatrix} 5.65 & 106 \\ 106 & 79666 \end{bmatrix} \\ &= 79666 \begin{bmatrix} 7.1 \times 10^{-5} & 0.0013 \\ 0.0013 & 1 \end{bmatrix} \end{aligned} \quad (5)$$

The matrices above are also shown with the largest parameter (i.e., γ) factored out in the form

$$P^{-1} = \gamma \begin{bmatrix} \alpha/\gamma & \beta/\gamma \\ \beta/\gamma & 1 \end{bmatrix}. \quad (6)$$

As we move from the least viscous “liquid” to the most viscous “thick jelly”, we observe a dramatic decrease in each of α , β , and γ , with each reducing by a factor of 2, approximately. However, in the factored form, we observe a relatively small change in α/γ and β/γ , with no clear increasing or decreasing trend. We further observe that, if we simply assume constant average values of $\alpha/\gamma = 7.1 \cdot 10^{-5}$ and $\beta/\gamma = 0.0013$ across lubricant types, we would find that the error between each of the experimentally determined parameters and their respective average is at most 17%.

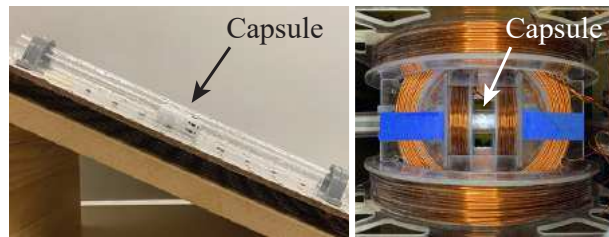


Fig. 2 (Left) Experiment with constant force and no torque. The capsule is dropped through the lubricated tube at 31° from horizontal. (Right) Experiment with constant torque and no force. A rotating uniform field is applied to the capsule using Helmholtz coils. As the capsule moves through the tube, the tube is moved in the opposite direction to keep the capsule in the central workspace of the coils.

DISCUSSION

Our results suggest that it is reasonable to express the propulsion matrix of a given screw-type capsule in a given environment, which has three independent parameters, as the product of a constant matrix and a single scalar parameter that varies as a function of the environment. The scalar parameter appears to be proportional to the environmental fluid viscosity, as expected based on the analogous model for microswimmers. The two-parameter constant portion, as well as a good initial guess for the factored term, can be determined experimentally (offline)—using a single environment, or results can be averaged over a small number of environments—and the scalar parameter can then be fit to new environments previously unencountered. The scalar parameter could be allowed to evolve in time to update the propulsion matrix as the capsule encounters variations in properties throughout the lumen, which will likely lead to improved performance of model-based controllers.

REFERENCES

- [1] G. Ciuti *et al.*, “Frontiers of robotic endoscopic capsules: a review,” *J. Micro-Bio Robot.*, vol. 11, no. 1-4, pp. 1–18, 2016.
- [2] K. Ikeuchi *et al.*, “Low invasive propulsion of medical devices by traction using mucus,” *Wear*, vol. 209, no. 1-2, pp. 179–183, 1997.
- [3] M. Sendoh *et al.*, “Fabrication of magnetic actuator for use in a capsule endoscope,” *IEEE Trans. Magn.*, vol. 39, no. 5, pp. 3232–3234, 2003.
- [4] Y. Zhang *et al.*, “A variable-diameter capsule robot based on multiple wedge effects,” *IEEE/ASME Trans. Mechatronics*, vol. 16, no. 2, pp. 241–254, 2011.
- [5] H. Zhou *et al.*, “Modeling and experimental characterization of propulsion of a spiral-type microrobot for medical use in gastrointestinal tract,” *IEEE Trans. Biomed. Eng.*, vol. 60, no. 6, pp. 1751–1759, 2013.
- [6] A. W. Mahoney and J. J. Abbott, “Generating rotating magnetic fields with a single permanent magnet for propulsion of untethered magnetic devices in a lumen,” *IEEE Trans. Robot.*, vol. 30, no. 2, pp. 411–420, 2014.
- [7] K. M. Popek *et al.*, “First demonstration of simultaneous localization and propulsion of a magnetic capsule in a lumen using a single rotating magnet,” in *Proc. IEEE Int. Conf. Robotics and Automation*, 2017, pp. 1154–1160.
- [8] E. M. Purcell, “The efficiency of propulsion by a rotating flagellum,” *Proc. Natl. Acad. Sci. USA*, vol. 94, p. 11307–11311, 1997.
- [9] A. W. Mahoney *et al.*, “Velocity control with gravity compensation for magnetic helical microswimmers,” *Adv. Robot.*, vol. 25, pp. 1007–1028, 2011.

Cable-Driven Linear Haptic Display for Medical Interventions

Max B. Schäfer, Julia Nawratil, Moritz Hemmer, Sophie Weiland, Peter P. Pott

Institute of Medical Device Technology, University of Stuttgart, Germany
max.schaefer@imt.uni-stuttgart.de

INTRODUCTION

The technological state-of-the-art in numerous medical procedures involves high-end actively actuated equipment, leading the surgeon to only telecontrol the device, which is actually in contact with the patient, instead of guiding it directly by hand. Well-known examples are robot-assisted surgical interventions, where the user telecontrols the instrument via an input console, or procedures, which need to be performed using x-ray imaging, such as needle placement during biopsies or for drug injection [1]. Thus, potentially leading to improved accuracy, a lack of haptic sensation aggravates the process of perceiving important information for the surgeon, such as the mechanical characteristics of tissue boundary layers during needle insertion.

In most disciplines, the forces during tool-tissue interaction are rather small and only slight changes of those interaction forces contain valuable information. This could be a threshold force from which a material will start to rip, or the force difference when a needle tip enters the next layer of tissue. To render these mechanical characteristics to the user, a dynamic haptic display with high mechanical bandwidth is required. These needs are perfectly met by haptic displays based on cable-driven parallel kinematics due to high stiffness and low inertia. Cable-driven haptic displays have been explored for various applications, such as for virtual reality or as a locomotion interface [2, 3], however, no research about application in medical telemanipulation was found.

In this work, the capabilities and characteristics of a cable-driven haptic display for telemanipulation in the medical field have been investigated. As an exemplary application, the needle insertion process was chosen since there is only one degree of freedom (DOF) and very small changes in the tool-tissue interaction force. Cable-driven parallel kinematics have the advantage that they can be easily reconfigured and expanded to include additional DOF. In this paper, the mechanical setup and the dynamic characteristics of a cable-driven linear haptic display, in the following referred to as the *haptic display*, are presented.

MATERIALS AND METHODS

The haptic display is oriented horizontally to avoid influence of gravitational forces aligned with the actuated DOF, which could lead to direction dependent influence on the user's perception. The haptic display consists of two winch units, two pulleys, and an endeffector handle, designed for a three-finger precision grip. Each winch unit consists of a Faulhaber type 4490 BS brushless DC motor (Dr. Fritz Faulhaber GmbH & Co. KG, Germany), a Faulhaber HEDS 5500 incremental

encoder, two Ø 8 mm pedestal bearings, a steel shaft (Ø 8 mm), a shaft coupling, and a 3D-printed winch with a spooling diameter of 15 mm. A polyethylene Dyneema® cable, (D-Pro, LIROS GmbH, Germany) with a diameter of 1.5 mm is used. The weight of the cable is 1.3 g/m while having a breaking load of 230 daN. To ensure a proper spooling of the cable, an acceptable deflection between cable axis and winch perpendicular is achieved by a distance of 330 mm between winch and pulley. A working range of 400 mm is achieved with a distance of 570 mm between both pulleys, the geometry of the endeffector, and a mechanical end stop to prevent the user from overrunning the pulley. All components are mounted on an aluminum breadboard (Fig. 1).

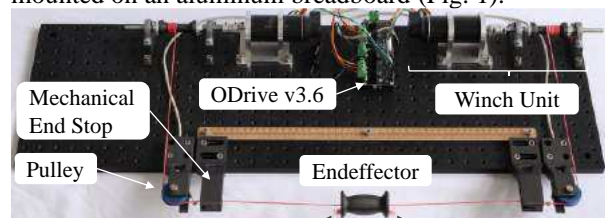


Fig. 1 Mechanical setup of the linear haptic display.

Both motors are controlled via an ODrive motor control board v3.6 (ODrive Robotics Inc., USA). The control concept is designed using SIMULINK (The MathWorks Inc., USA) on a host PC and a Raspberry Pi 4 Model B (Raspberry Pi Foundation, UK) as the target hardware, communicating via XCP on TCP/IP, while the ODrive is connected to the Raspberry Pi via USB. A mechanical end stop, electrical limit switches, and an emergency stop button ensure a safe operation.

For the haptic interaction, a task space impedance control approach was chosen to display virtual objects with varying characteristics regarding object stiffness, damping, and texture. No force sensor is used to preserve resource-efficient scalability with further DOF. Instead, depending on the position, velocity and acceleration of the endeffector measured by the encoder, a resulting force vector is calculated based on a virtual spring-mass-damper model. According to this calculated force vector, the required motor torques are determined and commanded to the motor control board. On the control board, field-oriented control (FOC) is implemented to control the torque via a PI-current-controller.

The minimum motor torque is set to 0.07 Nm, which results in a cable force of 9.33 N and thus a sagging angle of less than 1°. The maximum motor torque is limited to 0.17 Nm, resulting in a cable force of 22.67 N.

Static and dynamic behavior of the winch unit was evaluated. To assess the dynamic behavior, the transmission of an input force F_{in} was obtained. Displayed forces F_{disp} were measured using a type

KD40s100N force sensor ($f_{0_sensor} = 2.5$ kHz) with a measurement rate of 625 Hz (ME-Meßsysteme GmbH, Germany) (Fig. 2). Force transmission was measured in three configurations (winch only, winch and cable pulley, winch and cable pulley with improved stiffness) by sweeping a sinusoidal input force from 1 Hz to 150 Hz with an amplitude of 2.67 N. The dynamic force transmission function was determined following the equation $G(f) = F_{disp}/F_{in}$. The bandwidth of the system was obtained by applying the ± 3 dB criterion.

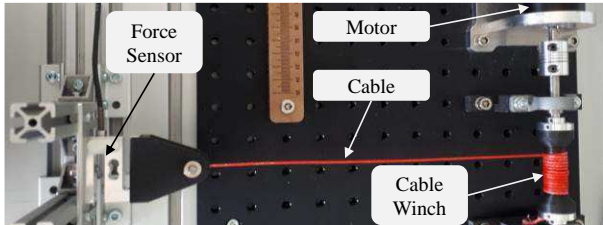


Fig. 2 Measurement setup with the cable winch for evaluation of the static and dynamic behavior of the winch unit.

Preliminary tests with three individuals were carried out to validate the haptic perception and to initially assess the system's performance. Virtual objects with varying stiffness (resembling workspace boundaries), damping (emulating movement through viscous fluid), and sinusoidal feedback force functions (resembling surface texture), were modeled and displayed using SIMULINK. Since the control system's performance is influenced by the endeffector's velocity, the individuals are asked to roughly follow the speed of an animation on a screen. By changing model parameters (stiffness; damping; frequency and amplitude of the sine function), absolute and differential perception thresholds were estimated.

RESULTS

The investigation of the cable-driven haptic display shows, that force values up to 22.67 N can be displayed over the complete linear workspace of 400 mm. When there is no pulley used for cable guidance, forces can be displayed up to 47 Hz. When using the winch and a pulley, the frequency range is limited to 25 Hz. Using the winch and an improved pulley with increased mechanical stiffness, a maximum of 30 Hz can be reached. For all setups, a clear resonance peak can be seen (see Fig. 3).

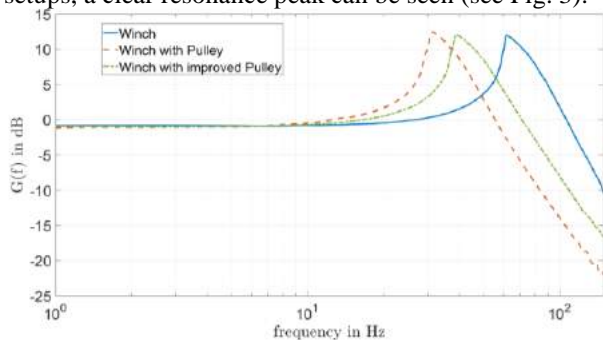


Fig. 3 Amplitude response of the dynamic force transmission function $G(f)$ for three different configurations.

Changes from 0.002 to 0.005 Ns/mm of the damping constant were perceivable by the individuals. The absolute perception threshold was not measured since the

existing damping of the mechanical setup was already noticeable. The absolute perception threshold regarding stiffness shows a wide distribution from 0.014 to 0.046 N/mm, while the differential perception threshold was less than 0.012 N/mm. In case of the displayed sinusoidal textures, amplitudes between 0.4 N and 1.2 N could already be felt by the individuals (period length of 3 mm). The differential perception threshold regarding the amplitude was between 0.4 N to 0.8 N.

DISCUSSION

The proposed setup of the linear cable-driven kinematic as a haptic display shows promising results for a resource-efficient and easy to reconfigure haptic user interface. The ability to display delicate forces with good dynamic behavior but yet simple setup has great potential for various applications, especially in the medical sector. The mechanical bandwidth of the proposed setup shows to be strongly dependent of the number and stiffness of cable-guiding elements. As a result, even for small cable forces, a stiff mechanical setup must be ensured to be able to transmit forces with high frequency. Adding DOFs to the setup might further limit the transmittable frequency. Preliminary tests revealed the discriminability of small interaction forces for different objects and structures which resembled the use of the haptic display in a realistic setup. However, since the performance of the system depends on the velocity of the endeffector in the workspace and the velocity was only roughly estimated, the perception thresholds must be reevaluated in a more accurate setting and with more participants. Nevertheless, the gained values enable an estimation on the achievable performance of the haptic display.

Slight variations in the displayed force occurred depending on the endeffector position. This might be caused by torque ripple [4], which especially is present for low load and low speed, or the mechanical setup.

In case of the application of telecontrolled needle insertion, more DOFs (translational and rotational) need to be added, to enable the user to perceive the evading of the needle's tip in the tissue caused by the bevel orientation. Future work will address the investigation of cable-driven haptic displays in planar and spatial configurations with translational and rotational DOFs, and the synthesis of workspaces with yet compact setups.

REFERENCES

- [1] Alterovitz R, Branicky M, Goldberg K. Motion Planning Under Uncertainty for Image-guided Medical Needle Steering. *Int J Rob Res.* 2008; 27(11-12):1361-1374.
- [2] Kim S, Hasegawa S, Koike Y, Sato M. Tension based 7-DOF force feedback device: SPIDAR-G. *Proceedings IEEE Virtual Reality 2002*; 283-284.
- [3] Gosselin C, Poulin R, Laurendeau D. A Planar Parallel 3-DOF Cable-Driven Haptic Interface. *12th World Multi-Conference on Systemics, Cybernetics and Informatics*, vol. 3, Orlando, FL, USA, 2008, pp. 266-271.
- [4] Bieber J, Bernstein D, Schuster M, Beitelschmidt, M. Entwicklung einfacher modularer Seilroboter ohne Verwendung von Kraftsensorik. *VDI Mechatroniktagung, Darmstadt, März 2021. Tagungsband: 211-216.*

Comparison of Performance Metrics for Real-Time Haptic Feedback in Surgical Skill Training

L.R. Johnson¹, M.D. Byrne², and M.K. O'Malley¹

¹*Department of Mechanical Engineering, Rice University*

²*Department of Psychological Sciences, Rice University*

Lianne.R.Johnson@rice.edu

INTRODUCTION

Endovascular surgery involves minimally invasive surgical techniques that can result in significantly shorter operation times and hospital stays, lower complication rates, less blood loss, and lower rates of postoperative mechanical ventilation and atrial fibrillation than the equivalent open procedures [1], [2]. Repeated practice is central to skill acquisition, and minimally invasive procedures like endovascular surgery may require more or specialized practice compared to traditional surgery. For example, despite known benefits of endovascular aortic valve replacement compared to traditional surgical methods, Smith et al. attributed observations of higher rates of stroke, transient ischemic attacks, and major vascular complications to a protracted learning curve for the endovascular approach [3].

Virtual reality endovascular surgical simulators can be loaded with a patient's pre-operative CT scan, enabling rehearsal of difficult cases before operating. Simulators are also accessible to trainees, giving opportunities for additional practice in navigating to hard-to-reach vascular structures, or exposure to rare procedures. Still, surgical simulators lack the provision of real-time and objective performance feedback. Instead, feedback is only available after the completion of a surgical task, and often does not provide the trainee with insight into *how* they should change their task performance strategies to achieve performance goals.

Objective measures of skill derived from endovascular guidewire movement kinematics that characterize tool tip movement smoothness have been shown to correlate with expertise [4], [5]. Such metrics have not yet been used during training as real-time performance feedback, despite evidence that providing feedback can improve training outcomes [6].

Our approach to providing real-time performance feedback during surgical skill training is intended to address this gap. We propose to use estimates of spectral arc length (SPARC), idle time, and average velocity to quantify task performance, then encode these measures as vibrotactile cues displayed to trainees in a wearable haptic device (see Fig. 1). We have shown the provision of feedback based on SPARC to be effective for

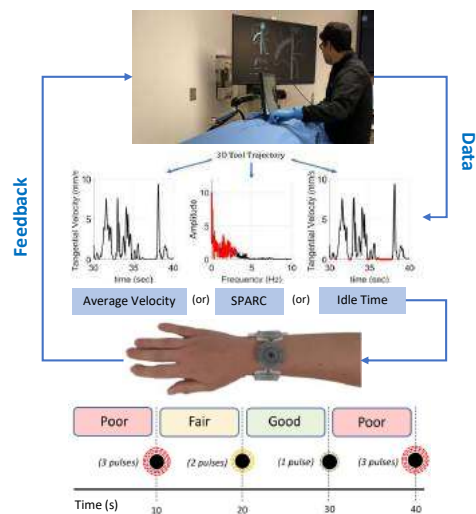


Fig. 1 Our method for providing real-time haptic feedback for training in endovascular surgery. Trainees perform navigation tasks with the AngioMentor. Data are streamed and performance metrics are computed. Metrics are encoded as a haptic cue provided to the trainee with a wearable vibrotactile bracelet.

enhancing performance during a mirror-tracing task that emulates endovascular navigation [7]. It was noted that trainees faced difficulties in interpreting and understanding the SPARC-based performance feedback that was provided, likely due to the non-intuitive nature of this frequency-domain measure of movement smoothness. More recently, we have explored alternative performance measures that may be easier for trainees to understand, namely average velocity and idle time, which are time-domain measures of smoothness [8].

In this work, we examine trainee performance of an endovascular navigation task using a commercial endovascular surgical simulator. We retrospectively analyze performance that was recorded without real-time feedback, and explore the nature of the real-time feedback that trainees would have received based on online computation of SPARC, average velocity, and idle time. Our goal is to determine the best performance metric on which to base real-time haptic feedback that encodes task performance.

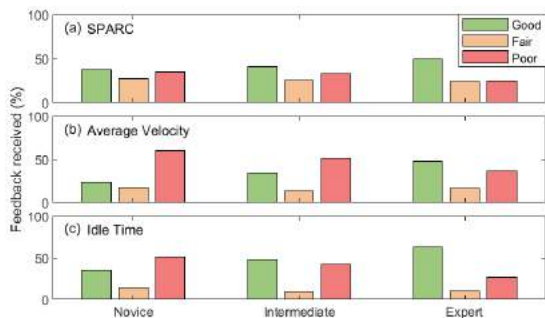


Fig. 2 Distribution of feedback received by novices, intermediates and experts for each performance metric

		SPARC		
		Good	Fair	Poor
Average Velocity	Good	38%	43%	22%
	Fair	15%	17%	15%
	Poor	47%	39%	63%

		SPARC		
		Good	Fair	Poor
Idle Time	Good	48%	59%	36%
	Fair	8%	14%	13%
	Poor	43%	27%	51%

		Idle Time		
		Good	Fair	Poor
Average Velocity	Good	61%	28%	6%
	Fair	18%	28%	9%
	Poor	21%	45%	85%

Fig. 3 Mapping of observed feedback for SPARC, average velocity and idle time

MATERIALS AND METHODS

We evaluated guidewire tool tip kinematic data that were collected in a previous study involving 75 participants (57 male, 18 female; 31 novices, 25 intermediates, and 19 experts determined by prior caseload) [8]. Participants were asked to perform four different navigation tasks comprising the FEVS (Fundamentals of Endovascular Surgery) [9] using a commercial virtual reality simulator (AngioMentor, Surgical Science). Real-time performance feedback was not provided to the trainees. Tangential velocity profiles were determined from tool tip data and used to compute the performance measures (SPARC, average velocity, and idle time). Scores were categorized as good, fair, or poor based on performance thresholds computed from prior studies (see Murali et al. [8]). We analyzed the distribution of good, fair, and poor feedback that participants would have received if real-time performance feedback had been provided based on each of the proposed metrics. We also analyzed the agreement in performance feedback between metrics.

RESULTS

Overall, the frequency of “good” feedback increases as participant expertise increases, as expected (see Fig. 2). Feedback based on average velocity and idle time is more likely to indicate “poor” performance than when based on SPARC. “Fair” feedback is rare when based on average velocity or idle time.

Despite prior studies showing good correlation between SPARC and both idle time and average velocity [8], our analysis shows that the feedback categories based on these metrics are rarely in agreement with those based on SPARC (see Fig. 3). For example, 47% of the “good” feedback for SPARC is mapped to “poor” feedback for average velocity. Similarly, 43% of “good” feedback cues for SPARC are mapped to “poor” feedback for idle time.

DISCUSSION

Studies in motor learning show that while corrective feedback can accelerate adaptation and learning, positive feedback can improve retention of skill [10]. In our study, movement smoothness feedback based on SPARC offers a more distributed set of feedback cues with “fair” and “good” feedback provided more frequently compared to feedback based on average velocity and idle time. Positive feedback has potential for increased self-efficacy [11] and intrinsic motivation [12]. Smoothness feedback based on SPARC has been successfully used to improve performance in endovascular-like tasks [7], and the variability in positive and negative feedback makes SPARC the preferred choice for surgical training.

REFERENCES

- [1] M. Prinssen, E. L. Verhoeven, J. Buth, P. W. Cuypers, M. R. van Sambeek, R. Balm, E. Buskens, D. E. Grobbee, and J. D. Blankensteijn, “A randomized trial comparing conventional and endovascular repair of abdominal aortic aneurysms,” *New England Journal of Medicine*, vol. 351, no. 16, pp. 1607–1618, 2004.
- [2] F. A. Lederle, T. C. Kyriakides, K. T. Stroupe, J. A. Freischlag, F. T. Padberg Jr, J. S. Matsumura, Z. Huo, and G. R. Johnson, “Open versus endovascular repair of abdominal aortic aneurysm,” *New England Journal of Medicine*, vol. 380, no. 22, pp. 2126–2135, 2019.
- [3] C. R. Smith, M. B. Leon, M. J. Mack, D. C. Miller, J. W. Moses, L. G. Svensson, E. M. Tuzcu, J. G. Webb, G. P. Fontana, R. R. Makkar, M. Williams, T. Dewey, S. Kapadia, V. Babaliaros, V. H. Thourani, P. Corso, A. D. Pichard, J. E. Bavaria, H. C. Herrmann, J. J. Akin, W. N. Anderson, D. Wang, and S. J. Pocock, “Transcatheter versus surgical aortic-valve replacement in high-risk patients,” *The New England Journal of Medicine*, vol. 364, no. 23, pp. 2187–2198, 2011.
- [4] V. M. Belvroy, B. Murali, M. G. Sheahan, M. K. O’Malley, and J. Bismuth, “In the Fundamentals of Endovascular and Vascular Surgery model motion metrics reliably differentiate competency,” *Journal of Vascular Surgery*, vol. 72, no. 6, pp. 2161–2165, 2020.
- [5] S. Estrada, C. Duran, D. Schulz, J. Bismuth, M. D. Byrne, and M. K. O’Malley, “Smoothness of surgical tool tip motion correlates to skill in endovascular tasks,” *IEEE Transactions on Human-Machine Systems*, vol. 46, no. 5, pp. 647–659, 2016.
- [6] A. Malpani, S. S. Vedula, H. C. Lin, G. D. Hager, and R. H. Taylor, “Effect of real-time virtual reality-based teaching cues on learning needle passing for robot-assisted minimally invasive surgery: a randomized controlled trial,” *International Journal of Computer Assisted Radiology and Surgery*, no. 15, p. 1187–1194, 2020.
- [7] J. L. Sullivan, S. Pandey, M. Byrne, and M. K. O’Malley, “Haptic feedback based on movement smoothness improves performance in a perceptual-motor task,” *IEEE Transactions on Haptics*, pp. 1–1, 2021.
- [8] B. Murali, V. M. Belvroy, S. Pandey, J. Bismuth, M. D. Byrne, and M. K. O’Malley, “Velocity-Domain Motion Quality Measures for Surgical Performance Evaluation and Feedback,” *Journal of Medical Devices*, vol. 15, no. 1, p. 011107, 2021.
- [9] C. Duran, S. Estrada, M. O’Malley, M. G. Sheahan, M. L. Shames, J. T. Lee, and J. Bismuth, “The model for Fundamentals of Endovascular Surgery (FEVS) successfully defines the competent endovascular surgeon,” *Journal of vascular surgery*, vol. 62, no. 6, pp. 1660–1666, 2015.
- [10] D. Sternad and K. P. Kording, “Carrot or stick in motor learning,” *Nature neuroscience*, vol. 18, no. 4, pp. 480–481, 2015.
- [11] K. A. Karl, A. M. O’Leary-Kelly, and J. J. Martocchio, “The impact of feedback and self-efficacy on performance in training,” *Journal of Organizational Behavior*, vol. 14, no. 4, pp. 379–394, 1993.
- [12] C. Burgers, A. Eden, M. D. van Engelenburg, and S. Buningh, “How feedback boosts motivation and play in a brain-training game,” *Computers in Human Behavior*, vol. 48, pp. 94–103, 2015.

Predictable therapeutic microswarm dispersion for targeted drug delivery application

Kiana Abolfathi¹, Mohammad Reza Hairi Yazdi^{2,3}, and Ali Kafash Hoshiar¹

¹*School of Computer Science and Electronic Engineering, University of Essex,*

²*School of Mechanical Engineering, University of Tehran,*

³*Department of Mechanical Engineering, Lassonde School of Engineering, York University, Toronto, Canada*

a.kafashhoshiar@essex.ac.uk

INTRODUCTION

The magnetic nanoparticles (MNPs) based micro-nanorobots are emerging drug carriers. Controllability by an external magnetic field is the major advantage of these drug carriers. However, they are facing several challenges including controllability of the individual motion of MNPs under a global magnetic field. The microswarm control where collective MNPs were guided by a magnetic field was proposed as a solution [1]. Steering the MNPs as a microswarm to the targeted region has many advantages which include increasing the delivered drug to the site, preserving the healthy organs from drug penetration, and decreasing the negative side effects.

In recent studies, particle swarms were guided using a rotating/oscillating magnetic field [2], [3]. A simulation platform for steering the aggregated MNPs based on the gradient field was developed [4]. Despite studies on the separation, no computational platform for predicting changes in particle dispersion under different magnetic field conditions has been introduced. After reaching the position of interest, the aggregates also had to be separated to ensure successful drug delivery.

In this study using mathematical modelling, a separation platform has been developed. More details on the mathematical model used here can be found in [5]. The paper is divided into two sections. First, the accuracy of the simulation platform is discussed and then the effective parameters have been studied.

MODELLING ROTATING MAGNETIC FIELD

In this study, the magnetic field strength (MFS) is considered in two directions (Fig. 1). The coefficient of variation of the MFS is defined as follows:

$$\begin{cases} f_x + f_y = 1 \\ f_x = 0, 0 \leq t < T_1 & ; & f_x = 1, T_1 \leq t \leq T_2 \end{cases} \quad (1)$$

where f_x and f_y are the coefficients of variation in directions x and y .

The applied magnetic field is described with three parameters: the coefficient of variation $\vec{f} = (f_x, f_y, 0)$, the frequency of the magnetic field $1/T_2$ and the period ratio $\alpha = T_2/T_1$ (Fig. 1-a).

MODEL VERIFICATION

The simulation results are compared to experiments in [6]. This simulation uses 1000 particles with a radius of

125 nm. The applied field has a frequency of 10 Hz with a frequency ratio of 2. Considering the particles' size, the Brownian force is assumed to be zero. For describing the change of particle's location in a specific time, two user-defined geometrical parameters were introduced (details can be found in [5]). These parameters are dispersion and the ideal percentage of dispersion changes (IPDC). Dispersion is a parameter that shows the average distance of particles from the gravity center of the whole particles. IPDC illustrates the difference between the dispersion at the determined time and the ideal dispersion of the particles. The ideal dispersion is the minimum concentration of particles. The ideal dispersion is a function of the number, diameter, and coefficient of elasticity of the particles. Fig. 1 offers a diagram of the IPDC with respect to time for both the simulation and experimental results. As shown in the diagram, both the simulation and experimental results follow the same trend of deceleration before settling down after 10 s. The final ideal percentage of dispersion change (IPDC) is inclined to 62% and 58% for the experimental and the simulation results (error =9.7—the difference between experimental and simulation results).

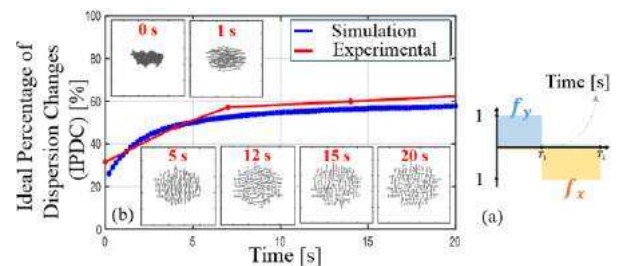


Fig. 1 (a) Schematic of the change of the variation coefficient over time. (b) The IPDC and the particles' position per time.

RESULTS

To evaluate the effect of the number of MNPs, we perform three simulations with 500, 1000 and 1500 particles number. Fig. 2-a presents these results. The particle radius and simulation time are equal to 125 nm and 35 s, respectively, for all cases. The applied magnetic field has a frequency and MFS of 10 Hz and 10 mT with a period ratio of 2. The results show that the IPDC changes over time are independent of the number of MNPs, and the trends of the diagrams are similar in all cases. To better describe the process of changing the results, we introduced two terms: the final IPDC and the stability time. The final IPDC indicates the ultimate limit

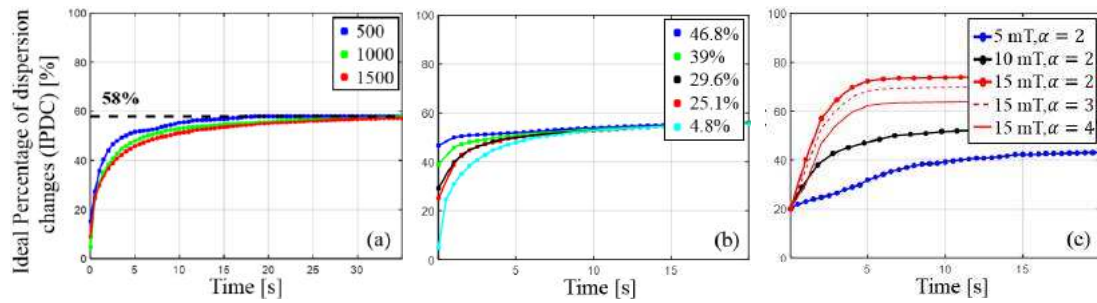


Fig. 2 (a)-(c) The diagram of the effect of the particle number, initial dispersion, MFS and the period ratio on IPDC changes over time.

of the dispersion changes, and when the particles reach their final IPDC, the particles' dispersion value stabilises itself, and the magnetic field becomes inert. The stability time determines the duration of the applied magnetic field by which the dispersion changes stabilise. After that time, the imposed field no longer affects the particles as, in time, the particles become so distanced and dipole force decreases ($F_{dipij} \propto 1/\hat{r}_{ij}^4$). The results of Fig. 2-a show that when the other effective parameters are the same, the final IPDC and the stability time are independent of the number of particles.

Fig. 2-b depicts the results of the simulations, which reveal that under any initial dispersion value, the IPDC converges to the same value. In all cases, the diameters of all particles are equal to 250 nm. Other parameters, such as the number of MNPs, frequency, MFS and period ratio, are set to equal 1000, 10 Hz, 10 mT and 2, respectively. All cases showed acceptable stability for the dispersion time. In Fig. 2-b, where the $IPDC_{t=0}=46.8\%$, the IPDC changes begin to slow, and the value of the IPDC becomes almost stable after 1s, but where the $IPDC_{t=0}=4.8\%$, the elapsed time required for the IPDC to reach the constant value of 57.2% is approximately 7 s.

Fig. 2-c illustrates the effects of the MFS and the period ratio on the dispersion stability time and the final IPDC when the MNPs number, diameter and frequency are equal to 1000, 250 nm and 10 Hz. The results reveal that the larger the MFS, the less stable the dispersion of particles in time. When the MFS is equal to 15 mT, the dispersion stabilises in 5 s, and the IPDC reaches 74.5%. When the MFS is equal to 10 mT and 5 mT, however, the dispersion stabilises itself after 7 s and 10 s, respectively, with IPDC values of 57.6% and 42.3%. Therefore, the stronger the magnetic field becomes, the sooner the dispersion process stabilises, and the higher the final IPDC tendency's value reaches. The dipole force is responsible for this phenomenon. Three cases are used to study the effect of the period ratio (Fig. 2-c). In all cases, the MFS is equal to 15 mT, and three-period ratios, namely, 2, 3 and 4, are used. The results demonstrate that a decrease in the period ratio is directly related to a simultaneous increase in the value of the IPDC. In these simulations, the slope of the curve is similar, and the stability time is equal to 5 s. However, the cases have different final IPDC values; for the period ratios of 2, 3 and 4, the value of the IPDC reaches 74.5%, 70.1% and 63%, respectively. Therefore, we conclude that the

dispersion stability time is independent of the period ratio and only affects the final IPDC's value.

DISCUSSION AND CONCLUSION

In this study, we demonstrate a numerical platform that has the ability to predict the separation of the microswarms under the oscillating magnetic field. A study of the effective parameters shows that independent of any environmental, geometric and process conditions, the dispersion changes are slow, and the dispersion becomes stable after 20 s. In addition, the value of the final dispersion of MNPs is related to the MFS value, period ratio, and particle diameter. The results showed that at a very high and very low frequency, microswarm dispersion does not have high scattering and the final scattering changes are very small. In general, the introduced platform can be useful for predicting the dispersion of the particles under different magnetic conditions. The platform can be used to predict recently introduced therapeutic microswarms.

REFERENCES

- [1] H. Xie et al., "Reconfigurable magnetic microrobot swarm: Multimode transformation, locomotion, and manipulation," *Science Robotics*, vol. 4, no. 28, pp. 1–15, 2019, doi: 10.1126/scirobotics.aav8006.
- [2] A. K. Hoshidar, S. D. Javan, T. Le, M. R. H. Yazdi, and J. Yoon, "Studies on Aggregated Nanoparticles Steering during Deep Brain Membrane Crossing," *Nanomaterial*, vol. 11, no.10, pp. 1–16, 2021.
- [3] A. K. Hoshidar, T. A. Le, P. Valdastrì, and J. Yoon, "Swarm of magnetic nanoparticles steering in multi-bifurcation vessels under fluid flow," *Journal of Micro-Bio Robotics*, 2020, doi: 10.1007/s12213-020-00127-2.
- [4] P. Vartholomeos and C. Mavroidis, "In Silico Studies of Magnetic Microparticle Aggregations in Fluid Environments for MRI-Guided Drug Delivery," *IEEE Transactions on Biomedical Engineering*, vol. 59, no. 11, pp. 3028–3038, Nov. 2012, doi: 10.1109/TBME.2012.2213340.
- [5] K. Abolfathi, M. R. H. Yazdi, and A. K. Hoshidar, "Studies of Different Swarm Modes for the MNPs under the Rotating Magnetic Field," *IEEE Transactions on Nanotechnology*, vol. 19, pp. 849–855, 2020, doi:10.1109/TNANO.2020.3041798.
- [6] B. Wang, K. F. Chan, J. Yu, Q. Wang, and L. Yang, "Reconfigurable Swarms of Ferromagnetic Colloids for Enhanced Local Hyperthermia," *Advanced Functional Material*, vol. 1705701, pp. 1–12, 2018, doi: 10.1002/adfm.201705701.

Modeling Telescoping Tendon-actuated Continuum Robots

Yash Chitalia, Abdulhamit Donder, and Pierre E. Dupont

Department of Cardiovascular Surgery, Boston Children's Hospital,
Harvard Medical School, Boston

INTRODUCTION

Tendon actuation is the most common method for producing flexure in continuum medical devices. Examples include catheters, ureteroscopes, bronchoscopes and colonoscopes. These devices are comprised of an elongated tube with a short steerable tip portion and a long passively flexible proximal portion. The shape of the proximal portion conforms to the shape of the body lumen as it is advanced into the body while the tendon-actuated tip portion provides for tip positioning and steering.

While many of these devices are comprised of a single elongated tube, there are important clinical examples for which a single steerable tip section is insufficient and the increased steerability provided by additional telescoping steerable sections is needed (Fig. 1). For example, the delivery systems used for heart valve repair and replacement employ 2-3 tendon-actuated telescoping sections [1]. Additional examples include Hansen Medical's robotic electrophysiology catheter [2] and Auris Health's robotic endoscope for peripheral lung biopsies [3] each of which possess two telescoping steerable sections.



Fig. 1. Example tendon-actuated catheter comprised of two telescoping tubes.

While a variety of models mapping tendon actuation to robot shape have been developed, they are all limited to consideration of a single tube [4-6]. They cannot accurately predict the shape of multi-tube robots because they do not model the twisting that occurs between the tubes. The contribution of this paper is to produce a model that includes tube twisting and to illustrate it experimentally using the system of Fig. 1.

MECHANICS-BASED MODEL

Each tube is modeled as a Cosserat rod and tendons are modeled as Cosserat strings similar to [6]. The rod model expresses static equilibrium using differential equations for bending moment, $m \in \mathbb{R}^3$, and shear force, $n \in \mathbb{R}^3$, as functions of arc length, s . Kinematic inputs are given as tendon tension forces, f . Each tendon generates distributed forces along the length of the rod as well as concentrated forces and moments at their distal ends where they attach to the rod. Tendon equilibrium is

described by a differential equation in shear force. Assuming no tendon friction, the tendon tension is constant along its length and shear force is tangent to the tendon.

Using constitutive laws relating bending moment and shear force to curvature and shear strain, respectively, Rucker and Webster show that these models result in a set of decoupled linear differential equations in curvature and shear strain [6]. To extend this model to multiple telescoping tubes, additional constraints and derivational techniques must be applied to arrive at a comparable set of linear differential equations.

Owing to the length of the derivation, only a summary of the approach and model are presented. For a set of telescoping tubes, each with its own tendons, the nominal set of state variables to be integrated for tube i is comprised of curvature, $u_i \in \mathbb{R}^3$, and shear strain, $v_i \in \mathbb{R}^3$. In the overlapping portions, however, the tubes conform to the same (body-frame) centerline, $p^b \in \mathbb{R}^3$. Using body-frame coordinates with the z axis directed tangentially, this constrains the x and y (bending) components of curvature to be equal for all overlapping tubes. Similarly, the cross-sectional (x and y) shear strain components must be equal in the overlapping portion.

Imposing these constraints reduces the number of independent state variable for q fully overlapping tubes from $6q$ (3 curvature components and 3 shear strain components for each tube) to $6 + 2(q - 1)$. Here, the first 6 state variables are the curvature and strain components of the first tube (u_1 and v_1) while the additional state variables correspond to the z components of curvature and shear strain for tubes 2, ..., q .

Defining the torsional twist between tubes as $\alpha_i(s) = \theta_i(s) - \theta_1(s)$, in the body frame of tube 1, we have $\dot{\alpha}_i(s) = u_{i,z}(s) - u_{1,z}(s)$ where $\dot{\alpha}(s) = d\alpha(s)/ds$. For all functions of arc length, such as $\alpha(s)$, the s term is dropped in the remainder of this paper. The relationship between overlapping tube curvatures is given by

$$u_i = R_z^T(\alpha_i)u_1 + \dot{\alpha}_i e_3 \quad (1)$$

Here, $R_z(\alpha)$ is rotation matrix about the z -axis. Differentiation with respect to arc length,

$$\dot{u}_i = R_z^T(\alpha_i)u_1 + \dot{\alpha}_i [e_3]^T R_z^T(\alpha_i)u_1 + \ddot{\alpha}_i e_3 \quad (2)$$

Similarly, the constraint on shear deformation of the overlapping tube cross sections is given by

$$v_i|_{x,y} = R_z^T(\alpha_i)v_1|_{x,y} \quad (3)$$

Assuming that the untensioned tubes are straight, the constitutive model for each tube is given as

$$\begin{bmatrix} m_i \\ n_i \end{bmatrix} = \begin{bmatrix} K_{bt} & 0 \\ 0 & K_{se} \end{bmatrix} \begin{bmatrix} u_i \\ v_i - v_i^0 \end{bmatrix}, \quad v_i^0 = e_3, \quad (4)$$

We write the overall moment-curvature equilibrium equation by summing over all the overlapping tubes. For compactness, the expression below is written for two tubes and $[x]$ represents the skew symmetric form of $x \in \mathbb{R}^3$:

$$\dot{m}_1 + [u_1]m_1 + \left\{ [u_1]R_z(\alpha) + \frac{dR_z(\alpha)}{d\alpha}\dot{\alpha} \right\} m_2 + R_z(\alpha)\dot{m}_2 + [v_1]n_1 + R_z(\alpha)[v_2]n_2 + \tau_1 + R_z(\alpha)\tau_2 = 0 \quad (5)$$

Here, τ_i represent the sum of moments applied to a tube by its tendons together with any external moments. Since, the tubes can be independently twisted, an additional equation is needed for the torsional moment of the second tube:

$$\dot{m}_{2,z} + ([u_2]m_2 + [v_2]n_2 + \tau_2)|_z = 0 \quad (6)$$

The shear strain equilibrium equation is obtained similarly. Here, summing for total shear strain equilibrium is done to cancel the distributed shear forces that each tube applies to the others. For two tubes, this yields:

$$\dot{n}_1 + [u_1]n_1 + \left\{ [u_1]R_z(\alpha) + \frac{dR_z(\alpha)}{d\alpha}\dot{\alpha} \right\} n_2 + R_z(\alpha)\dot{n}_2 + f_1 + R_z(\alpha)f_2 = 0 \quad (7)$$

Distributed forces, f_i , are due to tendons and external loads. Since the tubes can stretch independently, an additional equation is needed for axial elongation of the second tube:

$$\dot{n}_{2,z} + ([u_2]n_2 + f_2)|_z = 0 \quad (8)$$

Using (1)-(4), the equilibrium equations can be written purely in terms of the state variables, namely,

$x = [u_{1,x}, u_{1,y}, u_{1,z}, v_{1,x}, v_{1,y}, v_{1,z}, u_{2,z}, v_{2,z}]^T$. Tendon forces and moments can be formulated as in [6] resulting in a set of linear differential equations of the form

$$A\dot{x} = Bx + c \quad (9)$$

While expressions for A, B, c are too lengthy to include here, this equation can be integrated by inverting A at every time step. Kinematic inputs are the tendon tensions along with the relative tube translations and rotations at the base. Since tendon tensions produce point loads and moments at their distal ends [6], the equations are solved as a two-point boundary value problem.

EXPERIMENTAL MODEL COMPARISON

To demonstrate the twisting predicted by the multi-tube model, Fig. 2 provides a comparison with the single tube model for the catheter of Fig. 1. For comparison, the tips of the two tubes are aligned axially and the same overall cross section is used (two tubes: OD1 = 8mm, ID1 = 7.4mm; OD2 = 7.4mm, ID2 = 6.4mm versus one tube: OD = 8mm, ID = 6.4mm). Elastic moduli were experimentally estimated for the tubes and actual tendon radii were 3.9mm (outer tube) and 3.6mm (inner tube). The outer tube tendon is in the x - z plane and the inner tube tendon is in the y - z plane. Tendons were loaded individually and simultaneously to 14.7 N (1.5 kgf).

Fig. 2a shows that when a single tendon is loaded, both the single- and two-tube systems experience only bending and the two models overlap. When both tendons are loaded at 90° to each other, however, the two tubes twist along their length and more accurately predict the

experimental tip position. Model-predicted twisting between the tendons that accounts for the difference in tip is plotted in Fig. 2b.

DISCUSSION

Initial experimental validation of the multi-tube model suggests its usefulness for real-time control of robotic catheters and endoscopes. Future work will investigate its use for controlling a robotic catheter for interventional cardiology.

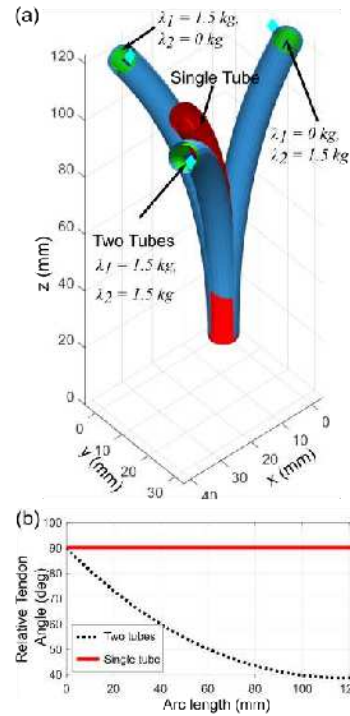


Fig. 2. Experimental comparison of single- and multi-tube models. (a) Catheter shape with tendons tensioned individually and simultaneously. (b) Relative tendon angle versus arc length.

REFERENCES

- [1] M. Sherif, L. Paranskaya, S. Yucel, S. Kische, O. Thiele, G. D'Ancona, A. Neuhausen-Abramkina, J. Ortak, H. Ince, and Oner, "Mitraclip step by step; how to simplify the procedure," *Netherlands heart journal*, vol. 25, no. 2, pp. 125–130, 2017.
- [2] Al-Ahmad, J. D. Grossman, and P. J. Wang, "Early experience with a computerized robotically controlled catheter system," *Journal of Interventional Cardiac Electrophysiology*, vol. 12, no. 3, pp. 199–202, 2005.
- [3] A. Agrawal, D. K. Hogarth, and S. Murgu, "Robotic bronchoscopy for pulmonary lesions: a review of existing technologies and clinical data," *Journal of Thoracic Disease*, vol. 12, no. 6, p. 3279, 2020.
- [4] P. Rao, Q. Peyron, S. Lilje and J. Burgner-Kahrs, "How to Model Tendon-Driven Continuum Robots and Benchmark Modelling Performance," *Frontiers in Robotics and AI*. Vol. 7, 2021.
- [5] F. Renda and C. Laschi, "A general mechanical model for tendon-driven continuum manipulators," *Proc IEEE Int Conf Robotics and Autom*, Saint Paul, MN, 2012.
- [6] D. C. Rucker and R. J. Webster III, "Statics and Dynamics of Continuum Robots With General Tendon Routing and External Loading," *IEEE Transactions on Robotics*, vol. 27, pp. 1033–1044, 2011.

Preliminary findings of a multimodal sensor system for measuring surgeon cognitive workload

Ravi Naik^{1, 2}, Kaizhe Jin^{1,2}, Alexandros Kogkas^{1,2}, Hutan Ashrafian,¹ Ara Darzi^{1, 2}, George Mylonas^{1,2}

¹Department of Surgery and Cancer, St Mary's Hospital, Imperial College London, UK,

²Hamlyn Centre for Robotic Surgery, Institute of Global Health Innovation, Imperial College London, UK

ravi.naik15@imperial.ac.uk

INTRODUCTION

The operating room represents a high-risk environment centred around the safe and efficient delivery of patient care. It is a complex ecosystem that encompasses many factors including communication within the multidisciplinary surgical team often led by the operating surgeon as well as execution of precise technical surgical skill. These factors are associated with the mental or cognitive workload (CWL) of the surgeon.

CWL, also described as the mental effort exerted while undertaking a task, is a construct derived from the cognitive load theory first described in the eighties during problem solving exercises [1]. There has been a growing emphasis on the measurement of CWL since then on individuals working in high-stake environments such as aviation [2]. Measurement of CWL in surgery is moving from solitary traditional subjective measures such as the Surgical Task Load Index (SURG-TLX) to objective measurement of physiological parameters secondary to changes in the CWL of the surgeon which are less exposed to subjective bias [3]. These have included heart rate variability (HRV), pupil metrics, electromyography (EMG), electroencephalography (EEG), skin conductance and functional near-infrared spectroscopy (fNIRS). More recently, there is increasing evidence to demonstrate the use of multiple sensors, or a multimodal sensor system designed to measure CWL with greater accuracy [4].

The aim of this paper is to demonstrate the use of a pilot synchronised system of multiple sensors to measure the real-time cognitive workload of surgeons in a simulated setting to demonstrate a proof of concept and to discuss the early findings.

MATERIALS AND METHODS

Ethics: Ethical approval was obtained from the research governance and integrity team at Imperial College (No: 20IC6361).

Participants: Five surgical residents from the academic surgical department at Imperial College London were recruited following study explanation and obtaining informed consent.

Surgical task: Laparoscopic peg transfer, a component of the Fundamentals of Laparoscopic surgery curriculum, was performed by participants twice per task condition. This was undertaken with standard laparoscopic equipment using the Olympus Elite system with a fixed 2D zero-degree 10mm laparoscope.

Task conditions: Participants were asked to perform the skill under four separate conditions in randomised order to minimise order effects bias and included 1. A control with no distractions (CS), 2. Mental arithmetic during the task (MA) which comprised of subtracting serial sevens from one thousand, 3. Noise from a recurring hospital bleep (ND) and 4. Dual distractions comprising of conditions 2 and 3 simultaneously (DD).

Subjective measures: Participants were asked to complete the SURG-TLX questionnaire tool after each task which consists of a multidimensional scale and pair-wise comparisons of cognitive domains including mental demands, physical demands, temporal demands, task complexity, situational stress and distractions.

Objective measures: Time to complete each task, number of pegs dropped, peg handling errors and miscalculations were recorded under each task condition and logged in real-time using a time stamp.

Physiological measures: The following physiological sensors were used: fNIRS (Artinis Brite24 2 x 11 system configured to the prefrontal cortex), EEG (TMSi Mobita 32 channel EEG system), eye tracker (Pupil Labs Pupil Core), photoplethysmography (PPG), galvanic skin response (GSR), electrocardiogram (ECG), electromyography (EMG) and skin temperature (Consensys Shimmer3 units). The arrangement of the wearable sensors is demonstrated in Figure 1A. Synchronisation of sensor data was undertaken using Lab Streaming Layer (LSL) and a bespoke graphical user interface was developed to facilitate recording.

Experimental protocol: Participants were consented and familiarised with the system. Participants were fitted with all sensors which were calibrated. An instructional video was shown, and participants were given five minutes to practice using the setup. Baseline recordings were then taken before each task condition. Participants then completed each task in a randomised order and completed the SURG-TLX questionnaire following each task. Preliminary analysis of SURG-TLX scores, pupil data, HRV and EEG is being undertaken with the

aim to analyse other physiological measures in due course.

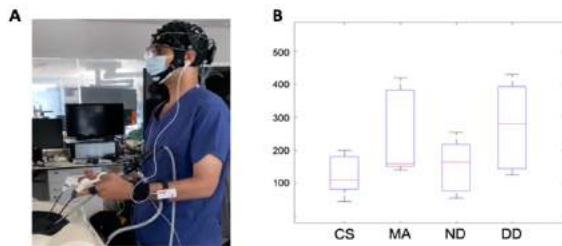


Figure 1A. Demonstration of the multimodal sensor network in use during a simulated laparoscopic peg transfer task. fNIRS, EEG, PPG, GSR sensors can be seen in use together with a wearable eye tracker. **Figure 1B.** Box plot to demonstrate distribution of overall adjusted SURG-TLX scores for each task for participants as a collective.

RESULTS

Table 1 and Figure 1B summarise the technical performance and subjective workload feedback results respectively. Participants subjectively recorded that task conditions MA and DD were significantly ($p < 0.05$) more difficult when compared to the control (CS) based on overall SURG-TLX scores ($p = 0.0071$ and $p = 0.0284$ respectively) and took longer to complete.

Figure 2 demonstrates the mean blink rate, mean single channel EEG recording and mean HRV (RMSSD) of participants during the CS and MA task. Although there was an increase in mean blink rate, single channel EEG and HRV, these were not statistically significant ($p = 0.067, 0.254$ and 0.149 respectively). There was a weak correlation between overall SURG-TLX score and time to complete task (Pearsons correlation coefficient = $0.347, p = 0.325$). There was a strong positive correlation between raw mental demand scores and blink rate for tasks CS and MA (Pearsons correlation coefficient = $0.855, p = 0.007$).

Participant	Task 1 (CS)			Task 2 (MA)			Task 3 (ND)			Task 4 (DD)		
	Duration (secs)	Pegs dropped	Errors in subtraction	Duration (secs)	Pegs dropped	Errors in subtraction	Duration (secs)	Pegs dropped	Errors in subtraction	Duration (secs)	Pegs dropped	Errors in subtraction
1	163.63	0	327.81	1	6	142.47	1	226.29	1	3		
2	284.09	2	289.39	3	2	222.51	1	195	0	1		
3	197.62	0	268.52	1	5	344.47	4	383.09	5	12		
4	232.16	3	286.47	3	3	176.39	0	198.68	2	1		
5	186.95	2	200.42	1	4	180.22	3	202.96	0	1		
Mean	212.89	1.4	274.522	1.8	4	213.212	1.8	241.204	1.6	3.6		

Table 1. Summary of task technical performance.

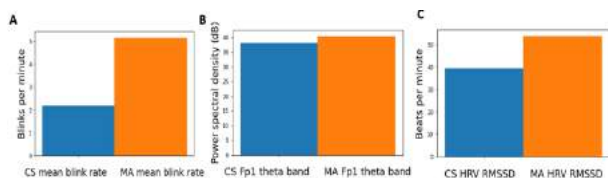


Figure 2. A) Mean blink rate of participants over task CS and MA. B) Mean HRV between task CS and MA. C) Mean change in EEG (Theta band) between task CS and MA.

DISCUSSION

The surgical task conditions designed in this pilot study successfully increased CWL when measured subjectively. There was successful synchronisation of sensors although signal loss of eye tracking and EEG

data for one participant. This study demonstrates the integration and synchronisation of the physiological data required to measure CWL using LSL. Initial findings from this study support the use of heart rate variability and blink rate as measures of CWL.

Preliminary results have demonstrated a positive relationship between blink rate and subjective task difficulty (CS vs MA) in keeping with current literature [5]. A single EEG channel (Fp1) was selected for preliminary analysis as this was thought to best represent activity of the prefrontal cortex, and was also found to be higher in the MA task.

The current sample size is recognised as a limitation and a larger number of participants of the same skill level is required to establish significant correlations between task performance, subjective and objective measures of CWL. Additional exploration is also required to ensure improved signal to noise ratio when considering fusion of multimodal data to ensure benefit over single sensors.

Future work will entail quantitative analysis of the data to demonstrate causation and correlation of increased CWL to rationalise and justify components of the multimodal sensor system however, preliminary results so far support the use of a multimodal sensor system to improve reliability and overcome individual variability when compared to single sensors used to measure CWL.

There is scope for further development to utilise machine learning techniques to recognise changes in CWL in an automated fashion and thus enable future integration into a smart operating environment in real-time.

Funding: This project is funded by the EPSRC Transformative Healthcare Technologies grant EP/W004755/1 and Imperial College Healthcare NHS Trust BRC.

REFERENCES

- Sweller J. Cognitive load during problem solving: Effects on learning. *Cogn Sci.* 1988;12(2):257-285. doi:10.1016/0364-0213(88)90023-7
- Wanyan X, Zhuang D, Zhang H. Improving pilot mental workload evaluation with combined measures. *Biomed Mater Eng.* 2014;24(6):2283-2290. doi:10.3233/BME-141041
- Wilson MR, Poolton JM, Malhotra N, Ngo K, Bright E, Masters RSW. Development and validation of a surgical workload measure: The surgery task load index (SURG-TLX). *World J Surg.* 2011;35(9):1961-1969. doi:10.1007/s00268-011-1141-4
- Zakeri Z, Mansfield N, Sunderland C, Omurtag A. Physiological correlates of cognitive load in laparoscopic surgery. *Sci Rep.* 2020;10(1):1-13. doi:10.1038/s41598-020-69553-3
- Gao J, Liu S, Feng Q, et al. Subjective and objective quantification of the effect of distraction on physician’s workload and performance during simulated laparoscopic surgery. *Med Sci Monit.* 2019;25:3127-3132. doi:10.12659/MSM.914635

Reinforcement Learning for Path Generation for Surgical Robot Maneuver

Junhong Chen¹, Zeyu Wang¹, Ruiqi Zhu², Ruiyang Zhang¹,
Weibang Bai¹, and Benny Lo, *Senior Member, IEEE*¹

¹Hamlyn Centre for Robotic Surgery ²King's College London
junhong.chen16@imperial.ac.uk

INTRODUCTION

In the last decades, surgical robots have been widely used in Robot-Assisted Minimally Invasive Surgery (RAMIS), which benefits surgeons by reducing their burdens and leads to safer operations. However, RAMIS tasks are still mainly relied on surgeon's control, thus the performance of a task mostly depends on the level and proficiency of a surgeon, and prone to human errors due to fatigue. However, despite their extensive experience, operators often make small mistakes and corrections during the tasks. Therefore, their kinematics data usually contains small differences to an ideal trajectory. To make full use of Learning from Demonstration(LfD) as well as reduce the dependence on kinematics data, a novel path generation method based on reinforcement learning(RL) is proposed in this paper. The da Vinci Research Kit, as the open-source robotic platform, is used to validate the model. And simulation is used for model training and early validation.

The contributions in this work: a) a quick path generation method for transferring tasks via RL; b) a new training strategy for surgical tasks based on surgeme[1]; c) the validation results of the proposed through transferring the learnt model from simulation to real robots.

MATERIALS AND METHODS

The overview of the proposed path generation for automatic transferring is shown in Fig.1. In most surgical tasks, transferring objects or purely moving tools are inevitable. Peg transfer is one of the standard tasks that are suitable for transferring training. In order to train, develop and test the peg transfer task, Asynchronous Multi-Body Framework (AMBF)[2] is used as the simulated environment based on our previous work[3], and then validate on the da Vinci Robot. Fig.2 shows the simulation environment (a) and da Vinci Robot (b) used in validation of the proposed. In Peg transfer task, the transferring process happens when the gripper is carrying the peg or moving tools to reach the peg. Therefore, the transferring would started from a random pillar with the peg to another random pillar as the target. The starting and targeting points are defined as:

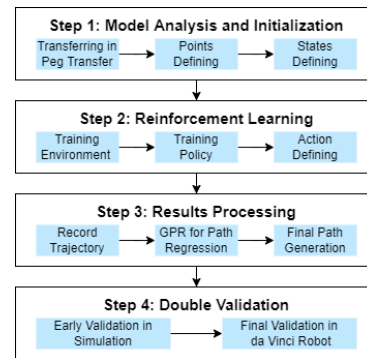


Fig. 1 Framework of the proposed path generation method

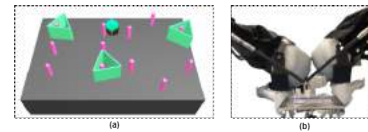


Fig. 2 Overview of the training environment (a) and the validation environment (b)

$$\begin{cases} P_0 = [x_0, y_0, z_0] \\ P_e = [x_e, y_e, z_e] \end{cases} \quad (1)$$

The gripper state contains its position as well as its orientation. Using quaternion to represent its orientation, and its state in time t is defined as:

$$S(t) = \begin{bmatrix} p_x(t), p_y(t), p_z(t), \\ o_x(t), o_y(t), o_z(t), o_w(t) \end{bmatrix} \quad (2)$$

Both the points and gripper state are in the global frame for easier processing. And the boundary for training depends on the size of pegboard. Here we have: $x \in [-0.72, 0.56]$, $y \in [-0.72, 12]$, $z \in [-0.5, 0.5]$. For training, the starting points are randomly picked from the range $[-0.1, 0.1]$ with equal probability in all x, y, z axes, while the targeting points are chosen randomly based on the pillar's position, a fixed coordinate throughout the training. Then three targeting points are chosen based on different distances between starting and targeting points, from close to far. For practical consideration, both gripper and peg are objects with volume, therefore, a round shape with radius $r = 0.08$ is defined as the peg. After initializing the environment, the action ΔS is defined as the variation of state of the gripper measured in the global frame. The action of the gripper can be represented as:

TABLE I Metrics in Simulation and Real robot

	S-Left	S-Mid	S-Right	R-Left	R-Mid	R-Right
M(m)	0.636	0.290	1.063	0.0440	0.0298	0.0327
t(s)	0.53	0.2	0.6	1.17	0.87	0.97
A(m/s)	1.200	1.446	1.772	0.0376	0.0342	0.0337

$$\Delta S(t) = S(t) - S(t-1) \quad (3)$$

This action will be the output command from the training model to control the gripper. Since the output control command is a vector with continuous values, thus the training policy is designed with the algorithm, Deep Deterministic Policy Gradients (DDPG)[4], which is widely used for continuous control[5]. The rewards are defined as:

$$R = \begin{cases} -1.0 & \text{if over boundary} \\ -\frac{d}{D} + k & \text{if moving away from the target} \\ -\frac{d}{D} & \text{if moving close to the target} \\ 1.0 & \text{if reaching the target} \end{cases} \quad (4)$$

where d is the distance between the current gripper position and the target point using Euclidean norm. D and k are constant for adjusting the rewards. The value of D is chosen empirically, otherwise, the gripper may collide or reach the boundary, and k must be a small negative, together with D to control the gripper. In our model, $D = 18$ and $k = -0.2$. Also, when t reaches maximum time steps, $R = -1.0$. Unlike other rewards functions, like [5], except the success or failure cases, the other two rewards aim to guide the agent following the way of approaching the target, which efficiently increases the training and path generation.

During the training, success happens when the gripper reaches the target point without collision or out-of-bounds. Once the simulation consecutively succeeds 100 times, the model stops training and records the trajectory in the simulation. These trajectories are treated as demonstrations, each one of them indicates one path to the target. To extract their features and generate the final path, Gaussian Process Regression (GPR) is used. With uncertainty of the training results, GPR will compute the final path as required and reduce errors. After that, further processing can ensure the endpoint will reach the close proximity to the target point. Through this method, the path generation of other tasks, like needle passing and pattern cutting could follow the training strategy. From the framework view, the only difference would be the Step 1 model analysis. For example, Needle passing could set several middle target while pattern cutting could change the rewards to follow the cutting curve.

RESULTS

The training curve is shown with average reward curve in Fig.3(a). The final success rate is close to 100%, while the average reward increases to its highest possible value. The final generated path is shown in Fig.3(b). In the figure, Red line indicates the final path, circle represents the volume of a peg and all blue points are point path before GPR process. The generated path will certainly reach the allowing range of targetting point. Fig.4 shows the frames of gripper

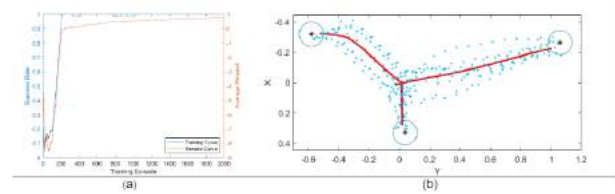


Fig. 3 a) Training and Reward curve. b) Generated path

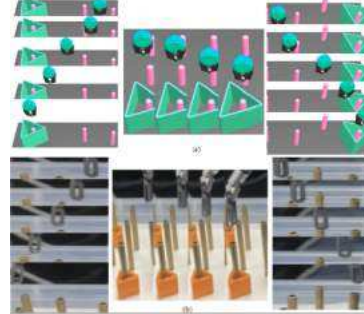


Fig. 4 a) Simulation validation frames, b) da Vinci validation frames

approaching the target based on the similar generated path in this framework. In the real-world validation, the initial position of end-effector tools are randomized. Fig.4 shows the frames of gripper approaching the target pillar when tested with the real da Vinci robot. And Table.I shows the metrics: i) path-length (M-m); ii) completion time (t-s); iii) average speed (A-m/s) during validations in both environments, simulation(S) and real(R).

DISCUSSION

In this paper, we present a novel method for path generation to conduct automatic transferring of pegs. The results of the generated path and their validation verified that the proposed path generation method could automate this repetitive surgical task. Unlike other research like [5], the method used after RL part aims for combining the strength of both LfD and RL. If integrated this work with our previous work on shared control[3], a surgeon will only need to pinpoint a few locations, the robot can then complete the whole peg transfer task.

REFERENCES

- [1] H. C. Lin, I. Shafran, D. Yuh, and G. D. Hager, "Towards automatic skill evaluation: Detection and segmentation of robot-assisted surgical motions," *Computer Aided Surgery*, vol. 11, no. 5, pp. 220–230, 2006.
- [2] A. Munawar, Y. Wang, R. Gondokaryono, and G. S. Fischer, "A real-time dynamic simulator and an associated front-end representation format for simulating complex robots and environments," in *2019 IEEE/RSJ International Conference on Intelligent Robots and Systems (IROS)*, Nov 2019, pp. 1875–1882.
- [3] J. Chen, D. Zhang, A. Munawar, R. Zhu, B. Lo, G. S. Fischer, and G.-Z. Yang, "Supervised semi-autonomous control for surgical robot based on banoian optimization," in *2020 IEEE/RSJ International Conference on Intelligent Robots and Systems (IROS)*, 2020, pp. 2943–2949.
- [4] T. P. Lillicrap, J. J. Hunt, A. Pritzel, N. Heess, T. Erez, Y. Tassa, D. Silver, and D. Wierstra, "Continuous control with deep reinforcement learning." in *ICLR (Poster)*, 2016. [Online]. Available: <http://arxiv.org/abs/1509.02971>
- [5] Z. Chiu, F. Richter, E. K. Funk, R. K. Orosco, and M. C. Yip, "Bimanual regrasping for suture needles using reinforcement learning for rapid motion planning," *CoRR*, vol. abs/2011.04813, 2020. [Online]. Available: <https://arxiv.org/abs/2011.04813>

Augmented Reality for Seamless Human-Robot Interaction in Surgery

H. Iqbal¹ and F. Rodriguez y Baena¹

¹*Mechatronics in Medicine, Imperial College London,
{hisham.iqbal13, f.rodriguez} [at] ic.ac.uk*



Fig. 1 A co-registered AR surgical workflow, using the HoloLens 2 and Navio[®] system. T_C^H : calibration matrix between tool pose in virtual world-frame T_P^H and surgical coordinates T_P^C .

INTRODUCTION

In the field of computer-assisted orthopaedic surgery (CAOS), new display technologies such as augmented reality (AR), defined as the superposition of computer-generated imagery onto the unoccluded, real environment [1], have the potential to transform the way clinicians manage patient-specific data during surgery. Modern CAOS systems require surgeons to visualise and interact with 3D medical data (e.g. MRI/CT scans, surgical cutting plans etc.) in the 2D environment of touchscreen monitors. Such user interfaces can divert the surgeon's attention from the operating site and require a mental coordinate mapping process to determine the spatial transformation between a surgeon's real viewpoint and the monitor's virtual view. In contrast, specialised AR user interfaces capable of directly projecting 3D information onto anatomy can allow a surgeon to maintain their line-of-sight to the operating site, and also improve the quality of human-robot interaction of CAOS systems through reductions in visual clutter and sight diversion, and improvements in situational awareness, as investigated in literature [2]. A novel, AR-centric workflow was designed to exploit the reported benefits of AR in the context of a simulated computer-assisted patellofemoral arthroplasty (PFA), using the Navio[®] (Smith & Nephew, UK), a commercially available CAOS platform. The constructed system co-registered the Navio[®] platform's optical tracker with the fixed virtual world frame of a HoloLens 2 (Microsoft, USA) headset, and provided in-situ holographic guidance during two surgical tasks

carried out during a PFA, patient-registration and robot-assisted cutting (cutting accuracy previously reported at [3]). A pre-clinical study was carried out to investigate the impact of the new AR workflow on mental-workload and usability measures when compared to the standard workflow delivered by the platform.

MATERIALS AND METHODS

The system structure (shown in Figure 1), consisted of two devices: a client Unity app (Unity Technologies, USA) deployed to the HoloLens, and a server-side software running on the surgical platform. On the server side, a customised build of the Navio[®] software was developed as part of a joint research collaboration with Smith & Nephew (Innovate UK, 103950). The customised software broadcasted tracking and medical data while carrying out a computer-assisted PFA. On the client side, the HoloLens app carried out two tasks – registering the surgical coordinate frame of the Navio[®] with the headset's fixed virtual world frame by using tools visible to both systems (as seen in Figure 1), while rendering and automatically positioning in-situ holographic guidance. By using native sensor data, the HoloLens detected IR-reflective marker arrays mechanically fixed to surgical tools or anatomy when using the Navio[®]. Following calibration, the workflow provided overlaid holographic guidance during two surgical tasks: patient-registration, and computer-assisted cutting. Patient registration was achieved by tracing over the surface of the distal femur with an optically tracked probe. Visual feedback on task progress was provided through a display monitor for standard procedures, whereas the AR workflow rendered a holographic point-cloud directly onto the surgical site. After setting an implant plan, the surgical robot generated a cut plan, displayed to the user as a virtual colour-coded cut-plan showing the depth and locations of required cuts. In the standard procedure, a model of the cutting-plan was shown on the monitor, and required inputs from the surgeon to adjust the view as desired, however, the AR workflow directly rendered a trackable overlay of the cut-plan onto the surgical site (see Figure 2), which dynamically updated as the bone was burred. As part of a pre-clinical study, six non-clinical volunteers were recruited to carry out standard and AR-enhanced PFA procedures with the Navio[®].

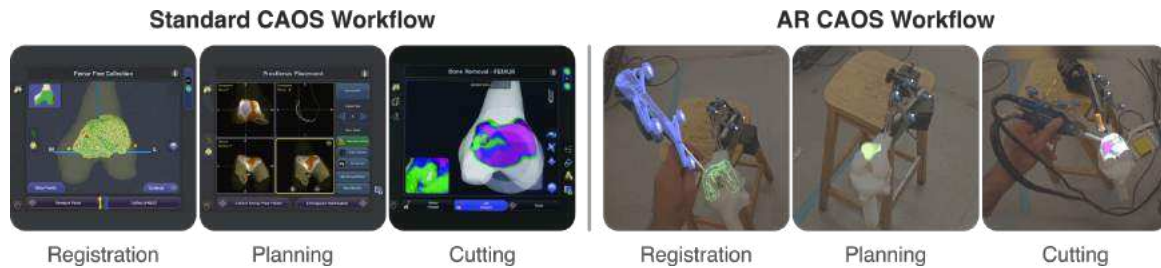


Fig. 2 Examples of standard and novel AR-centric workflow for Navio®

Mean TLX Scores for Patient-Registration Task			Mean TLX Scores for Bone-Cutting Task		
TLX Dimension	Standard	AR	TLX Dimension	Standard	AR
Mental Demand	32.5	29.167	Mental Demand	55	52.5
Physical Demand	18.333	14.583	Physical Demand	58.333	60.833
Temporal Demand	45.833	41.667	Temporal Demand	43.333	41.667
Performance	71.667	80	Performance	75.83	77.5
Effort	34.167	35.833	Effort	58.333	55.833
Frustration	20	17.5	Frustration	54.167	52.5

Fig. 3 Tables of TLX survey responses when using standard and AR workflows during two surgical tasks.

After completing a patient registration task, volunteers were asked to complete the surgical plan and mill plastic bone using visual guidance provided by the standard and AR workflows. To determine the usability and mental workload when using the standard and AR workflow in the two tasks, volunteers were asked to complete a usability survey using the NASA Task Load Index (TLX) format, assessing six categories: mental demand, physical demand, temporal demand, performance, effort, and frustration.

RESULTS

Mean TLX scores for each workload dimension (mental, physical etc.) were calculated for the patient registration and cutting tasks. TLX scores were assigned between 0-100 in steps of 5 in response to each TLX dimension. Mean TLX data are shown in Figure 3. For the first task, patient registration, AR outperformed the standard in every TLX dimension except 'Effort'. 5 Wilcoxon signed-rank tests across each TLX dimension found no statistically significant difference between the standard and AR TLX responses (p values from: .0625 – 1, $\alpha = .05$). For the second task, cutting, survey responses showed AR outperformed the standard workflow in every TLX dimension except 'Physical Demand'. Once more, no statistically significant differences were found between the standard and AR datasets (p values from: .6875 – 1, $\alpha = .05$).

DISCUSSION

This study describes the development and initial testing of a novel AR workflow designed to complement an established surgical robot's workflow. We report an initial analysis of the results, a usability survey based on the NASA TLX format, with further quantitative assessments of user performance (e.g. quality of patient-registration and economy of tool motion during cutting)

currently being processed for analysis. To the best of the authors' knowledge, this study is one of the first to fully integrate a mixed-reality workflow for knee-arthroplasty with a commercially available CAOS system. The reported setup provided holographic guidance for the duration of a procedure, providing an immersive platform to assist with patient registration, implant planning, and cutting via a dynamically updating holographic cut-map (see Figure 3). The positive trends in the study's findings regarding mental workload add to existing studies which report beneficial reductions in mental workload when using AR for surgical scenarios, such as catheter-insertion [4] and skull-base surgery [5]. Whilst no statistically significant gains in usability were obtained with this study cohort, a notable limitation was the recruitment protocol, which could not actively target clinical volunteers, making it challenging to decouple the effects of AR on surgical task performance and the learning curve associated with using CAOS technologies as a novice user. Future work aims to build upon the findings of this study to establish whether the novel AR workflow impacts surgical task-performance and mental workload in a clinically trained study population, in a setting more representative of the operating theatre (e.g. cadaveric testing in surgical labs), along with exploring physical discomfort associated with continuous use of HMDs during surgery.

REFERENCES

- [1] R. Azuma, Y. Baillot, R. Behringer, S. Feiner, S. Julier, and B. Macintyre, "Recent advances in augmented reality. IEEE Comput Graphics Appl," *Computer Graphics and Applications, IEEE*, vol. 21, pp. 34–47, 12 2001.
- [2] L. Qian, J. Y. Wu, S. P. DiMaio, N. Navab, and P. Kazanzides, "A Review of Augmented Reality in Robotic-Assisted Surgery," *IEEE Transactions on Medical Robotics and Bionics*, vol. 2, no. 1, pp. 1–16, 2020.
- [3] M. Casper *et al.*, "Accuracy assessment of a novel image-free handheld robot for Total Knee Arthroplasty in a cadaveric study," *Computer Assisted Surgery*, vol. 23, no. 1, pp. 14–20, 1 2018. [Online]. Available: <https://doi.org/10.1080/24699322.2018.1519038>
- [4] E. Azimi *et al.*, "An Interactive Mixed Reality Platform for Bedside Surgical Procedures BT - Medical Image Computing and Computer Assisted Intervention – MICCAI 2020," A. L. Martel, P. Abolmaesumi, D. Stoyanov, D. Mateus, M. A. Zuluaga, S. K. Zhou, D. Racoceanu, and L. Joskowicz, Eds. Cham: Springer International Publishing, 2020, pp. 65–75.
- [5] L. Li, J. Yang, Y. Chu, W. Wu, J. Xue, P. Liang, and L. Chen, "A Novel Augmented Reality Navigation System for Endoscopic Sinus and Skull Base Surgery: A Feasibility Study." *PLoS one*, vol. 11, no. 1, p. e0146996, 2016.

A Modular ROS-based dVRK Teleoperation Controller Architecture

R. Gondokaryono^{1,2}, M. Haiderbhai^{1,2}, A. Munawar³,
T. Looi², J. Drake², and L. A. Kahrs^{1,2}

¹ *Department of Computer Science, University of Toronto,*

² *The Wilfred and Joyce Posluns CIGITI, SickKids, Toronto,*

³ *Department of Computer Science, John Hopkins University*
radian.gondokaryono@mail.utoronto.ca

INTRODUCTION

The da Vinci Research Kit (dVRK) [1], a hardware and software stack for research development, implements the teleoperation control of the Patient Side Manipulators (PSMs) using the Master Tool Manipulators (MTMs), with the original capabilities of the da Vinci Surgical System such as input device clutching, rotated vision perspective control, and input output position scaling.

A recent research trend in automation and learning [2], uses 3D simulators such as AMBF [3], SurRol [4], and UnityFlexML [5]. These simulators re-implement the teleoperation controller and kinematics solver due to the non-modularity of the dVRK software (Fig. 1a). We argue that future dVRK research requires an architecture, that supports testing algorithms in simulation and real hardware, with a singular teleoperation controller and kinematics. This in turn will provide a robust robot test workflow and standardized algorithm comparisons and benchmarks.

Another research trend is the use of alternative input devices to control simulated PSMs. AMBF incorporates a large variety of input device options. Additionally, there has been work in using the MTM to teleoperate industrial robots [6]. In all of these cases, the teleoperation controller and kinematics are re-implemented.

To the best of our knowledge, there does not exist a formal definition of the dVRK teleoperation interfaces. We propose a modular dVRK teleoperation controller architecture, that is based on the Robot Operating System (ROS), with the original capabilities and further improvements such as:

- A lightweight and minimal dependency software implementation with a modular kinematics solver
- Defined input interface to integrate a variety of input devices
- Defined output interfaces that integrates to existing dVRK simulations and hardware

MATERIALS AND METHODS

In this architecture, the input devices, output modalities, and teleoperation controller and kinematics are separated

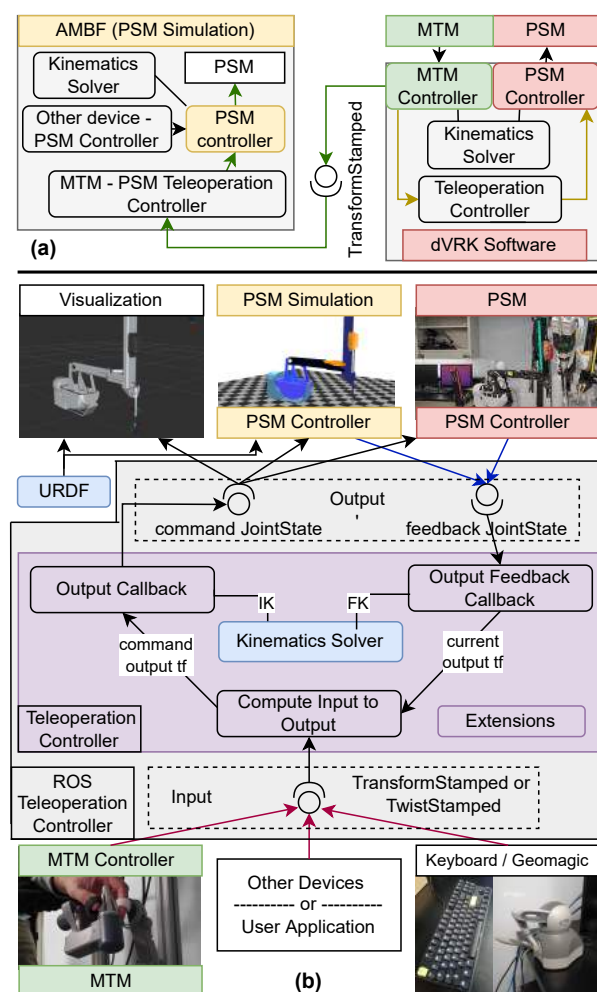


Fig. 1 a) Current dVRK teleoperation (yellow arrows) and AMBF MTM-PSM teleoperation (green arrows). b) Our modular ROS-based dVRK teleoperation controller architecture. FK is forward kinematics, IK is inverse kinematics, and URDF is Unified Robotics Description Format. Yellow, red, and green components are same as in a. Only one red and one blue arrow is valid at a time. Blue components have identical kinematics.

into individual components which communicate with each other through ROS. This is shown in Fig. 1b. The

components on the top are output modalities, which refer to any joint controller that interacts with the simulated or real robot.

The top grey box shows the output interfaces. An output command, which uses the *servo_jp sensor_msgs/JointState* Collaborative Robotics Toolkit (CRTK) definition [7], is an interface that sets the target joint positions to the PID controller without interpolation. This allows the controller to remain agnostic to different robot dynamics, as the joint controls are handled by the simulator or hardware controller. An output feedback is the current joint positions of the output modality which uses the *measured_js sensor_msgs/JointState* CRTK definition. By only supporting JointState for the output interfaces, the dependency of the kinematics provided by the dVRK software/simulations is removed, our solution replaces the kinematics solver within the controller (purple box).

The bottom grey box shows the input interface which uses ROS message types that are chosen as part of CRTK interface definitions. Namely, *geometry_msgs/TransformStamped* for the follower teleoperation and *geometry_msgs/TwistStamped* for the increment teleoperation. A follower teleoperation will compute the output transform (tf) so that the difference of the output tf and start output tf is the same as the difference of the current input tf and start input tf. An increment teleoperation will simply increment the current output tf at every input. This input interface behaves like the *servo_jp* command with no underlying interpolation. The architecture is event-driven where the output command will be issued every time an input is received.

This architecture uses a closed form kinematics solver, for the PSM, that was developed for AMBF. The URDF, used for simulators and visualization, along with the kinematics solver both use identical kinematics (blue boxes).

RESULTS

The proposed control architecture is tested using either a keyboard, a Geomagic Touch haptic device, or the MTM as input devices, as output modalities a PSM in Unity simulation, a PSM in AMBF, and the real PSM. Fig. 1b illustrates these components. The Unity and AMBF simulation use a PSM model described by a URDF [8]. We continuously move the input device which results in moving the output modality to record latencies seen in Table I. The latency is defined as the duration from when the input is sent to when it is received by the output modality, similar to the ROS latency tests [1]. We provide videos of the tests here.

DISCUSSION

We implement a dVRK teleoperation controller architecture that is lightweight and modular. It will be beneficial for the development of algorithms for higher levels of

TABLE I Output latency test results of different scenarios of teleoperation control. All values are averages over the test duration of 3 minutes. ¹

Input	Output	Input [Hz]	Latency [ms]
Keyboard	AMBF PSM	15.51	0.668
Keyboard	Unity PSM	25.02	0.773
Keyboard	Real PSM	20.33	0.802
Geomagic	AMBF PSM	100.00	0.691
Geomagic	Unity PSM	100.00	0.679
Geomagic	Real PSM	100.00	0.742
MTM	AMBF PSM	99.442	0.818
MTM	Unity PSM	99.44	0.692
MTM	Real PSM	99.49	0.743
MTM	AMBF and Real PSM	90.42	0.868

autonomy, especially those that utilize simulators and must be verified with the real dVRK. The latencies (Table I) are on average similar to the reported 0.792 ms latency for a ROS publisher subscriber running at 1 kHz [1], and as previously stated, is negligible for systems running at 100 Hz or less. The keyboard input is limited by the default Linux keyboard repeat rate. The test video qualitatively shows smooth control for every output modality.

The extensions component (Fig. 1b) allows future developments to provide capabilities such as virtual fixtures, workspace constraints, collision checking, etc. Here, we will add visualizations of robot kinematics and teleoperation transforms. Additionally, we plan to auto generate the kinematics solver together with URDF kinematics which allows researchers to introduce new tools for sim-to-real development. Furthermore, this dVRK teleoperation controller architecture enables implementation of other kinematics solvers to control a different robot such as an industrial robot arm. While the sole dependency is ROS and its' upstream packages, the defined interfaces allow other implementations of communication in the future. Our source code will be released once these contributions are finalized.

REFERENCES

- [1] Z. Chen *et al.*, "Software architecture of the da vinci research kit," in *First IEEE Intern. Conf. on Robotic Computing (IRC)*, 2017, pp. 180–187.
- [2] C. D'Ettorre *et al.*, "Accelerating surgical robotics research: A review of 10 years with the da vinci research kit," *IEEE Robotics and Automation Magazine*, vol. 28, no. 4, pp. 56–78, 2021.
- [3] A. Munawar *et al.*, "A real-time dynamic simulator and an associated front-end representation format for simulating complex robots and environments," in *2019 IEEE/RSJ Intern. Conf. on Intelligent Robots and Systems (IROS)*, 2019, pp. 1875–1882.
- [4] J. Xu *et al.*, "Surrol: An open-source reinforcement learning centered and dvrk compatible platform for surgical robot learning," in *IEEE/RSJ Intern. Conf. on Intelligent Robots and Systems (IROS)*, 2021, pp. 1821–1828.
- [5] E. Tagliabue *et al.*, "Soft tissue simulation environment to learn manipulation tasks in autonomous robotic surgery," in *IEEE/RSJ Intern. Conf. on Intelligent Robots and Systems (IROS)*, 2020, pp. 3261–3266.
- [6] J. Liang *et al.*, "Using dvrk teleoperation to facilitate deep learning of automation tasks for an industrial robot," in *IEEE Intern. Conf. on Automation Science and Engineering (CASE)*, 2017, pp. 1–8.
- [7] Y.-H. Su *et al.*, "Collaborative robotics toolkit (crtk): Open software framework for surgical robotics research," in *Fourth IEEE Intern. Conf. on Robotic Computing (IRC)*, 2020, pp. 48–55.
- [8] R. A. Gondokaryono *et al.*, "An approach to modeling closed-loop kinematic chain mechanisms, applied to simulations of the da vinci surgical system," *Acta Polytechnica Hungarica*, vol. 16, no. 8, pp. 29–48, 2019.

¹Hardware: Intel® Core™ i7-8700 CPU (3.20GHz), 16 GB RAM, NVIDIA GTX 1050 Ti. Software: Ubuntu 20.04.3 LTS, ROS Noetic.

fMRI and MEG Compatible Hand Motion Sensor

L Lyu, E Monfort Sanchez, M Runciman, G Mylonas, J Avery

The Hamlyn Centre, Imperial College London, London, UK

james.avery@imperial.ac.uk

INTRODUCTION

Functional magnetic resonance imaging (fMRI) and magnetoencephalography (MEG) are two of the most important neuroscience tools, providing spatial and temporal localisation of brain activity [1]. Investigations of somatosensory function or neuroplasticity in rehabilitation greatly benefit from the correlation of neuroimaging and motion sensor data [2], particularly considering recent MEG breakthroughs which enable more accurate assessment of brain function during real world visuomotor coordination tasks [3]. However, constructing wearable sensors suitable for these environments presents a significant design challenge. Interaction between the MR environment and ferromagnetic components present safety concerns. Further electronics and changes in the static magnetic field i.e., from moving metal components, can produce interference. Existing MR compatible sensor systems, such as fibre optic sensors [2][4] or Vision-Based Motion Analysis [5] are either non-cost-effective or require line of sight from multiple angles, which may not always be feasible in fMRI or MEG rooms. We propose a MR/MEG compatible joint sensor, Fig. 1, to track finger motion during grasping tasks, common in rehabilitation or functional experiments. Using the Skinfoflow [6] principle of fluidic transmission and metal free construction, the sensor has the potential to track the joint angle without creating artefacts in the neuroimaging data, at a lower cost than fibre optic sensors, and without the need for line of sight.

MATERIALS AND METHODS

The sensor consists of two soft components: a soft liquid sensor positioned on the finger joint, and a computer vision (CV) system to detect the liquid level at the opposite end of the tubing. Bending of the finger joint displaces the coloured water within the sensor chamber, which is transmitted a sufficient distance from the sensitive equipment through tubing to a glass display tube. The computer vision system then detects displacement of the liquid in the display tube.

The sensor body, Fig. 1B, contains a network of fluid chambers, which are compressed during bending and displace the liquid down the attached tube. This design also reduces the resistance to the natural bending motion at the finger joints. The sensor was constructed from two moulded Sylgard 186 (Dow, Inc.,U.S.) parts glued together with SilPoxy (Smooth-On, Inc.,U.S). Silicone tubing was used to connect the sensor inlet to the CV system. The fluid level inside the tubing was obtained by segmentation of video recorded at 30 fps using a

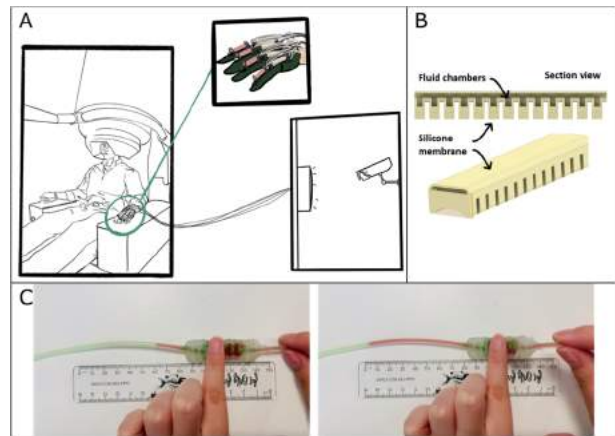


Fig 1. fMRI/MEG compatible sensor concept: (a) fluid displacement from hand motion transmitted to computer vision system away from sensitive equipment (b) sensor geometry (c) demonstration of working principle

webcam (Logitech Brio). The edge within each row of pixels within the liquid segmentation was then averaged to obtain a single fluid level in mm. The total tube length from sensor to CV was 1.5 m.

Initially a motorised hinge was used to evaluate the relationship between bending angle and the change in displaced fluid. The sensor was connected to both leaves of the hinge, and a single leaf was driven directly by a 0.9° stepper motor (uStepper), Fig. 2A. Thus, the motor angle represented the ground truth bending angle, enabling the characterisation of the accuracy and repeatability of the sensor. The hinge joint was

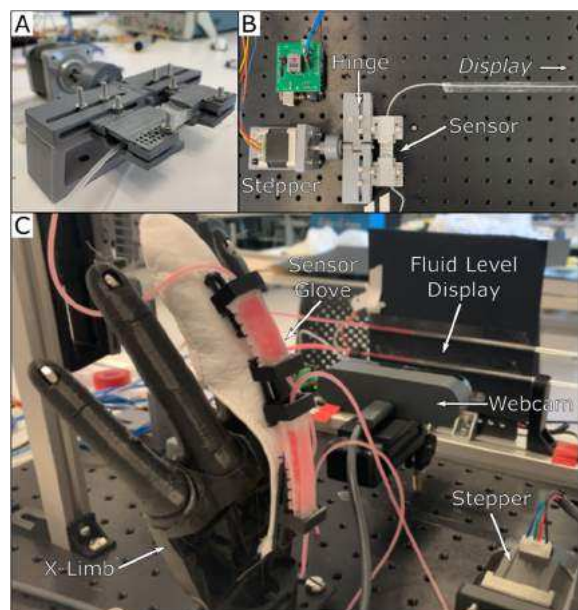


Fig 2. Experimental setup: (a) Sensor in motorised hinge (b) full hinge setup (c) sensor glove on X-Limb prosthetic

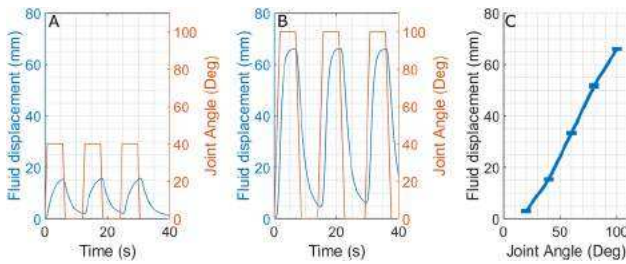


Fig 3. Hinge experiment results: fluid displacement captured by CV system during (a) 40° (b) 100° actuation (c) repeatability of final displacement with joint angle (mean±std)

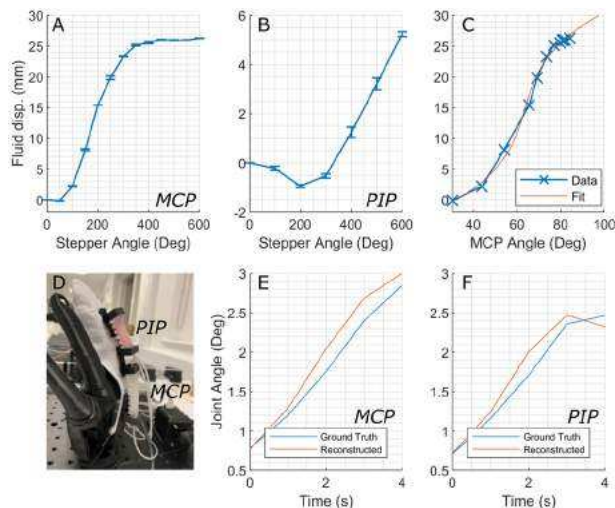


Fig 4. X-Limb experimental results: fluid displacement recorded by CV system during cable driven grip motion (a) MCP (b) PIP joint (c) comparison with ground truth angle (d) finger glove embodiment on X-Limb prosthetic (e) and (f) reconstructed joint angle for MCP and PIP

repeatedly actuated ($n=10$) from 20° to 100° with a 5 second settling time.

The sensor was then tested using a flexible 3D-printed cable driven finger from the open-source X-Limb prosthetic [7], Fig 2C. A repeatable grip motion was created using a stepper motor and the ground truth of each joint angle was obtained through tracking four markers using OpenCV. The sensor was placed on the Metacarpophalangeal (MCP) and Proximal Interphalangeal (PIP) joints, and data from 10 repeated grip motions was used in a polynomial regression to convert fluid level to joint angle. The joint angle of a further three repeats were used to estimate the accuracy of the reconstructed finger pose.

RESULTS

In the hinge experiments the sensor demonstrated a linear response for bending angles 20° and above ($R^2=0.99$), Fig. 3C, with a mean repeatability error of 0.25 mm (< 1%). The results from both the MCP and PIP joints on the X-Limb prosthetic finger, Fig. 4, were similarly repeatable with errors of 0.13 mm (< 1%). However, the correlation between fluid level measured and joint angle was not linear during the grip motion, thus a 4th order polynomial was used in the regression model. The finger pose was successfully reconstructed with an accuracy of 8.8° (6.8%) with the greatest error.

DISCUSSION

Overall, the results demonstrate the principle that the finger joint angle can be sensed using fluidic transmission in a sensor with metal free construction. The sensor is also lightweight (10g per joint) and low cost, using ~ £7 of materials excluding the camera. The results of the hinge experiments demonstrate the highly repeatable and linear response of the system for angles between 20-100°. The motion of the sensors on the X-Limb finger was a combination of both joints and orientation changes, and thus a higher order polynomial fit was required to estimate the joint angle. Integrating the sensor into the wearable housing did not adversely affect the performance as the repeatability error was unchanged from hinge experiments (<1%). This was sufficient to reconstruct the finger pose during a grip motion. This demonstrates the feasibility of the sensor as a wearable device for tracking hand motion during simple grasping tasks for neuroimaging.

The dynamic response of the sensor requires improvement before it is ready to incorporate into more complicated experiments, as the settling time for the largest angle changes are approximately 4s. This lag was also the cause of the larger error in reconstructed angle when the prosthetic was in motion. This error could be reduced, as per the Hagen-Poiseuille equation, by changing the tubing material to reduce friction (e.g., PTFE) and increasing the diameter to reduce the resistance to flow. However, increasing cross sectional area would also reduce the change in fluid level and would thus be harder to detect with the current CV system. Future work in improving the CV system would also be beneficial for measuring the smaller angle changes ($\leq 10^\circ$), which were not reliably detected.

REFERENCES

- [1] N. Williams and R. N. Henson, "Recent advances in functional neuroimaging analysis for cognitive neuroscience," *Brain Neurosci. Adv.*, vol. 2, Jan. 2018.
- [2] H. K. Yap, et al., "A Magnetic Resonance Compatible Soft Wearable Robotic Glove for Hand Rehabilitation and Brain Imaging," *IEEE Trans. Neural Syst. Rehabil. Eng.*, vol. 25, no. 6, pp. 782–793, 2017.
- [3] E. Boto et al., "Moving magnetoencephalography towards real-world applications with a wearable system," *Nature*, vol. 555, no. 7698, pp. 657–661, 2018.
- [4] F. Taffoni, D. Formica, P. Saccomandi, G. D. Pino, and E. Schena. Optical fiber based mr-compatible sensors for medical applications: An overview. *Sensors*, 13(10):14105–14120, 2013. pages 5, 6
- [5] R. Poppe. Vision-based human motion analysis: An overview. *Computer vision and image understanding*, 108(1-2):4–18, 2007. pages 7
- [6] G. Soter, M. Garrad, A. T. Conn, H. Hauser, and J. Rossiter. Skinflow: A soft robotic skin based on fluidic transmission. In 2019 2nd IEEE International Conference on Soft Robotics (RoboSoft), pages 355–360. IEEE, 2019. pages 7, 8, 11
- [7] A. Mohammadi, J. Lavranos, H. Zhou, R. Mutlu, G. Alici, Y. Tan, P. Choong, and D. Oetomo. A practical 3d-printed soft robotic prosthetic hand with multiarticulating capabilities. *PloS one*, 15(5):e0232766, 2020.

Signature Robot: A Miniature Robot for Orthopaedic Surgery

Spyridon Souipas*, Stephen G. Laws*, Ferdinando Rodriguez y Baena*, Brian L. Davies*

*Mechatronics in Medicine Laboratory, Imperial College London, UK

{stephen.laws14, spyridon.souipas14, f.rodriquez, b.davies}@imperial.ac.uk

I. INTRODUCTION

Imperial College London's first venture into orthopaedic robotic surgery was with a spinoff company called Acrobot Ltd. This was developed over many years, culminating in a series of uni-condylar knee replacement (UKR) surgery operations with excellent results [1]. Much was learned from this experience with many hardware iterations culminating in a trolley based cooperative system with 3 powered axes carrying a cutter that required large arm motions.

To exploit the resulting know-how, a new company, Signature Robot Ltd, was founded. This also uses a cooperative robot, but instead of being a "hands on" device, the cutter motor is held between the fingers while the wrist is supported comfortably on a robot platform. This gives excellent synergy, combining the sensitive finger control of the surgeon with the precision and safety constraints ('active constraints' [2]) of the robot. The small, light robot is clamped on a simple passive arm, as seen in Figure 1, which can be readily repositioned to access regions of the knee, e.g., the tibia and femur.

This paper presents the design for Signature Robot and how it addresses the limitations of the Acrobot, the accuracy of the positioning of the end effector is then quantified using a kinematic calibration routine.

II. METHODS AND MATERIALS

The long development of the ACROBOT system gave rise to considerable insights and development changes. Initially various gross positioning systems were developed to deal with the large cutting forces experienced in total knee replacement (TKR). It was only when unicondylar knee replacement was developed that the limited bone removal and low cutting forces allowed the use of a smaller trolley-mounted robot adjacent to the OR table. A 3 axes powered arm, carrying a passive orientation device that held an 8 mm diameter cutting burr, allowed registration of the robot to the patient to carry out the preoperative CT scan-based plan. The results of a small clinical trial demonstrated the improved accuracy of the robot compared to experienced surgeons using conventional minimally invasive surgery (MIS) [1]. The benefits of using active constraints to ensure safety of the cooperative robot were also demonstrated [3].

Benefiting from the Acrobot experience, the patented Signature Robot has been designed with a miniaturised parallel wrist mechanism, enabling motion across both pitch and yaw, as shown in Figure 2a, based on the mechanics of differential

gears. The robot can achieve 120° motion along each of these axes. The parallel system offers a threefold benefit over the serial manipulator of the original ACROBOT. Firstly, it provides identical impedance across pitch and yaw due to the parallel nature. Secondly, the two motors contribute to the force output of the pitch and yaw equally which, in turn, allows for the incorporation of smaller motors to output the same force. This miniaturisation ultimately leads to a reduction in the inertia and thus the impedance of the overall platform, significantly reducing the perceived impedance when back-driving the device. In addition to pitch and yaw, the Signature Robot can also move up to 100mm along a linear axis, this axis enjoys minimal impedance due to the integrated high precision linear bearings.



Figure 1: Visualisation of Signature Robot passive arm

The working volume of the Acrobot exceeded what was necessary for knee replacement surgery. Conversely, the working volume of the Signature Robot was designed with the purpose of performing UKR. Despite the small size of the robot there is no reduction in joint dexterity. Combining this design with the low impedance mechanism has allowed the Signature Robot to provide precise and dexterous finger-based movements to manipulate the end effector. The Signature Robot has also incorporated a 6 degree-of-freedom force/torque sensor between the operator's hand and the robot, as seen in Figure 2a. This placement permits new feed-forward algorithms to aid the desired motions, as well as the prerequisite active constraints

implementation.

Registration of the ACROBOT was a cumbersome procedure, and repositioning the platform was also difficult. Ultimately, the Signature Robot will incorporate a markerless registration and real-time tracking platform [4]. Furthermore, the Signature Robot will be mounted on an entirely passive gross positioning system, shown in Figure 1, that can be locked when the robot has been placed in a desired position with respect to the patient. This reduces the complexity, the size and cost of the platform.

The benefits of Signature Robot over the ACROBOT have been presented here in terms of size, workspace volume, ease of repositioning and registration. Further validation was performed to quantify the accuracy of the manufactured setup. An optical tracker (fusionTrack 500, Atracsys, Switzerland) was employed to compare the true position of the end effector with the position obtained by the motors. The forward kinematics of the robot include 13 fixed parameters that describe the kinematic geometry. The regression algorithm implemented converged these design parameters from the computer aided design (CAD) model to their true values.

III. RESULTS

Through kinematic calibration, the errors along the manufactured platform were explored. The culmination of individual errors allowed for a total positional error estimation of the end effector. This error has been plotted in Figure 2b. Ultimately, the mean positional RMS error of Signature Robot was calculated to 0.82 mm.

The robotic platform also boasts a reduced footprint of 150x140x150mm and weighs less than 2kg. The control system is capable of providing haptic feedback forces at the tool tip of up to 25N in the three axes whilst running a haptic control loop at 500Hz.

IV. DISCUSSION

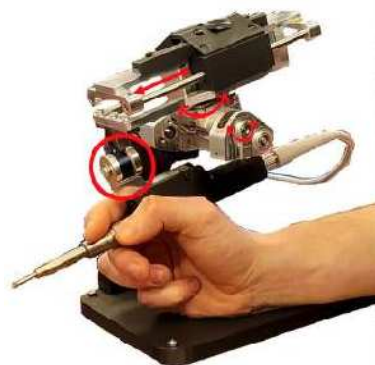
Since the clinical introduction of the ACROBOT 20 years ago, the benefits of incorporating highly accurate, robotic

assisted techniques in surgery have been constantly increasing. The Signature Robot now offers a significant footprint reduction compared to other orthopaedic robots, while also offering equal, minimal impedance across the 3 axes. By using the passive positioning arm the range of the system has increased, while also making robot repositioning in the operating room more convenient. The robot has been shown to have an end effector accuracy of 0.82 mm, this is an ideal first step in introducing the Signature Robot for cadaveric testing. Further optimisations to the design will only decrease this error further. Lastly, the integration of a new vision system will allow for real-time tissue registration, thus eliminating the need for the relatively time-consuming registration process that the ACROBOT suffered from.

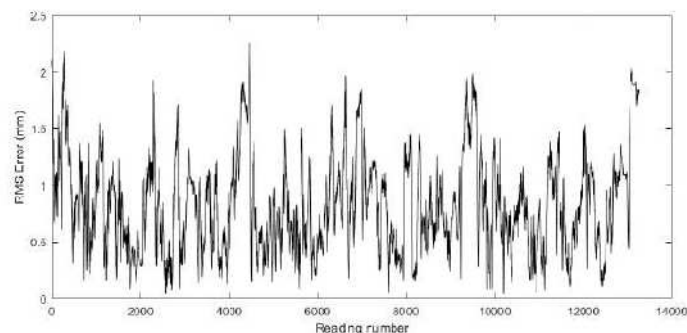
Future work will explore dissipative active constraint algorithms such as frictional constraints [5]. Two separate vision platforms will be incorporated in the robotic platform. One will allow for accurate, on-the-fly patient tissue registration and soft tissue tracking [4]. The second platform will allow for the identification of common surgical tools during operation, and subsequently will ensure that no collision occurs between robot and external agents.

REFERENCES

- [1] M. Jakopec, S.J. Harris, F. Rodriguez y Baena, P. Gomes, and B.L. Davies. Acrobot: a "hands-on" robot for total knee replacement surgery. In *7th International Workshop on Advanced Motion Control. Proceedings (Cat. No.02TH8623)*, pages 116–120, 2002.
- [2] Stuart A. Bowyer, Brian L. Davies, and Ferdinando Rodriguez y Baena. Active constraints/virtual fixtures: A survey. *IEEE Transactions on Robotics*, 30(1):138–157, 2014.
- [3] F Rodriguez, S Harris, M Jakopec, A Barrett, P Gomes, J Henckel, J Cobb, and B Davies. Robotic clinical trials of uni-condylar arthroplasty. *The International Journal of Medical Robotics and Computer Assisted Surgery*, 1(4):20–28, 2005.
- [4] Stephen G. Laws, Spyridon Souipas, Brian L. Davies, and Ferdinando Rodriguez y Baena. Toward automated tissue classification for markerless orthopaedic robotic assistance. *IEEE Transactions on Medical Robotics and Bionics*, 2(4):537–540, 2020.
- [5] Stuart Bowyer and Ferdinando Rodriguez y Baena. Dynamic frictional constraints in translation and rotation. pages 2685–2692, 05 2014.



(a) Degrees of freedom and integrated force sensor (circled)



(b) RMS Error (mm) across 13000 readings during kinematic calibration

Figure 2: Signature Robot

Optimizing Continuum Robot Tendon Routing for Minimally Invasive Brain Surgery

Margaret Rox¹, Aidan Coppinga², Robert P. Naftel³,
Robert J. Webster III¹, and Alan Kuntz²

¹*Department of Mechanical Engineering, Vanderbilt University*

²*School of Computing and Robotics Center, University of Utah*

³*Department of Pediatric Neurosurgery, Vanderbilt University Medical Center*

margaret.rox@vanderbilt.edu

INTRODUCTION

Tendon-driven continuum robots are compliant and capable of assuming complex curves, making them ideal for minimally invasive surgery in confined spaces with obstacles. These robots can achieve an infinite family of curves, determined by both actuation and design considerations, such as the tendon routing paths of tendons along the robot. Design optimization of surgical continuum robots has been studied (see [1] for review), but the idea of variable and complex tendon routing is newer, and although it has been modeled [2], it has yet to be used to design a practical surgical device. For tendon-driven continuum robots in general, design optimization has thus far focused on multi-segment robots that use straight (i.e. parallel to the backbone) segments of different lengths, where tendons terminate at various arclengths along the robot [3], [4]. The advantage of designing with nonlinearly routed tendons is the potential to enable a much more expressive family of shapes during actuation [2]. However, it has thus far been challenging to design nonlinear tendons because one is working in an infinite design space with mechanics-based models that require solving differential equations to compute robot kinematics.

Toward solving this problem, this paper presents a new tendon routing parameterization for tendon-driven robots and leverages it to optimize the routings for a design objective drawn from a practical neurosurgical application: choroid plexus cauterization for hydrocephalus [5]. This application was an early motivating example in the development of concentric tube robots, extended in [6], although physical size, achievable curvatures, and stiffness constraints have thus far limited practical fabrication of the robots designed in simulation. The endoscopic approach to choroid plexus cauterization requires maneuvering through tight spaces in the ventricles, which is challenging with traditional constant

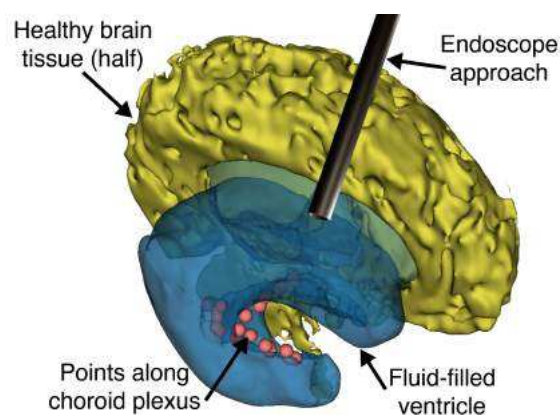


Fig. 1 Choroid plexus cauterization for hydrocephalus is a neurosurgical procedure where an endoscope is inserted into the open, fluid-filled ventricle, and then must reach points around the curvature of the ventricle.

curvature endoscopes (see Fig.1). Further, even in “successful” procedures, surgeons often want to cauterize more of the choroid plexus than they can currently reach and simply settle for what they can reach. Thus, a robot with nonlinear tendon routing that can access more of the choroid plexus would be a valuable tool.

MATERIALS AND METHODS

According to the model defined in [2], we can describe the tendon routing for a given robot by a vector in attached frame coordinates as a function of s : $\mathbf{r}_i(s) = [x_i(s) \ y_i(s) \ 0]^T$. Note that one can arbitrarily set x and y to any value (constrained by a maximum radius of the robot), but x and y do not have to be integer values. One can use any shape equation to define the tendon routing, as long as it is physically realizable.

To use this framework in designing an optimal robot for a given application, we propose a new way of parameterizing tendon routing which will enable complex routings in the design space, such that one does not have to assume a priori that the only candidates are lines or helices. We parameterize a given tendon routing path using polynomials in cylindrical coordinates, i.e., a polynomial describing the tendon’s angle around the

This work was supported in part by the National Science Foundation under Award # 2133027 and the National Institute of Health under the NIBIB training grant T32EB021937.

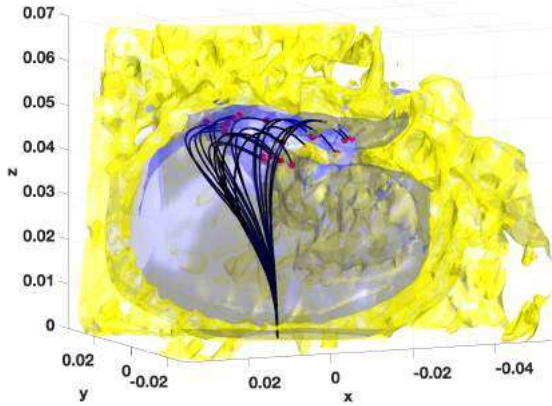


Fig. 2 After optimization, the robot is able to reach the desired points, which are shown in red. Also shown: the backbone of the tendon robot (black), brain tissue (yellow), and open ventricle space (blue).

backbone as a function of the backbone's arc length and a polynomial describing the tendon's distance from the backbone as a function of arc length.

This results in a set of polynomial basis functions with coefficients:

$$\begin{aligned}\varphi_i(s) &= C_{0i}s^0 + C_{1i}s^1 + C_{2i}s^2 + \dots + C_{ni}s^n \\ \rho_i(s) &= D_{0i}s^0 + D_{1i}s^1 + D_{2i}s^2 + \dots + D_{ni}s^n\end{aligned}\quad (1)$$

where s is arc length, φ is the angular position of the tendon on the projection plane located at s , ρ is the radial position of the tendon with respect to s , and with i indexing the i^{th} tendon. With the tendon routing formulated in this manner, we are now able to optimize the coefficients of these functions, searching over an expressive set of non-linear, generalized tendon routings. We can then convert the cylindrical equations back to a Cartesian frame using the standard conversion equations to be fed back into the model.

To apply this framework to hydrocephalus, we assumed a robot with 3 tendons and limited $\varphi_i(s)$ to 3 coefficients while keeping $\rho_i(s)$ fixed. We model the backbone with the physical properties of a nitinol tube of OD .686 mm and ID 0.533 mm, with an assumed disk diameter of 8 mm. We made these choices only as a proof-of-concept, and none are intrinsic to the approach. A pediatric neurosurgeon (co-author Naftel) selected targets defining the desired choroid plexus surface to be cauterized in an MRI scan of a brain from a hydrocephalus patient. He also selected the entry vector he would use for the endoscope if treating this patient, which defined the entry path for our robot. Next in our optimization, for a given tendon routing, we computed the forward kinematics of the robot at each combination of a discretized set of tension values (spanning 0 - 4.5 N) for each tendon. We then found the minimum distance from the tip of the robot to each desired point in the choroid plexus across all tension values. We tasked the optimizer with minimizing the sum of squared error for these distances, optimizing C_0 , C_1 , and C_2 for all 3 tendons (9 parameters total). We used MATLAB's `fminsearch` function with random initialization to perform the optimization.

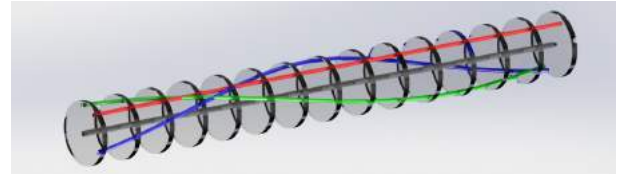


Fig. 3 Post-optimization tendon routing.

RESULTS

Our method found a set of tendon routings that enabled the robot to reach all 20 points with less than 0.8 mm of error and a mean error across all points of 0.5 mm (see Fig. 2). The optimization produced:

$$\begin{aligned}\varphi_1(s) &= -0.121 + 70.697s + 0.096s^2 \\ \varphi_2(s) &= 3.260 + 0.168s + 25.459s^2 \\ \varphi_3(s) &= 0.107 - 53.325s + -0.141s^2.\end{aligned}\quad (2)$$

with our fixed value of the radius set to $\rho_i(s) = 0.035$ for all tendons, which results in the nonlinear routing for each tendon shown in Fig. 3.

DISCUSSION

This paper presents a parameterization for nonlinear, expressive tendon routing for continuum robots. This parameterization results in a vector of coefficients that can be optimized using standard design optimization methods. We demonstrate the first generalized tendon routing optimization, while showing proof of concept in an example neurosurgical application in simulation. In future work, we plan to optimize not only the angle, but also include the radial distance from the backbone. We also intend to include either motion planning or another form of obstacle avoidance into the framework when evaluating design capabilities. We further intend to leverage the method to reduce the radius of the robot while maintaining capabilities and addressing physical fabrication feasibility. Lastly, we believe the method can be extended to many other surgical scenarios that involve touching a sequence of target positions.

REFERENCES

- [1] J. Burgner-Kahrs, D. C. Rucker, and H. Choset, "Continuum Robots for Medical Applications: A Survey," *IEEE Transactions on Robotics*, vol. 31, no. 6, pp. 1261–1280, 2015.
- [2] D. C. Rucker and R. J. Webster III, "Statics and Dynamics of Continuum Robots With General Tendon Routing and External Loading," *IEEE Transactions on Robotics*, vol. 27, no. 6, pp. 1033–1044, 2011.
- [3] C. Wang, S. Geng, D. T. Branson, C. Yang, J. S. Dai, and R. Kang, "Task space-based orientability analysis and optimization of a wire-driven continuum robot," *Proceedings of the Institution of Mechanical Engineers, Part C: Journal of Mechanical Engineering Science*, vol. 233, no. 23–24, pp. 7658–7668, 2019.
- [4] B. Ouyang, Y. Liu, and D. Sun, "Design and shape control of a three-section continuum robot," *IEEE/ASME International Conference on Advanced Intelligent Mechatronics, AIM*, pp. 1151–1156, 2016.
- [5] A. G. Weil, A. Fallah, P. Chamiraju, J. Ragheb, and S. Bhatia, "Endoscopic third ventriculostomy and choroid plexus cauterization with a rigid neuroendoscope in infants with hydrocephalus," *Journal of Neurosurgery: Pediatrics*, vol. 17, no. 2, pp. 163–173, 2016.
- [6] C. Bergeles, A. H. Gosline, N. V. Vasilyev, P. J. Codd, P. J. del Nido, and P. E. Dupont, "Concentric tube robot design and optimization based on task and anatomical constraints," *IEEE Transactions on Robotics*, vol. 31, no. 1, pp. 67–84, 2015.

Design, Fabrication, and Evaluation of a Biomimetic Soft Peristaltic Pump for Biomedical Applications

Sina Najjari¹, Peter Culmer², and Ali Alazmani³

University of Leeds,

el18sn@leeds.ac.uk, P.R.Culmer@leeds.ac.uk, A.Alazmani@leeds.ac.uk

INTRODUCTION

Peristaltic pumping can be observed in biological organs which contain hollow tubular cavities, including intestines, esophagus, and ureter [1, 2]. These act as positive displacement pumps where pumping is induced through sequential and periodic expansion and contraction in the tubular cavity [3]. Biomimetic peristaltic pumps are a subset of these pumps that mimic existing biological peristaltic systems closely in respect of size and transport parameters including generated pressure and flow rate. The potential to use soft materials and structures, and provide continuous actuation makes these pumps an appropriate substitute for their biological counterparts in in-vitro experiments. Experiments have been conducted to study the peristaltic rheology of the organs that demonstrate peristaltic actuation [1]. Despite recent advances in soft robotics, current biomimetic peristaltic pumps fail to replicate the pumping performance and self-actuation of biological pumps. Notably, their physical characteristics show limited structural flexibility [1, 4].

This research aims to design and develop a soft peristaltic pneumatic pump for use in biomedical applications, using a biomimetic approach. The contributions of this research include 1) utilizing fully soft materials in pump fabrication, 2) designing multiple identical units which enable the pump to have variable actuation sequences to achieve both forward and backward fluid transport, and 3) a new concept for an adaptable and flexible soft peristaltic pump for use in biological applications which can be tuned to mimic human organ performance (e.g. the ureter, fallopian tube, or esophagus) in an in-vitro environment.

MATERIALS AND METHODS

The primary design specification and requirements of the proposed Soft Peristaltic Actuator (SPEA) are based on common generic features of biological pumps found in human body. Requirements considered for this design include 1) an output pressure range of 1-15KPa which enables the pump to simulate existing pressures in various human organs including ureter and esophagus, 2) utilizing only soft compliant materials with high elasticity for fabrication, 3) ability to generate a range of sequential pressure patterns and also reverse pressure [5], and 4) scalable design dimensions to make the pump adjustable for various applications.

Concept: Biological peristaltic pumps are composed of soft circular conduits where deformable ring actuators are embedded throughout the pump's body. Ring

actuators enable the pump's body to achieve complete closure and sequential contraction and expansion, generating enough periodic pressure to pump the fluid inside. To develop the SPEA, embedded pneumatic chambers in the hollow conduit were selected which will generate the sequential actuation in the pump. For the initial model an actuator with a circular pneumatic chamber and inner conduit was developed. Dimensions of the SPEA were upscaled from biological examples to facilitate preliminary development and testing. The system configuration consists of five connected soft actuator units with an inner pneumatic chamber (Fig 1a). Each actuator has a separate air inlet, allowing it to individually inflate and thus mimic peristalsis through sequential activation of units in different patterns.

Fabrication: In this initial work, a single unit of the SPEA (Fig 1b) was fabricated in order to investigate and characterise the operational performance. This provides opportunity to compare different design geometries and materials. Ecoflex, 00-30 silicon rubber, was selected for manufacturing the first model due to its flexibility and high elongation at break (900%). Mould and casting was the primary fabrication method used. The fabrication was developed in three stages for a single unit actuator. Table 1 displays stages of fabrication along with mould CAD models and manufactured models in each stage.

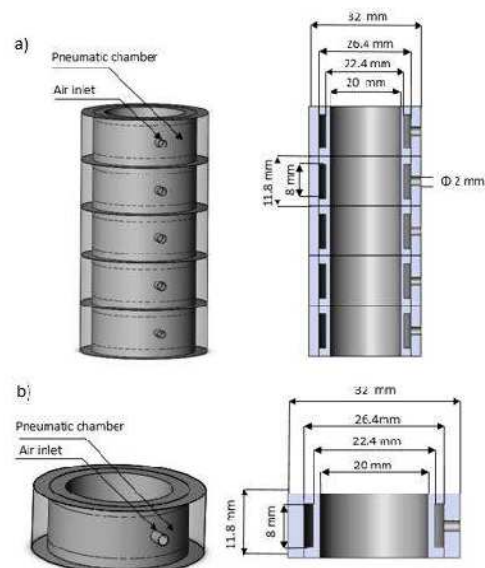




Figure 1 a) Schematic of the multi-unit soft peristaltic pump. b) Schematic of a single unit soft peristaltic pump.

At stage-1 a wax ring using the 'lost wax' technique was fabricated and used to create a cavity in the pump. At

stage-2, the inner conduit was fabricated by pouring the Ecoflex into the mould where the wax ring is placed on the existing dents inside. Additionally, a cylindrical pillar was installed in the centre of the mould to create a hollow section in the middle of the actuator. The manufactured inner conduit wall containing the wax ring from stage-2, was then placed inside the stage-3 mould where the outer surface of the actuator was fabricated using Ecoflex. A 2 mm hole was also created and filled with a rod of the same diameter on the side of the mould to produce an air inlet on the external surface of the actuator. As a post-casting process, the fabricated actuator was then placed in an oven to melt the wax and create a hollow inner cavity. Additionally, pneumatic tubing was attached to the actuator's air inlet using Elastosil E41 transparent silicone rubber. Finally, to maximize the inflation toward the inner side, the external layer of the SPEA was covered with a layer of paper solvy stabilizer which is inextensible and restrains expansion toward the outer direction. Fig 2c shows the manufactured single unit peristaltic pump. All moulds were manufactured by 3D printing of clear resin.

Characterisation: To test the performance of single unit SPEA, a test setup was developed in the form of a manometer where the pressure is set to 140 mmH₂O (10.3mmhg), to create a representative biological scenario (Fig 2a, b). To create the setup, a soft silicone tube was fabricated using SORTA_Clear 40 so that the applied pressure from SPEA could be transferred to the inner liquid with less resistance. The tube was then connected to the PVC tubes at the two ends creating the manometer. Finally, a single unit SPEA was installed around the silicone tube and was actuated through the pneumatic actuation system. The purpose of this test was to observe the generated pressure increase (ΔP) of a single unit SPEA. Characterization of the single unit SPEA was developed by supplying the SPEA with varying pneumatic PWM pressure inputs, supplied by a custom electro-pneumatic drive system.

Table. 1 Three-stage fabrication procedure.

Stages	Stage 1	Stage 2	Stage 3
Models			
Moulds			
Manufactured models			

RESULTS

The soft single unit SPEA was designed and manufactured successfully through a bespoke three-stage fabrication process. The manufacture process was found to be repeatable.

Testing explored a range of pneumatic actuation profiles for the single unit. This revealed that the single unit

achieved peak performance with a 25 KPa pressure supply at 1Hz, generating a 10 mmH₂O (0.735 mmHg) pressure increase in the manometer.

DISCUSSION

The initial test was performed on the single unit SPEA where a 0.7 mmHg pressure elevation was observed. Using alternative materials with different shore hardness for different sections of the pump (i.e. inner and outer), and utilizing multiple unit SPEAs instead of a single unit, offers the potential to further increase the generated pressure.

Future phases of this research are as follows: 1) Elevating the in-vitro test setup to a dynamic state by supplying a constant flow to the setup and creating a closed system via connecting tubes, 2) Measuring generated pressure and flow rate of the single unit SPEA in real-time in the dynamic setup, 3) Optimizing the single unit geometry by analysing recorded pressure and flow rate across different SPEA designs, and 4) Fabrication and characterization of multiple unit peristaltic actuators. The current trend to increase the use of soft materials in biomimetic pump fabrication could lead to new findings, including the development of low-energy micro-pumps. Most crucially soft peristaltic technical pumps have the potential to open new chapters in the use of artificial pumps for biomedical applications where conventional pumping approaches have failed [1].

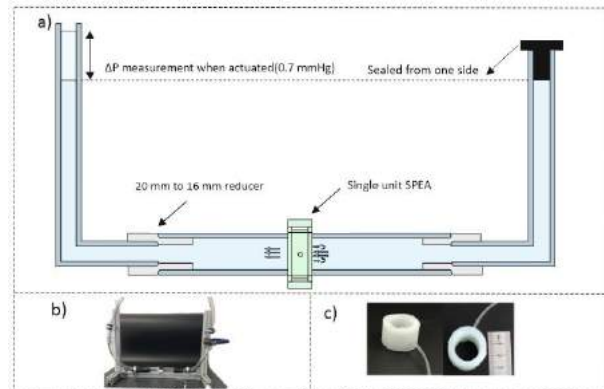


Fig. 2 a) Schematic of the manometer setup. b) The actual developed in-vitro test setup in the lab. c) Manufactured single unit peristaltic pump.

REFERENCES

- [1] F. Esser, et al, "Silent Pumpers: A Comparative Topical Overview of the Peristaltic Pumping Principle in Living Nature, Engineering, and Biomimetics," <https://doi.org/10.1002/aisy.201900009>, 2019.
- [2] S. Vogel, "Living in a physical world X. Pumping fluids through conduits," 2007.
- [3] W. Cullen, Institutions of medicine Part I. Physiology. For the use of students in the University of Edinburgh, 1777.
- [4] A. V. Bursian, "Structure of autorhythmic activity of contractile systems," 2012.
- [5] M. D. Rodefeld, et al, "Capopulmonary assist: (em)powering the univentricular fontan circulation," 2011.

Distal Joint Rotation Mechanism for Endoscopic Robot Manipulation

L.W. Cheung¹, *K.C. Lau^{1,2}, Flora F. Leung¹, Donald N.F. Ip¹,
Henry G.H. Chow¹, Philip W.Y. Chiu^{2,3}, and Y. Yam^{1,2}

¹Department of Mechanical and Automation Engineering, ²Multi-scale Medical Robotics Center, ³Department of Surgery, The Chinese University of Hong Kong

lwcheung@mae.cuhk.edu.hk, *Corresponding author: kclau@mrc-cuhk.com

INTRODUCTION

Robot-assisted Minimally Invasive Surgery (MIS) and Natural Orifice Transluminal Endoscopic Surgery (NOTES) are commonly adopted in Gastro-Intestinal (GI) cancer treatment with Endoscopic Submucosal Dissection (ESD). While using fully flexible cable-driven robots brings benefits to patients such as lower rate of complications and shorter healing time, the engineering challenges, for example, size and stiffness, manufacturability and sensorless environment, limit functionalities of robotic instruments and surgery performance. The rolling feature, rotation along the wrist of the instrument, is a good-to-have feature for surgical procedures with orientational and positional requirements such as tractioning and suturing with graspers. In traditional laparoscopy, rolling can be achieved by rotating the long straight rod of the instruments, which is straightforward and effective. However, this is not commonly found in cable-driven endoscopic robotic systems due to mechanical limit for linear-to-rolling motion conversion at distal-end and unmodelled friction resisting torque transmission from proximal-end.

Generally, researchers have three approaches to this problem. First, rotate the endoscope or overtube and the instrument together [1] [2]. However, this is not favorable to both surgeon and patient since rotating a twisted endoscope inside a patient's body requires a large amount of torque and rubbing would create discomfort to the patient. Second, rotate the torque coil or backbone of the instrument [3] [4]. Because friction inside the endoscope is unpredicted and rotation is coupled with roll, pitch, and yaw motion, sophisticated modeling, shape/orientation sensing feedback may be required for robotic automation. Third, develop a distal mechanism to convert cable linear motion into axial rotation [5] [6]. With this method, the coupling problem is solved and power transmission efficiency is improved but a larger and more complicated design is required, and an extra-rigid segment is usually unavoidable. The performance depends greatly on design and implementation.

This paper aims to demonstrate a scalable distal joint rotation mechanism for continuum endoscopic robots that can increase instrument dexterity and manipulability to ease the work of surgeons.

MATERIALS AND METHODS

Traditionally, barrel cam mechanism is used to convert rotational motion of the cam to linear motion of one or more followers. The distal joint rotation mechanism is based on the inverse of barrel cam mechanism, in which two rollers attached to push-pull wires turn the circular cam by out-of-phase linear oscillation. Compare with a single spiral slot, the barrel cam profile allows a larger lead angle without increasing the length of the mechanism dramatically, meaning a smoother and more efficient motion conversion. The out-of-phase actuation helps the rollers to transit to another segment of the repeating cam profile and achieve unlimited number of turns. It thus rotates at a specific step angle like a stepper motor, as shown in Fig. 1(a). The concept is similar to the operation principle of the linear stepper motor presented by Groenhuis and Stramigioli [7]. Surgical instruments such as graspers and scissors can be attached to the output shaft of the cam, which has an actuation wire passing through its center hole. And the mechanism will be attached to a continuum robotic arm that goes through an endoscope working channel.

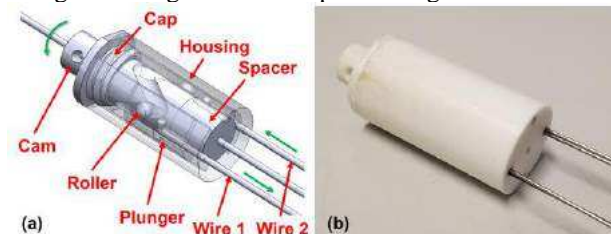


Fig. 1 (a) 3D model of inverse barrel cam mechanism (b) Actual 3D printed prototype of inverse barrel cam mechanism

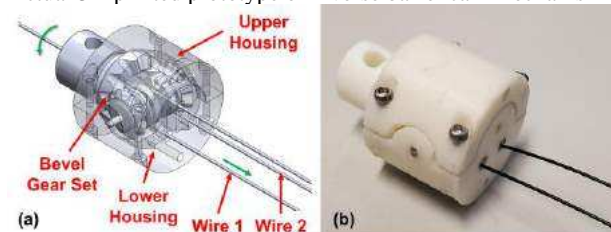


Fig. 2 (a) 3D model of bevel gear mechanism (b) Actual 3D printed prototype of bevel gear mechanism

From preliminary study, it is identified that the lead angle of the mechanism is the major parameter affecting its velocity, torque, and efficiency. A 20 mm prototype of inverse barrel cam mechanism is designed and fabricated using optimal lead angle (60°) obtained from static force analysis. Other parameters such as phase

width and cam radius are determined based on physical limitations. For comparison, a 20 mm bevel gear rotation mechanism is designed and fabricated, as shown in Fig. 2. It is designed to maintain the same overall diameter, have a rotation range of at least 180 degrees, and maximized torque.

A test platform, as shown in Fig. 3, is built to evaluate the performance of the distal joint rotation mechanism. The rotation mechanism is actuated by two wires driven by two rack pinion modules. A motor is attached at the end to serve as an adjustable torsional load. Output torque and position are recorded respectively. A current limiting approach is used for the comparison experiment. The experiment is repeated five times under constant motor speed (200, 400, 600, 800, 1000 rpm) and constant current limit (300, 400, 500, 600, 700 mA). Measurement will be terminated when torque is too low to be captured or the mechanism fails.

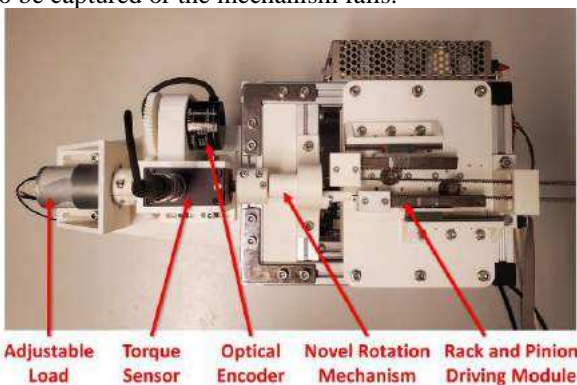


Fig. 3 Experimental setup with distal position, torque measurement, and adjustable load

RESULTS

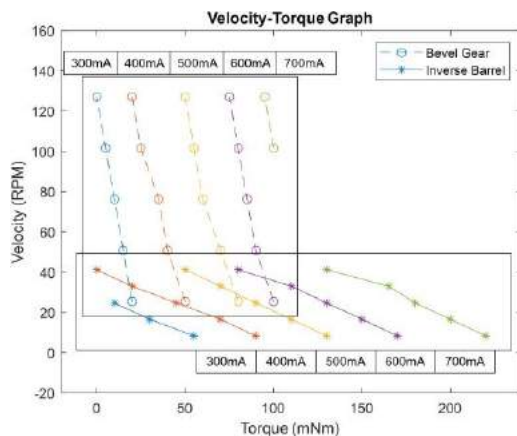


Fig. 4 Velocity-torque graph of bevel gear mechanism and inverse barrel cam mechanism

The experimental results show that the inverse barrel cam rotation mechanism can perform an unlimited number of revolutions with position tracking ability. This mechanism is non-backdrivable when the position of the wires is locked by the motors. Both mechanisms show a linear relationship between velocity and torque under constant current limit and a linear relationship between velocity and torque under constant motor speed. For inverse barrel cam setup, a maximum torque of 220 mNm is achieved at 8 rpm; for bevel gear setup,

a maximum torque of 102 mNm is achieved at 100 rpm, as shown in Fig. 4.

DISCUSSION

From the experimental results, it is observed that inverse barrel cam mechanism can deliver a significantly higher torque while bevel gear mechanism can rotate at a significantly higher speed. Since inverse barrel cam mechanism has a fair amount of friction, it cannot provide as much more torque as it sacrifice in term of velocity. Considering the application of endoscopic surgery, a high-torque and scalable inverse barrel cam mechanism would be a better choice. Compare with bevel gear mechanism, the structure of inverse barrel cam mechanism is much simpler, giving it much higher scalability with the help of technology such as micro-machining and micro-injection molding. It is expected that the output torque of the mechanism will decrease linearly with cam radius, as long as the lead angle can be maintained.

In order to provide smooth and reliable motion, correct phase tracking is essential because the kinematics and dynamics of the inverse barrel cam mechanism are unique in each phase. In the experiment, phase estimation is done by tracking motor position and introducing backlash compensation. But if the distal joint rotation mechanism is used in flexible endoscopes, phase estimation may be lost since varying friction and hysteresis are non-negligible. Given a sensorless environment, a combination of position and current sensing feedback may be suitable for phase determination in further development.

(This work is supported by InnoHK funding.)

REFERENCES

- [1] B.P.M. Yeung, T. Gourlay, "A technical review of flexible endoscopic," *Int J Surg*, vol. 10, no. 7, pp. 345-354, 2012.
- [2] SAGES, "A Novel Flexible Over-tube for Advanced Endoscopic Intervention Under Stabilized Visualization with Adjustable Tissue Traction," 2013.
- [3] L. Cao, X.G. Li., A. Tiong, P.T. Phan, "A Novel Robotic Suturing System for Flexible Endoscopic Surgery," *International Conference on Robotics and Automation*, 2019.
- [4] N. Simaan, K. Xu, A. Kapoor, W. Wei, P. Kazanzides, P. Flint, R. Talyor, "Design and Integration of a Telerobotic System for Minimally Invasive Surgery of the Throat," *Int J Rob Res*, vol. 9, pp. 1134-1153, 2009.
- [5] J. Ding, K. Xu, R.E. Goldman, P.K. Allen, "Design, Simulation and Evaluation of Kinematic Alternatives for Insertable Robotic Effectors Platforms in Single Port Access Surgery," *IEEE International Conference on Robotics and Automation*, 2010.
- [6] K.Y. Kim, H.S. Song, J.W Suh, J.J. Lee, "A Novel Surgical Manipulator with Workspace-Conversion Ability for Telesurgery," *IEEE/ASME Transactions on Mechatronics*, vol. 18, no. 1, pp. 200-211, 2013.
- [7] V. Groenhuis, S. Stramigioli, "Rapid Prototyping High-Performance MR Safe Pneumatic Stepper Motors," *IEEE/ASME Transactions on Mechatronics*, vol. 23, no. 4, pp. 1843-1853, 2018.

3D Printed Cups for Acetabular Reconstruction: a 3D-CT Implant Study

Anna Di Laura^{1,2}, Johann Henckel¹, Martin Belzunce¹,

Harry Hothi^{1,2}, Alister Hart^{1,3}

¹Royal National Orthopaedic Hospital, Stanmore, UK

²Department of Mechanical Engineering, University College London, UK

³Division of Surgery and Interventional Science, University College London, UK
anna.laura.14@ucl.ac.uk

INTRODUCTION

Custom 3D printed titanium acetabular implants have only recently been introduced and enable surgeons to treat traditionally unreconstructable massive acetabular defects. Whilst there is an accepted threshold for implant migration (proximal translation of >1 mm within 2 years) that constitutes loosening in primary and revision uncemented hip implants, there is no reference threshold for custom acetabular implants used to treat massive defects, with no long-term outcome studies [1].

Aim: We performed bone-to-bone registration of sequential CT imaging with the aim to help define radiological loosening of custom-made three-dimensionally 3D printed trabecular titanium cups for the management of massive acetabular defects.

Objectives: Our primary and secondary objectives were to assess implant position and orientation 1-year post surgery in comparison with the immediate post-operative CT imaging.

MATERIALS AND METHODS

This was a single-centre prospective cohort study of 19 patients from a single surgeon. We recruited patients with massive acetabular defects Paprosky type 3B or above treated with 3D printed custom implants, which 1-year post-operatively had no evidence of radiological or clinical implant loosening. The mean follow-up time was 46 months (32 to 62). Institutional approval was obtained. SE16.021

Using specialised software solutions, the CT images were rendered to produce 3D reconstructions of the patients' bony pelvis for relative comparison of the two imaging timepoints (immediate post-operative, 1-year post-operative). Bone-to-bone registration allowed for the assessment of implant movement over time, this was studied in terms of difference in centre of rotation (CoR), cup inclination INC and version VER.

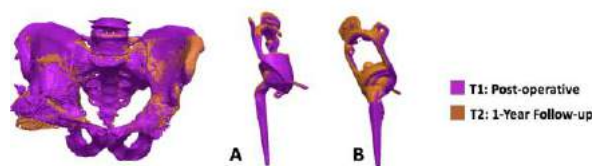


Fig. 2 Case example. 3D Reconstruction and registration of the pelvises at the two timepoints. (A) Anterior-posterior and (B) lateral views of the immediate post-operative (purple) and 1-year post-operative (orange) implant components.

Our primary outcome measure was the change in centre of rotation (CoR) between CT scans carried out immediately and 1 year post-operatively. Our secondary outcome measure was change in orientation (cup inclination and version). Meticulous patient follow-up by the operating surgeon to closely monitor for early complications was undertaken.

RESULTS

All patients presented acetabular defects classified Paprosky type 3B and beyond.

One year post-operatively the deviation of CoR was a mean (\pm SD) of -0.1 ± 0.9 mm (median = 0.1 mm; IQR -0.8, 0.6 mm, min = -1.9 mm, max = 1.3 mm) in the ML plane, $1.6 (\pm 1.6)$ (median = 1 mm; IQR 0.2, 3 mm, min = -0.8 mm, max = 5.4 mm) in the IS plane and $0.8 (\pm 2)$ (median = 0.2 mm; IQR -0.8, 2.4 mm, min = -2 mm, max = 4.4 mm) in the AP plane.

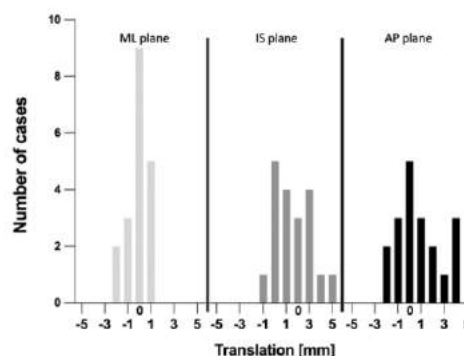


Fig. 1 Differences in CoR co-ordinates (mm) histograms for the ML, IS, AP planes at 1-year follow-up

The orientation of the acetabular implants changed on average by 1.4 and 2° (inclination and version respectively). The 3D analysis revealed local bony shifts around the implants suggestive of bone remodelling, in some cases the remodelling involved the whole hemipelvis.

There was no clinical indication of implant loosening, oxford hip score was a mean of 33/48, both plain radiographs and CT cross-sectional imaging did not show radiolucent lines at the bone/implant interface.

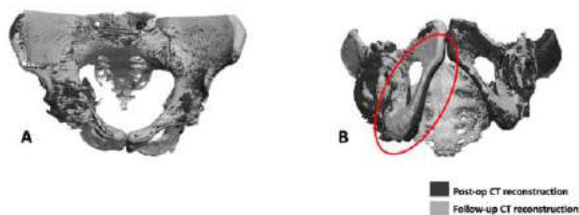


Fig. 3 Case example. Anteroposterior (A) and bottom-to-top view (B) showing co-registration between the immediate post-operative (dark grey) and 1-year follow-up CT pelvic reconstructions (light grey). Perfect alignment of the pelvises is seen overall except at the ischium, suggestive of bone remodelling.

DISCUSSION

Monitoring of 3D printed custom-made titanium cups is challenging due to the diversity in implant design, materials, manufacturers, surgical techniques and tools used worldwide.

Advances in medical image analysis, allowing robust assessment and monitoring of patients with newly introduced implants, provide novel insights in the evaluation of their in-vivo performance [2-3].

This study has showed that the threshold value of 1mm used to diagnose early loosening in THA is not applicable to custom-made acetabular implants designed to reconstruct massive acetabular defects.

REFERENCES

- [1] Abrahams JM, Callary SA, Munn Z, et al. Acetabular Component Migration Measured Using Radiostereometric Analysis Following Revision Total Hip Arthroplasty: A Scoping Review. *JBJS reviews*. 2020;8(4):e0170.
- [2] Brodén C, Sandberg O, Sköldenberg O, et al. Low-dose CT-based implant motion analysis is a precise tool for early migration measurements of hip cups: a clinical study of 24 patients. *Acta Orthopaedica*. 2020;91(3):260-265.
- [3] Scheerlinck T, Polfliet M, Deklerck R, Van Gompel G, Buls N, Vandemeulebroucke J. Development and validation of an automated and marker-free CT-based spatial analysis method (CTSA) for assessment of femoral hip implant migration In vitro accuracy and precision comparable to that of radiostereometric analysis (RSA). *Acta Orthopaedica*. 2016;87(2):139-145.

Results of in vivo cardiac arrhythmia ablations with an electro-magnetic navigation system

C. Chautems¹, C. On², N. Cesarovic⁴, P. Bode⁵,

B.J. Nelson¹, F. Duru^{2,3}

¹*Multi-Scale Robotics Lab, ETH Zurich*

²*Arrhythmia and Electrophysiology Division, University Heart Center Zurich*

³*Center for Integrative Human Physiology, University of Zurich*

⁴*Division of Surgical Research, University Hospital Zurich*

⁵*Institute of Surgical Pathology, University Hospital Zurich*

chautemc@ethz.ch

INTRODUCTION

In the last twenty years, radiofrequency ablation of cardiac arrhythmias has increasingly become the number one therapy as it is potentially curative and negates the need for long-term medication [1], [2]. Remote magnetic navigation is a proven technique used to reduce fluoroscopy [3] and assist navigation to sites with difficult anatomic locations [4], [5]. The Niobe system (Stereotaxis, USA) used in those studies has two movable permanent magnets [6]. In our electro-magnetic navigation system (eMNS), the movable permanent magnets are replaced with eight static electromagnets.

The eMNS system has an open design, which allows simultaneous fluoroscopy during ablation procedures. The system integrates third-party mapping to create endocardial anatomical maps using electrodes in the catheter to record electrical activity. The eMNS is capable of navigating a magnetic ablation catheter to a desired position [7]. The radiofrequency ablation catheter uses an alternating current that causes resistive heating of the tissue when in contact with the electrode tip [8]. The heated tissue becomes permanently damaged and stops conducting electrical signals.

In this paper, we present our initial in vivo experience using this innovative eMNS in our animal electrophysiology laboratory showing that static electromagnets could be an alternative to permanent magnets (Fig. 1).



Fig. 1 Animal electrophysiology lab in Zurich, Switzerland, where the first generation electro-magnetic navigation system (eMNS) is installed.

ELECTRO-MAGNETIC NAVIGATION SYSTEM

The patented electro-magnetic catheter steering system used in the in vivo trials is the first prototype of the system. It has eight electromagnets which are aligned in a hemispherical arrangement around the subject torso and is capable of steering a magnetic catheter accurately and efficiently by changing the direction of the magnetic field remotely from the control room.

The system requires 32 kW 400V 50-60 Hz, 3-phase power and is able to generate magnetic fields of up to 150 mT in a 12cm wide spherical region, which can be quickly moved in all directions. A control algorithm computes the electromagnet currents to obtain a desired magnetic field at a location [9]. The system is cooled with water, and when the system is not in operation, the electromagnets are switched off so no magnetic field is present. The precise insertion or retraction of the catheter is remotely controlled using a mechanical catheter advancer module.

METHODS

Two electrophysiologists generated three complete endocardial anatomical maps (EnSite NavX, St. Jude Medical, USA) of the right-sided intracardiac chambers in five farm pigs weighing 40-60kg using the electromagnetic catheter steering system, followed by mapping using the conventional manual approach.

Linear RF ablations were performed using 7Fr irrigated-tip ablation catheters (MagnoFlush G, Medfact, Germany) at 30W power to achieve a complete block in the cavo-tricuspid isthmus. Focal anatomical ablations were performed at a site in the right ventricular outflow tract. All heart specimens underwent histopathological analyses for safety and efficacy assessments.

RESULTS

Precise endocardial mapping was performed faster using the electromagnetic catheter steering system compared to manual mapping (12.64±0.91 min vs. 15.18±2.26 min, p<0.05). All predefined target sites were reached in an accurate, precise, and repeatable fashion and the

catheter was stable during mapping over all consecutive maps and trials.

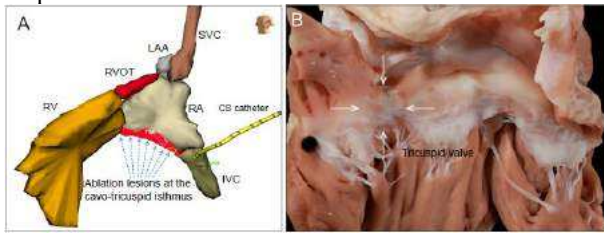


Fig. 2 A. LAO view of the generated map of the right heart chambers (Animal #3). The target regions were repeatedly reached in all animals. Linear ablation points along the cavo-tricuspid isthmus are shown in red. B. Pale ablation lesions with hemorrhagic rim at the cavo-tricuspid isthmus.

In addition, fluoroscopy durations were shorter and the corresponding radiation doses were lower for the animals using this technology (1.03 ± 0.39 min and 235.39 ± 80.26 cGy/cm² vs 1.55 ± 0.52 min and 364.98 ± 104.38 cGy/cm², respectively, both $p < 0.05$). The average time to achieve complete cavo-tricuspid isthmus block was 14.25 ± 2.78 min. The operator did not experience any X-ray radiation, as the catheter was operated from a control room protected from x-ray radiation. Both operators quickly adapted to using the eMNS, and as their experience increased, there was a trend towards a faster procedure with less fluoroscopy, however more data would be required to verify and quantify this trend.

All target sites were reached during ablations and no catheter slip events occurred, so a defined catheter position was maintained.

The histopathological analyses showed continuous linear lesions at the cavo-tricuspid isthmus and confirmed transmuralities of the lesions at all ablation sites with a uniform, continuous maximum depth of 6-7 mm each. No perforations were observed and the coronary arteries did not show any suspicious changes.

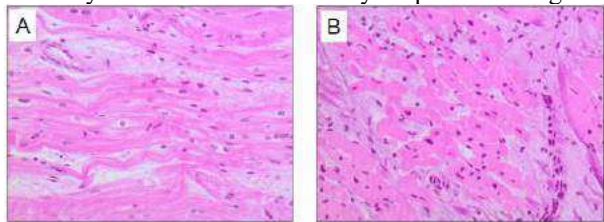


Fig. 3 A. Normal myocardium: Cardiomyocytes with normal morphology of nuclei. B. After ablation: Cardiomyocytes with hyper eosinophilic cytoplasm, loss of cross striation and pycnotic nuclei indicating cell death and necrosis.

DISCUSSION

This in vivo study demonstrated the feasibility of endocardial anatomical mapping and radiofrequency ablation by catheter steering using an eMNS with precision and accuracy, without compromising safety. In comparison to manual mapping, procedure durations were shorter and fluoroscopy exposures were lower using this system. Those results are similar to the one reported with the Niobe system. The advantage of using electromagnets over permanent magnet systems such as

the Niobe (Stereotaxis, USA), is the ability to turn off the magnetic field in three seconds. This allows to use equipment sensitive to magnetic field in the same operating room when the system is turned off. In the Niobe system only a magnetic torque can be applied on the catheter. In our eMNS, the magnetic force acting on a catheter can be controlled with the magnetic gradient [10].

Ongoing and future studies will focus on improving the system performance to reduce the procedure time by providing automation features, improving the catheter design, and reducing the eMNS size to facilitate installation in clinics.

ACKNOWLEDGEMENT

This work was partially supported by the Swiss National Science Foundation through grant number 200021-165564 and by BRIDGE through grant number 180861.

REFERENCES

- [1] F. Morady, "Radio-Frequency Ablation as Treatment for Cardiac Arrhythmias," *N. Engl. J. Med.*, vol. 340, no. 7, pp. 534–544, Feb. 1999.
- [2] J. P. Joseph and K. Rajappan, "Radiofrequency ablation of cardiac arrhythmias: past, present and future," *QJM*, vol. 105, no. 4, pp. 303–314, Apr. 2012.
- [3] M. K. Turagam *et al.*, "A meta-analysis of manual versus remote magnetic navigation for ventricular tachycardia ablation," *J. Interv. Card. Electrophysiol.*, vol. 49, no. 3, pp. 227–235, Sep. 2017.
- [4] A. Aryana *et al.*, "Remote magnetic navigation to guide endocardial and epicardial catheter mapping of scar-related ventricular tachycardia," *Circulation*, vol. 115, no. 10, pp. 1191–200, Mar. 2007.
- [5] M. Kawamura, M. M. Scheinman, Z. H. Tseng, B. K. Lee, G. M. Marcus, and N. Badhwar, "Comparison of remote magnetic navigation ablation and manual ablation of idiopathic ventricular arrhythmia after failed manual ablation," *J. Interv. Card. Electrophysiol.*, pp. 1–8, Jun. 2016.
- [6] S. Ernst *et al.*, "Initial experience with remote catheter ablation using a novel magnetic navigation system: magnetic remote catheter ablation," *Circulation*, vol. 109, no. 12, pp. 1472–5, Mar. 2004.
- [7] C. Chautems, S. Lyttle, Q. Boehler, and B. J. Nelson, "Design and Evaluation of a Steerable Magnetic Sheath for Cardiac Ablations," *IEEE Robot. Autom. Lett.*, vol. 3, no. 3, pp. 2123–2128, Jul. 2018.
- [8] G. Borggrefe, M. Hindricks, W. Haverkamp, W. Breithardt, M. Borggrefe, G. Hindricks, W. Haverkamp, and G. Breithardt, "Catheter Ablation Using Radiofrequency Energy," *Clin. Cardiol.*, vol. 131, no. 2, pp. 127–131, Feb. 1990.
- [9] M. P. Kummer, J. J. Abbott, B. E. Kratochvil, R. Borer, A. Sengul, and B. J. Nelson, "OctoMag: An Electromagnetic System for 5-DOF Wireless Micromanipulation," *IEEE Trans. Robot.*, vol. 26, no. 6, pp. 1006–1017, Dec. 2010.
- [10] C. Chautems and B. J. Nelson, "The tethered magnet: Force and 5-DOF pose control for cardiac ablation," in *2017 IEEE International Conference on Robotics and Automation (ICRA)*, 2017, pp. 4837–4842.

A drop-in robotic gamma probe for minimally invasive radioguided surgery

T. Pampiglione¹, L. Fumado², M.R. Grootendorst³, K. Vyas⁴, M. Chand¹

¹Department of Surgery and Interventional Sciences, GENIE Centre, University College London, UK

²Department of Urology, Hospital Del Mar, Barcelona, Spain

³Department of Clinical Affairs, Lightpoint Medical Ltd., Amsterdam, The Netherlands

⁴Department of Research and Development, Lightpoint Medical Ltd., Chesham, UK
tom.pampiglione@nhs.net

INTRODUCTION

Radioguided surgery (RGS) techniques have been developed to enable more accurate and selective nodal identification and dissection in cancer patients [1]. The most well-established application of RGS is sentinel lymph node biopsy (SLNB), and use of a technetium-99m (^{99m}Tc)-labelled radiotracer in combination with a fluorescent or blue dye is the recommended technique for optimal sentinel lymph node (SLN) detection in those malignancies [2-3]. Minimally-invasive radioguided SLN procedures currently rely on the use of rigid laparoscopic gamma probes (RLGPs), which have limited manoeuvrability and control due to their rigidity and dimensions. To address these limitations, miniaturised ‘drop-in’ gamma probes have been developed by different groups, with each probe having different design and performance features [4]. Our group has developed the SENSEI[®] drop-in gamma probe in collaboration with Lightpoint Medical Ltd. The probe can be used in both robotic and laparoscopic surgery due to its design. Here we present the design and technical characteristics of the device, the interim clinical trial results in prostate cancer (PCa) and the planned clinical study in rectal cancer (RCa).

MATERIALS AND METHODS

SENSEI[®] consists of a tethered probe connected to a control unit (Figure 1). The tethered probe measures 40 mm in length and is compatible with robot-assisted and laparoscopic surgery by fitting through a standard 12 mm laparoscopic port but can also be used for open surgery. The front-facing detector consists of a caesium iodide scintillator crystal and a silicon photomultiplier allowing the energy-specific detection of high energy photons. The grip feature is compatible with standard tissue graspers used for minimally invasive surgery, and the probe can be reoriented *in vivo* by using either a tissue grasper or needle holder to grasp the side pockets. The control unit provides a numerical and audible read out of the activity levels, and can be connected to an external display (e.g. da Vinci TilePro[™]) allowing for an ‘image-in-image’ display of radiation activity.

The probe is collimated in the forward direction with a full-width half maximum of 43° and has been optimised for the detection of ^{99m}Tc-labelled radiopharmaceuticals. An energy window centred at the 140.5 keV, accepts the ^{99m}Tc photopeak and rejects scattered photons with lower energies. The back and side shielding effectiveness is >99.97% as measured by NEMA NU 3-2004 standard testing.

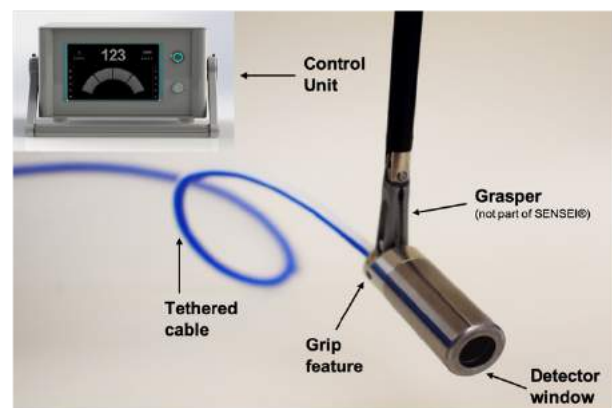


Figure 1: SENSEI[®] drop-in gamma probe system

A prospective, international, multicentre clinical trial evaluated SENSEI[®] for SLNB in PCa patients (ClinicalTrials.gov: NCT04632251). Following ethics approval and signed informed consent, a transrectal ultrasound-guided ^{99m}Tc-nanocolloid injection is given into each quadrant of the prostate. Planar lymphoscintigraphy scans are acquired 30-minutes and 2-hours post-injection. In the morning the next day, conventional laparoscopic or robot-assisted radical prostatectomy (RP) is performed followed by SLNB and extended pelvic lymph node dissection (ePLND). Suspected SLN locations are scanned *in vivo* with SENSEI[®] and subsequently with a RLGP. All excised SLNs and non-SLNs are measured *ex vivo* with both probes, and sent for post-operative histopathology. As predefined in the study protocol, an interim analysis was performed after N = 10 patients to assess the initial performance of SENSEI[®] including detection rate, diagnostic performance (using tumour status of ePLND lymph nodes as reference standard), and study-related adverse events.

RESULTS

In the PCa interim analysis, 8 patients underwent manual laparoscopic and 2 patients robot-assisted surgery. SENSEI® successfully detected a SLN in all 10 patients (detection rate: 100%). The total number of SLNs identified with SENSEI® was 27 (median 2 per patient, range 1 – 6). 1 SLN was located outside of the ePLND template in the left presacral area. The RLGP was used in 8 patients undergoing manual laparoscopy. The total number of SLNs identified with the RLGP was 17 (median 2, range 1 – 4). 2 SLNs identified by SENSEI® in the right internal iliac and left presacral region could not be detected with the RLGP due to the inability to precisely position the RLGP in these anatomically restricted areas. Histopathology identified 4 patients with positive nodes. All 4 had at least one metastatic SLN identified with SENSEI®. The RLGP also detected all LN-positive patients. No adverse events related to the SLNB procedure or SENSEI® device occurred.

DISCUSSION

The use of minimally-invasive surgical strategies, and specifically robotic surgery, has substantially increased in the last decade. The improved access and additional dexterity that robotic platforms allow means that technically challenging procedures can be undertaken with greater confidence and precision.

However, to further optimise surgical accuracy, there is a clear need for innovative technology to enable more confident identification of malignant tissue and thus the full potential of RGS in this setting. The innovative design of the SENSEI® drop-in gamma probe aims to facilitate this by combining a small form factor (i.e. the size of an AA battery) with an optimised grip and seamless integration of the numerical read-out on the robotic platform display.

The interim results from the prostate study show that SENSEI® can successfully detect SLNs in PCa patients undergoing both manual laparoscopic and robot-assisted surgery with the potential for improved SLNB compared with a RLGP. While awaiting the final study results, the ability of SENSEI® to detect SLNs with high sensitivity and in areas that can't be reached with the conventional RLGP holds promise for enabling more accurate lymph node staging.

Another interesting application in PCa is the use of SENSEI® in combination with a tumour-targeted prostate-specific membrane antigen (PSMA) radiotracer to detect lymph node metastases, and the performance of this technique is currently being evaluated in an ongoing clinical trial (NCT04857502)

In addition to PCa there are other pelvic cancers which may benefit from accurate targeting technology to treat lymph node disease. There is emerging evidence that removal of pelvic side wall (PSW) lymph nodes reduces local recurrence and may have a survival benefit in locally advanced RCa [5]. However, these nodes can be difficult and risky to dissect without intraoperative guidance, especially in obese patients. Lymph node

mapping with fluorescence has had some early promising results [6]. Therefore, we have designed a prospective, open label, single-centre pilot study to investigate the utility of dual radio-fluorescence guidance using SENSEI® in combination with the da Vinci's Firefly system to identify PSW lymph nodes in robotic RCa surgery. Patients will receive a peri-tumoural injection of ^{99m}Tc-nanocolloid and indocyanine green (ICG) into the submucosa and undergo single positron emission tomography/computed tomography (SPECT/CT) to assess transport of tracers in the lymphatic system and thus correlation with preoperative imaging. The PWS will then be examined intraoperatively to assess lymph node detection with SENSEI® and Firefly, as well as determining the usability of the probe and the depth penetration in this anatomical area.

Few studies have investigated the use of ^{99m}Tc RGS for detecting PSW lymph nodes in RCa, and those that have were in the open surgery and pre-chemoradiotherapy era [7]. Besides, no studies have used dual radio-fluorescence guidance in this cancer type. We therefore eagerly await the results from this planned clinical study evaluating this novel approach, with the ultimate aim to make PSW lymph dissection safer and allow for a general cross-specialty paradigm shift in how to manage PSW disease.

These studies demonstrate the real-world potential of SENSEI and RGS in an era of personalised medicine and minimally-invasive surgery.

REFERENCES

- [1] Hermann K, Nieweg OE, Povoski SP. Radioguided Surgery: Current Applications and Innovative Directions in Clinical Practice. Springer International Publishing; 2016.
- [2] Moncayo VM, Grady EE, Alazraki NP, Aarsvold JN. Sentinel-Lymph-Node Multicenter Trials. *Seminars in Nuclear Medicine*. 2020;50:56-74.
- [3] Chand M, Keller DS, Devoto L, McGurk M. Furthering Precision in Sentinel Node Navigational Surgery for Oral Cancer: a Novel Triple Targeting System. *Journal of Fluorescence* 2018 28:2. 2018;28:483-486.
- [4] Valdés Olmos RA, Rietbergen DDD, Rubello D, et al. Sentinel node imaging and radioguided surgery in the era of SPECT/CT and PET/CT: Toward new interventional nuclear medicine strategies. *Clinical Nuclear Medicine*. 2020;45:771-777.
- [5] Peacock O, Chang GJ. The Landmark Series: Management of Lateral Lymph Nodes in Locally Advanced Rectal Cancer. *Annals of Surgical Oncology* 2020 27:8. 2020;27:2723-2731.
- [6] Emile S, Elfeki H, Shalaby M, et al. Sensitivity and specificity of indocyanine green near-infrared fluorescence imaging in detection of metastatic lymph nodes in colorectal cancer: Systematic review and meta-analysis. *Journal of Surgical Oncology* 2017;116(6):730-740.
- [7] Kitagawa Y, Watanabe M, Hasegawa H, et al. Sentinel node mapping for colorectal cancer with radioactive tracer. *Diseases of the Colon and Rectum*. 2002;45:1476-1480.

The Virtuoso Surgical System: First Live Animal Experience

R. J. Hendrick¹, N. P. Dillon¹, L. M. Branscombe¹, T. J. Bruns¹, E. J. Blum¹, M. Oresi¹, S. Amack¹, S. D. Herrell III^{1,2,3,4}, and R. J. Webster III^{1,2,3,4}

¹*Virtuoso Surgical, Inc.*

²*Vanderbilt University Medical Center*

³*Vanderbilt University, Department of Mechanical Engineering*

⁴*Vanderbilt Institute for Surgery and Engineering (VISE)*

{richard.hendrick, robert.webster}@virtuososurgical.net

INTRODUCTION

The purpose of this paper is to describe initial animal experiences with the Virtuoso Surgical System, which is shown in Fig. 1. The Virtuoso System is a teleoperated system that delivers two concentric tube manipulators through a rigid endoscope. The manipulators are actuated by 10 motors (5 per manipulator) in a Motor Pack that is supported by a lightweight robot Holding Arm (Kuka, LBR MED 7). The surgeon operates the system from a Surgeon Workstation with custom five degree-of-freedom user interfaces. The Motor Pack accepts insertable and exchangeable Instrument Cartridges. The system can deliver tools for retraction (blunt retractors, snares, forceps) and energy delivery (laser, electrosurgery). The endoscope is a conventional setup for cystoscopy/hysteroscopy; it is 26 Fr at its largest diameter (8.67 mm) and contains an Inner Sheath and Outer Sheath for continuous flow irrigation (i.e. an endoscope and concentric tubes as in [1]). The endoscope can be inserted into the patient without the Motor Pack using conventional endoscopic tools (e.g. obturators).



Fig. 1: The Virtuoso System is made of three main subsystems: the Surgeon Workstation, the Motor Pack, and the Patient Cart.

The Holding Arm can be manipulated by hand, so that the endoscope can be re-oriented during the procedure. The robot arm operates in impedance mode to provide gravity compensation so that interaction feels weightless, from the surgeon's perspective. The surgeon also has the capability to remotely translate the endoscope along its axis via a foot pedal at the Surgeon Workstation. For more information on various versions of and applications for the Virtuoso System, see [2], [1], [3]. For a review on concentric tube manipulators themselves, see [4].

MATERIALS AND METHODS

This experiment took place in an anesthetized female porcine model (Fig. 2). The endoscope was introduced transcervically and delivered into the uterus; no other incisions were made for access or visualization. Continuous flow saline (0.9%) irrigation was initiated to distend the uterus and maintain a clear surgical field of view, as is standard for uterine interventions. Saline was used for irrigation because one of the two Instrument Cartridges was



Fig. 2: The endoscope inserted transcervically into the live porcine model, which is in lithotomy position.



Fig. 3: An initial resection into the uterine wall created a polypoid piece of tissue simulating a uterine fibroid. A snare was deployed from the left arm and surrounded the tissue. The left arm then lifted the tissue, applying countertraction to assist with electro-surgical (bipolar-in-saline) resection of the polypoid tissue.

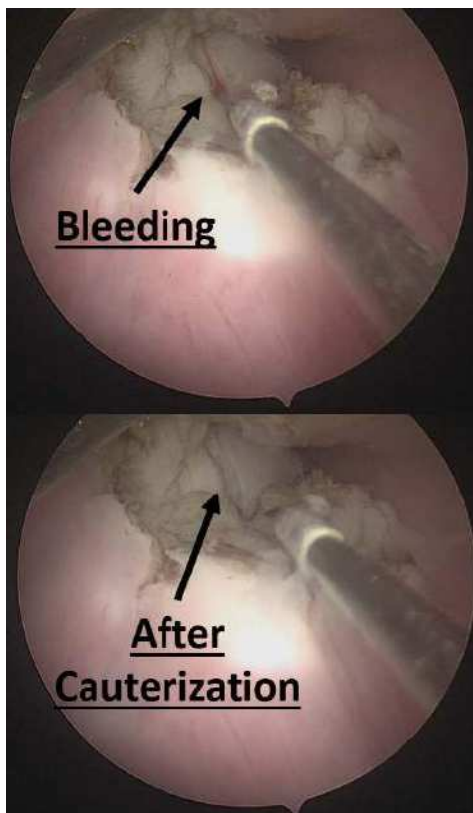


Fig. 4: During electro-surgical resection, observed bleeding was easily controlled using the electro-surgical tool.

a bipolar electro-surgical probe. The other Instrument Cartridge delivered a snare. The objective of the experiment was to remove tissue from the uterine wall, demonstrate traction and countertraction, demonstrate electro-surgical cutting, and control bleeding.

RESULTS

The results of the experiment are shown in Fig. 3 and 4. In Fig. 3 we illustrate the surgical procedure. First, an incision was made in the uterine wall using the electro-

surgical tool, at a site selected by the surgeon. Next (Step 1 in the Figure) a snare was deployed, maneuvered to surround the resulting attached polypoid tissue specimen, and then tightened and lifted. Thus the snare arm applied countertraction, while the electro-surgery arm cut the piece of tissue free. During the procedure, all bleeding that arose was controlled using the electro-surgery probe (see Fig. 4).

DISCUSSION

This paper has described the first animal experience with the Virtuoso Surgical System. We successfully removed tissue from the uterine wall in a porcine model. The experiment demonstrates the system's ability to perform an en bloc resection, which is useful in both uterine and bladder surgery, which use analogous endoscopy equipment. In both uterine fibroid and bladder cancer removal, the presence of a second hand to apply countertraction enables much more accurate cutting. This can prevent scarring in the uterus (enhancing subsequent fertility), and enable en bloc resection in the bladder (for cancer staging). The next steps with the Virtuoso System, now that feasibility has been demonstrated in a live animal model, are verification and validation testing toward human regulatory approval.

REFERENCES

- [1] L. Harvey, R. Hendrick, N. Dillon, E. Blum, L. Branscombe, S. Webster, R. J. Webster, and T. Anderson, "A novel robotic endoscopic device used for operative hysteroscopy," *Journal of Minimally Invasive Gynecology*, vol. 27, no. 7, pp. 1631–1635, 2020.
- [2] R. J. Hendrick, C. R. Mitchell, S. D. Herrell, and R. J. Webster III, "Hand-held transendoscopic robotic manipulators: A transurethral laser prostate surgery case study," *The International journal of robotics research*, vol. 34, no. 13, pp. 1559–1572, 2015.
- [3] J. B. Gafford, S. Webster, N. Dillon, E. Blum, R. Hendrick, F. Maldonado, E. A. Gillaspie, O. B. Rickman, S. D. Herrell, and R. J. Webster III, "A concentric tube robot system for rigid bronchoscopy: a feasibility study on central airway obstruction removal," *Annals of Biomedical Engineering*, vol. 48, no. 1, pp. 181–191, 2020.
- [4] A. W. Mahoney, H. B. Gilbert, and R. J. Webster III, "A review of concentric tube robots: Modeling, control, design, planning, and sensing," *Minimally Invasive Surgical Robotics, Encyclopedia of Medical Robotics*, pp. 181–202, 2018.

Note: The authors have financial interests in Virtuoso Surgical.

Robotic cervical fixation and sEEG depth electrode placement – pushing the boundaries

Brendan F. Judy, M.D.,¹ A. Daniel Davidar, M.B.B.S.,¹ Andrew Hersh, B.S.,¹ Carly Weber-Levine, M.S.,¹ Amanda N. Sacino, M.D.,¹ Brian Y. Hwang, M.D.,¹ Tej D. Azad, M.D.,¹ Ann Liu, M.D.,¹ Joshua Materi, B.S.,¹ Tara Dedrickson, B.S.,¹ William S. Anderson, M.D.,¹ Nicholas Theodore, M.D.¹

¹ Department of Neurosurgery, Johns Hopkins Hospital, Baltimore, Maryland, USA

Bjudy1@jhmi.edu

INTRODUCTION

The ExcelsiusGPS (Globus Medical, Inc., Audubon, PA) robot received clearance from the United States Food and Drug Administration for clinical use in 2017 with the first in human use for lumbar spine instrumentation at Johns Hopkins Hospital the same year. The applications of the robot soon expanded with the first interbody cage placement in 2020 and first deep brain stimulation performed in 2021. A metanalysis by Kosmopoulos et al¹ found that of 37,337 pedicle screws implanted by freehand, 34,107 (91.3%) were found to be placed accurately. Furthermore, there was a higher rate of accuracy in the navigation group (95.2%) compared to without navigation (90.3%). Initial studies with the ExcelsiusGPS robot reported successful lumbar pedicle screw placement rate of 97.4% (339/348)² and 99% (555/562).³ The ExcelsiusGPS robot has been shown to increase screw placement accuracy enabling utilization of longer screw length and diameters, reduce radiation exposure and surgical time.⁴ While conventional uses of the robot in spine surgery are pedicle screw placement and sacroiliac fusion, newer navigated interbody placement software hopes to minimize spinal cord injury during interbody placement. Current use in cranial surgery include biopsy, deep brain stimulation, and stereoelectroencephalography (sEEG).

High cervical fixation involving C1 and C2 is a complex surgery with potentially severe complications including screw malposition causing damage to neural and/or vascular structures. In a study evaluating the accuracy of free-hand technique of C2 pars screw placement, 11% of screws were mispositioned using the cortical-breach grading system⁵. Among high cervical transarticular screws, the most common complication included screw misposition at 7% while vertebral artery injury occurred in about 3% of patients⁶. It was noted that anatomic constraints for this procedure involve alignment of C1 and C2 while inadequate reduction of C1 and C2 contributed to screw misposition. Due to these complications, higher accuracy is needed. Common complications of depth electrode placement for sEEG are hemorrhage related (eg:

subdural hematoma, epidural hematoma or intracerebral hemorrhage) and hardware related complications such as malpositioning, electrode fracture, or electrode-recording malfunction⁷. Robotic navigation aims to reduce these events and increase accuracy. Here we report the first case series of high cervical fixation and sEEG depth electrode placement using the ExcelsiusGPS robot.

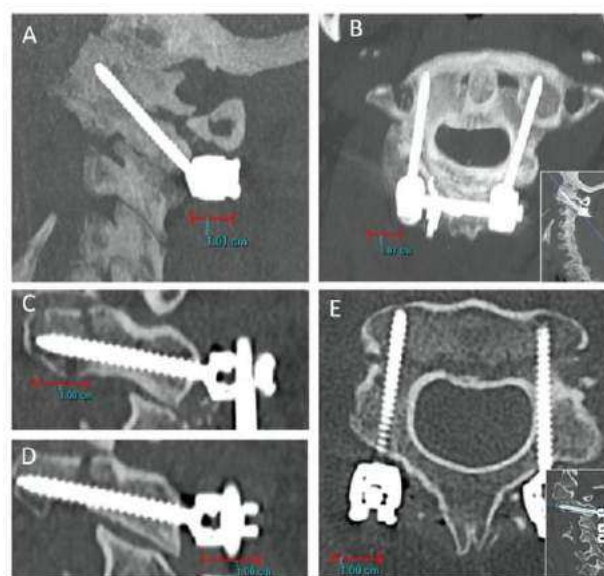


Fig 1. Sagittal (A) and axial (B) CT post-operative images showing excellent placement of C1-2 trans-articular screws attached by a horizontal rod. Sagittal (C and D) and axial (E) CT post-operative images of accurate screw placement in the C2 pars through the fracture line. One cm scale bar for reference.

MATERIALS AND METHODS

Patients who underwent robotic high cervical fixation and robotic sEEG depth electrode placement at a single tertiary care academic hospital were retrospectively reviewed for this study. The ExcelsiusGPS robotic system consists of a surgeon-controlled foot pedal attached to the robotic arm, a dynamic reference base (DRB; this is fixed onto the patient or attached to the Mayfield skull clamp), a surveillance marker attached close to the DRB and a camera that tracks movement. For cranial procedures, it includes an interchangeable end effector and a patient

stabilization stand placed underneath the surgeon table. The DRB is fixed to the skull clamp for cranial procedures and may be fixed to either the spinous process or skull clamp for cervical cases. The preoperative computed tomography scan is then merged with intraoperative fluoroscopic scans to enable the robot to navigate the field.

RESULTS

Two patients underwent high cervical robotic fixation. Indications for surgery included right side occipital neuralgia secondary to C1-2 joint arthritis and traumatic hangman's fracture. Surgery consisted of robotic C1-2 transarticular screw (Figure 1A-B) for occipital neuralgia and robotic C2 pars screws (Figure 1C-E) with C2-4 fusion for hangman's fracture. Both cervical spine patients had uncomplicated postoperative courses and at last follow up were asymptomatic. Five patients underwent robotic sEEG depth electrode placement for intractable seizure (Figure 2A and B). Leads were placed in the temporal lobes with a median of 11 leads per patient. There were no complications with placement or removal of leads.



Fig 2. Surgeon guides the robotic arm (A and B) for sEEG depth electrode placement. ExcelsiusGPS robot (C. From left to right: Robot system with real-time display and robotic arm with end effector attached, patient stabilization device used in cranial procedures, camera system).

DISCUSSION

Here we report the first robotic high cervical fixation and sEEG depth electrode placement using the ExcelsiusGPS

robot. All surgeries were performed successfully and there were no complications. Demonstrated benefits of robotic spine and cranial surgery are increased accuracy, decreased length of surgery and less invasiveness⁸. Limitations specific to this study include a small sample size and a single academic center. This study demonstrates the capability of the ExcelsiusGPS robot in both spine and cranial surgeries. Current ongoing research seeks to utilize preoperative magnetic resonance imaging instead of CT in order to further decrease radiation exposure. Future research is warranted to quantify the healthcare cost-savings and the learning curve for these complex robotic surgeries.

REFERENCES

1. Kosmopoulos V, Schizas C. Pedicle screw placement accuracy: a meta-analysis. *Spine (Phila Pa 1976)*. Feb 1 2007;32(3):E111-20. doi:10.1097/01.brs.0000254048.79024.8b
2. Vardiman AB, Wallace DJ, Crawford NR, Riggelman JR, Ahrendtsen LA, Ledonio CG. Pedicle screw accuracy in clinical utilization of minimally invasive navigated robot-assisted spine surgery. *J Robot Surg*. Jun 2020;14(3):409-413. doi:10.1007/s11701-019-00994-3
3. Huntsman KT, Ahrendtsen LA, Riggelman JR, Ledonio CG. Robotic-assisted navigated minimally invasive pedicle screw placement in the first 100 cases at a single institution. *J Robot Surg*. Feb 2020;14(1):199-203. doi:10.1007/s11701-019-00959-6
4. Maalouly J, Sarkar M, Choi J. Retrospective study assessing the learning curve and the accuracy of minimally invasive robot-assisted pedicle screw placement during the first 41 robot-assisted spinal fusion surgeries. *Mini-invasive Surg* 2021;5:35. <http://dx.doi.org/10.20517/2574-1225.2021.57>
5. Punyarat P, Buchowski JM, Klawson BT, Peters C, Lertudomphonwanit T, Riew KD. Freehand technique for C2 pedicle and pars screw placement: is it safe? *Spine J*. Jul 2018;18(7):1197-1203. doi:10.1016/j.spinee.2017.11.010
6. Elliott RE, Tanweer O, Boah A, et al. Atlantoaxial fusion with transarticular screws: meta-analysis and review of the literature. *World Neurosurg*. Nov 2013;80(5):627-41. doi:10.1016/j.wneu.2012.03.012
7. Mullin JP, Shriver M, Alomar S, Najm I, Bulacio J, Chauvel P, Gonzalez-Martinez J. Is sEEG safe? A systematic review and meta-analysis of stereo-electroencephalography-related complications. *Epilepsia*. 2016 Mar;57(3):386-401. doi: 10.1111/epi.13298. Epub 2016 Feb 21. PMID: 26899389.
8. Vo CD, Jiang B, Azad TD, Crawford NR, Bydon A, Theodore N. Robotic Spine Surgery: Current State in Minimally Invasive Surgery. *Global Spine J*. 2020;10(2 Suppl):34S-40S. doi:10.1177/2192568219878131

Index of Authors

—/ A /—

Abbott, Jake ...75, 81, 95, 123
 Abolfathi, Kiana.....129
 Aihara, Hiroyuki.....17
 Akhond, Saina..... 55
 Aktas, Ayhan..... 101
 Alazmani , Ali.....147
 Albu-Schäffer , Alin 93
 Alexander, Matthew D81
 Alian, Amirhosein.....15
 Amack, Stephanie.....157
 Anderson, Patrick..... 5
 Anderson, William S.....159
 Angel, Doug.....33
 Anichini, Giulio.....93
 Arezzo, Alberto.....53
 Ashrafian, Hutan.....133
 Avery, James.....11, 15, 55,
 65, 141
 Azad, Tej D.....159

—/ B /—

Bachmann, Ada L.....13
 Baena, Ferdinando Rodriguez
 Y..7, 15, 57, 67, 101, 137, 143
 Bai, Weibang.....135
 Ball, Tyler.....105
 Bano, Sophia.....47
 Barth, Eric.....105
 Batliwala, Rukaiya.....17
 Belzunce, Martin.....151
 Bergeles, Christos.....23
 Bernstein, Paul.....95
 Black, David.....91
 Blum, Evan.....157
 Bode, Peter.....153
 Bohler, Quentin,,,,,,79, 109
 Bosi, Giorgia.....31
 Branscombe, Lauren.....157
 Brockdorff, Michael.....73, 77
 Brumfiel, Timothy A.....103
 Bruns, Trevor.....157
 Burriesci, Gaetano.....31
 Byrne, Michael D.....127

—/ C /—

Caccianiga, Guido.....63
 Cajigas, Iahn.....107

Camp, Sophie.....93
 Casals, Alicia.....53
 Casella, Alessandro.....115,
 121
 Cesarovic, Nikola.....153
 Chand, Manish.....155
 Chandler, James.....73,77
 Chang, Doyoung.....107
 Chapman, Coley.....103
 Chautems, Christophe.....79,
 109, 153
 Chen, Junhong.....87, 135
 Chen, Yue.....97
 Chern, Joshua J.....103
 Cheung, L. W.....29, 149
 Chitalia, Yash.....99, 131
 Chiu, Philip W.Y.....149
 Chow, Henry.....149
 Ciuti, Gastone.....53
 Cleary, Kevin.....97
 Consumi, Vanni.....3
 Coote, Joanna.....39
 Coppinga, Aidan.....145
 Cui, Zejian.....67
 Culmer, Peter.....147

—/ D /—

D'Almeida, Jesse.....27, 69
 Daher, Rema.....45, 89
 Dall'Alba, Diego.....117
 Damian, Dana.....119
 Darzi, Ara.....65, 133
 David, Anna.....47, 49
 Davidar, A. Daniel.....159
 Davidson, Brian.....43
 Davies, Brian.....143
 Debuys, Christian.....19
 Dedrickson, Tara.....159
 Demircali, A.A.....101
 Deprest, Jan.....49
 Desai, Jaydev P.....103
 Dietsch, Solene.....39
 Dillon, Neal.....157
 Dimitrakakis, Emmanouil...39
 Dixon, Luke.....93
 Donder, Abdulhamit...67, 131

Doyle, Katie.....43
 Drake, James....99, 111, 139
 Dreyfus, Roland.....79
 Dromey, Brian.....49
 Dupont, Pierre.....99, 131
 Duru, Firat.....153
 Dwyer, George.....43
 Dyck, Michael.....93

—/ E /—

Englot, Dario.....105
 Esser, Daniel.....105

—/ F /—

Faoro, Giovanni.....41
 Favaretto, Martina.....83
 Felinska, Eleni.....85
 Ferrigno, Giancarlo.....121
 Fichera, Loris.....69
 Finocchiaro, Martina.....53
 Fiorini, Paolo.....117
 Fischer, Ryan.....107
 Franco, Enrico.....15
 Fu, Junling.....121
 Fuchs, Thomas.....85
 Fumado, Lluís.....155

—/ G /—

Gafford, Joshua.....5
 Galeazzi, Dario.....59
 Garrow, Sarah.....105
 Gerald, Arincheyan.....17
 Ghesu, Florin.....19
 Giacoppo, Giuliano13
 Giannarou, Stamatia ...89, 93
 Glöckner Anja M.....61
 Gondokaryono, Radian...139
 Grillo, Abby.....105
 Grissom, Will.....105
 Grootendorst, M.R.....155
 Gunderman, Anthony.....97

—/ H /—

Haiderbhai, Mustafa.....139
 Hart, Alister.....151
 Hemmer, Moritz.....61, 125
 Henckel, Johann.....151
 Hendrick, Richard.....157

Henley, Jessica.....	33
Henry, Ross.....	23
Hernansanz , Albert.....	53
Herrell, Stanley D.....	5, 157
Hersh, Andrew.....	159
Hong , Jaesung.....	1
Hoshiar, Ali Kafash	129
Hothi , Harry.....	151
Hsu , Patra.....	17
Hu , Xue.....	57
Hwang , Brian Y.....	159

—/ I /—

Iacovacci , Veronica.....	41
Iordache, Alice.....	121
Iovene, Elisa.....	121
Ip, N. D Fung.....	29, 149
Iqbal, Hisham.....	137
Ivan, Michael.....	107
Iyengar, Keshav.....	37

—/ J /—

Jackson, Benjamin.....	23
Jaramaz, Branislav	7
Jin, Kaizhe.....	133
Johnson , Lianne R.....	127
Joung , Sanghyun	1
Judy, Brendan F.....	159

—/ K /—

Kahrs, Lueder.....	139
Kendrick, Connah.....	89
Keunen, Benjamin.....	111
Kim, Hyunwook.....	1
Kim, J. S.....	107
Kim, Seunguk.....	1
Kim, Young-Ho.....	19
Kirby, Simon.....	33
Klodmann, Julian.....	93
Kogkas, Alexandros.....	85, 133
Koszowska, Zaneta.....	73
Kuchenbecker, Katherine.....	25, 63
Kuntz , Alan.....	81, 145

—/ L /—

L'Orsa, Rachael.....	25
Lahondes, Quentin.....	119
Lam, Chun Ping.....	29

Landers, Fabian C.....	109
Langari , Reza.....	19
Lau, K. C.....	29, 149
Laura, Anna Di.....	151
Laws , Stephen.....	143
Lee, Subin.....	1
Leff, Daniel.....	89
Leung, Flora.....	29, 149
Lindenroth , Lukas.....	3, 39, 43
Liu, Ann.....	159
Lo, Benny.....	51, 89, 135
Looi, Thomas.....	99, 111, 139
Lyu, Lingyu.....	141

—/ M /—

MacLean, Luke.....	9
Magbagbeola, Morenike.....	43
Maglio, Sabina.....	71
Mariani, Andrea.....	59
Marzullo, Aldo.....	83
Materi, Joshua.....	159
Mattos, Leonardo.....	115, 121
McDonald-Bowyer, Aoife.....	39
Meli, Daniele.....	117
Melkote, Shreyes N.....	103
Mencattelli, Margherita.....	99
Menciassi, Arianna.....	21, 41, 53, 59, 71
Miyashita, Shuhei.....	119
Moccia, Sara.....	41, 115
Modarelli, Giulia.....	71
Momi, Elena De.....	83, 115, 121
Müller-Stich, Beat.....	85
Munawar, Adnan.....	139
Muradore, Riccardo.....	117
Mylonas, George... ..	11, 15, 55, 85, 133, 141

—/ N /—

Naftel, Robert.....	105, 145
Naik, Ravi.....	133
Najjari, Sina.....	147
Nawratil, Julia.....	125
Neimat, Joseph.....	105
Nelson, Bradley	79, 109, 153
Neveu, Joannie.....	33
Nickel, Felix.....	85

—/ O /—

O'Malley, Marcia K.....	127
Obstein, Keith.....	5
Oresi, Moffat.....	157

—/ P /—

Pacheco, Nicholas.....	69
Paladini, Dario.....	115
Pampiglione, Tom.....	155
Pane, Stefano.....	41
Pané, Salvador.....	109
Paolis, Gaia Romana De ..	119
Paterno, Linda.....	21
Peebles, Donald M.....	49
Peine, Joseph.....	99
Persons, Brandon.....	69
Pessina, Federico.....	121
Peters, John.....	105
Piano, Matteo.....	121
Piccinelli, Nicola.....	117
Pichardo, Samuel.....	111
Picho, Kalani.....	69
Pinegar, Emma.....	75
Pittiglio, Giovanni.....	73, 77
Pore, Ameya.....	117
Posselli , Nicholas.....	75, 95
Pott, Peter P.....	13, 61, 125
Pourkand, Ashkan.....	99
Price , Karl.....	99

—/ R /—

Raghuram, Hrishikesh.....	111
Rai, Zainab.....	43
Rashid, Asif.....	103
Reynolds, Colin.....	69
Riva, Marco.....	121
Rolston, John D.....	81
Rossi, Giacomo De.....	117
Rox, Margaret.....	27, 145
Rucker, Daniel.....	5
Runciman, Mark.....	11, 15, 141
Russo, Sheila.....	17

—/ S /—

Sacino, Amanda N.....	159
Sadati, S.M.Hadi.....	23
Sahu, Sujit Kumar	21
Salcudean, Septimiu.....	91
Sanchez, Elena M.....	65, 141
Schäfer, Max B.....	61, 125

Schwehr, Trevor J.	81	Temelkuran, Burak.....	101	Weiland, Sophie.....	125
Secoli, Riccardo.....	101	Ten, Jarrett.....	119	Weld, Alistair.....	93
Sengupta, Saikat.....	97	Theodore, Nicholas.....	9, 159	Westwick, David.....	25
Shigematsu, Akiyuki.....	103	Thompson, Alex J.....	65	Wurdemann, Helge.....	31
Sigounas, Dimitri.....	97	Tognarelli, Selene.....	59, 71		
Sivakumaran, Derick.....	109			—/ Y /—	
Solzbacher, R.M.	1	—/ V /—		Yam, Yeung.....	29, 149
Soucier, Nathan.....	111	Valdastri, Pietro.....	73, 77	Yamamoto, Kent K.....	103
Souipas, Spyridon.....	143	Vasconcelos, Francisc.....	45,	Yao, Junke.....	31
Sozer, Canberk.....	21		47, 49	Yap, Moi Hoon	89
Sperry, Adam J.....	81, 123	Vece, Chiara Di.....	49	Yazdi, Reza Mohammad	129
Spurgeon, Sarah.....	37	Veiga, Tomas da.....	77	Ye, Jonathan.....	17
Stilli, Agostino.....	3, 39, 43	Vyas, Kunal.....	155		
Stoyanov, Danail.....	3, 37, 39,	—/ W /—		—/ Z /—	
	43, 45, 47, 49	Wang, Zeyu.....	87, 135	Zareinia, Kouros.....	25
Sutherland, Garnette.....	25	Waspé, Adam.....	111	Zari, Emilia.....	15
Szold, Amir.....	113	Weber-Levine, Carly.....	159	Zhang, Dandan.....	51
		Webster, Robert.....	5, 27, 105,	Zhang, Ruiyang.....	87, 135
—/ T /—			145, 157	Zhu, Ruiqi.....	51, 135
Tatti, Fabio.....	7, 57	Webster, Scott.....	5	Zuo, Katie.....	23